Title

Final Moments: Confined Circumstellar Material as a Singular Probe of Supernova Progenitor Systems

Author

Jacobson-Galán, Wynn Vicente

Publication Date

2024

Peer reviewed|Thesis/dissertation

Final Moments: Confined Circumstellar Material as a Singular Probe of Supernova Progenitor Systems

By

Wynn Vicente Jacobson-Galán

A dissertation submitted in partial satisfaction of the

requirements for the degree of

Doctor of Philosophy

in

Astrophysics

in the

Graduate Division

of the

University of California, Berkeley

Committee in charge:

Professor Raffaella Margutti, Chair
Professor Daniel Kasen
Professor Alexei Filippenko

Summer 2024

Final Moments: Confined Circumstellar Material as a Singular Probe of Supernova Progenitor Systems

Abstract

Final Moments: Confined Circumstellar Material as a Singular Probe of Supernova Progenitor Systems

by

Wynn Vicente Jacobson-Galán

Doctor of Philosophy in Astrophysics

University of California, Berkeley

Professor Raffaella Margutti, Chair

The liberation of gas from a star's outer layers (i.e., mass loss) is a fundamental part of its evolution from stellar conception to demise. However, given that most of the resolved, local stars in the Universe will not explode on a human timescale, alternate probes of late-stage stellar evolution are required to quantify the mass-loss rates of stars in their final years, decades, and centuries. One such method is observing the collision between ejected stellar material in a supernova (SN) and pre-existing circumstellar material (CSM), the latter being formed from stellar activity (e.g., steady winds, turbulent eruptions, and/or binary interaction) prior to the terminal explosion, which produces the former. In this thesis, I demonstrate how early-time (∼days post-explosion), multi-wavelength observations of CSM-interacting supernovae can be synthesized to directly constrain both progenitor identity and mass-loss history during the final stages of stellar evolution for a variety of SN subtypes, both from massive and compact stars.

For a girl and her two cats.

Contents

Acknowledgments

I will begin by thanking by partner Cebe Loomis. There really is no way to adequately describe the role that Cebe has played in the completion of my PhD without writing a whole other thesis so, for the sake of the reader, I will try to be brief and concise. Whether she believes it or not, Cebe has contributed to every single day of my PhD through her unconditional love and support for everything I do, both inside and outside of graduate school. She has made such immense sacrifices over the past few years in support of me finishing my degree that I am not sure if one lifetime will be enough to thank her. The life that Cebe continues to artistically curate for us is beyond appreciated, even in times of hardship or mental/physical absence. This thesis, my PhD, and every achievement along the way is just as much hers as it is mine; I would not be here without her. I love you Cebe, more and more each passing day.

To my mom Kathryn, dad Seth, stepmom Cindy, stepdad Dan, grandparents Jean, and brothers Layne and Skye: the endless love you give as I pursue this weird dream of being an astrophysicist is more than I could ever ask for. I am nothing but a reflection of your wisdom, bolstered by your unwavering support. Also, even though they are no longer with me, the PhD and Master's degrees obtained by my grandparents Lou, Howard and Dana were a major inspiration for getting a PhD of my own.

To my PhD advisor Raffaella Margutti: I went to graduate school to work with you and, in doing so, I learned more about the transient Universe than I could have ever imagined. You (pretty much) always say "yes" to the things I ask to do and your diligent support of my scientific explorations through the last 5 years has allowed me to be the scientist I am today, for which I am extremely grateful. To my undergraduate advisor Ryan Foley: you gave me a shot when I was nothing but a transfer student and got me hooked on the beautiful world of time-domain astronomy. To my colleague, friend and (likely) life-long mentor Charlie Kilpatrick: the support you have shown me in the last 8 years is unparalleled and I owe so much of what I have achieved to your patience, care and insight. To Luc Dessart: thank you for being such an amazing collaborator and for you unconditional passing of knowledge. To David Matthews: for being my best friend and most caring colleague, in all times.

A huge thank you to the amazing friends I had the priviledge of sharing joy and science with during graduate school: Huei Sears, Andrea Antoni, Lindsay DeMarchi, Candice Stauffer, Aprajita Hajela, Jillian Rastinejad, Joseph Michail, Nick Kaaz and so many others. Lastly, I am incredibly thankful for the amazing collaborations that I have been apart of

such as the Young Supernova Experiment and the Global Supernova Project, and all the amazing people I have been able to do science with. Every discovery presented in this thesis began with a telescope, an instrument that I hope humanity continues to value and employ.

Chapter 1

Introduction

Circumstellar material (CSM) is a mixture of gas and dust that is derived from a stellar system. The construction of CSM is reliant on partial and/or complete liberation of gas from the surface of a star, i.e., overcoming the stellar gravitational potential. This process is often generalized as "mass loss," which can take a variety of forms depending on the specific stellar system involved. A star's mass-loss rate can be described through mass conservation:

$$\frac{dM}{dt} = \dot{M} = 4\pi r^2 \rho(r) v_w \tag{1.1}$$

where $\rho(r)$ is the radial, pre-explosion CSM density profile assuming spherical symmetry and v_w is the wind velocity of the CSM i.e., stellar surface escape velocity. In a steady-state mass-loss scenario, the CSM density profile goes as $\rho \propto r^{-2}$, which is commonly adopted in the simulations of massive stars through core collapse. Additionally, the CSM wind velocity profile can be parameterized as:

$$v_w(r) = v_0 + (v_\infty - v_0)\left(1 - \frac{R_0}{r}\right)^\beta \tag{1.2}$$

where v_0 is the initial CSM velocity at the stellar surface, v_∞ is the CSM velocity post-acceleration, R_0 is the location where the wind is launched, and β is a dimensionless parameter that can be used to describe the degree of wind acceleration i.e., lower β is a higher degree of pre-explosion acceleration (Moriya et al. 2017b).

In single star evolution, the classic picture of mass-loss involves the line-driven mechanism in which radiation pressure on the stellar envelope from absorption and scattering by metals at ultraviolet (UV) wavelengths will drive a steady-state wind (Lucy & Solomon 1970; Castor et al. 1975; Puls et al. 2008). This mechanism is commonly adopted in stellar evolution codes as time-averaged prescriptions for stellar mass loss that depend on stellar luminosity, metallicity, and temperature (Langer 2012), but ignores complexities such as clumping (Sundqvist & Owocki 2013). In this simplified scenario, the maximum mass-loss rate that can occur through line-driven winds is $\dot{M}_{\rm max} = 7 \times 10^{-3} Z L_6$ $\mathrm{M_\odot}$ $\mathrm{yr^{-1}}$, where Z is stellar metallicity and L_6 is stellar luminosity in units of 10^6 $\mathrm{L_\odot}$ (Gayley 1995; Smith & Owocki 2006). While line driving is most applicable to hot Wolf Rayet (WR) and OB-type stars, cooler massive

stars such as red and yellow supergiants (YSGs and RSGs) lose mass via convective envelope pulsations that lift material to a few stellar radii at which point the gas will cool, form dust, and then be accelerated beyond the star's surface gravity by radiation pressure (Gehrz & Woolf 1971; Wilson et al. 2000; Yoon & Cantiello 2010). However, as the observed mass-loss rates of massive stars continue to be revised to lower values than past prescriptions (Beasor et al. 2020; Beasor & Smith 2022), the existence of both massive stars with mass-loss rates exceeding the line-driving limit (e.g., $\dot{M} > 10^{-4}$ $M_\odot$ yr^{-1} for $L_\star < 10^6$ $L_\odot$; Smith et al. 2001) and supernovae (SNe) from stars that have partial and/or complete removal of their hydrogen as well as their helium envelopes (e.g., type IIb/Ibc SNe; Smith et al. 2011a; Yoon et al. 2017) necessitates a means for more enhanced mass-loss rates. Furthermore, SNe that interact with dense CSM for months-to-years post-explosion (e.g., type IIn SNe) reinforce the need for dramatic, non-standard mass-loss mechanisms (Smith 2017).

An increase in the stellar luminosity beyond the Eddington limit (e.g., $\Gamma = \kappa L/(4\pi GMc) > 1$, where κ is opacity, L is luminosity, G is the graviational constant, M is the stellar mass, and c is the speed of light), for example, can induce a "Super-Eddington" wind, which is driven by radiation pressure via electron scattering in the dense CSM (Shaviv 2001b,a; Owocki et al. 2004). This scenario may be invoked to explain the large mass-loss rates observed in Luminous Blue Variable (LBV) stars, but it is unclear whether such a process is capable of explaining the ejection of > 10 $M_\odot$ of material in extreme stellar systems such as η Car (Smith 2014). Beyond this enhanced wind scenario, non-terminal explosions/eruptions have been invoked to explain above-average mass-loss rates. Simply put, the deposition of energy at the base of a stellar envelope that is comparable to the envelope's binding energy will cause the ejection of stellar material. While this phenomenon has been applied agnostically to the underlying energy injection mechanism (e.g., Dessart et al. 2010; Tsang et al. 2022; Takei et al. 2022), many numerical simulations have explored the link to a stellar process e.g., gravity wave-driving (Quataert et al. 2016; Fuller 2017; Wu & Fuller 2021), unsteady/explosive nuclear burning (Smith & Arnett 2014; Woosley & Heger 2015), or stellar mergers/collisions (Smith & Frew 2011; Kochanek et al. 2014). Furthermore, significant amounts of CSM ($0.01 - 0.1$ $M_\odot$) may be created via convection and shocks in RSG envelopes, leading to hydrostatic "cocoons" of material known as chromospheres or effervescent zones (Soker 2021; Fuller & Tsuna 2024). Given the uncertainties and limitations with inciting enhanced mass-loss in single stellar systems, binary interaction is a naturally invoked process given the high rate of massive star binaries that will interact ($\sim 60 - 70\%$; Sana & Evans 2011; Sana et al. 2012) and the large numbers of free parameters that can be used to match observables. For massive stars in binary systems, mass transfer can be initiated when the primary star fills its Roche Lobe, this process being capable of driving large mass-loss rates (e.g., $> 10^{-3}$ $M_\odot$ yr^{-1}) depending on the mass ratio of primary to secondary stars (Langer 2012; Smith 2014; Yoon et al. 2017). Beyond massive stars, binary interaction is also relevant to the circumstellar environments of thermonuclear SNe (e.g., type Ia/Iax SNe). Here, the primary star is a white dwarf that is accompanied by either a non-degenerate star (e.g., Sun-like main sequence, red giant, helium-star, etc) or another white dwarf; the interaction of the two stars and/or the wind of the non-degenerate companion is intrinsically

linked to the formation of CSM. For example, white dwarf systems may participate in steady nuclear burning mass accretion ($\dot{M} > 3 \times 10^{-7}$ M$_\odot$ yr^{-1}), recurrent nova eruptions, or even tidal interactions/disruptions, all of which influence the local CSM (Shen & Bildsten 2007, 2009; Chen et al. 2011; Raskin & Kasen 2013; Zenati et al. 2019a).

By framing mass-loss in the context of time-domain astronomy and terminal explosions of some stellar systems, we see that the creation of CSM via any of the above mass-loss mechanisms during late-stage evolution (i.e., ∼1-10000 years before stellar demise) will have a direct, and often observable, impact on a newly formed SN. More importantly, studying the CSM-ejecta interaction in SNe, especially at very early times (e.g., ∼days post-explosion), provides a unique window into the the mass-loss history and chemical composition of the progenitor system during its final moments. While the CSM around SN progenitors can be extremely diverse, the collision and subsequent interaction of fast-moving SN ejecta and slow-moving CSM can be described analytically as well as modelled effectively in radiation hydrodynamics and radiative transfer simulations (Dessart et al. 2015; Moriya et al. 2017b; Dessart et al. 2017, 2023; Khatami & Kasen 2023). In general, CSM interaction begins right after "shock breakout," a phenomenon described as a brilliant release of radiation following the arrival of a SN shockwave at a characteristic optical depth, $\tau_{\rm shock} \approx c/v_{\rm shock}$ (Waxman & Katz 2017; Goldberg et al. 2022). The timescale, energy and temperature of shock breakout are dependent on the progenitor star with larger stars (e.g., RSGs) displaying bright UV shock breakout emission for hours to a day while compact stars (e.g., white dwarfs) can have shock breakout emission for ∼seconds that peaks in γ-ray bands (Matzner & McKee 1999; Nakar & Sari 2010). Furthermore, it is worth noting that because shock breakout depends on optical depth, the presence of dense CSM at the stellar surface can extend the shock breakout signal from ∼hours to ∼days by shifting the breakout location to within the CSM (Chevalier & Irwin 2011; Svirski et al. 2012; Haynie & Piro 2021; Dessart et al. 2023).

Following breakout flash/pulse, the most local CSM will remain ionized on the recombination timescale, $t_{\rm rec} \propto 1/n_e$, where n_e is number density of free electrons (Osterbrock & Ferland 2006). Afterward, the expanding SN ejecta will collide with the CSM gas, leading to the formation of two strong shocks: a forward shock (FS) propagating outward into the unshocked CSM and a reverse shock (RS) which recedes (in mass coordinates) into the SN ejecta. Here, the dynamics of the post-shock gas can be described as a momentum equation that balances the ram pressure of the CSM and colliding SN ejecta, assuming that the shocked gas can be treated as a thin shell (Chevalier 1982a, 1990; Chevalier & Fransson 2017):

$$M_{\rm sh}\frac{dv_{\rm sh}}{dt} = 4\pi r_{\rm sh}[\rho_{\rm ej}(v_{\rm ej} - v_{\rm sh})^2 - \rho_{\rm CSM}v_{\rm sh}^2] \tag{1.3}$$

where $M_{\rm sh}$ is the mass of both shocked CSM gas and SN ejecta, $v_{\rm sh}[r_{\rm sh}]$ is the shock velocity[radius], and $\rho_{\rm ej}[\rho_{\rm CSM}]$ is the density of the ejecta[CSM]. For SNe in low density environments, the photosphere quickly recedes into the fastest moving ejecta and there is little/no observational signature of CSM-interaction in UV/optical photometry or in early-time spectra. However, if the CSM is dense enough (i.e., higher progenitor $\dot{M}$) and the reverse shock is

radiative, the mass of the shocked CSM can be significant enough to form a "cold dense shell" (CDS) between the forward and reverse shocks, while the photosphere remains in the ionized, pre-shock CSM for days to weeks depending on the CSM density/extent (Chevalier & Fransson 1994, 2017). During this phase, the photosphere is located within the pre-shock CSM gas, which remains photo-ionized by radiation from FS material. Observationally, the spectrum of an interacting SN during this phase will be dominated by Lorentzian-shaped emission line profiles that are formed from two components: (1) a narrow core ($\sim 10 - 1000$ km s^{-1}) and (2) symmetrically broadened "wings" that extend to ~1000s of km s^{-1}. The velocity of the former can reflect the pre-explosion wind velocity but it is likely that radiative acceleration will cause larger velocities to be measured in the narrow core. For the latter, the Lorentzian "wings" are the result of electron scattering of recombination photons with free electrons in the photo-ionized pre-shock CSM, where a single scattering traces the thermal velocity of the free electrons ($v_e \approx 10^3 (T/10^{4.5}\ \mathrm{K})^{1/2}$ km s^{-1}) and multiple scatterings can be produced in CSM that is optically thick e.g., $\tau_e \approx 3 - 10$ (Chugai 2001; Dessart et al. 2009; Huang & Chevalier 2018). Observers label this multi-component profile a "IIn-like feature" or classify an object as a "type IIn SN (SN IIn)" when narrow lines like this are present. However, this is purely an observational trait that only reflects that, at the time of the spectrum, the SN was interacting with CSM and therefore cannot be used to classify the underlying SN and/or identify the likely progenitor star.

The narrow-line-dominated spectrum (i.e., IIn-like) of an interacting SN will persist on a timescale that is driven by the CSM density profile that the outgoing shock "sees." More specifically, the kinetic luminosity of the shock goes as:

$$L_{\rm sh} = 2\pi r_{\rm sh}^2 \rho(r_{\rm sh}) v_{\rm sh}^3 = \dot{M} v_{\rm sh}^3 / 2 v_w \tag{1.4}$$

Consequently, for high enough CSM densities at a given shock radius, the FS is capable of continually photo-ionizing the pre-shock gas, which in turn allows for the persistence of the electron-scattering broadened line profiles. However, the CSM density also influences the persistence/strength of these line profiles because the line emissivity depends on density ($j_\nu \propto n^2$) and the line width depends on the optical depth to electron scattering ($\tau \approx \kappa_{\rm T} \rho_{\rm CSM} r_{\rm sh}$) i.e., for $\tau = 1$, $t_{\rm IIn} = [\kappa_{\rm T} \rho_{\rm CSM} r_{\rm sh}]^{-1}$. Following the end of the optically thick interaction, the SN photosphere can recede to within the dense shell of post-shock gas, if present. Here, the observer will see intermediate-width line profiles in absorption and emission ($v \approx 2000 - 8000$ km s^{-1}) that trace the velocity of the post-shock gas. Depending on the amount of material swept up into the dense shell region, the photosphere will eventually recede enough to reveal the Doppler-broadened spectral line profiles of the SN ejecta.

Beyond spectroscopic line profiles, CSM-interaction is intrinsically a multi-wavelength phenomenon, comprised of both thermal and non-thermal emission components. For example, under the assumption of equipartition between ions and electrons, the shocked gas behind the FS is heated to large temperatures:

$$T_{\rm FS} \approx 2 \times 10^9 \mu \left(\frac{v_{\rm sh}}{10^4\ \mathrm{km\,s^{-1}}} \right)\ \mathrm{K} \tag{1.5}$$

where μ is the mean molecular weight of the post-shock gas, (Chevalier & Fransson 2017). Depending on the power-law index n of the ejecta density profile, the RS temperature will scale as $T_{\rm RS} = T_{\rm FS}/(n-3)^2$ (Chevalier 1982a), assuming that the SN ejecta profile can be approximated as a steep power law (i.e., $\rho_{\rm ej} \propto r^{-n}$) and the CSM density profile is "wind-like" (i.e., $\rho_{\rm CSM} \propto r^{-2}$). Given these high temperatures, the emission will peak in X-ray bands (e.g., 1-20 keV) as the post-shock gas cools primarily through free-free emission i.e., a thermal bremsstrahlung spectrum (Chevalier 1982b; Chevalier & Irwin 2012). However, for electron temperatures of $T_e < 2.6 \times 10^7$ K, line emission can start to influence the cooling (Chevalier & Fransson 2017). For high enough CSM densities, the FS will cool radiatively via free-free (ff) emission on a timescale of:

$$t_{\rm cool,ff} \approx 10^2 \left(\frac{T_{\rm FS}}{10^5\ {\rm K}}\right)^{0.5} \left(\frac{\rho}{10^{-12}\ {\rm gcm^{-3}}}\right)^{-1}\ {\rm s} \tag{1.6}$$

assuming (1) that the temperature in the post-shock gas is high enough that line emission does not dominate cooling, (2) equipartition of electrons and ions, and (3) solar abundances in the CSM. Here, the FS will be radiative so long as the cooling timescale is less than the dynamical timescale of the FS (Khatami & Kasen 2023). The shock is radiative or adiabatic based on the ratio of the cooling time to the SN age:

$$t_{\rm cool}/t_{\rm age} = 0.44 \left(\frac{t_{\rm age}}{1\ {\rm d}}\right) \left(\frac{10^{-4}}{{\rm M_\odot\ yr^{-1}}}\right) \left(\frac{v_w}{100\ {\rm km\,s^{-1}}}\right) \tag{1.7}$$

where $t_{\rm cool}/t_{\rm age} > 1$ implies a radiative shock (Chevalier & Fransson 2017). For higher post-shock temperatures, faster shocks and lower densities, the shock cannot cool efficiently (i.e., adiabatic) and there will be inefficient thermalization. Furthermore, high shock temperatures also likely imply a significant amount of cooling through Inverse Compton scattering, depending on the pool of seed photons required for upscattering (Chevalier & Irwin 2012; Margalit et al. 2022). However, notably, a radiative shock can be extremely efficient at converting the SN kinetic energy into radiation e.g., $> 50\%$ in an interacting SN compared to the $\sim 1\%$ kinetic energy that is radiated in a normal type II SN (Smith 2017; Khatami & Kasen 2023). While the radiative efficiency during CSM interaction is not well understood, this phenomenon leads to enhanced bolometric luminosities and temperatures relative to SNe with little CSM-interaction.

In addition to X-ray emission, additional emission processes can arise from ejecta-CSM interaction. For example, particle acceleration at the FS will produce synchrotron emission from relativistic electrons that gyrate in magnetic fields within the post-shock gas (Chevalier 1998; Weiler et al. 2002). The resulting emission manifests observationally as a "bell-shaped" spectrum that peaks in radio bands, comprised of optically thick ($F_\nu \propto \nu^{5/2}$) and thin ($F_\nu \propto \nu^{(1-p)/2}$) spectral components (Granot & Sari 2002; Chevalier & Fransson 2017). Radio synchrotron emission is an essential observation for determining the magnetic field strength, CSM emitting radius and progenitor mass-loss rate (e.g., Chevalier & Fransson 2006; Soderberg et al. 2006; Chandra et al. 2015; Margutti et al. 2017; Bietenholz et al. 2021; Stroh et al. 2021; Brethauer et al. 2022; DeMarchi et al. 2022). Additionally, ejecta-CSM

interaction can be the site of cosmic-ray acceleration (Longair 2011; Caprioli & Spitkovsky 2014; Caprioli 2023). Here, the collision of high-energy protons (>300 MeV) accelerated at the shock front will lead to pion generation and decay that will then produce high-energy γ-rays and neutrinos (Murase et al. 2011). While still a theoretical phenomenon for extragalactic SNe, future telescopes such at the Cherenkov Telescope Array (CTA) will be able to detect such emission, unless a very nearby (<10 Mpc) SN II with strong CSM interaction occurs before this array is constructed (Murase et al. 2014).

As the field of time-domain astronomy has grown over the past several decades, so has the diversity of CSM-interacting SNe that are discovered. As mentioned above, the "IIn" SN classification is commonly given to any transient with narrow emission lines in its optical spectrum, regardless of future spectral evolution out of a narrow-line-dominated phase. However, the long-term label of "SN IIn" does in fact apply to some core-collapse SNe, which belong to a physically distinct class of objects with enduring CSM interaction (Filippenko 1997; Smith 2017). This class is still quite diverse, with these events displaying IIn-like features of mainly H I and He I for weeks, months and even years post-explosion, many becoming increasingly bright in the radio and X-ray bands (e.g., Margutti et al. 2014; Chandra et al. 2015) as well as showing detectable precursor emission that may be related to the formation of such dense, extended CSM (e.g., Ofek et al. 2014; Strotjohann et al. 2021). The spread in luminosity of enduring SNe IIn can be quite large (Nyholm et al. 2020), with some events (e.g., SNe 2006gy and 2010jl; Ofek et al. 2007; Smith et al. 2007, 2011b) even considered "superluminous" SNe. Consequently, the inferred CSM masses for these SNe are also diverse e.g., $M_{\rm CSM} \approx 1 - 20$ M$_\odot$ (e.g., Dessart et al. 2015; Smith 2017; Villar et al. 2017). Classical SNe IIn are intrinsically rare events ($\sim$7% of the SN population; Smith et al. 2011a; Li et al. 2011) and are thought to arise from a wide variety of massive star progenitors e.g., LBVs, extreme RSG/YHGs (Foley et al. 2011; Gal-Yam et al. 2007; Gal-Yam & Leonard 2009; Smith et al. 2011b; Mauerhan et al. 2013; Margutti et al. 2014). Overall, the interaction timescale in these SNe IIn indicates enhanced and sustained progenitor mass loss that may extend from centuries to millennia before core collapse (e.g., see Brethauer et al. 2022 for summary plots).

A natural extension of enduring SNe IIn are explosions of massive stars where the narrow features only persist for days to weeks post-explosion. Sometimes dubbed "flash-ionization", "flash spectroscopy" or "flasher" events, these SNe display IIn-like profiles typical of long-lived SNe IIn as well as high-ionization narrow lines of He II, C III/IV, N III/IV/V, and O V/VI, all of which fade within days of first light, indicating a more compact CSM located within radii of $< 10^{15}$ cm from the progenitor star (Gal-Yam et al. 2014; Shivvers et al. 2015; Smith et al. 2015; Yaron et al. 2017; Dessart et al. 2017; Terreran et al. 2016, 2022; Bruch et al. 2021b, 2023a; Jacobson-Galán et al. 2024). After the fading of these IIn-like features, the explosion will evolve similarly to more normal type II-P/L SNe that are known to arise from RSG progenitors. Consequently, the current explanation for these SNe II with such high mass-loss rates (e.g., $\dot{M} \approx 10^{-3} - 10^{-1}$ M$_\odot$ yr^{-1}) is that they arise from RSG stars that form dense amounts of CSM within their final years. While the intrinsic rates of these events are uncertain and could be as high as 40% of SNe II by volume (Bruch et al. 2023a), their

existence points toward an unknown mechanism of mass loss that is restricted to the last years of a RSG's life.

Beyond H-rich CSM interaction, there also exist massive-star explosions wherein the SN ejecta collide with He- or C/O-rich CSM. The former, known as type Ibn SNe (SNe Ibn), display strong narrow and intermediate-width He I spectral lines as well as luminous, fast-evolving light curves (Hosseinzadeh et al. 2017). It should be noted that SNe Ibn are distinct from the subset of H-poor SNe (e.g., SNe Ibc) that collide with H-rich CSM months-to-years after explosion e.g., SNe 2014C (Milisavljevic et al. 2015; Margutti et al. 2017; Bietenholz et al. 2018; Brethauer et al. 2022) and 2019yvr (Ferrari et al. 2024). Similar to enduring SNe IIn, multiple SNe Ibn have shown pre-SN emission (i.e., precursor events) that could connect the presence of their He-rich CSM to progenitor eruptions, outbursts and/or binary interaction (Pastorello et al. 2007; Foley et al. 2007; Strotjohann et al. 2021; Wang et al. 2023; Brennan et al. 2024; Dong et al. 2024). Given the degree of envelope removal likely needed for SNe Ibn, binary progenitor channels have been proposed e.g., WR primary star (Foley et al. 2007) or He star plus compact object (Dong et al. 2024). Recently, the class of type Icn SNe (SNe Icn) has emerged, which includes explosions from stars that are stripped of both H and He, but interact with C/O-rich CSM upon exploding (Fraser et al. 2021; Gal-Yam et al. 2022; Perley et al. 2022; Pellegrino et al. 2022; Davis et al. 2023a). Given its infancy as a class of interacting SNe, the observational and progenitor diversity of SNe Icn is a large unknown. It remains to be seen if even more extreme events (e.g., type Idn SNe) with CSM that is rich in higher mass elements (e.g., Ne or Si) exist in the Universe.

The landscape of CSM-interacting transients also extends to thermonuclear SN varieties. For example, "type Ian" or "type Ia-CSM" SNe are SNe Ia that arise from white dwarf explosions yet interact with H-rich, and sometimes He-rich, CSM (Hamuy et al. 2003; Dilday et al. 2012; Silverman et al. 2013; Kool et al. 2023). While CSM-interacting SNe Ia are rare, they do point to the existence of binary channels where mass transfer from either a degenerate or non-degenerate companion with the white dwarf primary is enhanced and/or non-conservative in the final years-to-decades before explosion. Similarly, some type Iax SNe (Foley et al. 2013) have evidence for interaction with He-rich CSM (Jacobson-Galán et al. 2019), which aligns with the preferred He star + white dwarf progenitor channel for these events. Lastly, a growing number of Calcium-rich transients (Filippenko et al. 2003; Kasliwal et al. 2010, 2012) have be discovered with evidence for ejecta interaction with dense, confined CSM e.g., X-ray emission, IIn-like features, and double-peaked light curves (De et al. 2018b; Jacobson-Galán et al. 2020b, 2022b; Karthik Yadavalli et al. 2023; Irani et al. 2024).

The intrinsic connection between SN ejecta-CSM interaction and the identity/mass-loss of SN progenitors is the driving theme of the work described in this thesis. In Chapters 2, 3, & 4, I present observations and analysis of three CSM-interacting Calcium-rich transients, two with the first-ever detection of X-ray emission. These results helped to reveal new diversity within this peculiar explosion class as well as to constrain their unknown progenitor channels. In Chapters 5, 6, & 7, I present observations and analysis of three SNe II that show spectroscopic evidence of CSM interaction within ∼days of explosion, revealing unprecedented and enhanced RSG mass loss in the final ∼years before core collapse. Notably,

Chapter 5 presents SN 2020tlf, the first SN II from a RSG progenitor with a precursor event. Lastly, in Chapters 8 & 9, I present the largest sample study to date of SNe II with early-time spectroscopic evidence for CSM interaction (i.e., similar to the single objects presented in Ch. 5-7).

Chapter 2

SN 2019ehk: A Double-Peaked Ca-rich Transient with Luminous X-ray Emission and Shock-Ionized Spectral Features

This chapter was previously published as Jacobson-Galán et al., 2020b, ApJ, 898, 166.

2.1 Abstract

We present panchromatic observations and modeling of the Calcium-rich supernova (SN) 2019ehk in the star-forming galaxy M100 (d≈16.2 Mpc) starting 10 hours after explosion and continuing for $\sim$ 300 days. SN 2019ehk shows a double-peaked optical light curve peaking at $t = 3$ and 15 days. The first peak is coincident with luminous, rapidly decaying *Swift*-XRT discovered X-ray emission ($L_x \approx 10^{41}$ erg s^{-1} at 3 days; $L_x \propto t^{-3}$), and a Shane/Kast spectral detection of narrow Hα and He II emission lines ($v \approx 500\,\mathrm{km\,s^{-1}}$) originating from pre-existent circumstellar material (CSM). We attribute this phenomenology to radiation from shock interaction with extended, dense material surrounding the progenitor star at $r < 10^{15}$ cm and the resulting cooling emission. We calculate a total CSM mass of $\sim 7 \times 10^{-3}$ M$_\odot$ ($M_{\rm He}/M_{\rm H} \approx 6$) with particle density $n \approx 10^9\,\mathrm{cm^{-3}}$. Radio observations indicate a significantly lower density $n < 10^4\,\mathrm{cm^{-3}}$ at larger radii $r > (0.1 - 1) \times 10^{17}$ cm. The photometric and spectroscopic properties during the second light curve peak are consistent with those of Ca-rich transients (rise-time of $t_r = 13.4 \pm 0.210$ days and a peak B-band magnitude of $M_B = -15.1 \pm 0.200$ mag). We find that SN 2019ehk synthesized $(3.1 \pm 0.11) \times 10^{-2}$ M$_\odot$ of ^{56}Ni and ejected $M_{\rm ej} = (0.72 \pm 0.040)$ M$_\odot$ total with a kinetic energy $E_{\rm k} = (1.8 \pm 0.10) \times 10^{50}$ erg. Finally, deep *HST* pre-explosion imaging at the SN site constrains the parameter space of viable stellar progenitors to massive stars in the lowest mass bin (~ 10 M$_\odot$) in binaries that lost most of their He envelope *or* white dwarfs (WDs).

The explosion and environment properties of SN 2019ehk further restrict the potential WD progenitor systems to low-mass hybrid HeCO WD + CO WD binaries.

2.2 Introduction

Calcium-rich (Ca-rich) transients are a new class of faint, rapidly evolving astronomical transients that has been identified in the past two decades (Filippenko et al. 2003; Perets et al. 2010a; Kasliwal et al. 2012). Observationally, Ca-rich transients are characterized by peak magnitudes of -14 to -16.5 mag, rise-times $t_r < 15$ days, and strong calcium features in photospheric and nebular phase spectra (Taubenberger 2017). The majority of these objects exhibit low ejecta and ^{56}Ni masses of $\lesssim 0.5$ M$_\odot$ and $\lesssim 0.1$ M$_\odot$, respectively. Ca-rich transients do not necessarily have larger than average Ca mass but rather are "rich" in [Ca II] emission during the nebular phase. Consequently, Ca-rich spectra typically exhibit minimal [O I] $\lambda\lambda 6300, 6364$ emission and contain an integrated [Ca II]/[O I] flux ratio greater than $\sim$2.

The "Ca-rich" naming convention was reinforced by the Ca and O abundances of 0.135 and 0.037 M$_\odot$ derived from the nebular spectrum of prototypical event, SN 2005E (Perets et al. 2010a). However, subsequent modeling of Ca-rich transient nebular spectra using optical and near-infrared data highlight uncertainty in this estimate and suggest that chemical abundances may vary widely between events (Milisavljevic et al. 2017). A potential explanation for the prominence of Ca II emission relative to other species is that the distribution of ^{56}Ni throughout the SN ejecta over-excites calcium ions (Polin et al. 2019a). Because of this, we choose to adopt the label suggested by Shen et al. (2019) and refer to these objects as "Calcium-Strong Transients" (CaSTs) from this point forward.

Early-time spectra of "gold sample" CaSTs (Shen et al. 2019) resemble that of core-collapse type Ib SNe (SNe Ib) with detectable photospheric He I and no observed Hα emission. However, the large fraction of objects found in old stellar environments on the outskirts of early-type galaxies disfavors a massive star origin for most CaSTs (Perets et al. 2011; Kasliwal et al. 2012). Parenthetically, CaSTs tend to occur in group or cluster environments of early-type elliptical galaxies with no evidence for local star formation or globular clusters (Perets et al. 2010a; Lyman et al. 2014; Foley 2015; Lunnan et al. 2017). Perets (2014a) finds the location of CaSTs to be mostly consistent with older stellar populations, with many of these objects having large separations from early-type host galaxies known to have large stellar halos. Shen et al. (2019) also find that the radial distribution of CaSTs is consistent with old (>5 Gyr), metal-poor stellar populations. However, a non-negligible fraction of CaSTs were found in disk-shaped galaxies (Perets et al. 2010a; Perets 2014a; De et al. 2020).

A variety of progenitor scenarios have been proposed to explain the observed properties of CaSTs and their environments. Shen et al. (2019) outline the three scenarios that are most consistent with current observations. First, ultra-stripped-envelope SNe could reproduce the low ejecta and ^{56}Ni masses and rapidly evolving light curves, but cannot reconcile the lack of star formation at most CaST explosion sites. Similar discrepancies disfavor the second scenario wherein a WD is tidally disrupted by a neutron star (NS) or an intermediate-mass

black hole (IMBH) (Rosswog et al. 2008; Metzger 2012; MacLeod et al. 2014; Sell et al. 2015; Margalit & Metzger 2016; Bobrick et al. 2017; Zenati et al. 2019b,a). While such a system is likely to occur in dense stellar systems like globular or super star clusters, there is currently no evidence for CaSTs occurring in such environments. However, SN kicks may push such systems outside of their typical cluster environments and still allow NS/BH + WD systems to reside at CaST explosion sites. Furthermore, NS+WD binaries occur at only 0.3-3% of the type Ia SN (SN Ia) rate for similar age populations, which is much less than the CaST rate of 10-94% with respect to SNe Ia (Perets et al. 2010a; Frohmaier et al. 2018; Toonen et al. 2018; De et al. 2020). Lastly, the detonation of a helium shell on the surface of a WD remains a viable option for CaSTs since its application in the study of SN 2005E (Perets et al. 2010a; Waldman et al. 2011; Woosley & Kasen 2011). In this case, the detonation of the He-shell could lead a partial second detonation of the C/O core for low mass WDs and still match the CaST observables. A complete second detonation of a near-Chandrasekhar mass WD would otherwise result in a SN Ia (Nomoto 1982; Woosley et al. 1986; Fink et al. 2010; Waldman et al. 2011; Polin et al. 2019b; Townsley et al. 2019; Perets et al. 2019; Zenati et al. 2019a). Given the proper conditions needed for helium shell detonations, this explosion scenario can successfully produce heightened Ca abundances through which the ejecta can effectively cool and subsequently produce the prominent Ca II emission lines seen in CaSTs (Holcomb et al. 2013; Polin et al. 2019a).

Despite attempts to find a singular progenitor scenario, some diversity is observed amongst SNe that display unusually large [Ca II]/[O I] flux ratios. This then suggests that CaSTs might be a heterogeneous class of objects with different physical origins. For example, the large inferred ejecta mass ($\sim 2-4$ $M_\odot$) for iPTF15eqv is difficult to reconcile with other homogeneous properties of CaSTs (Milisavljevic et al. 2017). However, iPTF15eqv was only observed after optical peak, and its light curve is consistent with being more luminous than any of the known CaSTs. Together with its prominent Hα emission during nebular phase (also shown by the CaST PTF09dav, Sullivan et al. 2011), these findings might imply that iPTF15eqv is unrelated to the general sample of CaSTs, thus demonstrating the existence of different explosion channels responsible for Ca-rich emission at late times in SNe. An additional outlier amongst CaSTs is "Calcium-strong" SN 2016hnk (Galbany et al. 2019; Jacobson-Galán et al. 2020a), which fits observationally within the class based on its peak luminosity, rise-time and [Ca II]/[O I] ratio, yet has a slowly decaying light curve as well as similarities to "SN 1991bg-like" SNe. This object may represent the extremes of the "Ca-rich" classification while still remaining consistent with the helium shell detonation scenario that is now considered to be a feasible explosion mechanism for CaSTs (De et al. 2020).

While the [Ca II]/[O I] flux ratio is the common metric for classifying new CaSTs, it is now clear that there is a substantial spread in this ratio amongst events: some objects such as SN 2003dg, PTF09dav and PTF10iuv have negligible [O I] emission, while SN 2012hn has an oxygen composition comparable to type IIb/IIP SNe (e.g., Valenti et al. 2014a). Furthermore, type Iax SNe (SNe Iax) are also thermonuclear explosions that are rich in [Ca II] emission at nebular times, yet do not belong to the typical CaST class (Foley et al. 2009, 2016).

Similar to other transients in the "thermonuclear zoo", CaSTs have never been detected in X-ray observations (Sell et al. 2015; Milisavljevic et al. 2017; De et al. 2018b; Sell et al. 2018; Prentice et al. 2019). The earliest X-ray follow-up of a CaST was at $t \approx 26$ days after explosion by Sell et al. (2018) who was testing a progenitor scenario involving the tidal disruption of a WD by an IMBH for SN 2016hnk. However, the fact that multiple other studies have also found X-ray non-detections in CaSTs suggests that either (i) these objects resulted from progenitor environments where X-ray production is not possible or (ii) X-ray emission occurs in CaSTs at yet un-observed phases i.e., extremely early-times, $\sim 0-25$ days after explosion. Furthermore, no CaST has been detected in radio observations (Chomiuk et al. 2016). Progenitor mass-loss rates of $\leq 7 \times 10^{-5}$ and $\leq 2 \times 10^{-6}$ $M_{\odot}yr^{-1}$ were derived from radio non-detections in iPTF15eqv and iPTF16hgs, respectively (Milisavljevic et al. 2017; De et al. 2018b).

In this paper we present, analyze and model multi-wavelength observations (X-ray to radio) of a new CaST, SN 2019ehk, discovered by astronomer Joel Shepherd on 2019 April 29 (MJD 58602.24) using a TEC 140mm APO refracting telescope and Atik 460 EX Mono camera with an SDSS g filter (Grzegorzek 2019). SN 2019ehk has a discovery apparent magnitude of 17.1 mag and is located at $\alpha = 12^{h}22^{m}56.13^{s}$, $\delta = +15°49'33.60''$. The last non-detection of SN 2019ehk was on 2019 April 28 (MJD 58601.25), with a reported limiting r-band apparent magnitude of > 17.9 mag. We fit a power law to the early-time data and derive a time of explosion of MJD 58601.8 ± 0.1.

We first classified SN 2019ehk as a young core-collapse SN with a blue, featureless continuum and strong Na I D absorption (Dimitriadis et al. 2019). Later observations of SN 2019ehk suggested a SN Ib classification with strong calcium features present in the photospheric spectra. However, the spectral time series of SN 2019ehk, coupled with its light curve evolution, indicated that it belonged to the CaST class.

SN 2019ehk is located 17.4″ east and 13.9″ north of the nucleus of the SAB(s)bc galaxy M100 (NGC 4321). In this paper, we use a redshift-independent host-galaxy distance of 16.2 Mpc reported by Folatelli et al. (2010), which is consistent with the Cepheid distance estimated by Freedman et al. (2001). However, it should be noted that there is a significant spread in reported distances for M100, which has influence on derived SN parameters. We use a redshift $z = 0.00524$ and standard ΛCDM cosmology ($H_0 = 72$ km s^{-1} Mpc^{-1}, $\Omega_M = 0.27$, $\Omega_\Lambda = 0.73$). The main parameters of SN 2019ehk and its host-galaxy are displayed in Table A1.

SN 2019ehk presents a remarkable opportunity to advance our understanding of this class of objects. Our observational coverage of this SN includes constraining pre-explosion *Hubble Space Telescope (HST)* imaging combined with a double-peaked light curve wherein the first peak is temporally consistent with luminous X-ray emission and "flash-ionized" Balmer series and He II spectral features. In §2.3 we outline the reduction and analysis of archival *HST*, *Spitzer* and *Chandra* observations of the SN 2019ehk explosion site. In §2.4 we describe all optical, IR, UV, radio and X-ray observations of SN 2019ehk. In §5.5 we present metallicity and star formation estimates for the explosion site in M100. In §4.5 and §4.6 we present analysis and comparisons of SN 2019ehk's optical photometric and spectroscopic

properties, respectively, with chemical abundances of the SN and circumstellar medium derived spectroscopically in §2.7.2 and §4.6.2. In §4.7 we describe and model the first peak of the optical light curve of SN 2019ehk, while in §4.8 we infer properties of the explosion's immediate environment using X-ray and radio observations. Finally, in §4.9 we discuss the possible progenitor systems responsible for SN 2019ehk. Conclusions are drawn in §2.11. All uncertainties are quoted at the 68% confidence level (c.l.) unless otherwise stated.

2.3 Pre-explosion observations and data analysis

2.3.1 HST observations

We analyze archival *HST* images of M100 from the Mikulski Archive for Space Telescopes (MAST) to search for the progenitor system of SN 2019ehk. These observations span from 31 December 1993 to 12 November 2009 and include a variety of filters on the Wide Field and Planetary Camera 2 (WFPC2) and the Wide Field Camera 3 (WFC3). Post-explosion Advanced Camera for Surveys (ACS) F814W imaging of SN 2019ehk was obtained under *HST* program PID-15645 (Sand 2018) on 23 May 2019. We follow the procedure outlined in Kilpatrick et al. (2018a) to reduce all *HST* data with the `astrodrizzle` (Gonzaga 2012) reduction package.[1]

We perform a fine alignment between pre- and post-explosion images in order to accurately look for a coincident progenitor source. For this we use the ACS F814W image of SN 2019ehk on 23 May 2019 and the deepest WFPC2 archival image in F555W taken on 7 January 1997. These specific images are presented in Figure 3.1 for reference. We first run `sextractor` (Bertin & Arnouts 1996) on both images to determine common sources to be used in the alignment process, with cuts made based on an individual sources' full width at half maximum (FWHM) and relative flux. We find 220 common sources between pre- and post-explosion images.

We then performed image registration on the ACS image with IRAF[2] tasks `ccmap` and `ccsetwcs`. We used a fourth order polynomial in `ccmap` to fit pixel coordinates of all common sources in the WFPC2 image to the tangent plane projection of the right ascensions and declinations of the same sources in the ACS image. We then adjusted the WCS solution of the WFPC2 image with `ccsetwcs`. We calculate an astrometric uncertainty of $\sigma_\alpha = 4.05 \times 10^{-4}{}''$ and $\sigma_\delta = 2.71 \times 10^{-4}{}''$ on the explosion site of SN 2019ehk in pre- and post-explosion images.

We apply the WCS solution from our fine alignment to all pre-explosion images and run `dolphot` to search for a source at the location of SN 2019ehk. We find no detectable source in any pre-explosion images within the uncertainty range of the relative astrometry. We then calculate 3σ upper limits on a possible source coincident with SN 2019ehk by injecting fake stars and performing PSF photometry on these sources with `dolphot`. We present the upper

[1] https://github.com/charliekilpatrick/hst123

[2] IRAF, the Image Reduction and Analysis Facility, is distributed by the National Optical Astronomy Observatory, which is operated by the Association of Universities for Research in Astronomy (AURA) under cooperative agreement with the National Science Foundation (NSF).

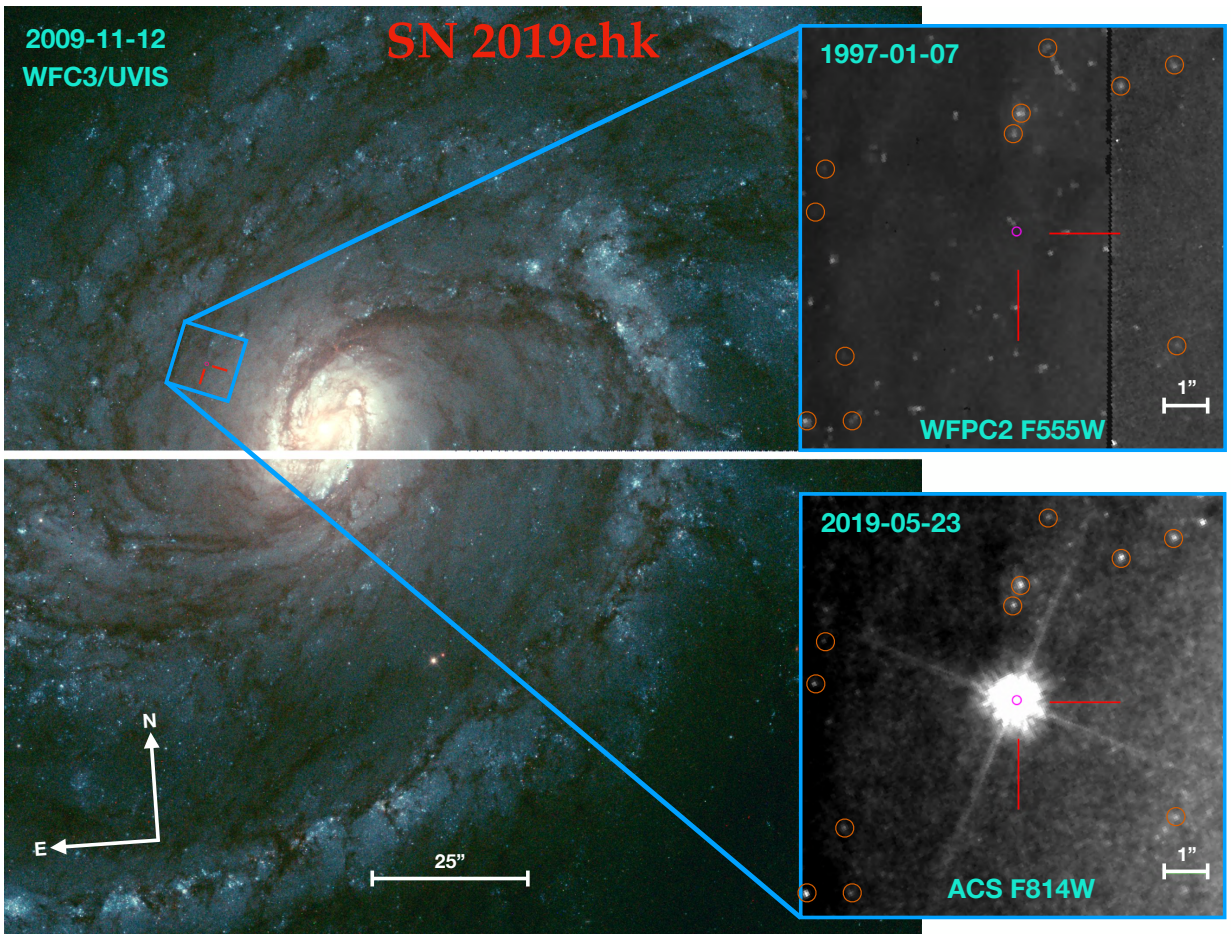

Figure 2.1 *Left:* False color, *HST* RGB pre-explosion image of host galaxy M100. *Right Top Panel:* Zoomed-in pre-explosion image with WFPC2. *Right Bottom Panel:* Post-explosion image of SN 2019ehk with ACS. Common sources between pre-/post-explosion epochs have been marked by orange circles. SN location is marked by red lines and the alignment uncertainty (at 200σ) is indicated by pink ellipses.

limits in apparent magnitude (Vega system) for each pre-explosion *HST* filter in Table A1 and flux limits with respect to filter functions in Figure 2.26 of the Appendix.

All *HST* limiting magnitudes are used to constrain the luminosity and temperature of the SN 2019ehk stellar progenitor. First, we use `pysynphot` to generate a grid of luminosities ($10^{-2} - 10^{8}$ $L_{\odot}$) and temperatures ($100 - 10000$ K) assuming a blackbody stellar model. Each blackbody luminosity is normalized using the SN distance and uncertainty. For each luminosity and temperature in our grid, we convolve the associated spectrum with each *HST* filter in order to calculate the expected apparent magnitude. Then, in each filter, we cross-match the synthetic magnitude against the limit derived from fake star injection. If every synthetic magnitude is smaller than the pre-explosion limits then the luminosity/temperature grid point is rejected from the SN 2019ehk progenitor parameter space. We present the allowed/ruled out regions of pre-explosion parameter space (§2.10.2) and discuss its implications for the progenitor of SN 2019ehk on the Hertzsprung-Russell diagram.

2.3.2 Spitzer observations

We perform a similar analysis of *Spitzer* pre-explosion imaging as in §2.3.1. We collect archival data of M100 from the Spitzer Heritage Archive that included multi-channel observations from 21 August 2014 to 12 April 2019 (Kasliwal et al. 2013, 2014, 2016, 2018). For the fine alignment, we utilized explosion imaging of SN 2019ehk taken on 11 May 2019 under *Spitzer* program DD-14089 (Kasliwal et al. 2018). As in §2.3.1, we perform relative astrometry with IRAF and use `dolphot` to measure photometry of all detected sources. Upon inspection, we detect no pre-explosion source coincident with the location of SN 2019ehk. We then perform fake star injection with `dolphot` to estimate the limiting magnitudes of the SN 2019ehk progenitor. We report our 3σ limits in the AB magnitude system in Table A2 and flux limits with respect to filter functions in Figure 2.26 of the Appendix. While the limits are not as constraining as those derived from *HST* imaging, we discuss implications of these observations in the context of dusty progenitors in §2.10.2.

2.3.3 CXO observations

The *Chandra X-ray Observatory* (CXO) observed the location of SN 2019ehk with ACIS-S on multiple occasions between 1999 November 6 and 2012 February 16, for a total exposure time of 149.3 ks (observation IDs 400, 6727, 9121, 12696, 14230; PIs Garmire, Immler, Patnaude). We followed standard ACIS-S data reduction routines within `CIAO v.4.12` employing the latest calibration files. Specifically, we reprocessed the data with `chandra_repro` and generated a merged event file from the individually re-projected files; this action also created a merged exposure map and a combined exposure map weighted PSF file. Running the source detection algorithm `wavdetect` on the merged event file using the exposure-map weighted PSF file we find no evidence for statistically significant X-ray emission from a point source at the location of SN 2019ehk. Adopting Poisson statistics we infer a 0.5-8 keV count-rate upper limit of 7×10^{-5} c s^{-1} ($3\,\sigma$ c.l.), which translates into an unabsorbed flux

limit in the range $F_x < (1.7-4.0)\times10^{-15}$erg s^{-1}cm^{-2} (0.3-10 keV) for a power-law spectrum with index $\Gamma = 2$, Galactic absorption 2×10^{20} cm^{-2} (Kalberla et al. 2005), and intrinsic absorption $NH_{\rm int} = (1 - 10^2) \times 10^{20}$ cm^{-2}. For a blackbody spectrum with $kT = (0.1 - 10)$ keV and $NH_{\rm int} = (1 - 10^2) \times 10^{20}$ cm^{-2} the flux limit is $F_x < (1 - 10) \times 10^{-15}$erg s^{-1}cm^{-2} (0.3-10 keV).

2.4 Post-explosion observations and data analysis

Table 2.1 Main parameters of SN 2019ehk and its host galaxy

Host Galaxy	M100 (NGC 4321)
Galaxy Type	SAB(rs)c
Galactic Offset	23″(1.8 kpc)
Redshift	0.005 ± 0.0001
Distance	16.2 ± 0.400 Mpc[3]
Distance Modulus, μ	31.1 ± 0.100 mag
RA_{SN}	$12^h22^m56.15^s$
Dec_{SN}	$+15°49'34.18''$
Time of Explosion (MJD)	58601.8 ± 0.1
$E(B-V)_{MW}$	0.02 ± 0.001 mag
$E(B-V)_{host}$	0.47 ± 0.10 mag
$E(B-V)_{host,\ H\,II}$	0.34 ± 0.14 mag[4]
m_B^{peak}	18.0 ± 0.0150 mag
M_B^{peak}	-15.1 ± 0.0210 mag[56]
Δm_{15}	1.7 ± 0.014 mag[d]

Note. — No extinction corrections have been applied to the presented apparent magnitudes.

2.4.1 UV/Optical/NIR Photometry

We started observing SN 2019ehk with the Ultraviolet Optical Telescope (UVOT; Roming et al. 2005) onboard the Neil Gehrels *Swift* Observatory (Gehrels et al. 2004) on 1 May 2019 until 26 May 2019 (δt = 2.8 – 27.3 days since explosion). We performed aperture photometry with a 3″ region with `uvotsource` within HEAsoft v6.26 (and corresponding calibration files), following the standard guidelines from Brown et al. (2014). We detect UV emission from the SN at the time of the first optical peak (Figure 5.4) until $t \approx 5$ days after

explosion. Subsequent non-detections in $U, W1, M2, W2$ bands indicate significant cooling of the photosphere.

SN 2019ehk was imaged between 30 April 2019 and 1 August 2019 (δt = 1.2 – 94.2 days since explosion) with the Direct camera on the Swope 1-m telescope at Las Campanas Observatory, Chile and the PlaneWave CDK-700 0.7m telescope at Thacher Observatory in Ojai, California. Observations were performed in Johnson BV and Sloan $ugriz$ filters. For these data, we performed bias-subtraction and flat-fielding, stitching, registration, and photometric calibration using `photpipe` (Rest et al. 2005). For our photometric calibration, we used stars in the PS1 DR1 catalog (Flewelling et al. 2016a) transformed from gri magnitudes to the $uBVgri$ Swope natural system following the Supercal method (Scolnic et al. 2015). Difference imaging in gri bands was performed using PS1 templates. Final photometry was performed in the difference images with DoPhot (Schechter et al. 1993).

Las Cumbres Observatory (LCO) $UBVgri$-band data of SN 2019ehk were obtained with the Sinistro cameras on the 1m telescopes at Sutherland (South Africa), CTIO (Chile), Siding Spring (Australia), and McDonald (USA), through the Global Supernova Project. Using `lcogtsnpipe`[7], a PyRAF-based photometric reduction pipeline, PSF fitting was performed. Reference images were obtained after the SN faded, and image subtraction was performed using PyZOGY (Guevel & Hosseinzadeh 2017), an implementation in Python of the subtraction algorithm described in Zackay et al. (2016). UBV-band data were calibrated to Vega magnitudes (Stetson 2000) using standard fields observed on the same night by the same telescope. gri-band data were calibrated to AB magnitudes using the Sloan Digital Sky Survey (SDSS, Albareti et al. 2017a).

SN 2019ehk was also observed with ATLAS, a twin 0.5m telescope system installed on Haleakala and Mauna Loa in the Hawai'ian islands that robotically surveys the sky in cyan (c) and orange (o) filters (Tonry et al. 2018a). The survey images are processed as described in Tonry et al. (2018a) and photometrically and astrometrically calibrated immediately (using the RefCat2 catalogue; Tonry et al. 2018c). Template generation, image subtraction procedures and identification of transient objects are described in Smith et al. (2020). Point-spread-function photometry is carried out on the difference images and all sources greater than 5σ are recorded and all sources go through an automatic validation process that removes spurious objects (Smith et al. 2020). Photometry on the difference images (both forced and non-forced) is from automated point-spread-function fitting as documented in Tonry et al. (2018a). The photometry presented here are weighted averages of the nightly individual 30 sec exposures, carried out with forced photometry at the position of SN2019ehk. We searched for pre-explosion outbursts in archival ATLAS observations of the SN explosion site from MJD $57400 - 58599$ ($1201 - 2$ days before explosion). We assume Gaussian errors on the flux and test different phase-dependent binning combinations of pre-explosion data but do not find any photometric detections at $> 3\sigma$ significance.

Additional follow-up photometry on SN 2019ehk was gathered at the Konkoly Observatory, Hungary, using the 0.8m RC80 telescope equipped with a 2048×2048 FLI Proline

[7] https://github.com/svalenti/lcogtsnpipe

23042-1 back-illuminated CCD camera and $BVg'r'i'z'$ filters. The frames are geometrically registered to a common pixel position then median-combined to create a deeper frame in each filter; transformation to the WCS was done by applying `astrometry.net` (Lang et al. 2010). Using IRAF tasks, image subtraction was applied using PS1 *griz* frames as templates, after pixel resampling, geometric registration, PSF- and flux-matching transformations of the template images. We then applied the publicly available `Yoda` code (Drory 2003) to get simple aperture photometry on both the SN and the local comparison stars. Transformation to the standard photometric system was done using the standard magnitudes of the local comparison stars from the PS1-catalog (Flewelling et al. 2016b). Uncertainties on the final magnitudes are computed by combining the photometric errors as given by `Yoda` and the residuals of the photometric zero points derived from the local comparison stars.

The Milky Way V-band extinction and color excess along the SN line of site is A_V = 0.070 mag and *E(B-V)* = 0.0227 mag (Schlegel et al. 1998; Schlafly & Finkbeiner 2011), respectively, which we correct for using a standard Fitzpatrick (1999) reddening law (R_V = 3.1). In order to estimate the effect of host galaxy extinction, we use a spectroscopic observation at the SN location from the Multi Unit Spectroscopic Explorer (MUSE), which observed M100 before the SN explosion on 28 April 2019 through ESO program PID 1100.B-0651 (PI Schinnerer). We apply a 0.77″ aperture (equal to the underlying H II region) to the MUSE data cube in order to extract a host spectrum. After accounting for the stellar absorption with Single Stellar Population (SSP) modeling within `STARLIGHT` (Cid Fernandes et al. 2005) as in Galbany et al. (2016), we measure a Hα and Hβ line flux ratio of 4.23 and estimate the Balmer decrement through standard assumptions of Case B recombination (Osterbrock & Ferland 2006) and Fitzpatrick (1999) extinction law (R_V = 3.1). We derive a line of sight host galaxy reddening of $E(B-V) = 0.339 \pm 0.135$ mag.

In addition to the color excess derived from Balmer decrement in M100, there appears to be significant host galaxy extinction in the local SN environment. All photospheric spectra show prominent Na I D absorption with Equivalent Width EW ∼3 Å, at the host-galaxy redshift. We attempt to use Equation 9 in Poznanski et al. (2012) to convert the Na I EW to an intrinsic *E(B-V)*, but the empirical relation shown in their Figure 9 becomes tenuous for EW $\gtrapprox$ 1.5 Å. Consequently, in order to derive an appropriate host extinction, we compare the *r-i* color to a sample of type Ic SNe (SNe Ic) (see §8.4.1). We find that *E(B-V)*=0.47 mag (corresponding to EW = 1.3 Å) is a reasonable estimate for host-galaxy extinction because it represents an average between the large extinction needed to match SNe Ic colors and a negligible extinction that is consistent with the observed color evolution in other CaSTs.

The complete light curve of SN 2019ehk is presented in Figure 5.4 and all photometric observations are listed in Appendix Table A10. In addition to our observations, we include photometry from the Zwicky Transient Facility (ZTF; Bellm et al. 2019; Graham et al. 2019) public data stream. The most notable feature of the light curve is the presence of two peaks at $\delta t \approx 3$ days and $\delta t \approx 15$ days after explosion. Potential power sources of the first peak are presented in §4.7 while the luminosity of the later peak is considered to be derived from standard ^{56}Ni decay modeled in §4.5.2.

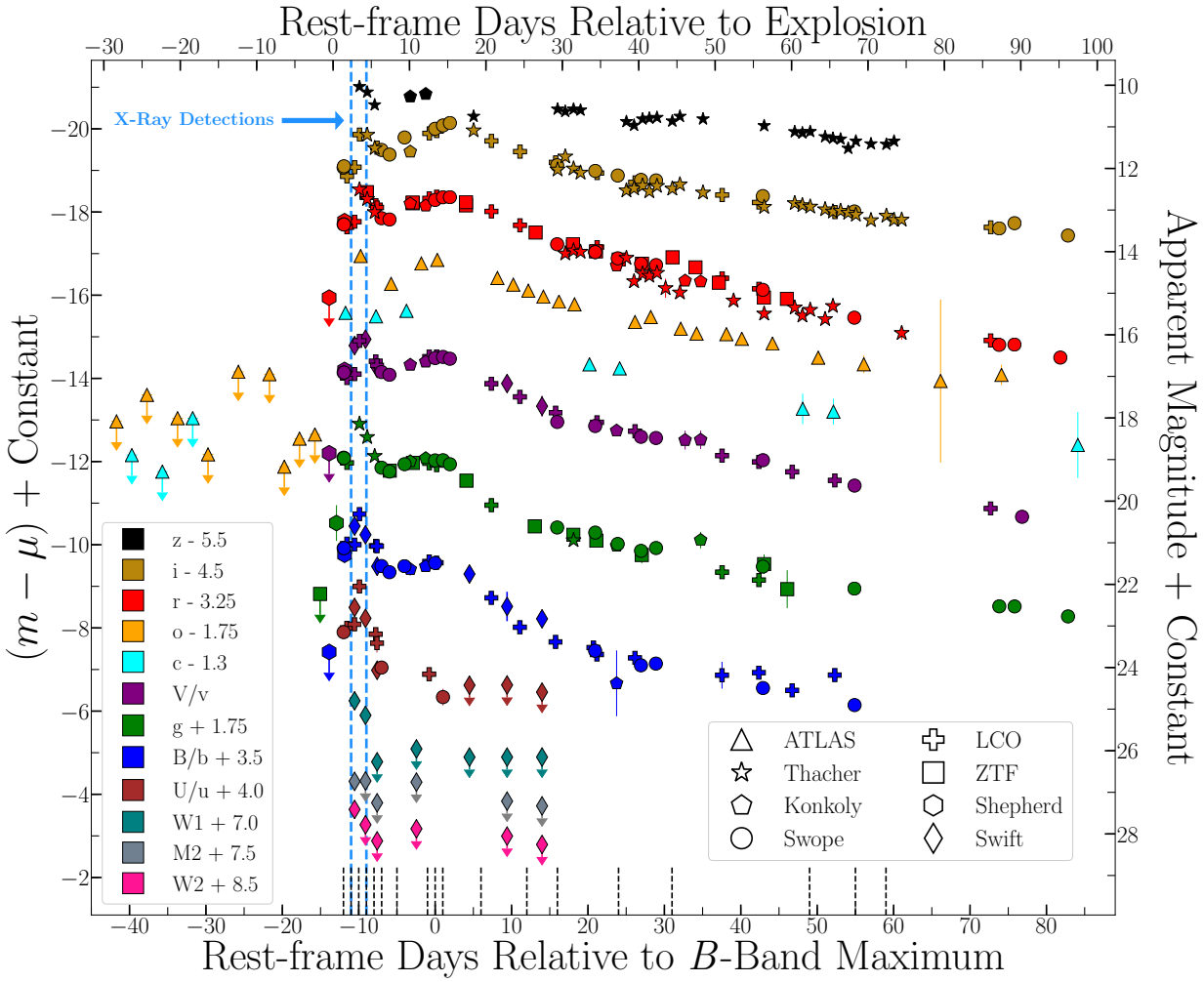

Figure 2.2 UV/Optical light curve of SN 2019ehk with respect to second B-band maximum. Observed photometry presented in AB magnitude system. ATLAS data/3σ upper limits are presented as triangles, Swope as circles, LCO as plus signs, Thacher as stars, ZTF as squares, Konkoly as polygons and J. Shepherd as hexagons. The epochs of our spectroscopic observations are marked by black dashed lines. Grey vertical dashed lines mark the time of the X-ray detections of SN 2019ehk.

2.4.2 Optical/NIR spectroscopy

In Figures 2.3 and 2.4, we present the complete series of optical spectroscopic observations of SN 2019ehk from -12 to +257d relative to the second B-band maximum ($\delta t = 1.34 - 270$ days relative to explosion). A full log of spectroscopic observations is presented in Appendix Table A1.

SN 2019ehk was observed with Shane/Kast (Miller & Stone 1993), SOAR/Goodman (Clemens et al. 2004) and Keck/LRIS (Oke et al. 1995) between -12d and +257d relative to the second light curve peak. For all these spectroscopic observations, standard CCD processing and spectrum extraction were accomplished with IRAF. The data were extracted using the optimal algorithm of Horne (1986). Low-order polynomial fits to calibration-lamp spectra were used to establish the wavelength scale, and small adjustments derived from night-sky lines in the object frames were applied. We employed custom IDL routines to flux calibrate the data and remove telluric lines using the well-exposed continua of the spectrophotometric standard stars (Wade & Horne 1988; Foley et al. 2003). Details of these spectroscopic reduction techniques are described in Silverman et al. (2012).

SN 2019ehk was observed using EFOSC2 (Buzzoni et al. 1984) at the 3.58 m ESO New Technology Telescope (NTT) on 13 May 2019 through the ePESSTO+ program (Smartt et al. 2015; Nicholl et al. 2019). Grism #13 was used, with spectral coverage of 3500-9300 Å and resolution of 21 Å. The exposure time was 1500 s. Standard data reduction processes were performed using the PESSTO pipeline (Smartt et al. 2015)[8]. The reduced spectrum was then extracted, and calibrated in wavelength and flux.

Las Cumbres Observatory (LCO) optical spectra were taken with the FLOYDS spectrographs mounted on the 2m Faulkes Telescope North and South at Haleakala (USA) and Siding Spring (Australia), respectively, through the Global Supernova Project. A 2″ slit was placed on the target at the parallactic angle. One-dimensional spectra were extracted, reduced, and calibrated following standard procedures using the FLOYDS pipeline[9] (Valenti et al. 2014b).

One low resolution optical spectrum was taken with the 300 l/mm grating on the Boller & Chivens (B&C) spectrograph mounted on the 2.3m Bok telescope on Kitt Peak using a 1.5 arcsec slit width on 5 June 2019. Additionally, one moderate resolution spectrum was taken with the Binospec spectrograph (Fabricant et al. 2019a) on the MMT using the 600 l/mm grating and 1" slit on 3 June 2019. Both the B&C and Binospec spectra were reduced using standard techniques in IRAF, including bias subtraction, flat-fielding, and sky subtraction. Flux calibration was done with spectrophotometric standard star observations taken on the same night at similar airmass.

The spectroscopic observations of SN 2019ehk were also collected using the Xinglong 2.16-m telescope (+BFOSC), and the Lijiang 2.4-m telescope (+YFOSC) (Fan et al. 2015) in China. The SN was observed between -11 to -7 days relative to second B-band maxiumum. All the spectra were reduced using routine tasks within IRAF and the flux was calibrated

[8] https://github.com/svalenti/pessto

[9] https://github.com/svalenti/FLOYDS_pipeline

with spectrophotometric standard stars observed on the same nights. Telluric lines are removed from all of these spectra whenever possible.

On 22 June 2019 (MJD 58656.0), we used the Triple-Spec instrument at SOAR to obtain a set of 3 ABBA observations of SN 2019ehk. We used the Spextool IDL package (Cushing et al. 2004a) to reduce the Triple-Spec data, we subtracted consecutive AB pairs to remove the sky and the bias level, then we flat fielded the science frames dividing by the normalized master flat. We calibrated 2D science frames in wavelength by using comparison lamps obtained in the afternoon before the observations. To correct for telluric features and to flux calibrate our SN spectra, we observed the A0V telluric standard HD 111744 after the SN and at a similar airmass. Finally, we extracted the SN and the telluric star spectra from the 2D wavelength calibrated frames. After the extraction of the individual spectra, we used the `xtellcorr` task (Vacca et al. 2003) included in the Spextool IDL package (Cushing et al. 2004a), to perform the telluric correction and the flux calibration of the spectra of SN 2019ehk. We combined individual observations of SN 2019ehk in a single spectrum shown in Figure 2.5.

2.4.3 X-ray observations with *Swift*-XRT and Chandra

The X-Ray Telescope (XRT, Burrows et al. 2005) on board the *Swift* spacecraft (Gehrels et al. 2004) started observing the field of SN 2019ehk on 01 May 2019, until 25 May 2019 ($\delta t \approx 3-24$ d since explosion with a total exposure time of 11.4 ks, IDs 11337 and 11339). We analyzed the data using HEASoft v 6.22 and followed the prescriptions detailed in Margutti et al. (2013), applying standard filtering and screening. A bright source of X-ray emission is clearly detected with significance of $> 5\sigma$ against the background. Visual inspection reveals the presence of extended emission from the host galaxy at the location of the SN. Using Poisson statistics we find that X-ray emission from SN 2019ehk is detected with significance $> 3\,\sigma$ at $t \leq 4.2$ d since explosion. No X-ray emission is detected above the host-galaxy level at later times.

We used *Swift*-XRT pre-explosion data acquired in 2005-2006 to estimate the level of emission from the host galaxy at the SN location (IDs 35227 and 30365). Merging all the available pre-explosion observations (exposure time of ∼59.1 ks), and extracting a spectrum from a 20″ region centered at the SN location, we find that the host-galaxy emission is well modeled by a power-law spectrum with photon index $\Gamma = 2.1 \pm 0.1$, corresponding to a 0.3-10 keV unaborbed flux $F_x = (1.0 \pm 0.1) \times 10^{-13}\,\mathrm{erg\,s^{-1}cm^{-2}}$. The Galactic neutral hydrogen column density along our line of sight is $\mathrm{NH_{MW}} = 2.0 \times 10^{20}\,\mathrm{cm^{-2}}$ (Kalberla et al. 2005). We use this model to account for the contribution of the host galaxy in the two post-explosion epochs where an excess of X-ray emission from SN 2019ehk is detected (at $t = 2.8$ d and 4.2 d).

For each of these two epochs we extracted a spectrum using a 20″ region centered at the location of the SN. We find that the X-ray spectrum of the SN emission has a best-fitting photon index $\Gamma = 0.1 \pm 0.3$ and $\Gamma = 0.2 \pm 0.9$ for the first and second epoch, respectively, corresponding to an unabsorbed 0.3-10 keV flux of $F_x = 4.4 \times 10^{-12}\,\mathrm{erg\,s^{-1}cm^{-2}}$ and $F_x =$

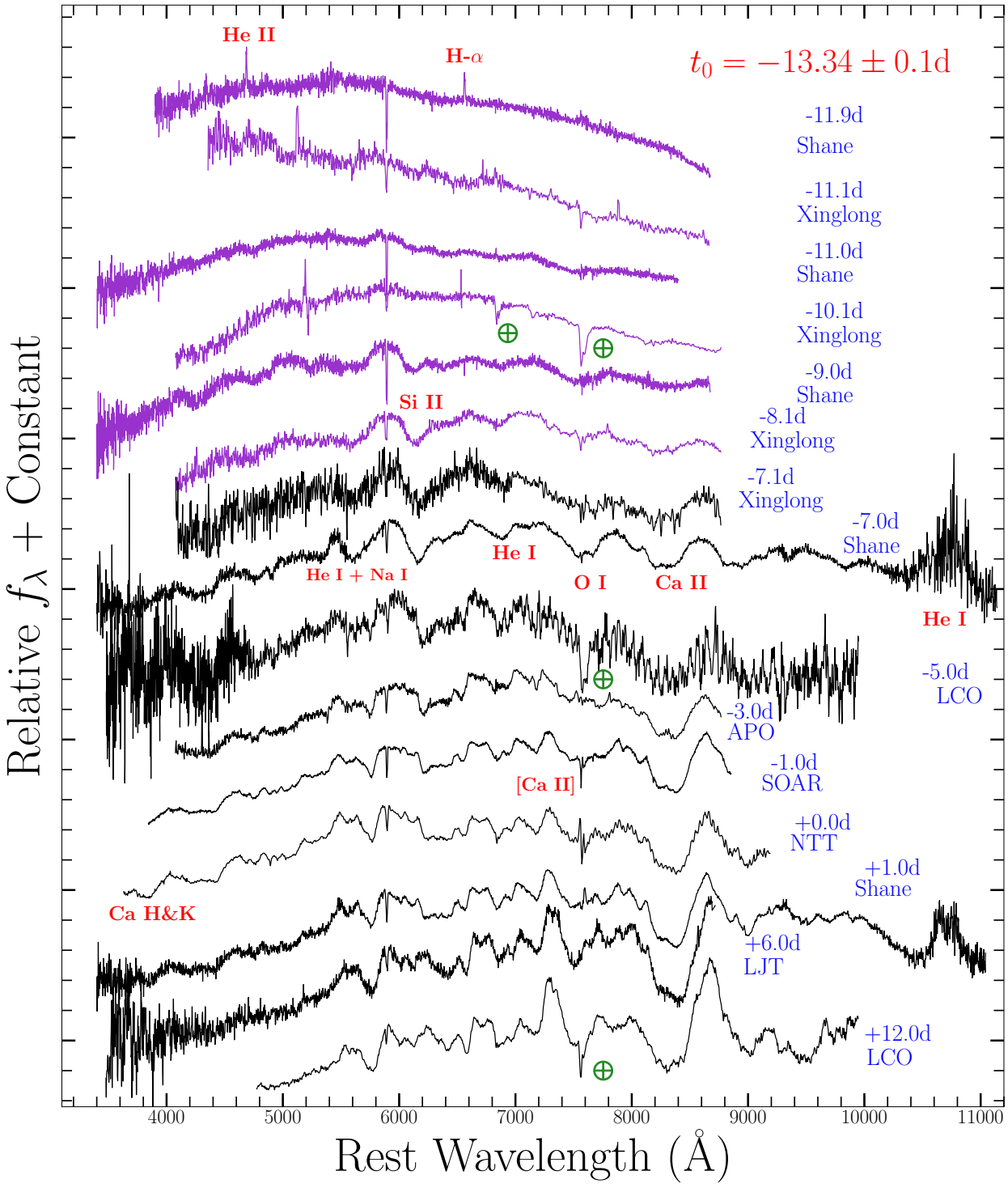

Figure 2.3 Spectral observations of SN 2019ehk with phases (blue) marked with respect to second B-band maximum. Spectra during the first light curve peak are plotted in purple. Green circles with a plus indicate telluric absorption. As shown in the extremely early-time epochs, flash-ionized Balmer series and He II emission lines are only detected until $\delta t \approx 2$ days after explosion.

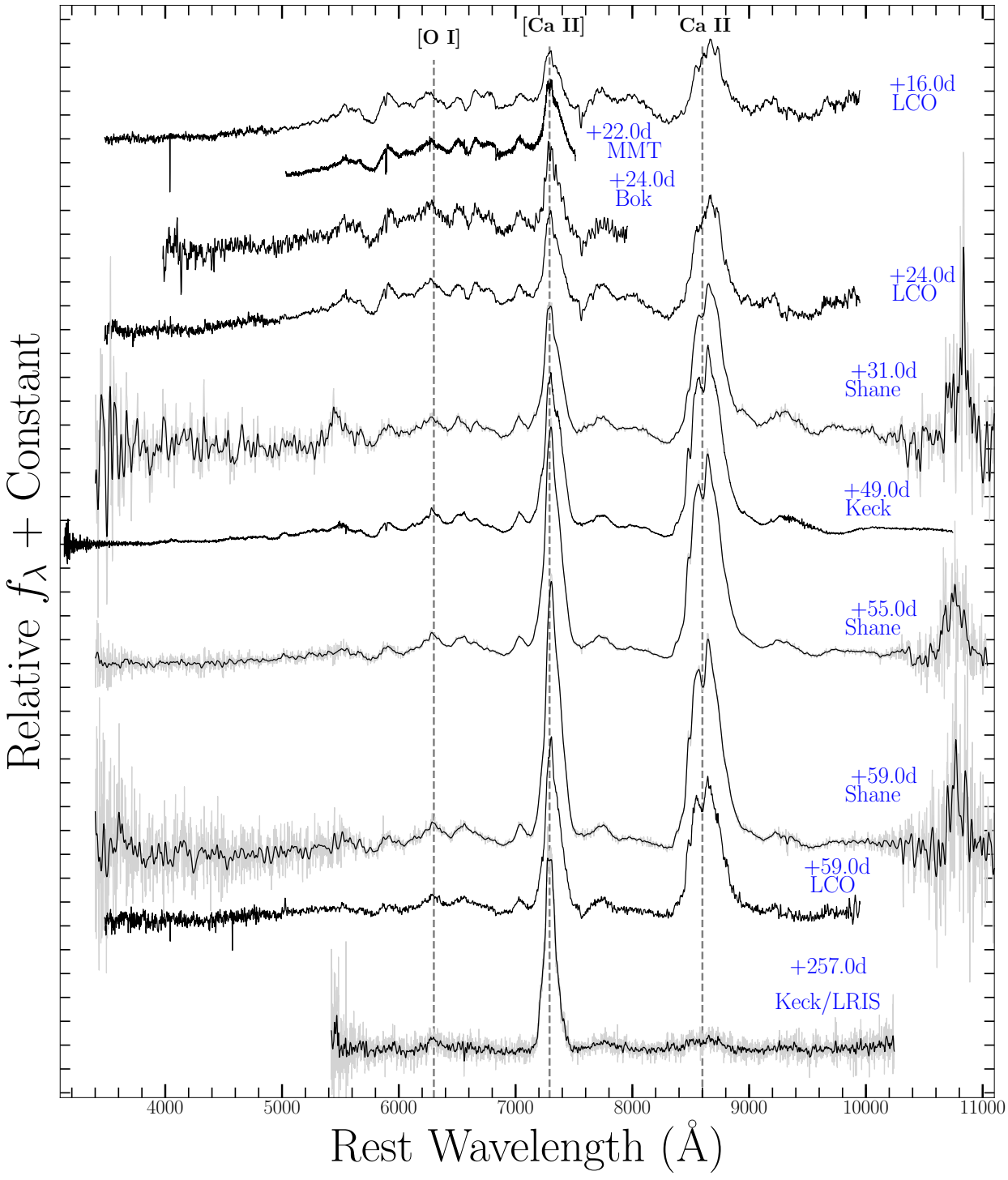

Figure 2.4 Spectral observations of SN 2019ehk with phases (blue) marked with respect to *B*-band maximum. Raw spectra are shown in gray, and smoothed spectra with black lines.

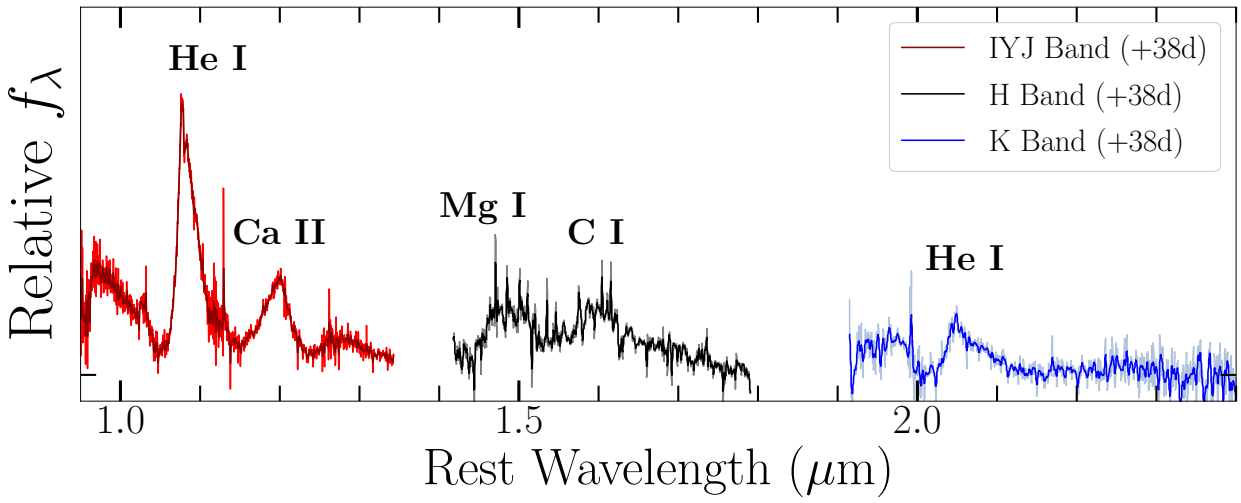

Figure 2.5 SOAR Triple Spec NIR spectrum of SN 2019ehk on MJD 58655.9 or +38d relative to second B-band peak. Prominent line transitions are marked in black.

$1.3 \times 10^{-12}\,\mathrm{erg\,s^{-1}cm^{-2}}$. No evidence for intrinsic neutral hydrogen absorption is found ($NH_{int} < 4 \times 10^{22}\,\mathrm{cm^{-2}}$ at $3\,\sigma$ c.l. from the first epoch). We use the best-fitting spectral parameters inferred from the second epoch of observations to flux-calibrate the count-rate upper limits derived for the following epochs (Table A1). At the distance of SN 2019ehk these measurements indicate a steeply decaying, large X-ray luminosity with $L_x \propto t^{-3}$ and $L_x \geq 3 \times 10^{40}\,\mathrm{erg\,s^{-1}}$ at very early times $t \leq 4.2$ d (Figure 4.5). The very luminous X-ray emission from SN 2019ehk at $t \approx 2.8$ d $L_x \approx 10^{41}\,\mathrm{erg\,s^{-1}}$ rivals that of GRB 980425. Since no other CaST has been observed in the X-rays a few days since explosion, it is unclear if this luminous X-ray display is a common trait of the class.

The hard 0.3-10 keV X-ray spectrum of SN 2019ehk is suggestive of thermal bremsstrahlung emission with temperature $T > 10$ keV. Fitting the SN contribution with a bremsstrahlung spectral model with $T = 10 - 200$ keV the inferred emission measure $EM = \int n_e n_I dV$ is $EM = (7-10) \times 10^{63}\,\mathrm{cm^{-3}}$ (at $\delta t = 2.8$ d) and $EM = (2-3) \times 10^{63}\,\mathrm{cm^{-3}}$ (at $\delta t = 4.2$ d), where n_e and n_I are the number densities of electrons and ions, respectively.

The location of SN 2019ehk was serendipitously observed by the Chandra X-ray Observatory (CXO) on 15 February, 2020 ($\delta t = 292.2$ d since explosion, exposure time of 9.95ks, ID 23140, PI Stroh) as part of follow-up observations of another supernova, SN 2020oi, that exploded in the same host galaxy. We analyzed the data with the `CIAO` software package v4.12 and corresponding calibration files. We find no evidence for X-ray emission at the location of SN 2019ehk and we place a 3σ count-rate upper limit of $3.01 \times 10^{-4}\mathrm{c\,s^{-1}}$ (0.5-8 keV, pure Poisson statistics). We adopt the spectral parameters from the latest epoch of *Swift*-XRT observations that led to a detection and we infer an unabsorbed 0.3-10 keV flux limit $F_x < 1.07 \times 10^{-14}\,\mathrm{erg\,s^{-1}cm^{-2}}$, which corresponds to $L_x < 3.3 \times 10^{38}\,\mathrm{erg\,s^{-1}}$. This is the deepest limit on the late-time X-ray luminosity of a CaST to date (Figure 4.5).

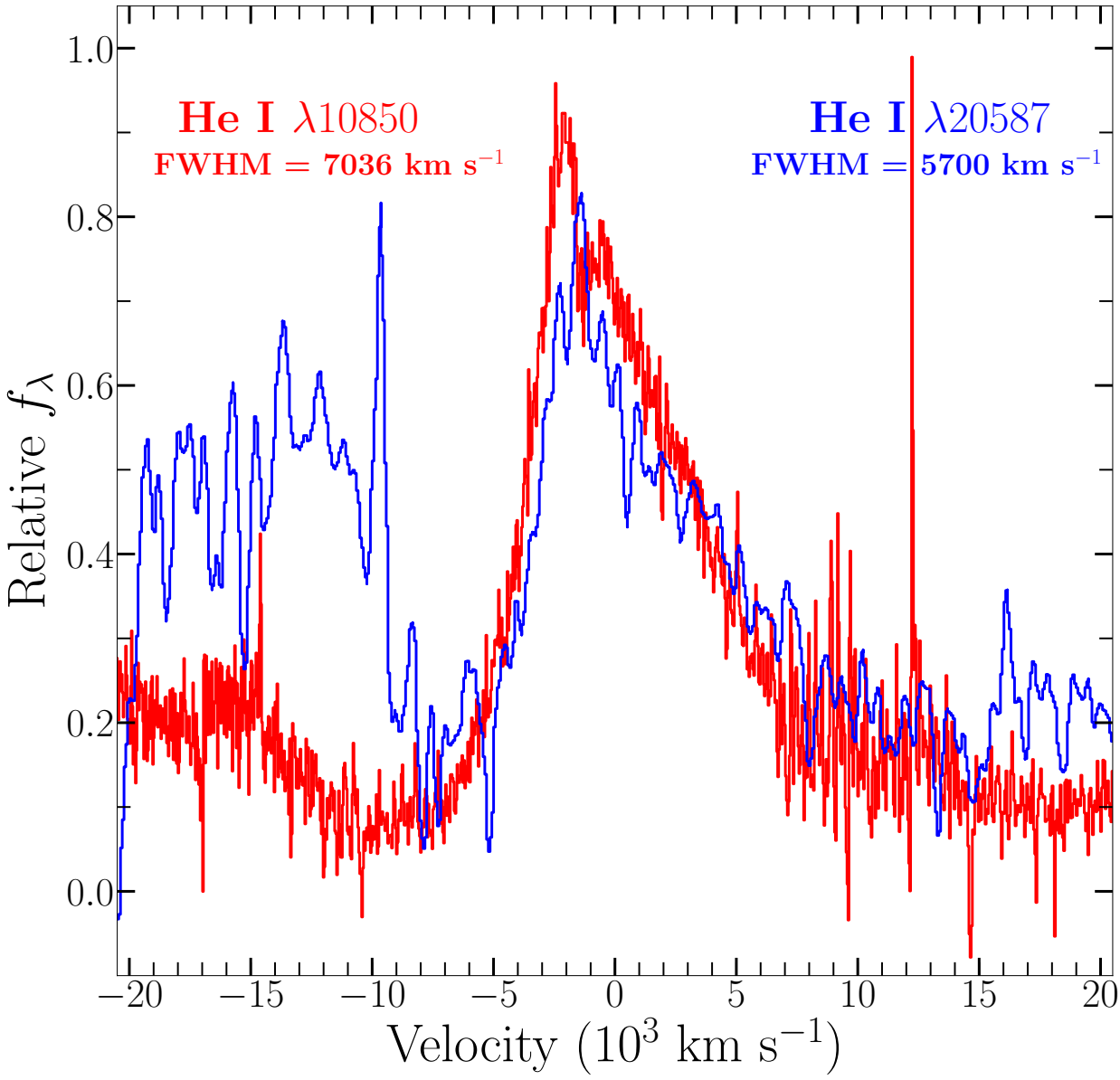

Figure 2.6 NIR He I λ10850 and λ20587 line velocity profiles (Fig. 2.5). The P-Cygni line profile indicates that the helium is photospheric and expanding up to $\sim$7000 km s^{-1}. However, the broad emission feature may either indicate a detached ejecta component of helium in the circumstellar material (CSM) or a blending of spectral features near 1μm. The profile of the He I λ20589 line at +38 days after second B-band maximum shows that it becomes optically thin at lower velocity than does the He I λ10830 line, presumably because of a lower population of the 1s2s ^{1}S metastable levels, which results from its much higher Einstein A value.

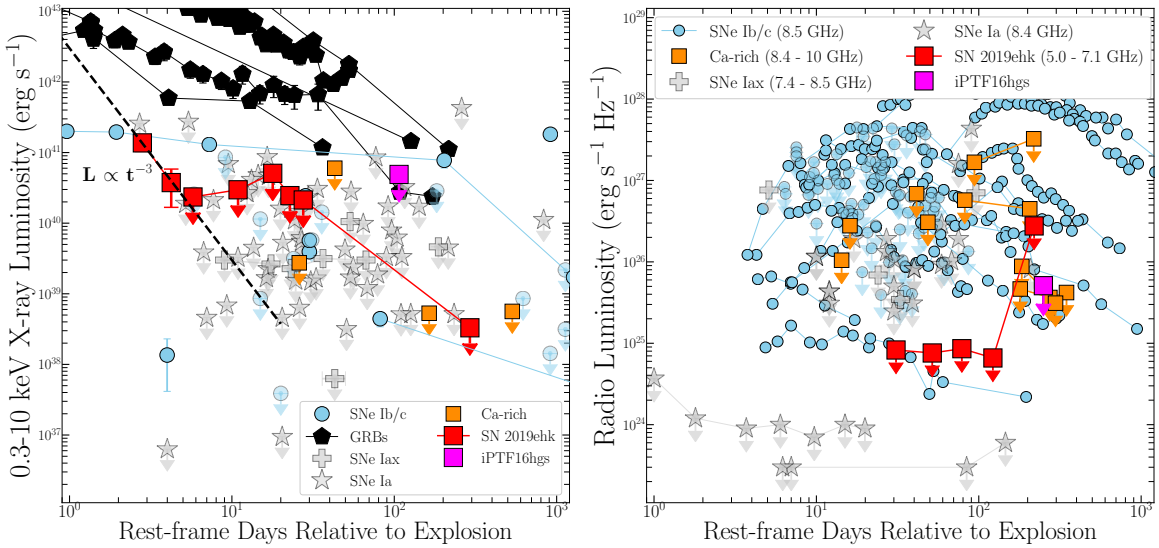

Figure 2.7 (a) X-Ray light curve of SN 2019ehk (red squares) and other thermonuclear transients e.g., SNe Iax (grey plus signs), SNe Ia (grey stars) and CaSTs (orange squares). Core-collapse SNe Ib/c are shown as light blue circles and GRBs are displayed as black polygons. The decline rate of SN 2019ehk's X-ray emission ($L_x \propto t^{-3}$) is shown as a black dashed line. (b) Radio non-detections of SN 2019ehk (red squares) compared to non-detection limits of thermonuclear SNe and SNe Ib/c.

2.4.4 Radio observations with the VLA

We acquired deep radio observations of SN 2019ehk with the Karl G. Jansky Very Large Array (VLA) at $\delta t = 30.5 - 219.7$ days post explosion through project VLA/19A-271 (PI D. Coppejans). All observations have been obtained at 6.05 GHz (C-band) with 2.048 GHz bandwidth in standard phase referencing mode, with 3C286 as a bandpass and flux-density calibrator and QSO J1224+21 (in A and B configuration) and QSO J1254+114 (in D configuration) as complex gain calibrators. The data have been calibrated using the VLA pipeline in the Common Astronomy Software Applications package (CASA, McMullin et al. 2007) v5.4.1 with additional flagging. Briggs weighting with a robust parameter of 2 was used to image. SN 2019ehk is not detected in our observations. We list the inferred flux densities in Appendix Table A4 and show how these measurements compare to radio observations of thermonuclear transients and core-collapse SNe in Figure 4.5(b).

2.5 Host Galaxy and Explosion Site

2.5.1 Metallicity

We determine an oxygen abundance 12 + log(O/H) at the explosion site by using a MUSE spectroscopic observation taken on 28 April 2019 (PI Schinnerer). Data were reduced and analyzed following the prescriptions outlined in Galbany et al. (2016). The spectrum was corrected for a host galaxy reddening of $E(B-V) = 0.34$ mag and stellar absorption is accounted for with a SSP model (e.g., see §8.3.2). Using a combination of line flux ratios ([O III] / Hβ and [N II]/Hα) into Equation 3 of Pettini & Pagel (2004), we determine a host metallicity of 12 + log(O/H) = 8.70 ± 0.12 dex (1.03 ± 0.120 Z$_\odot$). We obtain a similar value if we use the method presented in Dopita et al. (2016): 12 + log(O/H) = 9.04 ± 0.20 dex (1.46 ± 0.290 Z$_\odot$). The ∼0.3 dex difference between methods is expected given known offsets amongst calibrators (Kewley & Ellison 2008). Furthermore, both values are similar to the metallicities calculated by Pohlen et al. (2010) from the radial distribution of gas across M100.

2.5.2 Star Formation Rate

We utilize the same pre-explosion MUSE spectrum to determine a star formation rate at the location of SN 2019ehk. We calculate a total Hα emission line luminosity of $L_{\rm H\alpha} = (1.16 \pm 0.37) \times 10^{37}$ erg s^{-1} from a 0.7″ aperture that encompasses the local H II region at the SN location. We then use Equation 2 from Kennicutt (1998) to estimate a star formation rate of SFR = $(9.2 \pm 2.9) \times 10^{-5}$ M$_\odot$ yr^{-1} at the explosion site. We also derive an effective star formation rate of $(5.3 \pm 1.7) \times 10^{-3}$ M$_\odot$ yr^{-1} kpc^{-2}. These SFR values are reasonable considering the lack of observed star formation found at most CaST explosion sites. Our inferred rate is consistent with the low observed SFR values derived from $\gtrsim 90\%$ of CaST explosion sites. With regards to core-collapse SNe, the Hα luminosity at the explosion site of

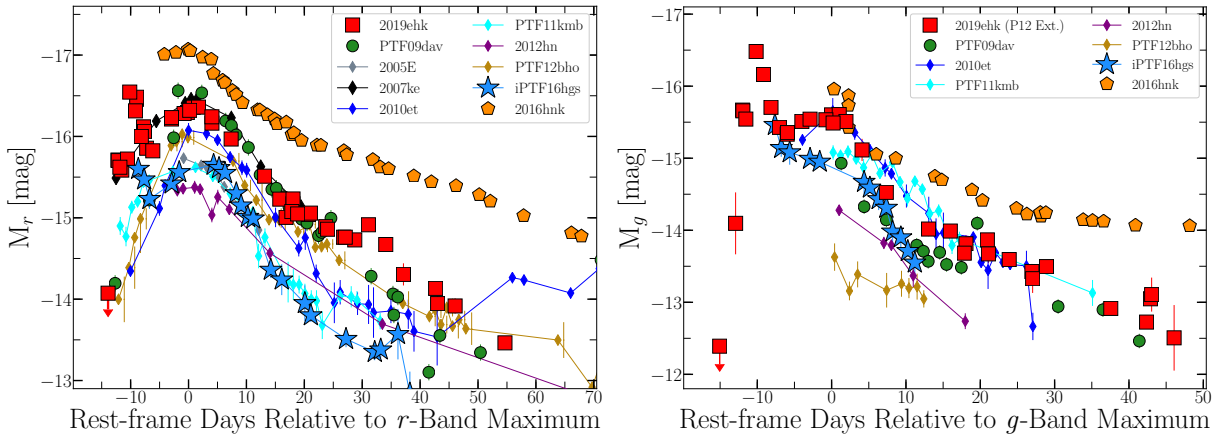

(a) (b)

Figure 2.8 (a) Early-time $r-$band comparison of SN 2019ehk (red squares) and classified CaSTs. The peculiar, "calcium-strong" SN 2016hnk also presented for reference (orange polygons). SN 2019ehk is now the second object in this class to show a double-peaked light curve, iPTF16hgs (light blue stars) being the first. (b) $g-$band comparison of SN 2019ehk (red squares) and classified CaSTs.

SN 2019ehk is only consistent with the H II region luminosity at the location of $\sim 20-30\%$ of H-stripped SNe (e.g., Galbany et al. 2018; Kuncarayakti et al. 2018).

2.6 Optical Light Curve Analysis

2.6.1 Photometric Properties

SN 2019ehk is the third observed CaST with a double-peaked optical light curve (the others being iPTF 16hgs, De et al. 2018b and SN 2018lqo, De et al. 2020). Consequently, we define its phase relative to the secondary, "Nickel-powered" peak and discuss the potential power sources of the first peak in §4.7. We fit a low-order polynomial to the SN 2019ehk light curve to find best fit B- and r-band peak absolute magnitudes of $M_B = -15.1 \pm 0.0210$ mag at MJD 58615.15 ± 0.1 and $M_r = -16.36 \pm 0.01$ mag at MJD 58616.18 ± 0.2, respectively. We calculate a Phillips (1993) decline parameter value of $\Delta m_{15}(B) = 1.71 \pm 0.0140$ mag from our B-band light curve fits. We calculate a rise-time of $t_r = 13.4 \pm 0.210$ days using the adopted times of explosion and B-band peak.

We present $r-$ and $g-$band light curve comparisons of SN 2019ehk and CaSTs in Figures 2.8(a)/(b). Overall, SN 2019ehk has comparable light curve evolution to other confirmed CaSTs: $t_r < 15$ days and declines in luminosity at a similar rate. SN 2019ehk is less luminous in $r-$band than "Calcium-strong" SNe 2016hnk (Galbany et al. 2019; Jacobson-Galán et al. 2020a) and PTF09dav (Sullivan et al. 2011), but has a similar light curve

evolution to the next most luminous CaST SN 2007ke (Lunnan et al. 2017). Furthermore, its $r-$band evolution is consistent with iPTF16hgs (De et al. 2018b), the only other CaST with a confirmed double-peaked light curve. This duplicate first light curve peak may indicate similar underlying physics between the two objects despite the fact that SN 2019ehk is $\sim$1 mag more luminous than iPTF16hgs and declines at a slower rate. Additionally, we present Δm_{15}(B) vs. M_B for SN 2019ehk with respect to CaSTs and other thermonuclear varieties in Figure 2.9. From this comparison, SN 2019ehk is broadly consistent with the CaST class due to its $B-$band light curve evolution from peak out to 15 days. SN 2019ehk is clearly distinct from normal and sub-luminous SNe Ia/Iax, but has a comparable Phillips (1993) decline parameter value to 91bg-like SNe Ia.

In Figure 8.5, we present $g-r$, $B-V$ and $r-i$ color comparison plots of SN 2019ehk, CaSTs, SNe Ia/Iax and SNe Ic. Given the relative uncertainty on SN 2019ehk's host-galaxy extinction, we display color curves that have no host extinction applied (red squares) as well as colors where the adopted value of $E(B-V) = 0.47$ mag is used to correct for extinction (blue line). As shown in Figures 8.5(a)/(c), SN 2019ehk's de-reddened colors are consistent to within 0.1 mag in $g-r$ and 0.2 mag in $r-i$ of the typical CaSTs; all objects exhibiting a noticeably "red" color evolution. Consequently, SN 2019ehk's intrinsically red colors deviate significantly from all flavors of SNe Ia shown in Figures 8.5(b). SN 2019ehk is $\sim$0.3 mag redder than the reddest SN Ia, 2005ke and SN Iax, 2012Z.

We present $r-$band light curve comparisons of SN 2019ehk and type IIb/Ib SNe (SNe IIb/Ib) in Figure 2.11(a). SN 2019ehk has a similar peak magnitude to SN Ib, iPTF13bvn and a higher peak magnitude than prototypical SN Ib, SN 2008D. While SN 2019ehk's $r-$band evolution is quite similar to iPTF13bvn, it has a significantly shorter rise-time than any SNe Ib. With respect to SNe IIb, SN 2019ehk is less luminous at peak and evolves faster than both SNe 1993J and 2011dh. Furthermore, the first light curve peak observed in SNe IIb occurs on a longer timescale ($\sim 10-15$ days) than that observed in SN 2019ehk ($\sim$5 days). The first peak in these SNe is also typically less luminous than the secondary maximum, which is reversed in SN 2019ehk. However, the double-peaked light curve in SN 2019ehk may be physically connected to a explosion scenario wherein the SN shock "breaks out" into an extended envelope, which then rapidly cools. Such a mechanism has been invoked as an explanation for the primary peak in SNe IIb and we further discuss this model in §2.8.3.

2.6.2 Pseudo-Bolometric Light Curve

We construct a pseudo-bolometric light curve by fitting the broad-band photometry with a blackbody model that is dependent on radius and temperature. Each spectral energy distribution (SED) was generated from the combination of multi-color optical photometry in $uBVcgoriz$ bands (3000-9000Å). In regions without complete color information, we extrapolated between light curve data points using a low-order polynomial spline. We present SN 2019ehk's bolometric light curve in addition to its blackbody radius and temperature evolution in Figure 2.12. We display the inferred blackbody luminosities, temperatures and radii that resulted from both host-galaxy extinction corrected photometry and non-corrected

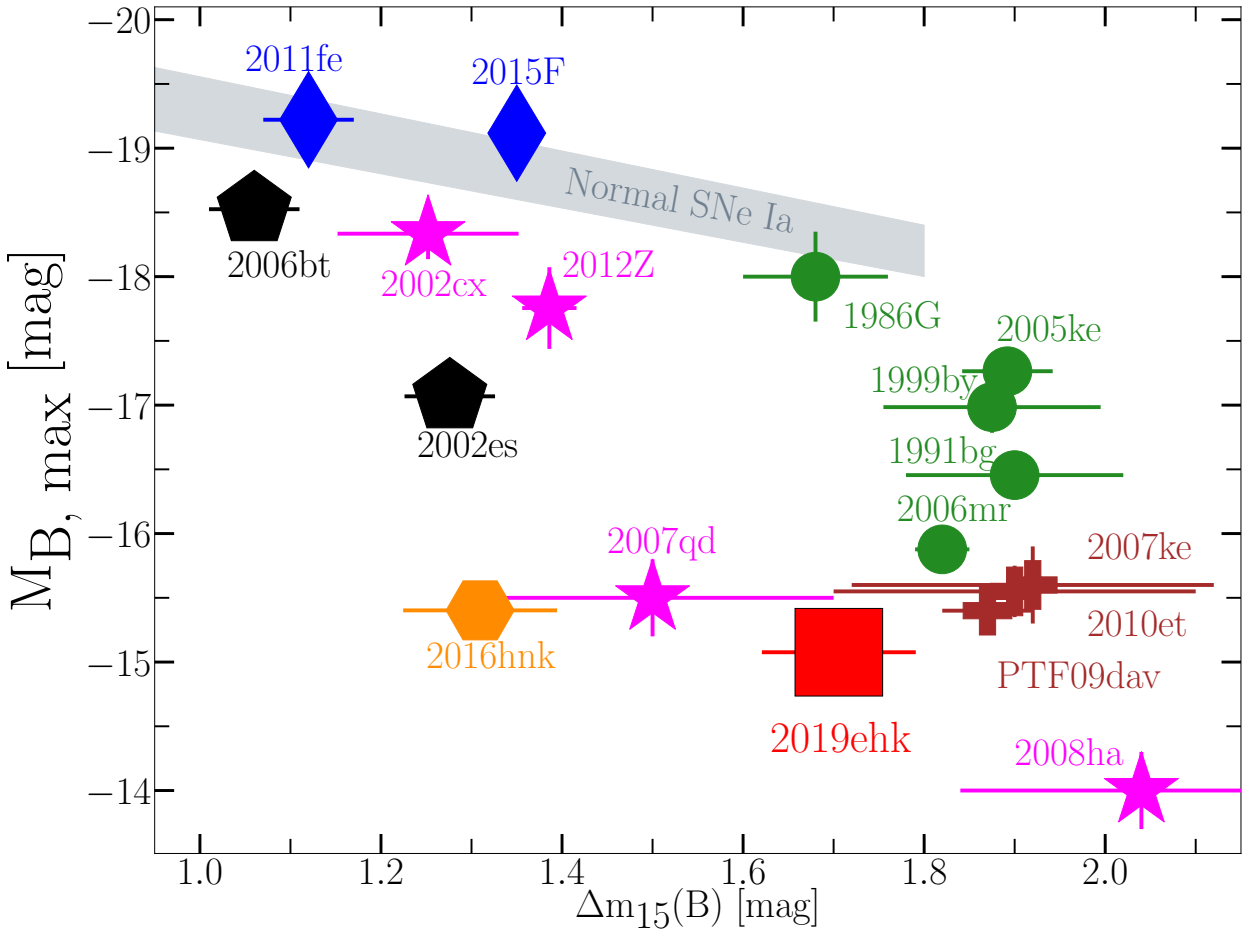

Figure 2.9 Δm_{15} vs. $M_{B,max}$ for SN 2019ehk (red square), normal SNe Ia (diamonds + grey region), 91bg-like SNe Ia (circles), SNe Iax (stars), 02es-like SNe Ia (pentagons), other CaSTs (plus signs), peculiar thermonuclear SN 2006bt (pentagon) and "Calcium-strong" SN 2016hnk (hexagon). Some uncertainities on $M_{B,max}$ are smaller than plotted marker size.

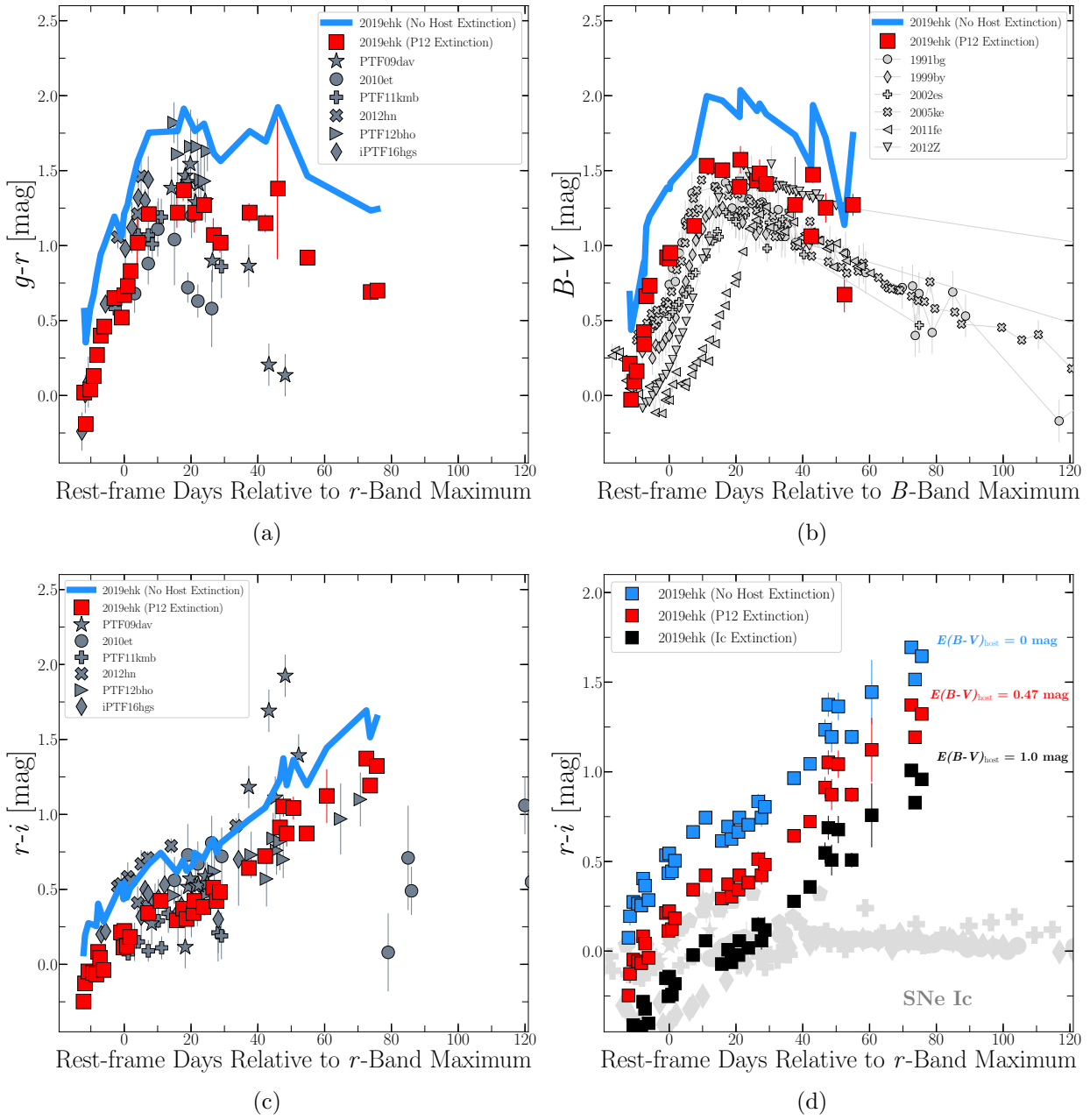

Figure 2.10 (a) g-r color comparison of SN 2019ehk and CaSTs. SN 2019ehk colors from photometry are presented as a blue line. The red squares represent the photometric colors that have been de-reddened according to the Poznanski et al. (2012) (P12) extinction relation and host galaxy reddening $E(B-V) = 0.47$. (b) B-V color comparison of SN 2019ehk and various types of SNe Ia. (c) r-i color comparison of SN 2019ehk and CaSTs. (d) SN 2019ehk's r-i color evolution for different levels of host extinction: 0 mag (black), 0.47 mag (red) and 1.0 mag (blue). These are compared to the r-i colors of a sample of type Ic SNe (grey).

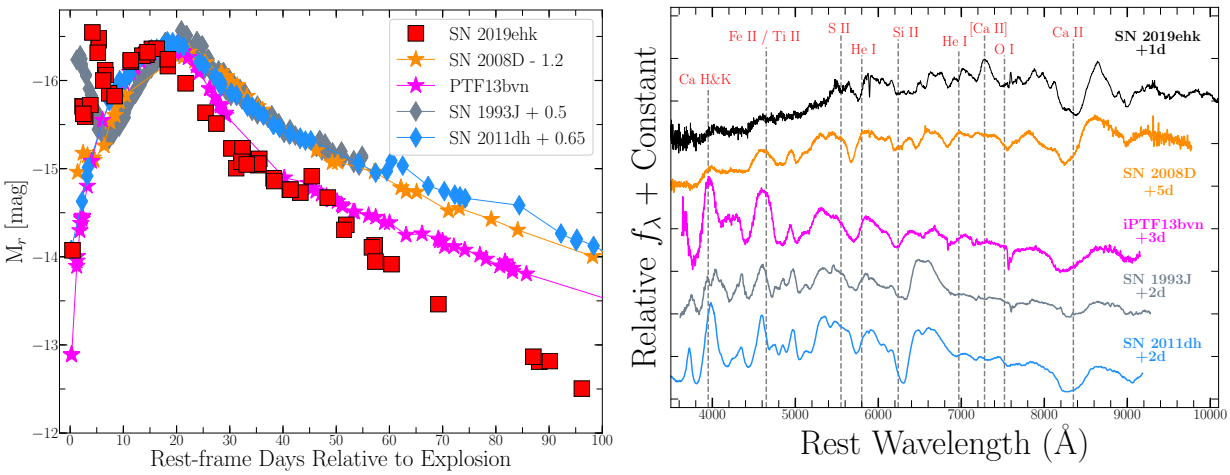

(a) (b)

Figure 2.11 (a) Photometric comparison of SN 2019ehk (red squares) with respect to SNe Ib (stars; Soderberg et al. 2008; Malesani et al. 2009; Modjaz et al. 2009; Fremling et al. 2016) and SNe IIb (diamonds; Wheeler et al. 1993; Arcavi et al. 2011). (b) Spectral comparison of SN 2019ehk (without reddening correction) and SNe Ib/IIb. While there are some individual similarities between SN 2019ehk and SNe Ib/IIb, the apparent contrast in its photometric and spectral evolution is indicative of different underlying explosion physics, which then distances this SN from a SN Ib/IIb classification.

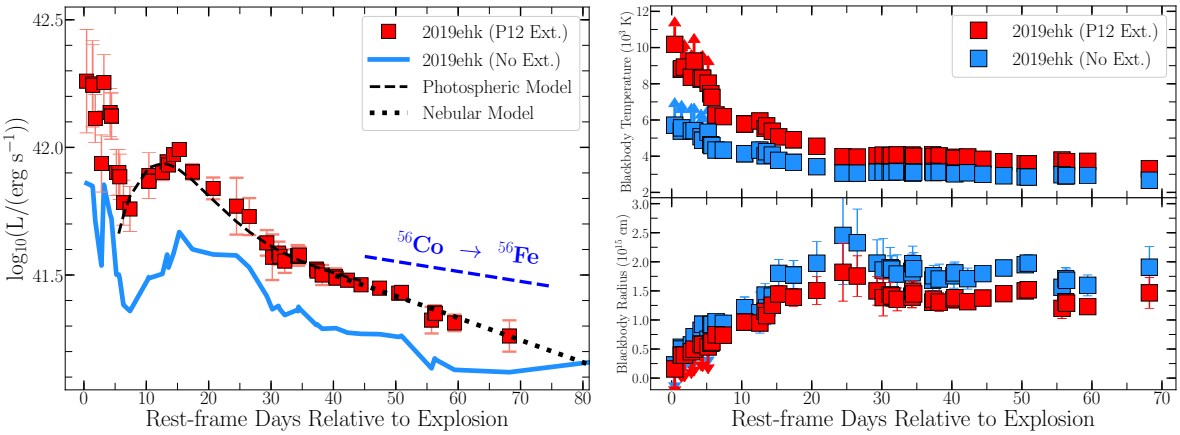

(a) (b)

Figure 2.12 (a) Pseudo-bolometric light curve of SN 2019ehk for different host-galaxy reddening: $E(B-V) = 0.47$ (red squares) and $E(B-V) = 0.0$ (blue line). Points at $t < 6$d were calculated using a linearly increasing photosphere radius (e.g., see §4.7, Fig. 2.19) Separate photospheric light curve models for the early-time light curve (§4.5.2) are plotted as dashed black line. Modeling of the nebular phase data plotted as dotted black line. (b) Blackbody radii and temperatures derived from SED modeling of all multi-color optical photometry. Red squares indicate a host extinction correction of $E(B-V) = 0.47$ and blue squares indicate $E(B-V) = 0$. Radii and temperatures at $t < 6$ days are displayed as upper and lower limits, respectively.

photometry. All uncertainties on blackbody radii and temperature were calculated using the co-variance matrix generated by the SED fits. It should be noted that the blackbody approximation breaks down when emission lines begin to dominate the spectrum of SN 2019ehk at $t > 30$ days after explosion. Therefore a blackbody assumption for SN 2019ehk at late-times is most likely an over-simplification and could result in additional uncertainty on the presented bolometric luminosities and the resulting estimates on physical parameters of the SN. For the secondary, Nickel-powered light curve peak, we find a peak bolometric luminosity of $(9.81 \pm 0.15) \times 10^{41}$ erg s^{-1}.

In order to determine physical parameters of the explosion, we model the bolometric light curve with the analytic expressions presented in Appendix A of Valenti et al. (2008a). We exclude the first light curve peak from this analysis and model the bolometric evolution of SN 2019ehk for $t > 8$ days post-explosion. These models are divided into two distinct parts: the photospheric phase ($t < 30$ days past explosion), which is based on Arnett (1982) and the nebular phase ($t > 60$ days past explosion), which is derived from prescriptions outlined in Sutherland & Wheeler (1984) and Cappellaro et al. (1997) (however see Wheeler et al. 2015 for corrected Arnett 1982 equations). Furthermore, this analytic formalism self-consistently implements the possibility of incomplete γ-ray trapping in the expanding SN ejecta throughout the modeling process. A typical opacity of $\kappa = 0.1$ cm^2 g^{-1} is applied in each model. The free parameters of each model are kinetic energy ($E_{\rm k}$), total mass of synthesized ^{56}Ni ($M_{\rm Ni}$), and ejecta mass ($M_{\rm ej}$). However, there is a known degeneracy within these models between kinetic energy and ejecta mass:

$$M_{\rm ej} = \frac{10}{3}\frac{E_{\rm k}}{v^2} \tag{2.1}$$

where we follow standard practice and use $v \approx v_{ph}$, i.e. the photospheric velocity at peak. We use $v_{ph} \approx 6500$ km s^{-1}, which is estimated from Si II absorption at peak. Our photospheric and nebular models are presented in Figure 2.12(a) as the dashed and dotted lines, respectively. From these models, we calculate $M_{\rm Ni} = (3.1 \pm 0.11) \times 10^{-2}$ M$_\odot$, $E_{\rm k} = (1.8 \pm 0.1) \times 10^{50}$ erg and $M_{\rm ej} = (0.72 \pm 0.04)$ M$_\odot$. We discuss the modeling of the first light curve peak in §2.8.2. Furthermore, we show that the nebular phase light curve decline is slightly faster than the typical decay of ^{56}Co $\rightarrow$ ^{56}Fe that assumes complete trapping of γ-rays.

In Figure 2.12(b), we present the evolution of SN 2019ehk's blackbody radius and temperature for different extinction values from 0.44 to 73.2 days after explosion. For phases 0.44-6d, it should be noted that the peak of the blackbody curve is not visible in our model fits i.e., the blackbody peaks in the near-to-far UV. Thus we cannot be confident that the reported blackbody radii and temperatures during these times are completely accurate. As is further discussed in §4.7.1, these specific radii and temperatures are best treated as upper and lower limits, respectively.

At the time of first detection in $g-$band, SN 2019ehk had a minimum blackbody temperature of $\gtrsim 10,200$ K and a maximum initial radius of $\leq 1.6 \times 10^{14}$ cm (2300 R$_\odot$). This was conservatively calculated by assuming no color evolution between first and second epochs

and then fitting a blackbody model. We can thus better constrain the initial radius at $t = 0.44$d by fitting a blackbody model to the initial $g-$band detection for a range of fiducial temperatures $T = (2-4) \times 10^4$ K. In this case we find photospheric radii of $7-4 \times 10^{13}$ cm (1000-500 $R_\odot$). Extended progenitors for SN 2019ehk are ruled out in §2.10.2. Therefore, considering a compact massive progenitor with radius of $\sim$10 $R_\odot$, we estimate a shock velocity of $v_s \approx 1.8 \times 10^4$ km s^{-1} in order to reach a blackbody radius of 7×10^{13} cm at $t = 0.44$d. This is also a reasonable estimate for shock breakout from a WD progenitor. Because the shock could be ahead of the photosphere, we consider v_s to be a lower limit on the true shock velocity, which is consistent with being larger than the photospheric velocities derived from SN 2019ehk spectra.

2.7 Optical/NIR Spectral Analysis

2.7.1 Spectroscopic Properties

We model the SN 2019ehk spectrum near peak in order to understand the chemical composition of the explosion. To do this, we utilize the spectral synthesis software `SYNAPPS` (Thomas et al. 2011), which is dependent on generalized assumptions about the SN such as spherical symmetry, local thermal equilibrium, and homologous expansion of ejecta. We present a `SYNAPPS` fit to the +1 day spectrum as the red line in Figure 2.13. As shown in blue, we detect the following species in SN 2019ehk near peak: He I, C II, O I, Na I, Mg I, Si II, S II, Ca II, Ti II, Fe II and Fe III. While the C II absorption is weak relative to the continuum, it does appear to be contributing to the overall flux near $\lambda\lambda$6580,7234. The model also appears to be over-producing the line flux between 5500-6000Å, which we attribute to possible deficiency in fitting species such as S II, Ti II and Fe II. However, the overall spectral profiles are matches in that region, which allows us to conclude that those ions are in fact present in the SN ejecta.

We perform additional spectral modeling to explore the possibility that hydrogen or exotic Fe-group elements such as Cr II, Sc II and Sr II are present in SN 2019ehk. After multiple iterations of `SYNAPPS` modeling, we find no detectable Hα or Balmer series lines in the maximum light spectrum. Furthermore, the addition of Cr II, Sc II and Sr II to our `SYNAPPS` models does not improve the overall fit, specifically bluewards, and thus we cannot claim a confident detection of these ions. All identified ions in SN 2019ehk are typical of canonical CaSTs (e.g., 2005E-like) and indicate a similar chemical composition to be expected for an object within the class.

We track the expansion velocity of different ions through modeling of P-Cygni and pure emission line profiles. We estimate the photospheric velocities of various ions from first detection of spectral line formation at -9d to the last pre-nebular spectrum taken at +59d relative to the second $B-$band peak. At -9d, the fastest moving ions in the SN ejecta is Si II at -11700 ± 250 km s^{-1} and Ca II at -10400 ± 300 km s^{-1}; this is measured from the fitted minimum of the λ6355 absorption profile. These profiles, including O I and He I,

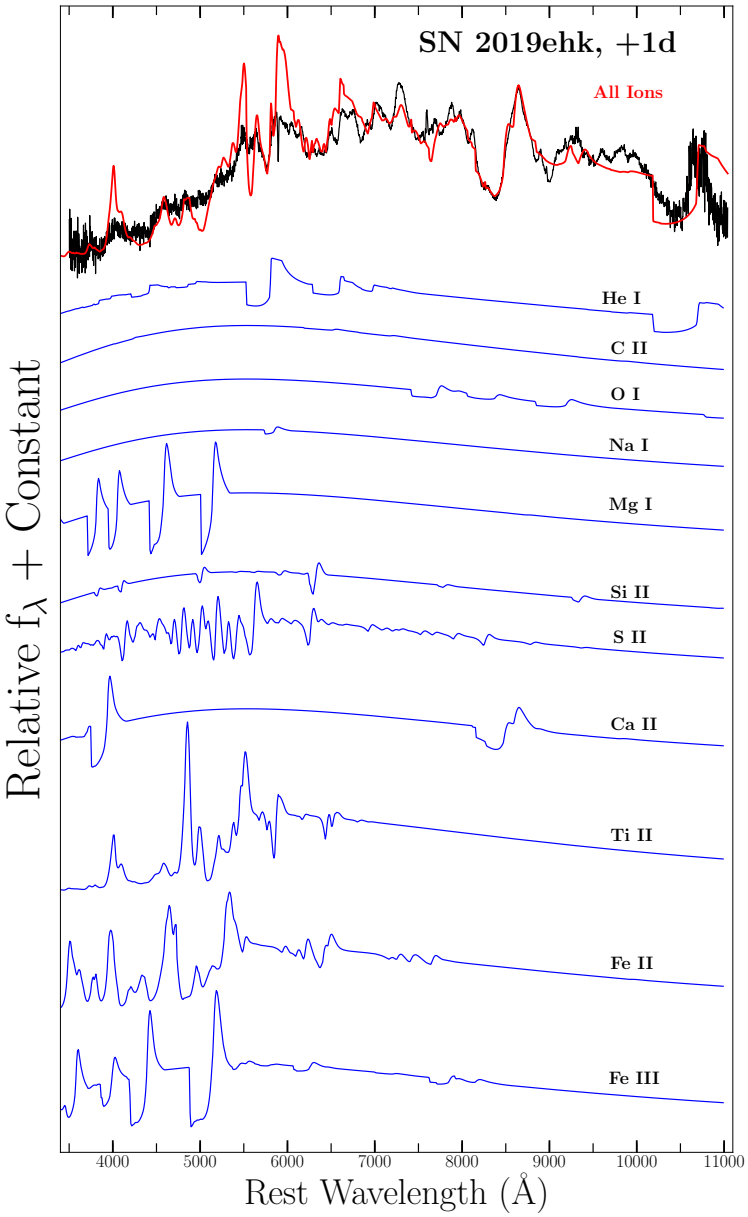

Figure 2.13 Decomposition of active ions in `SYNAPPS` fit. Phase relative to second B-band maximum. Total fit is shown in red, while blue lines mark each individual ion's contribution.

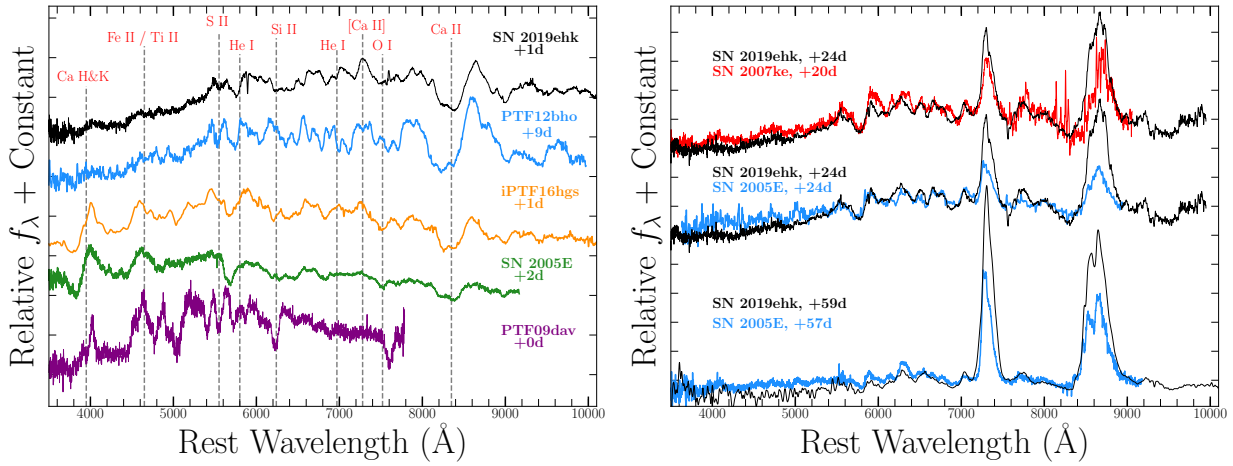

(a) (b)

Figure 2.14 (a) Spectral comparison of SN 2019ehk (black) and other CaSTs at approximately the same phase (Perets et al. 2010b; Sullivan et al. 2011; Lunnan et al. 2017; De et al. 2018b). Common ions are marked by grey lines. (b) Direct spectral comparison of SN 2019ehk (black) and CaSTs SNe 2007ke and 2005E at approximately the same phase (Perets et al. 2010b; Lunnan et al. 2017). Almost every line transition is matched between spectra, with SN 2019ehk showing stronger Ca II emission than both other objects.

show similar declines in velocity as the SN expands and becomes optically thin. We also measure Ca II and [Ca II] velocities from the FWHM of the λ8542 and λ7291 profiles, which remain approximately constant out to nebular times at ~ 9000 km s^{-1} and ~ 6000 km s^{-1}, respectively.

In the +38d NIR/IR spectrum of SN 2019ehk (Fig. 2.5), we identify similar ions to those found in our optical spectral modeling: He I, C I, Mg I and Ca II. We present the velocity profiles of He I $\lambda\lambda$10850, 20587 in Figure 2.6. Both IR He I lines have identical P-Cygni line profiles, with λ10850 showing a strong emission component and faster absorption minimum. The FWHM of the λ10850 line is 7036 km s^{-1} and the λ20587 line is 5700 km s^{-1}.

We present early-time spectral comparisons of SN 2019ehk and other CaSTs in Figure 2.14. Near (second) maximum light, SN 2019ehk is most similar visually to PTF12bho (Lunnan et al. 2017) and iPTF16hgs (De et al. 2018b). All three objects have strong Ca II absorption, prominent He I profiles and the fast emergence of a [Ca II] profile relative to peak. SN 2019ehk and PTF12hbo both show little bluewards flux from Fe-group elements, which is unlike the prominent Fe-group transitions seen in iPTF16hgs, SN 2005E (Perets et al. 2010a) and PTF09dav (Sullivan et al. 2011). This may indicate either a low total Nickel mass (typical for these objects) or variation in the mixing of Fe-group elements in the outer layers of SN ejecta. This process can then result in the suppression of bluewards flux.

As shown in Figure 2.14(b), SN 2019ehk is nearly identical to SNe 2007ke and 2005E near +24 days after second maximum light. These pre-nebular spectra are dominated by [Ca II]

and Ca II emission but are not yet optically thin given the observed P-Cygni profiles of He I and Ca II. Nonetheless, the prominence of [Ca II] emission at such an early phase indicates a rapid evolution towards the nebular regime and low enough ejecta densities to allow for efficient cooling through forbidden transitions. Furthermore, we compare nebular spectra of the majority of CaSTs to SN 2019ehk in Figure 2.15. Similar to all other CaSTs, there is no detectable emission from Fe-group elements in the bluewards spectrum; the majority of the observed flux being in [Ca II] emission, which shows no apparent [Ni II] λ7378 line blending.

A common CaST classifier is a [Ca II]/[O I] line flux ratio greater than 2. We show the evolution of this ratio, in addition to a direct comparison of [O I] to [Ca II] lines in Figure 4.13. As seen in 4.13(a), even after reddening corrections, SN 2019ehk has the highest observed [Ca II]/[O I] ratio of any known CaST at $t < 150$ days. This indicates that SN 2019ehk is not only more O-poor than most CaSTs, but it also has the fastest observed evolution to the optically thin regime. A quantitative discussion of elemental abundances in SN 2019ehk is presented in §4.6.2.

While the spectral characteristics of SN 2019ehk appear to confidently place it within the CaST class, we explore the similarities between this SN and SNe Ib/IIb. As shown in Figure 2.11(b), SN 2019ehk, like other CaSTs, has similar spectral features to SNe Ib 2008D near peak such as detectable He I and Si II profiles and strong Ca II absorption. Compared to SNe IIb, the most apparent difference is the lack of a P-Cygni Hα and Hβ profiles in SN 2019ehk, which only showed narrow Hα emission within $\sim$2 days of explosion. This suggests a H-rich CSM in SN 2019ehk while the broad Hα profiles in SNe IIb are indicative of H attached to an expanding photosphere. Finally, the line velocities in SN 2019ehk are slower overall than the photospheric velocities observed in SNe Ib and IIb: He I velocity is $\sim$6500 km s^{-1} in SN 2019ehk, $\sim$9000 km s^{-1} in iPTF13bvn and $\sim$7100 km s^{-1} in SN 2011dh. These spectral differences may indicate that SN 2019ehk is the result of a different explosion scenario than these core-collapse SNe, but does not necessarily rule out a massive star progenitor.

2.7.2 Inferences from "Flash-Ionized" H+He Spectral Lines at $t <$ 3 days

The earliest spectrum obtained -11.9 days before second B-band maximum (1.45d since explosion) shows narrow Hα and He II λ4686 emission lines with width of $\sim$500 km s^{-1}. The observed velocities are greater than the spectral resolution of the Kast spectrograph ($\lesssim$ 100 km s^{-1}) used to detect this spectral features. These lines are partially detected in the spectrum acquired on day -11.1, but not on day -10.8 (2.3 and 2.6 days since explosion, respectively) (Figure 2.17). Furthermore, we visually identify potential narrow He I emission near λ6678 in the earliest spectrum with a $\sim 1\sigma$ detection confidence. We present its velocity profile for reference in Figure 2.17 and note that, if real, the species is below the 3σ detection threshold. Accounting for the brightening of the underlying continuum we conclude that there is evidence for fading of Hα and He II line flux by a factor $\geq$2 at 3σ c.l. between the second and third epoch. These emission profiles are similar to those found in young

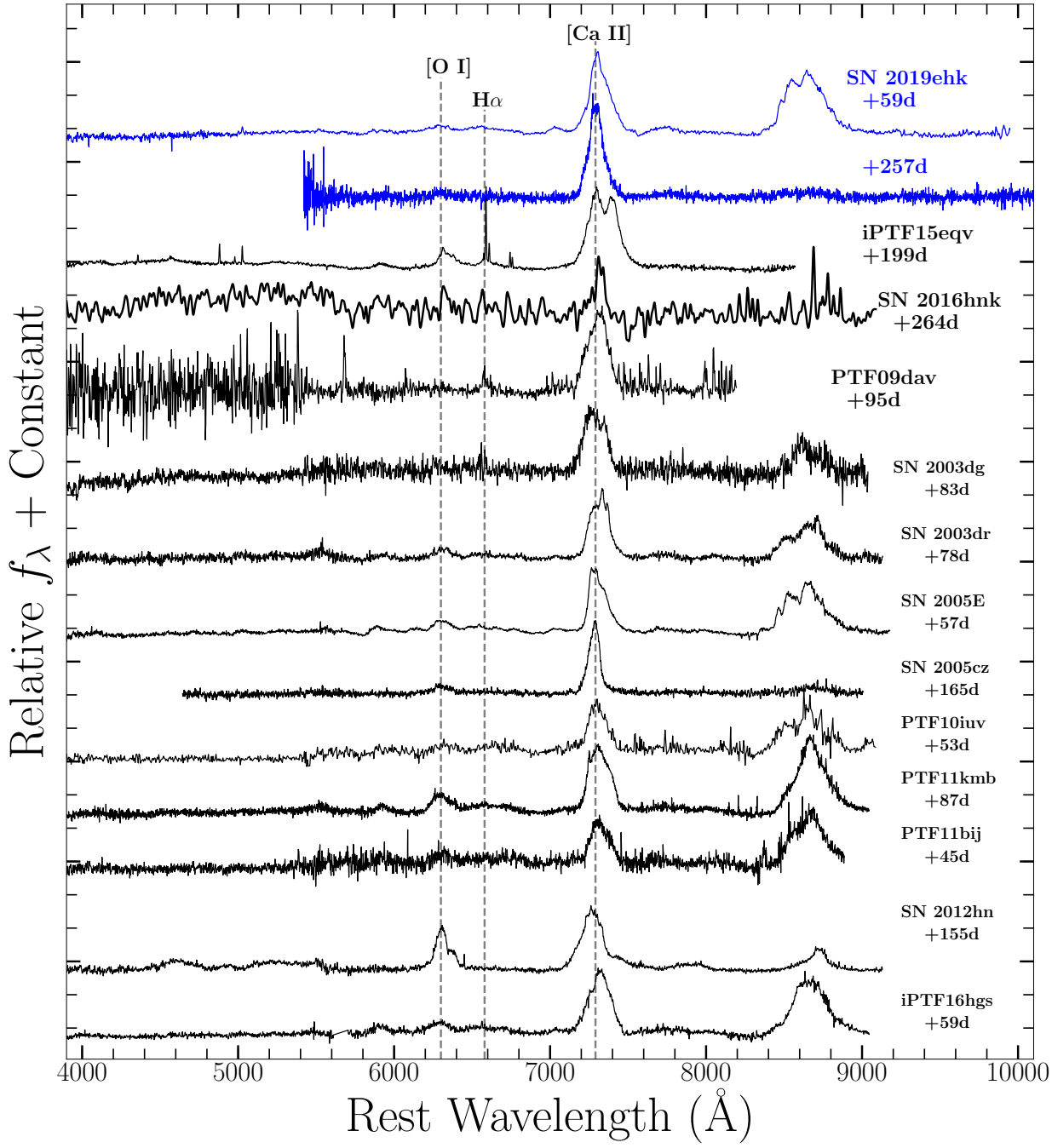

Figure 2.15 Nebular spectra of all classified CaSTs. Pre-nebular (+59d) and fully nebular (+257d) spectra of SN 2019ehk shown in blue. Prominent [O I] and [Ca II] lines as well as Hα marked by dashed grey lines.

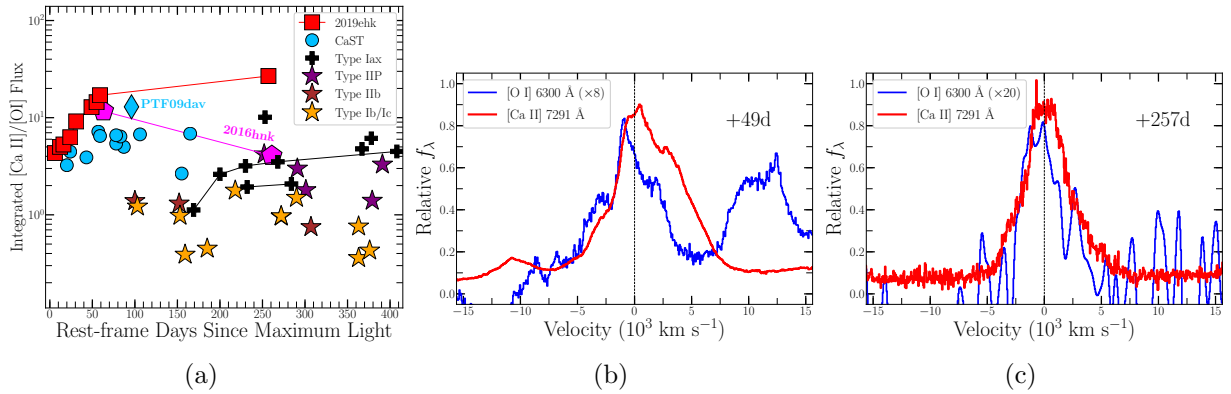

(a) (b) (c)

Figure 2.16 (a) Ratio of integrated [Ca II] and [O I] flux with respect to phase for SN 2019ehk, PTF09dav, SN 2016hnk, CaSTs SNe Iax and assorted types of core-collapse SNe. [Ca II]/[O I] values for all Type II/Ibc objects from Milisavljevic et al. (2017). (b)/(c) Velocity profiles of [Ca II] $\lambda\lambda$ 7291,7324 (red) and scaled [O I] $\lambda\lambda$ 6300, 6364 (blue) in SN 2019ehk at +49d and +257d post second maximum light.

core-collapse SNe and are thought to form from "flash" or shock-ionized CSM surrounding the progenitor star (Gal-Yam et al. 2014; Kochanek 2019).

The line width of $\sim$500 km s^{-1} (Figure 2.17), significantly lower than the velocity of material in the explosion's photosphere (§8.4.2), indicates that the emission arises from CSM produced via mass-loss *before* the explosion (as opposed to originating in the explosion's ejecta). The detection of H and He emission lines with these properties thus establishes the presence of H and He-rich CSM around SN 2019ehk. The time of their disappearance and relative luminosity enable inferences on the location of the CSM and its chemical composition, as we detail below.

The Hα and He II λ4686 luminosities of 2.0×10^{38} and 3.1×10^{38} erg s^{-1}, respectively, measured at 1.45 days since explosion imply $n_{\rm He++}/n_{\rm H+} = 0.44$ assuming Case B recombination (Hummer & Storey 1987). The luminosity limit of the He I λ7065 line $< 4.0 \times 10^{37}$ erg s^{-1} can be used to infer an upper limit on the amount of He$^+$ using recombination rates from Benjamin et al. (1999), so that we find

$$0.44 < n_{\rm He}/n_{\rm H} < 0.88 \tag{2.2}$$

implying partial burning of hydrogen.

The SN shock break out radiation cannot be responsible for the ionization of the CSM at $t \geq 1.4$ days, as the recombination timescale for H+ and He++ is $t_{\rm rec} \propto 1/n_e$ and $t_{\rm rec} \leq$ a few hours for gas temperatures $\sim 10^5 - 10^6$ K and free electron densities $n_e \geq 10^8$ cm^{-3} (e.g. Lundqvist & Fransson 1996). The source of ionizing radiation can be provided by the luminous X-ray emission (Fig. 4.5) that resulted from the SN shock interaction with the CSM (§2.9.1). In this scenario the fading of the H and He recombination lines is related to the time when the SN shock overtakes the CSM shell. We infer an outer CSM shell radius

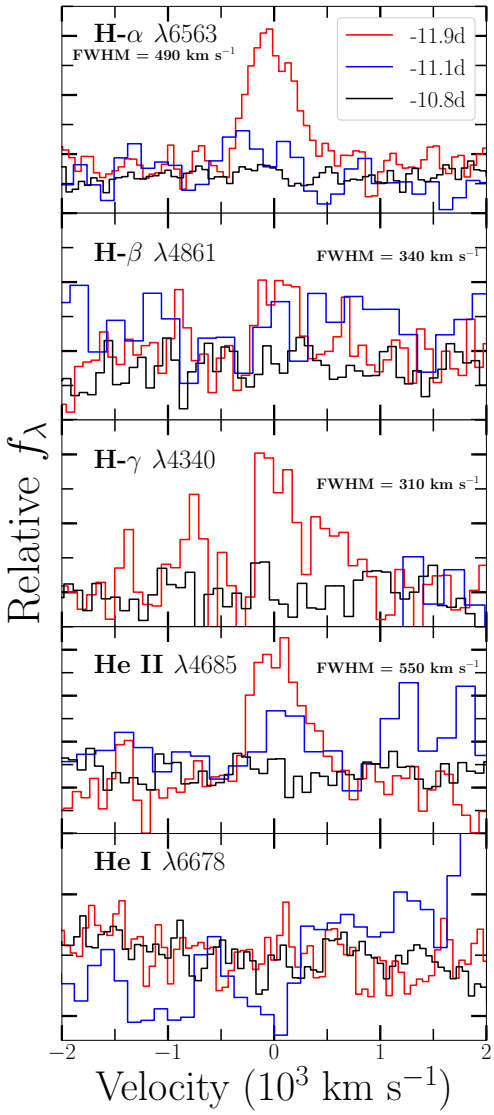

Figure 2.17 Velocity profiles of "flash-ionized" H Balmer series and He II lines in the first three epochs of spectroscopic observations. He I λ6678 is shown in the bottom panel for reference. Phases presented are relative to the second B-band maximum with the red, blue and black lines at -11.9, -11.1 and -10.8 days, respectively, corresponding to 1.45, 2.33, and 2.55 days since explosion. These observations indicate the presence of pre-explosion CSM composed of H- and He-rich material moving with velocities of $\sim$400 km s^{-1} and $\sim$500 km s^{-1}, respectively.

$r \leq 10^{15}$ cm, for the SN shock to reach it in ∼2 days (for a typical shock velocity ∼0.1c), and an emission measure $EM \approx 4 \times 10^{63}$ cm^{-3} to account for the observed recombination line luminosities at 1.45 days after explosion. From these inferences we derive a CSM density[10] $n \approx 10^{9}$ cm^{-3} and a CSM shell mass of $M_{\rm CSM} \approx 2 \times 10^{-3}$ M$_{\odot}$ assuming a spherical shell ($R_{\rm CSM} = 10^{15}$cm) and unity filling factor. Note that the filling factor cannot be less than about 0.3 without reducing the ionization parameter to less than 30 and producing too much He I emission. Based on the abundance by number shown in Eqn. 2.2, we estimate a CSM H mass in the range $(1.2 - 4.8) \times 10^{-4}$ M$_{\odot}$ and a He mass of $(1.5 - 1.9) \times 10^{-3}$ M$_{\odot}$.

We end by noting that for these physical parameters, the resulting ionization parameter $\xi = L_{\rm ion}/nr^2$ (where $L_{\rm ion}$ is supplied by the X-ray luminosity) has values intermediate between those needed to doubly ionize helium (as observed), but lower than those necessary to produce high ionization lines such as [Fe X], which are not seen in the spectra of SN 2019ehk (but detected in other SNe with CSM interaction, e.g., SN2014C, Milisavljevic et al. 2015).

2.7.3 Inferences from Nebular Phase Spectroscopy at $t \geq 30$ days

Table 2.2 lists the emission line luminosities measured from spectra acquired on 31, 38 and 59 days since second B-band maximum. Recombination lines of He I, C I, O I and Mg I are detected, along with forbidden lines of [O I] and [Ca II] and permitted lines of Ca II, while we consider the possible Hα feature to be an upper limit. Uncertainties in the underlying continuum and the wavelength ranges of some of the lines cause up to factor of ∼2 errors in the inferred luminosities, especially for lines that show prominent P-Cygni profiles. With this caveat in mind, we find that the ratios of He I line fluxes approximately agree with those predicted with the atomic rates of Benjamin et al. (1999) for densities up to $\sim 10^{10}$ cm^{-3} at a temperature of $\sim 10^{4}$ K.

The inferred blackbody radius at ∼59 days after second B-band maximum (∼72 days since explosion) is $\sim 1.5 \times 10^{15}$ cm (Figure 2.12). The maximum velocity shift of the [Ca II] emission feature is $v_{\rm [Ca\,II]} \approx 5000$ km s^{-1}, corresponding to a radius of $v_{\rm [Ca\,II]} \times t \approx 3.2 \times 10^{15}$ cm. The nebular emission is produced between those radii, so we take the volume to be about 1.1×10^{47} cm^{3}. The observed He I line luminosities and inferred volume require $n_e\ n_{\rm He\,II} \approx 10^{16}$ cm^{-6} at 59 days since second B-maximum. We note that the He I λ7065 line is stronger than expected, probably because of repeated scatterings that convert He I λ3889 photons into emission at λ7065. This scenario is supported by the prominent P-Cygni profiles of the He I NIR lines, which indicate large optical depths and a substantial population of the 1s2s ^{3}S metastable level.

The relative luminosities and recombination rates from Hummer & Storey (1987) and Julienne et al. (1974) imply number density ratios $n_{\rm HII}/n_{\rm He\,II} \leq 1.3$ and $n_{\rm O\,II}/n_{\rm He\,II} = 1.5$. If no other elements contribute significant numbers of free electrons, the densities of electrons, He^{+}, H^{+} and O^{+} are 3.8, 1.0, <1.3 and 1.5×10^{8} cm^{-3}, respectively. If carbon contributes free electrons, n_e will be correspondingly higher and the densities of the ions correspondingly

[10]Note that this is the density of the unshocked CSM gas illuminated and ionized by the X-ray emission from the SN shock.

lower. The limit on the ratio of He^+ to H^+ is similar to the He/H ratio derived for the CSM (§2.7.2), so H:He:O ratio may be similar to the values above.

At densities above 10^7 cm^{-3}, the [O I] and [Ca II] lines are in their high density limits, and their luminosities are given by the populations of the excited states multiplied by the Einstein A values:

$$L_{[\mathrm{O\,I}]} = n_{\mathrm{O\,I}}\ A_{[\mathrm{O\,I}]}\ h\nu_{[\mathrm{O\,I}]}\ (5/14)\ e^{-22000/T} \tag{2.3}$$

$$L_{[\mathrm{Ca\,II}]} = n_{\mathrm{Ca\,II}}\ A_{[\mathrm{Ca\,II}]}\ h\nu_{[\mathrm{Ca\,II}]}\ (10/11)\ e^{-19700/T} \tag{2.4}$$

where hν is the photon energy, the exponentials are the Boltzmann factors (T is in K) and the numerical factors are statistical weights. The observed luminosities of the [Ca II] lines are much higher than the [O I] luminosities ($L_{[\mathrm{Ca\,II}]}/L_{[\mathrm{O\,I}]} \approx 25$ at 257 days since second B-band maximum, Figure 4.13). From Eqn. 2.3-2.4:

$$\frac{L_{[\mathrm{Ca\,II}]}}{L_{[\mathrm{O\,I}]}} = \frac{28}{11}\frac{n_{\mathrm{Ca\,II}}}{n_{\mathrm{O\,I}}}\frac{A_{[\mathrm{Ca\,II}]}}{A_{[\mathrm{O\,I}]}}\frac{\nu_{[\mathrm{Ca\,II}]}}{\nu_{[\mathrm{O\,I}]}}e^{2300/T} \approx\ 1100\frac{n_{\mathrm{Ca\,II}}}{n_{\mathrm{O\,I}}} \tag{2.5}$$

where we used $T = 10^4$ K, $A_{[\mathrm{Ca\,II}]} = 2.6\,\mathrm{s}^{-1}$ and $A_{[\mathrm{Ca\,II}]} \approx 390 A_{[\mathrm{O\,I}]}$. We thus infer $\frac{n_{\mathrm{O\,I}}}{n_{\mathrm{Ca\,II}}} \approx 30$. Since there is a strong overlap of the temperature and ionization parameter ranges where O I and Ca II exist, we expect $\frac{n_{\mathrm{OI}}}{n_{\mathrm{CaII}}} \approx \frac{n_{\mathrm{O}}}{n_{\mathrm{Ca}}}$, implying that, as in iPTF15eqv (Milisavljevic et al. 2017), the prominent Ca lines result from the density and ionization state of the ejecta rather than an overabundance of Ca with respect to O. We note that the [O I] and [Ca II] lines are likely to arise from a region of lower electron density than the recombination lines, because the forbidden lines are strongly suppressed at densities above 10^8 cm^{-3}, leading to higher ratios of the λ8600 calcium triplet to the [Ca II] lines than are observed. The Ca II feature at λ11873 is much stronger than expected for optically thin emission, even if the 4s-5p lines from the ground state are converted to λ11873 through multiple scatterings. It is possible that the He II λ1640 line pumps the 4s-5p transition, since the separation is about 1700 km s^{-1}. If so, the He II line is formed by recombination, and this would be the only indication of doubly ionized helium in the nebular gas.

Assuming temperatures of $\sim 10^4$ K for the recombination lines and 5000 K for the forbidden lines, the densities and volume yield rough mass estimates from the day +59 spectrum (from second B-band max) of 0.008, 0.037, 0.10 and 0.004 $M_\odot$ for He^+, O^+, O^0 and Ca^+, respectively. It should be noted that at these phases the SN is not fully nebular and therefore the derived masses may be lower than the true elemental masses in the explosion.

2.8 The optical "Flare"

Here we describe the observational properties of the first light curve peak and present physical models that can explain this initial increase in total flux. In an effort to be succinct, we hereafter refer to this primary light curve evolution as the "flare." In this section, all times are referred with respect to the explosion.

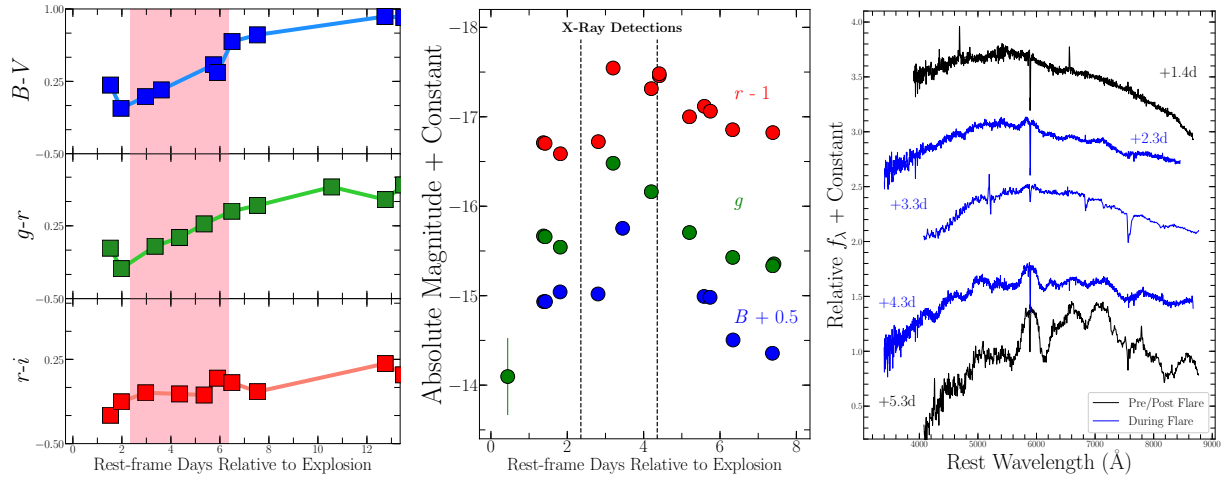

(a) (b) (c)

Figure 2.18 (a) Highlighted by the pink shaded region are extinction corrected colors in SN 2019ehk during the optical "flare." This color evolution indicates that the flare was quite blue as the colors do not become redder until after the first light curve peak. (b) *Bgr*-band, extinction corrected photometry during the flare with the times of the X-ray detections from *Swift*-XRT shown as vertical black dashed lines. (c) Spectral evolution during the flare shown in blue, with observations before and after presented in black. The peak of the flare occurs at +3.3 days with respect to explosion, which has an observed increase in optical flux as shown in the spectrum. Following the flare, regions of line formation in the photosphere emerge in the spectra and known ions can be more easily identified.

2.8.1 Observational Properties

The flare is observed across all UV, optical and NIR photometric bands from the first $g-$band detection at 0.44 days until $\sim$7 days after explosion. We present SN 2019ehk's color, photometric and spectral evolution during the flare in Figure 2.18. We observe an initial rise in $g-$band flux from 0.44-1.38 days and then seemingly constant flux between 1.38 and 2.81 days. However, in some photometric bands (e.g., $gVri$) the flux in this phase range appears to be decreasing. This indicates that there could be 2 separate peaks within the flare or possibly separate emission mechanisms at these early-times. Then, as shown in Figure 2.18(b), the most dramatic flux increase occurs in < 1 day and peaks at $t_p = 3.2 \pm 0.1$ days. This is reflected by a $\sim$1 mag flux increase in all photometric bands. During the early rise, the flare spectrum is blue and mostly featureless, with transient H and He recombination lines that soon subside (§2.7.2). Clear photospheric spectral features (e.g., Si II, O I, Ca II) first appear after the flare's peak at $t \approx 3$ days after explosion (Figure 2.18c).

We present SN 2019ehk's blackbody radius $R(t)$, temperature $T(t)$ and resulting bolometric luminosity evolution during the flare in Figure 2.19 (shown as squares). As discussed in §4.5.2, at $t \lesssim 5$ days the blackbody SED peak lies in the mid-UV, outside the range covered by our complete photometric dataset. At these times the data provide lower limits on the blackbody temperature and upper limits on the radius, which results in a lower limit on the true bolometric luminosity (arrows in Figure 2.19). The bolometric light curve at $t < 3$ days was likely dominated by UV radiation and decreased rapidly from a peak luminosity potentially larger than $L_{\rm bol}(t_p) \approx 10^{42}$ erg s^{-1} shown in Figure 2.19 with red squares.

A reasonable assumption for stellar explosions at early times is that of a photosphere expanding homologously in time (e.g., Liu et al. 2018). Here we make the simplistic assumption of a linear evolution of the photospheric radius with time, $R(t) = R_e + v_e * t \approx v_e * t$, where we take $v_e \approx 12000$ km s^{-1}, similar to the velocities observed in the first photospheric spectra and R_e is the initial envelope radius (black dotted line in Fig. 2.19, lower panel). Interestingly, the resulting $R(t)$ matches the photospheric radius at $t \geq 5$ days. Freezing the blackbody radius to the values implied by the linear evolution with time in our blackbody fits leads to larger inferred temperatures, as expected (Fig. 2.19, middle panel). The resulting bolometric luminosity is also consequently larger (Fig. 2.19, upper panel). While we consider these estimates to lead to a more realistic bolometric output at early times, we caution that the assumption of a linearly increasing photospheric radius is likely an over-simplification and that accelerated expansion could have a significant influence on the very early-time SN evolution.

2.8.2 Nickel Powered Model

A possible power source for the flare emission is the radioactive decay of an amount of ^{56}Ni that was heavily mixed into the outer layers of ejecta. This ^{56}Ni mass is distinct from the centrally located ^{56}Ni that is responsible for the main SN optical peak. As discussed

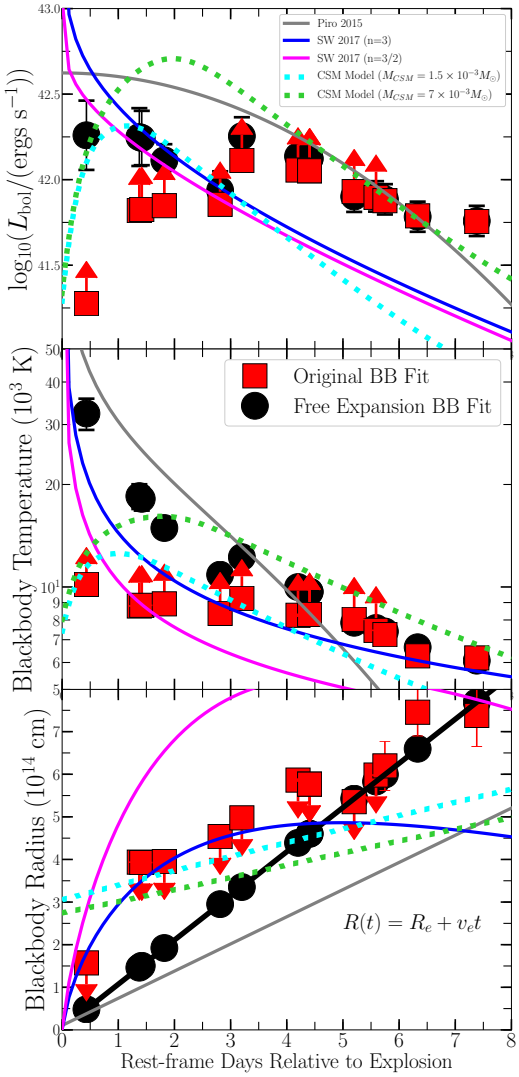

Figure 2.19 *Top:* Inferred bolometric luminosity during the flare presented as red squares and black dots (fixed blackbody radius). Shock interaction models for different CSM masses are plotted in green and cyan dashed lines (see §2.8.4). Shock cooling models are plotted as solid lines: Piro (2015) in grey, Sapir & Waxman (2017) n = 3/2[3] in pink[blue]. *Middle:* Lower limits and more realistic estimates of the blackbody temperature during the flare. For the interaction model we show the effective blackbody temperature. *Bottom:* Upper limits and more realistic estimate of the blackbody radius assuming a linear increase of the photospheric radius with time ($v_e \approx 12,000$ km s^{-1}). The shock interaction model presents the radius of the emitting region.

in De et al. (2018b) for iPTF16hgs, this distribution of ^{56}Ni could result in two distinct light curve peaks, each powered by its own supply of ^{56}Ni (e.g., see also Drout et al. 2016). We test the validity of this model for SN 2019ehk by applying the same analytic model for a radioactively powered light curve as that presented in §4.5.2. We find $E_{\rm k} \approx 10^{47}$ ergs and $M_{\rm Ni} \approx 3 \times 10^{-2}$ M$_\odot$. A total ejecta mass of $M_{\rm ej} \approx 10^{-4}$ M$_\odot$ is estimated using $v_{\rm ph} \approx 12000$ km s^{-1}, which is derived from Si II absorption near the peak of the flare.

This model both produces a poor fit to the flare's bolometric luminosity as well as results in a $M_{\rm Ni}/M_{\rm ej}$ ratio greater than 1, which is clearly unphysical. Furthermore, this model is disfavored because it does not naturally explain the presence of early-time X-ray emission. If an exterior plume of ^{56}Ni is the power-source behind the flare, an additional, independent ingredient would need to be invoked to explain the X-rays, which would have occurred coincidentally at the same time as the optical flare, but would otherwise have no physical connection to the flare. More natural scenarios are those where the optical flare and the X-ray emission are different manifestations in the electromagnetic spectrum of the same physical process (§2.8.3, §2.8.4).

2.8.3 Shock Breakout and Envelope Cooling Model

It is now understood that shock breakout through an extended distribution of material (e.g., stellar envelope) can increase the SN flux above the typical radioactively powered continuum emission. The resulting observational signature is a double-peaked light curve where the first peak originates from the expansion and cooling of the shocked envelope, followed by the standard SN peak of emission. This is typically observed in SNe IIb (e.g., SNe 1993J, 2011dh and 2016gkg; Wheeler et al. 1993; Arcavi et al. 2011, 2017a; Piro et al. 2017) and numerous models have been put forward to explain this observational signature with breakout and cooling emission into an expanding envelope (Nakar & Piro 2014; Piro 2015; Sapir & Waxman 2017).

As discussed in §4.7.1, the light curve exhibits nearly constant flux at $t < 2.5$ days before the dramatic rise and decline in magnitude from $3 < t < 6$ days. Furthermore, as illustrated by the magenta and grey dotted lines in Figure 2.20, H and He emission lines persist in SN 2019ehk spectra until $t \approx 2.5$ days and fade in visibility when the primary peak of the flare occurs at $t \approx 3$ days. These observational signatures suggest separate emission components within the flare: one that allows for H + He spectral emission in addition to unremitting flux ($t < 2$ days), and one that induces a substantial rise in flux without "flash-ionized" spectral lines ($2 < t < 6$ days). Consequently, we choose to model each of the observationally distinct regimes within the flare separately.

In the following sections, we describe and apply three models for a shock cooling emission mechanism to explain the entire evolution of the optical flare in SN 2019ehk. At the time of explosion, each model produces constraints on the envelope mass, M_e, envelope radius, R_e, the velocity of the shock or envelope, v_e and the time offset from explosion t_o (consistent with our explosion time estimate). In this analysis, we use `emcee`, a Python-based application of an affine invariant MCMC with an ensemble sampler (Foreman-Mackey et al. 2013). We

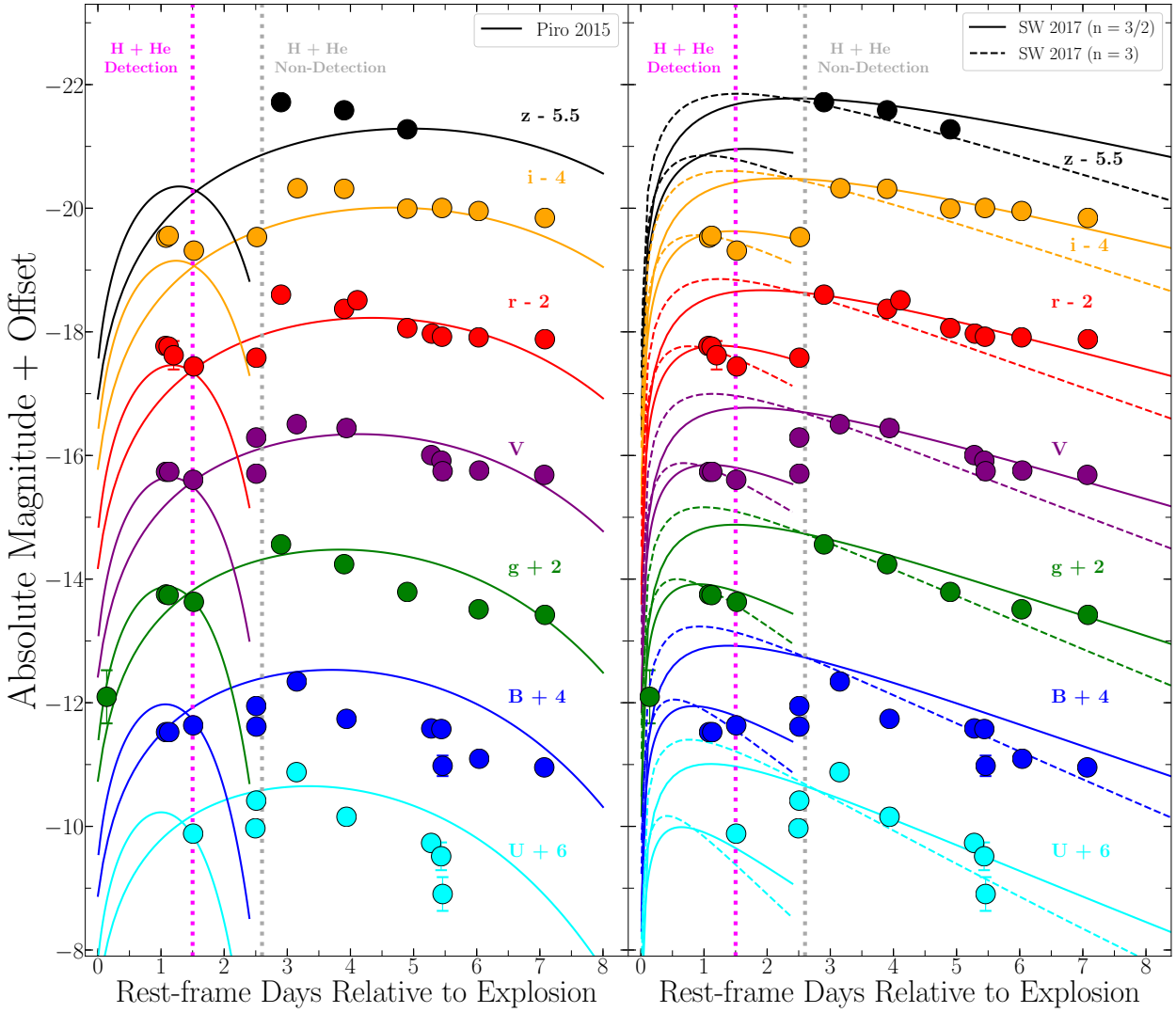

Figure 2.20 Multi-color shock cooling model fits to the flare assuming a blackbody SED. *Left:* Piro (2015) models are presented as solid lines with the phases of "flash-ionized" H and He detection and non-detection presented as dotted magenta and grey lines, respectively. *Right:* Sapir & Waxman (2017) models shown as dashed (n=3) and solid (n=3/2) lines. We model the flare in two components due to temporal variability at $t < 2$ days. Model specifics are discussed in §2.8.3 and physical parameters are presented in Table 4.12.

compile the best fit parameter estimates from each model in Table 4.12. While in §2.8.3 we model the flare emission with two cooling-envelope components, we note that the presence of H and He emission in the first flare component requires a persistent source of ionizing radiation that might not be provided by pure cooling-envelope models, which motivates our investigation of models that also include ongoing CSM interaction in §2.8.4

2.8.3.1 Nakar & Piro (2014) Model

Nakar & Piro (2014) present scaling relations for "non-standard" core-collapse SN progenitors with compact cores surrounded by extended envelopes. By showing that the peak of the optical flux will occur when the mass depth (i.e., photon diffusion distance within mass) is equal to the envelope mass (M_e), they construct the following analytic expression for M_e:

$$M_e \approx 5 \times 10^{-3} \kappa_{0.34}^{-1} \left(\frac{v_e}{10^9 \text{ cm s}^{-1}} \right) \left(\frac{t_p}{1 \text{ day}} \right)^2 \text{M}_\odot \tag{2.6}$$

where v_e is the expansion velocity of the extended envelope, t_p is the time to first light curve peak and the opacity is $\kappa_{0.34} = \kappa / 0.34$ cm^2 g^{-1}. As discussed in §2.8.3, it is likely that the flare is the product of separate emission mechanisms, each occurring on different timescales. As a result, we apply the Nakar & Piro (2014) model to each "peak" within the flare at times $t_{p1} = 0.44 \pm 0.10$ and $t_{p2} = 3.2 \pm 0.10$ days. We estimate an envelope velocity of $\sim 1.2 \times 10^9$ cm s^{-1} from the absorption minimum of the He I λ5976 transition, which is the first detectable spectral feature to appear at 2.2 ± 0.10 days after explosion.

Furthermore, from Nakar & Piro (2014), the envelope radius can be expressed as:

$$R_e = 2 \times 10^{13} \kappa_{0.34} L_{43} \left(\frac{v_e}{10^9 \text{ cm s}^{-1}} \right)^{-2} \text{cm} \tag{2.7}$$

where $L_{43} = L_{bol}(t_p)/10^{43}$ erg s^{-1}. At $t_{p1} = 0.44 \pm 0.10$ days and $t_{p2} = 3.2 \pm 0.10$ days, we calculate peak bolometric luminosities of $L_{bol}(t_{p1}) = 1.8 \pm 0.9 \times 10^{42}$ and $L_{bol}(t_{p2}) = 1.8 \pm 0.10 \times 10^{42}$ erg s^{-1}, respectively. They also predict the observed temperature at t_p as:

$$T_{\text{obs}}(t_p) \approx 3 \times 10^4 \kappa_{0.34}^{-0.25} \left(\frac{R_e}{10^{13} \text{ cm}} \right)^{0.25} \left(\frac{t_p}{1 \text{ day}} \right)^{-0.5} \text{K} \tag{2.8}$$

Using this expression for t_{p1} and t_{p2}, we calculate observed flare temperatures of $2.5 \pm 0.30 \times 10^4$ and $1.7 \pm 0.90 \times 10^4$ K, respectively; both of which are consistent with derived blackbody temperatures at the same phase as shown in Figure 2.19. Overall, we caution against the accuracy of these model outputs due to uncertainties surrounding the bolometric luminosities at $t < 6$ days. As discussed in §4.5.2, we can only place solid constraints on upper and lower limits on the blackbody radii and temperature during the flare, which then affect the bolometric luminosity at those times. Thus the M_e and R_e values derived from the Nakar & Piro (2014) models should be treated as lower limits given the uncertainty on each

peak luminosity. For the main peak of the flare and opacity $\kappa = 0.2$ cm^2 g^{-1}, we estimate an envelope mass of $M_e \approx 0.1$ M$_\odot$ and radius of $R_e \approx 100$ R$_\odot$.

2.8.3.2 Piro (2015) Model

Starting from the scaling relations at t_p from Nakar & Piro (2014), Piro (2015) presents a generalized analytic model that allows a direct, detailed comparison to the observed flux evolution with time. The SN shock is assumed to propagate into extended material of mass M_e of unknown chemical composition surrounding the progenitor star core with mass M_c. This is a one-zone model that does not include a prescription for the density profile, gradient or chemical composition of the extended material. Following Piro (2015) the expansion velocity v_e and the energy E_e passed into the extended material read:

$$v_e \approx (2 \times 10^9) E_{51}^{0.5} \left(\frac{M_c}{\mathrm{M}_\odot}\right)^{-0.35} \left(\frac{M_e}{0.01\mathrm{M}_\odot}\right)^{-0.15} \mathrm{cm\ s^{-1}} \tag{2.9}$$

$$E_e \approx (4 \times 10^{49}) E_{51} \left(\frac{M_c}{\mathrm{M}_\odot}\right)^{-0.7} \left(\frac{M_e}{0.01\mathrm{M}_\odot}\right)^{0.7} \mathrm{erg} \tag{2.10}$$

where $E_{51} = E_{SN}/10^{51}$erg. Piro (2015) show that the shocked extended material will expand (with characteristic radius $R(t) = R_e + v_e\, t$) and cool, with an observed peak of emission occurring at time t_p:

$$t_p \approx 0.9 \kappa_{0.34}^{0.5} E_{51}^{-0.25} \left(\frac{M_c}{\mathrm{M}_\odot}\right)^{0.17} \left(\frac{M_e}{0.01\mathrm{M}_\odot}\right)^{0.57} \mathrm{day} \tag{2.11}$$

In their Eqn. 15, Piro (2015) present a predicted bolometric luminosity from shock cooling as:

$$L(t) = \frac{t_e E_e}{t_p^2} \exp\left[\frac{-t(t+2t_e)}{2t_p^2}\right] \tag{2.12}$$

where $t_e = R_e/v_e$.

Following Arcavi et al. (2017a) and Piro (2015), we model the emission from the extended mass as a blackbody spectrum with radius $R(t) = R_e + v_e t$ and temperature:

$$T(t) = \left[\frac{L(t)}{4\pi\sigma_{\mathrm{SB}} R^2(t)}\right]^{1/4} \tag{2.13}$$

We calculate the expected apparent magnitudes for individual photometric bands from this model using the `pysynphot` Python package and we fit these models to the (extinction-corrected) apparent magnitudes of SN 2019ehk in $uBVgriz$ bands at $t < 6$ days. As before, we fit the data at $t < 2$d and $t < 6$ days as two separate components. For all models we adopt $E_{SN} = 1.8 \times 10^{50}$ erg, $\kappa = 0.2$ cm^2 g^{-1} and $M_c = 1$ M$_\odot$ (§4.5.2). It should be noted that the chosen core mass M_c has little impact on the final inferred parameters. We present all multi-color light curve fits using these models as the solid lines in Figure 2.20. As shown in

the plot, this simplified model provides a reasonable match to the data for both components of the flare. The best fitting values for both components are reported in Table 4.12.

2.8.3.3 Sapir & Waxman (2017) Model

Sapir & Waxman (2017) present an updated version of the model by Rabinak & Waxman (2011), which applies to the immediate post-shock breakout evolution at $t \approx$ few days, when the emission is dominated by radiation from the external envelope layers, and extends the solutions by Rabinak & Waxman (2011) to later times, when the observed emission originates from the inner envelope layers and depends on the progenitor density profile. Sapir & Waxman (2017) adopt a progenitor structure with a polytropic hydrogen-dominated envelope, which they demonstrate numerically can power an initial light curve peak through shock cooling.

Below we present the analytic expression for the envelope's bolometric luminosity that was derived by Arcavi et al. (2017a) starting from Sapir & Waxman (2017):

$$L(t) = 1.88[1.66] \times 10^{42} \times \left(\frac{v_{s,8.5}^2 R_{13}}{\kappa_{0.34}}\right)\left(\frac{v_{s,8.5} t^2}{f_p M \kappa_{0.34}}\right)^{-0.086[-0.175]} \times \exp\left\{-\left[\frac{1.67[4.57]t}{(19.5\kappa_{0.34} M_e v_{s,8.5}^{-1})^{0.5}}\right]^{0.8[0.73]}\right\} \text{erg s}^{-1} \tag{2.14}$$

where $R_{13} \equiv R_e/10^{13}$cm, $v_{s,8.5} \equiv v_s/10^{8.5}$ cm s^{-1}, $M = M_e + M_c$ and t is in days. This model is for a polytropic index of $n = 3/2[3]$, which encompasses both stars with convective envelopes as well as radiative envelopes e.g., RSGs[BSGs], respectively. Same as for the Piro (2015) models, we adopt $M_c = 1\,\mathrm{M}_\odot$. The dimensionless scaling factor f_p from Sapir & Waxman (2017) is:

$$f_p \approx \begin{cases} (M_e/M_c)^{0.5}, & n = 3/2 \\ 0.08(M_e/M_c), & n = 3 \end{cases} \tag{2.15}$$

Finally, Arcavi et al. (2017a) present an envelope temperature derived by Sapir & Waxman (2017) to be:

$$T(t) \approx 2.05[1.96] \times 10^4 \times \left(\frac{v_{s,8.5}^2 t^2}{f_p M \kappa_{0.34}}\right)^{0.027[0.016]} \left(\frac{R_{13}^{0.25}}{\kappa_{0.34}^{0.25}}\right) t^{-0.5} \text{ K} \tag{2.16}$$

We assume a blackbody spectrum and perform the same analysis as in §2.8.3.2 to extract apparent magnitudes from the predicted luminosity and temperature. We model the flare by the same methods and present light curve fits for an $n = 3/2$ and $n = 3$ polytropes as solid and dashed lines, respectively, in Figure 2.20. We find that the first flare component at $t < 2$d can be fit accurately with our MCMC model. For the first peak within the flare, we estimate envelope radii and masses of $R_e \approx 40[30]$ R$_\odot$ and $M_e \approx 0.8[0.2]$ M$_\odot$ for n = 3[3/2] polytropes. The MCMC routine, however, does not formally converge when we attempt to fit the entire data set at $t < 6$d. In Figure 2.20 we show a representative model,

with parameter values indicated in Table 4.12. These values should be treated as order of magnitude estimates.

We end by noting that the model by Sapir & Waxman (2017) is valid for times:

$$t > 0.2 \frac{R_{13}}{v_{s,8.5}} \max\left[0.5, \frac{R_{13}^{0.4}}{(f_p \kappa_{0.34} M)^{0.2} v_{s,8.5}^{0.7}}\right] \text{days} \tag{2.17}$$

$$t < 7.4 \left(\frac{R_{13}}{\kappa_{0.34}}\right)^{0.55} \text{days} \tag{2.18}$$

We test the validity of our derived model parameters (Table 4.12) with Equations 2.17 and 2.18 and we find that our model parameters satisfy the relations above. For the first peak in the flare we find: $\sim 0 < t < 4.09$ days (n = 3/2) and $\sim 0 < t < 8.94$ days (n = 3). For the second peak we find: $\sim 0 < t < 4.31$ days (n = 3/2) and $\sim 0 < t < 9.74$ days (n = 3). All derived timescales are valid for the duration of the flare.

In the previous three subsections we have investigated a shock cooling model as a power source for the flare. Because of its temporal structure, we have modeled the flare in two components ($t < 2$ and $t < 6$ days) in order to derive physical parameters (e.g., radius, mass, velocity) of a shock heated envelope needed to match optical the optical light curve. Figure 2.20 demonstrates that modeling the entire flare with one shock cooling model cannot reproduce the observations but the corresponding radii and masses for each model represent upper limits on the total amount of shocked material capable of powering the flare.

2.8.4 CSM Interaction Model

Another potential source of energy to power the optical flare emission is via ongoing SN shock interaction with the medium. This scenario has physical similarities to that discussed in §2.8.3 with the key difference being that rather than powering this rapid light curve peak via post-breakout cooling emission, the CSM interaction model allows for continuous energy injection due to the ongoing conversion of shock kinetic energy into radiation. The presence of CSM around the SN 2019ehk progenitor is evident given the detection of flash-ionized H and He features in the first optical spectrum at 1.45 days since explosion. The estimated blackbody radius at the time of the first spectrum is $\leq 4 \times 10^{14}$cm (§4.5.2) and the velocities of H- and He-rich material are ~ 400 and 500km s^{-1}, respectively (§2.7.2). The flash-ionized CSM lies in front of the photosphere at radii $> 4 \times 10^{14}$cm. Therefore, this H+He rich material was lost by the stellar progenitor to the environment $\gtrsim 3$ months prior to explosion.

We quantitatively test the scenario of a SN shock interacting with a shell of CSM through 1D numerical radiation hydrodynamics simulations with the `CASTRO` code (Almgren et al. 2010). Equations for radiation hydrodynamics are solved using a gray flux-limited non-equilibrium diffusion approximation. The models are similar to those applied to the SN Ic-BL, 2018gep (Ho et al. 2019) and the fast-evolving luminous transient KSN 2015K (Rest et al. 2018), but have been adapted to the observables in SN 2019ehk.

Our simulations assume spherical symmetry wherein the SN ejecta expands homologously and is characterized by a broken power-law density profile ($\rho_{\rm ej} \propto r^{-n}$, with $n = 3$), ejecta mass $M_{\rm ej}$, energy E_{ej}, initial outer radius $R_{\rm ej}$, outer velocity $v_{\rm ej}$ and ejecta temperature $T_{\rm ej} = 10^4$ K. The CSM shell is assumed to have constant density and is initialized with temperature $T_{\rm csm} = 10^3$ K. We adopt a static CSM (i.e. $v_{\rm csm} = 0\,{\rm km\,s^{-1}}$) whose velocity has no affect on the model results so long as $v_{\rm csm} << v_{\rm ej}$. The shell is described physically by its mass $M_{\rm csm}$, radius $R_{\rm csm}$ and thickness $\delta R_{\rm csm}$. Once the ejecta have reached homology we use the radiative transfer code `Sedona` (Kasen et al. 2006) to generate synthetic bolometric light curves as well as the temporal evolution of the effective blackbody temperature and radius in each model. Unlike other CSM interaction codes (e.g., MOSFIT, Guillochon et al. 2018; TigerFit, Chatzopoulos et al. 2016) that use the semi-analytic Arnett approximation with a parameterized heating term, our simulations self-consistently solve for the time-dependent light curves by evolving the coupled radiation hydrodynamics equations with `CASTRO`.

From a grid of shock interaction simulations, we find that the first component of the flare is best fit by shock breakout emission into a CSM characterized by the following parameters: mass $M_{\rm csm} = 1.5 \times 10^{-3}$ M$_\odot$, radius $R_{\rm csm} = 2 \times 10^{14}$ cm, thickness $\delta R_{\rm csm} = 4 \times 10^{13}$ cm and opacity $\kappa = 0.4$ cm^2 g^{-1}. This model was initialized for a SN with $M_{\rm ej} \approx 1$ M$_\odot$, which is based on observations as constrained by our modeling of §4.5.2. This model is presented with respect to SN 2019ehk's bolometric luminosity, temperature and radius evolution during the flare in Figure 2.19. We also show a CSM interaction model that is able to power the entire flare ($t < 7$d) with $M_{\rm csm} = 7 \times 10^{-3}$ M$_\odot$ and the same physical parameters as above. These CSM properties are consistent with the masses independently inferred from the optical spectral modeling of §2.7.2 and X-ray modeling of §2.9.1.

2.9 Radio/X-ray data Modeling

2.9.1 Inferences on the explosion's local environment from X-ray observations

The luminous ($L_x \approx 10^{41}\,{\rm erg\,s^{-1}}$), rapidly-decaying X-ray emission ($L_x \propto t^{-3}$) with a hard spectrum is consistent with thermal bremsstrahlung from shocked CSM gas in adiabatic expansion. In this scenario the X-ray luminosity scales as the emission measure $EM = \int n_e n_I dV$, and $EM \propto r^{-3} \propto t^{-3}$ once the shock has swept up most of the CSM gas. For $n_e \approx n_I$, the EM measured from the first epoch of X-ray observations at ~ 2.8 d indicates a particle density $n \approx 10^9 R_{\rm csm,15}^{-1} \delta R_{\rm csm,15}^{-0.5} f^{-0.5}\,{\rm cm^{-3}}$, where $R_{\rm csm,15}$ and $\delta R_{\rm csm,15}$ are the radius and thickness of the shocked shell of gas in units of 10^{15} cm, respectively, and f is a volume filling factor. This density estimate is remarkably similar to the density of the pre-shocked CSM gas that we have inferred from the H and He recombination lines (§2.7.2). The inferred mass of the shocked gas is $M_{\rm csm} \approx 0.01 R_{\rm csm,15}^{-1} \delta R_{\rm csm,15}^{-0.5} f^{-0.5}$ M$_\odot$.

For a typical SN shock velocity of $\sim 0.1c$, the forward shock radius at 2.8 d is $r \approx 7 \times 10^{14}$ cm. The disappearance of the H and He recombination lines by 2.4 d post explosion

and the rapid fading of the X-ray luminosity detected at 2.8 d indicate that the shock has overtaken the shell of CSM by this time. Using $R_{\rm csm} \approx 7 \times 10^{14}\,{\rm cm}$ and assuming $\delta R_{\rm csm} \approx R_{\rm csm}$ we infer a particle density of $n \approx 10^9\,{\rm cm^{-3}}$ and a total CSM shell mass of $M_{\rm csm} \approx 7 \times 10^{-3}\,{\rm M_\odot}$ (for $f = 1$). This result is consistent with the mass of pre-shocked CSM gas $\sim 2 \times 10^{-3}\,{\rm M_\odot}$ that was in front of the shock at $t = 1.4$ d since explosion derived in §2.7.2. Together with the modeling of the flare optical continuum of §4.7, these results strengthen the scenario where the detected X-rays and continuum optical emission originate from pre-existing H/He rich CSM shocked by the SN blastwave, while the H and He recombination lines result from pre-shocked CSM gas lying in front of the SN shock and ionized by its X-ray emission. If the chemical composition of the entire shell is similar to that constrained by the H+He emission lines of §2.7.2, and under the assumption of $f \approx 1$, the total CSM H mass is in the range $(4. - 17.) \times 10^{-4}$ M$_\odot$ and the total CSM He mass is constrained within the range $(5.3 - 6.7) \times 10^{-3}$ M$_\odot$.

2.9.2 Inferences on the explosion's environment at $R \geq 10^{16}\,{\rm cm}$ from radio observations

We interpret the radio upper limits of §5.4.4 in the context of synchrotron emission from electrons accelerated to relativistic speeds at the explosion's forward shock, as the SN shock expands into the medium. We adopt the synchrotron self-absorption (SSA) formalism by Chevalier (1998) and we self-consistently account for free-free absorption (FFA) following Weiler et al. (2002). For the calculation of the free-free optical depth $\tau_{\rm ff}(\nu)$ we adopt a wind-like density profile $\rho_{\rm csm} \propto r^{-2}$ in front of the shock, and we conservatively assume a gas temperature $T = 10^4\,{\rm K}$ (higher gas temperatures would lead to tighter density constraints). The resulting SSA+FFA synchrotron spectral energy distribution depends on the radius of the emitting region, the magnetic field, the environment density and on the shock micro-physical parameters ϵ_B and ϵ_e (i.e. the fraction of post-shock energy density in magnetic fields and relativistic electrons, respectively).

Figure 7.7 shows the part of the density vs. shock velocity parameter space that is ruled out by the upper limits on the radio emission from SN 2019ehk for three choices of microphysical parameters. Specifically, we show the results for $\epsilon_B \approx 0.1$ and $\epsilon_e \approx 0.1$ (which have been widely used in the SN literature) to allow a direct comparison with other SNe (black dots in Figure 7.7). We find that SN 2019ehk shows a combination of lower environment density and lower shock velocity when compared to core-collapse SNe with radio detections. As a final step, we self-consistently solve for the shock dynamics in a wind medium adopting the explosion's parameters inferred in §4.5.2 (kinetic energy $E_{\rm k} \approx 1.8 \times 10^{50}\,{\rm erg}$ and ejecta mass $M_{\rm ej} \approx 0.7\,{\rm M_\odot}$). We show the resulting shock velocity $\Gamma\beta$ as a function of the environment density for an outer density profile of the ejecta of the exploding star typical of compact massive stars ($\rho_{\rm ej} \propto v^{-n}$ with $n \approx 10$, Matzner & McKee 1999) or relativistic WDs (e.g., Chomiuk et al. 2012 and references therein). The SN shock decelerates with time as it plows through the medium. Figure 7.7 illustrates the range of shock velocities during the time of our radio observations at $\delta t \approx 30 - 220$ d for the two choices of stellar

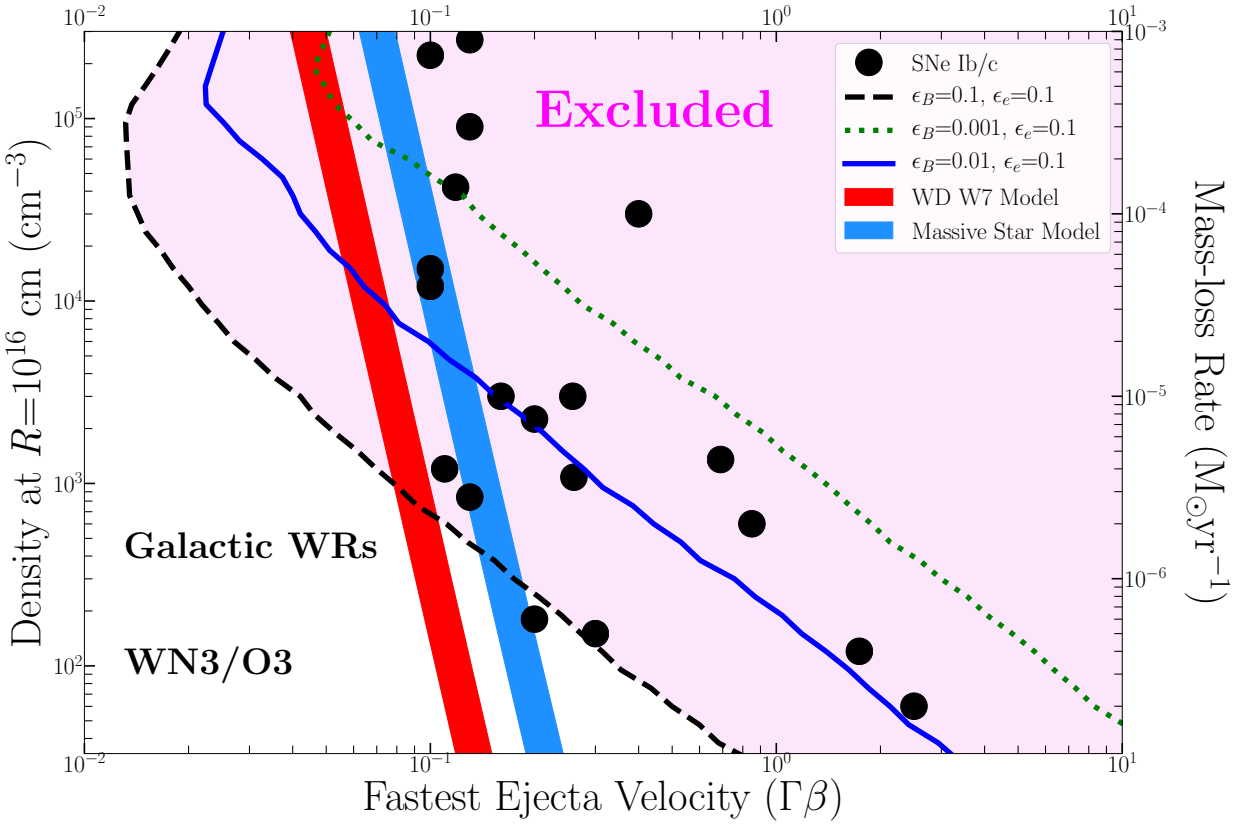

Figure 2.21 Environment density $\rho_{\rm CSM} \propto r^{-2}$ vs. shock velocity parameter space. Radio non-detections of SN 2019ehk rule out the vast majority of the parameter space of Ib/c SNe (black dots, Drout et al. 2016), for which $\epsilon_B = 0.1$ and $\epsilon_e = 0.1$ are typically assumed (black dashed line). The parameter space to the right of the thick blue line and green dotted line is ruled out for a different choice of microphysical parameters ($\epsilon_B = 0.01$ and $\epsilon_B = 0.001$, respectively). Red (blue) band: range of SN 2019ehk shock velocities during our radio monitoring ($\delta t = 30 - 220$ d) for an explosion with $E_{\rm k} = 1.8 \times 10^{50}$ erg and $M_{\rm ej} = 0.7\,{\rm M}_\odot$ (§4.5.2) and a massive star (blue) or WD (red) outer ejecta density profile. Grey shaded regions: range of mass-loss rates $\dot{M}$ for Galactic WRs (Crowther 2007; Massey et al. 2015) for a wind velocity $v_w = 1000\,{\rm km\,s^{-1}}$.

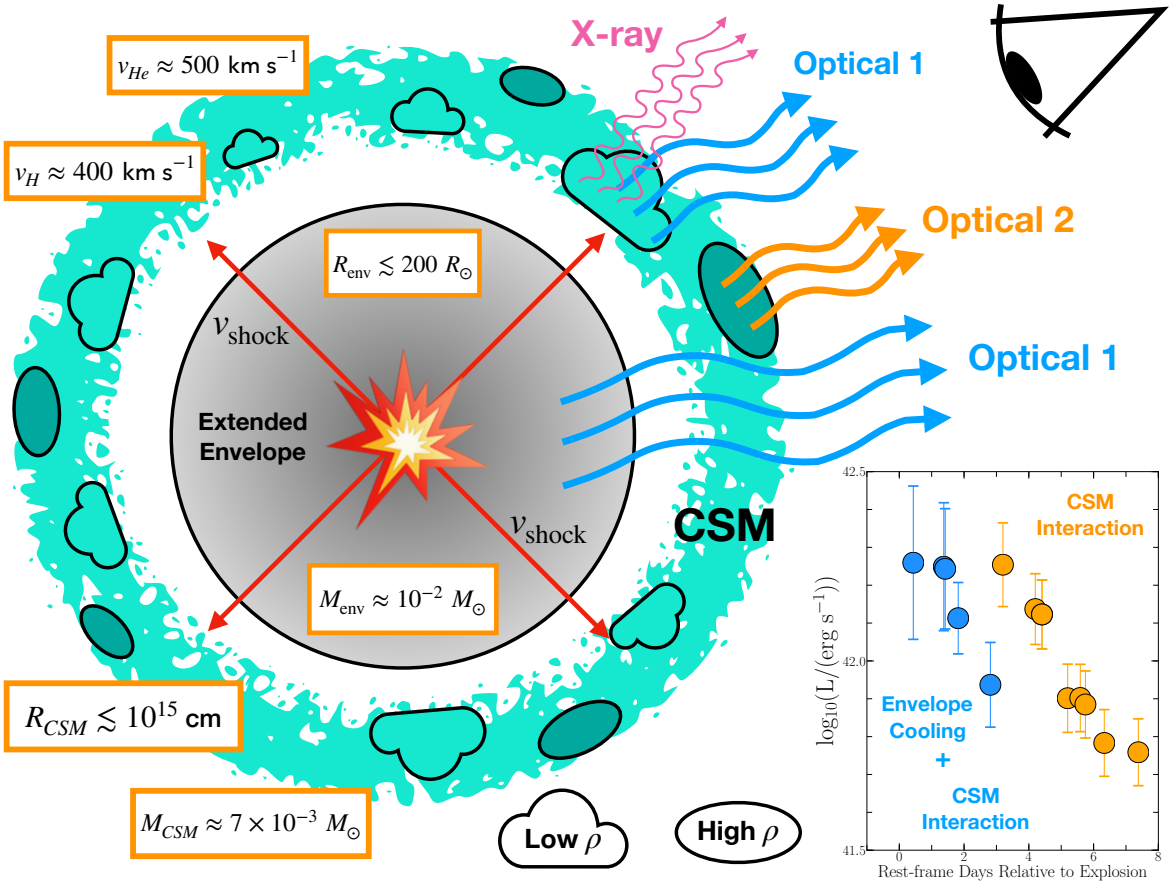

Figure 2.22 Visual representation of SN 2019ehk's progenitor environment at the time of explosion (§4.9.1). Here, the SN shock breaks out from an extended envelope and collides with lower density, outer CSM, inducing X-ray emission and flash-ionized spectral lines. A combination of envelope cooling and shock interaction produces the first part of the flare (blue light curve points), while high density or "clumpy" CSM causes delayed optical emission at $t > 2$d (orange light curve points). CSM velocities and abundances are derived from flash-ionized spectral lines, while the total mass is calculated from X-ray detections. The physical scale and mass of the inner extended material are estimated from shock cooling models. The bolometric light curve during the flare is presented in lower right for reference.

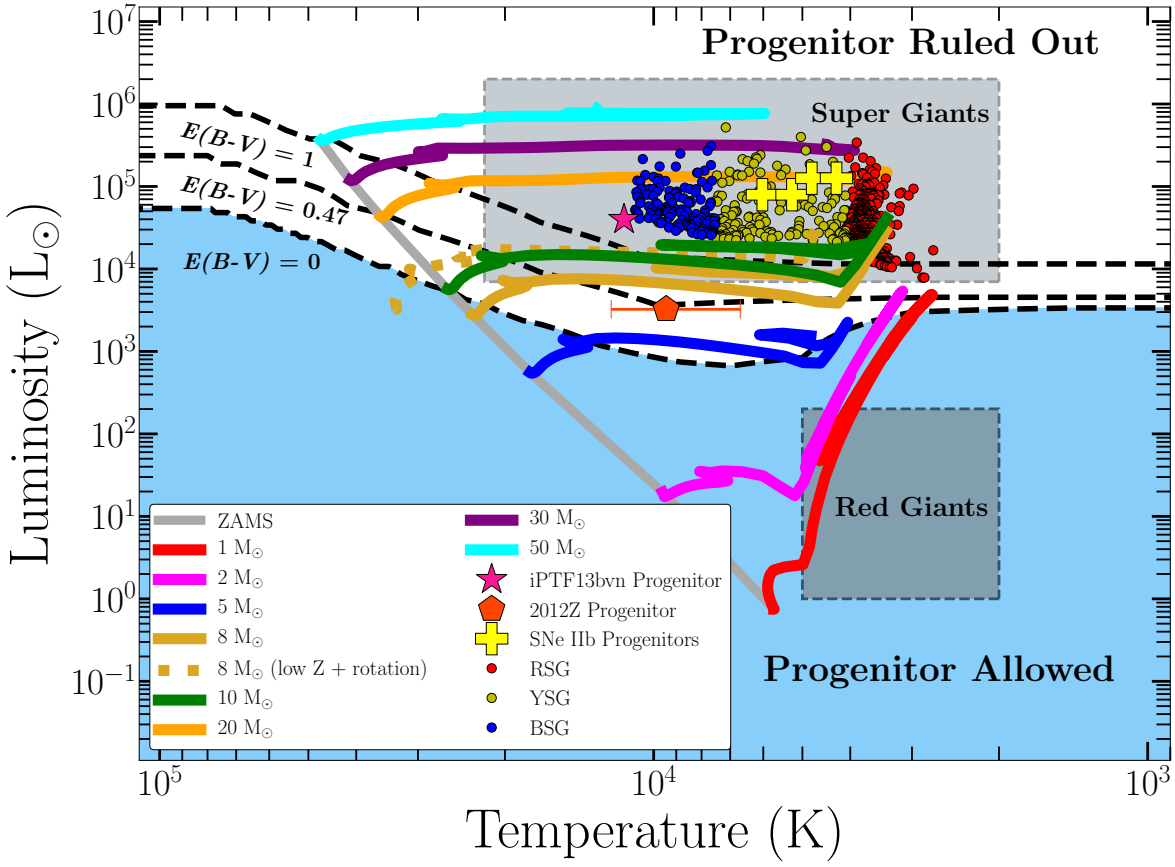

Figure 2.23 H-R diagram showing the inferred limits on the stellar progenitor of SN 2019ehk from pre-explosion HST imaging. Permitted regions for different local extinctions are shown as dashed lines in the shaded violet-to-blue region and the excluded region is presented in pink. We plot `MESA` stellar evolutionary tracks from 1-50 $M_\odot$ single stars with no rotation, and solar metallicity as solid lines. For completeness, an 8 $M_\odot$ single star track with rotation and sub-solar metallicity is plotted as a dashed line. The progenitors of SN Ib iPTF13bvn and SN Iax, 2012Z are displayed as a pink star and a red diamond, while progenitors of SNe IIb are shown as yellow plus signs (Maund et al. 2011; Cao et al. 2013; McCully et al. 2014). Dashed grey squares represent the range of Supergiants (top) and Red Giants (bottom). A representative sample of Red, Yellow and Blue supergiants in the LMC are plotted as circles (Neugent et al. 2012). With the most conservative choice of local extinction ($E(B-V) = 1$ mag) the HST limits rule out all single massive stars capable of exploding, while a realistic choice of extinction correction ($E(B-V) = 0.47$ mag) extends the masses of single stars progenitors that are ruled out to $\gtrsim 8$ $M_\odot$.

progenitors. For more realistic choices of microphysical parameters ($\epsilon_B = 0.01$, $\epsilon_e = 0.1$), our results imply a mass-loss rate limit $\dot{M} < 10^{-5}\,\mathrm{M_\odot yr^{-1}}$ for an assumed wind velocity $v_w = 500\,\mathrm{km\,s^{-1}}$ similar to the observed velocities of H and He-rich material (Figure 2.17). This limit applies to distances $r \approx 10^{16} - 10^{17}\,\mathrm{cm}$ from the explosion site, and it is shown in Figure 7.6 in the context of predictions from WD merger models. These merger simulations are discussed in greater detail in §2.10.3.

2.10 Discussion

2.10.1 A Physical Progenitor Model

Panchromatic observations have provided an unprecedented picture of this CaST both before and after explosion. In Figure 2.22, we attempt to combine inferences made from observation and modeling to create a visualization of the explosion and surrounding environment. Our model is a snapshot of the SN at explosion and contains physical scales and parameters such as distance, velocity and composition estimates.

It is most likely the case that the flare is powered by shock interaction or cooling emission in an extended mass of material, regardless of the type of progenitor that exploded. The progenitor could have accrued an extended envelope located at < 200 $\mathrm{R_\odot}$ (light grey circle; Fig. 2.22), while mass-loss in the progenitor's final months may have placed H- and He-rich material in the circumstellar environment (shown in sea foam green; Fig. 2.22) with velocities of $\sim$ $400 - 500$ $\mathrm{km\,s^{-1}}$ and at distances $\lesssim 10^{15}$ cm. The detection of early-time X-ray emission and flash-ionized H and He spectral lines is clear evidence for a SN shock colliding with removed CSM. The observed CSM velocities might be difficult to explain given typical WD escape velocities of $\gtrsim 1000$ $\mathrm{km\,s^{-1}}$ needed for mass ejection from a WD surface. However, material might be ejected at low velocities during mass-transfer in WD binaries prior to the merger (see §2.10.3).

Based on our modeling of the flare in §2.8.3 and §2.8.4, we propose a physical scenario that could have produced this first optical light curve peak. In the picture, the flare is powered by two physically distinct emission components: shock interaction with more distant CSM in addition to the cooling of hot, shocked material a smaller radii. Following shock breakout, the inner extended envelope will cool, producing some of the emission on timescales $t < 2$ days (blue light curve points; Fig. 2.22). Once the shock collides with more distant H- and He-rich CSM it will induce "flash-ionized" spectral lines that are powered until 1.5 days via X-ray emission from the shock propagating through the CSM shell. The same low density region of the CSM responsible for X-rays and narrow emission lines can also power the early-time light curve ($t < 2$d). Our analysis has indicated that this shell had a mass of $\sim 7 \times 10^{-3}$ $\mathrm{M_\odot}$ and is located between 4×10^{13} - 10^{15} cm from the progenitor.

At $t > 2$d, the flare's power source and the complete explosion picture becomes more ambiguous. By the start of the main peak of the flare (orange light curve points; Fig. 2.22), the narrow emission lines are no longer detectable and the X-ray emission from the initial

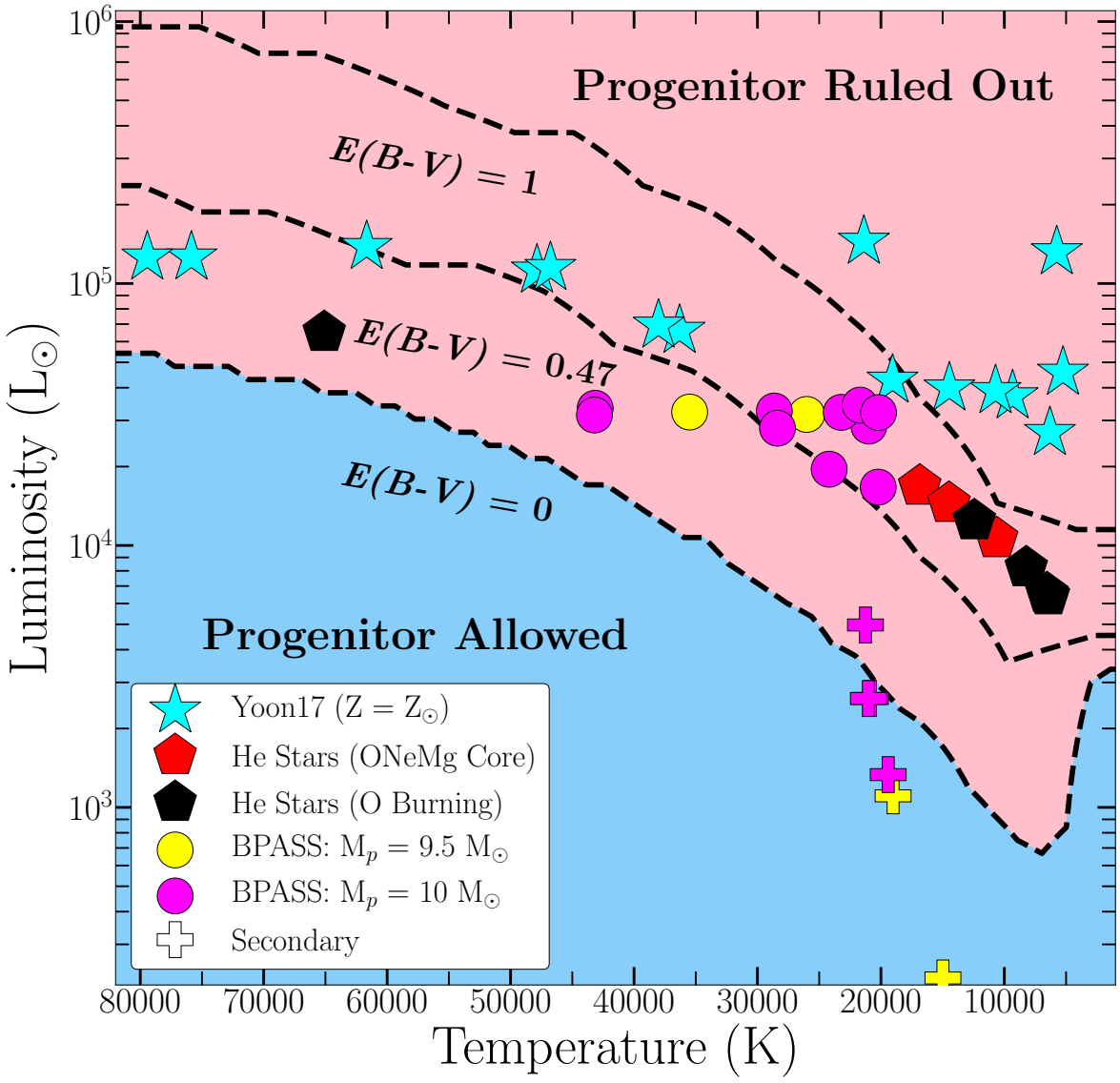

Figure 2.24 `BPASS` models consistent with pre-explosion limits and SN properties. Primary and secondary stars are shown as circles and plus signs, respectively. Cyan stars represent the primary star in binary models by Yoon et al. (2017) that result in SNe IIb/Ib. Helium star models where different amounts of the envelope is removed are shown as polygons. Final states of these models are either an ONeMg core (red) or O-burning (black) in the core. The same color coding as Fig. 2.23 is used to indicate allowed regions of the parameter space for different intrinsic $E(B-V)$.

shock is rapidly decaying, suggesting that the shock has overtaken the entire CSM shell. Here we propose two plausible expanations for the rapid increase in flux at $t \approx 2$d. (i) Delayed optical emission from the high density, optically thick regions of the CSM shell begin to cool and radiate in the optical bands following shock interaction. (ii) The shock encounters additional CSM material at $r > 10^{15}$cm which induces optical emission from shock interaction.

While this physical progenitor model does account for most of the observables, there are many caveats and unknowns about such a system. First, this model assumes spherically symmetric distributions of mass, both in the inner extended envelope and the outer CSM. Alternatively, this material could have formed a torus where more mass is located in the equatorial regions rather than at the poles. Secondly, neither the shock cooling (§2.8.3) nor the shock interaction models (§2.8.4) takes into account the chemical composition of the shocked material that then causes the flare. It is likely that the extended masses have significant density gradients, which could lead to variations on how the radiation is able escape the material. Such a scenario would be best tested through numerical modeling (e.g., Piro et al. 2017) in which the density gradients and composition are taken into account, but is ultimately beyond the scope of this paper. Nonetheless, our observations have allowed for the most complete picture of CaST explosion mechanisms and their circumstellar environments. In the following sections we discuss the stellar systems capable of producing the SN 2019ehk observables.

2.10.2 Pre-Explosion Constraints on a Massive star Progenitor

Figure 2.23 shows the constraints on the progenitor system of SN 2019ehk in the H-R diagram, as derived from pre-explosion HST multi-band imaging. In the context of single stars, only compact objects (e.g., WD, NS, BH) and massive stars ($8-10$ M$_\odot$) are consistent with observations. Specifically, we plot the `MESA` evolutionary tracks (Choi et al. 2016) of non-rotating single massive stars with the same metallicity as the host galaxy ($Z = Z_\odot$). We find that only stars with mass ∼8-10 M$_\odot$ satisfy the limits for the most extreme choice of intrinsic $E(B-V) \approx 1$ mag. This is also true for low metallicity stellar tracks with rotation included e.g., dashed goldenrod line of 8 M$_\odot$ progenitor. However, a more realistic choice of intrinsic $E(B-V) = 0.47$ mag would effectively rule out the vast majority of parameter space corresponding to various types of single massive stars ($\gtrsim 8$ M$_\odot$). Furthermore, we explore the potential of a single He star progenitor (Table 2.13) that would be responsible for a core-collapse SN Ib-like explosion. As shown in Figure 2.24, this model is only consistent with the most highly reddened pre-explosion limits and requires a mechanism to remove its outer H-rich envelope. Overall, we conclude that single massive stars are unlikely progenitors of SN 2019ehk.

We then explore the possibility of a binary progenitor system. To this aim, we employ the large grid of Binary Population and Spectral Synthesis (`BPASS`) models by Eldridge et al. (2017) to find binary systems that fit the observational parameters of SN 2019ehk. Firstly, we exclude binary models whose final luminosity and temperature do not reside

within the "allowed" parameter region of Figure 2.23 (blue shaded regions). This includes the final luminosity and temperature of both the primary and secondary stars; neither of which should be detected in archival *HST* imaging. Additionally, we only include systems whose final helium mass is > 0.1 M$_\odot$ and final hydrogen mass is < 0.01 M$_\odot$ (e.g., §8.3.3). To meet the `BPASS` condition for a resulting SN, we only include systems where the primary's CO core mass is >1.35M$_\odot$ and total mass is >1.5 M$_\odot$. Following these conditions, we look for systems whose ejecta mass is $< 1.0\,$M$_\odot$ for a weak SN explosion ($E_{\rm k} \approx 10^{50}$erg), both of which are inferred from observations (§4.5.2). When this cut is made on predicted ejecta mass, we recover *no* consistent binary systems within the SN 2019ehk parameter space. However, because parameters associated with a predicted SN in `BPASS` are uncertain, we choose to include systems that have a predicted ejecta mass $M_{\rm ej} < 2$ M$_\odot$ for completeness. We plot the final luminosities and temperatures of 13 potential binary systems in Figure 2.24 and display significant BPASS parameters of each model in Table A8. Overall, these binary configurations have primary stars with masses of $9.5 - 10$ M$_\odot$ and radii < 15 R$_\odot$.

We further test the possibility that SN 2019ehk is the result of a more exotic binary system through He-star modeling in `MESA`. We initialize $2.7 - 3.0$ M$_\odot$ He-stars with C/O cores and track their luminosity and temperature evolution until the exhaustion of He-burning and the onset of O core burning or the formation of an ONeMg core. We test the following mass-loss scenarios: no mass-loss, standard Wolf-Rayet (WR) winds, artificial envelope removal and binary interaction with NS companion (with varying orbital periods). We present the specifics of each model in Table 2.13 and plot each final luminosity/temperature as red and black polygons in Figure 2.24. These are compared to binary models in Yoon et al. (2017) that result in normal SNe Ib/IIb (plotted as cyan stars).

Overall, our presented He-star models are consistent with the pre-explosion parameter space for host extinctions of $E(B-V) = 0.5$ - 1 mag. We can rule out some of these systems based on the final mass if we assume that the total ejecta mass will be this mass minus $\sim$1.4 M$_\odot$. The estimated ejecta mass in SN 2019ehk is $\sim$0.7 M$_\odot$, which is consistent with an artificial envelope removal (models #2, 4) and a He-star + NS binary (models #7,8), both ending in O core burning. However, these models do not naturally reconcile the presence of H-rich CSM in the SN 2019ehk progenitor environment.

We can further constrain the presence of a dusty progenitor for SN 2019ehk by utilizing the *Spitzer* pre-explosion limits (Table A2). We use the most constraining limit of > 23.87 mag from Channel 2 and assume that the majority of the flux is emitted about an effective wavelength of $\lambda_{\rm eff} = 4.493$ μm. We then apply the spherically symmetric dust shell model shown in Equation 1 of Kilpatrick et al. (2018b). As in their study, we also assume that the dust shell emits isotropically in the optically thin limit (Fox et al. 2010) and have a flux density that goes as $F_\nu \approx M_d B_\nu(T)\kappa_\nu/d^2$, where M_d is the shell mass, d is the distance to SN 2019ehk and $B_\nu(T)$ is the Planck function. Applying this simple approximation, we derive dust shell masses limits of $< 6.6 \times 10^{-8} - 5.3 \times 10^{-6}$ M$_\odot$ for shell temperatures $T_{\rm s} = 1500 - 500$ K, respectively.

Our inferred dust mass is a factor ~ 4 smaller than that derived by Kilpatrick et al. (2018b) for LBV outburst Gaia16cfr and an order of magnitude lower than typical dust

masses observed around type IIn SNe (Fox et al. 2011). Furthermore, the total dust luminosity of the Gaia16cfr progenitor was 2.4×10^5 $L_\odot$, which is more than an order of magnitude larger than the NIR F160W *HST* pre-explosion limits (e.g., Fig. 2.23). Since our derived dust shell mass is similar to Gaia16cfr, a massive star progenitor with a small dust shell would have been detected in pre-explosion images of the SN explosion site. While this analysis is highly simplified, our findings make a dusty progenitor for SN 2019ehk highly unlikely given the observations.

Finally, it should be noted that the luminosity limit derived from *Chandra* pre-explosion imaging does not constrain the existence of a luminous supersoft X-ray source (SSS) at the location of SN 2019ehk. Such a system has been invoked as a precursor to SNe Ia wherein a nuclear-burning WD accretes mass from a non-degenerate companion. This process in turn produces X-ray luminosities of order 10^{38} erg s^{-1}. However, it has been demonstrated that there are not enough observed SSSs that retain luminous X-ray emission on the same timescale as is needed for quasi-steady burning on the WD surface (Di Stefano 2010). Therefore a single-degenerate scenario, or related event, cannot be constrained with our current *Chandra* X-ray limits.

From this analysis, we can rule out all single massive stars > 8 $M_\odot$ as progenitors of SN 2019ehk. With regards to binary systems, the pre-explosion parameter space allows for only the lowest mass massive star binaries ($9.5 - 10$ $M_\odot$) or He stars whose envelopes are removed through a mass-loss mechanism. However, while our pre-explosion limits greatly constrain the massive star parameter space, progenitor systems involving a WD cannot be excluded based on detection limits.

2.10.3 White Dwarf Explosion Models

Given the pre-explosion limits, every progenitor system involving a WD is permitted in the progenitor parameter space of SN 2019ehk. Nevertheless, we can exclude some of these scenarios based on observed properties of the explosion. As shown in Figure 2.23, the progenitor of SN Iax, 2012Z is not ruled out and has been proposed to be a He star + WD binary (McCully et al. 2014). However, this progenitor channel cannot account for the H-rich material observed in SN 2019ehk's circumstellar environment nor the photospheric He in its spectra without significant buildup of unburned He on the WD surface at the time of explosion. Furthermore, explosion models for this configuration generally produce SN Ia, or Iax-like events from failed detonation/deflagration (Jordan et al. 2012; Kromer et al. 2013a) that do not match the observed photometric or spectroscopic evolution of CaSTs. The same reasoning rules out a main sequence (MS) companion model typical of SN Ia models. Because common single degenerate progenitor channels appear unlikely for SN 2019ehk, we explore double degenerate explosion scenarios capable of reproducing CaST observables such as those from SN 2019ehk.

Recently, Perets et al. (2019) suggested a double WD (DWD) merger scenario for the origin of SNe Ia, where a CO-WD merges with a hybrid HeCO WD (Zenati et al. 2019b and references therein). In this hybrid + CO DWD (HybCO) model, the disruption of a hybrid

WD by a more massive (¿0.75 $M_{\odot}$) CO WD can give rise to normal SNe Ia (Perets et al. 2019), through a detonation of a He-mixed material on the CO WD surface, followed by a detonation of a CO core due to its compression by the first He-detonation. In cases where the primary WD was of a low mass ($\lesssim 0.65$ $M_{\odot}$), only the first He-detonation occurs while the CO core is left intact leaving a remnant WD behind. In such cases, and in particular when the progenitor is a hybrid-WD disrupting a lower-mass CO WD (or another hybrid WD), Zenati et al. 2020 (in prep.) find that the He-detonation gives rise to a faint transient, potentially consistent with CaSTs.

In this specific double-degenerate channel, mass that is lost from the secondary WD prior to its disruption can give rise to CSM, possibly consistent with the observations of SN 2019ehk, as we describe below (a more detailed discussion will be provided in Bobrick et al. 2020, in prep.). This scenario has been explored in the context of SNe Ia wherein the merger is preceded by the ejection of mass as "tidal tails" and placed at distances $r \approx 10^{15}$ cm (Raskin & Kasen 2013). Further in, material around the primary WD can "settle down" to form an extended envelope ($r \approx 10^{11}$ cm); this process can occur on timescales of < 1000 yrs before merger (Shen et al. 2012; Schwab et al. 2016).

Before the actual merger, DWDs spiral-in due to gravitational wave emission. As the binary components gradually come into contact and the donor starts losing mass, the mass transfer rate in the system gradually grows, starting from small values below 10^{-12} $M_{\odot}yr^{-1}$ and continually increasing, which leads to the eventual disruption over several years' time. Mass-loss during this phase leads to material ejected at typical velocities of likely a few hundreds up to thousand $km\,s^{-1}$, which expands to characteristic radii of $10^{15} - 10^{16}$ cm by the time the actual merger happens, while some material could be ejected shortly before the final merger of the WDs. Here we focus on the mass transfer and ejection prior to the merger/disruption of the WDs, which can contribute to the CSM far from the WD and may explain the observations. Levanon & Soker (2017) discussed the possibility of very high velocity CSM from material ejected after the disruption of a WD, and just shortly before the merger; this is however unlikely to explain, or be consistent with, the observations shown here.

We compute the density distribution in the ejecta by solving the equations of secular evolution of the mass transfer rate and binary orbital properties (masses and separation, M_1, M_2, a) in DWD binaries driven by gravitational wave emission starting from early phases of mass transfer (see e.g., Marsh et al. 2004; Gokhale et al. 2007; Bobrick et al. 2017). We represent the WD donor by one-dimensional, corotating and perfectly-degenerate models following the Helmholtz equation of state Timmes & Swesty (2000) and calculate the mass transfer rate following Kolb & Ritter (1990). The binaries are evolved from the moment mass transfer rate reaches 10^{-12} $M_{\odot}yr^{-1}$ until the mass transfer rate reaches 10^{-2} $M_{\odot}yr^{-1}$, shortly before the merger. We assume that a fixed fraction of mass is ejected from the systems at some characteristic velocity during the process of mass transfer, both parameters being free parameters of the model.

We explored several physically-motivated cases which cover most of the parameter space of possible assumptions in the model, as summarised in Table 2.3. As the fiducial model, we

Table 2.2. Nebular emission line luminosities for three epochs of spectroscopy at 31, 38 and 59 days after second B-band maximum light.

Wavelength (Å)	Line ID	Day +31 (10^{38} erg s^{-1})	Day +38 (10^{38} erg s^{-1})	Day +59 (10^{38} erg s^{-1})
5876	He I	17	–	2.3
6303,6363	[O I]	19	–	7.3
7065	He I	14	–	4.5
7291,7324	[Ca II]	220	–	130
7774	O I	18	–	4.9
8579	Ca II	290	–	150
9224	O I	21	–	5.0
10830	He I	94	162	29.
11873	Ca II	–	72	–
14878	Mg I	–	14	–
15900	C I	–	16	–
20589	He I	–	16	–

Note. — In our latest spectrum at +257d, [Ca II] and [O I] luminosities are 3.1×10^{38} erg s^{-1} and 1.2×10^{37} erg s^{-1}, respectively.

Model Name	$M_{\rm donor} + M_{\rm acc}$ ($M_\odot$)	$f_{\rm ej}$	$v_{\rm ej}$ (km s^{-1})	Abund. (donor)
Fiducial	$0.5 + 0.6$	0.99	300	CO
Reduced mass loss	$0.5 + 0.6$	0.1	500	CO
Fast ejecta	$0.5 + 0.6$	0.99	1000	CO
Heavy accretor	$0.5 + 0.9$	0.99	500	CO
Hybrid donor	$0.53 + 0.6$	0.99	500	HeCO
Super-Chandra	$0.75 + 0.95$	0.99	500	CO

Table 2.3 WD explosion models presented in §2.10.3. The columns show the model name, the masses of the primary and the secondary in solar masses, the fraction of the transferred material which is ejected from the system, the velocity of the ejecta and the chemical composition of the donor. The accretor has a C/O composition.

chose a $0.5 + 0.6\,M_\odot$ DWD binary, which represents potential progenitors of CaSTs in the hybCO scenario. In the fiducial model, we assume that 99% of mass is lost due to direct-impact accretion expected in these binaries and we assigned ejecta velocities of 500 $\mathrm{km\,s^{-1}}$, comparable to the orbital velocity in the binary. In the exploratory models, we considered the cases where only 10% of mass is lost, where the ejecta is launched at 1000 $\mathrm{km\,s^{-1}}$, where the accretor is a $0.9\,M_\odot$ CO WD and where the donor is a hybrid HeCO WD $0.53\,M_\odot$, based on the detailed model from Zenati et al. (2019b). Additionally, we simulated a super-Chandrasekhar binary with 0.75+0.95 $\mathrm{M_\odot}$ CO WDs, which is expected to produce brighter SNe Ia instead. As may be seen from Figure 7.6, the density distributions from the models agree well with the density limits derived from the X-ray detections, flash-ionized spectral lines and radio non-detections. The agreement is also robust to the assumptions in the model, apart from the model with the $0.9\,M_\odot$ CO accretor, for which the ejecta density at late times (small radii) disagrees with the X-ray limits. Indeed, this latter case is not expected to give rise to a CaST SN in the HybCO model.

Throughout the evolution, mass transfer gradually peels the donor starting from the outermost layers, and therefore the ejected mass inherits the composition profiles of the donor WD. We use `MESA` models of WDs stripped during binary evolution and find that $0.53\,M_\odot$ CO WDs contain about $3 \times 10^{-3}\,M_\odot$ of H, while hybrid WDs contain less. For example, a 0.53 $\mathrm{M_\odot}$ HeCO WD model contains only $2 \times 10^{-5}\,M_\odot$ of H and is based on the models from Zenati et al. (2019b). In contrast, models of single WDs predict $\sim 10^{-4}$ $\mathrm{M_\odot}$ of surface H (Lawlor & MacDonald 2006) for low-mass WDs ($\lesssim 0.6$ $\mathrm{M_\odot}$) and orders of magnitude lower H abundances on higher mass WDs. Since H is initially in the outermost layer of the donor, it ends up in the outermost parts of the CSM, being replaced-by/mixed-with He at typical separations 10^{14}–10^{15} cm, assuming H layers between $10^{-3}\,M_\odot$ and $10^{-4}\,M_\odot$. Depending on the mass of the He layer, He is replaced by CO at separations between 10^{12} and 10^{14} cm, assuming He fraction between $10^{-2}\,M_\odot$ and $10^{-3}\,M_\odot$. For hybrid-WDs containing > 0.03 $\mathrm{M_\odot}$ of He, no CO is stripped until the final disruption of the hybrid-WD.

The inferred composition of the CSM around SN 2019ehk is broadly consistent with a ~ 0.53 $\mathrm{M_\odot}$ CO or a ~ 0.48 $\mathrm{M_\odot}$ hybrid-WD donor model; both of which formed during binary evolution, and not as isolated single WDs. In particular, these are consistent with the expectations of the HybCO model for CaST SNe progenitors. In the HybCO model interpretation, future observations of CaSTs may potentially be used to put strong constraints on the progenitor systems, and even the surface composition of WDs.

The exact velocity and the geometry of the material lost to the surroundings are the main uncertainties in the pre-merger stripping model. While this material is expected to have velocities comparable to the orbital velocities, the exact detailed hydrodynamical picture of the secular mass-loss in direct-impact DWD binaries is uncertain. In particular, the material may be ejected in an outflow from the disc, a more tightly-collimated jet from near the accretor, or as a more isotropic cloud-like structure powered by the feedback from accretion. When it comes to the fraction of the mass lost from the binary, even within a wide range of assumed efficiencies of mass-loss (range of $5 - 100$% ejection efficiency), the CSM ejecta profiles agree well with the observations. They explain (i) the cut-off at large

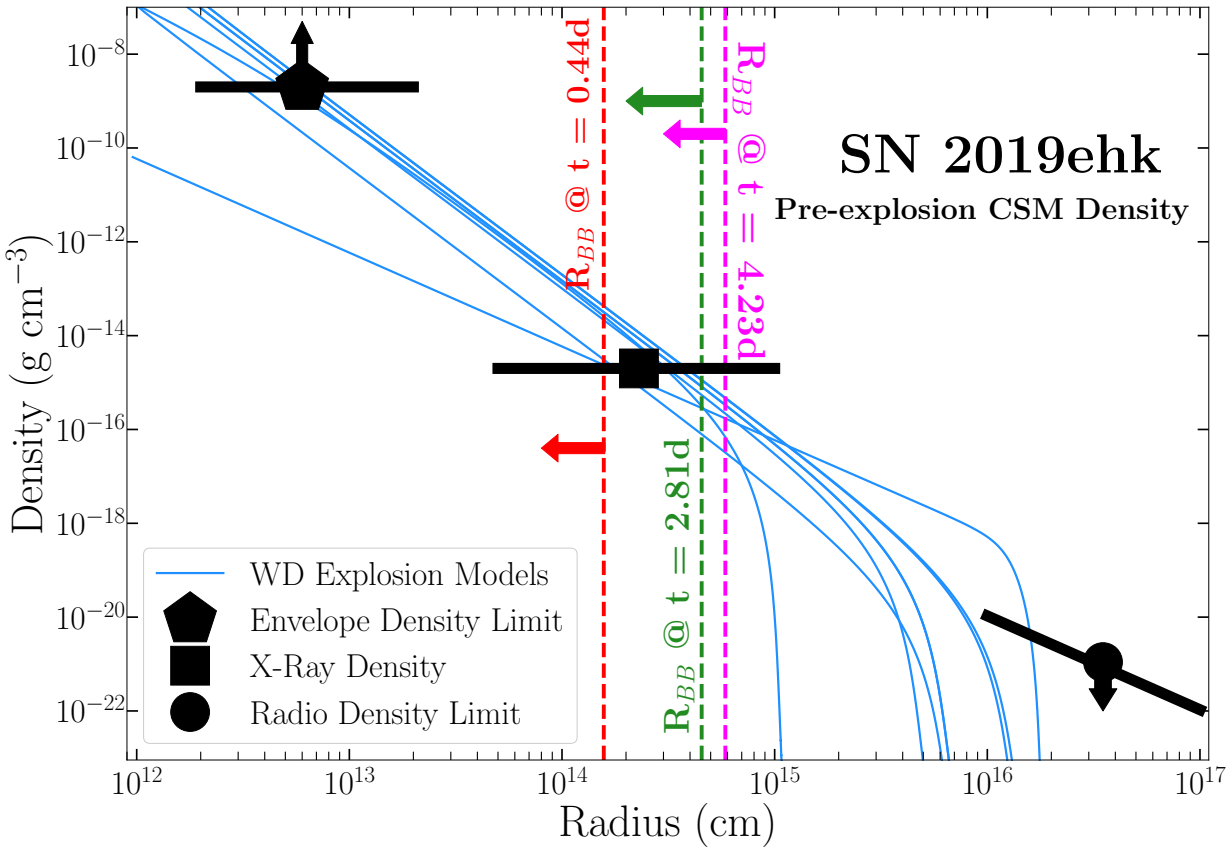

Figure 2.25 Density profile of the SN 2019ehk explosion environment. Shown as black squares are density limits derived from X-ray detections and presented at radii derived from black-body modeling. The black circle is the density limit derived from modeling of the radio non-detections. Blue lines are CSM models for WD mergers at the time of explosion (see §2.10.3).

separations, due to the time when the secondary WD gradually overfills its Roche lobe and before which no significant stripping initiates; (ii) the overall density profile of the CSM; (iii) the overall composition and the transition between the outer and inner regions due to the compositional structure on the stripped WD surface and (iv) the observed low CSM velocities derived from early-time Hα and He II lines. It should also be noted that similar observables could be obtained from the disruption of HybCO (hybrid He/C/O) WD by a NS (e.g., see Fernández et al. 2019) although the rates associated with such binary systems are not consistent with CaSTs.

2.10.4 Tidal Disruption by an Intermediate-Mass Black Hole

A proposed model for CaSTs is the tidal disruption of a low mass WD by an intermediate mass black hole (IMBH) (Rosswog et al. 2008; Metzger 2012; MacLeod et al. 2014; Sell et al. 2015; Tanikawa et al. 2017). One prominent signature of this accretion process would be the presence of X-ray emission above the Eddington luminosity. Since we observed luminous X-ray emission from the CaSTs SN 2019ehk for the first time, we briefly discuss this scenario here. Sell et al. (2015) first explore this scenario for the CaST 2012hn to constrain the potential masses of the IMBH and of the disrupted WD via X-ray upper limits at 533 days after explosion. Milisavljevic et al. (2017) employ a similar method for iPTF15eqv, for which these authors infer an IMBH mass $\lessapprox 100 M_\odot$ on an accretion timescale of <164 days. We apply the same method to SN 2019ehk here.

The X-ray luminosity of SN 2019ehk $L_x \approx 10^{41}$ erg s^{-1} at ~ 3 days since explosion (Figure 4.5) is consistent with the Eddington luminosity of a $\sim 10^3$ M$_\odot$ BH, for which the timescale of fallback accretion is (e.g. Milisavljevic et al. 2017):

$$t_{\rm Edd} = \left(\frac{M_{\rm BH}}{10^3\ {\rm M}_\odot}\right)^{-2/5} \left(\frac{M_{\rm WD}}{0.6\ {\rm M}_\odot}\right)^{1/5} \left(\frac{R_{\rm WD}}{5\times10^{-2}\ {\rm R}_\odot}\right)^{3/5} {\rm yr}, \tag{2.19}$$

which indicates that for fiducial values of $M_{\rm WD}$ and $R_{\rm WD}$, such a transient would have an accretion luminosity above the Eddington limit for $t_{\rm Edd} \approx 1$ yr. This timescale is not consistent with observations of SN 2019ehk as its X-ray emission fades quickly on timescales of days as $L_x \propto t^{-3}$ after the first detection. The IMBH scenario can be further constrained by using the deepest X-ray luminosity limit of $< 3.3 \times 10^{38}$ erg s^{-1} obtained with *Chandra* at 292 days since explosion. Using $t_{\rm Edd} = 292.2$ d (the phase of observation), we calculate a limit on the BH mass of $\lesssim 2000$ M$_\odot$, assuming fiducial WD parameters. From the X-ray luminosity limit, and assuming an accretion efficiency of 10%, we calculate a BH mass limit of $\lesssim 33$ M$_\odot$. Furthermore, as discussed in §4.8, we find no evidence for an off-axis jet in our modeling of the radio emission, which is assumed to be associated with an accretion event such as the tidal disruption of a WD by an IMBH. Lastly, a IMBH progenitor is expected to be associated with a cluster, yet we find no sources near the SN location in the pre-explosion images. Based on these inferences, we conclude that the tidal disruption of a WD by an IMBH is an extremely unlikely physical scenario for SN 2019ehk.

2.10.5 SN 2019ehk in the "Calcium-strong" Class

SN 2019ehk is currently the CaST with the most extended and detailed observational data set across the electromagnetic spectrum. A key question is how representative SN 2019ehk is of the entire "Calcium-strong" class of transients? As discussed in §8.4.1, the optical light curve ($M_B^{\rm peak} = -15.10 \pm 0.0210$ mag, $\Delta {\rm m}_{15} = 1.71 \pm 0.0140$ mag) and color evolution of SN 2019ehk are consistent with the class of CaSTs (e.g., Figures 2.8 & 8.5). However, the main photometric difference is its prominent double (triple?) peaked light curve with the initial "flare" only matching one other object in the class, iPTF16hgs (De et al. 2019).

iPTF16hgs was not discovered as early but does show consistency spectroscopically (Figure 2.14(a)) to SN 2019ehk. Both objects were found in star forming host galaxy environments, in contrast with the majority of the sample (e.g. Shen et al. 2019). Furthermore, De et al. (2018b) also find that shock breakout emission can reproduce the increase in flux prior to the Ni-powered light peak. These combined similarities suggest a shared progenitor scenario amongst these two objects (and potentially other CaSTs).

Spectroscopically, SN 2019ehk shows near remarkable consistency with CaSTs SNe 2005E and 2007ke (Figure 2.14b). This level of similarity is intriguing given that the large-scale environments of these two CaSTs relative to SN 2019ehk are quite different (SNe 2005E and 2007ke are located on the outskirts of early-type galaxies while SN 2019ehk is embedded in a late-type spiral galaxy). SN 2005E was modeled via a helium shell detonation of a sub-Chandra WD (Perets et al. 2010b; Waldman et al. 2011), and SN 2007ke is thought to arise from a compact object progenitor given the lack of star formation at its explosion site (Lunnan et al. 2017). Generally, SN 2019ehk shares clear spectroscopic similarities with the rest of the class: Type I spectrum, visible He I, weak Fe-group element and O I transitions, and dominant Ca II emission at late-times. SN 2019ehk has the largest [Ca II]/[O I] ratio yet observed amongst CaSTs (and known transients as a whole) and has the earliest visible detection of [Ca II] (-5 days). Out to nebular times, SN 2019ehk shows persistent [Ca II] emission that is similar to other CaSTs. Therefore, SN 2019ehk's [Ca II]/[O I] ratio is consistent with the overall classification of CaSTs and it is the "richest" known object in Ca emission.

SN 2019ehk is located in a star-forming region of a barred spiral host-galaxy. SN 2019ehk thus adds to the increasing evidence for a wide distribution of both early and late type host galaxies for CaSTs. The SN is also embedded in its host galaxy (offset $\sim$ 2 kpc), which suggests that CaST class cannot be completely defined by large galactic offsets. Overall, a large fraction of the current CaSTs sample are located at large offsets from early-type galaxies and/or with limited to no visible star formation (Perets et al. 2010a, 2011; Kasliwal et al. 2012; Lyman et al. 2013a, 2014; Lunnan et al. 2017; De et al. 2020). However, multiple confirmed CaSTs and candidate objects have deviated from this trend. iPTF15eqv, iPTF16hgs and SN 2016hnk are all located in spiral host-galaxies and analysis of the explosion sites indicate the presence of star formation (Milisavljevic et al. 2017; De et al. 2018b; Galbany et al. 2019; Jacobson-Galán et al. 2020a). Similarly, CaSTs PTF09dav, SN 2001co, SN 2003H, SN 2003dr and 2003dg appear to have exploded in or offset from disk-galaxies (Sullivan et al. 2011; Kasliwal et al. 2012; Perets 2014a; Foley 2015).

The older stellar populations where a large fraction of CaSTs are found makes it difficult to reconcile a massive star progenitor for the entire class. In the context of WD progenitors, the increased discovery of CaSTs in late-type galaxies with a young stellar population component is still compatible with an older progenitor given the frequency of WDs in a variety of host environments. A larger sample of stellar ages near CaST explosion sites will confirm whether a broad(er) delay time distribution is needed to explain the presence of some CaSTs in younger stellar populations. Nevertheless, the existence of star-forming host galaxies does potentially still allow for a massive stellar progenitor channel (and hence a

core-collapse origin) as an explanation for some CaSTs, as suggested by Milisavljevic et al. (2017). SN 2019ehk has greatly constrained the massive star progenitor parameter space by illustrating that only the lowest mass stars (∼8-10 $M_\odot$) in binary systems are permitted progenitors of a CaST. Increasing the sample size of CaSTs with detailed observational coverage across the spectrum will help to reveal whether this class truly has multiple associated progenitor scenarios.

Finally, the detection of luminous X-ray emission in SN 2019ehk represents a newly discovered observational signature of CaSTs. Based on the observational coverage at X-ray wavelengths, it has become apparent that CaSTs may only exhibit X-ray emission at very early-times. No other CaSTs has X-ray observations before +25d after explosion yet we now know that X-ray emission in SN 2019ehk only lasted until +4 days. This indicates two possibilities: the explosion and environment of SN 2019ehk are unique *or* CaSTs do show X-ray emission directly after explosion that has been missed observationally until now. If the latter is true, then extremely early observations of CaSTs is imperative to understand the progenitor environments of these objects.

2.11 Summary and Conclusions

In this paper we have presented pre- and post-explosion (0.4-292 days) panchromatic observations of the nearby CaST SN 2019ehk located in a region of high star formation near the core of the SAB(rs)c galaxy M100 at $d \sim 16.2$ Mpc. Our observations cover the electromagnetic spectrum from the X-rays to the radio band, before and after the explosion. Below we summarize the primary observational findings that make SN 2019ehk the CaST with the richest data set to date:

- SN 2019ehk was detected ∼0.44 days after explosion and its UV/optical/NIR photometric evolution shows a double-peaked light curve in all multi-color bands, similar to CaST iPTF16hgs (De et al. 2018b). However, different from iPTF16hgs, these very early observations of SN 2019ehk were also able to capture the rapid rise to the first light curve peak. With respect to its second broader light curve peak, SN 2019ehk has a rise-time $t_r = 13.4 \pm 0.210$ days, a peak B-band magnitude $M_B = -15.1 \pm 0.0210$ mag and Phillips (1993) decline parameter of $\Delta m_{15}(B) = 1.71 \pm 0.0140$ mag.

- Within 24 hrs of discovery, three optical spectra were acquired starting at $t \approx 1.4$ days since explosion, and revealed the rapid disappearance of "flash-ionized" H Balmer series and He II emission lines with velocities of ~ 400 and ~ 500 km s^{-1}, respectively. These spectral features were detected at the time of the first light curve peak, and provide first evidence for H+He-rich CSM in the immediate vicinity of a CaST.

- SN 2019ehk showed luminous, rapidly-decaying X-ray emission ($L_x \approx 10^{41}$ erg s^{-1} with $L_x \propto t^{-3}$). The luminous X-ray emission detected with *Swift*-XRT at +3 and +4d after explosion constitutes a newly discovered observational signature of CaSTs and results

from the exploration of a pristine portion of the X-ray parameter space within this class. The X-ray emission is temporally coincident with the first optical light curve peak ("the flare"). At later times (+292d) *Chandra* observations provided the deepest constraints on a CaST to date ($L_x < 3.3 \times 10^{38}$ erg s^{-1}).

- Our deep radio monitoring with the VLA provided the tightest constraints on the radio luminosity from a CaST at phases >30 days after explosion $L_\nu < 10^{25}$ erg s^{-1} Hz^{-1}.

- SN 2019ehk has the latest spectroscopic follow-up of any CaST at +257d after explosion. The spectrum revealed the largest [Ca II]/[O I] line flux ratio yet reported (~ 25).

- The explosion site of SN 2019ehk has extremely deep pre-explosion imaging with *Chandra*, *Spitzer* and *HST*. No source is detected in any archival image with an astrometric uncertainty of $\sigma_\alpha = 4.05 \times 10^{-4''}$ and $\sigma_\delta = 2.71 \times 10^{-4''}$.

By modeling these observations we place tight constraints on the SN progenitor, its environment and the explosion mechanism:

- Bolometric light curve models show that the explosion synthesized $(3.1 \pm 0.11) \times 10^{-2}\,M_\odot$ of ^{56}Ni, produced $0.72 \pm 0.04\,M_\odot$ of ejecta and had a kinetic energy of $(1.8 \pm 0.1) \times 10^{50}$ erg.

- The H+He-rich material is part of the CSM and preceded the SN explosion. "Flash-ionized" emission lines indicate the presence of pre-shock CSM gas with mass $M_{\rm csm} \approx 2 \times 10^{-3}$ M$_\odot$ and composition in the range $0.44 < n_{\rm He}/n_{\rm H} < 0.88$ by number. The total CSM mass as inferred from X-ray observations is $M_{\rm csm} \approx 7 \times 10^{-3} M_\odot$, comprised of $(4 - 17) \times 10^{-4}$ and $(5.3 - 6.7) \times 10^{-3}$ M$_\odot$ of H- and He-rich material, respectively. Both observations combined revealed a CSM density of $\rho_{\rm csm} = 2 \times 10^{-15}$ g cm^{-3} at $R_{\rm csm} = (0.1 - 1) \times 10^{15}$cm.

- For realistic microphysical parameters ($\epsilon_B = 0.01$ and $\epsilon_e = 0.1$), radio non-detections suggest a mass-loss rate of $\dot{M} < 10^{-5}\,M_\odot {\rm yr}^{-1}$ for a wind velocity $v_w = 500$ km s^{-1} at distances $r \approx 10^{16} - 10^{17}$ cm from the explosion site.

- We model the early-time optical emission with two models: (i) shock interaction with CSM and (ii) shock cooling following breakout into extended material. Given an observed SN ejecta mass $M_{\rm ej} \approx 1\,M_\odot$, the former yields a CSM mass of $M_{\rm csm} = 1.5 \times 10^{-3}$ M$_\odot$ and radius of $R_{\rm csm} = 4 \times 10^{13}$ cm. This model can adequately power the persistent SN optical emission at $t < 6$d and is consistent with the duration of visible H+He emission lines. The latter model provides a potential physical mechanism for the increased optical emission at $t < 2$d and indicates extended material of mass $M_e \approx 7 \times 10^{-2}\,M_\odot$ and radius $R_e \approx 200\,R_\odot$. These values are broadly consistent with our inferences from the H+He spectral lines and the modeling of the X-ray emission,

suggesting that the presence of an extended distribution of (H+He rich) material with which the SN shock interacted can reasonably account for three key observational findings in SN 2019ehk (e.g., the X-ray emission, the optical flare and the transient H+He lines).

Pre-explosion imaging at the location of SN 2019ehk rules out a vast portion of the parameter space associated with both massive stars and WD explosions. Specifically, we find that pre-explosion limits rule out all *single* massive stars with mass $\gtrsim 8$ $M_\odot$ as the progenitor of CaST SN 2019ehk for a host reddening of $E(B-V) = 0.47$. We explore the available binary system parameter space and find that our limits only allow for systems with a $9.5 - 10$ $M_\odot$ primary star or a low-mass He star whose envelope was removed through mass-loss and/or binary interaction. Furthermore, the observed explosion properties make it unlikely that SN 2019ehk was produced by the explosion of a C/O WD with a He or main sequence star companion. However, we find that a model for the disruption of a low-mass C/O WD or a hybrid HeCO WD ($\sim 0.5 - 0.6$ $M_\odot$) by another, likely low-mass hybrid WD is consistent with the CSM densities, abundances and dynamics inferred for SN 2019ehk, and would possibly be able to account for the increasingly large fraction of CaSTs embedded in young stellar populations by allowing for a broader time delay distribution. Complete multi-wavelength observations of future CaSTs will be instrumental in differentiating between these two possible progenitor scenarios.

2.12 Acknowledgements

We thank David Matthews, Enrico Ramirez-Ruiz, Brian Metzger and Nathan Smith for stimulating conversations and constructive comments in regards to this work.

W.J-G is supported by the National Science Foundation Graduate Research Fellowship Program under Grant No. DGE-1842165 and the Data Science Initiative Fellowship from Northwestern University. R.M. is grateful to KITP for hospitality during the completion of this paper. This research was supported in part by the National Science Foundation under Grant No. NSF PHY-1748958. R.M. acknowledges support by the National Science Foundation under Award No. AST-1909796. Raffaella Margutti is a CIFAR Azrieli Global Scholar in the Gravity & the Extreme Universe Program, 2019. The Margutti's team at Northwestern is partially funded by the Heising-Simons Foundation under grant # 2018-0911 (PI: Margutti).

The National Radio Astronomy Observatory is a facility of the National Science Foundation operated under cooperative agreement by Associated Universities, Inc. GMRT is run by the National Centre for Radio Astrophysics of the Tata Institute of Fundamental Research.

The scientific results reported in this article are based in part on observations made by the Chandra X-ray Observatory. This research has made use of software provided by the Chandra X-ray Center (CXC) in the application packages CIAO. Partial support for this work was provided by the National Aeronautics and Space Administration through Chandra Award Number DD0-21114X issued by the Chandra X-ray Center, which is operated by the

Smithsonian Astrophysical Observatory for and on behalf of the National Aeronautics Space Administration under contract NAS8-03060.

W. M. Keck Observatory [and/or MMT Observatory] access was supported by Northwestern University and the Center for Interdisciplinary Exploration and Research in Astrophysics (CIERA).

The UCSC transient team is supported in part by NSF grant AST-1518052, NASA/*Swift* grant 80NSSC19K1386, the Gordon & Betty Moore Foundation, the Heising-Simons Foundation, and by a fellowship from the David and Lucile Packard Foundation to R.J.F. Research at Lick Observatory is partially supported by a generous gift from Google.

A.H. is partially supported by the Future Investigators in NASA Earth and Space Science and Technology (FINESST) Award No. 80NSSC19K1422. HBP acknowledges support from the Kingsely distinguished-visitor program at Caltech, and the KITP visitor program. KJS is supported by NASA through the Astrophysics Theory Program (NNX17AG28G). PJB is supported by a NASA Swift Guest Investigator grant 80NSSC19K0316. TMB was funded by the CONICYT PFCHA / DOCTORADOBECAS CHILE/2017-72180113. SCY is supported by the National Research Foundation of Korea (NRF) grant (NRF-2019R1A2C2010885). MG is supported by the Polish NCN MAESTRO grant 2014/14/A/ST9/00121. DAH, JB, DH, and CP are supported by NSF AST-1911225 and NASA grant 80NSSC19K1639. JD and EB are supported in part by NASA Grant 80NSSC20K0456. SJS acknowledges funding from STFC Grant ST/P000312/1. M.R.S. is supported by the National Science Foundation Graduate Research Fellowship Program under Grant No. 1842400.

Research by DJS is supported by NSF grants AST-1821967, 1821987, 1813708, 1813466, and 1908972. This research is based on observations made with the NASA/ESA Hubble Space Telescope obtained from the Space Telescope Science Institute, which is operated by the Association of Universities for Research in Astronomy, Inc., under NASA contract NAS 5-26555. These observations are associated with program 15645.

X. Wang is supported by the National Natural Science Foundation of China (NSFC grants 11325313, 11633002, and 11761141001), and the National Program on Key Research and Development Project (grant no. 2016YFA0400803). We acknowledge the support of the staff of the Xinglong 2.16-m telescope. This work was partially supported by the Open Project Program of the Key Laboratory of Optical Astronomy, National Astronomical Observatories, Chinese Academy of Sciences." Funding for the LJT has been provided by Chinese Academy of Sciences and the People's Government of Yunnan Province. The LJT is jointly operated and administrated by Yunnan Observatories and Center for Astronomical Mega-Science, CAS.

Based on observations obtained at the Southern Astrophysical Research (SOAR) telescope, which is a joint project of the Ministério da Ciência, Tecnologia, Inovações e Comunicações (MCTIC) do Brasil, the U.S. National Optical Astronomy Observatory (NOAO), the University of North Carolina at Chapel Hill (UNC), and Michigan State University (MSU).

Observations reported here were obtained at the MMT Observatory, a joint facility of the University of Arizona and the Smithsonian Institution.

Some of the data presented herein were obtained at the W. M. Keck Observatory, which is operated as a scientific partnership among the California Institute of Technology, the University of California and the National Aeronautics and Space Administration. The Observatory was made possible by the generous financial support of the W. M. Keck Foundation. The authors wish to recognize and acknowledge the very significant cultural role and reverence that the summit of Maunakea has always had within the indigenous Hawaiian community. We are most fortunate to have the opportunity to conduct observations from this mountain. We wish to recognize the destructive history of colonialism endured by native Hawaiians as we strive to hear the voice of those whose sacred land we continue to utilize for scientific gain.

This work includes data obtained with the Swope Telescope at Las Campanas Observatory, Chile, as part of the Swope Time Domain Key Project (PI: Piro, Co-Is: Drout, Phillips, Holoien, French, Cowperthwaite, Burns, Madore, Foley, Kilpatrick, Rojas-Bravo, Dimitriadis, Hsiao). We wish to thank Swope Telescope observers Jorge Anais Vilchez, Abdo Campillay, Nahir Munoz Elgueta and Natalie Ulloa for collecting data presented in this paper.

This research has made use of the XRT Data Analysis Software (XRTDAS) developed under the responsibility of the ASI Science Data Center (ASDC), Italy. The SN group at Konkoly Observatory is supported by the project "Transient Astrophysical Objects" GINOP 2.3.2-15-2016-00033 of the National Research, Development and Innovation Office (NKFIH), Hungary, funded by the European Union. Based on observations collected at the European Southern Observatory under ESO programme 1103.D-0328.

This work has made use of data from the Asteroid Terrestrial-impact Last Alert System (ATLAS) project. ATLAS is primarily funded to search for near earth asteroids through NASA grants NN12AR55G, 80NSSC18K0284, and 80NSSC18K1575; byproducts of the NEO search include images and catalogs from the survey area. The ATLAS science products have been made possible through the contributions of the University of Hawaii Institute for Astronomy, the Queen's University Belfast, and the Space Telescope Science Institute.

2.13 Appendix

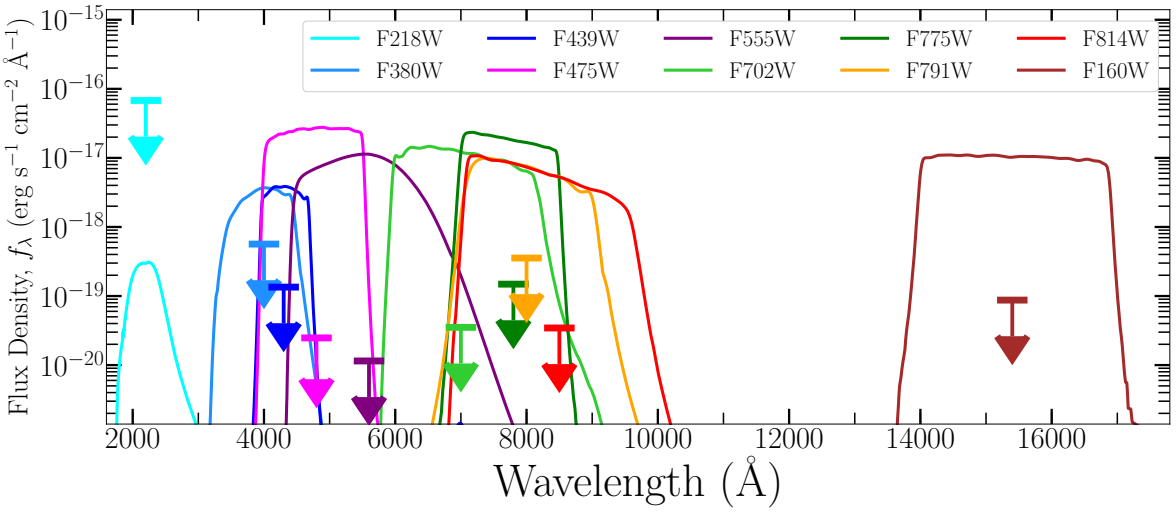

Figure 2.26 *HST* pre-explosion limits with respect to filter functions.

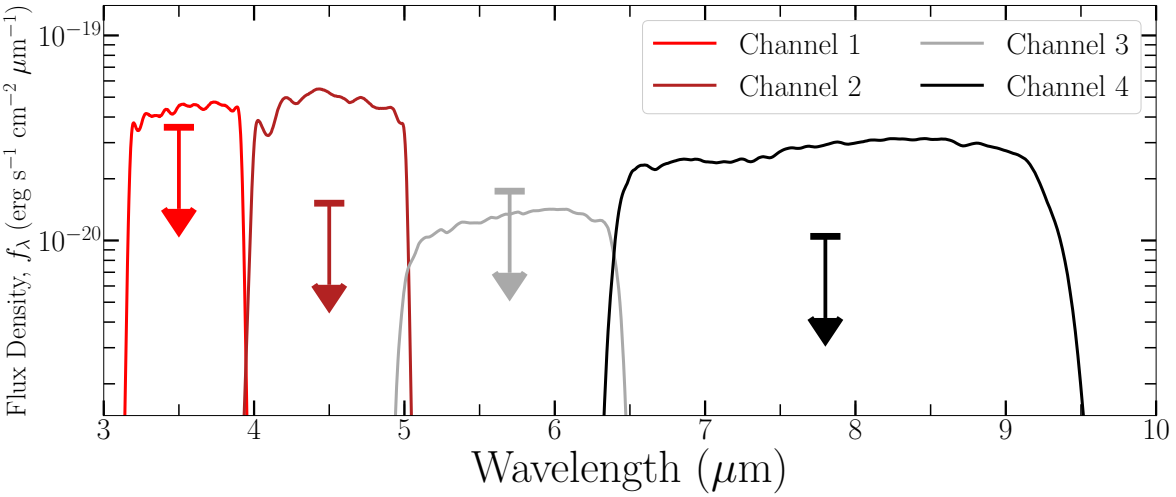

Figure 2.27 *Spitzer* pre-explosion limits with respect to filter functions.

Table A1. *HST* Pre-explosion Limits on Progenitor

Instrument	Aperture	Filter	UT Date Obs.	Exp. Time (s)	Proposal No.	3σ Limit[a] (mag)
WFPC2	WF	F218W	1999-02-02	1200	6358	21.2
WFPC2	WF	F380W	2008-01-04	1000	11171	25.2
WFPC2	WF	F439W	1993-12-31 – 2008-01-04	60 – 900	5195, 11171	26.6
WFC3	UVIS	F475W	2009-11-12	300-670	6358	28.2
WFPC2	WF	F555W	1993-12-31 – 2008-01-04	10 – 1000	5195, 5972, 9776	28.7
WFPC2	WF	F702W	1993-12-31 – 2008-01-04	5 – 600	5195, 11171	27.0
WFC3	UVIS	F775W	1999-02-02	1200	6358	25.2
WFPC2	WF	F791W	2008-01-04	500	11171	24.2
WFPC2	WF	F814W	1994-05-12 – 1996-04-27	350 – 2100	5972, 15133	26.6
WFC3	IR	F160W	2018-02-04	596	15133	24.3

[a]All apparent magnitudes in Vega system.

Table A2. *Spitzer* Pre-explosion Limits on Progenitor

UT Date Obs. Range	Channel 1	Channel 2	Channel 3	Channel 4[a]
2015-09-06 – 2019-10-27	23.49 mag	23.87 mag	23.21 mag	23.08 mag

[a]All apparent magnitudes in AB system.

Table A3. X-ray Observations of SN 2019ehk

MJD	Phase[a] (days)	Photon Index (Γ)	0.3-10 keV Unabsorbed Flux (10^{-12} erg s^{-1} cm^{-2})	Instrument
58604.61	+2.81	0.1 ± 0.4	$4.3^{+0.9}_{-0.8}$	*Swift*-XRT
58606.03	+4.23	0.2 ± 0.9	$1.3^{+0.9}_{-0.6}$	*Swift*-XRT
58607.56	+5.76	–	< 0.7[b]	*Swift*-XRT
58612.71	+10.91	–	< 0.9	*Swift*-XRT
58619.64	+17.84	–	< 1.6	*Swift*-XRT
58624.56	+22.76	–	0.8	*Swift*-XRT
58629.30	+27.50	–	< 0.7	*Swift*-XRT
58894.00	+292.2	–	$< 1.1 \times 10^{-2}$	*Chandra*

[a]Relative to explosion (MJD 58601.8).

[b]Flux calibration performed assuming same spectral parameters inferred at $t =$ 4.2 d.

Table A4. VLA radio observations of SN 2019ehk

Start Date (UT)	Time[a] (days)	Frequency (GHz)	Bandwidth (GHz)	Flux Density[b] (μJy/beam)
2019-05-29	30	6.05	2.048	≤ 27
2019-06-18	51	6.05	2.048	≤ 24.8
2019-07-15	78	6.10	2.048	≤ 28
2019-08-29	122	6.10	2.048	≤ 21
2019-12-04	220	6.05	2.048	≤ 880

[a]Relative to second B maximum (MJD 58615.156)

[b]Upper-limits are quoted at 3σ.

Table A5. Shock Cooling Models

Model	Phase Range	$E(B-V)_{host}$	R_e $R_\odot$	M_e $[\times 10^{-2}]$ $M_\odot$	v_e $[\times 10^3]$ km s^{-1}	t_{off} days
Nakar & Piro (2014)	$t < 2$	0.47	110 ± 50	0.9 ± 0.6	12.0	–
Nakar & Piro (2014)	$t < 6$	0.47	105 ± 27	10.4 ± 3.3	12.0	–
Piro (2015)	$t < 2$	0.47	$174.1^{+3.1}_{-4.4}$	$0.51^{+0.1}_{-0.1}$	9.5 ± 0.3	$0.01^{+0.01}_{-0.00}$
Piro (2015)	$t < 6$	0.47	$208.2^{+5.3}_{-6.5}$	$7.2^{+1.1}_{-1.1}$	7.9 ± 0.20	$0.01^{+0.01}_{-0.00}$
Sapir & Waxman (2017) [n=3/2]	$t < 2$	0.47	$7.2^{+2.9}_{-2.9}$	$20.2^{+14.1}_{-6.3}$	$13.0^{+1.6}_{-0.7}$	$0.17^{+0.2}_{-0.1}$
Sapir & Waxman (2017) [n=3/2]	$t < 6$	0.47	~ 30	~ 30	~ 12	–
Sapir & Waxman (2017) [n=3]	$t < 2$	0.47	$7.6^{+4.3}_{-3.0}$	$83.3^{+17.0}_{-20.2}$	$20.6^{+7.9}_{-3.2}$	$0.3^{+0.1}_{-0.1}$
Sapir & Waxman (2017) [n=3]	$t < 6$	0.47	~ 43	~ 120	~ 19	–

Table A6. Helium Star Models

Model	$M_{\rm i}$ ($M_\odot$)	$M_{\rm f}$ ($M_\odot$)	$M_{\rm He}$ ($M_\odot$)	$M_{\rm C/O}$ ($M_\odot$)	$L_{\rm f}$ ($L_\odot$)	$T_{\rm eff}$ (K)	$Y_{\rm s}$	End Point	$T_{\rm max}$ (10^9 K)	Comments
#1	3.00	2.61	1.10	1.51	4.50	6552	0.98	O-burning	2.0	Single He-star
#2	3.00	1.77	0.20	1.57	4.50	64094	0.97	O-burning	1.9	Single He-star
#3	2.70	2.61	1.20	1.50	4.54	10625	0.98	ONeMg Core	1.2	Single He-star
#4	2.70	1.75	0.34	1.41	4.46	6428	0.98	O-burning	1.9	Single He-star
#5	2.70	1.50	0.11	1.38	4.41	16856	0.96	ONeMg Core	1.2	Single He-star
#6	2.70	1.41	0.05	1.36	4.71	14486	0.65	ONeMg Core	1.1	Single He-star
#7	3.00	1.89	0.46	1.43	3.49	8226	0.94	O-burning	2.0	Binary
#8	3.00	1.78	0.35	1.43	4.41	12436	0.98	O-burning	1.8	Binary

Note. — L in log space. Y_s is the surface helium mass fraction. Model luminosity and temperature presented in Figure 2.24: black polygons for O-burning end state and red polygons for a ONeMg core.

Table A7. Binary Progenitor Models from Yoon et al. (2017)

$M_{\rm p}$	$M_{\rm p}$ ($M_\odot$)	$M_{\rm f}$ ($M_\odot$)	$L_{\rm f}$ ($L_\odot$)	$R_{\rm f}$ ($R_\odot$)	$T_{\rm eff}$ (K)	$H_{\rm env}$	$M_{\rm H}$ ($M_\odot$)	$M_{\rm He}$ ($M_\odot$)	$\dot{M}$ ($M_\odot$ yr^{-1})	SN
Sm13p50	13	3.88	4.82	6.50	4.56	0.00	0.00	1.63	-5.65	Ib
Sm13p50	13	3.96	4.84	6.20	4.58	0.00	0.00	1.65	-5.63	Ib
Sm16p50	16	4.99	5.05	4.90	4.68	0.00	0.00	1.66	-5.35	Ib
Sm16p300	16	5.01	5.06	5.10	4.67	0.00	0.00	1.65	-5.34	Ib
Sm16p1700	16	6.08	5.14	3.20	4.79	0.02	0.00	2.25	-5.27	IIb (BSG)
Sm18p50	18	5.44	5.10	2.10	4.88	0.00	0.00	1.57	-5.29	Ib
Sm18p500	18	5.55	5.10	1.90	4.90	0.00	0.00	1.61	-5.29	Ib
Sm18p2000	18	6.62	5.19	1.70	4.94	0.00	0.00	2.16	-5.18	Ib
Sm18p2200	18	7.04	5.16	1.70	4.93	0.08	0.01	2.53	-5.36	IIb (BSG)

Note. — L, T, $\dot{M}$ in log space.

Table A8. BPASS Binary Progenitor Models

M_i $M_\odot$	L_f $L_\odot$	T_f K	R_f $R_\odot$	$M_{p,f}$ $M_\odot$	$M_{s,f}$ $M_\odot$	$M_{\rm H}$ $M_\odot$	$M_{\rm He}$ $M_\odot$	M_{Ni} $M_\odot$	$M_{\rm ej}$ $M_\odot$	Delay Time yrs
9.50	4.50	4.42	8.77	1.69	3.87	0.000	0.22	0.006	1.76	7.49
9.50	4.51	4.55	4.76	1.61	6.08	0.000	0.19	0.005	1.46	7.49
10.00	4.51	4.46	7.35	1.65	1.00	0.000	0.19	0.008	1.61	7.46
10.00	4.51	4.32	13.52	1.69	7.75	0.000	0.20	0.006	1.78	7.45
10.00	4.52	4.63	3.28	1.63	6.60	0.000	0.18	0.005	1.54	7.46
10.00	4.45	4.45	6.94	1.69	2.01	0.000	0.25	0.007	1.79	7.46
10.00	4.29	4.38	7.97	1.59	3.06	0.000	0.12	0.006	1.40	7.46
10.00	4.50	4.64	3.17	1.57	1.00	0.000	0.13	0.005	1.34	7.46
10.00	4.46	4.32	12.82	1.72	3.04	0.000	0.20	0.006	1.90	7.45
10.00	4.51	4.37	11.11	1.70	2.01	0.000	0.20	0.006	1.83	7.45
10.00	4.54	4.34	13.14	1.74	1.00	0.000	0.24	0.006	1.98	7.45
10.00	4.22	4.31	10.55	1.74	7.55	0.000	0.22	0.010	1.99	7.45
10.00	4.51	4.31	14.67	1.70	9.03	0.000	0.21	0.004	1.83	7.45

Note. — L, T and delay time in log space. Weak SN (10^{50} erg), CO Core mass ¡ 1.35 $M_\odot$, $M_{p,f} > 1.5$ $M_\odot$ $M_{\rm ej} < 2$ $M_\odot$, $M_{\rm H} < 0.01$ $M_\odot$, $M_{\rm He} > 0.1$ $M_\odot$

Table A9. Optical Spectroscopy of SN 2019ehk

UT Date	MJD	Phase[a] (days)	Telescope	Instrument	Wavelength Range (Å)
2019-04-30	58603.3	−11.9	Shane	Kast	4000–8600Å
2019-05-01	58604.1	−11.1	Xinglong	BFOSC	4200–8600Å
2019-05-01	58604.2	−11.0	Shane	Kast	3500–8200Å
2019-05-02	58605.1	−10.1	Xinglong	BFOSC	4200–8600Å
2019-05-03	58606.2	−9.0	Shane	Kast	3500–8600Å
2019-05-04	58607.1	−8.1	Xinglong	BFOSC	4200–8200Å
2019-05-05	58608.1	−7.1	Xinglong	BFOSC	4200–8200Å
2019-05-05	58608.2	−7.0	Shane	Kast	3500–11000Å
2019-05-07	58610.1	−5.0	Faulkes North	FLOYDS	3500–10000Å
2019-05-07	58610.2	−5.1	Xinglong	BFOSC	4200–8800Å
2019-05-09	58612.1	−3.0	Xinglong	BFOSC	4200–8800Å
2019-05-11	58614.1	−1.0	SOAR	Goodman	4000–9000Å
2019-05-12	58615.1	0.0	NTT	EFOSC2	3600–9200Å
2019-05-13	58616.1	+1.0	Shane	Kast	3500–11000Å
2019-05-18	58621.1	+6.0	LJT	YFOSC	3500–8800Å
2019-05-24	58627.1	+12.0	Faulkes North	FLOYDS	4800–10000Å
2019-05-28	58631.1	+16.0	Faulkes North	FLOYDS	3500–10000Å
2019-06-03	58637.1	+22.0	MMT	Binospec	4800–7500Å
2019-06-05	58639.1	+24.0	Bok	B&C	4000–7800Å
2019-06-05	58639.1	+24.0	Faulkes North	FLOYDS	3500–10000Å
2019-06-14	58648.1	+31.0	Shane	Kast	3500–11000Å
2019-06-21	58655.1	+38.0	SOAR	Triple Spec	9000–25000Å
2019-06-30	58664.1	+49.0	Keck I	LRIS	3200–10800Å
2019-07-06	58670.1	+55.0	Shane	Kast	3500–11000Å
2019-07-10	58674.1	+59.0	Shane	Kast	3500–11000Å
2019-07-10	58674.1	+59.0	Faulkes North	FLOYDS	3500–10000Å
2020-01-24	58872.1	+257.0	Keck I	LRIS	5400–10200Å

[a]Relative to second B-band maximum (MJD 58615.156)

Table A10. Optical Photometry of SN 2019ehk

MJD	Phase[a]	Filter	Magnitude	Uncertainty	Instrument
58603.18	−11.98	u	19.15	0.02	Swope
58603.22	−11.93	u	18.69	0.06	Swope
58608.13	−7.02	u	20.00	0.06	Swope
58616.18	+1.02	u	20.71	0.20	Swope
58675.00	+59.84	u	24.00	0.20	Swope
58603.18	−11.97	B	17.63	0.01	Swope
58603.23	−11.93	B	17.63	0.01	Swope
58608.14	−7.02	B	18.06	0.01	Swope
58609.17	−5.98	B	18.21	0.02	Swope
58611.14	−4.02	B	18.06	0.02	Swope
58615.16	+0.00	B	17.99	0.01	Swope
58636.09	+20.94	B	20.10	0.02	Swope
58642.09	+26.93	B	20.45	0.09	Swope
58644.04	+28.89	B	20.41	0.05	Swope
58658.06	+42.90	B	20.99	0.05	Swope
58670.04	+54.89	B	21.40	0.07	Swope
58603.18	−11.98	V	16.91	0.01	Swope
58603.23	−11.93	V	16.91	0.01	Swope
58608.14	−7.02	V	16.89	0.01	Swope
58609.17	−5.98	V	16.96	0.01	Swope
58615.15	−0.00	V	16.56	0.01	Swope
58616.19	+1.03	V	16.53	0.01	Swope
58617.08	+1.92	V	16.58	0.01	Swope
58631.13	+15.98	V	18.09	0.10	Swope
58636.10	+20.94	V	18.19	0.01	Swope
58642.09	+26.93	V	18.45	0.02	Swope
58644.05	+28.90	V	18.48	0.02	Swope
58658.05	+42.90	V	19.01	0.02	Swope
58670.04	+54.88	V	19.63	0.02	Swope
58691.96	+76.81	V	20.38	0.04	Swope
58603.18	−11.98	g	17.20	0.01	Swope
58603.22	−11.94	g	17.21	0.01	Swope
58608.13	−7.02	g	17.44	0.01	Swope
58609.18	−5.98	g	17.54	0.01	Swope

Table A10 (cont'd)

MJD	Phase[a]	Filter	Magnitude	Uncertainty	Instrument
58611.15	−4.00	g	17.36	0.01	Swope
58615.15	−0.01	g	17.27	0.01	Swope
58616.18	+1.02	g	17.27	0.01	Swope
58617.08	+1.93	g	17.36	0.01	Swope
58631.12	+15.97	g	18.88	0.10	Swope
58636.11	+20.95	g	19.01	0.02	Swope
58639.05	+23.89	g	19.28	0.02	Swope
58642.10	+26.94	g	19.44	0.11	Swope
58644.06	+28.91	g	19.38	0.03	Swope
58658.04	+42.89	g	19.82	0.02	Swope
58670.02	+54.87	g	20.35	0.03	Swope
58688.98	+73.83	g	20.78	0.05	Swope
58690.98	+75.83	g	20.78	0.04	Swope
58697.98	+82.82	g	21.02	0.07	Swope
58603.17	−11.98	r	16.59	0.01	Swope
58603.22	−11.94	r	16.60	0.01	Swope
58608.13	−7.03	r	16.45	0.01	Swope
58609.18	−5.97	r	16.48	0.01	Swope
58615.14	−0.01	r	16.01	0.01	Swope
58616.18	+1.02	r	15.94	0.01	Swope
58617.08	+1.93	r	15.94	0.01	Swope
58631.12	+15.96	r	17.07	0.01	Swope
58636.08	+20.93	r	17.26	0.01	Swope
58636.11	+20.96	r	17.26	0.01	Swope
58639.05	+23.90	r	17.41	0.01	Swope
58642.10	+26.95	r	17.54	0.01	Swope
58644.07	+28.91	r	17.57	0.01	Swope
58658.04	+42.88	r	18.17	0.01	Swope
58670.01	+54.86	r	18.84	0.01	Swope
58688.97	+73.81	r	19.49	0.02	Swope
58690.97	+75.81	r	19.48	0.02	Swope
58696.97	+81.82	r	19.80	0.04	Swope
58603.18	−11.98	i	16.48	0.01	Swope
58603.22	−11.94	i	16.45	0.01	Swope

Table A10 (cont'd)

MJD	Phase[a]	Filter	Magnitude	Uncertainty	Instrument
58608.13	−7.02	i	16.05	0.01	Swope
58609.18	−5.97	i	16.17	0.01	Swope
58611.15	−4.00	i	15.76	0.01	Swope
58615.14	−0.01	i	15.55	0.01	Swope
58616.18	+1.02	i	15.47	0.01	Swope
58617.08	+1.93	i	15.41	0.01	Swope
58631.12	+15.97	i	16.42	0.01	Swope
58636.11	+20.96	i	16.56	0.01	Swope
58639.05	+23.89	i	16.67	0.01	Swope
58642.10	+26.95	i	16.77	0.01	Swope
58644.07	+28.91	i	16.79	0.01	Swope
58658.04	+42.88	i	17.17	0.01	Swope
58670.02	+54.86	i	17.53	0.01	Swope
58688.98	+73.82	i	17.94	0.01	Swope
58690.98	+75.82	i	17.82	0.01	Swope
58697.97	+82.82	i	18.11	0.01	Swope
58601.28	−13.88	B	>20.12	–	Joel Shepherd
58603.30	−11.86	B	17.79	0.16	Joel Shepherd
58601.28	−13.88	V	>18.85	–	Joel Shepherd
58603.30	−11.86	V	16.84	0.17	Joel Shepherd
58602.24	−12.92	g	18.78	0.43	Joel Shepherd
58601.28	−13.88	r	>18.36	–	Joel Shepherd
58603.30	−11.86	r	16.52	0.09	Joel Shepherd
58600.10	−15.06	g	>20.48	–	ZTF
58609.21	−5.94	g	17.52	0.03	ZTF
58612.25	−2.90	g	17.33	0.02	ZTF
58619.25	+4.10	g	17.76	0.15	ZTF
58628.19	+13.04	g	18.86	0.10	ZTF
58633.23	+18.07	g	19.06	0.12	ZTF
58636.25	+21.09	g	19.20	0.13	ZTF
58642.20	+27.04	g	19.54	0.20	ZTF
58658.21	+43.05	g	19.77	0.24	ZTF
58661.23	+46.07	g	20.36	0.46	ZTF
58606.21	−8.95	r	15.84	0.01	ZTF

Table A10 (cont'd)

MJD	Phase[a]	Filter	Magnitude	Uncertainty	Instrument
58612.21	−2.94	r	16.09	0.01	ZTF
58619.19	+4.04	r	16.14	0.06	ZTF
58628.30	+13.15	r	16.79	0.02	ZTF
58633.20	+18.05	r	17.13	0.03	ZTF
58636.21	+21.05	r	17.24	0.03	ZTF
58639.18	+24.02	r	17.44	0.04	ZTF
58642.22	+27.07	r	17.54	0.04	ZTF
58646.23	+31.07	r	17.39	0.08	ZTF
58649.22	+34.06	r	17.63	0.08	ZTF
58652.28	+37.12	r	18.00	0.14	ZTF
58658.18	+43.02	r	18.36	0.09	ZTF
58661.20	+46.04	r	18.39	0.10	ZTF
58606.21	−8.95	r	15.82	0.03	ZTF
58612.21	−2.94	r	16.07	0.04	ZTF
58619.19	+4.04	r	16.06	0.04	ZTF
58633.20	+18.05	r	17.07	0.04	ZTF
58611.90	−3.26	B	18.14	0.15	Konkoly
58613.92	−1.24	B	18.07	0.10	Konkoly
58638.90	+23.74	B	20.88	0.79	Konkoly
58647.87	+32.71	B	21.27	0.12	Konkoly
58611.90	−3.26	V	16.72	0.04	Konkoly
58613.92	−1.24	V	16.65	0.03	Konkoly
58638.90	+23.74	V	18.30	0.08	Konkoly
58647.87	+32.71	V	18.53	0.23	Konkoly
58649.90	+34.74	V	18.52	0.22	Konkoly
58611.90	−3.26	g	17.29	0.06	Konkoly
58613.92	−1.24	g	17.22	0.02	Konkoly
58638.90	+23.74	g	19.33	0.12	Konkoly
58649.90	+34.74	g	19.19	0.20	Konkoly
58611.90	−3.26	r	16.10	0.02	Konkoly
58613.92	−1.24	r	16.14	0.01	Konkoly
58638.90	+23.74	r	17.58	0.03	Konkoly
58647.87	+32.71	r	17.95	0.11	Konkoly
58649.90	+34.74	r	17.97	0.06	Konkoly

Table A10 (cont'd)

MJD	Phase[a]	Filter	Magnitude	Uncertainty	Instrument
58611.90	−3.26	*i*	16.10	0.02	Konkoly
58613.92	−1.24	*i*	16.14	0.01	Konkoly
58638.90	+23.74	*i*	17.58	0.03	Konkoly
58647.87	+32.71	*i*	17.95	0.11	Konkoly
58649.90	+34.74	*i*	17.97	0.06	Konkoly
58611.90	−3.26	*z*	15.77	0.04	Konkoly
58613.92	−1.24	*z*	15.71	0.02	Konkoly
58638.90	+23.74	*z*	16.88	0.03	Konkoly
58647.87	+32.71	*z*	17.02	0.04	Konkoly
58573.46	−41.70	*o*	>19.58	–	ATLAS
58577.44	−37.72	*o*	>18.94	–	ATLAS
58581.44	−33.71	*o*	>19.51	–	ATLAS
58585.43	−29.73	*o*	>20.38	–	ATLAS
58589.40	−25.75	*o*	>18.39	–	ATLAS
58593.47	−21.68	*o*	>18.45	–	ATLAS
58595.41	−19.74	*o*	>20.67	–	ATLAS
58597.41	−17.75	*o*	>20.00	–	ATLAS
58599.42	−15.74	*o*	>19.90	–	ATLAS
58605.40	−9.75	*o*	15.61	0.02	ATLAS
58609.39	−5.76	*o*	16.28	0.03	ATLAS
58613.35	−1.81	*o*	15.79	0.02	ATLAS
58615.44	+0.28	*o*	15.70	0.07	ATLAS
58623.30	+8.15	*o*	16.13	0.10	ATLAS
58625.38	+10.22	*o*	16.29	0.02	ATLAS
58627.34	+12.19	*o*	16.44	0.01	ATLAS
58629.32	+14.16	*o*	16.58	0.02	ATLAS
58631.36	+16.20	*o*	16.70	0.02	ATLAS
58633.39	+18.24	*o*	16.77	0.06	ATLAS
58641.31	+26.15	*o*	17.19	0.06	ATLAS
58643.37	+28.22	*o*	17.07	0.10	ATLAS
58647.30	+32.14	*o*	17.36	0.03	ATLAS
58649.37	+34.21	*o*	17.47	0.13	ATLAS
58653.27	+38.11	*o*	17.48	0.15	ATLAS
58655.29	+40.13	*o*	17.60	0.14	ATLAS

Table A10 (cont'd)

MJD	Phase[a]	Filter	Magnitude	Uncertainty	Instrument
58659.30	+44.14	*o*	17.71	0.14	ATLAS
58665.29	+50.13	*o*	18.05	0.10	ATLAS
58671.26	+56.10	*o*	18.21	0.21	ATLAS
58681.30	+66.14	*o*	18.61	1.96	ATLAS
58689.27	+74.11	*o*	18.46	0.24	ATLAS
58575.46	−39.70	*c*	>19.89	–	ATLAS
58579.45	−35.70	*c*	>20.29	–	ATLAS
58583.42	−31.73	*c*	>19.00	–	ATLAS
58603.42	−11.73	*c*	16.77	0.04	ATLAS
58607.41	−7.74	*c*	16.86	0.06	ATLAS
58611.40	−3.75	*c*	16.72	0.03	ATLAS
58635.35	+20.20	*c*	18.01	0.09	ATLAS
58639.31	+24.15	*c*	18.11	0.09	ATLAS
58663.26	+48.10	*c*	19.08	0.37	ATLAS
58667.28	+52.12	*c*	19.15	0.31	ATLAS
58699.26	+84.11	*c*	19.95	0.79	ATLAS
58603.61	−11.55	*u*	17.55	0.01	LCO
58604.59	−10.56	*u*	17.46	0.02	LCO
58605.25	−9.91	*u*	16.55	0.02	LCO
58607.38	−7.78	*u*	17.70	0.06	LCO
58607.54	−7.62	*u*	17.91	0.22	LCO
58614.37	−0.78	*u*	18.66	0.10	LCO
58603.61	−11.54	*B*	17.52	0.02	LCO
58604.61	−10.55	*B*	17.55	0.02	LCO
58605.25	−9.91	*B*	16.81	0.02	LCO
58607.38	−7.77	*B*	17.57	0.03	LCO
58607.54	−7.62	*B*	17.58	0.06	LCO
58614.38	−0.78	*B*	17.95	0.02	LCO
58615.34	+0.19	*B*	17.98	0.03	LCO
58622.50	+7.35	*B*	18.82	0.05	LCO
58626.24	+11.09	*B*	19.53	0.01	LCO
58630.91	+15.76	*B*	19.88	0.03	LCO
58635.87	+20.72	*B*	20.02	0.05	LCO
58636.33	+21.17	*B*	20.19	0.07	LCO

Table A10 (cont'd)

MJD	Phase[a]	Filter	Magnitude	Uncertainty	Instrument
58641.31	+26.15	B	20.27	0.06	LCO
58652.70	+37.54	B	20.68	0.32	LCO
58657.51	+42.36	B	20.62	0.09	LCO
58661.88	+46.72	B	21.05	0.09	LCO
58667.45	+52.30	B	20.68	0.11	LCO
58603.61	−11.54	V	17.04	0.02	LCO
58604.61	−10.55	V	16.94	0.02	LCO
58605.25	−9.90	V	16.14	0.02	LCO
58607.38	−7.77	V	16.64	0.03	LCO
58607.54	−7.61	V	16.74	0.04	LCO
58614.38	−0.77	V	16.53	0.01	LCO
58615.35	+0.19	V	16.52	0.01	LCO
58622.51	+7.35	V	17.18	0.02	LCO
58626.25	+11.09	V	17.49	0.02	LCO
58630.92	+15.77	V	17.87	0.02	LCO
58636.34	+21.18	V	18.10	0.06	LCO
58641.32	+26.16	V	18.32	0.03	LCO
58652.70	+37.55	V	18.91	0.01	LCO
58657.52	+42.37	V	19.06	0.02	LCO
58661.88	+46.73	V	19.29	0.04	LCO
58667.46	+52.31	V	19.50	0.04	LCO
58687.85	+72.69	V	20.18	0.16	LCO
58603.62	−11.54	g	17.33	0.02	LCO
58614.39	−0.77	g	17.34	0.01	LCO
58615.35	+0.20	g	17.38	0.01	LCO
58622.51	+7.36	g	18.35	0.02	LCO
58652.71	+37.55	g	19.96	0.06	LCO
58657.52	+42.37	g	20.15	0.05	LCO
58603.62	−11.54	r	16.92	0.01	LCO
58604.61	−10.54	r	16.78	0.01	LCO
58607.39	−7.77	r	16.38	0.02	LCO
58607.55	−7.61	r	16.44	0.02	LCO
58614.39	−0.77	r	16.22	0.01	LCO
58615.36	+0.20	r	16.18	0.02	LCO

Table A10 (cont'd)

MJD	Phase[a]	Filter	Magnitude	Uncertainty	Instrument
58622.52	+7.36	r	16.53	0.02	LCO
58626.26	+11.10	r	16.87	0.02	LCO
58636.35	+21.20	r	17.39	0.03	LCO
58652.71	+37.56	r	18.14	0.02	LCO
58657.53	+42.38	r	18.39	0.03	LCO
58687.86	+72.70	r	19.64	0.02	LCO
58603.62	−11.53	i	16.69	0.05	LCO
58604.62	−10.54	i	16.47	0.01	LCO
58605.26	−9.90	i	15.69	0.01	LCO
58607.55	−7.61	i	16.00	0.03	LCO
58614.39	−0.77	i	15.66	0.02	LCO
58615.36	+0.21	i	15.60	0.02	LCO
58622.52	+7.36	i	15.84	0.02	LCO
58626.26	+11.10	i	16.10	0.01	LCO
58630.93	+15.78	i	16.35	0.01	LCO
58636.35	+21.20	i	16.61	0.01	LCO
58641.33	+26.18	i	16.84	0.03	LCO
58652.72	+37.56	i	17.14	0.02	LCO
58657.54	+42.38	i	17.32	0.02	LCO
58667.48	+52.32	i	17.55	0.02	LCO
58687.86	+72.71	i	17.92	0.02	LCO
58605.25	−9.90	g	16.39	0.02	Thacher
58606.26	−8.89	g	16.71	0.02	Thacher
58607.24	−7.91	g	17.17	0.02	Thacher
58633.27	+18.11	g	19.19	0.07	Thacher
58605.25	−9.90	r	15.76	0.01	Thacher
58606.26	−8.89	r	15.99	0.01	Thacher
58607.24	−7.91	r	16.30	0.03	Thacher
58632.18	+17.03	r	17.30	0.03	Thacher
58633.27	+18.11	r	17.22	0.02	Thacher
58634.18	+19.03	r	17.25	0.02	Thacher
58640.18	+25.03	r	17.40	0.03	Thacher
58641.19	+26.03	r	17.96	0.08	Thacher
58642.30	+27.14	r	17.78	0.03	Thacher

Table A10 (cont'd)

MJD	Phase[a]	Filter	Magnitude	Uncertainty	Instrument
58643.19	+28.03	r	17.83	0.04	Thacher
58644.19	+29.03	r	17.76	0.06	Thacher
58645.31	+30.15	r	18.13	0.23	Thacher
58647.19	+32.03	r	18.23	0.08	Thacher
58654.21	+39.06	r	18.43	0.06	Thacher
58658.21	+43.06	r	18.74	0.06	Thacher
58662.21	+47.06	r	18.60	0.05	Thacher
58663.21	+48.06	r	18.79	0.06	Thacher
58664.24	+49.08	r	18.65	0.07	Thacher
58666.19	+51.03	r	18.87	0.07	Thacher
58667.21	+52.06	r	18.56	0.07	Thacher
58676.21	+61.06	r	19.21	0.16	Thacher
58606.26	−8.89	i	15.69	0.01	Thacher
58607.24	−7.91	i	16.01	0.01	Thacher
58620.19	+5.03	i	15.59	0.02	Thacher
58631.18	+16.02	i	16.53	0.02	Thacher
58632.18	+17.03	i	16.22	0.14	Thacher
58633.27	+18.11	i	16.50	0.02	Thacher
58634.18	+19.03	i	16.60	0.02	Thacher
58640.18	+25.03	i	17.03	0.03	Thacher
58641.19	+26.03	i	16.98	0.03	Thacher
58642.30	+27.14	i	16.92	0.03	Thacher
58643.19	+28.03	i	17.05	0.03	Thacher
58644.19	+29.03	i	16.92	0.04	Thacher
58646.19	+31.03	i	16.99	0.04	Thacher
58647.19	+32.03	i	16.88	0.06	Thacher
58650.21	+35.06	i	17.08	0.04	Thacher
58658.21	+43.06	i	17.43	0.03	Thacher
58662.21	+47.06	i	17.34	0.03	Thacher
58663.21	+48.06	i	17.38	0.03	Thacher
58664.24	+49.08	i	17.42	0.05	Thacher
58666.19	+51.03	i	17.48	0.03	Thacher
58667.21	+52.06	i	17.54	0.04	Thacher
58668.21	+53.06	i	17.52	0.04	Thacher

Table A10 (cont'd)

MJD	Phase[a]	Filter	Magnitude	Uncertainty	Instrument
58669.21	+54.06	i	17.57	0.04	Thacher
58670.21	+55.06	i	17.61	0.04	Thacher
58672.19	+57.03	i	17.75	0.08	Thacher
58674.21	+59.05	i	17.64	0.06	Thacher
58675.21	+60.06	i	17.74	0.06	Thacher
58676.21	+61.06	i	17.73	0.08	Thacher
58605.25	−9.90	z	15.53	0.02	Thacher
58606.26	−8.89	z	15.66	0.02	Thacher
58607.24	−7.91	z	15.97	0.02	Thacher
58620.19	+5.03	z	16.25	0.06	Thacher
58631.18	+16.02	z	16.07	0.03	Thacher
58632.18	+17.03	z	16.13	0.04	Thacher
58633.27	+18.11	z	16.07	0.03	Thacher
58634.18	+19.03	z	16.10	0.03	Thacher
58640.18	+25.03	z	16.37	0.04	Thacher
58641.19	+26.03	z	16.46	0.06	Thacher
58642.30	+27.14	z	16.31	0.04	Thacher
58643.19	+28.03	z	16.29	0.03	Thacher
58644.19	+29.03	z	16.27	0.04	Thacher
58646.19	+31.03	z	16.36	0.06	Thacher
58647.19	+32.03	z	16.25	0.03	Thacher
58650.21	+35.06	z	16.31	0.04	Thacher
58658.21	+43.06	z	16.47	0.03	Thacher
58662.21	+47.06	z	16.62	0.04	Thacher
58663.21	+48.06	z	16.65	0.03	Thacher
58664.24	+49.08	z	16.61	0.10	Thacher
58666.19	+51.03	z	16.74	0.04	Thacher
58667.21	+52.06	z	16.77	0.05	Thacher
58668.21	+53.06	z	16.79	0.05	Thacher
58669.21	+54.06	z	17.02	0.07	Thacher
58670.21	+55.06	z	16.84	0.05	Thacher
58672.19	+57.03	z	16.91	0.08	Thacher
58674.21	+59.05	z	16.92	0.08	Thacher
58675.21	+60.06	z	16.84	0.07	Thacher

Table A10 (cont'd)

MJD	Phase[a]	Filter	Magnitude	Uncertainty	Instrument
58604.61	−10.55	B	17.10	0.10	*Swift*
58606.04	−9.12	B	17.31	0.11	*Swift*
58607.56	−7.60	B	18.07	0.17	*Swift*
58619.64	+4.49	B	18.25	0.00	*Swift*
58624.57	+9.41	B	19.03	0.35	*Swift*
58629.14	+13.99	B	19.33	0.00	*Swift*
58604.61	−10.55	V	16.26	0.11	*Swift*
58606.04	−9.12	V	16.11	0.13	*Swift*
58607.56	−7.60	V	16.80	0.14	*Swift*
58624.57	+9.41	V	17.17	0.19	*Swift*
58629.14	+13.99	V	17.72	0.25	*Swift*
58604.61	−10.55	U	17.05	0.12	*Swift*
58606.04	−9.12	U	17.32	0.13	*Swift*
58607.56	−7.60	U	18.57	0.27	*Swift*
58619.64	+4.49	U	18.93	0.00	*Swift*
58624.57	+9.41	U	18.92	0.00	*Swift*
58629.14	+13.99	U	19.09	0.00	*Swift*
58604.61	−10.55	$W1$	17.80	0.15	*Swift*
58606.04	−9.12	$W1$	18.15	0.17	*Swift*
58607.56	−7.60	$W1$	19.27	0.00	*Swift*
58612.70	−2.45	$W1$	18.96	0.27	*Swift*
58619.64	+4.49	$W1$	19.15	0.00	*Swift*
58624.57	+9.41	$W1$	19.15	0.00	*Swift*
58629.14	+13.99	$W1$	19.15	0.00	*Swift*
58604.61	−10.55	$W2$	18.91	0.22	*Swift*
58606.04	−9.12	$W2$	19.28	0.00	*Swift*
58607.56	−7.60	$W2$	19.67	0.00	*Swift*
58612.70	−2.45	$W2$	19.38	0.00	*Swift*
58624.57	+9.41	$W2$	19.55	0.00	*Swift*
58629.14	+13.99	$W2$	19.75	0.00	*Swift*
58604.61	−10.55	$M2$	19.24	0.24	*Swift*
58606.04	−9.12	$M2$	19.23	0.00	*Swift*
58607.56	−7.60	$M2$	19.75	0.33	*Swift*
58612.70	−2.45	$M2$	19.25	0.00	*Swift*

Table A10 (cont'd)

MJD	Phase[a]	Filter	Magnitude	Uncertainty	Instrument
58624.57	+9.41	$M2$	19.71	0.00	*Swift*
58629.14	+13.99	$M2$	19.83	0.34	*Swift*

[a]Relative to second B-band maximum (MJD 58615.156)

Chapter 3

Late-time Observations of Calcium-Rich Transient SN 2019ehk Reveal a Pure Radioactive Decay Power Source

This chapter was previously published as Jacobson-Galán et al., 2021, ApJL, 908, L32

3.1 Abstract

We present multi-band *Hubble Space Telescope* imaging of the Calcium-rich supernova (SN) 2019ehk at 276 - 389 days after explosion. These observations represent the latest B-band to NIR photometric measurements of a Calcium-rich transient to date and allow for the first opportunity to analyze the late-time bolometric evolution of an object in this observational SN class. We find that the late-time bolometric light curve of SN 2019ehk can be described predominantly through the radioactive decay of ^{56}Co for which we derive a mass of $M(^{56}\mathrm{Co}) = (2.8 \pm 0.1) \times 10^{-2}$ $\mathrm{M}_{\odot}$. Furthermore, the rate of decline in bolometric luminosity requires the leakage of γ-rays on timescale $t_{\gamma} = 53.9 \pm 1.30$ days, but we find no statistical evidence for incomplete positron trapping in the SN ejecta. While our observations cannot constrain the exact masses of other radioactive isotopes synthesized in SN 2019ehk, we estimate a mass ratio limit of $M(^{57}\mathrm{Co})/M(^{56}\mathrm{Co}) \leq 0.030$. This limit is consistent with the explosive nucleosynthesis produced in the merger of low-mass white dwarfs, which is one of the favored progenitor scenarios in early-time studies of SN 2019ehk.

3.2 Introduction

Calcium-rich (Ca-rich) transients are a peculiar class of thermonuclear transients that were identified almost two decades ago and studied extensively ever since (Filippenko et al.

2003; Perets et al. 2010a; Kasliwal et al. 2012). These supernovae (SNe) are defined observationally by fast-evolving light curves ($t_r < 15$ days) and low overall luminosities ($M_{\rm peak} > -16$ mag), both photometric properties being consistent with typical ejecta and ^{56}Ni mass estimates of $\lesssim 0.5$ M$_\odot$ and $\lesssim 0.1$ M$_\odot$, respectively (Taubenberger 2017). The "Ca-rich" naming convention is in part derived from their spectroscopic evolution wherein these transients exhibit prominent [Ca II] emission features in their photospheric and nebular phase spectra compared to [O I] emission ([Ca II]/[O I] > 2; Milisavljevic et al. 2017). However, while Ca-rich transients appear to cool most efficiently through Ca II transitions over O I, it is debated whether these explosions are in fact more abundant in calcium ions than oxygen by mass (Perets et al. 2010a; Milisavljevic et al. 2017). As a result, we choose to adopt the nomenclature presented by Shen et al. (2019) and refer to these objects as "Calcium-strong transients" (CaSTs) throughout the paper.

The majority of known CaSTs are located in the outskirts of early-type host galaxies (Perets et al. 2011; Kasliwal et al. 2012). However, as the number of confirmed CaSTs increases, there appears to be a substantial spread in their host morphology that includes both disk-shaped as well as elliptical galaxies (Perets et al. 2010a; Perets 2014a; Milisavljevic et al. 2017; De et al. 2020). Additionally, CaSTs are typically found in galaxy groups or cluster environments with no evidence of star formation and their explosion sites are generally associated with old stellar populations (Perets et al. 2010a, 2011; Lyman et al. 2014; Foley 2015; Lunnan et al. 2017). Consequently, typical progenitor systems proposed for CaSTs have included a white dwarf (WD) with a neutron star (NS), a black hole (BH), another WD or a non-degenerate main sequence star companion (Rosswog et al. 2008; Perets et al. 2010a; Metzger 2012; MacLeod et al. 2014; Sell et al. 2015; Margalit & Metzger 2016; Bobrick et al. 2017; Zenati et al. 2019b,a). Nevertheless, the observed diversity in host galaxies and explosion characteristics suggests heterogeneity amongst CaST progenitors (Milisavljevic et al. 2017). Therefore, increasing the sample size of objects and performing novel studies of new CaSTs will help uncover the origins of this unique explosion class.

On 2019 April 29 (MJD 58602.24), the closest known CaST, SN 2019ehk, was detected in the nearby galaxy NGC 4321 (M100) at 16.2 ± 0.4 Mpc (Jacobson-Galán et al. 2020b; Nakaoka et al. 2020). Observations of SN 2019ehk were acquired as early as $\sim$10 hours after explosion ($t_{exp} = 58601.8 \pm 0.1$ days, in MJD), which allowed for unprecedented multi-wavelength coverage of this event. Fast-cadence observations revealed a double-peaked light curve in optical bands, with the primary peak being temporally coincident with luminous X-ray emission ($L_X \approx 10^{41}$ erg s^{-1}); the first instance of X-ray detections in a CaST. Combined with flash-ionized Hα and He II spectral lines at +1.5d after explosion, these observations revealed the presence of dense circumstellar material (CSM) in a compact shell surrounding the progenitor system at the time of explosion. Jacobson-Galán et al. (2020b) (hereafter WJG20a) also presented deep *Hubble Space Telescope (HST)* pre-explosion imaging of the explosion site that constrained the possible progenitor of SN 2019ehk to be either a massive star in the lowest mass bin ($\lesssim 10$ M$_\odot$) or a WD in a binary system. Alternatively, Nakaoka et al. (2020) suggest that SN 2019ehk is an ultra-stripped SN candidate that arose from a He (or C/O) star + NS binary configuration. This latter scenario, however, is difficult

to reconcile with the presence of H-rich material in the local circumstellar environment. Recently, based on derived Oxygen mass, De et al. (2021) concluded that the progenitor of SN 2019ehk was a low-mass massive star ($M_{\rm ZAMS} \approx 9 - 9.5$ M$_\odot$) that lost most of its H envelope via binary interaction prior to explosion. We explicitly address the viability of this alternative scenario of a "Calcium-rich type IIb" SN proposed by De et al. (2021) in Section 3.5.3 and we offer an additional, independent calculation of the Oxygen mass parameter.

Photometric observations of SNe at late time phases ($t \gtrsim 300$ days) enables the study of explosion power sources and, consequently, the progenitor system responsible for a given transient. To date, only a few CaSTs and CaST candidates have been detected in photometric observations at $\gtrsim 250$ days after explosion e.g., PTF10iuv (Kasliwal et al. 2012), SN 2012hn (Valenti et al. 2014a), and SN 2018gwo (De et al. 2020). The close proximity of SN 2019ehk provides the first opportunity to accurately reconstruct the late-time bolometric light-curve evolution of a CaST using multi-color observations that span from B-band to the NIR at $t \gtrsim 250$ days. In this paper, we present late-time *HST* observations of SN 2019ehk and modeling of the bolometric light curve out to ~ 400 d post-explosion. In §8.3 we present observations and data reduction of SN 2019ehk. In §8.4 we present modeling of SN 2019ehk's bolometric light curve evolution and derive physical properties of the radioactive decay-powered explosion. In §8.6 we discuss how SN 2019ehk compares to other late-time SN light curves and how these new observations constrain the SN progenitor system.

3.3 Observations

Early-time observations of SN 2019ehk were conducted with a variety of ground-based telescopes from 28 April to 02 August 2019 ($\sim 0.5-96.2$ days after explosion). Specifics about reductions techniques and instruments used are presented in WJG20a. Following WJG20a, we adopt a host galaxy distance of 16.2 ± 0.400 Mpc, distance modulus $\mu = 31.1\pm0.100$ mag, redshift $z = 0.005\pm0.0001$ and time of explosion $t_{exp} = 58601.8\pm0.1$ days (MJD). The Milky Way color excess along the SN line of sight is $E(B\text{-}V) = 0.0227$ mag (Schlegel et al. 1998; Schlafly & Finkbeiner 2011) and the host galaxy reddening is $E(B-V) = 0.47 \pm 0.10$ mag[1] (WJG20a), both of which we correct for using a standard Fitzpatrick (1999) reddening law ($R_V = 3.1$). Understanding if alternative R_V values are more appropriate descriptors of the host galaxy extinction is beyond the scope of this paper and we proceed with $R_V = 3.1$ so as to remain consistent with other studies on SN 2019ehk.

We obtained additional late-time, ground-based imaging of SN 2019ehk on 1 January 2020 ($\sim$247.2 days after explosion) in $r-$ and $i-$band with the Inamori-Magellan Areal

[1] Nakaoka et al. 2020 and De et al. 2021 assume a host galaxy reddening range of 0.5-1.0 mag that is derived from a comparison between SN 2019ehk and two particular SNe. Our adopted color excess from WJG20a lies at the lower end of this range and it is based on (i) direct measurements of Balmer decrement of the H II region from pre-explosion spectroscopy of the SN explosion site and (ii) color comparisons to CaST and SNe Ic samples (e.g., Fig. 10 in WJG20a).

Camera and Spectrograph (IMACS; Dressler et al. 2011) on the Magellan Baade 6.5-m Telescope. The data were first bias-subtracted and flat-fielded, then three frames per filter were averaged using `PyRAF`. From these observations, we measure an i-band AB magnitude of 21.40 ± 0.06 mag and derive an r-band upper limit of > 23.51 mag.

Late-time *HST* imaging of SN 2019ehk was first obtained in F275W, F336W, F438W, F555W and F814W filters (2000-10000Å) with the Wide Field Camera 3 (WFC3) through *HST* program PID-15654 (PI Lee) on 29 January and 15 March 2020 (∼276.2 and 321.8d after explosion, respectively). Additional UVIS/IR WFC3 imaging was taken in F555W, F814W, F110W and F160W filters (0.45 - 1.7 μm) on 21 May 2020 (∼389.0d after explosion) under *HST* program PID-16075 (PI Jacobson-Galán). Following methods in Kilpatrick et al. (2018a), we reduced all *HST* imaging using the `hst123`[2] python-based reduction package. We downloaded all relevant calibrated WFC3/UVIS and IR images (`flc`/`flt` frames) from the Mikulski Archive for Space Telescopes.[3] Each image was then aligned to a common reference frame using `TweakReg`. We then drizzled images from common filters and epochs using `astrodrizzle`. Finally, we performed photometry in the original, calibrated images using `dolphot` (Dolphin 2000). We present the observed apparent magnitudes (AB system), as well as 3-σ upper limits derived from fake star injection, for all late-time *HST* filters in Table A1. The late-time false color RGB image of SN 2019ehk and its host galaxy is shown in Figure 3.1. The complete multi-band light curve of SN 2019ehk is shown in Figure 3.2(a).

3.4 Analysis

In §3.4.1 we describe the derivation of SN 2019ehk's bolometric light curve which spans ∼0.5 to 388.8 days after explosion. In §7.4.3 we apply an analytic formalism for a radioactive-decay powered emission to fit the late-time light curve evolution of SN 2019ehk and derive physical parameters of the explosion.

3.4.1 Pseudo-Bolometric Light Curve

At $t < 97$ days, we construct a pseudo-bolometric light curve of SN 2019ehk through a combination of multi-band photometry from multiple ground-based telescopes (e.g., see WJG20a). For each epoch, luminosities are calculated through trapezoidal integration of SN flux in $uBVcgoriz$ bands (3000-10000 Å). Uncertainties are estimated through a Monte Carlo simulation that includes 1000 realizations of the data. In time intervals without complete color information, we interpolated between light curve data points using a low-order polynomial spline. This method is different than that used by WJG20a who created a bolometric light curve of SN 2019ehk through fitting of the spectral energy distribution (SED) with a blackbody model. The two methods lead to consistent luminosities for $t \lesssim$ 40 days. However, the blackbody model over-predicts the total flux at later phases due

[2] https://github.com/charliekilpatrick/hst123

[3] https://archive.stsci.edu/hst/

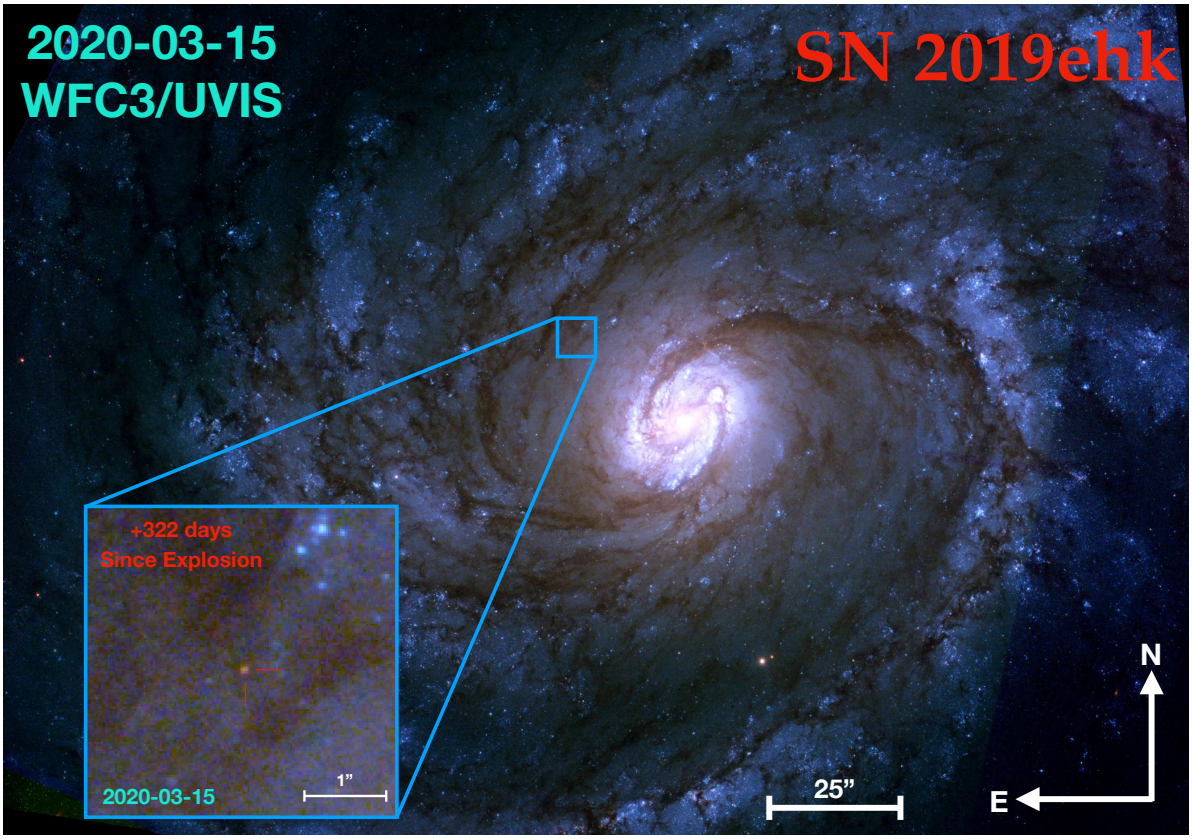

Figure 3.1 False color, *HST* RGB image of SN 2019ehk in host galaxy M100 at +322 days after explosion. The SN is marked in red within the zoomed-in blue box in lower left corner.

to the prominent [Ca II] and Ca II line transitions that dominate the SED flux in some bands. As expected, the blackbody model becomes an inadequate description of the observed emission as soon as the SN transitions to an emission dominated spectrum in the nebular phase. Therefore, we apply the trapezoidal integration method to determine the bolometric luminosity at all phases for consistency.

For late-time observations at $t > 276$ days, we also perform trapezoidal integration of SN 2019ehk's spectral energy distribution (SED) in *HST* filters (0.3-1.7 μm). Because infrared (IR) *HST* imaging was only taken during the last epoch (+389d, Fig. 3.2a), we extrapolate backwards in time in order to apply an IR correction that constitutes ∼30% of the bolometric flux to the *HST* observations at +276 and +322d after explosion. We proceed with the assumption that such a correction is not necessary for early-time epochs ($t \lesssim 100$ days) where IR contribution is negligible. Furthermore, we note that there may be a small fraction ($\lesssim 5\%$) of UV SN flux that is not taken into account when constructing the late-time bolometric luminosities due to observed non-detections in the F275W, F336W and F475W *HST* filters. The complete bolometric light curve of SN 2019ehk is presented in Table A2 and plotted in Figure 3.2(b).

3.4.2 Radioactive Decay Model

The late-time light curve evolution of most SNe is governed primarily by the energy deposition rate of the radioactive decay chain $^{56}\mathrm{Ni} \xrightarrow{t_{decay} = 8.77\,d} {}^{56}\mathrm{Co} \xrightarrow{t_{decay} = 111.3\,d} {}^{56}\mathrm{Fe}$ (Arnett 1982). γ-rays released in this process are then thermalized in the expanding SN ejecta and, for phases $t \gtrsim 60$ days after explosion, ^{56}Co beta-decay will power the bolometric light curve until the decays of other radioactive species such as ^{57}Co and ^{55}Fe become dominant (e.g., $t \gtrsim 500$ days after explosion; orange dot-dashed line in Fig. 3.2b).

In this section, we describe the components of a purely radioactive decay powered model and apply it to fit the bolometric light curve of SN 2019ehk at late times. The total energy generated in each beta-decay can be defined by (i) γ-rays released in the decay chain, (ii) kinetic energy of emitted positrons and (iii) γ-rays produced from electron-positron annihilation. Regardless of the generation process, all γ-rays produced have a finite probability of escaping the ejecta before depositing their energy. The limiting case where the γ-ray photons from the ^{56}Co decay are completely trapped and thermalized within the expanding ejecta is shown in Fig. 3.2b (green dot-dashed line). However, observations of Type Ia SNe (SNe Ia) and stripped envelope Type Ib/c SNe (SNe Ib/c) clearly show more rapid light curve decays, indicating that a fraction of γ-rays is able to escape before depositing their energy into the ejecta (Cappellaro et al. 1997; Wheeler et al. 2015). Following Clocchiatti & Wheeler (1997), the γ-ray leakage can be parameterized in terms of a trapping timescale, t_γ. The kinetic energy from positrons can also be thermalized and therefore their potential leakage from the SN ejecta can be described by a positron trapping timescale, t_{e^+}.

To model the late-time light curve of SN 2019ehk, we apply the formalism outlined in the appendix of Valenti et al. (2008a) for energy deposition from radioactive decay during the nebular phase ($t \gtrsim 60$ days). This model is very similar to the Bateman equation (e.g.,

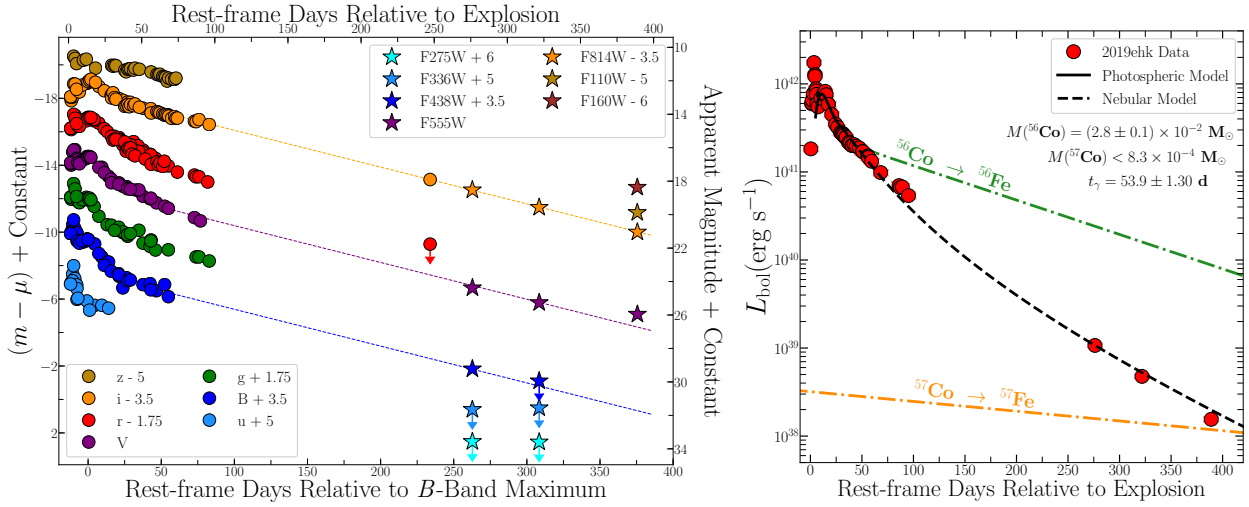

Figure 3.2 (a) UV/Optical/IR light curve of SN 2019ehk with respect to second B-band maximum. Observed photometry is presented in the AB magnitude system. Circles denote ground-based photometry, the majority of which were presented in WJG20a. Stars represent late-time *HST* detections and upper limits. Dashed lines provide visual extrapolation between early and late-time data in filters that are roughly consistent between *HST* and ground-based filters. (b) Bolometric light curve data of SN 2019ehk shown in red circles with respect to the radioactive decay model fit (dashed line) discussed in §7.4.3. Solid black line is the photospheric model from WJG20a that fits the early-time data around peak using SN parameters $M(^{56}\mathrm{Ni})$, E_k and M_{ej}. Dotted-dashed green and orange lines represent the decays of ^{56}Co and ^{57}Co, respectively, for the complete trapping of γ-rays and positrons.

see eqn. 16 in Seitenzahl et al. 2014) in how it can be used to derive masses of radioactive isotopes and trapping timescales, t_γ and t_{e^+}. However, unlike the Bateman formalism, this method self-consistently accounts for the trapping of γ-rays created through electron-positron annihilation.

The total luminosity generated by radioactive decay of ^{56}Ni and ^{57}Ni during the nebular phase ($t \gtrsim 60$ days) is described by the following expression, originally presented by Sutherland & Wheeler (1984) and Cappellaro et al. (1997) and summarized here for clarity:

$$L_{\rm neb}(t) = S^{^{56}\rm Ni}(\gamma) \; + \; S^{^{56}\rm Co}(\gamma) \; + \; S^{^{56}\rm Co}_{e^+}(\gamma) \; + S^{^{56}\rm Co}_{e^+}(KE) \; + \; S^{^{57}\rm Co}(\gamma) \tag{3.1}$$

$S^{^{56}\rm Ni}(\gamma)$ is the energy deposition due to ^{56}Ni decay:

$$S^{^{56}\rm Ni}(\gamma) = M(^{56}\rm Ni)\epsilon_{^{56}\rm Ni}e^{-t/\tau_{^{56}\rm Ni}} \tag{3.2}$$

where $M(^{56}\rm Ni)$ is the mass of ^{56}Ni, $\epsilon_{^{56}\rm Ni} = 3.9 \times 10^{10}$ erg s^{-1} g^{-1} is the energy rate generated by the decay of ^{56}Ni per unit mass and a decay time scale of $\tau_{^{56}\rm Ni} = 8.77$ days. The remaining terms in Equation 3.1 constitute the energy deposition rate due to the respective decays of ^{56}Co and ^{57}Co. 81% of the energy released by the ^{56}Co decay is emitted in the form of γ-rays:

$$S^{^{56}\rm Co}(\gamma) = 0.81\mathcal{E}\left(1 - e^{-(t_\gamma/t)^2}\right) \tag{3.3}$$

The term $(1 - e^{-(t_\gamma/t)^2})$ accounts for the trapping probability of the γ-rays in the ejecta and $\mathcal{E}$ is the rate of energy production from the ^{56}Co decay:

$$\mathcal{E} = M(^{56}\rm Ni)\epsilon_{^{56}\rm Co}\left(e^{-t/\tau_{^{56}\rm Co}} - e^{-t/\tau_{^{56}\rm Ni}}\right) \tag{3.4}$$

where $\epsilon_{^{56}\rm Co} = 6.8 \times 10^9$ erg s^{-1} g^{-1} and $\tau_{^{56}\rm Co} = 111.3$ days. The remaining 19% of energy from ^{56}Co decay is released via positrons and is partly described by the following expression for energy deposition from γ-rays created in positron annihilation:

$$S^{^{56}\rm Co}_{e^+}(\gamma) = 0.164\mathcal{E}\left(1 - e^{-(t_\gamma/t)^2}\right)\left(1 - e^{-(t_{e^+}/t)^2}\right) \tag{3.5}$$

where the terms $(1 - e^{-(t_\gamma/t)^2})$ and $(1 - e^{-(t_{e^+}/t)^2})$ account for the trapping probabilities of the γ-rays and positrons, respectively. The remaining source of energy in ^{56}Co decay is kinetic energy from positrons and is expressed by:

$$S^{^{56}\rm Co}_{e^+}(KE) = 0.036\mathcal{E}\left(1 - e^{-(t_{e^+}/t)^2}\right) \tag{3.6}$$

Lastly, we consider the contribution of ^{57}Co decay to the bolometric light curve, which we parameterize as follows:

$$S^{^{57}\rm Co}(\gamma) = M(^{57}\rm Co)\epsilon_{^{57}\rm Ni}e^{-t/\tau_{^{57}\rm Co}} \tag{3.7}$$

where $\epsilon_{^{57}\mathrm{Ni}} = 8.9 \times 10^6$ erg s^{-1} g^{-1} for no γ-ray trapping, $\epsilon_{^{57}\mathrm{Ni}} = 7.0 \times 10^7$ erg s^{-1} g^{-1} for complete γ-ray trapping, and $\tau_{^{57}\mathrm{Co}} = 392.11$ days. We adopt the energy rate $\epsilon_{^{57}\mathrm{Ni}}$ that assumes no trapping of γ-rays and complete trapping of X-rays and Auger electrons (e.g., see Seitenzahl et al. 2009, Graur et al. 2016). This description of energy deposition from γ-rays released in ^{57}Co decay will yield the most conservative estimate on the total ^{57}Co mass in SN 2019ehk. We also ignore any "freeze-out" effects that typically influence the SN light curve at $t > 600$ days (Fransson & Kozma 1993; Fransson & Jerkstrand 2015; Graur et al. 2017).

In this model, free variables include the total masses of ^{56}Co and ^{57}Co as well as the timescales of γ-ray and positron escape, t_γ and t_{e^+}, respectively. We do not fit for other physical parameters that define these timescales such as the density profile, opacity, mass and kinetic energy of the expanding ejecta. These dependencies are discussed in the context of derived trapping timescales in Equations 3.8 and 3.9. To fit the bolometric light curve, we use the non-linear least squares package `curve_fit` in `scipy` (Virtanen et al. 2020). Our final model fit to the late-time light curve is shown as the dashed black line in Figure 3.2(b).

Using Equation 3.1, we first attempt to model the bolometric light curve of SN 2019ehk with the inclusion of partial trapping of positrons e.g., including t_{e^+}. We find that the model is insensitive to the positron trapping timescale and no meaningful statistical boundary can be constrained. We then model the bolometric light curve under the assumption of complete positron trapping (i.e., $(1 - e^{-(t_{e^+}/t)^2}) = 1$) and derive a total ^{56}Co mass of $M(^{56}\mathrm{Co}) = (2.8 \pm 0.10) \times 10^{-2}$ M$_\odot$ and a γ-ray trapping timescale of $t_\gamma = 53.9 \pm 1.30$ days. The estimated ^{56}Co mass is consistent with the ^{56}Ni mass of $M_{\mathrm{Ni}} = (3.1 \pm 0.11) \times 10^{-2}$ M$_\odot$ derived from photospheric modeling of the SN 2019ehk light curve at $t < 30$ days after explosion (WJG20a). This indicates that the early-time luminosity of SN 2019ehk during its second light curve peak was primarily powered by radioactive decay and not by additional power sources such as CSM interaction. Conversely, the first light curve peak at $t < 7$ days after explosion was powered by interaction with dense CSM (WJG20a).

Because SN 2019ehk's bolometric light curve only extends to ∼400 days after explosion, the model fit is not fully sensitive to the contribution of ^{57}Co decay to the overall SN luminosity. Consequently, we derive an upper limit on the total mass of ^{57}Co in SN 2019ehk to be $M(^{57}\mathrm{Co}) < 8.3 \times 10^{-4}$ M$_\odot$, which represents a 3σ statistical deviation relative to the late-time light curve data. Based on these mass estimates, we find a ratio of radioactive isotope masses in SN 2019ehk to be $M(^{57}\mathrm{Co})/M(^{56}\mathrm{Co}) \leq 0.030$. As previously stated, this mass ratio represents the most conservative limit under the assumption of no γ-ray trapping from ^{57}Co decay. However, for complete γ-ray trapping from this decay chain, the least conservative limit on ^{57}Co mass in SN 2019ehk is $M(^{57}\mathrm{Co}) < 1.1 \times 10^{-4}$ M$_\odot$, which yields a mass ratio of $M(^{57}\mathrm{Co})/M(^{56}\mathrm{Co}) \leq 0.004$. It is likely that the true ^{57}Co mass and mass ratio limits for SN 2019ehk are within this range given the evidence of partial γ-ray trapping from ^{56}Co decay at late-times. Finally, given the uncertainty on SN 2019ehk's host extinction, we also calculate the $M(^{57}\mathrm{Co})/M(^{56}\mathrm{Co})$ mass ratio limit after correcting the data for a maximum color excess of $E(B-V) = 1$ mag as presented in the range by Nakaoka et al. (2020). We find mass ratio limits of ≤ 0.0044 and ≤ 0.034 for complete and no γ-ray trapping from ^{57}Co

decay, respectively. These limits are consistent to those calculated with our preferred host extinction value presented in §8.3. We also note that the estimated mass ratio limits are marginally dependent on the bolometric correction to the IR flux at late times as discussed in §3.4.1.

As shown by Clocchiatti & Wheeler (1997), the trapping timescales of both γ-rays and positrons are physical parameters that are defined based on properties of the SN ejecta. For γ-ray trapping, the expression is:

$$t_\gamma = \left(C(\eta)\kappa_\gamma M_{ej}^2 E_k^{-1}\right)^{1/2} \tag{3.8}$$

where the ejecta opacity to γ rays is $\kappa_\gamma = 0.027$ cm^2 g^{-1}, M_{ej} is the ejecta mass, E_k is the kinetic energy of the ejecta and the density function $C(\eta)$, under the assumption of spherical symmetry, is written as:

$$C(\eta) = (\eta - 3)^2\Big[8\pi(\eta - 1)(\eta - 5)\Big]^{-1} \tag{3.9}$$

where η defines the density profile of ejecta i.e., $\rho_{ej} \propto r^{-\eta}$.

Following Valenti et al. (2008a), we assume the ejecta is homogeneous and has a flat density profile of $\eta = 0$ within Eqn. 3.9, which then yields $C(0) = 0.072$. For the known γ-ray energies of the beta-decays, the γ-ray opacity of the ejecta is expected to be $\kappa_\gamma = 0.027$ cm^2 g^{-1} (Colgate et al. 1980; Woosley et al. 1989; Clocchiatti & Wheeler 1997). To check this assumption, we solve for κ_γ in Eqn. 3.8 using $C(0)$ listed above, t_γ from our model fits as well as $M_{ej} = 0.7$ M$_\odot$ and $E_k = 1.6 \times 10^{50}$ erg as derived in WJG20a from early-time light curve modeling. With these values, we estimate a γ-ray opacity of $\kappa_\gamma = 0.026 \pm 0.0019$ cm^2 g^{-1}, which is consistent with the fiducial value used in other studies. Furthermore, this agreement suggests that the SN 2019ehk ejecta structure can be consistent with being homogeneous and spherically symmetric, with synthesized Ni located at the center.

3.5 Discussion

3.5.1 Comparison to Late-time SN Studies

SN 2019ehk is the only confirmed CaST to be observed long enough after explosion so as to probe the effects of energy deposition from multiple radioactive isotopes on the bolometric light curve. Studying this object at such late-times also allows for the first test of γ-ray and positron trapping in a SN that exhibits the typical spectroscopic and photometric evolution of a CaST. As shown in Figure 3.3(a), the peculiar, "Calcium-strong" SN 2016hnk was observed to ∼300 days after explosion and Jacobson-Galán et al. (2020a) found that including $t_\gamma \approx 60$ days was necessary to fit the bolometric light curve at late-times. However, while SN 2016hnk follows a similar light curve evolution as SN 2019ehk out to late-times,

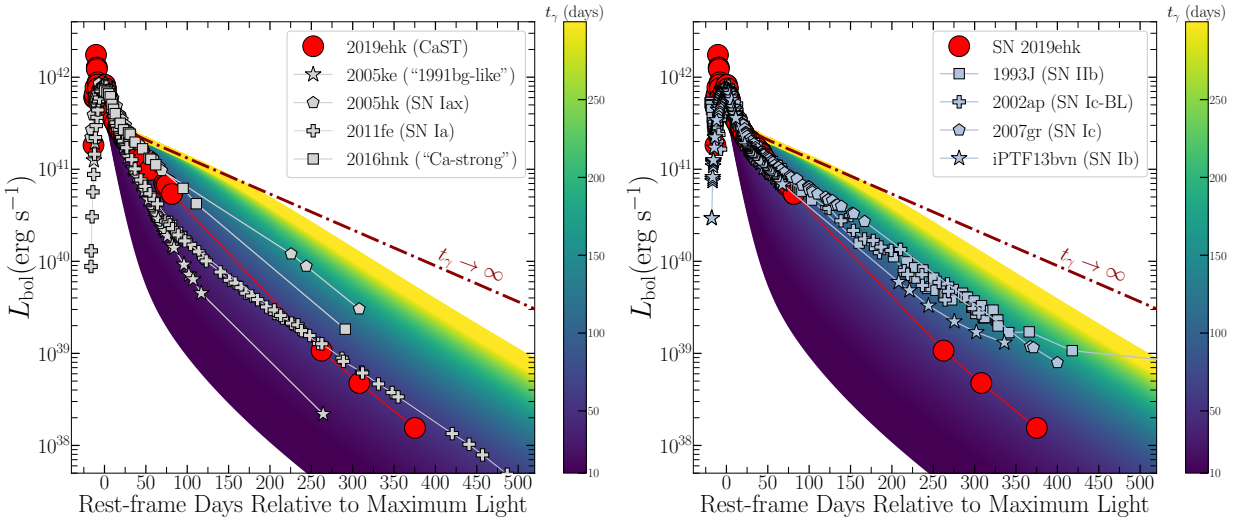

Figure 3.3 (a) Bolometric light curve comparison of SN 2019ehk and thermonuclear SN varieties such as SNe Ia (SN 2011fe; grey plus signs, Zhang et al. 2016), 1991bg-like (SN 2005ke; grey stars, Contreras et al. 2010), SNe Iax (SN 2005hk; grey polygons, Sahu et al. 2008) and Calcium-strong SNe (SN 2016hnk; grey squares, Galbany et al. 2019; Jacobson-Galán et al. 2020a). Comparison objects have been shifted in luminosity and phase space to match SN 2019ehk's light curve maximum. Dark red dashed-dotted line represents a radioactive decay light curve model fit to SN 2019ehk with complete γ-ray trapping. The colorbar gradient demonstrates the decline rate dependency on trapping timescale, t_γ in a radioactive decay powered model fit to the SN 2019ehk data. (b) Comparison between SN 2019ehk and H-poor SN varieties such as SNe IIb (SN 1993J; light blue squares, Zhang et al. 2004), SNe Ic-BL (SN 2002ap; light blue plus signs, Tomita et al. 2006), SNe Ic (SN 2007gr; light blue polygons, Valenti et al. 2008b) and SNe Ib (iPTF13bvn; light blue stars, Srivastav et al. 2014; Fremling et al. 2016). The colorbar gradient is based on a fit to SN 2019ehk's light curve and thus cannot be used to directly compare t_γ values for different SNe.

it is not considered a typical CaST given its similarities to "1991bg-like" SNe Ia (Galbany et al. 2019).

With regards to other thermonuclear SN varieties shown in Figure 3.3(a), SN 2019ehk has a similar overall light curve evolution out to ∼400 days after explosion. Compared to normal and sub-luminous SN Ia, 2011fe and 2005ke, respectively, SN 2019ehk has a consistent decline rate. Furthermore, given the differences in SN parameters e.g., M_{ej} and E_k between SN types, it is understandable that the estimated trapping timescale ($t_\gamma \propto M_{ej}/E_k^{1/2}$; Eqn. 3.8) is higher in SN 2019ehk (∼54 days) than in SNe Ia ($\lesssim$ 35 days). The difference in γ-ray trapping between objects is illustrated through the t_γ colorbar in Figure 3.3. Finally, SN 2019ehk shows a slightly faster bolometric decline than "Calcium-strong" SN 2016hnk and Type Iax SN (SN Iax) 2005hk (Sahu et al. 2008), which suggests that it has less efficient γ-ray trapping than these low luminosity thermonuclear events. For a phase range of 100−300 days, SN 2019ehk has a smaller fractional change in luminosity than SN 2005ke but a larger change than all other thermonuclear transients used for comparison.

We explore the similarities between SN 2019ehk and SNe Iax given that it is a low luminosity transient where the explosion of a WD is a favored progenitor scenario (WJG20a). At late times, we find no evidence for significant change in color to IR bands nor a late-time flattening of the light curve that deviates from a Ni-powered decline, as seen in some SNe Iax (e.g., SN 2005hk and 2014dt). Furthermore, unlike SNe Iax, SN 2019ehk has no detectable excess of NIR/MIR flux, which has been used as evidence for both a super-Eddington wind launched from a surviving, bound remnant star (e.g., Foley et al. 2016; Shen & Schwab 2017; Kawabata et al. 2018) or dust formation (Fox et al. 2016) in SN Iax, 2014dt. Such scenarios are disfavored based on SN 2019ehk's late-time light curve evolution.

SN 2019ehk has a faster decline rate and larger fractional change in luminosity (100 − 300 days) than all stripped-envelope SN varieties such as Type IIb, Ibc and broad-lined Ic SNe. As illustrated by Figure 3.3(b), all of the example H-poor SN sub-types are more efficient at trapping γ-rays in their ejecta than SN 2019ehk. This suggests values of t_γ that are a factor of two greater than that of SN 2019ehk and is consistent with the trapping timescales $\gtrsim$ 100 days found by Wheeler et al. (2015) for a sample of stripped-envelope events. Furthermore, all SNe in that study have larger observed M_{ej} and E_k values than SN 2019ehk despite some objects having comparable total masses of ^{56}Ni.

3.5.2 CSM Interaction and Dust Formation

SN 2019ehk represents the first CaST with direct evidence for confined CSM surrounding the progenitor star at the time of explosion (WJG20a). Shock-ionized spectral lines and luminous X-ray emission revealed that the CSM was H- and He-rich, had a mass of $\sim 7 \times 10^{-3}$ M$_\odot$ and a velocity of $\sim$ 500 km s^{-1}. These observations jointly confirmed that this compact shell of material extended out to a radius of $r < 10^{15}$ cm from the progenitor and had a density of $n \approx 10^9\,\mathrm{cm}^{-3}$ ($\dot{M} < 10^{-5}\,\mathrm{M}_\odot\mathrm{yr}^{-1}$). Radio observations from $\sim 30 - 220$ days after explosion indicated a significantly lower density $n < 10^4\,\mathrm{cm}^{-3}$ at larger radii $r > (0.1 - 1) \times 10^{17}$ cm. Furthermore, there is no evidence of circumstellar interaction in the

latest nebular spectrum of SN 2019ehk at a phase of ∼270 days.

Prior to the late-time imaging presented in this analysis, all multi-wavelength observations have indicated that the material ejected by the progenitor was dense, small in quantity, and confined to the immediate circumstellar environment. Based on the light curve modeling in Section 7.4.3, we find no statistical evidence for a power source in addition to ^{56}Ni; the same amount of ^{56}Ni that powers the early-time light curve is enough to account for the entire bolometric luminosity up to 400 days. Here, we quantify the contribution of CSM interaction to the late-time light curve, employing a modified version of the simplified formalism by Smith et al. (2010):

$$L_{\rm CSM} = \frac{1}{2}\epsilon w v_s^3 \tag{3.10}$$

where ϵ is the efficiency of conversion of shock kinetic energy into radiation and v_s is the shock velocity. The wind density parameter w is defined by $\dot{M}/v_w$, where we adopt $v_w \approx 500$ km s^{-1} as estimated in WJG20a. For the explosion parameters of SN 2019ehk (M_{ej} and E_k), and a wind-like environment (see WJG20a), the shock velocity is:

$$v_s = 10^4 \left[\left(\frac{\dot{M}}{\rm M_\odot\ yr^{-1}} \right)^{0.12} \left(\frac{t}{\rm days} \right)^{0.12} \right]^{-1} \ {\rm km\,s^{-1}} \tag{3.11}$$

We treat Eqn. 3.10 as an extra energy term to be added to Eqn. 3.1 and we derive a 3σ limit on mass-loss of $\dot{M} \lesssim 10^{-10}$ M$_\odot$yr^{-1} for an optimistic efficiency of 80%. This result indicates very low densities in the SN environment of $n < 10^4$ cm^{-3}, consistent with the radio non-detections. Our mass-loss estimate suchs a "very clean" environment that is natural in a WD+WD system (WJG20a) but more difficult to reconcile with the environments around massive stars.

Finally, we consider the case of dust formation in SN 2019ehk for completeness. As shown in the optical/IR light curve in Figure 3.2(a), the late-time SED of SN 2019ehk is gradually being shifted bluewards, which is not reflective of dust formation that would induce the opposite effect and is likely an effect of fading Ca II emission at redward wavelengths. Furthermore, our WFC3/IR observations at +389 days after explosion extend from $\sim 0.9 - 1.7$ μm and would be able to detect emission from a dust shell that typically peaks around ~ 2 μm. Consequently, we can conclude that there is no evidence for dust formation in SN 2019ehk at phases $\lesssim$ 400 days after explosion.

3.5.3 Oxygen Ejecta Mass

The mass of oxygen in the ejecta can constrain the type of progenitor and the explosion mechanism. WJG20a estimated $M_O > 0.14$ M$_\odot$ from O I and [O I] emission lines in the +72 day spectrum and De et al. (2021) found a less stringent, but consistent mass limit of $M_O > 0.005 - 0.05$ M$_\odot$ from a spectrum at +270 days using only the [O I] line transition. Both of these analyzes assumed temperatures of the emission region (e.g., T = 5000 K by

WJG20a and T = 3400 - 4000 K by De et al. 2021) that were not directly constrained by the data. Here we re-analyze the +72 day spectrum, adding to our analysis the inferences made from an estimated upper limit on the [O I] 5577 luminosity to constrain the temperature and obtain a robust lower limit to M_O. We then present two independent estimates of M_O based on the ^{56}Co mass obtained in this paper.

3.5.3.1 Lower limit from +72 day spectrum

In order to obtain a lower limit to M_O from the +72 day spectrum, we use L_{6300}, the [O I] $\lambda\lambda$6303,6363 luminosity and L_{7774}, the recombination line luminosity from WJG20a. We add a constraint for the [O I] λ5577 line by re-scaling to the +44 day spectrum in order to determine the continuum, resulting in a line ratio of $L_{5577}/L_{6300} < 0.2$ and assuming a constant continuum shape between epochs. We note that a change in the line ratio of $\pm$30% would influence the excitation rate in λ6303 by $\pm$25%, which in turn will modify the final O mass estimate by $\mp$25%. We then computed a grid of models over a range of density, temperature and ionization fraction for various values of the oxygen mass using atomic rates from CHIANTI (Dere et al. 1997). We find that an O mass of $M_O > 0.08$ M$_\odot$ is required to match the observed line luminosities, which lies in the upper end of the lower limits presented by De et al. (2021). For this minimum mass, the other parameters are constrained to log(n_e) = 8.6, T = 5350 K and O$^+$/O $\sim$ 0.25. For larger M_O, wider ranges of the other parameters are allowed. This is a robust lower limit on the O mass because (i) some oxygen could be inside the photosphere at this stage as the spectrum is not yet fully nebular, and (ii) we assume a single temperature. If, as is likely, a range of temperatures is present and the higher temperature gas is more highly ionized, then both the neutral mass ($M \propto e^{22800/T}$) and the ionized mass ($M \propto T^{1/2}$) will increase. We note that we can not confirm the approximated formula by Uomoto (1986) used by De et al. (2021) with CHIANTI. Using the same parameters as De et al. (2021) in CHIANTI, we would infer an O mass that is a factor 1.6 lower than that reported by De et al. (2021). We speculate that updated atomic parameters of CHIANTI might be responsible for the difference.

3.5.3.2 Estimate from L_{7774} in +270 day spectrum

We measure a O I recombination line luminosity $L_{7774} = 1.8 \times 10^{37}$ erg s^{-1} in the +270 spectrum. It is known that $\sim$ 37% of the recombinations produce that line, and each recombination must balance an ionization (Julienne et al. 1974). We have shown that the original mass of ^{56}Co is 0.028 M$_\odot$, but by +270 days, only 0.0025 M$_\odot$ remains. With a 77.2 day half-life, that implies 5.4×10^{45} decays per second at t = 270 days, each of which carries 2.11 MeV of energy. Victor et al. (1994) computed the number of ionizations per 1000 eV as a particle slows down in pure oxygen gas. They did not include photo-ionization by emission lines created in the process and while the O I emission lines cannot photo-ionize oxygen, O II lines such as those at 834 Å can ionize O I. We use this information to quantify the amount of energy released by ^{56}Co decay that is channeled solely to O I emission. We note that Ca

is excited by a population of electrons at significantly lower energies that would not lead to O emission. Adding in those photo-ionizations, we find $26-45$ ionizations per 1000 eV. For a radius of 6×10^{15} cm based on the expansion speed and phase, the energy flux is 2.7×10^{13} MeV cm^{-2} s^{-1}, and the absorption cross section based on $\kappa_\gamma = 0.027$ cm^2 g^{-1} yields $(5.1-8.7) \times 10^{-7}$ ionizations per second. Thus the observed λ7774 luminosity requires $M_O \approx 0.30-0.50$ M$_\odot$. This estimate applies if the ^{56}Co is located well inside the absorbing shell but the local γ-ray flux will be higher if the ^{56}Co is just inside the absorbing shell (i.e., large degree of mixing). The geometrical correction could reduce the required oxygen mass by as much as a factor of 1.5, and the final estimate is $M_O \approx 0.20 - 0.33$ M$_\odot$. We also explore the effect of a large host extinction on the SN 2019ehk O mass. Using a color excess of $E(B-V) = 1.0$ mag, we find a O I line luminosity $L_{7774} = 4.3 \times 10^{37}$ erg s^{-1} which yields an O mass range of $M_O \approx 0.70-1.20$ M$_\odot$ by the steps outlined above. While these values violate the total ejecta mass estimates from light curve modeling and support a lower host extinction value, it is possible that the assumptions made in this analysis do not fully account for all the details of SN physics e.g., the application of Victor et al. (1994) is technically for pure O gas.

3.5.3.3 Estimate from opacity at +270 days

Figure 3.2(b) shows that all but ∼4% of the radioactive decay energy escapes from the oxygen SN ejecta shell, which indicates an optical depth of ∼0.04. We assume that the source of γ-rays (i.e., ^{56}Co) is centrally located. With an opacity $\kappa_\gamma = 0.027$ cm^2 g^{-1}, that implies a mass column of 1.48 g cm^{-2}. Multiplying by the area of a 6×10^{15} cm shell gives an O mass of ~ 0.3 M$_\odot$. WJG20a found that there is a significant amount of He in the ejecta, which would reduce the O mass range to ~ 0.27 M$_\odot$. Carbon might be present as well, which could lower the O mass by as much as 1/3.

A further geometric correction should also be considered. The estimate above implicitly assumes that the γ-rays move radially, and that is a good approximation if the ^{56}Co is located well inside the absorbing shell. If the ^{56}Co is located just inside the absorbing shell, a photon will move at some angle to the radial and will encounter more material. The correction factor depends on the thickness of the shell, but for a plausible range of $1.5 < r_{outer}/r_{inner} < 2$, the mass estimate could be decreased by a factor of 1.5 to 1.32. If the ^{56}Co is mixed with the absorbing material, some γ-rays will escape more easily, bringing the correction factor back toward 1. The mass estimate based on the opacity thus becomes ~ 0.20 M$_\odot$. This O mass, as well as other estimates discussed above, are consistent with the O abundances in merging hybrid + C/O WDs (e.g., Zenati et al. 2019b) that WJG20a present as a favored progenitor scenario for SN 2019ehk.

3.5.4 Progenitor Channels

As the sample of known CaSTs continues to grow, the exact progenitor systems responsible for these SNe remains unknown. While the older stellar environments and significant

host galaxy offsets observed for many CaSTs is consistent with a WD origin, the increasing diversity of CaST explosion sites indicates that their progenitors may be heterogeneous and include some types of massive stars. For the progenitor of SN 2019ehk, Nakaoka et al. (2020) conclude that the SN may have arisen from the explosion of a ultra-stripped, low mass He (or C/O) star in a binary system with a companion NS. Alternatively, WJG20a find that the disruption of a hybrid WD by a C/O WD companion is most consistent with observations. However, as identified in WJG20a, pre-explosion imaging also allows for a low-mass, massive star progenitor ($\sim$10 $M_\odot$) in a binary system.

In the context of late-time studies of SNe Ia, the ratio of odd to even radioactive isotope masses (e.g., ^{57}Co / ^{56}Co) provides information on the density structure of the explosion which, in turn, can help constrain the progenitor system of these SNe (Seitenzahl et al. 2013a; Graur et al. 2016; Shappee et al. 2017; Dimitriadis et al. 2017; Jacobson-Galán et al. 2018). Here, we use the mass ratio $M(^{57}\mathrm{Co})/M(^{56}\mathrm{Co})$ derived in §7.4.3 as a unique and novel probe of possible CaST progenitor scenarios. In Figure 3.4, we compare SN 2019ehk's radioactive isotope mass ratio limit and total ejecta mass to those predicted in a variety of explosion models. The complete list of models used in this plot are presented in Table A3. It should be noted that the complexity of the nuclear reaction network may vary between each type of explosion model.

With respect to single degenerate and double degenerate models for SN Ia-like explosions of WDs, SN 2019ehk has a lower total ejecta mass but is consistent with the mass ratio of some explosion models. A progenitor scenario with similar nucleosynthesis that instead involved the explosion of a sub-Chandrasekhar mass WD (e.g., He-shell double detonations) would match these specific observables in SN 2019ehk. However, any WD explosion model of this variety would need to reconcile the H- and He-rich CSM in near SN 2019ehk's progenitor star (WJG20a).

More exotic progenitor scenarios such as disruptions of low-mass WDs by another WD or a NS can also be constrained. As shown in Figure 3.4, SN 2019ehk is inconsistent with the predicted ejecta masses and nucleosynthesis of CO or ONe WD + NS merger models (Zenati et al. 2020; Bobrick et al. 2022). However, the exact unbound ejecta mass produced in these models is uncertain and could match $M_{\rm ej}$ estimated for SN 2019ehk. Nonetheless, most of these models synthesize higher amounts of ^{57}Co than could be present in SN 2019ehk (Fig. 3.4) and thus are not viable progenitor systems.

An explosion scenario that is consistent with SN 2019ehk is the disruption of a lower-mass CO WD (or hybrid HeCO WD) by a hybrid WD (Zenati et al. 2019b), which can produce fast-rising, faint CaST-like events (Zenati et al. 2023). The explosion model can result in $\sim$0.4 - 0.6 $M_\odot$ of ejecta and synthesize low enough masses of ^{57}Co so as to remain within the limit set by the late-time light curve modeling. WJG20a also find this progenitor scenario to be consistent with the H- and He-rich CSM composition found in the SN progenitor environment. While this late-time analysis confirms one of the favored models in WJG20a, further tests should be done to understand how well this type of explosion can quantitatively match SN 2019ehk's early-time light curve and spectra.

Lastly, we compare estimates of M_{ej} and mass ratio values to those predicted by a variety

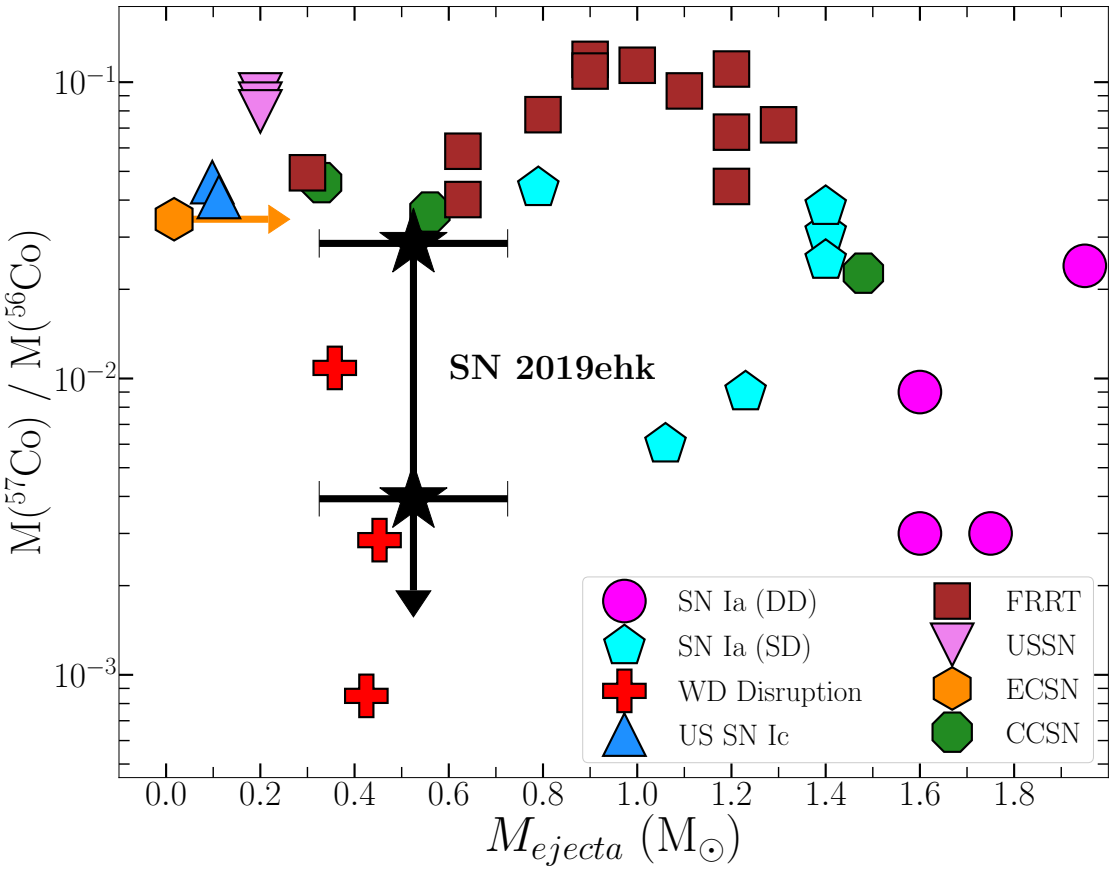

Figure 3.4 Comparison of cobalt isotope mass ratio to M_{ej} for SN 2019ehk (black star) with respect to values predicted by various explosion models. SN 2019ehk's mass ratio is shown as range of most to least conservative limits based on no trapping to complete γ-ray trapping, respectively, in ^{57}Co decay. These limits are not dependent on the assumed host galaxy extinction (e.g., see §7.4.3). Single and double degenerate SN Ia-like explosions are presented as cyan polygons and magenta circles, respectively. WD disruption models for CaSTs are shown as red plus signs and different ultra-stripped (US) SN models presented as blue/pink up/down triangles. Model for WD+NS/BH disruptions leading to a Faint Rapid Red Transient (FRRT) are shown as brown squares. Electron-capture (EC) and core-collapse (CC) SN models for low mass progenitors ($\lesssim$ 11 $\mathrm{M}_\odot$) are shown as orange hexagons and green octagons, respectively. All model parameters presented in Table A3. The uncertainty on M_{ej} for SN 2019ehk reflects the range of values estimated in both WJG20a and Nakaoka et al. (2020).

of core-collapse (CC) SN models. In Figure 3.4, we show that SN 2019ehk is not consistent with both the nucleosynthetic yields and ejecta masses produced in the explosion of massive stars in the lowest mass bins ($\lesssim 8-11$ M$_\odot$; Wanajo et al. 2018). Similarly, electron-capture (EC) SN models for low mass progenitors (8.8 M$_\odot$; Wanajo et al. 2018) cannot reproduce the SN 2019ehk observables despite their proposed link to fastly evolving transients such as CaSTs (Moriya & Eldridge 2016; Milisavljevic et al. 2017). Furthermore, we explore the possible connection between SN 2019ehk and ultra-stripped SN (USSN) models. Such a progenitor system was favored by Nakaoka et al. (2020) for SN 2019ehk and involves the explosion of a He or CO star that has had most of its outer H and He envelope removed due to its NS companion. In Figure 3.4 we include explosion models for ultra-stripped SNe Ic (Yoshida et al. 2017) and USSNe of varying explosion energies (Moriya et al. 2017b). Both models produce less M_{ej} than SN 2019ehk and synthesize too much ^{57}Co to be consistent with the most conservative mass ratio limit. Nonetheless, additional modeling of USSNe is needed to understand the range of ejecta and isotope masses generated through the explosion of compact, stripped massive stars.

Based on a lower limit on the O mass of $M_O > 0.005-0.05$ M$_\odot$, De et al. (2021) favor a stripped envelope progenitor ($M_{\rm ZAMS} \approx 9-9.5$ M$_\odot$) for SN 2019ehk with $\gtrsim 0.02$ M$_\odot$ of H on the stellar surface. The mass of potential photospheric H is based on a qualitative analogy between one peak spectrum of SN 2019ehk and SNe IIb models (e.g., Hachinger et al. 2012) despite the overall dissimilarity between the photometric and spectroscopic evolution, as well as explosion parameters, of H-poor SNe compared to SN 2019ehk (Nakaoka et al. 2020, WJG20a). While the O mass lower limit by De et al. (2021) shows consistency with USSN models (e.g., Moriya et al. 2017b; Yoshida et al. 2017), such a progenitor scenario is inconsistent with even the most conservative mass ratio limit shown in Figure 3.4 as well as alternative methods for calculating O mass discussed in Section 3.5.3. Furthermore, the range of nucleosynthetic yields and M_{ej} values produced in the core-collapse of normal to ultra-stripped, $9-11$ M$_\odot$ SN progenitors cannot reproduce those observed in SN 2019ehk.

Additionally, it is difficult to reconcile the specific progenitor scenario proposed by De et al. (2021) with the detection of a dense, confined shell of H- and He-rich CSM in the SN 2019ehk progenitor environment. From X-ray detections and flash-ionized spectral lines, WJG20a derived a CSM H mass of $\sim 3\times10^{-4}$ M$_\odot$ around SN 2019ehk's progenitor, which is incompatible with the estimate proposed by De et al. (2021) of $\gtrsim 0.03$ M$_\odot$ near or on the surface of the progenitor. Furthermore, the progenitor environment of SN 2019ehk is unlike that of any double-peaked, H-poor SNe with extensive radio observations (e.g., see Kamble et al. 2016) and the lack of radio detections indicates a low density environment at distances $r > 10^{16}$ cm, which is inconsistent with a stripped-envelope, massive star progenitor system. Also, our radio limits, as well as the presence of a H-rich CSM, are inconsistent with most of the ultra-stripped SN progenitor configurations presented by Matsuoka & Maeda (2020). Nonetheless, SN 2019ehk radio limits and ejecta mass are consistent with two binary models that include a fraction of gas escaping the system $f_{\dot{M}} = 0.1$ and final orbital separation $a_{\rm fin} = 1-10$ R$_\odot$, but these models cannot reconcile the presence of H in the local SN environment. Furthermore, we note the large uncertainties on the efficiency of non-conservative mass

transfer in these systems during the Roche lobe overflow stage of binary evolution. It is unclear how mass-loss in a stripped, $\sim 9-9.5$ $M_\odot$ massive star progenitor could allow for the presence of only $\sim 10^{-4}$ $M_\odot$ of dense H-rich material in its local environment ($r < 10^{15}$ cm), while also ejecting several $M_\odot$ worth of H via binary interaction that was not detected in any panchromatic observations of SN 2019ehk out to late-time phases.

3.6 Conclusions

In this paper, we have presented *HST* WFC3 imaging of CaST SN 2019ehk at 276-389 days after explosion. Photometric detections in all optical/IR filters enabled the creation of a bolometric light curve that extended out to phases yet unexplored in a CaST. We show that the late-time light curve evolution can be modeled solely through the radioactive decay of isotope ^{56}Co with a mass of $M(^{56}\mathrm{Co}) = (2.8 \pm 0.1) \times 10^{-2}$ $M_\odot$. Additionally, we find evidence for γ-ray leakage on the timescale of $t_\gamma = 53.9 \pm 1.3$ d but do not find statistical evidence for incomplete positron trapping in SN 2019ehk's ejecta. The bolometric light curve of SN 2019ehk does not extend to late enough phases to precisely quantify the mass of ^{57}Co synthesized in the explosion and therefore we derive the most conservative limit on the mass ratio of odd to even isotopes to be $M(^{57}\mathrm{Co})/M(^{56}\mathrm{Co}) \leq 0.030$.

We compare this mass ratio limit and the total SN 2019ehk ejecta mass to that predicted by various explosions models involving WDs and stripped, compact massive stars. We show that these observables make SN 2019ehk incompatible with single- and double-degenerate explosion scenarios that typically produce SN Ia-like explosions. Additionally, SN 2019ehk is inconsistent with the projected nucleosynthetic yields of WD+NS binary mergers as well as CC and EC SNe from normal to ultra-stripped massive stars ($M_{\mathrm{ZAMS}} \approx$ 9-11 $M_\odot$). However, these derived values in SN 2019ehk do match the mass ratio and M_{ej} produced in the tidal disruption of a low-mass C/O WD by a larger, hydrid WD. Additional modeling of these explosion mechanisms, as well as more late-time observations of nearby CaSTs, will be essential in constraining CaST progenitor systems.

3.7 Acknowledgements

Research at Northwestern University and CIERA is conducted on the stolen land of the Council of Three Fires, the Ojibwe, Potawatomi, and Odawa people, as well as the Menominee, Miami and Ho-Chunk nations.

We thank Takashi Yoshida, Takashi Moriya and Shinya Wanajo for model yields. W.J-G is supported by the National Science Foundation Graduate Research Fellowship Program under Grant No. DGE-1842165 and the IDEAS Fellowship Program at Northwestern University. W.J-G acknowledges support through NASA grants in support of *Hubble Space Telescope* program GO-16075. R.M. is grateful to KITP for hospitality during the completion of this paper. This research was supported in part by the National Science Foundation under Grant No. NSF PHY-1748958. R.M. acknowledges support by the National Science Foundation

under Award No. AST-1909796. Raffaella Margutti is a CIFAR Azrieli Global Scholar in the Gravity & the Extreme Universe Program, 2019. The Margutti's team at Northwestern is partially funded by the Heising-Simons Foundation under grant # 2018-0911 (PI: Margutti). C.D.K. acknowledges support through NASA grants in support of *Hubble Space Telescope* programmes GO-15691 and AR-16136. P.K.B. is supported by a CIERA Postdoctoral Fellowship. HBP acknowledges support from the Kingsely distinguished-visitor program at Caltech, the KITP visitor program (supported in part by the National Science Foundation under Grant No. NSF PHY-1748958), and the European Union's Horizon 2020 research and innovation program under grant agreement No 865932-ERC-SNeX.

The UCSC transient team is supported in part by NSF grant AST-1518052, NASA/*Swift* grant 80NSSC19K1386, the Gordon & Betty Moore Foundation, the Heising-Simons Foundation, and by a fellowship from the David and Lucile Packard Foundation to R.J.F. Research at Lick Observatory is partially supported by a generous gift from Google.

This paper includes data gathered with the 6.5 meter Magellan Telescopes located at Las Campanas Observatory, Chile. CHIANTI is a collaborative project involving George Mason University, the University of Michigan (USA), University of Cambridge (UK) and NASA Goddard Space Flight Center (USA).

3.8 Appendix

Table A1. *HST* Imaging of SN 2019ehk

Instrument	Aperture	Filter	MJD	Phase (days)	Exp. Time (s)	Proposal No.	Magnitude[a] (mag)	Error
WFC3	UVIS	F275W	58877.92	321.78	2190.0	15654	>26.93	–
WFC3	UVIS	F275W	58923.58	321.78	2190.0	15654	>26.59	–
WFC3	UVIS	F336W	58877.90	276.10	1110.0	15654	>26.65	–
WFC3	UVIS	F336W	58923.58	321.78	1110.0	15654	>26.55	–
WFC3	UVIS	F438W	58877.89	276.10	1050.0	15654	25.73	0.10
WFC3	UVIS	F438W	58923.57	321.78	1050.0	15654	>26.44	–
WFC3	UVIS	F555W	58877.93	276.10	670.0	15654	24.38	0.04
WFC3	UVIS	F555W	58923.59	321.78	670.0	15654	25.26	0.08
WFC3	UVIS	F555W	58990.73	388.93	1500.0	16075	25.96	0.07
WFC3	UVIS	F814W	58877.89	276.10	836.0	15654	22.03	0.01
WFC3	UVIS	F814W	58923.57	321.78	836.0	15654	23.07	0.03
WFC3	UVIS	F814W	58990.70	388.93	900.0	16075	24.55	0.06
WFC3	IR	F110W	58990.64	388.84	1211.75	16075	24.88	0.05
WFC3	IR	F160W	58990.64	388.84	1211.75	16075	24.37	0.07

[a]All apparent magnitudes in AB system. No extinction corrections have been made for MW or host reddening.

Table A2. Bolometric Light Curve Data

MJD	Phase[a] days	Luminosity[b] erg s^{-1}	Uncertainty erg s^{-1}
58602.23	+0.43	1.83e+41	1.15e+40
58603.17	+1.37	5.94e+41	2.99e+40
58603.22	+1.42	6.10e+41	3.07e+40
58603.62	+1.82	6.53e+41	3.55e+40
58604.61	+2.81	7.76e+41	4.03e+40
58605.25	+3.45	1.75e+42	9.28e+40
58606.21	+4.41	1.27e+42	7.12e+40
58606.21	+4.41	1.27e+42	7.05e+40
58606.26	+4.46	1.22e+42	6.88e+40
58607.24	+5.44	8.80e+41	5.34e+40
58607.39	+5.59	8.33e+41	5.25e+40
58607.55	+5.75	7.59e+41	7.77e+40
58608.13	+6.33	5.91e+41	3.04e+40
58609.18	+7.38	5.48e+41	2.88e+40
58612.21	+10.41	6.86e+41	3.75e+40
58612.21	+10.41	6.86e+41	3.72e+40
58614.39	+12.59	7.63e+41	4.06e+40
58615.14	+13.34	7.84e+41	4.04e+40
58615.36	+13.56	8.03e+41	4.27e+40
58616.18	+14.38	8.23e+41	4.30e+40
58617.08	+15.28	7.54e+41	4.05e+40
58619.19	+17.39	5.87e+41	3.88e+40
58619.19	+17.39	5.87e+41	3.81e+40
58622.52	+20.72	4.50e+41	2.88e+40
58626.26	+24.46	3.49e+41	1.93e+40

Table A2 (cont'd)

MJD	Phase[a] days	Luminosity[b] erg s^{-1}	Uncertainty erg s^{-1}
58628.30	+26.50	3.21e+41	1.80e+40
58631.12	+29.32	2.81e+41	1.62e+40
58632.18	+30.38	2.74e+41	2.02e+40
58633.20	+31.40	2.72e+41	1.62e+40
58633.20	+31.40	2.72e+41	1.64e+40
58633.27	+31.47	2.66e+41	1.52e+40
58634.18	+32.38	2.58e+41	1.49e+40
58636.08	+34.28	2.45e+41	1.34e+40
58636.11	+34.31	2.45e+41	1.34e+40
58636.21	+34.41	2.44e+41	1.46e+40
58636.35	+34.55	2.47e+41	1.51e+40
58639.05	+37.25	2.17e+41	1.29e+40
58639.18	+37.38	2.16e+41	1.34e+40
58640.18	+38.38	2.10e+41	1.30e+40
58642.10	+40.30	1.99e+41	1.26e+40
58642.22	+40.42	2.00e+41	1.31e+40
58644.07	+42.27	2.05e+41	1.25e+40
58646.23	+44.43	1.95e+41	1.43e+40
58649.22	+47.42	1.87e+41	1.40e+40
58652.28	+50.48	1.70e+41	1.49e+40
58652.71	+50.91	1.70e+41	1.34e+40
58657.53	+55.73	1.52e+41	9.97e+39
58658.04	+56.24	1.48e+41	8.88e+39
58658.18	+56.38	1.46e+41	9.21e+39
58661.20	+59.40	1.32e+41	8.76e+39

Table A2 (cont'd)

MJD	Phase[a] days	Luminosity[b] erg s^{-1}	Uncertainty erg s^{-1}
58670.01	+68.21	9.83e+40	6.95e+39
58687.86	+86.06	6.99e+40	6.94e+39
58688.97	+87.17	6.64e+40	5.75e+39
58690.97	+89.17	6.75e+40	5.33e+39
58696.97	+95.17	5.39e+40	4.26e+39
58877.93	+276.13	1.07e+39	4.68e+37
58923.59	+321.79	4.76e+38	2.19e+37
58990.73	+388.93	1.55e+38	9.05e+36

[a]Relative to explosion.

[b]Covers wavelength range 3000-10000 Å

Table A3. Explosion Model Characteristics

Model	Description	SN Type	M_{ej} ($M_\odot$)	M(^{56}Ni) ($M_\odot$)	^{57}Co/^{56}Co	Reference
W7	Deflagration[a]	SN Ia	1.38	0.59	0.041	Iwamoto et al. 1999
ddt_n100	Delayed Detonation[a]	SN Ia	1.40	0.60	0.031	Seitenzahl et al. 2013b
det_1.06	Detonation[a]	SN Ia	1.06	0.56	0.006	Sim et al. 2010
doubledt_CSDD-S	Double Detonation[a]	SN Ia	0.79	0.21	0.044	Sim et al. 2012
def_N100def	Pure Deflagration[a]	SN Ia	1.40	0.36	0.038	Fink et al. 2014
det_ONe15e7	O-Ne WD Detonation[a]	SN Ia	1.23	0.96	0.009	Marquardt et al. 2015
gcd_GCD200	Detonation[a]	SN Ia	1.40	0.74	0.025	Seitenzahl et al. 2016
merger_11+09	Violent Merger[b]	SN Ia	1.95	0.10	0.024	Pakmor et al. 2012
merger_09+09	Violent Merger[b]	SN Ia	1.75	0.10	0.003	Pakmor et al. 2010
merger_09+076_Z1	Violent Merger[b]	SN Ia	1.6	0.18	0.009	Kromer et al. 2013b
merger_09+076_Z0.01	Violent Merger[b]	SN Ia	1.6	0.18	0.003	Kromer et al. 2016
0.55+0.63_Carich	WD Merger	CaST	0.45	0.013	0.0028	Zenati et al. 2023
0.52+0.63_Carich	WD Merger	CaST	0.43	0.052	0.00084	Zenati et al. 2023
0.50+0.58_Carich	WD Merger	CaST	0.36	0.011	0.011	Zenati et al. 2023
03HeWD+14NS	NS + He WD	FRRT[c]	0.30	0.0036	0.049	A. Bobrick
063COWD+14NS	NS + CO WD	FRRT[c]	0.63	0.0049	0.040	Zenati et al. 2020
063COWD+20NS	NS + CO WD	FRRT[c]	0.63	0.0061	0.058	Zenati et al. 2020
08COWD+14NS	NS + CO WD	FRRT[c]	0.80	0.029	0.078	Zenati et al. 2020
09ONeWD+14NS	NS + ONe WD	FRRT[c]	0.9	0.023	0.120	Bobrick et al. 2022
09COWD14NS	NS + CO WD	FRRT[c]	0.9	0.026	0.11	Bobrick et al. 2022
10ONeWD14NS	NS + ONe WD	FRRT[c]	0.9	0.029	0.11	Bobrick et al. 2022
11ONeWD14NS	NS + ONe WD	FRRT[c]	1.1	0.046	0.093	Bobrick et al. 2022
12ONeWD14NS	NS + ONe WD	FRRT[c]	1.2	0.054	0.11	Bobrick et al. 2022
12ONeWD20NS	NS + ONe WD	FRRT[c]	1.2	0.034	0.068	Bobrick et al. 2022
12ONeWD50BH	BH + ONe WD	FRRT[c]	1.2	0.010	0.044	Bobrick et al. 2022

Table A3 (cont'd)

Model	Description	SN Type	M_{ej} ($M_\odot$)	M(^{56}Ni) ($M_\odot$)	^{57}Co/^{56}Co	Reference
13ONeWD14NS	BH + ONe WD	FRRT[c]	1.3	0.090	0.072	Bobrick et al. 2022
CO145	CO Star Core-Collapse	USSN[d]	0.098	0.0097	0.046	Yoshida et al. 2017
CO150	CO Star Core-Collapse	USSN[d]	0.11	0.0057	0.041	Yoshida et al. 2017
ussn_E1e50erg	Core-Collapse, 10^{50} erg	USSN[d]	0.20	0.026	0.091	Moriya et al. 2017b
ussn_E2.5e50erg	Core-Collapse, 2.5×10^{50} erg	USSN[d]	0.20	0.030	0.085	Moriya et al. 2017b
ussn_E5e50erg	Core-Collapse, 5×10^{50} erg	USSN[d]	0.20	0.034	0.080	Moriya et al. 2017b
e8.8	Core-Collapse, $M_{\rm ZAMS} = 8.8$ $M_\odot$	ECSN[e]	0.017	0.0029	0.034	Wanajo et al. 2018
z9.6	Core-Collapse, $M_{\rm ZAMS} = 9.6$ $M_\odot$	CCSN[f]	0.56	0.0025	0.036	Wanajo et al. 2018
u8.1	Core-Collapse, $M_{\rm ZAMS} = 8.1$ $M_\odot$	CCSN[f]	0.33	0.0016	0.046	Wanajo et al. 2018
s11	Core-Collapse, $M_{\rm ZAMS} = 11$ $M_\odot$	CCSN[f]	1.48	0.0039	0.023	Wanajo et al. 2018

[a]Single Degenerate Channel

[b]Double Degenerate Channel

[c]"Faint Rapid Red Transient"

[d]"Ultra-stripped supernova"

[e]"Electron-capture supernova"

[f]"Core-collapse supernova"

Chapter 4

The Circumstellar Environments of Double-Peaked, Calcium-strong Transients 2021gno and 2021inl

This chapter was previously published as Jacobson-Galán et al., 2022b, ApJ, 932, 58

4.1 Abstract

We present panchromatic observations and modeling of calcium-strong supernovae (SNe) 2021gno in the star-forming host galaxy NGC 4165 and 2021inl in the outskirts of elliptical galaxy NGC 4923, both monitored through the Young Supernova Experiment (YSE) transient survey. The light curves of both SNe show two peaks, the former peak being derived from shock cooling emission (SCE) and/or shock interaction with circumstellar material (CSM). The primary peak in SN 2021gno is coincident with luminous, rapidly decaying X-ray emission ($L_x = 5 \times 10^{41}$ erg s^{-1}) detected by Swift-XRT at $\delta t = 1$ day after explosion, this observation being the second ever detection of X-rays from a calcium-strong transient. We interpret the X-ray emission in the context of shock interaction with CSM that extends to $r < 3 \times 10^{14}$ cm. Based on X-ray modeling, we calculate a CSM mass $M_{\rm CSM} = (0.3 - 1.6) \times 10^{-3}$ M$_\odot$ and density $n = (1 - 4) \times 10^{10}$ cm^{-3}. Radio non-detections indicate a low-density environment at larger radii ($r > 10^{16}$ cm) and mass loss rate of $\dot{M} < 10^{-4}$ M$_\odot$ yr^{-1}. SCE modeling of both primary light curve peaks indicates an extended progenitor envelope mass $M_e = 0.02 - 0.05$ M$_\odot$ and radius $R_e = 30 - 230$ R$_\odot$. The explosion properties suggest progenitor systems containing either a low-mass massive star or a white dwarf (WD), the former being unlikely given the lack of local star formation. Furthermore, the environments of both SNe are consistent with low-mass hybrid He/C/O WD + C/O WD mergers.

4.2 Introduction

Calcium-rich (Ca-rich) transients are a peculiar class of stellar explosions whose progenitor system remains ambiguous (Filippenko et al. 2003; Perets et al. 2010a; Kasliwal et al. 2012). These SNe are defined primarily based on an observed integrated emission line flux ratio of [Ca II]/[O I] > 2 when the explosion has reached its nebular phase (Milisavljevic et al. 2017) and the current sample consists of $N \gtrsim 25$ confirmed objects. Consequently, these SNe are labeled as "Ca-rich" compared to other transients when observed in their optically thin regime. However, because modeling of these SNe has indicated that they do not in fact produce more Ca in abundance relative to O (Milisavljevic et al. 2017; Jacobson-Galán et al. 2020b, 2021), but rather are simply "rich" in Ca II emission, we choose to adopt an alternative naming convention and refer to these as "Ca-strong transients" (CaSTs) from this point forward (Shen et al. 2019).

Beyond their prominent Ca II emission, CaSTs have other observational characteristics that make them a well-defined explosion class. Firstly, these SNe are typically low-luminosity explosions ($M_{\rm peak} > -16.5$ mag) that have a fast photometric evolution (e.g., rise-times $\lesssim 15$ days) (Taubenberger 2017). Physically, CaSTs are typically low energy explosions ($E_k \approx 10^{50}$ erg) that produce small amounts of ejecta ($\lesssim 0.6$ M$_\odot$) and ^{56}Ni ($\lesssim 0.1$ M$_\odot$); the latter being the dominant radioactive isotope that dictates their peak light curve luminosities. Spectroscopically, most CaSTs exhibit type I spectra with prominent He I transitions at early-times and then experience an expedited transition to nebular phases where [Ca II] dominates. Lastly, the explosion environments of early samples of CaSTs showed a strong preference towards the outskirts of early-type galaxies where no star formation was detected, indicating a compact progenitor star e.g., a white dwarf (WD) system (Perets et al. 2010a, 2011; Kasliwal et al. 2012; Lyman et al. 2014; Foley 2015; Lunnan et al. 2017; Dong et al. 2022). However, as the sample of confirmed CaSTs has grown, there has been increased diversity in the host environments of new objects. For example, CaSTs such as iPTF15eqv (Milisavljevic et al. 2017), iPTF16hgs (De et al. 2018b), SN 2016hnk (Galbany et al. 2019; Jacobson-Galán et al. 2020a) and SN 2019ehk (Jacobson-Galán et al. 2020b; Nakaoka et al. 2020) were all discovered in star-forming host galaxies, while a number of CaSTs reported in a recent sample by De et al. (2020) continued to show a preference towards early-type hosts.

Many of these SNe were found at relatively large offsets from their host galaxy nuclei (Perets & Beniamini 2021, and references therein), showing a different offset distribution than type Ia SNe (Kasliwal et al. 2012), which prompts suggestions of the progenitors residing in globular clusters or ejected at high velocities from their original formation closer to the host galaxy nuclei (Perets et al. 2010a; Foley 2015; Shen et al. 2019). However, a more detailed study (Perets & Beniamini 2021) showed that the large offsets originate from the SNe in early-type galaxies (also consistent with the two new SNe we discuss here), where a large fraction of the CaST SNe are found. In such galaxies the old stellar population extend to large distances, and the overall large offset distribution is consistent with the distribution of the old stellar populations in such galaxies, further supporting an old stellar progenitors for likely the majority of the CaST SNe (Perets 2014b; Perets & Beniamini 2021).

While the heterogeneous environments of CaSTs make it difficult to constrain a single progenitor channel, there have been significant constraints made to the parameter space of viable CaST progenitor systems. Firstly, the discovery of multiple CaSTs with double-peaked light curves (e.g., iPTF16hgs, SN 2018lqo, SN 2019ehk; De et al. 2018b, 2020; Jacobson-Galán et al. 2020b) has indicated that the progenitors of at least some of these transients must arise from stars surrounded by either extended envelopes or confined CSM. Another major breakthrough in the study of these objects came from the discovery of the closest CaST to date, SN 2019ehk, which exploded in the spiral host galaxy M100 at $D \approx 16.2$ Mpc (Jacobson-Galán et al. 2020b; Nakaoka et al. 2020; De et al. 2021). SN 2019ehk was detected within ∼10 hours of explosion and produced luminous X-ray emission, coincident with shock-ionized spectral emission lines and a double-peaked light curve (Jacobson-Galán et al. 2020b, hereafter WJG20a). The combination of these observations (X-ray to radio) revealed that the SN 2019ehk progenitor star exploded into a confined shell of H- and He-rich CSM with mass of $\sim 7 \times 10^{-3}$ $M_\odot$. Furthermore, SN 2019ehk is the first CaST with pre-explosion *HST* imaging, which revealed no detectable progenitor, but did constrain the possible progenitor channels to a low-mass massive star (<10 $M_\odot$) or a WD system. Lastly, given its close proximity, SN 2019ehk was imaged out to ∼400 days post-explosion, which allowed for the tightest constraints to date to be made on the total amount of synthesized radioactive decay isotopes ^{56}Ni and ^{57}Ni in a CaST; the isotope mass ratio suggesting a progenitor channel involving the merger of low-mass WDs (Jacobson-Galán et al. 2021).

In this paper, we present, analyze and model multi-wavelength observations (X-ray to radio) of two new CaSTs, SNe 2021gno and 2021inl, both with double-peaked optical light curves. SN 2021gno was discovered with an apparent magnitude of 18.2 mag by the Zwicky Transient Facility (ZTF) on 20 March 2021 (MJD 59293.2) and is located at $\alpha = 12^{\rm h}12^{\rm m}10.29^{\rm s}$, $\delta = +13^\circ14'57.04''$ (Bruch et al. 2021a). While SN 2021gno was originally classified as both a type II and type IIb SN (Hung et al. 2021), the spectral time series, coupled with its light curve evolution, indicates that it belongs in the CaST class. SN 2021inl was discovered by ZTF on 07 April 2021 (MJD 59311.2) with a detection magnitude of 19.5 mag and is located at $\alpha = 13^{\rm h}01^{\rm m}33.24^{\rm s}$, $\delta = +27^\circ49'55.10''$ (Munoz-Arancibia et al. 2021). SN 2021inl was classified as a type Ib-peculiar and was noted to be spectroscopically consistent with the "Ca-rich" transient class (Taggart et al. 2021).

SN 2021gno is located 23.3″ NW of the nucleus of the SABa galaxy NGC 4165. For SN 2021gno, we use the redshift-independent distance of 30.5±5.6 Mpc, which was calculated using the Tully-Fisher relation (Theureau et al. 2007). For SN 2021inl, we use a redshift $z = 0.0182 \pm 0.0001$ (Albareti et al. 2017b), which corresponds to a distance of 79.9 ± 0.4 Mpc for standard ΛCDM cosmology ($H_0 = 70$ km s^{-1} Mpc^{-1}, $\Omega_M = 0.27$, $\Omega_\Lambda = 0.73$); unfortunately no redshift-independent distance is available. Possible uncertainties on the SN 2021inl distance could be the choice of H_0 and/or peculiar velocities of the host galaxy, the uncertainty on the former can, for example, contribute to $\lesssim 5\%$ uncertainty of the SN luminosity. For each SN, we define the time of explosion as the mean phase between last non-detection and first detection. This results in a time of explosion of MJD 59292.7 ± 0.6 days (19 March 2021) for SN 2021gno and MJD 59309.4±0.1 days (05 April 2021) for SN 2021inl.

Table A1 Main parameters of SN 2021gno and its host galaxy

Host Galaxy	NGC 4165
Galaxy Type	SAB(r)a
Galactic Offset	24.3″(3.6 kpc)
Redshift	0.0062 ± 0.0002
Distance	30.5 ± 5.6 Mpc[1]
Distance Modulus, μ	32.4 ± 0.4 mag
RA_{SN}	$12^h12^m10.29^s$
Dec_{SN}	$+13°14'57.04''$
Time of Explosion (MJD)	59292.7 ± 0.6
$E(B-V)_{MW}$	0.030 ± 0.001 mag
$E(B-V)_{host}$	0.0[2]
m_g^{peak}	17.50 ± 0.03 mag
M_g^{peak}	-14.9 ± 0.1 mag[3,4]

Note. — No extinction corrections have been applied to the presented apparent magnitudes.

The main parameters of SNe 2021gno and 2021inl and their host-galaxies are displayed in Tables A1 and A2, respectively.

4.3 Observations

4.3.1 UV/Optical/NIR Photometry

SN 2021gno was observed with the Ultraviolet Optical Telescope (UVOT; Roming et al. 2005) onboard the Neil Gehrels *Swift* Observatory (Gehrels et al. 2004) from 20 March 2021 until 21 April 2021 (δt = 0.84 – 33.0 days since explosion). We performed aperture photometry with a 5″ region with `uvotsource` within HEAsoft v6.26[9], following the standard guidelines from Brown et al. (2014). In order to remove contamination from the host galaxy, we employed images acquired at $t \approx 122$ days after explosion, assuming that the SN contribution is negligible at this phase. This is supported by visual inspection in which we found no flux associated with SN 2021gno. We subtracted the measured count rate at the location of the SN from the count rates in the SN images following the prescriptions of Brown et al. (2014). Consequently, we detect bright UV emission from the SN directly after explosion (Figure 5.4) until maximum bolometric light. Subsequent non-detections in $w1, m2, w2$ bands indicate significant cooling of the photosphere and/or Fe-group line blanketing.

[9]We used the calibration database (CALDB) version 20201008.

Table A2 Main parameters of SN 2021inl and its host galaxy

Host Galaxy	NGC 4923
Galaxy Type	E/S0
Galactic Offset	60.0″(23.3 kpc)
Redshift	0.0182 ± 0.0001[5]
Distance	79.9 ± 0.4 Mpc
Distance Modulus, μ	34.50 ± 0.01 mag
RA_{SN}	$13^h01^m33.24^s$
Dec_{SN}	$+27°49'55.10''$
Time of Explosion (MJD)	59309.4 ± 0.1
$E(B-V)_{MW}$	0.008 ± 0.001 mag
$E(B-V)_{host}$	0.0[6]
m_g^{peak}	20.2 ± 0.1 mag
M_g^{peak}	-14.3 ± 0.2 mag[78]

Note. — No extinction corrections have been applied to the presented apparent magnitudes.

Additional *griz*-band imaging of SN 2021gno and SN 2021inl was obtained through the Young Supernova Experiment (YSE) (Jones et al. 2021) with the Pan-STARRS telescope (PS1; Kaiser et al. 2002) between 24 March 2021 and 21 July 2021 ($\delta t = 4.80 - 123.5$ days since explosion) and 06 April 2021 and 10 June 2021 ($\delta t = 0.97 - 66.0$ days since explosion), respectively. PS1 images of SNe 2021gno and 2021inl are presented in Figure 5.1. Furthermore, SN 2021gno was observed with the DECam Extension survey of YSE between 22 March 2021 and 09 January 2022 ($\delta t = 1.49 - 294.7$ days) on the Cerro Tololo Inter-American Observatory Blanco 4-m telescope (Rest et al. 2022). The YSE photometric pipeline is based on `photpipe` (Rest et al. 2005). Each image template was taken from stacked PS1 exposures, with most of the input data from the PS1 3π survey. All images and templates are resampled and astrometrically aligned to match a skycell in the PS1 sky tessellation. An image zero-point is determined by comparing PSF photometry of the stars to updated stellar catalogs of PS1 observations (Chambers et al. 2017). The PS1 templates are convolved with a three-Gaussian kernel to match the PSF of the nightly images, and the convolved templates are subtracted from the nightly images with `HOTPANTS` (Becker 2015). Finally, a flux-weighted centroid is found for each SN position and PSF photometry is performed using "forced photometry": the centroid of the PSF is forced to be at the SN position. The nightly zero-point is applied to the photometry to determine the brightness of the SN for that epoch.

Both SNe 2021gno and 2021inl were observed with ATLAS ($\delta t = 0.70 - 84.6$ and $\delta t = 0.10 - 28.1$ days since explosion, respectively), a twin 0.5m telescope system installed

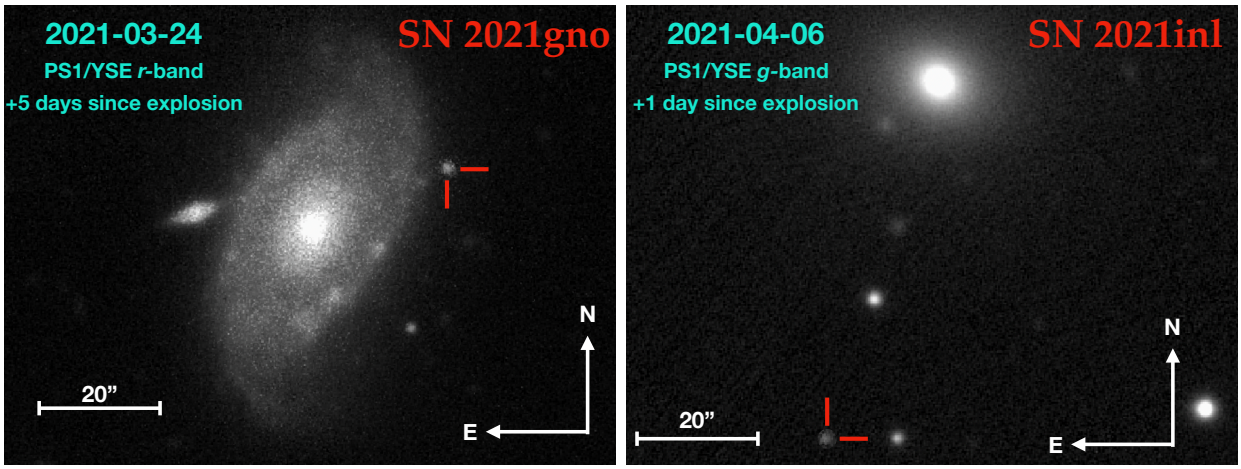

(a) (b)

Figure 4.1 (a) PS1/YSE $r-$band explosion image of Ca-strong SN 2021gno in host galaxy NGC 4165. (b) PS1/YSE $g-$band explosion image of Ca-strong SN 2021inl, offset from host galaxy NGC 4923 by 60″.

on Haleakala and Mauna Loa in the Hawai'ian islands that robotically surveys the sky in cyan (c) and orange (o) filters (Tonry et al. 2018a). The survey images are processed as described in Tonry et al. (2018a) and photometrically and astrometrically calibrated immediately (using the RefCat2 catalogue; Tonry et al. 2018c). Template generation, image subtraction procedures and identification of transient objects are described in Smith et al. (2020). Point-spread-function photometry is carried out on the difference images and all sources greater than 5σ are recorded and all sources go through an automatic validation process that removes spurious objects (Smith et al. 2020). Photometry on the difference images (both forced and non-forced) is from automated point-spread-function fitting as documented in Tonry et al. (2018a). The photometry presented here are weighted averages of the nightly individual 30 sec exposures, carried out with forced photometry at the position of the SNe.

The complete light curves of SNe 2021gno and 2021inl are presented in Figures 5.4 and 4.3, respectively, and all photometric observations are listed in Appendix Table A4. In addition to our observations, we include $g/r-$band photometry of SNe 2021gno and 2021inl from the Zwicky Transient Facility (ZTF; Bellm et al. 2019; Graham et al. 2019) forced-photometry service (Masci et al. 2019), which span from 20 March 2021 to 15 June 2021 ($\delta t = 0.54-87.5$ days since explosion) and 07 April 2021 to 08 May 2021 ($\delta t = 1.85-32.9$ days since explosion).

The Milky Way (MW) V-band extinction and color excess along the SN 2021gno line of sight is $A_V = 0.093$ mag and $E(B\text{-}V) = 0.03$ mag (Schlegel et al. 1998; Schlafly & Finkbeiner 2011), respectively, which we correct for using a standard Fitzpatrick (1999) reddening law ($R_V = 3.1$). Additionally, the MW V-band extinction and color excess along the SN 2021inl

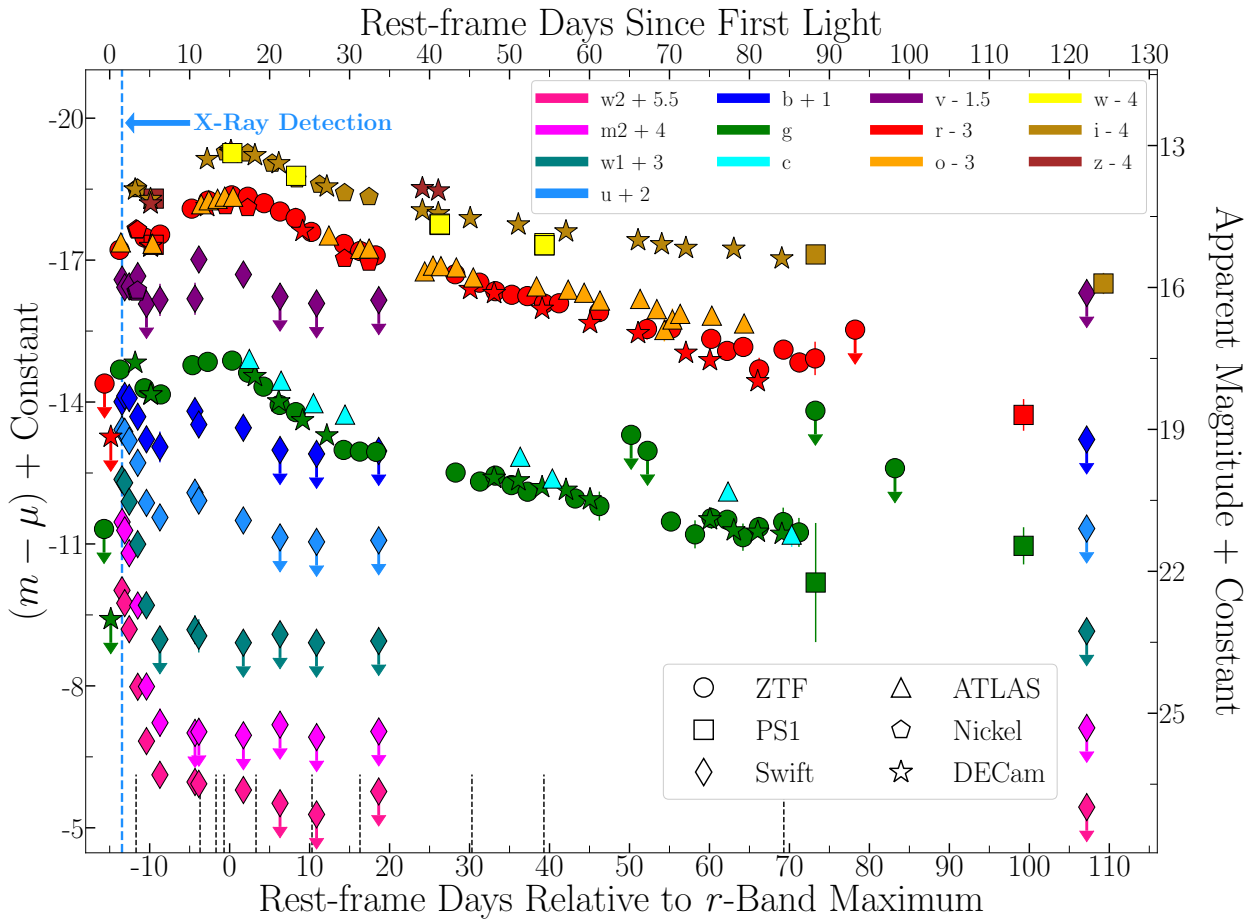

Figure 4.2 UV/Optical/NIR light curve of SN 2021gno with respect to second r-band maximum ($\delta t \approx 15$ days). Peak of primary light curve peak occurs at phase $\delta t \approx 2$ days. Observed photometry (absolute and apparent magnitudes) is presented in the AB magnitude system. ATLAS data/3σ upper limits are presented as triangles, PS1/YSE as squares, *Swift* as diamonds, ZTF as circles, Nickel as polygons, and DECam as stars. The epochs of our spectroscopic observations are marked by black dashed lines. Blue vertical dashed line mark the time of the X-ray detection in SN 2021gno.

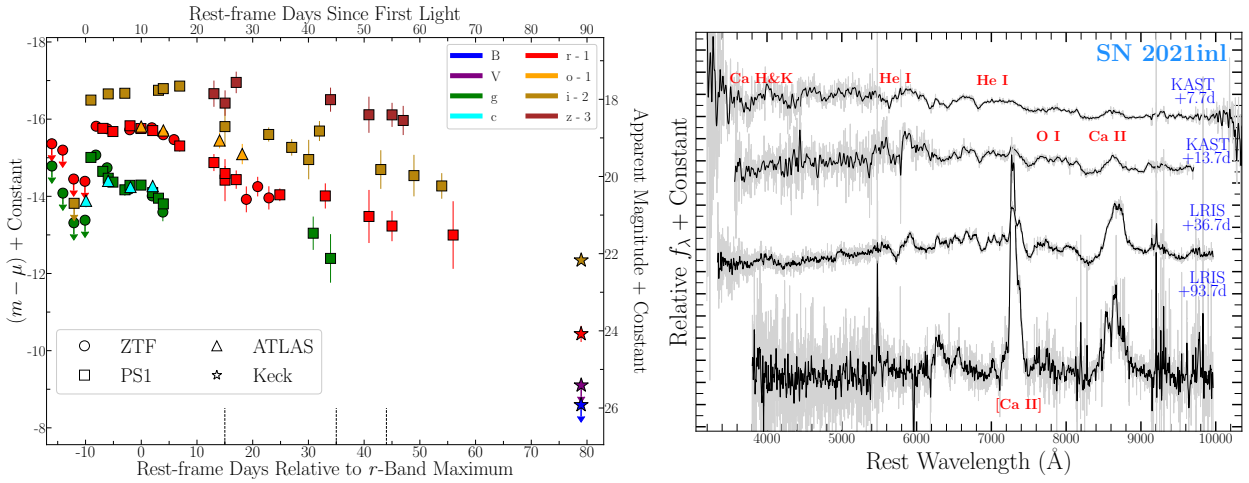

(a) (b)

Figure 4.3 (a) Optical/NIR light curve of SN 2021inl with respect to second r-band maximum ($\delta t \approx 10$ days). Peak of primary light curve peak occurs at phase $\delta t \approx 2$ days. Observed photometry presented in AB magnitude system. ATLAS data/3σ upper limits are presented as triangles, PS1/YSE as squares, *Swift* as diamonds, ZTF as circles, and Keck LRIS as stars. The epochs of our spectroscopic observations are marked by black dashed lines. (b) Spectral observations of SN 2021inl with phases (blue) marked with respect to explosion. Raw spectra are shown in gray, and smoothed spectra with black lines.

line of sight is $A_V = 0.025$ mag and $E(B\text{-}V) = 0.008$ mag (Schlegel et al. 1998; Schlafly & Finkbeiner 2011). For both SNe, we do not correct for host-galaxy contamination given the absence of Na I D absorption in all spectra at the host redshift.

4.3.2 Optical/NIR spectroscopy

In Figures 4.4 and 4.3(b), we present the complete series of optical spectroscopic observations of SN 2021gno and SN 2021inl from $\delta t = 3 - 84$ days and $\delta t = 25 - 111$ days relative to explosion, respectively. A full log of spectroscopic observations is presented in Appendix Tables A2 and A3.

SNe 2021gno and 2021inl were observed with Shane/Kast (Miller & Stone 1993) and Keck/LRIS (Oke et al. 1995) between $\delta t = 3 - 54$ days and $\delta t = 25 - 111$ days relative to explosion, respectively. For all these spectroscopic observations, standard CCD processing and spectrum extraction were accomplished with IRAF[10]. The data were extracted using the optimal algorithm of Horne (1986). Low-order polynomial fits to calibration-lamp spectra were used to establish the wavelength scale and small adjustments derived from night-sky lines in the object frames were applied. We employed custom IDL routines to flux calibrate the data and remove telluric lines using the well-exposed continua of the spectrophotometric standard stars (Wade & Horne 1988; Foley et al. 2003). Details of these spectroscopic reduction techniques are described in Silverman et al. (2012).

Spectra of SN 2021gno were also obtained with the Alhambra Faint Object Spectrograph (ALFOSC) on The Nordic Optical Telescope (NOT), as well as Binospec on MMT, and SpeX at the NASA Infrared Telescope Facility (IRTF). All of the spectra were reduced using standard techniques, which included correction for bias, overscan, and flat-field. Spectra of comparison lamps and standard stars acquired during the same night and with the same instrumental setting have been used for the wavelength and flux calibrations, respectively. When possible, we further removed the telluric bands using standard stars. Given the various instruments employed, the data-reduction steps described above have been applied using several instrument-specific routines. We used standard IRAF commands to extract all spectra.

4.3.3 X-ray observations with *Swift*-XRT

The X-Ray Telescope (XRT, Burrows et al. 2005) on board the *Swift* spacecraft (Gehrels et al. 2004) started observing the field of SN 2021gno from 20 March 2021 to 06 Nov. 2021 ($\delta t = 0.81 - 233.6$ days since explosion with a total exposure time of 28.8 ks, IDs 14199 and 14214). We analyzed the data using HEAsoft v6.26 and followed the prescriptions detailed in Margutti et al. (2013), applying standard filtering and screening. A bright source of X-ray emission is clearly detected in each individual observation with significance of $> 3\sigma$ against the background in the first two epochs ($\delta t = 0.81 - 1.14$ days; total exposure time of 4.73

[10]https://github.com/msiebert1/UCSC_spectral_pipeline

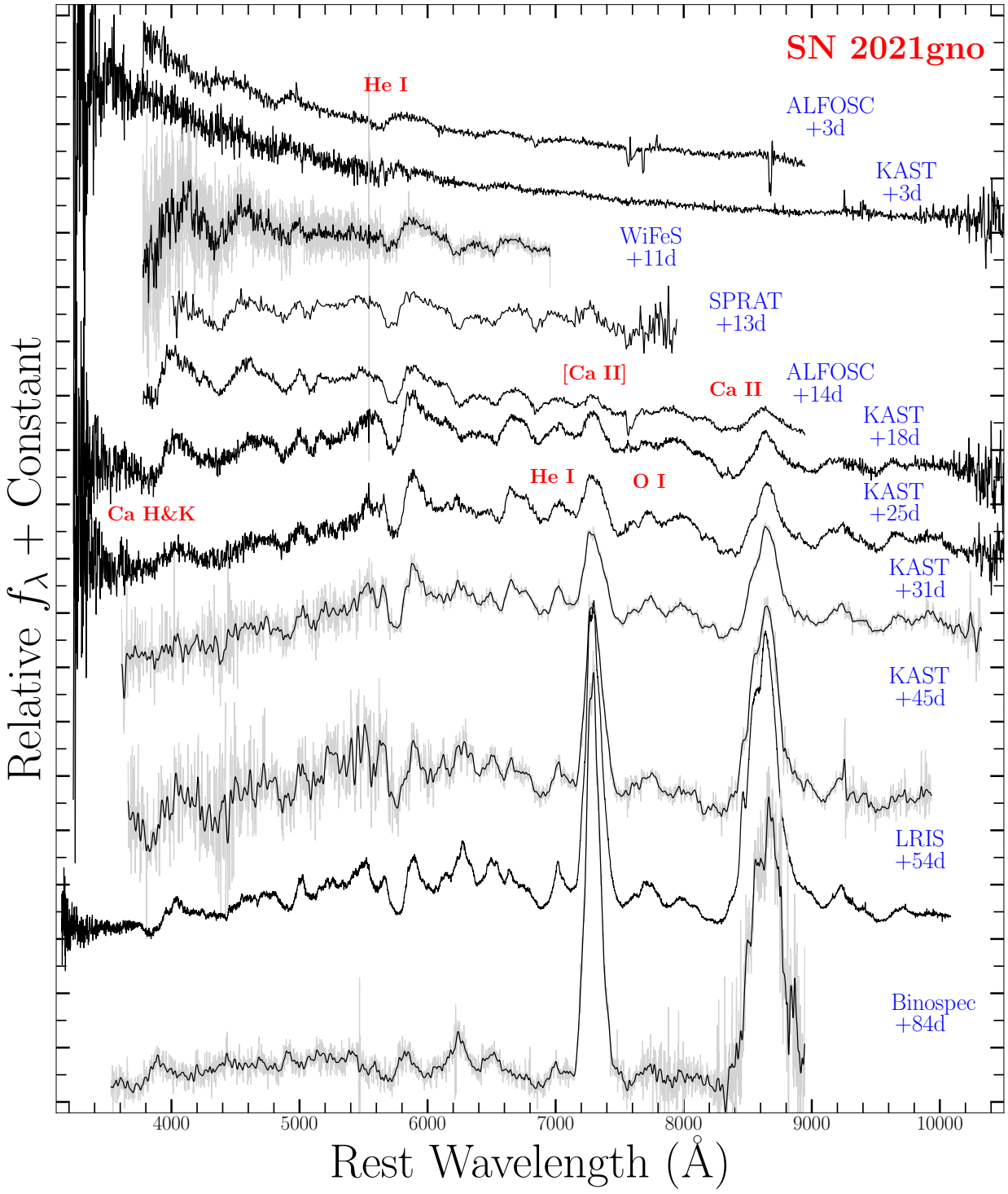

Figure 4.4 Spectral observations of SN 2021gno with phases (blue) marked with respect to explosion. Raw spectra are shown in gray, and smoothed spectra with black lines.

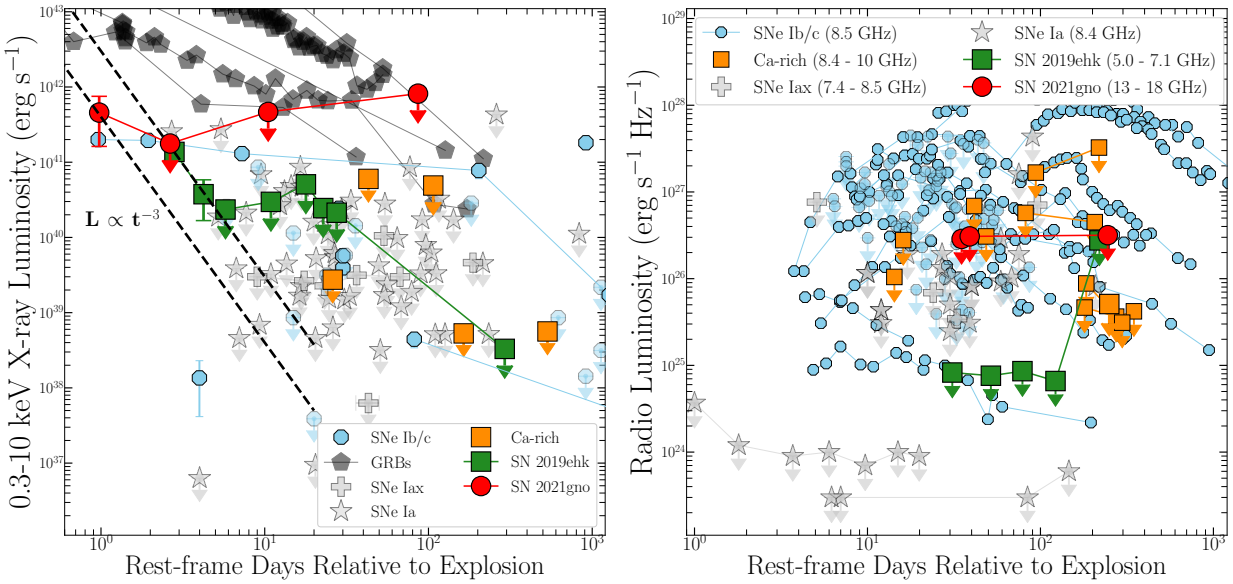

(a) (b)

Figure 4.5 (a) X-Ray light curve of SN 2021gno (red circles) and other thermonuclear transients e.g., SNe Iax (grey plus signs), SNe Ia (grey stars) and CaSTs (orange squares). Core-collapse SNe Ib/c are shown as light blue octagons and GRBs are displayed as black polygons. The decline rate of SN 2019ehk's X-ray emission (green squares; $L_x \propto t^{-3}$) is shown as a black dashed line, which is also consistent with SN 2021gno's decline rate (black dashed line). (b) Radio non-detections of SN 2021gno (red circles) compared to non-detection limits of thermonuclear SNe and SNe Ib/c.

ks) and count rates of $(3.8 \pm 1.6) \times 10^{-3}$ and $(2.3 \pm 1.1) \times 10^{-3}$ c s^{-1}, respectively. Given how close in time the first XRT observations are to one another, we chose to merge the two event files and use the combined epoch for analysis of the X-ray spectrum.

To test the validity of the X-ray emission observed in SN 2021gno, we first employ a binomial test to understand the likelihood that the fading X-ray emission was a chance coincidence. In this test, we compared the observed counts in the combined early-time epoch to a late-time, template XRT image (3.6 ks) of the explosion site at ~ 234 days. We find a probability of chance fading X-ray emission of only $\sim 0.34\%$, further indicating that the observed X-ray photons were in fact derived from the SN at early-times. Furthermore, in the template image, no X-ray emission is detected above the background level at later phases. The complete X-ray light curve is presented in Figure 4.5(a).

From the merged event file at $t \leq 2.1$ days, we extracted a spectrum using a 15″ region centered at the location of SN 2021gno. We find that the X-ray spectrum of the SN emission has a best-fitting photon index $\Gamma = 0.7 \pm 0.5$ (1σ error) corresponding to an unabsorbed 0.3-10 keV flux of $F_x = (4.1 \pm 2.2) \times 10^{-12}\,\mathrm{erg\,s^{-1}cm^{-2}}$. No evidence for intrinsic neutral hydrogen absorption is found ($\mathrm{NH_{MW}} < 2.2 \times 10^{18}\,\mathrm{cm^{-2}}$). The Galactic neutral hydrogen column density along our line of sight is $\mathrm{NH_{MW}} = 2.4 \times 10^{20}\,\mathrm{cm^{-2}}$ (Kalberla et al. 2005), which is used to account for the contribution of the host galaxy in modeling the X-ray excess. We then use the best-fitting spectral parameters inferred from the merged observations to flux-calibrate the count-rate upper limits derived for the following epochs (Table A1). Given the distance to SN 2021gno, these measurements indicate a steeply decaying, large X-ray luminosity of $L_x \leq 4.6 \times 10^{41}\,\mathrm{erg\,s^{-1}}$ at $t \leq 2.1$ days (Figure 4.5), rivaling even the gamma-ray burst SN, 1998bw (Kouveliotou et al. 2004). This very early-time observation represents only the second X-ray detection in a CaST, the first being SN 2019ehk, which showed luminous rapidly fading X-ray emission at $t \leq 4.2$ days since explosion (WJG20a). Furthermore, SN 2021gno's decay in X-ray luminosity is consistent with the steep light curve slope of $L_x \propto t^{-3}$ found in SN 2019ehk. However, because SN 2021gno only has one X-ray detection, it is important to note that its X-ray decline rate could vary differently than that observed in SN 2019ehk.

The hard 0.3-10 keV X-ray spectrum of SN 2019ehk is suggestive of thermal bremsstrahlung emission with temperature $T > 10$ keV. Consequently, we fit the SN 2021gno contribution with a bremsstrahlung spectral model with $T = 20$ keV and find an inferred emission measure of $EM = \int n_e n_I dV$ is $EM = (1.8 \pm 0.7) \times 10^{64}\,\mathrm{cm^{-3}}$ (at $\delta t \approx 1.0$ d), where n_e and n_I are the number densities of electrons and ions, respectively. Furthermore, in §4.8, we apply the estimated EM from the XRT detections to derive parameters of the CSM surrounding the progenitor system of SN 2021gno .

4.3.4 Radio observations

We observed SN 2021gno with the Arcminute Microkelvin Imager Large Array (AMI-LA; Zwart et al. 2008; Hickish et al. 2018) on 21, 25 April and 19 Nov. 2021 ($\delta t =$ 35, 39, & 245 days since explosion) and found no evidence for radio emission from the

SN. These data were all taken at a central frequency of 15.5 GHz across a 5 GHz bandwidth consisting of 4096 channels, which we average down to 8 for imaging. Radio frequency interference (RFI) flagging and bandpass and phase reference calibration were performed using a custom reduction pipeline (Perrott et al. 2013). Additional flagging and imaging was performed in the Common Astronomy Software Applications (CASA; McMullin et al. 2007) package. For imaging we use natural weighting with a clean gain of 0.1. To measure the source flux density we use the CASA task IMFIT. The resolution of the AMI-LA (characteristic beam dimensions 400 x 3000) when observing at the declination of J1820 means that the source is unresolved in all epochs. Details of each observation are presented in Appendix Table A2 and the derived radio luminosity limits for SN 2021gno are plotted in Figure 4.5(b).

4.4 Host Galaxy and Explosion Site

SN 2021gno is located 3.6 kpc in projection from the nucleus in the outer arm of its SBa type host galaxy NGC 4165 (Fig. 5.1a). We determine the host galaxy oxygen abundance 12 + log(O/H) by using an SDSS spectroscopic observation taken on 20 April 2004 of the galactic core; given the SN location, the metallicity at the explosion site is likely lower. Using a combination of line flux ratios ([O III] / Hβ and [N II]/Hα) in Equations 1 & 3 of Pettini & Pagel (2004), we determine a range of host metallicities of 12 + log(O/H) = 8.94 − 9.15 dex (1.03 − 1.06 $Z_{\odot}$). Using the same spectrum, we find an Hα emission line luminosity of $L_{H\alpha} = 8.7 \times 10^{39}$ erg s^{-1}, which corresponds to a star formation rate of SFR = 0.07 $M_{\odot}$ yr^{-1} (Kennicutt 1998).

In order to understand the SFR and metallicity at the exact location of SN 2021gno, we acquired an additional host spectrum at the explosion site using the Goodman spectrograph on SOAR on 27 January 2021, when the SN emission is not expected to be detected given its brightness at this phase and the S/N of the spectrum. We find no detectable host galaxy emission lines at the SN location and perform a manual, optimal Gaussian extraction with a 6σ region, 3σ on each side of the SN location, which translates to distance of 0.22 kpc. We then derive a limit on the Hα emission line luminosity by simulating a marginal detection as a Gaussian profile (FWHM = 100 km s^{-1}) with a peak flux of three times the spectrum's root-mean-square (RMS) flux. We then calculate $L_{H\alpha} < 4.3 \times 10^{36}$ erg s^{-1} and a local SFR of $< 3.4 \times 10^{-5}$ $M_{\odot}$ yr^{-1}. This estimate is consistent with the low SFR of $\sim 9.2 \times 10^{-5}$ $M_{\odot}$ yr^{-1} inferred from the explosion site of SN 2019ehk (WJG20a) and suggests that SN 2021gno is more likely to have originated from an older progenitor system (e.g., low-mass massive star or WD binary). Furthermore, the Hα luminosity at the explosion site of SN 2019ehk is only consistent with the H II region luminosity at the location of $\sim$ 20% of H-stripped SNe (Galbany et al. 2018; Kuncarayakti et al. 2018).

Similar to many other CaSTs, SN 2021inl is located at a large projected offset ($\sim$23 kpc) from early-type, E/S0 host galaxy NGC 4923 (Fig. 5.1b). While the explosion site indicates no star formation at the SN location, we also use an SDSS spectroscopic observation taken

on 22 Feb. 2007 of the galactic core to infer properties of NGC 4923. To derive properties of the host galaxy, we model the SDSS spectrum as well as *GALEX* All-Sky Survey Source Catalog (GASC; Seibert et al. 2012) UV, SDSS *ugriz*, and NIR Two Micron All Sky Survey (2MASS; Jarrett et al. 2000) JHK_s photometry with the Fitting and Assessment of Synthetic Templates code (FAST; Kriek et al. 2009). Our model grid includes stellar initial mass functions by Salpeter (1955) and Chabrier (2003), star-formation history that is exponentially decreasing and a delayed function, and stellar population libraries presented by Bruzual & Charlot (2003) and Conroy et al. (2009). For models without host galaxy dust reddening, we find a total stellar mass of $M_\star \approx (4.6 - 7.6) \times 10^{10}$ M$_\odot$, metallicity of $Z \approx Z_\odot$ and SFR $\lesssim 10^{-5}$ M$_\odot$ yr^{-1}. We also find consistent $M_\star$ and Z measurements within a grid of models that included dust ($A_V = 0.6$), but all models found an SFR = 0. Overall, these models indicate that SN 2021inl, given its large offset from a host with no apparent star formation, is *not* from a massive star progenitor.

4.5 Optical Light Curve Analysis

4.5.1 Photometric Properties

SNe 2021gno and 2021inl are the fourth and fifth confirmed CaSTs with clearly defined double-peaked light curves as shown in Figure 5.4 & 4.3(a), respectively. The other double-peaked objects in the present CaST sample are iPTF16hgs (De et al. 2018b), SN 2018lqo (De et al. 2020), and SN 2019ehk (Jacobson-Galán et al. 2020b; Nakaoka et al. 2020; De et al. 2021). Similar to other double-peaked SNe, we define the phase of these SNe relative to both the secondary, "Nickel-powered" peak and to explosion as defined at the end of §8.2. For both CaSTs, we calculate the time of maximum by fitting a third-order polynomial to $g-$ and $r-$band photometry. For SN 2021gno, we find best-fit g- and r-band peak absolute magnitudes of $M_g = -14.90 \pm 0.03$ mag at MJD 59305.2 ± 0.6 and $M_r = -15.3 \pm 0.2$ mag at MJD 59307.6 ± 0.6, respectively, resulting in an r-band rise-time of $t_r = 15.3 \pm 0.6$ days. For SN 2021inl, we find best-fit g- and r-band peak absolute magnitudes of $M_g = -14.3 \pm 0.1$ mag at MJD 59318.6 ± 0.1 and $M_r = -14.8 \pm 0.2$ mag at MJD 59317.4 ± 0.1, respectively, resulting in an $r-$band rise-time of $t_r = 8.04 \pm 0.10$ days.

In Figure 4.7, we present $r-$ and $g-$band light curve comparisons of SNe 2021gno and 2021inl to a sample of confirmed CaSTs. Overall, both objects have a consistent light curve evolution to other CaSTs e.g., $t_r \lesssim 15$ days, $M_{\rm peak} > -16.5$ mag, and fast-decaying post-maximum photometry. Both SNe are amongst the lowest luminosity events compared to other CaSTs, with SN 2021inl being $\sim$1 mag fainter than SNe 2005E (Perets et al. 2010a) and 2019ehk (Jacobson-Galán et al. 2020b; Nakaoka et al. 2020) and $\sim$2 mag less luminous than the peculiar "Calcium-strong" SN 2016hnk (Galbany et al. 2019; Jacobson-Galán et al. 2020a). Despite being intrinsically fainter, SN 2021gno's overall photometric evolution is most similar to SN 2019ehk and iPTF16hgs (De et al. 2018b); all three objects contain double-peaked light curves, as well as consistent rise-times and post-peak decline rates in both

$g-$ and $r-$bands. SN 2021inl's post-maximum decline is also consistent with SNe 2019ehk, 2021gno and iPTF16hgs, with all objects exhibiting a relatively rapid decay in $g-$band flux following the Ni-powered SN peak. Additionally, we compare the $g-r$ colors of SNe 2021gno and 2021inl to a CaST sample in Figure 8.5. Same as the photometric evolution, the overall $g-r$ color evolution of these two objects at $\delta t < 70$ days post-peak is quite consistent with the colors typically observed in other CaSTs. Similar to other objects observed early and with high cadence observations (e.g., iPTF16hgs, SN 2019ehk), SNe 2021gno and 2021inl display blue colors at the start of their evolution ($g-r < 0$ mag), but quickly transform into instrinsically red explosions ($g-r > 1$ mag) following SN peak.

4.5.2 Bolometric Light Curve

For SN 2021gno, we construct a bolometric light curve by fitting the ZTF, PS1, Nickel, ATLAS and *Swift* photometry with a blackbody model that is dependent on radius and temperature. The extremely blue UV colors and early-time color evolution of SN 2021gno during its first light peak impose non-negligible deviations from the standard *Swift*-UVOT count-to-flux conversion factors. We account for this effect following the prescriptions by Brown et al. (2010). Each spectral energy distribution (SED) of SN 2021gno was generated from the combination of multi-color UV/optical/NIR photometry in the $w2$, $m2$, $w1$, u, b, v, g, c, o, r, i, and z bands (1500–10000 Å). Similarly, for SN 2021inl, we construct a bolometric light curve by fitting the ZTF, PS1, Nickel, and ATLAS photometry with the same blackbody model to multi-band g, c, o, r, i, and z bands (3000–10000 Å). For both SNe, we extrapolated between light curve data points using a low-order polynomial spline in regions without complete color information. All uncertainties on blackbody radii and temperature were calculated using the co-variance matrix generated by the SED fits. For the secondary, Nickel-powered light curve peak, we find peak bolometric luminosities of $(4.12 \pm 1.57) \times 10^{41}$ erg s^{-1} and $(2.37 \pm 0.05) \times 10^{41}$ erg s^{-1} for SN 2021gno and SN 2021inl, respectively.

In Figures 4.8(a)/(b), we present the bolometric light curves of SNe 2021gno and 2021inl, in addition to their blackbody radius and temperature evolution in Figure 4.9. In both figures, we also present the bolometric luminosities, blackbody radii and temperatures of CaST SN 2019ehk (WJG20a). Overall, both SNe are less luminous than SN 2019ehk throughout all of their bolometric evolution except the very first data point of the first light curve peak where the luminosities are comparable. However, the post-peak bolometric decline in SNe 2021gno and 2021inl is consistent with the rate observed in SN 2019ehk; all of these objects declining faster than the typical decay of ^{56}Co $\rightarrow$ ^{56}Fe that assumes complete trapping of γ-rays. Furthermore, as shown in Figure 4.9, the blackbody temperature of SNe 2019ehk, 2021gno, and 2021inl are all nearly identical throughout the early-time evolution, $\delta t < 70$ days since explosion. However, the blackbody radius of SN 2019ehk is larger than both SNe throughout their evolution, while SN 2021gno and SN 2021inl are consistent with one another for most early-time epochs. Additionally, it should be noted that the blackbody approximation may not be appropriate when emission lines (e.g., Ca II) begin to dominate the spectrum

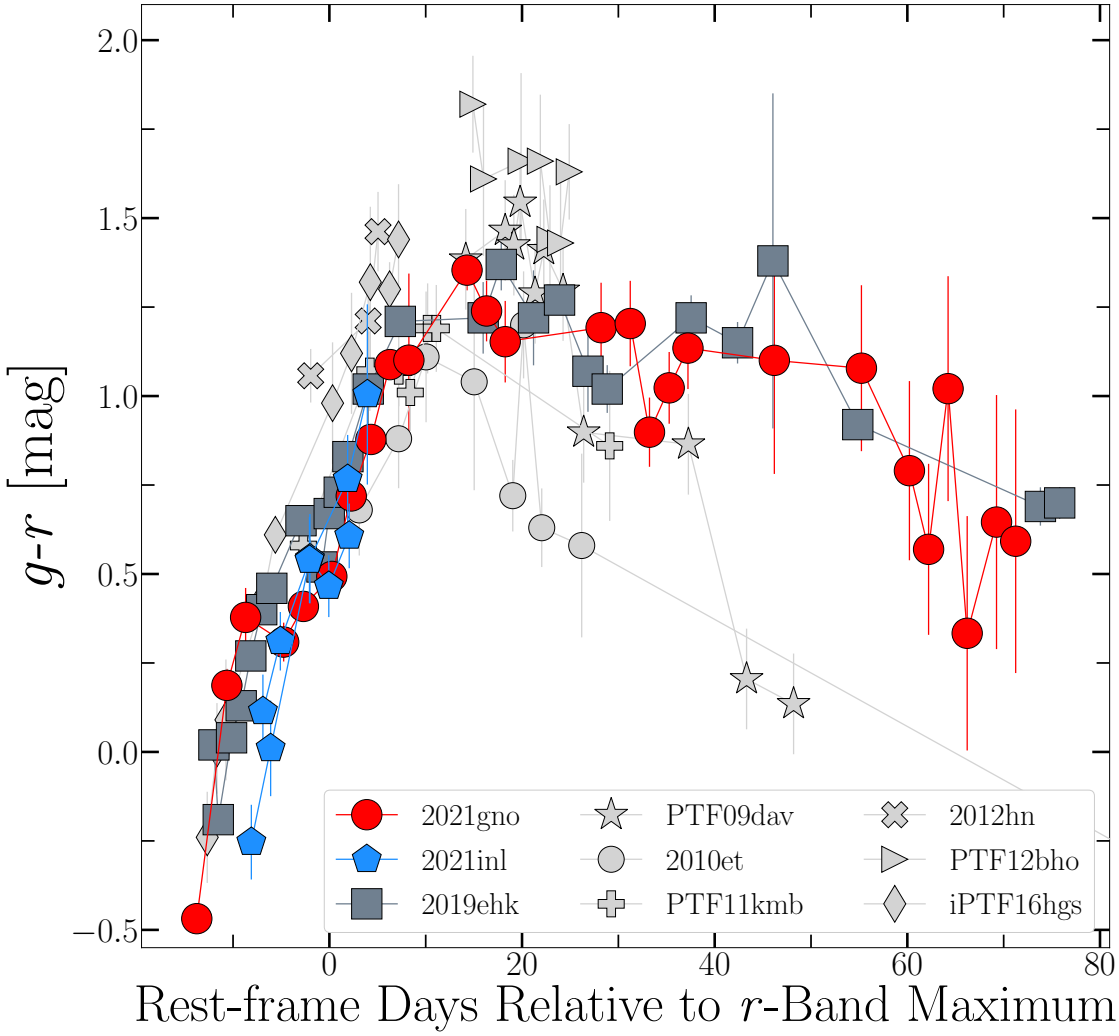

Figure 4.6 g-r color comparison of SN 2021gno (red circles), SN 2021inl (blue polygons), and current sample of CaSTs. All photometry has been extinction corrected.

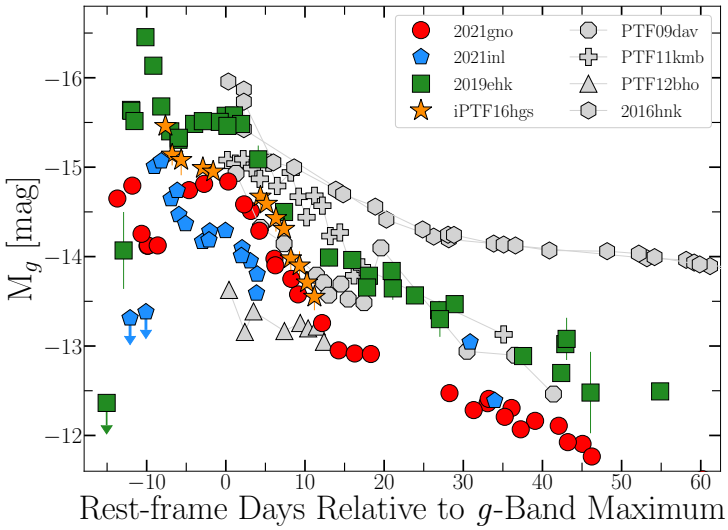

(a)

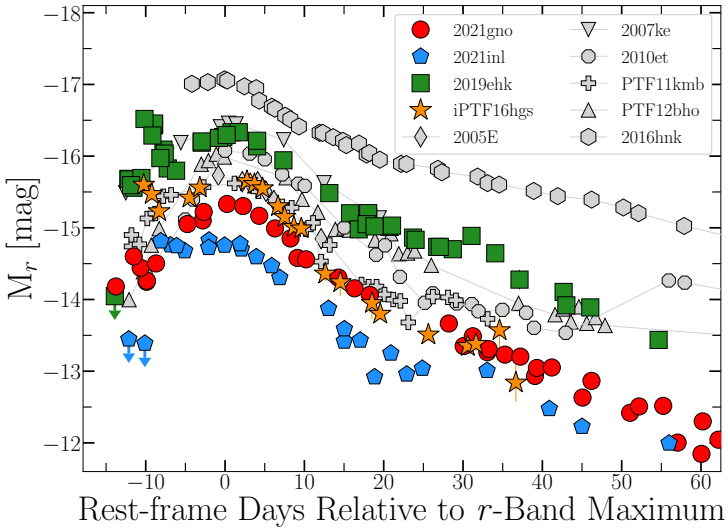

(b)

Figure 4.7 (a) Early-time $g-$band comparison of SN 2021gno (red circles), SN 2021inl (blue polygons), and classified CaSTs (Sullivan et al. 2011; Lunnan et al. 2017; De et al. 2018b; Jacobson-Galán et al. 2020b,a). The peculiar, "calcium-strong" SN 2016hnk also presented for reference (gray hexagons). SNe 2021gno and 2021inl are the fourth and fifth objects in this class to show a double-peaked light curve, iPTF16hgs (orange stars), SN 2019ehk (green squares), and SN 2018lqo (De et al. 2020) being the first three confirmed cases. (b) $r-$band comparison of SN 2021gno (red circles), SN 2021inl (blue polygons), and classified CaSTs.

of SNe 2021gno and 2021inl, which occurs $t > 40$ days after explosion. Consequently, a blackbody assumption for these objects in those phases is most likely an over-simplification and could result in additional uncertainty on the presented bolometric luminosities.

For SN 2021gno, the earliest inferred blackbody radius is $\sim 9 \times 10^{13}$ cm ($\sim$1300 $R_\odot$) at $\delta t = 0.84$ days since explosion. This suggests a compact progenitor star with radius $R_\star \lesssim 10 - 100$ $R_\odot$, which allows for the first detected blackbody radius to be reached given a shock velocity of $v_s \approx 1.2 \times 10^4$ km s^{-1}. Similarly, the first blackbody radius of $\sim 10^{14}$ cm ($\sim$1400 $R_\odot$) in SN 2021inl at $\delta t = 0.97$ days also allows for a compact progenitor radius of $R_\star \lesssim 10-100$ $R_\odot$ for $v_s \approx 1.2\times10^4$ km s^{-1}. Similar inferences we made for SN 2019ehk whose initial blackbody radius at $\delta t \approx 0.4$ days after explosion rules out an extended progenitor. Furthermore, in all three SNe, WD progenitors are still permitted given the time it would take the SN shock to reach the first blackbody radii from a much smaller initial stellar radius.

To determine physical parameters of both SNe such as ejecta mass ($M_{\rm ej}$), kinetic energy ($E_{\rm k}$), and ^{56}Ni mass ($M_{\rm Ni}$), we model both bolometric light curves with the analytic expressions presented in Appendix A of Valenti et al. (2008a) and in Wheeler et al. (2015). Same as in SN 2019ehk, we exclude the first light curve peak and model two distinct phases of the light curve: photospheric ($\delta t < 30$ days; Arnett 1982) and nebular ($\delta t > 40$ days; Sutherland & Wheeler 1984; Cappellaro et al. 1997). The analytic formalism applied in this modeling self-consistently implements the possibility of incomplete γ-ray trapping and a typical opacity of $\kappa = 0.1$ cm^2 g^{-1} is applied in each model. Furthermore, we correct for the known degeneracy between kinetic energy and ejecta mass (e.g., see Eqn. 1 in WJG20a) by applying photospheric velocities of $v_{\rm ph} \approx 6000$ km s^{-1} for SN 2021gno and $v_{\rm ph} \approx 7500$ km s^{-1} for SN 2021inl, both of which are derived from Si II absorption features in the SN spectra. For SN 2021gno, we find an ejecta mass of $M_{\rm ej} = 0.60 \pm 0.01$ $M_\odot$, kinetic energy of $E_{\rm k} = (1.3 \pm 0.2) \times 10^{50}$ erg, and ^{56}Ni mass of $M_{\rm Ni} = (1.20 \pm 0.02) \times 10^{-2}$ $M_\odot$. For SN 2021inl, we calculate an ejecta mass of $M_{\rm ej} = 0.29 \pm 0.01$ $M_\odot$, kinetic energy of $E_{\rm k} = (9.6 \pm 0.4) \times 10^{49}$ erg, and ^{56}Ni mass of $M_{\rm Ni} = (6.90 \pm 0.06) \times 10^{-3}$ $M_\odot$. In both SNe, the photospheric and nebular model fits (shown in Fig. 4.8) return consistent parameter values. We note that all uncertainties on these explosion parameters are purely statistical and there are likely larger systematic errors derived from the construction of the bolometric light curve, as well as the assumed opacity and velocity of the SN ejecta. Overall, the explosion parameters in SN 2021gno are very consistent with those derived for SN 2019ehk (WJG20a) despite a slightly lower $M_{\rm Ni}$, which explains the larger luminosities observed in SN 2019ehk. However, SN 2021inl's explosion parameters are all lower than that observed in SNe 2019ehk and 2021gno, but are consistent with the values generally found in the CaST class (De et al. 2020). We compile all explosion parameters of SNe 2021gno and 2021inl, in addition to SN 2019ehk, iPTF16hgs and objects studied in De et al. (2020), in Appendix Table A5.

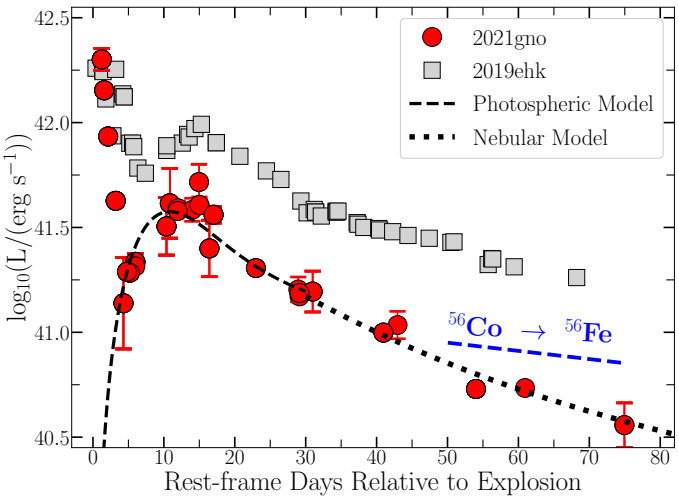

(a)

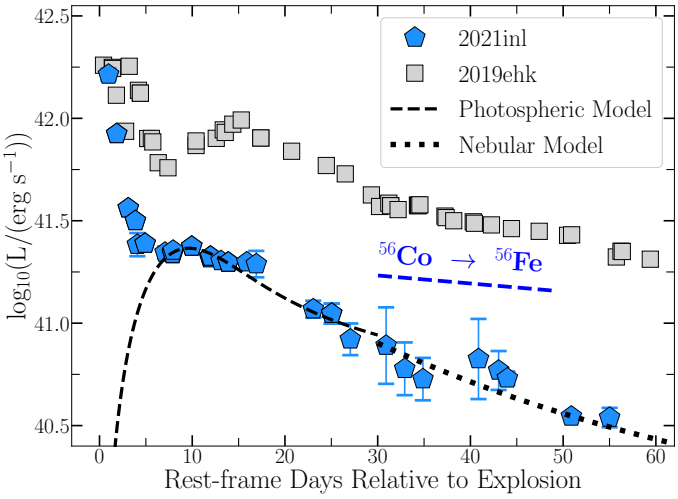

(b)

Figure 4.8 (a) Bolometric light curves of SNe 2021gno (red circles) and 2019ehk (gray squares). Secondary, ^{56}Ni-powered peak in SN 2021gno is at a phase of $\delta t \approx 10$ days, while the primary peak from shock cooling emission or CSM interaction is during phases $\delta t < 5$ days. Photospheric light curve model for the early-time light curve of SN 2021gno (§4.5.2) is plotted as dashed black line. Modeling of the nebular phase data plotted as dotted black line. Blue dashed line shows the luminosity decline rate for a radioactive decay powered light curve with complete $\gamma-$ray trapping. (b) Bolometric light curves of SNe 2021inl (blue polygons) and 2019ehk (gray squares). Secondary, ^{56}Ni-powered peak in SN 2021inl is at a phase of $\delta t \approx 10$ days.

4.6 Optical/NIR Spectral Analysis

4.6.1 Spectroscopic Properties

The complete spectral series of SNe 2021gno and 2021inl are presented in Figures 4.4 and 4.3(b), both of which include obvious ion identifications for both SNe. During their photospheric phase, both SNe display prominent He I, O I, Ca II, Si II and Fe-group element transitions; neither SNe showing evidence for detectable H I. In the first spectrum of SN 2021gno at +3 days post-explosion, we find that all the broad features can be identified as fast-moving He I $\lambda\lambda$ 4471, 5016, 5876, 6678 profiles and find a consistent expansion velocity of $\sim 1.3 \times 10^4$ km s^{-1} from the minimum of the absorption profile. Based on the absorption profiles in the SN 2021gno maximum light spectrum, we find characteristic ejecta velocities of $\sim 7000 - 8000$ km s^{-1} for He I, ~ 6500 km s^{-1} for Si II, and ~ 7000 km s^{-1} for Ca II. We find similar expansion velocities in SN 2021inl, such as $\sim (1 - 1.2) \times 10^4$ km s^{-1} for He I, ~ 7500 km s^{-1} for Si II, and ~ 8000 km s^{-1} for Ca II. Overall, the ejecta velocities estimated for both SNe are consistent with ion velocities found for SN 2019ehk (WJG20a) and other CaSTs (Kasliwal et al. 2012; Lunnan et al. 2017; De et al. 2020).

In Figure 4.10, we present the IR spectra of SN 2021gno at +10 days after second maximum compared to SN 2019ehk at +38 days; these two observations being the only confirmed IR spectra of a CaST during the photospheric phase. The IR spectrum of SN 2021gno shows nearly identical transitions to SN 2019ehk, both objects showing clear P-Cygni profiles of Ca II, He I, C I, and Mg I. Furthermore, the expansion velocities of these transitions are consistent with the ejecta velocities derived from optical spectra e.g., $\sim 1.1 \times 10^4$ km s^{-1} for He I and ~ 9000 km s^{-1} for Ca II.

In Figure 4.11(a), we present early-time spectral comparisons of SNe 2021gno and 2021inl to other CaSTs near (second) maximum light. Overall, both SNe show consistent spectral features to all plotted CaSTs, but are most similar to SN 2019ehk and iPTF16hgs at this phase. All four objects show prominent He I and Ca II transitions as well as the fast emergence of a [Ca II] emission profile relative to peak. Furthermore, we compare the mid-time spectra of SN 2021gno at +19 days to SNe 2005E, 2007ke, and 2019ehk in Figure 4.11(b). At this phase, SN 2021gno shows nearly identical transitions to these CaSTs such as prominent [Ca II] and marginal [O I]. These spectral comparisons are further indication that both SNe 2021gno and 2021inl are clear members of the CaST class.

4.6.2 Inferences from Nebular Phase Spectroscopy

Similar to other CaSTs, SNe 2021gno and 2021inl show a fast transition from the photospheric to the optically thin regime where their spectra become dominated by forbidden emission lines such as [Ca II] and [O I] (Fig. 4.12). For SN 2021gno, the transition to the nebular regime occurs at $\sim$13-18 days after explosion, which is evident from the presence of [Ca II] emission in the early-time spectra; this transition then comes to dominate the spectra at later phases (Fig. 4.4). Despite lower cadence spectroscopic observations, a similar be-

havior is observed in SN 2021inl, whose first spectrum at +8 days shows marginal evidence for [Ca II] emission, which later becomes the dominant transition by +94 days (Fig. 4.3b).

Once in the optically thin regime, we calculate [Ca II]/[O I] line flux ratio, which, if greater than 2, is a common classifier of CaSTs and present this quantity in Figure 4.13(a) for both SNe. Based on this metric, we find that both objects are significantly "rich" in [Ca II] emission as shown by a maximum line flux ratio of [Ca II]/[O I] ≈ 10. These flux ratios are consistent with other CaSTs presented in Figure 4.13(a), but neither SN has as large of a [Ca II]/[O I] ratio as SN 2019ehk, which remains the member of CaST with largest [Ca II] flux relative to [O I] at all phases. Furthermore, in Figures 4.13(b)/(c), we present the velocity profiles [Ca II] and [O I] of SNe 2021gno and 2021inl, respectively, with the O emission scaled to match the Ca feature. We find that in both objects, these forbidden line transitions are consistent in shape and indicate [Ca II] and [O I] expansion velocities of $\sim 5000-6000$ km s^{-1} based on the FWHM of the emission profiles.

In order to understand the Ca and O abundance in each explosion, we apply a similar analysis to that outlined in Section 6.3 of WJG20a where the observed luminosities of [Ca II] and [O I] are related to the populations of the excited states, ion number densities ($n_e > 10^7$ cm^{-3}), and Einstein A coefficient values of each ion:

$$L_{[\mathrm{O\,I}]} = n_{\mathrm{O\,I}}\ A_{[\mathrm{O\,I}]}\ h\nu_{[\mathrm{O\,I}]}\ (5/14)\ e^{-22000/T} \tag{4.1}$$

$$L_{[\mathrm{Ca\,II}]} = n_{\mathrm{Ca\,II}}\ A_{[\mathrm{Ca\,II}]}\ h\nu_{[\mathrm{Ca\,II}]}\ (10/11)\ e^{-19700/T} \tag{4.2}$$

where $h\nu$ is the photon energy, n is the ion number density, $A_{[\mathrm{Ca\,II}]} = 2.6$ s^{-1}, $A_{[\mathrm{Ca\,II}]} \approx 390 A_{[\mathrm{O\,I}]}$, the exponentials are the Boltzmann factors (T is in K), and the numerical factors are statistical weights. To find the ion number densities and subsequent masses in each SN, we first estimate the forbidden line luminosities to be $L_{[\mathrm{O\,I}]} = 3.9 \times 10^{38}$ erg s^{-1} and $L_{[\mathrm{Ca\,II}]} = 3.5 \times 10^{39}$ erg s^{-1} for SN 2021gno ($\delta t = 84$ days since explosion), and $L_{[\mathrm{O\,I}]} = 8.2 \times 10^{38}$ erg s^{-1} and $L_{[\mathrm{Ca\,II}]} = 3.6 \times 10^{39}$ erg s^{-1} for SN 2021inl ($\delta t = 111$ days since explosion). In the analytic relations above, we choose to calculate Ca and O masses for a range of temperatures $T = 5000 - 10^4$ K, for completeness.

For SN 2021gno, we calculate O and Ca masses of $M(\mathrm{O}) = (0.6 - 6) \times 10^{-2}$ M$_\odot$ and $M(\mathrm{Ca}) = (1 - 9) \times 10^{-4}$ M$_\odot$, for temperatures $T = 10^4 - 5000$ K. Similarly, for SN 2021inl, we find O and Ca masses of $M(\mathrm{O}) = 0.01 - 0.1$ M$_\odot$ and $M(\mathrm{Ca}) = (1 - 10) \times 10^{-4}$ M$_\odot$, for $T = 10^4 - 5000$ K. These abundances are lower overall, but still somewhat consistent, to those found by WJG20a for SN 2019ehk e.g., $M(\mathrm{O}) = 0.10$ M$_\odot$ and $M(\mathrm{Ca}) = 4 \times 10^{-3}$ M$_\odot$. However, it should be noted that at these phases both SNe are not fully nebular and therefore the derived masses may be lower than the true elemental masses in the explosion. Nevertheless, these mass estimates continue to prove that the "richness" of Ca emission in CaSTs is not due to a larger intrinsic amount of Ca relative to O, but rather it is likely the result of relative abundances and ionization temperatures in the inner, low density ejecta.

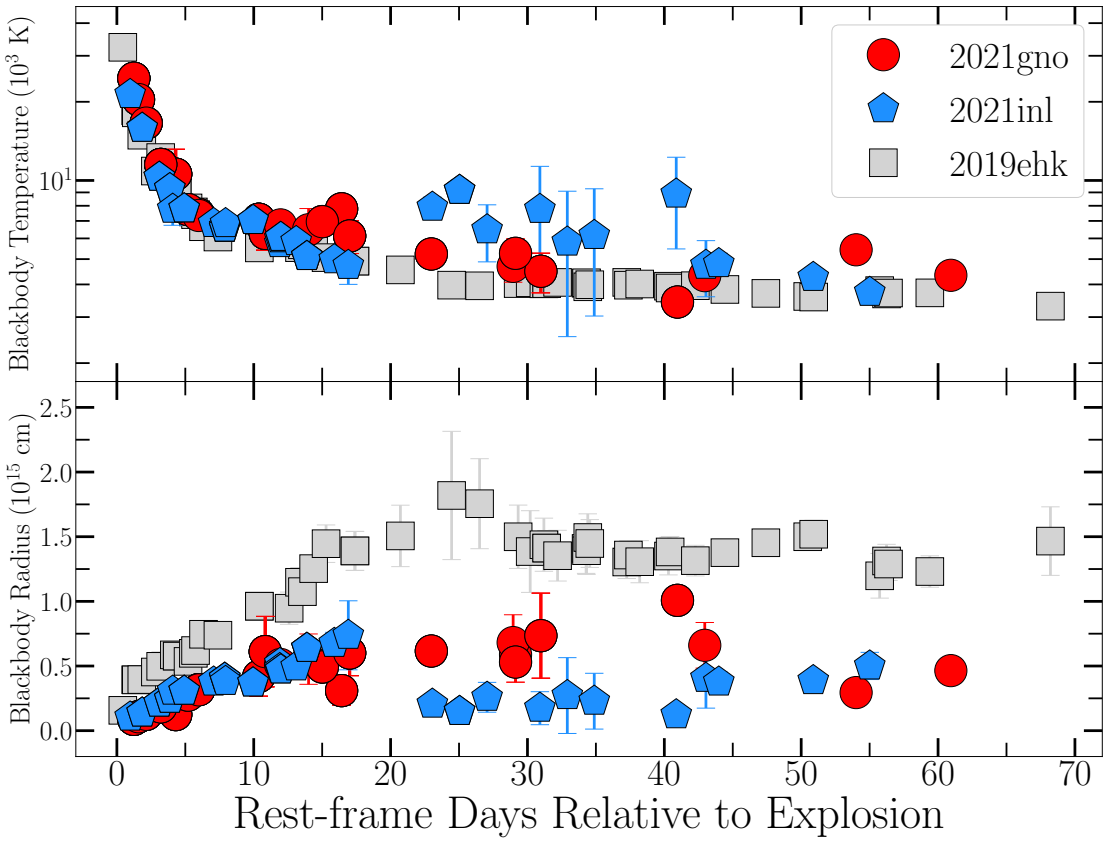

Figure 4.9 Blackbody radii (bottom panel) and temperatures (top panel) derived from SED modeling of all multi-color optical photometry from SNe 2021gno (red circles), 2021inl (blue polygons), and 2019ehk (gray squares).

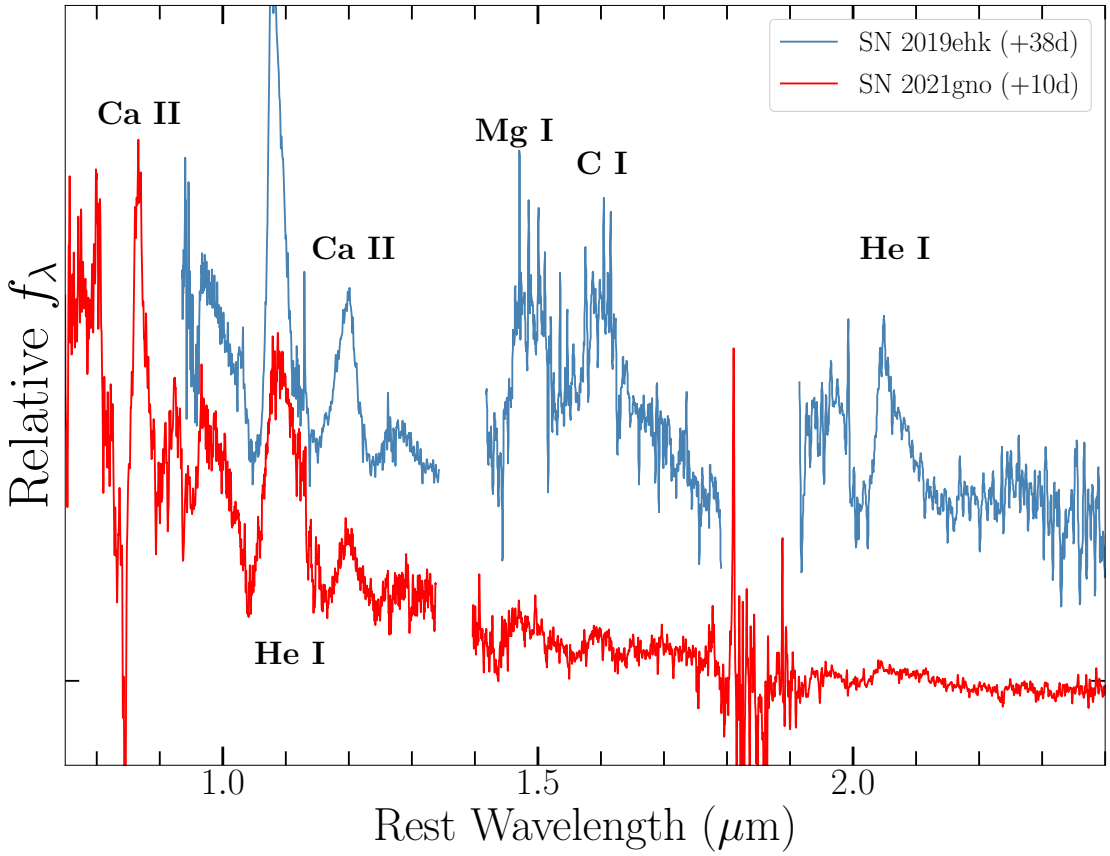

Figure 4.10 SPEX NIR spectrum (red) of SN 2021gno at +10 days relative to second B-band peak. NIR spectrum of SN 2019ehk shown in blue (WJG20a); these being the only early-time NIR spectra taken of CaSTs. Prominent line transitions are marked in black.

4.7 Early-time Flux Excess

4.7.1 Observational Properties

Similar to other double-peaked CaSTs, the early-time excess in flux above the ^{56}Ni-powered continuum is observed in all available UV/optical/NIR filters used to observe SNe 2021gno and 2021inl. Additionally, these very early-time observations of both SNe represent the only other instances where the initial rise of the primary light curve peak was recorded in a CaST, the first being in SN 2019ehk. In Figure 4.14, we present the $g-r$ colors, as well as $r-$ and $g-$band light curves of SNe 2019ehk, 2021gno, 2021inl, and iPTF16hgs during their primary light curve phase.

For all four double-peaked CaSTs in Figure 4.14(a), the $g-r$ color evolution during the flux excess follows a consistent trend: all objects show a linear increase in color following first detection and all begin with quite blue colors e.g., $g-r < -0.2$ mag. Seemingly, the physical process behind this early-time flux excess is responsible for a retention of high blackbody temperatures and, consequently, blue colors until the SN emission becomes dominated by energy injection from ^{56}Ni decay.

As shown in Figures 4.14(b)/(c), SN 2019ehk remains the most luminous double-peaked CaST, with its flux excess peaking at $M \approx -16.5$ mag in $g-$ and $r-$bands. SNe 2021gno and 2021inl are lower luminosity events than SN 2019ehk and iPTF16hgs, with their primary $g-$ and $r-$band light curves peaking at $M \approx -14.8$ mag and $M \approx -15.2$ mag, respectively. Furthermore, the light curve slopes during this phase varies between all CaSTs. SN 2021gno shows a $g-$band decline rate of $\Delta\mathrm{m(g)}_5 = 0.52$ mag during the $\sim$5 day primary peak duration while SN 2021inl has a decline rate of $\Delta\mathrm{m(g)}_7 = 0.64$ mag. Additionally, SN 2019ehk has a very fast decline rate of $\Delta\mathrm{m(g)}_5 = 1.1$ mag during its largest flare in early-time flux, while iPTF16hgs has a similarly rapid decline of $\Delta\mathrm{m(g)}_3 = 0.75$ mag.

4.7.2 Shock Breakout and Envelope Cooling Model

For stellar progenitors with an extended envelope, the energy deposited by the passage of a shock through their envelopes manifests in detectable shock cooling emission (SCE) on a timescale of $t \lesssim$ days after shock breakout. This process has been modeled both analytically (e.g., Nakar & Piro 2014; Piro 2015) and numerically (e.g., Sapir & Waxman 2017; Piro et al. 2017, 2021), these models being highly effective at reproducing the early time double-peaked light curves of SNe IIb (e.g., SNe 1993J, 2011dh, 2016gkg, 2017jgh; Wheeler et al. 1993; Arcavi et al. 2011, 2017a; Piro et al. 2017; Armstrong et al. 2021), super-luminous SNe (e.g., DES14X3taz; Smith et al. 2016), SNe Ic (e.g., SNe 2014ft, 2020bvc, 2020oi; De et al. 2018a; Ho et al. 2020; Gagliano et al. 2022), fast-risers (e.g., 2019dge; Yao et al. 2020 and CaSTs (e.g., iPTF16hgs, SN 2019ehk; De et al. 2018b; Nakaoka et al. 2020; Jacobson-Galán et al. 2020b). Furthermore, by fitting the primary light curve peaks of these double-peaked SNe, information about the extended material around the progenitor star at the time of explosion can be derived, such as the envelope mass and radius, as well as the shock velocity.

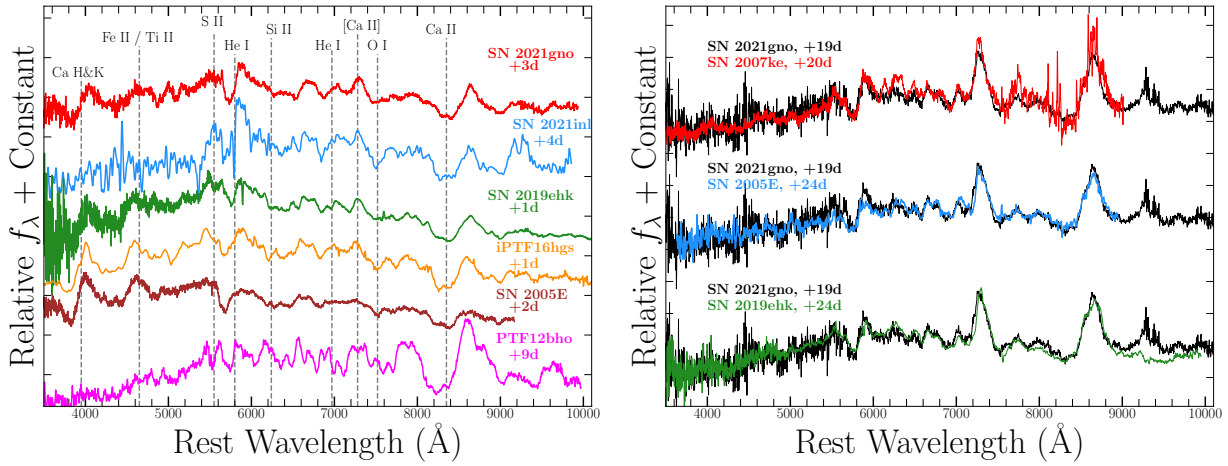

(a) (b)

Figure 4.11 (a) Spectral comparison of SN 2021gno (red), SN 2021inl (blue), and other CaSTs near maximum light (Perets et al. 2010b; Sullivan et al. 2011; Lunnan et al. 2017; De et al. 2018b). Common ions are marked by grey lines. (b) Direct spectral comparison of SN 2021gno (black) and CaSTs SNe 2007ke, 2005E, and 2019ehk at approximately the same phase (Perets et al. 2010b; Lunnan et al. 2017). Almost every line transition is matched between spectra, with SN 2021gno showing similar Ca II emission to all other objects.

In order to understand the physical origin of their early-time flux excess, we fit the primary light curve peaks of SNe 2021gno and 2021inl with models for SCE of extended material. We apply four models to fit the SN light curves: the original SCE model by Piro (2015) as well as the revised two-component formalism presented in Piro et al. (2021), in addition to the models of Sapir & Waxman (2017) who numerically model SCE from both red and blue supergiant, H-rich envelopes (polytropic index of n = 3/2 and n = 3, respectively). Presentation of the analytic expressions behind these models can be found in Arcavi et al. (2017a) or Section 7.3 of WJG20a. Following shock breakout, each model produces constraints on the envelope mass, M_e, envelope radius, R_e, the velocity of the envelope, v_e, and the time offset from explosion t_o (consistent with our explosion time estimate). In this analysis, we use `emcee`, a Python-based application of an affine invariant MCMC with an ensemble sampler (Foreman-Mackey et al. 2013). We compile the best fit parameter estimates from each model in Table 4.12.

In Figures 4.15 & 4.16, we present the best-fitting multi-color light curves of the aforementioned models for SNe 2021gno and 2021inl, respectively. We also present model bolometric light curves, as well as their blackbody temperatures and radii, in Figure 4.17 with respect to the SNe 2021gno and 2021inl data. In general, we find that SCE can accurately reproduce the early-time flux excess in both objects, with the models of Sapir & Waxman (2017) providing the best fit and lowest χ^2 value overall. From all four model fits, the SN 2021gno light curve is best reproduced by an extended mass $M_e \approx 0.013 - 0.47$ $M_\odot$ with radius

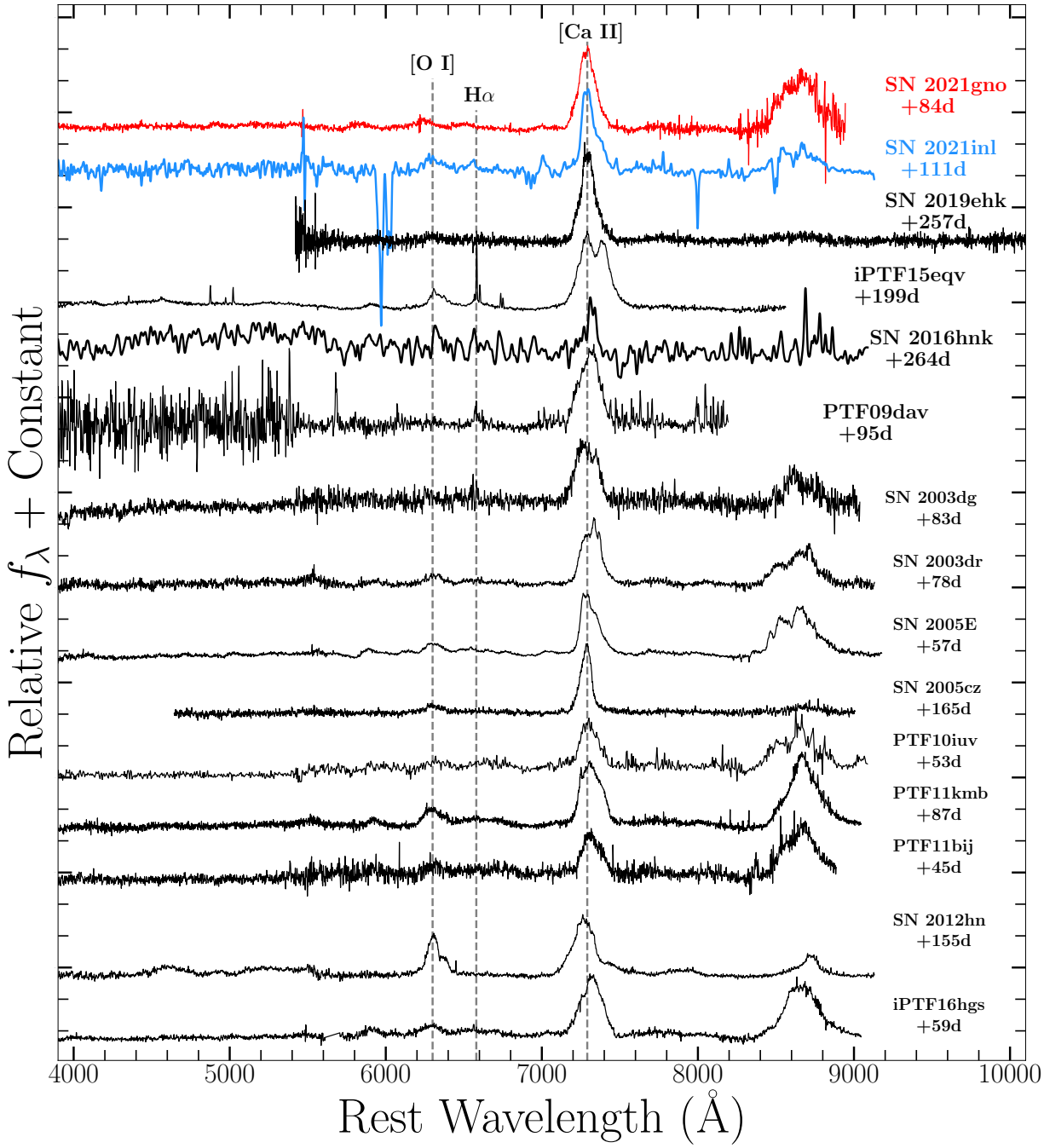

Figure 4.12 Nebular spectra of all confirmed CaSTs (Sullivan et al. 2011; Kasliwal et al. 2012; Foley 2015; Lunnan et al. 2017; Milisavljevic et al. 2017; Jacobson-Galán et al. 2020b,a). Nebular spectra of SN 2021gno at +84 days and SN 2021inl at +111 days, shown in red and blue, respectively, both spectra further establishing these objects as CaSTs. Prominent [O I] and [Ca II] lines as well as Hα marked by dashed grey lines.

$R_e \approx 27.5 - 385$ $R_\odot$ and shock velocity $v_e \approx (4.5 - 7.8) \times 10^4$ km s^{-1}. Furthermore, we find two best fitting times of explosions: 59292.3 MJD for Piro (2015); Piro et al. (2021) models and 59293.01 MJD for Sapir & Waxman (2017) models, both values being consistent with the model-independent estimate of $t_{\rm exp} = 59292.7 \pm 0.55$ MJD. Additionally, for SN 2021inl, we find best fitting SCE model parameters of $M_e \approx 0.02 - 1.61$ $M_\odot$, $R_e \approx 20.5 - 207$ $R_\odot$ and $v_e \approx (4.5 - 7.8) \times 10^4$ km s^{-1}; there is no change to the original explosion date estimate. Lastly, we caution against using the M_e derived from the blue supergiant SCE model by Sapir & Waxman (2017) to best understand the progenitor environments of these CaSTs given that the estimated envelope mass is larger than the ejecta mass in SN 2021inl and a significant fraction of the mass of SN 2021gno, both scenarios being unphysical in nature. We therefore conclude that the most physical range of best fitting extended masses for both objects are $M_e = (1.5 - 4.5) \times 10^{-2}$ $M_\odot$ for SN 2021gno and $M_e \approx 2.3 \times 10^{-2}$ $M_\odot$ for SN 2021inl; only the Piro (2015) model returned a mass that was not comparable in size, and consequently unphysical, to SN 2021inl's total ejecta mass.

In Figure 4.18, we attempt to compare the radius and mass of the extended material estimated from the SCE modeling of SNe 2021gno and 2021inl to other double-peaked events whose primary light curve peak was modeled in a similar fashion. As shown in the plot, the SCE parameter space of all five double-peaked CaSTs is highly consistent: on average, these objects can be modeled with SCE from extended material that has a compact radius of ∼50-120 $R_\odot$ and mass of ∼0.05-0.1 $M_\odot$. Compared to SCE model parameters presented in the literature, CaSTs show a similar extended mass to fast-rising events such as SN 2019dge (Yao et al. 2020) and SNe IIb (Wheeler et al. 1993; Arcavi et al. 2011, 2017a; Piro et al. 2017; Armstrong et al. 2021), the latter typically exhibiting larger extended radii, likely indicating a more massive progenitor star than what produces CaSTs. Furthermore, the SCE parameter space of CaSTs is unlike that of SNe Ic (De et al. 2018a; Ho et al. 2020; Gagliano et al. 2022) and super-luminous SNe (Smith et al. 2016), the former showing a much larger range of radii and smaller masses, while the latter is best fit by a much larger extended material mass and radius. However, we note that the parameters derived for all CaSTs presented were done using four separate SCE models (e.g., Piro 2015; Piro et al. 2021; Sapir & Waxman 2017, while other objects shown were only modeled with one of these formalisms. Therefore, direct comparison of the SCE parameters may not be completely accurate.

4.7.3 CSM Interaction Model

In addition to the SCE model, we explore interaction of the explosion's shock with a circumstellar medium as a mechanism to explain the primary light curve peaks of SNe 2021gno and 2021inl. We model the interaction as homologously expanding ejecta interacting with a detached CSM shell. In this picture, the CSM is sufficiently optically thick that the radiation becomes visible only after shock breakout from the outer edge of the CSM. The light curve is then powered by the resulting shock cooling emission of the swept up CSM and ejecta.

In this model, we assume a broken power-law ejecta with density profile $\rho_{\rm ej} \propto r^{-1}$ and $\rho_{\rm ej} \propto r^{-10}$ in the inner and outer ejecta, respectively; and assume the ejecta is expanding homologously with a kinetic energy of $E_{\rm sn}$. The CSM of mass $M_{\rm csm}$ extends from an inner radius $R_{\rm csm}$ with a width of $\Delta R_{\rm csm}$. The density profile follows a $\rho_{\rm csm} \propto r^{-2}$ profile out to $R_{\rm csm}+\Delta R_{\rm csm}$.

We run numerical simulations using the radiation hydrodynamics code Sedona (Kasen et al. 2006). The equations of radiation hydrodynamics are solved in one-dimensional spherical symmetry using implicit Monte Carlo radiative transfer (Roth & Kasen 2015) coupled to a moving mesh hydrodynamics code based off of Duffell (2016). We assume a grey electron scattering opacity of $\kappa_{\rm es} = 0.1$ cm^2 g^{-1} and an absorptive opacity of $\kappa_{\rm abs} = \epsilon\kappa_{\rm es}$, with $\epsilon = 10^{-3}$ to account for Compton thermalization. We assume $M_{\rm ej} = 0.3 - 0.6$ M$_\odot$ (i.e., $M_{\rm ej}$ for SN 2021gno and SN 2021inl, respectively) , $E_{\rm sn} = (1-2) \times 10^{50}$ erg s^{-1} (i.e., E_k for SN 2021gno and SN 2021inl, respectively), $M_{\rm csm} = 0.02$ M$_\odot$, $R_{\rm csm} = 10^{13}$ cm, $\Delta R_{\rm csm} = 10^{13}$ cm. These CSM properties are based on SCE model parameters (§4.7.2) and X-ray/radio observations (§4.8), and allow us to create a fiducial model for both comparison to observations as well as rough estimation of CSM properties in both objects.

These models are presented with respect to both object's bolometric luminosity during the early-time flux excess in Figure 4.17. As shown in the plot, both model light curves overestimate the total luminosity in the primary light curve peak for both SNe; this indicates that the CSM mass is likely lower than that used in the simulations i.e., $M_{\rm csm} \lesssim 0.02$ M$_\odot$. For reference, we also plot the CSM interaction model designed for SN 2019ehk's early-time excess ($M_{\rm csm} = 1.5 \times 10^{-3}$ M$_\odot$, $R_{\rm csm} = 10^{14}$ cm), which yields a better match to the light curve peak in SNe 2021gno and 2021inl. Furthermore, based on these model comparisons, the inferred CSM properties in SN 2021gno are consistent with the CSM mass independently inferred from X-ray modeling in §4.8.

4.8 CSM Constraints from X-ray/Radio Emission in SN 2021gno

SN 2021gno is the second CaST, after SN 2019ehk (WJG20a), to show luminous X-ray emission ($L_x \approx 5 \times 10^{41}$ erg s^{-1}) at very early-time phases ($\delta t \approx 1$ days), as shown in Figure 4.5(a). Given the consistency with a rapidly-decaying X-ray emission ($L_x \propto t^{-3}$) and the hard spectrum (§5.4.3), we suggest that, like SN 2019ehk, the X-ray luminosity observed in SN 2021gno is most likely derived from thermal bremsstrahlung emission from shocked CSM gas in adiabatic expansion. Emission measure goes as $EM = n^2 V$ and we can derive properties of the local CSM density in SN 2021gno by the following relation:

$$n = \left[(EM)(\mu_e \mu_I)(4\pi R^2 \Delta R f)^{-1}\right]^{1/2} \tag{4.3}$$

where μ_e, μ_I are the electron and ion molecular weights, respectively, R is the radius of the CSM, ΔR is the CSM thickness, and f is the filling factor (i.e., how homogeneous the shell

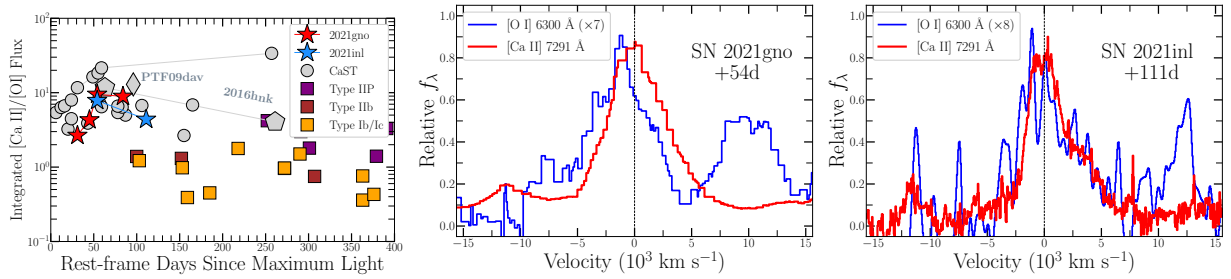

(a) (b) (c)

Figure 4.13 (a) Ratio of integrated [Ca II] and [O I] flux with respect to phase for SN 2021gno (red stars), SN 2021inl (blue stars), and current sample of CaSTs (gray circles, diamonds and polygons), and assorted types of core-collapse SNe. All CaSTs, including SNe 2021gno and 2021inl, show [Ca II]/[O I] > 2. [Ca II]/[O I] values for all Type II/Ibc objects from Milisavljevic et al. (2017). (b)/(c) Velocity profiles of [Ca II] $\lambda\lambda$ 7291,7324 (red) and scaled [O I] $\lambda\lambda$ 6300, 6364 (blue) in SN 2021gno at +54 days and SN 2021inl at +111 days post-explosion.

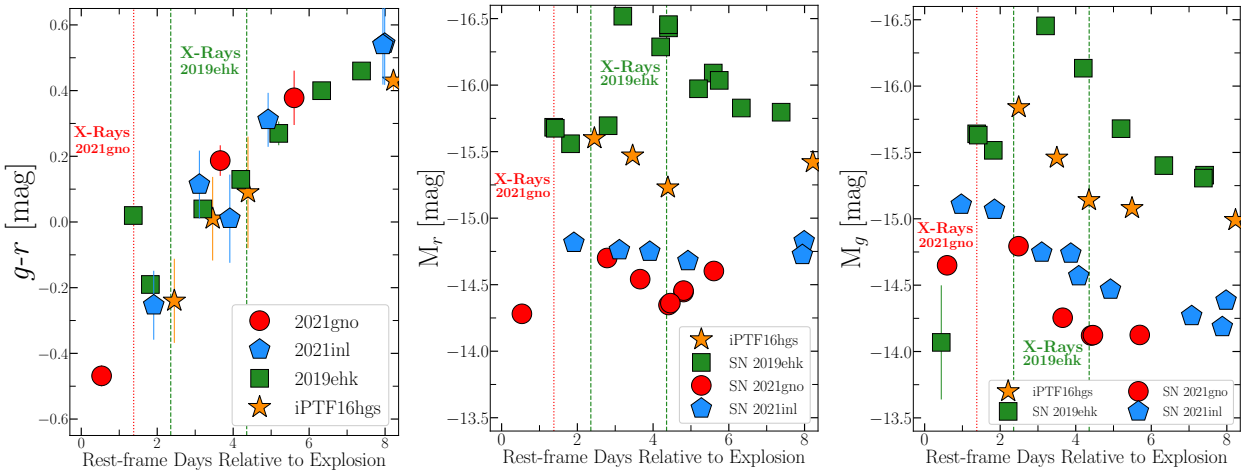

(a) (b) (c)

Figure 4.14 (a) g-r color comparison of SNe 2021gno (red circles), 2021inl (blue polygons), 2019ehk (green squares), and iPTF16hgs (orange stars) during the primary light curve peak. Phases of X-ray detections in SNe 2021gno and 2019ehk shown as dotted red and dashed green lines, respectively. (b)/(c) Absolute magnitude $r-$ and $g-$band (left and right) photometry of all four CaSTs during their primary light curve peak.

of CSM is around the progenitor). For the expression above, we use an emission measure of $EM = (1.8 \pm 0.7) \times 10^{64}$ cm^{-3}, filling factor $f = 1$, $\mu_e = \mu_I$ assuming H-rich CSM, and that the CSM thickness goes as $\Delta R \approx R$. Because the exact CSM extent is unknown, we calculate multiple possible particle densities based on different CSM geometries. For a shock travelling with speed $v_s = 0.1c$, the location of the blastwave at the time of X-ray emission ($\delta t \approx 1$ day) gives $R_{\rm CSM} = 3 \times 10^{14}$ cm and thus a particle density of $n = (9.4 \pm 1.9) \times 10^9$ cm^{-3}. Assuming a H-rich CSM composition, this yields a CSM density of $\rho_{\rm CSM} = (1.6 \pm 0.3) \times 10^{-14}$ g cm^{-3} and mass of $M_{\rm CSM} = (1.6 \pm 0.3) \times 10^{-3}$ M$_\odot$, assuming a spherical geometry. If the CSM radius is in fact comparable to the blackbody radius at $\delta t \approx 1$ day (e.g., $R_{\rm CSM} = 9 \times 10^{13}$ cm), as was done for the X-ray analysis of SN 2019ehk (WJG20a), we find a CSM density and mass of $\rho_{\rm CSM} = (7.4 \pm 1.5) \times 10^{-14}$ g cm^{-3} and $M_{\rm CSM} = (3.4 \pm 0.7) \times 10^{-4}$ M$_\odot$, respectively.

At larger distances from the progenitor, we interpret the radio upper limits discussed in §4.3.4 ($\delta t = 35 - 245$ days) in the context of synchrotron emission from electrons accelerated to relativistic speeds at the explosion's forward shock, as the SN shock expands into the medium. To derive parameters of the medium, we adopt the synchrotron self-absorption (SSA) formalism by Chevalier (1998) and we self-consistently account for free-free absorption (FFA) following Weiler et al. (2002) (however, see Terreran et al. (2022) and Jacobson-Galán et al. (2022a) for application and additional details on these derivations). For the calculation of the free-free optical depth $\tau_{\rm ff}(\nu)$, we adopt a wind-like density profile $\rho_{\rm csm} \propto r^{-2}$ in front of the shock, and we conservatively assume a gas temperature $T = 10^4$ K (higher gas temperatures would lead to tighter density constraints). The resulting SSA+FFA synchrotron spectral energy distribution depends on the radius of the emitting region, the magnetic field, the environment density and on the shock microphysical parameters ϵ_B and ϵ_e (i.e. the fraction of post-shock energy density in magnetic fields and relativistic electrons, respectively).

At the time of the latest radio non-detection in SN 2021gno, the shock will have probed distances of $r \approx 2 \times 10^{16}$ cm for $v_s = 10^4$ km s^{-1}; however this distance could vary based on the chosen shock speed. We find that, for typical microphysical parameters $\epsilon_B = 0.01$ and $\epsilon_e = 0.1$ (same as for CaST SN 2019ehk; WJG20a), the lack of radio emission indicates a low density medium that corresponds to a progenitor mass loss rate of $\dot{M} < 10^{-4}\,{\rm M}_\odot\,{\rm yr}^{-1}$, for an adopted wind speed of $v_w = 500$ km s^{-1}. This v_w value is the same as in SN 2019ehk, which had direct detections of CSM velocity based on shock-ionized emission lines in the early-time spectra (WJG20a). Overall, the mass loss limits of both SNe 2021gno and 2019ehk are consistent with one another, the latter being more constraining given the depth of the radio observations.

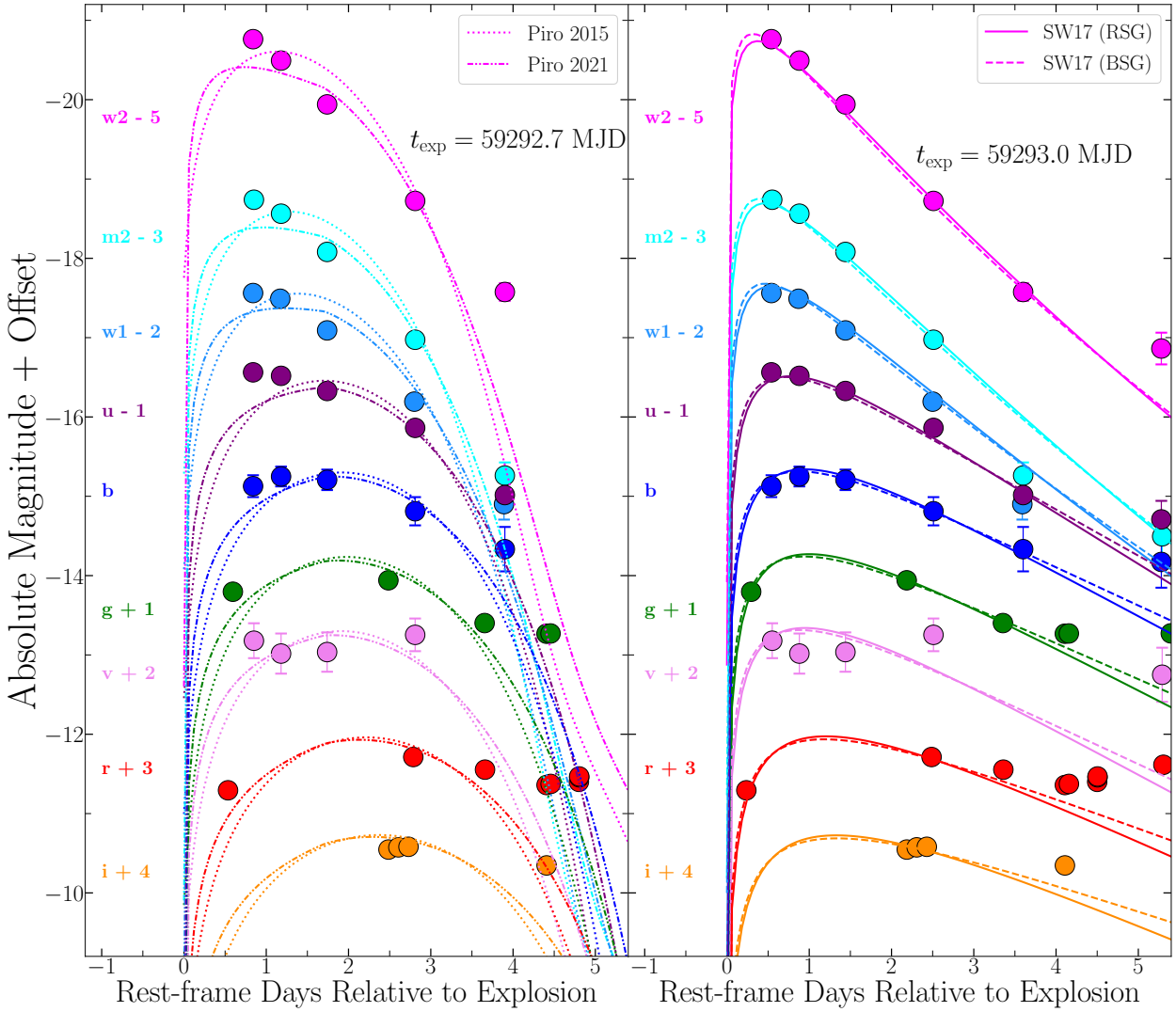

Figure 4.15 Multi-color shock cooling model fits to the first light curve peak in SN 2021gno assuming a blackbody SED. *Left:* Piro (2015) and Piro et al. (2021) models are presented as dotted and dot-dash lines, respectively. *Right:* Sapir & Waxman (2017) models shown as dashed (n=3) and solid (n=3/2) lines. Model specifics are discussed in §4.7.2 and physical parameters are presented in Table 4.12.

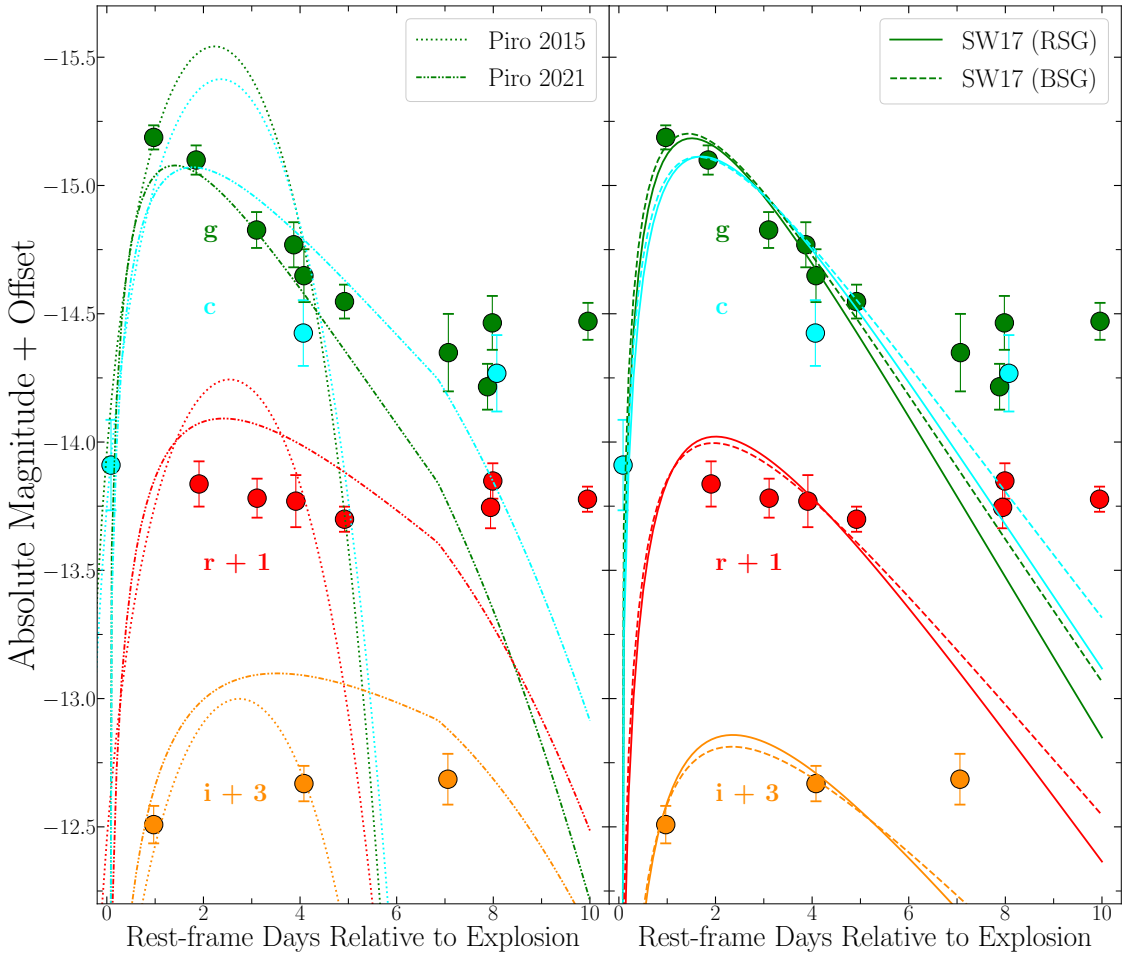

Figure 4.16 Multi-color shock cooling model fits to the first light curve peak in SN 2021inl assuming a blackbody SED. *Left:* Piro (2015) and Piro et al. (2021) models are presented as dotted and dot-dash lines, respectively. *Right:* Sapir & Waxman (2017) models shown as dashed (n=3) and solid (n=3/2) lines. Model specifics are discussed in §4.7.2 and physical parameters are presented in Table 4.12.

4.9 Discussion

4.9.1 A Physical Progenitor Model

The high-cadence, multi-wavelength follow-up of SNe 2021gno and 2021inl allows for some of the best constraints to be made on CaST progenitor systems to date. For SN 2021gno, modeling of the bolometric light curve has revealed that the explosion was low energy ($E_k \approx 1.3 \times 10^{50}$ erg), which produced $\sim$0.6 $M_\odot$ of ejecta and synthesized $\sim$0.012 $M_\odot$ of ^{56}Ni. Furthermore, the multi-band light curve revealed a flux excess above the radioactive decay powered continuum emission that lasted $\sim$ 5 days post-explosion. Modeling of this primary light curve peak (e.g., §4.7.2) suggests that the progenitor star could have had an extended envelope of material with radius $R_e = 30 - 230$ $R_\odot$ and mass $M_e = (1.5 - 4.5) \times 10^{-2}$ $M_\odot$. Additionally, modeling of the luminous X-ray emission detected in SN 2021gno at $\sim$1 day after explosion indicates that the progenitor system also contained a shell of CSM that extended to $R \approx (0.9 - 3) \times 10^{14}$ cm and was comprised of $\sim(0.3 - 1.6) \times 10^{-3}$ $M_\odot$ of H- and/or He-rich gas, if the CSM composition is similar to SN 2019ehk. In Figure 4.17, we show that this amount of CSM can also be the power-source behind the multi-band primary light curve peak; this material being ejected by the progenitor star in the final months before explosion for a possible wind velocity of $\sim$ 500 km s^{-1}. Lastly, radio non-detections at late-times suggest a relatively clean progenitor environment at distances of 10^{16-17} cm and a progenitor mass loss rate in the final year(s) before explosion of $\dot{M} < 10^{-4}\,M_\odot\,\mathrm{yr}^{-1}$.

The above information allows for decent constraints to be made on the potential progenitor star(s) responsible for SN 2021gno. One progenitor scenario is that SN 2021gno resulted from a low-mass, massive star ($\sim$8-11 $M_\odot$) that experienced enough enhanced mass loss prior to explosion to remove all stellar H-rich material as well as to place $\sim(1 - 4) \times 10^{-2}$ $M_\odot$ of extended material/envelope at distances $\lesssim$230 $R_\odot$ and/or $\sim(0.3 - 1.6) \times 10^{-3}$ $M_\odot$ CSM at $r \lesssim 3 \times 10^{14}$ cm. A massive star progenitor is also consistent with the location of SN 2021gno in the spiral arm of a star-forming host galaxy. However, increased mass loss in such a progenitor could only have taken place in the final months before explosion given the low mass loss rate of $\dot{M} < 10^{-4}\,M_\odot\,\mathrm{yr}^{-1}$ in the progenitor's final year(s). Compared to simulations, SN 2021gno's ejecta mass is consistent with the collapse of a $9 - 10$ $M_\odot$ progenitor (Wanajo et al. 2018), but the total synthesized Ni mass is, on average, an order of magnitude lower in these models. Similarly, from `BPASS` library (Eldridge et al. 2017), all massive star explosions occurring in binary systems in the lowest mass bins (e.g., 8-11 $M_\odot$) produce $>$ 1.5 $M_\odot$ of ejecta and synthesize a total ^{56}Ni mass that is inconsistent with SN 2021gno. Furthermore, while ultra-stripped SN (USSN) progenitor models (e.g., Yoshida et al. 2017; Moriya et al. 2017b) produce $M_{\rm ej} \lesssim 0.2$ $M_\odot$, they can reproduce the Ni yield observed in SN 2021gno, but it is unclear whether these progenitors can retain enough of a He-rich envelope to produce SCE as well as CSM capable of luminous X-ray emission via shock interaction. Lastly, a promising progenitor candidate is a He-star binary system capable of producing a type Ib-like explosion (e.g., see Yoon et al. 2017; Jung et al. 2021). Based on the models presented in Table A6 of WJG20a, the ejecta mass of SN 2021gno is consistent with a He-star with

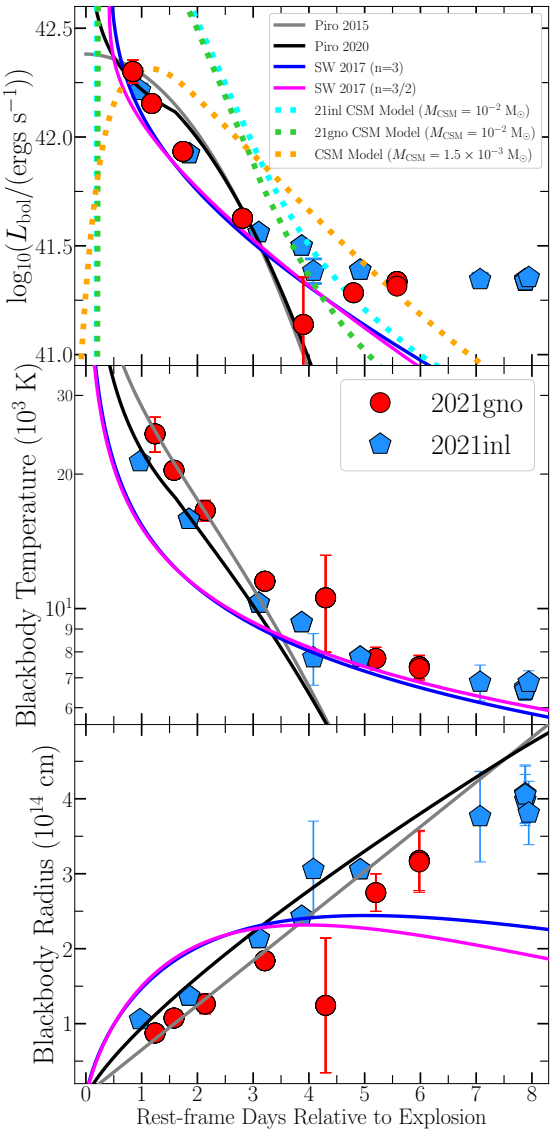

Figure 4.17 *Top:* Bolometric luminosity during the primary light curve peaks in SNe 2021gno and 2021inl. Shock interaction models plotted as orange/cyan/green dashed lines (see §4.7.3). Shock cooling models are plotted as solid lines: Piro (2015) in grey, Piro et al. (2021) in black, Sapir & Waxman (2017) n = 3/2[3] in pink[blue]. SCE model parameters: $M_e = 0.02 - 0.5$ M$_\odot$, $R_e = 40 - 230$ R$_\odot$, and $v_e = (7 - 9) \times 10^4$ km s^{-1}. *Middle:* Blackbody temperatures during the primary light curve peak. For the interaction model we show the effective blackbody temperature. *Bottom:* Blackbody radii during the primary light curve peak. The shock interaction model presents the radius of the emitting region.

artificial envelope removal (e.g., models #2, 4) and a He-star + NS binary (models #7,8), both ending in O core burning. However, all of these models would be ruled out if the X-ray emission is derived from H-rich CSM. Furthermore, it is difficult to reconcile a massive star progenitor with the non-detection of a star forming region at the SN 2021gno explosion site (§5.5) and a SFR of $< 3.4 \times 10^{-5}$ $M_\odot$ yr^{-1}, under the assumption of on-going star formation. Given these constraints on a massive star progenitor for SN 2021gno, it may be the case that a WD system is better suited to reproduce the SN observables, as discussed below for SN 2021inl.

In terms of constraining the progenitor of SN 2021inl, the large offset of the SN from an early-type elliptical galaxy makes a massive star progenitor system very unlikely. Consequently, a more plausible scenario is one that involves the explosion of a WD in a binary system. However, such an explosion needs to produce $\sim$0.3 $M_\odot$ of ejecta and $\sim$0.012 $M_\odot$ of ^{56}Ni, as well as allow for either SCE from a confined ($\sim$20-150 $R_\odot$) and low mass ($\sim$0.02 $M_\odot$) extended envelope and/or $\lesssim 10^{-3}$ $M_\odot$ of CSM. While such a SN is unable to be formed by typical SN Ia explosion channels, the formation of a confined, extended envelope can occur during the ejection of material in "tidal tails" that then "settles" around the primary WD prior to merger (Raskin & Kasen 2013; Shen et al. 2012; Schwab et al. 2016).

We explore the possibility that SN 2021inl resulted from a double degenerate system containing a hybrid and a CO WD, which was initially presented by WJG20a to explain SN 2019ehk. In this scenario, the tidal disruption of the hybrid HeCO WD by lower-mass CO WD (or another hybrid WD) can induce a He-detonation that can lead to CaST-like transient (Bobrick et al. 2017; Perets et al. 2019; Zenati et al. 2019b,a). Furthermore, prior to the disruption, significant mass transfer ($\dot{M} \approx 10^{-2}\,M_\odot\,\mathrm{yr}^{-1}$) will place CSM in the local environment, capable of powering the initial light curve peak observed in SN 2021inl. We note that such a system could also reproduce the observables in SN 2021gno such as $M_{\rm ej}$ and $M(^{56}\mathrm{Ni})$ (e.g., see Table A4 of Jacobson-Galán et al. 2021), as well as X-ray emission from CSM interaction and the lack of detectable star formation at the explosion site. In Figure 4.19, we show the density profiles in the pre-explosion environments of SNe 2019ehk, 2021gno, 2021inl, and iPTF16hgs derived from SCE models as well as X-ray and radio modeling for SNe 2019ehk and 2021gno specifically. We show that the pre-explosion environments are consistent with the CSM density profiles of WD disruption models discussed above, further indicating that this scenario may be a plausible model to explain these CaSTs.

4.9.2 SNe 2021gno and 2021inl in the "Calcium-strong" Class

Based on the observational properties of both SNe 2021gno and 2021inl, it is evident that these objects fit within the confines of the CaST observational class. As discussed in §8.4.1, both SNe display low luminosity ($M_{\rm r,peak} \approx -15$ mag) and rapidly evolving ($t_r \approx 8-15$ days) light curves whose color evolution is consistent with other confirmed CaSTs (e.g., Fig. 8.5). Furthermore, the spectroscopic evolution of SNe 2021gno and 2021inl also solidifies their place in this observational class: both objects showing type I spectra near peak, which quickly transitions to an optically thin regime where all nebular emission is dominated by

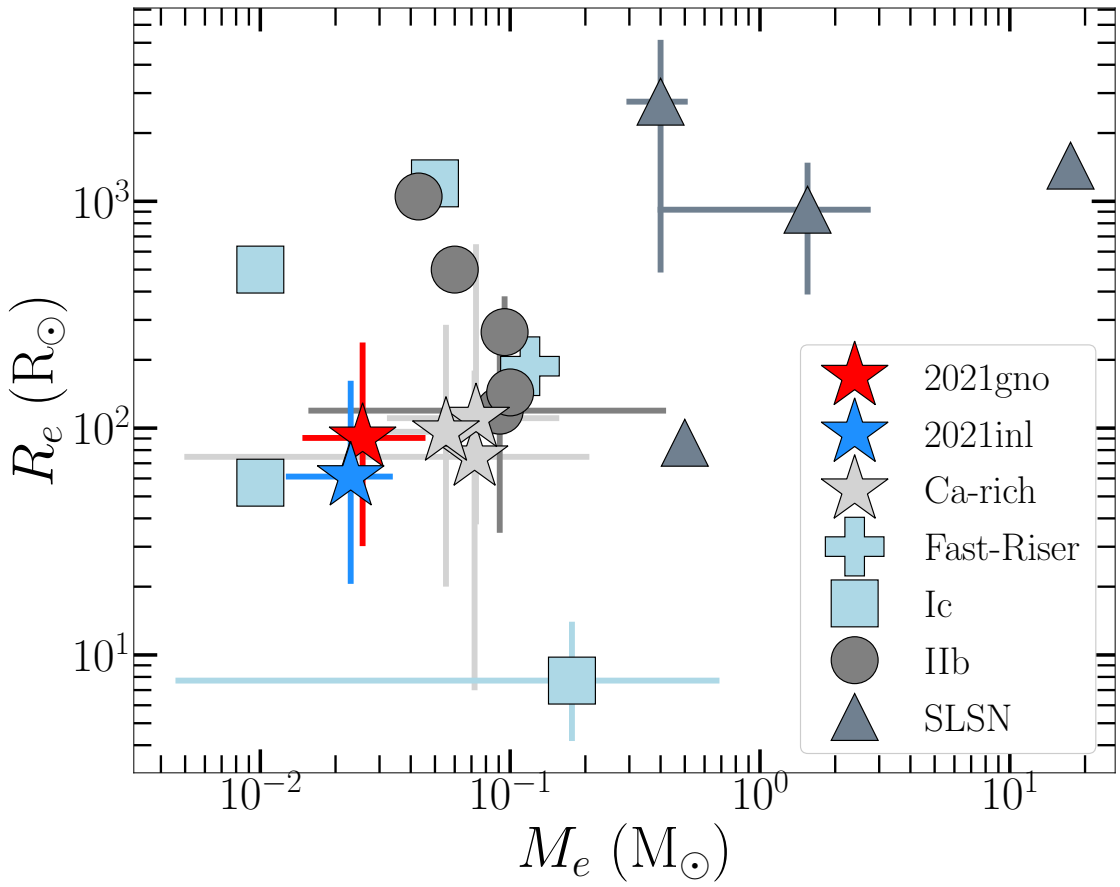

Figure 4.18 Radius versus mass of extended material derived from light curve modeling with shock cooling emission models (e.g., see §4.7.2 for discussion of representative sample). Double-peaked CaSTs shown as stars (2021gno in red, 2021inl in blue), fast-rising transients as blue plus signs, SNe Ic as blue squares, SNe IIb as grey circles, and super-luminous SNe as grey triangles. Note that not all of these double-peaked SN light curves were fit with exactly the same SCE models.

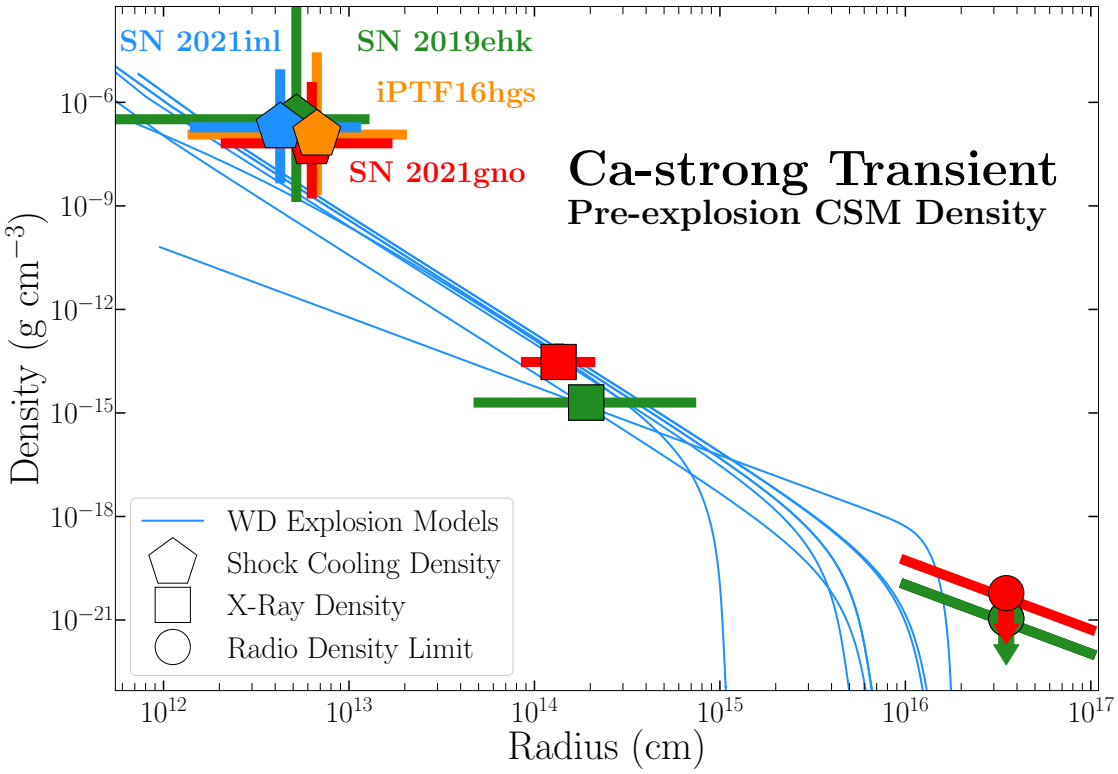

Figure 4.19 Density profile of the explosion environment of CaSTs 2021gno (red), 2021inl (blue), 2019ehk (green), and iPTF16hgs (orange). Densities plotted as polygons are derived from shock cooling modeling. Shown as red and green squares are density limits derived from X-ray detections in SNe 2021gno and 2019ehk, respectively. The red and green circles are the density limit derived from modeling of the radio non-detections in SNe 2021gno and 2019ehk (WJG20a), respectively. Blue lines are CSM models for WD mergers at the time of explosion (see §4.9.1)

[Ca II] emission and weak [O I] (e.g., [Ca II]/[O I] $>$ 2; Fig. 4.13).

Nonetheless, these SNe do appear to deviate from normative CaST characteristics based on their double-peaked light curves and pre-explosion environments. With regards to the former, SNe 2021gno and 2021inl now represent the 4th and 5th confirmed CaSTs with an early-time flux excess, the other events being iPTF16hgs, SN 2018lqo, and SN 2019ehk. The observation of this primary light curve peak confirms the presence of an extended stellar envelope capable of producing SCE and/or a dense CSM that powers the initial flux excess through SN shock interaction in at least some CaST progenitor systems. Of the 9 CaSTs discovered $<$3 days after explosion and with $<$2 day photometric cadence, 5 (55%) show a clear early-time flux excess: iPTF16hgs, SNe 2018lqo, 2019ehk, 2021gno and 2021inl. However, it is possible that 100% of these objects show this signature given the marginal detections of a very early-time flux excess in the remaining sub-sample objects PTF11kmb,

PTF12bho, SN 2018kyj and SN 2019hty, indicating that this feature is potentially ubiquitous to CaSTs.

In terms of their progenitor environments, both SNe exist in visibly different host galaxies, the large projected offset of SN 2021inl from its early-type host galaxy being most similar to the environments of many other CaSTs (Perets et al. 2010a, 2011; Kasliwal et al. 2012; Lyman et al. 2013b, 2014; Perets 2014b; Foley 2015; Lunnan et al. 2017; De et al. 2020; Perets & Beniamini 2021). Additionally, despite the fact that SN 2021gno exploded in a star-forming, late-type galaxy, there is no evidence for star formation at the explosion site (similar to SN 2019ehk), which makes this event quite similar to other CaSTs in spite of the visibly different host galaxy type. However, a number of CaSTs have been discovered in spiral host galaxies with explosion site star formation (e.g., iPTF15eqv, iPTF16hgs, SN 2016hnk; Milisavljevic et al. 2017; De et al. 2018b; Galbany et al. 2019), as well as in, or offset from, disk galaxies (e.g., PTF09dav, SN 2001co, SN 2003H, SN 2003dr, SN 2003dg; Sullivan et al. 2011; Kasliwal et al. 2012; Perets 2014a; Foley 2015). This spread in CaST host environments continues to indicate that the progenitor systems responsible for these transients are likely heterogeneous, some arising from certain types of massive stars and others coming from the explosion of compact stars such as WDs.

Lastly, SN 2021gno is now the second confirmed CaST to be detected in X-rays, a novel observational probe for this explosion class. The X-ray emission in SN 2021gno was detected earlier than SN 2019ehk (WJG20a), in addition to being more luminous, but was nonetheless consistent with a rapid decline rate of $L_x \approx t^{-3}$. Now that this behavior has been confirmed in more than one CaST, it is more likely that X-ray emission from shock interaction in a dense, confined shell of CSM is a trait that could be more common to the CaST class as a whole. However, detecting future CaSTs at X-ray wavelengths requires the discovery of future objects at $D \lesssim 40$ Mpc and the follow-up of these transients with X-ray telescopes in the first $\sim$day after explosion. Given that X-rays were detected in both SNe 2019ehk and 2021gno, the only two CaSTs where *Swift*-XRT was re-pointed at very early phases ($\delta t < 4$ days), it is highly likely that X-ray emission is present in all double-peaked, and possibly all single-peaked, CaSTs directly after explosion.

4.10 Conclusions

In this paper, we have presented multi-wavelength observations of two new CaSTs, SNe 2021gno and 2021inl. Despite their unique double-peaked light curves, both objects are photometrically and spectroscopically consistent with prototypical CaSTs throughout their evolution, which solidifies their place in this explosion class. Below we list the primary findings that make SNe 2021gno and 2021inl significant and novel additions to our understanding of these peculiar explosions:

- SN 2021gno was first detected within 0.5 days of explosion and is located on the outer edge of the star-forming spiral host galaxy NGC 4165. SN 2021inl was first detected

within 0.1 days of explosion and is located at a large offset from early-type host galaxy NGC 4923.

- Based on their fast light curve evolution ($t_r \lesssim 15$ days), low overall luminosities ($M_{\rm g,peak} > -15$ mag), and dominant [Ca II] emission lines (e.g., [Ca II]/[O I] ≈ 10), both SNe can be confidently classified as CaSTs. Furthermore, the ratio of ion masses derived for both SNe in §4.6.2 (e.g., $M({\rm O}) > M({\rm Ca})$) continues to indicate that these explosions are not "rich" in Ca abundance but rather are "rich" in Ca emission i.e., "Calcium-strong."

- Despite visibly different host galaxies, modeling of the host spectra reveals that the explosion sites of both SNe had very little ($\lesssim 10^{-5}$ M$_\odot$ yr^{-1}) or no recent star formation, which strongly suggests that neither SN came from a massive star progenitor.

- SN 2021gno is the second CaST with confirmed, luminous X-ray emission ($L_x \approx 5 \times 10^{41}$ erg s^{-1}) as detected by *Swift*-XRT at $\delta t \approx 0.8$ days post-explosion. Based on the rapid fading and modeling of the X-ray spectrum, we conclude that this emission was derived from shocked CSM gas comprised of $M_{\rm CSM} = (0.3-1.6) \times 10^{-3}$ M$_\odot$ of shocked gas that extended to distances $R = (0.9-3) \times 10^{14}$ cm, possibly comprised of H- and/or He-rich material. At larger distances from the progenitor star (e.g., $\sim 10^{16-17}$ cm), modeling of SN 2021gno radio observations indicates a progenitor mass loss rate of $\dot{M} < 10^{-4}\,{\rm M}_\odot\,{\rm yr}^{-1}$ ($v_w = 500$ km s^{-1}) in the final year(s) before explosion.

- SNe 2021gno and 2021inl are the fourth and fifth CaSTs with multi-color, double-peaked light curves. We model the initial flux excess using four analytic formalisms for shock cooling emission from extended material to derive best fit parameters of this material (§4.7.2). For SN 2021gno, we find that a radius and mass of extended material ranging from $R_e \approx 30 - 230$ R$_\odot$ and $M_e \approx 0.02 - 0.05$ M$_\odot$, respectively, can reproduce the early-time emission. Similarly, for SN 2021inl, we derive radius and mass of extended material of $R_e \approx 20 - 150$ R$_\odot$ and $M_e \approx 0.02$ M$_\odot$, respectively.

- Given the direct evidence for CSM interaction in SN 2021gno, we also model the primary light curve peak in both SNe with numerical models for shock interaction with confined CSM (§4.7.3). We find that the observed flux excess in SN 2021gno can be fit with $R_{\rm CSM} = 10^{13-14}$ cm and $M_{\rm CSM} \lesssim 10^{-2}$ M$_\odot$, both properties being consistent with X-ray modeling. For SN 2021inl, we find a similar best fit CSM radius and mass.

- Using a combination of shock cooling, shock interaction, X-ray, and radio modeling, as well as host galaxy SFR, we are able to place some of the tightest constraints to date on the density profile of the local CaST progenitor environment (Fig. 4.19). For both SNe 2021gno and 2021inl, as well as other double-peaked CaSTs SN 2019ehk and iPTF16hgs, the progenitor CSM density is consistent with models for the merger of low-mass, hybrid WDs. For SNe 2019ehk, 2021gno and 2021inl specifically, this

is supported by the lack of host galaxy star formation at the explosion sites of these events.

Future multi-wavelength (X-ray to radio) observations of double-peaked CaSTs at very early-time phases will be instrumental in filling out the progenitor environment phase space and constraining the progenitor channel of these peculiar explosions. Multi-color transient surveys with higher limiting magnitudes (> 21 mag) such as YSE currently and LSST in the future will greatly increase the number of CaSTs discovered within a day of explosion.

4.11 Acknowledgements

Research at UC Berkeley is conducted on the territory of Huichin, the ancestral and unceded land of the Chochenyo speaking Ohlone people, the successors of the sovereign Verona Band of Alameda County. Keck I/II, ATLAS, and PS1 observations were conducted on the stolen land of the kānaka ʻōiwi people. We stand in solidarity with the Pu'uhonua o Pu'uhuluhulu Maunakea in their effort to preserve these sacred spaces for native Hawai‘ians. MMT observations were conducted on the stolen land of the Tohono O'odham and Hia-Ced O'odham nations; the Ak-Chin Indian Community, and Hohokam people. ZTF observations were conducted on the stolen land of the Pauma and Cupeño tribes; the Kumeyaay Nation and the Payómkawichum (Luiseño) people. Shane 3-m observations were conducted on the stolen land of the Ohlone (Costanoans), Tamyen and Muwekma Ohlone tribes.

The Young Supernova Experiment and its research infrastructure is supported by the European Research Council under the European Union's Horizon 2020 research and innovation programme (ERC Grant Agreement No. 101002652, PI K. Mandel), the Heising-Simons Foundation (2018-0913, PI R. Foley; 2018-0911, PI R. Margutti), NASA (NNG17PX03C, PI R. Foley), NSF (AST-1720756, AST-1815935, PI R. Foley; AST-1909796, AST-1944985, PI R. Margutti), the David & Lucille Packard Foundation (PI R. Foley), VILLUM FONDEN (project number 16599, PI J. Hjorth), and the Center for AstroPhysical Surveys (CAPS) at the National Center for Supercomputing Applications (NCSA) and the University of Illinois Urbana-Champaign.

W.J-G is supported by the National Science Foundation Graduate Research Fellowship Program under Grant No. DGE-1842165. W.J-G acknowledges support through NASA grants in support of *Hubble Space Telescope* program GO-16075 and 16500. This research was supported in part by the National Science Foundation under Grant No. NSF PHY-1748958. R.M. acknowledges support by the National Science Foundation under Award No. AST-1909796 and AST-1944985. R.M. is a CIFAR Azrieli Global Scholar in the Gravity & the Extreme Universe Program, 2019. The Margutti's team at Northwestern and UC Berkeley is partially funded by the Heising-Simons Foundation under grant # 2018-0911 and #2021-3248 (PI: Margutti).

V.A.V acknowledges support by the National Science Foundation under Award No.AST-2108676. C. R. A. was supported by grants from VILLUM FONDEN (project numbers 16599 and 25501). Parts of this research were supported by the Australian Research Council

Centre of Excellence for All Sky Astrophysics in 3 Dimensions (ASTRO 3D), through project number CE170100013.

The UCSC team is supported in part by NASA grant 80NSSC20K0953, NSF grant AST–1815935, the Gordon & Betty Moore Foundation, the Heising-Simons Foundation, and by a fellowship from the David and Lucile Packard Foundation to R.J.F.

Some of the data presented herein were obtained at the W. M. Keck Observatory, which is operated as a scientific partnership among the California Institute of Technology, the University of California, and NASA. The Observatory was made possible by the generous financial support of the W. M. Keck Foundation. The authors wish to recognize and acknowledge the very significant cultural role and reverence that the summit of Maunakea has always had within the indigenous Hawaiian community. We are most fortunate to have the opportunity to conduct observations from this mountain.

A major upgrade of the Kast spectrograph on the Shane 3 m telescope at Lick Observatory was made possible through generous gifts from the Heising-Simons Foundation as well as William and Marina Kast. Research at Lick Observatory is partially supported by a generous gift from Google.

Based in part on observations obtained with the Samuel Oschin 48-inch Telescope at the Palomar Observatory as part of the Zwicky Transient Facility project. ZTF is supported by the NSF under grant AST-1440341 and a collaboration including Caltech, IPAC, the Weizmann Institute for Science, the Oskar Klein Center at Stockholm University, the University of Maryland, the University of Washington, Deutsches Elektronen-Synchrotron and Humboldt University, Los Alamos National Laboratories, the TANGO Consortium of Taiwan, the University of Wisconsin at Milwaukee, and the Lawrence Berkeley National Laboratory. Operations are conducted by the Caltech Optical Observatories (COO), the Infrared Processing and Analysis Center (IPAC), and the University of Washington (UW).

The Pan-STARRS1 Surveys (PS1) and the PS1 public science archive have been made possible through contributions by the Institute for Astronomy, the University of Hawaii, the Pan-STARRS Project Office, the Max-Planck Society and its participating institutes, the Max Planck Institute for Astronomy, Heidelberg and the Max Planck Institute for Extraterrestrial Physics, Garching, The Johns Hopkins University, Durham University, the University of Edinburgh, the Queen's University Belfast, the Harvard-Smithsonian Center for Astrophysics, the Las Cumbres Observatory Global Telescope Network Incorporated, the National Central University of Taiwan, STScI, NASA under grant NNX08AR22G issued through the Planetary Science Division of the NASA Science Mission Directorate, NSF grant AST-1238877, the University of Maryland, Eotvos Lorand University (ELTE), the Los Alamos National Laboratory, and the Gordon and Betty Moore Foundation.

IRAF is distributed by NOAO, which is operated by AURA, Inc., under cooperative agreement with the National Science Foundation (NSF).

4.12 Appendix

The complete photometry and spectroscopy dataset can found in Jacobson-Galán et al. (2022b).

Table A1. X-ray Observations of SN 2021gno

MJDs	Phase[a] (days)	Photon Index (Γ)	0.3-10 keV Unabsorbed Flux (10^{-12} erg s^{-1} cm^{-2})	Instrument
59293.51, 59293.84	0.81 – 1.14	$0.74^{+0.50}_{-0.52}$	$4.1^{+2.2}_{-2.1}$	*Swift*-XRT
59294.36 - 59296.23	1.66 – 3.53	–	< 1.6[b]	*Swift*-XRT
59298.28 - 59308.71	5.58 – 16.01	–	< 4.2	*Swift*-XRT
59313.30 - 59524.21	20.6 – 231.51	–	< 7.3	*Swift*-XRT

[a]Relative to explosion (MJD 59292.7).

[b]Flux calibration performed assuming same spectral parameters inferred at $t = +1.21 - 1.54$ d.

Table A2. Optical Spectroscopy of SN 2021gno

UT Date	MJD	Phase[a] (days)	Telescope	Instrument	Wavelength Range (Å)
2021-03-22	59295	+2.3	NOT	ALFOSC	3600–9000
2021-03-22	59295	+2.3	Shane	Kast	3300–10200
2021-03-30	59303	+10.3	ANU 2.3m	WiFES	3800–7000
2021-04-01	59305	+12.4	Liverpool Telescope	SPRAT	3800–8000
2021-04-02	59306	+13.3	NOT	ALFOSC	3600–9000
2021-04-06	59310	+17.3	Shane	Kast	3300–10200
2021-04-10	59314	+21.3	IRTF	SpeX	7000–25000
2021-04-13	59317	+24.3	Shane	Kast	3300–10200
2021-04-19	59323	+30.3	Shane	Kast	3300–10200
2021-05-03	59337	+44.3	Shane	Kast	3300–10200
2021-05-12	59346	+53.3	Keck	LRIS	3000–10000
2021-04-09	59376	+83.3	MMT	Binospec	3800–9200

[a]Relative to explosion (MJD 59292.7)

Table A3. Optical Spectroscopy of SN 2021inl

UT Date	MJD	Phase[a] (days)	Telescope	Instrument	Wavelength Range (Å)
2021-04-13	59317	+7.7	Shane	Kast	3300–10200
2021-04-19	59323	+13.7	Shane	Kast	3300–10200
2021-05-12	59346	+36.7	Keck	LRIS	3000–10000
2021-07-08	59403	+93.7	Keck	LRIS	3000–10000

[a]Relative to explosion (MJD 59309.4)

Table A4. VLA radio observations of SN 2021gno

Start Date (UT)	Time[a] (days)	Frequency (GHz)	Bandwidth (GHz)	Flux Density[b] (μJy/beam)
2021-04-21	35	15.5	5	≤ 258
2021-04-25	39	15.5	5	≤ 276
2021-11-19	245	15.5	5	≤ 285

[a]Relative to explosion (MJD 59292.7)

[b]Upper-limits are quoted at 3σ.

Table A5. Explosion Parameters

SN	Peak[a]Luminosity (erg s^{-1})	M_{ej} ($M_\odot$)	E_k (erg)	$M(^{56}Ni)$ ($M_\odot$)	v_{ph} (km s^{-1})
2021gno	$(4.12 \pm 1.57) \times 10^{41}$	0.60 ± 0.01	$(1.3 \pm 0.2) \times 10^{50}$	$(1.20 \pm 0.02) \times 10^{-2}$	6000
2021inl	$(2.37 \pm 0.05) \times 10^{41}$	0.29 ± 0.01	$(9.6 \pm 0.4) \times 10^{49}$	$(6.90 \pm 0.06) \times 10^{-3}$	7500
2019ehk[b]	$(9.81 \pm 0.15) \times 10^{41}$	0.72 ± 0.04	$(1.8 \pm 0.1) \times 10^{50}$	$(3.1 \pm 0.11) \times 10^{-2}$	6500
iPTF16hgs[c]	$\sim 3 \times 10^{41}$	0.38	2.3×10^{50}	8.0×10^{-3}	10000
Ca-Ib/c[d]	–	0.1-0.4	–	1.5×10^{-2}	$(6 - 10) \times 10^4$

[a]Second, radioactive decay powered light curve peak.

[b]Jacobson-Galán et al. (2020b)

[c]De et al. (2018b)

[d]De et al. (2021)

Table A6. Shock Cooling Models

Model	SN	Phase Range days	R_e $R_\odot$	M_e $[\times 10^{-2}]$ $M_\odot$	v_e $[\times 10^3]$ km s^{-1}	$t_{\rm off}$ days	χ^2_ν
Piro (2015)	2021gno	$t < 5$	$62.0^{+0.70}_{-0.69}$	$1.72^{+0.015}_{-0.013}$	6.6 ± 0.40	$0.001^{+0.002}_{-0.001}$	105
Piro et al. (2021)	2021gno	$t < 5$	$231.5^{+7.8}_{-8.2}$	$1.51^{+0.03}_{-0.03}$	$6.19^{+0.06}_{-+0.05}$	$0.01^{+0.001}_{-0.001}$	51.3
Sapir & Waxman (2017) [n=3/2]	2021gno	$t < 5$	$31.1^{+1.12}_{-1.10}$	$4.47^{0.10}_{-0.010}$	$7.07^{+0.14}_{-0.14}$	$0.28^{+0.010}_{-0.010}$	10.8
Sapir & Waxman (2017) [n=3]	2021gno	$t < 5$	$37.4^{+1.39}_{-1.25}$	$50.4^{+1.30}_{-1.26}$	$8.57^{+0.19}_{-0.19}$	$0.31^{+0.0091}_{-0.01}$	10.2
Piro (2015)	2021inl	$t < 6$	$156.8^{+6.93}_{-6.1}$	$2.29^{+0.10}_{-0.10}$	5.2 ± 0.20	$0.01^{+0.002}_{-0.001}$	40.1
Piro et al. (2021)	2021inl	$t < 6$	$21.2^{+1.71}_{-1.50}$	$37.1^{+24.7}_{-12.6}$	$9.46^{+0.63}_{-0.67}$	$0.003^{+0.004}_{-0.002}$	7.91
Sapir & Waxman (2017) [n=3/2]	2021inl	$t < 6$	$24.7^{+5.34}_{-4.03}$	$18.7^{+4.20}_{-3.50}$	$5.26^{+0.23}_{-0.23}$	$0.003^{+0.003}_{-0.002}$	5.57
Sapir & Waxman (2017) [n=3]	2021inl	$t < 6$	$42.7^{+7.13}_{-4.83}$	$170^{+19.5}_{-27.3}$	$5.15^{+0.23}_{-0.25}$	$0.004^{+0.004}_{-0.002}$	3.71

Chapter 5

Precursor Emission, Envelope Inflation, and Enhanced Mass loss Preceding the Luminous Type II Supernova 2020tlf

This chapter was previously published as Jacobson-Galán et al., 2022a, ApJ, 924, 15

5.1 Abstract

We present panchromatic observations and modeling of supernova (SN) 2020tlf, the first normal Type II-P/L SN with confirmed precursor emission, as detected by the Young Supernova Experiment (YSE) transient survey. Pre-SN activity was detected in $riz-$bands at -130 days and persisted at relatively constant flux until first light. Soon after discovery, "flash" spectroscopy of SN 2020tlf revealed narrow, symmetric emission lines that resulted from the photo-ionization of circumstellar material (CSM) shedded in progenitor mass loss episodes before explosion. Surprisingly, this novel display of pre-SN emission and associated mass loss occurred in a RSG progenitor with ZAMS mass of only 10-12 $M_{\odot}$, as inferred from nebular spectra. Modeling of the light curve and multi-epoch spectra with the non-LTE radiative transfer code CMFGEN and radiation-hydrodynamical code HERACLES suggests a dense CSM limited to $r \approx 10^{15}$ cm, and mass loss rate of 10^{-2} $M_{\odot}$ yr^{-1}. The luminous light-curve plateau and persistent blue excess indicates an extended progenitor, compatible with a RSG model with $R_{\star} = 1100$ $R_{\odot}$. Limits on the shock-powered X-ray and radio luminosity are consistent with model conclusions and suggest a CSM density of $\rho < 2 \times 10^{-16}$ g cm^{-3} for distances from the progenitor star of $r \approx 5 \times 10^{15}$ cm, as well as a mass loss rate of $\dot{M} < 1.3 \times 10^{-5}\, M_{\odot}\, yr^{-1}$ at larger distances. A promising power source for the observed precursor emission is the ejection of stellar material following energy disposition into the stellar envelope as a result of gravity waves emitted during either neon/oxygen burning or a

nuclear flash from silicon combustion.

5.2 Introduction

The behavior of massive stars in their final years of evolution is almost entirely unconstrained. However, we can probe these terminal phases of stellar evolution prior to the core-collapse of massive stars >8 $M_\odot$ by understanding the composition and origin of the high-density, circumstellar material (CSM) surrounding these stars at the time of explosion (Smith 2014). This CSM can be comprised of primordial stellar material or elements synthesized during different stages of nuclear burning, and is enriched as the progenitor star loses mass via wind and violent outbursts (Smith 2014 and references therein).

Early-time optical observations of young ($t < 10$ days since shock breakout; SBO) Type II supernovae (SNe II) is one such probe of the final stages of stellar evolution. In the era of all-sky transient surveys, rapid ("flash") spectroscopic observations have become a powerful tool in understanding the very nearby circumstellar environment of pre-SN progenitor systems in the final days to months before explosion (e.g., Gal-Yam et al. 2014; Groh 2014; Khazov et al. 2016; Bruch et al. 2021b). Obtaining spectra of young SNe II in the hours to days following shock breakout allows us to identify prominent emission lines in very early-time SN spectra that result from the recombination of unshocked, photo-ionized CSM. However, because the recombination timescale of ionized H-rich CSM is inversely related to the number density of free electrons $t_{\rm rec} \propto n_e^{-1}$ (Osterbrock & Ferland 2006), "flash" ionization from radiation associated with SBO is not responsible for the persistence of these narrow ($v_w \lesssim 500$ km s^{-1}), CSM-derived spectral features at $\gtrsim 1$ day after explosion (e.g., $t_{\rm rec} \leq$ a few hours for H-rich gas with $T \approx 10^5 - 10^6$ K and $n_e \geq 10^8$ cm^{-3}). The conversion of shock kinetic energy into high-energy radiation as it advances into the CSM provides a persistent source of ionizing photons that keep the CSM ionized for significantly longer timescales (e.g., $>> t_{\rm rec}$). The prominent, rapidly fading emission lines in the photo-ionization spectra of young SNe II are direct evidence of dense and confined CSM surrounding the progenitor star, comprised of elements ejected during episodes of enhanced mass loss days-to-months before explosion. The strength/brightness of these features is derived from the CSM density and chemical abundances at the time of explosion. This is a direct tracer of the progenitor's chemical composition (CNO abundances specifically) and recent mass loss at small distances $r < 10^{15}$ cm, as well as an indirect probe of progenitor identity.

Combining early-time spectroscopy with non-Local Thermal Equilibrium (non-LTE) radiative transfer modeling codes such as `CMFGEN` (Hillier & Miller 1998) have been a successful tool in constraining the progenitor systems responsible for a growing number of supernovae that undergo a relatively flat (Type II-P) or linear (Type II-L) fading during the photospheric phase in their optical light curve evolution. The latter may be the result of massive star progenitors that have lost more of their H-rich envelope in episodes of enhanced mass loss (Hillier & Dessart 2019). For such objects, radiative transfer modeling indicates that a dense ($\dot{M} = 10^{-4} - 10^{-2}$ $M_\odot$ yr^{-1}; $v_w \sim 100 - 200$ km s^{-1}) and compact ($r \lesssim 10^{15}$ cm) CSM

is present in order to produce the observed spectral profiles of high-ionization species such as He II, N III, C III/IV, or O IV/V in the early-time SNe II spectra (Shivvers et al. 2015; Terreran et al. 2016; Dessart et al. 2016, 2017; Yaron et al. 2017; Boian & Groh 2020; Tartaglia et al. 2021; Terreran et al. 2022). However, mass loss rates derived from SN spectral modeling are much larger than the generally inferred steady-state mass loss rates (e.g., $\lesssim 10^{-6}$ $M_\odot$ yr^{-1}; Beasor et al. 2020) observed in galactic, quiescent Red Supergiants (RSGs), which are considered the likely stellar type responsible for SNe II (Smartt 2009). In extreme cases, some RSGs, such as VY Canis Majoris, are estimated to be losing mass at enhanced rates of $\sim 10^{-3}$ $M_\odot$ yr^{-1} (Smith et al. 2009), which could match some lower mass loss estimates derived from `CMFGEN` modeling. However, VY CMa is more massive ($\sim 25-30$ $M_\odot$) than typical SN II RSG progenitors and contains a much more extended CSM ($\sim 2 \times 10^{16}$ cm). Overall, this deviation between theory and observation suggests that some RSGs must undergo enhanced mass loss in the final years before core-collapse. Furthermore, the identification and modeling of photo-ionization features in other objects such as Type IIb SN 2013cu (Gal-Yam et al. 2014), Calcium-strong SN 2019ehk (Jacobson-Galán et al. 2020b), Type Ibn SN 2010al (Pastorello et al. 2015), and electron-capture SN candidate 2018zd (Hiramatsu et al. 2021) represents a burgeoning technique for constraining the progenitor properties in a variety of SN sub-types beyond normal SNe II.

Indirect evidence of enhanced mass loss in SNe II progenitors is also shown through the non-LTE modeling of multi-band and bolometric SN optical light curves. Based on recent studies, the presence of dense, confined CSM around a RSG progenitor at the time of explosion manifests in a few key light curve properties. First, SBO into dense CSM can produce a longer-lasting, and thus potentially easier to observe, as well as more luminous SBO signature, peaking in UV bands of the spectral energy distribution (Chevalier & Irwin 2011; Moriya et al. 2011; Haynie & Piro 2021). Modeling of early-time SNe II light curves also revealed the need for local CSM ($r \lesssim 10^{15}$ cm) in order to reproduce the rapid rise time and brighter emission at peak observed in some objects (Dessart et al. 2017; Moriya et al. 2017a; Morozova et al. 2017, 2018) as well as the long plateau duration, delayed photometric decline rate, and H I line profile morphology (Hillier & Dessart 2019).

An additional observational probe of stellar behavior in the late-stage evolution of core-collapse SN progenitors is the detection of precursor emission prior to the terminal explosion. Optical flux has been observed as the precursors to a number of Type IIn supernovae (e.g., SN 2009ip, PTF 10bjb, SN 2010mc, PTF 10weh, SN 2011ht, PTF 12cxj, LSQ13zm, iPTF13z, SN 2016bdu, SN 2018cnf; Ofek et al. 2013b, 2014; Tartaglia et al. 2016; Nyholm et al. 2017; Pastorello et al. 2018, 2019), which show persistent spectral signatures of CSM interaction for all of their evolution, as well as H-poor, interacting Type Ibn supernovae (SNe Ibn) (Pastorello et al. 2007; Foley et al. 2007). The months-long, pre-SN flux observed in such SNe is typically found in the range of $M \approx -13$ to -17 mag and can occur anywhere from years to days prior to explosion. These eruptive events can also repeat in the years before explosion (e.g., SN 2009ip; e.g., Mauerhan et al. 2013; Pastorello et al. 2013; Ofek et al. 2013a; Margutti et al. 2014) or be one-time events, some of which are sustained for hundreds of days before core-collapse. In a recent sample study of precursor emission in ZTF-discovered

SNe, Strotjohann et al. (2021) found that ∼25% of SNe IIn have detectable pre-SN flux for ∼months prior to explosion associated with the ejection of ∼ 1 $M_\odot$ of material into the local progenitor environment. Unfortunately, no SNe II with photo-ionization spectra were detected in their search for precursor emission from massive star progenitors.

In recent years, there have been a number of theoretical explanations put forth to explain eruptive or heightened mass loss in core-collapse SN progenitors that could then be responsible for detectable precursor emission and/or photo-ionization features in early-time spectra. Enhanced mass loss observed in these progenitor stars cannot be explained by line-driven winds and thus more exotic scenarios are needed to drive off a considerable amount of material from the stellar surface. In lower mass RSGs (∼ 8-12 $M_\odot$), it is possible that nuclear flashes that ignite dynamical burning of oxygen, neon or silicon could lead to the ejection of outer layers of the stellar envelope in the final years to months before explosion (Woosley et al. 1980; Meakin & Arnett 2007; Arnett et al. 2009; Dessart et al. 2010; Woosley & Heger 2015). Alternatively, late-stage burning phases can induce gravity waves that propagate outwards and inject energy into the stellar envelope, leading to eruptions of ∼ 1$M_\odot$ worth of material in the final months before explosion (Quataert & Shiode 2012; Shiode & Quataert 2014; Fuller 2017; Wu & Fuller 2021). Additionally, super-Eddington continuum-driven winds can be induced at the stellar surface during late-stage nuclear burning, which can then cause enhanced mass loss and detectable pre-SN emission (Shaviv 2001b,a; Ofek et al. 2016). However, this mechanism is unlikely to be present in RSGs and is more suited to super-massive ($M_{\rm ZAMS} \gtrsim 30$ $M_\odot$) Luminous Blue Variable (LBV) stars.

In this paper we present, analyze, and model multi-wavelength observations (X-ray to radio) of the Type II SN 2020tlf (shown in Figure 5.1), discovered by the Asteroid Terrestrial-impact Last Alert System (ATLAS) on 16 Sept. 2020 (MJD 59108.72) in the $c-$band filter (Tonry et al. 2020). SN 2020tlf has an ATLAS discovery apparent magnitude of 15.89 mag and is located at $\alpha = 14^{\rm h}40^{\rm m}10.03^{\rm s}$, $\delta = +42°46'39.45''$. As shown in §5.3, the Pan-STARRS1 (PS1) telescope detected significant pre-explosion flux for ∼ 130 days prior to the discovery date reported above by ATLAS. We define the time of first light as the phase at which the observed magnitudes increased beyond the threshold of the pre-explosion PS1 detections. This results in a time of first light of MJD 59098.7 ± 1.5 days (06 Sept. 2020).

SN 2020tlf was classified as a young SN IIn with "flash-ionization" spectral features by Dimitriadis et al. (2020) and Balcon (2020) on 17 Sept. 2020. Following its classification, SN 2020tlf became sun-constrained for ground-based observatories. Once visible again at +95 days since first light, spectroscopic observations of SN 2020tlf revealed that the narrow, photo-ionized emission features had disappeared (unlike typical SNe IIn) and the SN had evolved into a normal Type II-like object.

SN 2020tlf is located 9.3″ east and 6.9″ south of the nucleus of the SABcd galaxy NGC 5731. In this paper, we use a redshift $z = 0.008463 \pm 0.0003$ (Oosterloo & Shostak 1993), which corresponds to a distance of 36.8 ± 1.29 Mpc for standard ΛCDM cosmology ($H_0 = 70$ km s^{-1} Mpc^{-1}, $\Omega_M = 0.27$, $\Omega_\Lambda = 0.73$); unfortunately no redshift-independent distance is available. Possible uncertainties on the distance could be the choice of H_0 and/or peculiar velocities of the host galaxy, the uncertainty on the former can, for example, con-

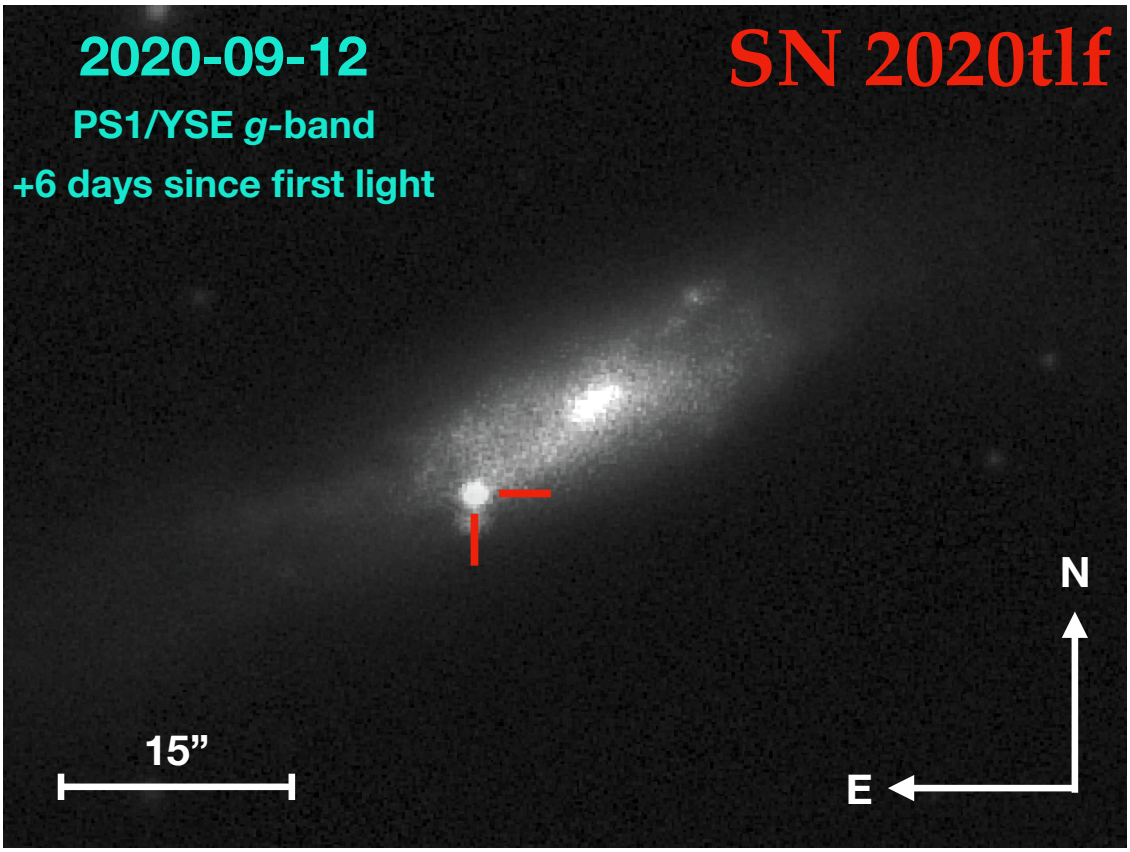

Figure 5.1 PS1/YSE $g-$band explosion image of Type II SN 2020tlf in host galaxy NGC 5731.

tribute to $\lesssim 5\%$ uncertainty of the SN luminosity. The main parameters of SN 2020tlf and its host-galaxy are displayed in Table A1. This paper represents the first installment in a series of studies that will focus on constraining the "final moments" of massive star evolution through the derivation of progenitor properties from precursor activity and "flash" spectroscopy.

5.3 Pre-Explosion Observations

5.3.1 Young Supernova Experiment Observations

SN 2020tlf was first reported to the Transient Name Server by ATLAS (Tonry et al. 2018b) on 16 Sept. 2020, but the earliest detections of the SN are from the Young Supernova Experiment (YSE; Jones et al. 2021) with the PS1 telescope (Kaiser et al. 2002) on 5 Sept. 2020. YSE began monitoring the field in which SN 2020tlf was discovered on 18 Jan. 2020.

YSE data is initially processed by the Image Processing Pipeline (IPP), described in Magnier et al. (2013), including difference imaging and photometry. Those data are passed to

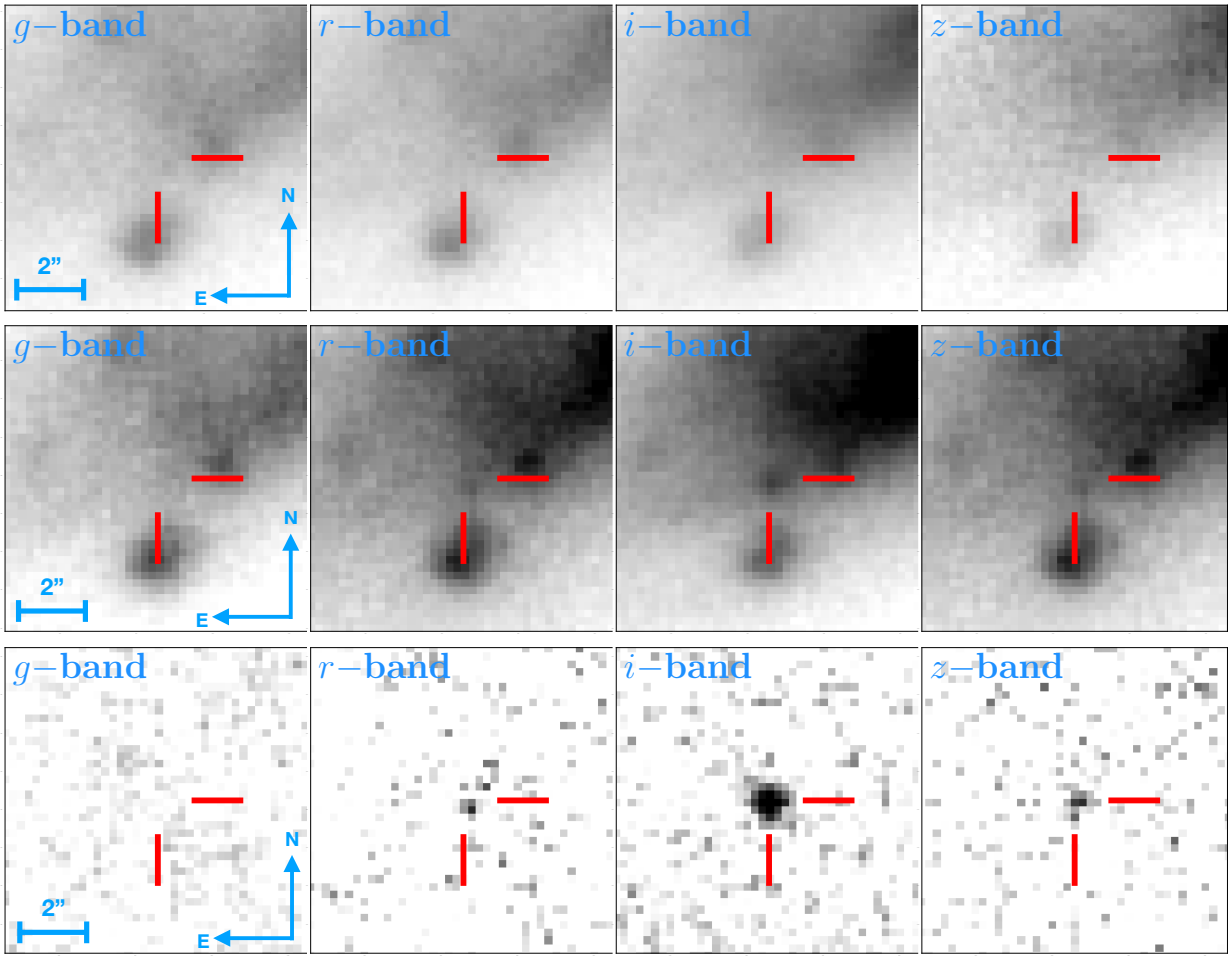

Figure 5.2 Pre-explosion PS1/YSE stacked $griz-$band template (top), detection (middle), and difference (bottom) images of progenitor precursor emission preceding SN 2020tlf. Stacked images were created from 13 $z-$band, 45 $i-$band, 23 $r-$band and 22 $g-$band pre-explosion observations spanning a phase range of $\delta t = -169.7$ to -3.7 days since first light (MJD 58929-59095). PS1 $g-$band is not detected.

the Transient Science Server (Smith et al. 2020), where catalog cross-matching and machine learning tools are used to identify potential transients in each image. The YSE team performs manual vetting of potential transients to remove artifacts, asteroids, and other contaminating sources, and finally sends new transient discoveries and initial photometric epochs to the Transient Name Server for followup by the community. We then load the transient data into YSE's transient management system, "YSE-PZ", which allows us to view Pan-STARRS data with that of other ongoing surveys and schedule follow-up observations. Further detail on this procedure is given in Jones et al. (2021) and references therein.

This process allows for identification and follow-up of fast-rising transients. For SN 2020tlf, we re-measured the pre-explosion photometry using `Photpipe` (Rest et al. 2005) to ensure highly accurate photometric measurements that took into account pixel-to-pixel correlations in the difference images and host galaxy noise at the SN location. `Photpipe` is a well-tested pipeline for measuring SN photometry and has been used to perform accurate measurements from Pan-STARRS in a number of previous studies (e.g., Rest et al. 2014; Foley et al. 2018; Jones et al. 2018; Scolnic et al. 2018; Jones et al. 2019). In brief, `Photpipe` takes as input IPP images that have been re-sampled and astrometrically aligned to match skycells in the PS1 sky tessellation and measures their zeropoints by using `DoPhot` (Schechter et al. 1993) to measure the photometry of stars in the image and comparing to stars in the PS1 DR2 catalog (Flewelling et al. 2016a). Then, `Photpipe` convolves a template image from the PS1 3π survey (Chambers et al. 2017) with data taken between the years 2010 and 2014, using a kernel that consists of three superimposed Gaussian functions, to match the point spread function (PSF) of the survey image and subtracts the template from the image. Finally, `Photpipe` uses `DoPhot` again to measure fixed-position photometry of the SN at the weighted average of its location across all images. Further details regarding this procedure are given in Rest et al. (2014) and Jones et al. (2019).

To account for the bright host galaxy of SN 2020tlf, which could cause larger-than-expected pre-explosion photometric noise in the difference image (Kessler et al. 2015; Doctor et al. 2017; Jones et al. 2017), we estimate the noise in the photometry by adding the Poisson noise at the SN location in quadrature to the standard deviation of fluxes measured in random difference-image apertures at coordinates with no pre-SN (or SN) light but approximately the same underlying host galaxy surface brightness as exists at the SN location. These apertures are placed in an annulus at the same elliptical radius from the center as SN 2020tlf to ensure similar surface brightness to the SN location. We find that the SN host galaxy does not contribute significantly to the uncertainty in the photometry ($\lesssim 15\%$ of the total error budget). We can also rule out contributions from a possible Active Galactic Nucleus (AGN) in NGC 5731 to fluxes at the SN location given the significant offset of SN 2020tlf from host center.

Based on the above data reduction, we find evidence for a statistically significant ($> 3\sigma$) pre-explosion flux excess at the SN location ($m \approx 20.7 - 21.9$ mag) in riz-bands from MJD 58971.42 – 59097.24 ($\delta t = -127.3$ to -1.49 days before first light). However, we find no evidence for similar pre-explosion emission in the YSE $g-$band images from $\delta t = -232.1$ to -17.49 days before first light. We present the pre-explosion $griz$-band stacked

Table A1 Main parameters of SN 2020tlf and its host galaxy

Host Galaxy	NGC 5731
Galaxy Type	SAcd[1]
Host Galaxy Offset	11.6″(2.10 kpc)
Redshift	0.008463 ± 0.0003[2]
Distance	36.8 ± 1.29 Mpc
Distance Modulus, μ	32.83 ± 0.10 mag
RA_{SN}	$14^h40^m10.03^s$
Dec_{SN}	$+42°46'39.45''$
Time of First Light (MJD)	59098.7 ± 1.5
Time of $B-$band Maximum (MJD)	59117.6 ± 0.2
$E(B-V)_{MW}$	0.014 ± 0.001 mag[3]
$E(B-V)_{host}$	0.018 ± 0.010 mag
m_B^{peak}	14.5 ± 0.0440 mag
M_B^{peak}	-18.5 ± 0.0440 mag

Note. — Extinction corrections have only been applied to the presented apparent magnitudes, not the absolute magnitudes.

PS1 images in Figure 5.2 over the phase range of $\delta t = -169.7$ to -3.7 days before first light (MJD 58929-59095). The multi-band, pre-explosion PS1 light curve is displayed in Figure 5.3. Furthermore, there is no evidence for significant flux in earlier pre-explosion PS1 3π survey imaging of the SN site from 28 Feb. 2011 to 21 Feb. 2014 ($\delta t = -3478$ to -2389 days before first light). For PS1 *griyz*-bands, we derived 3σ upper limits over this pre-explosion phase range of > 22.24, > 22.28, > 22.02, > 21.50, and > 21.75 mag, respectively.

5.3.2 Additional Pre-Explosion Observations

Pre-explosion imaging of SN 2020tlf was also acquired by the Zwicky Transient Facility (ZTF; Bellm et al. 2019; Graham et al. 2019) and ATLAS (Tonry et al. 2018a). ZTF $g/r-$band photometry was obtained through the ZTF forced-photometry service (Masci et al. 2019) and covers a phase range of $\delta t = -900.4$ to -34.5 days before first light. We follow the procedure outlined in the ZTF forced-photometry manual to apply a signal-to-noise threshold (SNT) of 3 to the data i.e., all photometry with SNR > 3 are considered $> 3\sigma$ detections. After the SNT is applied, we find evidence for tentative pre-explosion ZTF $r-$band flux ($m \approx 21.2$ mag) ranging from $\delta t = -128.4$ to -51.50 days since first light. To further test the validity of these "detections," we downloaded the public difference image

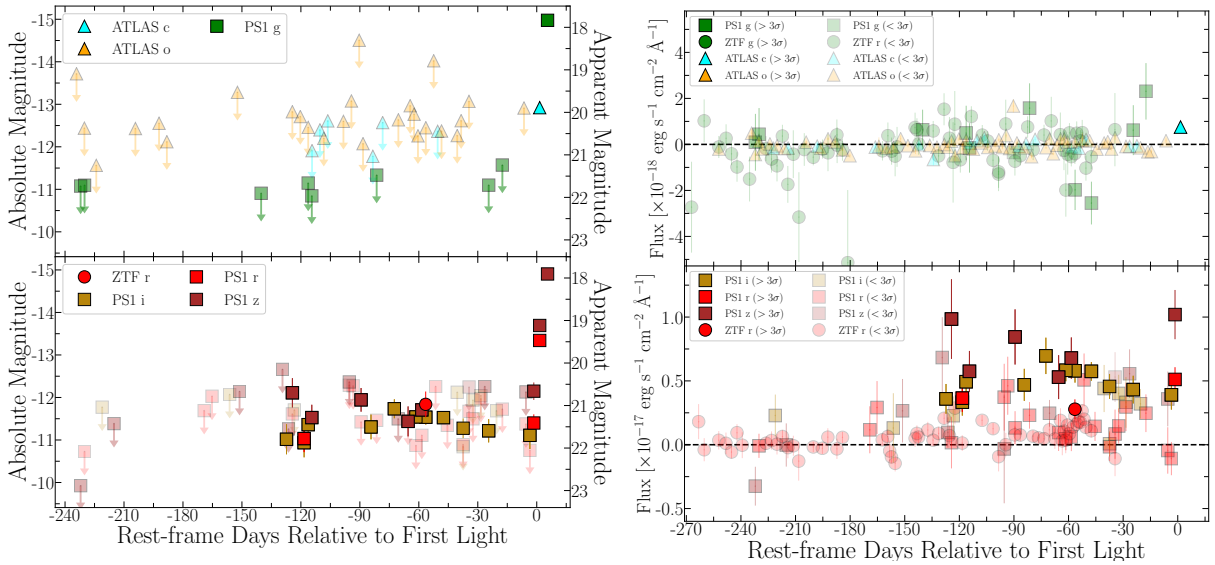

(a) (b)

Figure 5.3 (a)/(b) Pre-explosion $c/o-$band ATLAS (triangles), $r-$band ZTF (circles) and $riz-$band PS1 (squares) light curves; magnitudes presented to the left, apparent fluxes presented to the right. 3σ PS1 $riz-$band detections shown in bottom panel for ~ 130 days before first light.

pre-explosion data from the Infrared Processing and Analysis Center (IPAC)[4] and performed the same random background aperture analysis on the images as discussed in §5.3.1. We find evidence for $> 3\sigma$ emission in only one epoch of $r-$band ZTF data at a phase $\delta t = -56.5$ days prior to first light. This ZTF $r-$band detection is consistent with the PS1 detections and is presented in the pre-explosion light curve plot (Fig. 5.3a). Additionally, there is no evidence for detectable emission of pre-explosion flux in the ZTF $g-$band images ($m \geq 20.7$ mag).

Furthermore, we do not find evidence for significant emission in $c/o-$band ATLAS pre-explosion photometry during the phase range of $\delta t = -1714.1$ to -6.5 days since first light. Similar to the YSE/PS1 pre-explosion image analysis described above, we model the background noise by placing random apertures near the explosion site and performing aperture photometry of these regions. The flux is then recorded in each these random background apertures for each pre-explosion epoch and used to create background light curves i.e., control light curves. To attempt and meature significant pre-SN flux detection at the location of SN 2020tlf, we apply several cuts on the total number of individual as well as averaged data in order to remove bad measurements. Our first cut uses the χ^2 and uncertainty values of the PSF fitting to clean out bad data. We then obtain forced photometry of 8 control light curves located in a circular pattern around the location of the SN with a radius of $17''$. The flux of these control light curves is expected be consistent

[4]https://irsa.ipac.caltech.edu/applications/ztf

with zero within the uncertainties, and any deviation from that would indicate that there are either unaccounted systematics or underestimated uncertainties.

We search for such deviations by calculating the 3σ cut weighted mean of the set of control light curve measurements for a given epoch (for a more detailed discussion see Rest et al, in prep.). This weighted mean of these photometric measurements is expected to be consistent with zero and, if not, we flag and remove those epochs from the pre-SN light curve. This method allows us to identify potentially bad measurements in the SN light curve *without* using the SN light curve itself. We then bin the SN 2020tlf light curve by calculating a 3σ cut weighted mean for each night (typically, ATLAS has 4 epochs per night), excluding the flagged measurements from the previous step. We find that this method successfully removes bad measurements that can mimic pre-SN emission (Rest et al., in prep.). We then calculate the rolling sum of the S/N with a Gaussian kernel of 30 days for the pre-SN and the control light curves and identify any significant flux excess in the rolling sum. The kernel size of 30 days is chosen to maximize the detection of pre-SN emission with similar time scales. We use the peaks in the control light curves as our empirical detection limit: since there is no transient in the control light curves (barring an extremely unlikely coincidence with a transient unrelated to pre-SN emission at the location of SN 2020tlf), any peaks in the control light curves are false positives. We choose as our conservative detection limit a rolling sum value of 20, and we find no evidence of pre-SN activity in SN 2020tlf down to a magnitude limit of $m \gtrsim 20.3$ mag, which is consistent with PS1 and ZTF detections.

5.4 Post-Explosion Observations

5.4.1 UV/Optical photometry

We started observing SN 2020tlf with the Ultraviolet Optical Telescope (UVOT; Roming et al. 2005) onboard the Neil Gehrels *Swift* Observatory (Gehrels et al. 2004) on 9 Sept. 2020 until 18 Feb. 2021 (δt = 11.0 – 165.2 days since first light). We performed aperture photometry with a 5″ region with `uvotsource` within HEAsoft v6.26[5], following the standard guidelines from Brown et al. (2014). In order to remove contamination from the host galaxy, we employed images acquired at $t \approx 165$ days after first light, assuming that the SN contribution is negligible at this phase. This is supported by visual inspection in which we found no flux associated with SN 2020tlf. We subtracted the measured count rate at the location of the SN from the count rates in the SN images following the prescriptions of Brown et al. (2014). We detect bright UV emission from the SN near optical peak (Figure 5.4) until $t \approx 60$ days after explosion. Subsequent non-detections in $w1, m2, w2$ bands indicate significant cooling of the photosphere and/or Fe-group line blanketing.

Additional *griz*-band imaging of SN 2020tlf was obtained through the Young Supernova Experiment (YSE) sky survey (Jones et al. 2021) with the Pan-STARRS telescope (PS1; Kaiser et al. 2002) between 08 Sept. 2020 and 26 June 2021 ($\delta t = 1.5 - 292.3$ days since first

[5]We used the calibration database (CALDB) version 20201008.

light). The YSE photometric pipeline is based on `photpipe` (Rest et al. 2005). Each image template was taken from stacked PS1 exposures, with most of the input data from the PS1 3π survey. All images and templates are resampled and astrometrically aligned to match a skycell in the PS1 sky tessellation. An image zero-point is determined by comparing PSF photometry of the stars to updated stellar catalogs of PS1 observations (Chambers et al. 2017). The PS1 templates are convolved with a three-Gaussian kernel to match the PSF of the nightly images, and the convolved templates are subtracted from the nightly images with `HOTPANTS` (Becker 2015). Finally, a flux-weighted centroid is found for each SN position and PSF photometry is performed using "forced photometry": the centroid of the PSF is forced to be at the SN position. The nightly zero-point is applied to the photometry to determine the brightness of the SN for that epoch.

SN 2020tlf was observed with ATLAS ($\delta t = -9.40 - 157.8$ days since first light), a twin 0.5m telescope system installed on Haleakala and Mauna Loa in the Hawai'ian islands that robotically surveys the sky in cyan (c) and orange (o) filters (Tonry et al. 2018a). The survey images are processed as described in Tonry et al. (2018a) and photometrically and astrometrically calibrated immediately (using the RefCat2 catalogue; Tonry et al. 2018c). Template generation, image subtraction procedures and identification of transient objects are described in Smith et al. (2020). Point-spread-function photometry is carried out on the difference images and all sources greater than 5σ are recorded and all sources go through an automatic validation process that removes spurious objects (Smith et al. 2020). Photometry on the difference images (both forced and non-forced) is from automated point-spread-function fitting as documented in Tonry et al. (2018a). The photometry presented here are weighted averages of the nightly individual 30 sec exposures, carried out with forced photometry at the position of SN 2020tlf.

We observed SN 2020tlf with the Las Cumbres Observatory Global Telescope Network 1-m telescopes and Las Cumbres Observatory imagers from 21 Sept 2020 to 29 March 2021 ($\delta t = 14.34 - 203.5$ days since first light) in $ugri$-bands. We downloaded the calibrated BANZAI (McCully et al. 2018) frames from the Las Cumbres archive and re-aligned them using the command-line blind astrometry tool `solve-field` (Lang et al. 2010). Using the `photpipe` imaging and photometry package (Rest et al. 2005; Kilpatrick et al. 2018a), we regridded each Las Cumbres Observatory frame with `SWarp` (Bertin 2010) to a common pixel scale of $0.389''$ centered on the location of SN 2020tlf. We then performed photometry on these frames with `DoPhot` (Schechter et al. 1993) and calibrated each frame using PS1 DR2 standard stars observed in the same field as SN 2020tlf in $ugri$ bands (Flewelling et al. 2016a).

Observations of SN 2020tlf were obtained with the 1-m Lulin telescope located at Lulin Observatory on 09 Oct. 2020 ($\delta t = 32.71$ days since first light) in $BVgr$ bands. The individual frames were corrected for bias and flat-fielded using calibration frames obtained on the same night and in the same instrumental configuration. Within `photpipe`, we solved for the astrometric solution in each frame using 2MASS astrometric standards (Cutri et al. 2003) observed in the same field as SN 2020tlf. Finally, we performed photometry in each frame following the same procedures for Las Cumbres Observatory described above.

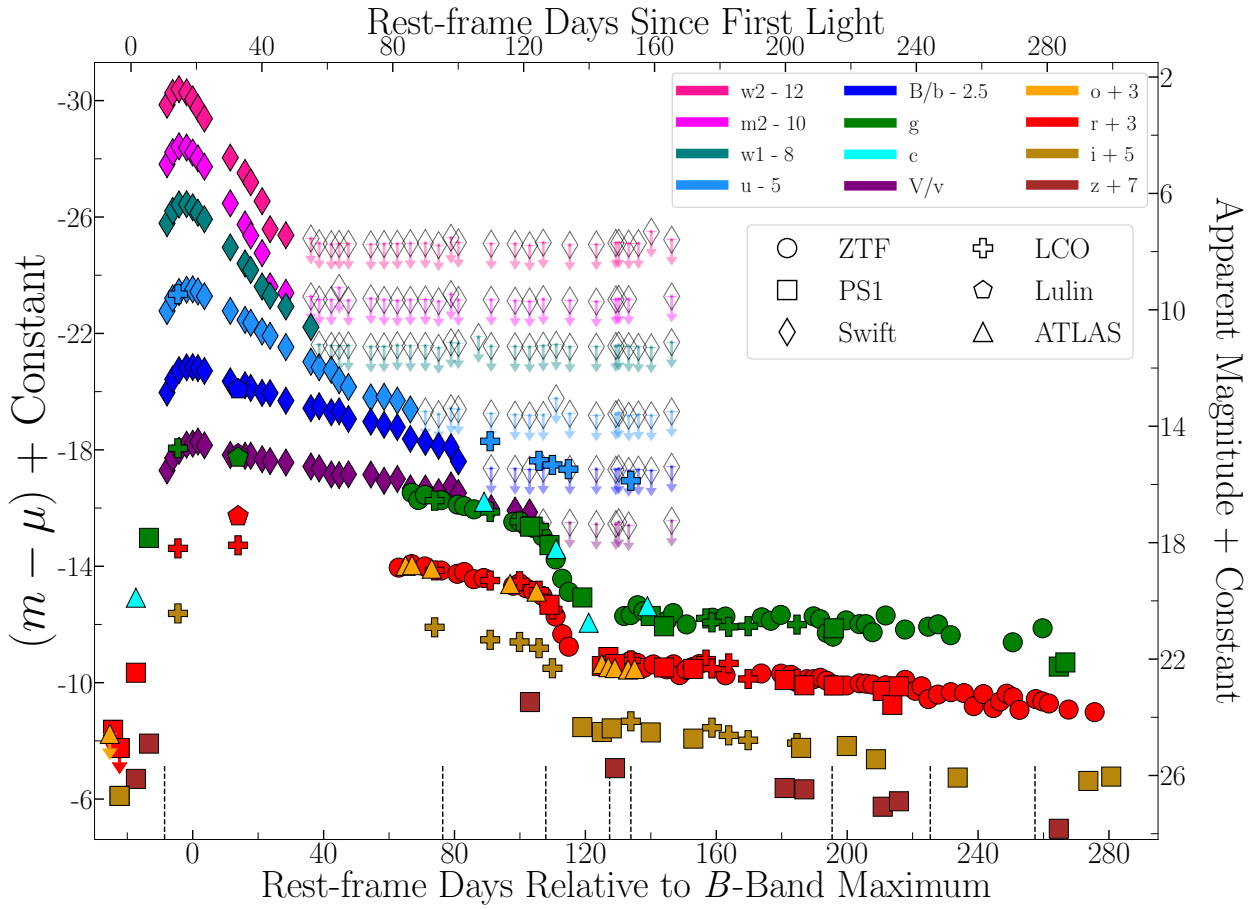

Figure 5.4 UV/Optical/NIR light curve of SN 2020tlf with respect to B-band maximum (bottom axis) and time since first light (top axis). Observed photometry presented in AB magnitude system and have not been corrected for any extinction. ATLAS data/3σ upper limits are presented as triangles, PS1/YSE as squares, Las Cumbres Observatory (LCO) as plus signs, *Swift* as diamonds, ZTF as circles, Lulin observatory as pentagons. The epochs of our spectroscopic observations are marked by vertical black dashed lines.

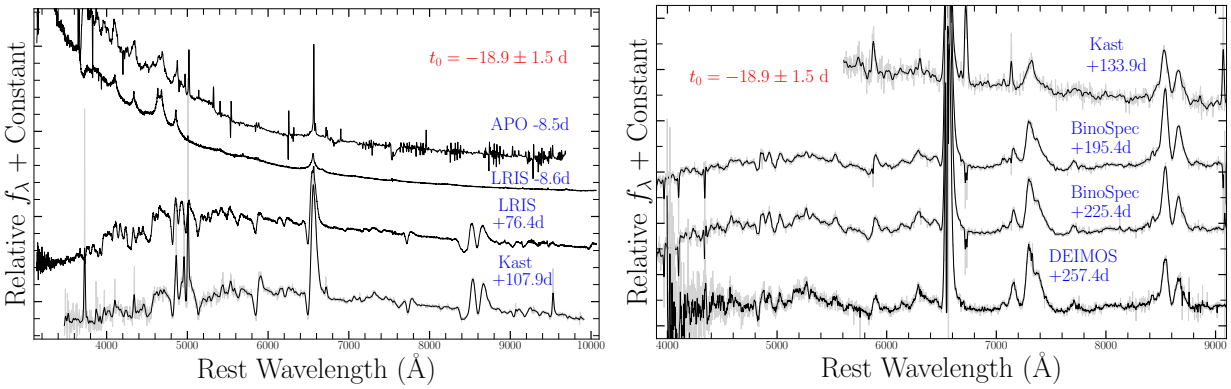

Figure 5.5 (a)/(b) Spectral observations of SN 2020tlf with phases (blue) marked with respect to B-band maximum. Time of first light relative to maximum listed in red. Unsmoothed spectra are shown in gray, and spectra shown in black have been smoothed with a Gaussian-filter.

For both Las Cumbres Observatory and Lulin photometry, we re-processed the final light curve by calculating the mean astrometric position of SN 2020tlf in all Las Cumbres Observatory and Lulin frames separately. We then performed forced photometry using a custom version of `DoPhot` at this position using the PSF parameters in each individual frame and solving only for the flux of SN 2020tlf at the time.

The complete light curve of SN 2020tlf is presented in Figure 5.4 and all photometric observations are listed in Appendix Table A4. In addition to our observations, we include $g/r-$band photometry from the Zwicky Transient Facility (ZTF; Bellm et al. 2019; Graham et al. 2019) forced-photometry service (Masci et al. 2019), which span from 27 Nov. 2020 to 28 June 2021 ($\delta t = 81.81 - 294.5$ days since first light).

The Milky Way (MW) V-band extinction and color excess along the SN line of site is $A_V = 0.043$ mag and $E(B\text{-}V) = 0.014$ mag (Schlegel et al. 1998; Schlafly & Finkbeiner 2011), respectively, which we correct for using a standard Fitzpatrick (1999) reddening law ($R_V = 3.1$). In addition to MW color excess, we estimate the contribution of galaxy extinction in the local SN environment. We use Equation 9 in Poznanski et al. (2012) to convert the Na I equivalent width (EW) of 0.10 ± 0.010 Å in the first SN 2020tlf spectrum to an intrinsic $E(B\text{-}V)$ and find a host galaxy extinction of $E(B-V)_{\rm host} = 0.018 \pm 0.003$ mag, also corrected for using the Fitzpatrick (1999) reddening law.

5.4.2 Optical/NIR Spectroscopy

In Figure 5.5, we present the complete series of optical spectroscopic observations of SN 2020tlf from -9 to +257 days relative to the B-band maximum ($\delta t = 10 - 270$ days relative to first light). A full log of spectroscopic observations is presented in Appendix

Table A1.

SN 2020tlf was observed with Shane/Kast (Miller & Stone 1993) and Keck/LRIS (Oke et al. 1995) between -9 and +257 days relative to the $B-$band maximum. For all these spectroscopic observations, standard CCD processing and spectrum extraction were accomplished with IRAF[6]. The data were extracted using the optimal algorithm of Horne (1986). Low-order polynomial fits to calibration-lamp spectra were used to establish the wavelength scale and small adjustments derived from night-sky lines in the object frames were applied. We employed custom IDL routines to flux calibrate the data and remove telluric lines using the well-exposed continua of the spectrophotometric standard stars (Wade & Horne 1988; Foley et al. 2003). Details of these spectroscopic reduction techniques are described in Silverman et al. (2012).

Spectra of SN 2020tlf were also obtained with Keck NIRES and DEIMOS, as well as Binospec on MMT and the Dual Imaging Spectrograph (DIS) on the Astrophysical Research Consortium (ARC) 3.5-m telescope at Apache Point Observatory (APO). All of the spectra were reduced using standard techniques, which included correction for bias, overscan, and flat-field. Spectra of comparison lamps and standard stars acquired during the same night and with the same instrumental setting have been used for the wavelength and flux calibrations, respectively. When possible, we further removed the telluric bands using standard stars. Given the various instruments employed, the data-reduction steps described above have been applied using several instrument-specific routines. We used standard IRAF commands to extract all spectra.

5.4.3 X-ray observations with Swift-XRT

The X-Ray Telescope (XRT, Burrows et al. 2005) on board the *Swift* spacecraft (Gehrels et al. 2004) started observing the field of SN 2020tlf on 9 Sept. 2020 until 18 Feb. 2021 (δt = 11.0 – 165.2 days since first light) with a total exposure time of 35.2 ks, (Source IDs 11337 and 11339). We analyzed the data using HEAsoft v6.26 and followed the prescriptions detailed in Margutti et al. (2013), applying standard filtering and screening using the latest CALDB files (version 2021008). We find no evidence for significant X-ray emission in any of the individual *Swift*-XRT epochs, nor in merged images near optical/UV peak and at all observed phases. From the complete merged image, we extracted an X-ray spectrum using `XSELECT`[7] at the source location with a 35″ source region (100″ background region) and estimated the count-to-flux conversion by fitting an absorbed simple power-law spectral model with Galactic neutral H column density of 1.25×10^{20} cm^{-2} (Kalberla et al. 2005) and spectral index $\Gamma = 2$ using `XSPEC` (Arnaud 1996). Using a merged, 0.3-10 keV XRT image around UV peak (δt = 11.0 – 23.0 days since first light), we derive 3σ upper limits on the count rate, unabsorbed flux and luminosity of $< 3.9 \times 10^{-3}$ ct s^{-1}, $< 1.7 \times 10^{-13}$ erg s^{-1} cm^{-2}, and $< 2.6 \times 10^{40}$ erg s^{-1}, respectively. These limits assume no intrinsic absorption from material in the local SN environment e.g., $n_{\rm H,host} = 0$. This $n_{\rm H,host}$ value is chosen so as

[6]https://github.com/msiebert1/UCSC_spectral_pipeline
[7]http://heasarc.nasa.gov/docs/software/lheasoft/ftools/xselect/

to provide the most conservative upper limit on X-ray emission despite the host reddening of $E(B-V)_{\rm host} = 0.018$ mag derived from optical spectra (§8.3.2).

5.4.4 Radio observations with the VLA

We acquired deep radio observations of SN 2020tlf with the Karl G. Jansky Very Large Array (VLA) at $\delta t = 146 - 320$ days since first light through project SD1096 (PI Margutti). All observations have been obtained at 10 GHz (X-band) with 4.096 GHz bandwidth in standard phase referencing mode, with 3C286 as a bandpass and flux-density calibrator and QSO J1224+21 (in A and B configuration) and QSO J1254+114 (in D configuration) as complex gain calibrators. The data have been calibrated using the VLA pipeline in the Common Astronomy Software Applications package (CASA, McMullin et al. 2007) v6.1.2 with additional flagging. SN 2020tlf is not detected in our observations. We list the inferred upper-limits on the flux densities in Appendix Table A4.

5.5 Host Galaxy Properties

We determine an oxygen abundance 12 + log(O/H) in host galaxy NGC 5731 by using an SDSS spectroscopic observation taken on 14 April 2004. This spectrum was taken near the galactic core and therefore the metallicity at the explosion site could be slightly different. Using a combination of line flux ratios ([O III] / Hβ and [N II]/Hα) into Equations 1 & 3 of Pettini & Pagel (2004), we determine a range of host metallicities of 12 + log(O/H) = $8.65 - 9.04$ dex ($0.99 - 1.04$ Z$_\odot$). Our derived metallicity range is higher than average SNe II host metallicities of $\sim 8.41 - 8.49$ dex (Anderson et al. 2016). However, the true metallicity at the SN explosion site could be lower than that estimated from the SDSS spectrum near the galactic core.

We utilize the same pre-explosion SDSS spectrum nearby the host galaxy center to determine a star formation rate. We calculate a total Hα emission line luminosity of $L_{\rm H\alpha} = 3.7 \times 10^{40}$ erg s^{-1}. We then use Equation 2 from Kennicutt (1998) to estimate a star formation rate of SFR = 0.29 M$_\odot$ yr^{-1} of the host galaxy. This star formation estimate is reflective of the star-forming characterization of host galaxy NGC 5731. The derived SFR is also consistent with with SFRs of other galaxies that hosted SNe II that displayed photo-ionized emission features in their early spectra. For example, Terreran et al. (2022) find a SFR of 0.25–0.39 M$_\odot$ yr^{-1} for the star-forming host of SN 2020pni.

5.6 Analysis

5.6.1 Photometric Properties

The complete post-explosion, multi-band light curve of SN 2020tlf is presented in Figure 5.4 and pre-explosion *gcroiz*−band light curves are displayed in Figure 5.3. We define the

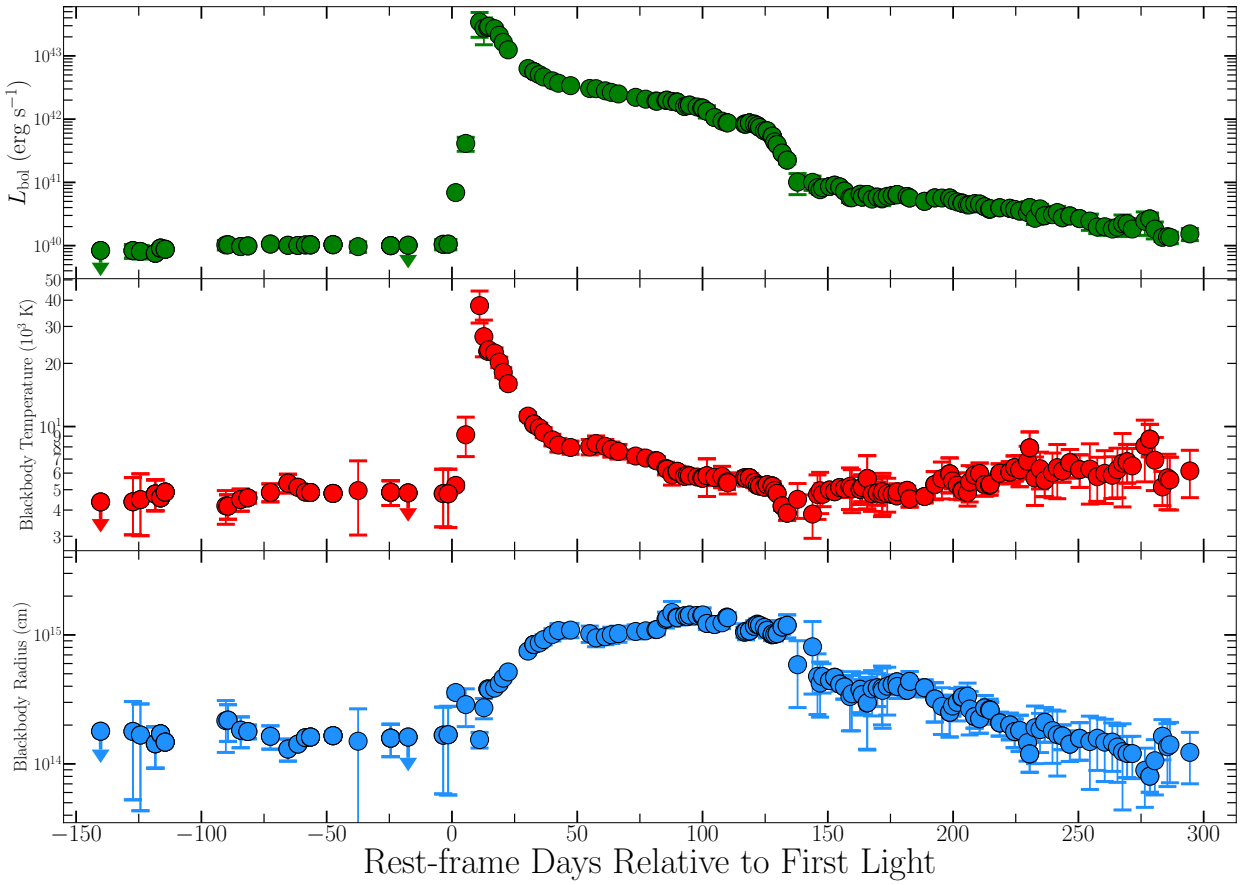

Figure 5.6 Complete pre- and post-explosion bolometric light curve (top), blackbody temperatures (middle) and radii (bottom). Data shown is derived from SED blackbody modeling of all multi-color optical photometry.

time of first light as the average phase between the last photometric detection at the pre-SN flux threshold ($M \approx -12$ mag) and the first multi-color detections that rose above that flux threshold ($M \lesssim -12$ mag). This yields a time of first light of $t_{\rm exp} = 59098.7 \pm 1.5$, which is then used for reference through the analysis. We discuss potential uncertainties on this time when modeling the bolometric light curve (e.g., §8.5). We fit a 3$^{\rm rd}$-order polynomial to the SN 2020tlf light curve to derive a peak absolute $B-$band magnitude of $M_B = -18.5 \pm 0.04$ mag at MJD 59117.6 ± 1.5, where the uncertainty on peak magnitude is the 1σ error from the fit and the uncertainty on the peak phase is the same as the error on the time of first light. Using the adopted time of first light, this indicates a rise time of $t_r = 18.9 \pm 1.5$ days with respect to B-band maximum.

As shown in Figure 5.11(b), we compare the r/V-band light-curve evolution of SN 2020tlf to popular SNe II discovered within a few days of explosion, many of which showed photo-ionization features in the early-time spectra e.g., SNe 1998S (Leonard et al. 2000; Fassia et al. 2001; Shivvers et al. 2015), 2013fs (Yaron et al. 2017), 2014G (Terreran et al. 2016), 2017ahn (Tartaglia et al. 2021), and 2020pni (Terreran et al. 2022). Compared to these SNe, the peak r/V-band absolute magnitude of SN 2020tlf is more luminous than that of SNe 2013ej, 2013fs, 2017ahn, and 2020pni, but less luminous than SNe 1998S and 2014G at peak. While the r/V-band rise time near maximum light is similar to SN 1998S, SN 2020tlf was discovered at an even earlier phase with a fainter detection absolute magnitude of $\sim$-13.5 mag. The linear photometric evolution of SN 2020tlf during its photospheric phase is comparable to most of these objects. However, SN 2020tlf has the longest lasting plateau, extending out to $\sim$110 days after maximum light, suggesting a larger ejecta mass and/or larger stellar radius than other SNe II with early-time signatures of CSM interaction.

5.6.2 Bolometric Light Curve

We construct a bolometric light curve by fitting the ZTF, PS1, Las Cumbres Observatory, ATLAS and *Swift* photometry with a blackbody model that is dependent on radius and temperature. The extremely blue UV colors and early-time color evolution of SN 2020tlf near maximum light impose non-negligible deviations from the standard *Swift*-UVOT count-to-flux conversion factors. We account for this effect following the prescriptions by Brown et al. (2010). Each spectral energy distribution (SED) was generated from the combination of multi-color UV/optical/NIR photometry in the $w2$, $m2$, $w1$, u, b/B, v/V, g, c, o, r, i, and z bands (1500–10000 Å). In regions without complete color information, we extrapolated between light curve data points using a low-order polynomial spline. We present SN 2020tlf's pre- and post-explosion bolometric light curve in addition to its blackbody radius and temperature evolution in Figure 5.6. All uncertainties on blackbody radii and temperature were calculated using the co-variance matrix generated by the SED fits. At the time of first spectrum with photo-ionization emission features, the blackbody radius, temperature and luminosity is $R_{\rm BB} = (1.5 \pm 0.21) \times 10^{14}$ cm, $T_{\rm BB} = (3.8 \pm 0.65) \times 10^4$ K and $L_{\rm bol} = (3.4 \pm 1.4) \times 10^{43}$ erg s^{-1}, respectively. This $R_{\rm BB}$ is technically the radius of thermalization ($\tau > 1$), which is much smaller than the photospheric radius ($\tau = 1$; Dessart

& Hillier 2005), and the assumption of a pure blackbody is not strictly accurate (see, e.g., Dessart et al. 2015). Consequently, this can lead to the reported luminosities from blackbody fitting to be possble lower limits on the true bolometric luminosity of SN 2020tlf.

As shown in Figure 5.7, we model the post-plateau ($t > 120$ days after maximum light) bolometric light evolution curve with energy injection from pure radioactive decay of newly synthesized ^{56}Co. The complete analytic formalism behind this model is outlined in Valenti et al. 2008a, Wheeler et al. 2015, and Jacobson-Galán et al. 2021. From this modeling, we derive a total ^{56}Co mass of $M_{\rm Co} = (2.7 \pm 0.070) \times 10^{-2}$ M$_\odot$ and a γ-ray trapping timescale of $t_\gamma = 261.1 \pm 9.57$ days. The inferred ^{56}Co mass is lower than other SNe II with early-time photo-ionization signatures e.g., SN 2014G ($\sim$0.06 M$_\odot$; Terreran et al. 2016) or SN 1998S ($\sim$0.15 M$_\odot$; Fassia et al. 2001). While the late-time light curve evolution is consistent with energy injection from the radioactive decay of ^{56}Co, there are possibly small, but overall negligible, contributions from additional power sources at these phases such as CSM interaction. Furthermore, the nebular spectra of SN 2020tlf (e.g., Fig. 5.5b) show typical O I and Ca II emission, which is compatible with ^{56}Co decay being absorbed by the metal-rich inner ejecta rather than late-time power coming from the outer ejecta ramming into CSM, as observed in SN 1998S.

5.6.3 Spectroscopic Properties

The complete spectroscopic sequence of SN 2020tlf from -8.6 to $+257.4$ days since maximum light is presented in Figure 5.5. In the earliest spectrum, SN 2020tlf shows narrow, symmetric emission features of H I, He I, He II, N III and C III (FWHM < 300 km s^{-1}). As shown in Figure 5.8, this spectrum is nearly identical to the early-time spectrum of SN 1998S at a phase of $+3$ days since first detection (-10 days from B-band peak; Fassia et al. 2001). However, the time of first light in SN 1998S is relatively uncertain given the last non-detection was 8 days prior to the first detection, indicating that the phase of this spectrum could be later than $+3$ days. Based on our adopted time of first light, SN 2020tlf is at later phase of $+10$ days since first light (-8.6 days relative to B-band peak), despite the overall spectral similarity. This could indicate that the true time of first light for SN 2020tlf is actually later than estimated, that first light emission from SN 2020tlf was detected at earlier phases given the depth of PS1 compared to the instruments used to discover SN 1998S (plus the uncertainty on the time of first light for SN 1998S), or that the environment around each of the two SNe is different i.e., variations in the properties of the most local CSM or intrinsic extinction from the SN host galaxies.

In Figure 5.8(b)/(c), we present velocity comparisons plots of H I and N III + He II emission profiles for SN 2020tlf and SN 1998S. The SN 1998S high-resolution spectrum is from Shivvers et al. (2015) and all line velocities can be resolved, unlike in the SN 2020tlf LRIS spectrum. Nonetheless, while line velocities in the SN 2020tlf LRIS spectrum can only be resolved to $\lesssim 300 - 400$ km s^{-1} and $\lesssim 200$ km s^{-1} in the APO DIS spectrum at the same phase, the overall similarity of the narrow features in SN 2020tlf compared to SN 1998S indicates that the wind velocities of CSM around the SN 2020tlf progenitor may be com-

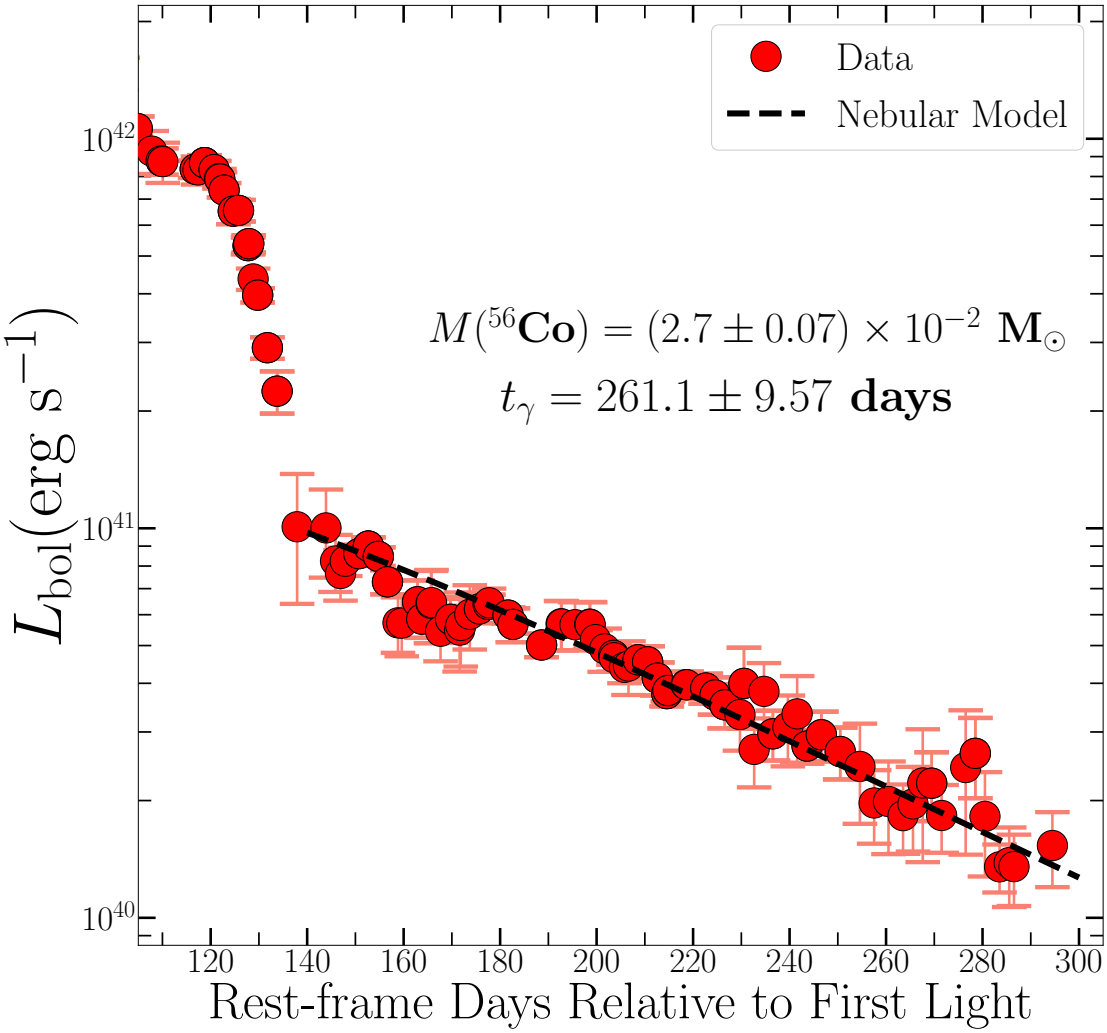

Figure 5.7 Post-plateau bolometric light curve of SN 2020tlf (red) with radioactive decay powered model shown in black for the energy released in ^{56}Co decay at late-times, following the decay of ^{56}Ni at early-times. The SN decline rate is consistent with a total ^{56}Co mass of ~ 0.03 M$_\odot$ and a γ-ray trapping timescale of $\sim$260 days.

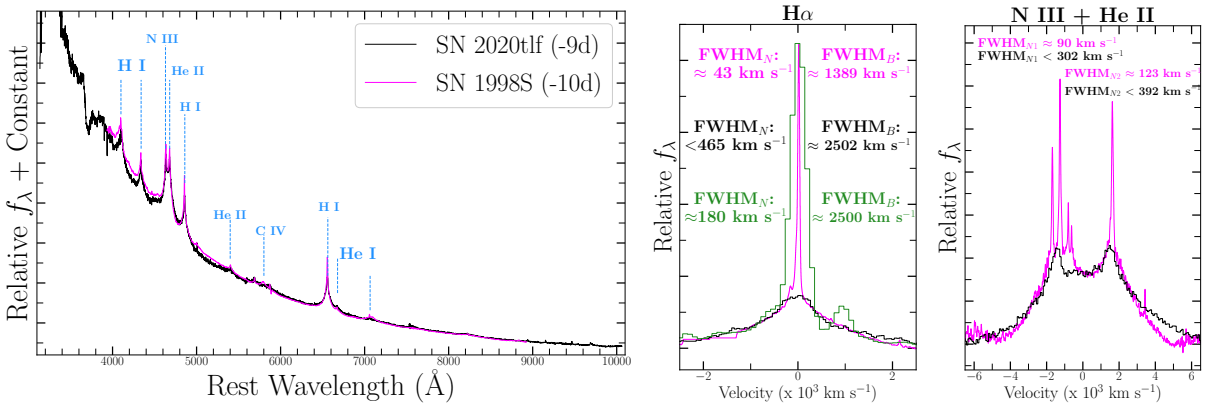

(a) (b) (c)

Figure 5.8 (a) Early-time spectra of SNe 1998S (magenta) and 2020tlf (black) with common narrow emission features labeled in blue; phases relative to $B-$band maximum. (b) Hα emission profiles of SNe 1998S (magenta) and 2020tlf (Keck LRIS in black, APO DIS in green). Narrow component velocity is resolved in the high-resolution spectrum of SN 1998S (Shivvers et al. 2015) to $v_w \approx 40$ km s^{-1}. (c) N III and He II emission profiles in SNe 1998S and 2020tlf spectra.

parable to that of the CSM in SN 1998S. To test this, we convolve the high-resolution SN 1998S spectrum to the instrumental resolution of the SN 2020tlf LRIS spectrum and find that the narrow Balmer series emission components in this spectrum, as well as those in the SN 1998S LRIS spectrum, can be modeled with a similar Lorentzian profile velocity ($\sim 300 - 400$ km s^{-1}) as observed in the SN 2020tlf spectrum. Therefore, based on the SN 1998S spectra, it is possible that the H-rich CSM in SN 2020tlf is moving at ~ 50 km s^{-1} (e.g., Fig. 5.8b) and other CSM ions such as He II or N III (e.g., Fig. 5.8c) are moving with wind velocities of ∼90-120 km s^{-1}. We present additional modeling of these photo-ionization line profiles in Figure 5.9 using combined Lorentzian profiles. Narrow components of each profile in the LRIS spectrum can only be resolved to FWHM $\lesssim 300$ km s^{-1} and FWHM $\lesssim 200$ km s^{-1} in the APO DIS spectrum, but the broad components of the profiles resulting from electron scattering (e.g., Chugai 2001; Dessart et al. 2009) are fit using Lorentzian profiles with FWHM $\sim 2000 - 3000$km s^{-1}. Based on the comparison to SN 1998S and the Lorentzian profile fits, we conclude that the SN 2020tlf progenitor likely had a wind velocity of $v_w \sim 50 - 200$ km s^{-1}. For the N III + He II feature shown in Figure 5.9(b), we explore the possibility of blueshifted, Doppler broadened He II from the SN ejecta being present in the line profile, in addition to the narrow He II and N III profiles derived from the wind. This specific combination of Lorentzian profiles is consistent with the overall profile shape as well as the flux excess on top of continuum emission, bluewards of the N III + He II feature. Doppler broadened He II from the SN ejecta has been proposed as an explanation for blue flux excesses in SNe II-P that do not show spectral signatures of CSM interaction (Dessart

et al. 2008).

In Figure 5.10, we compare the continuum-subtracted spectrum of SN 2020tlf to other well-studied events with photo-ionization features such as SNe 1998S, 2014G, 2013fs, 2017ahn, and 2020pni (Fassia et al. 2001; Terreran et al. 2016; Yaron et al. 2017; Tartaglia et al. 2021; Terreran et al. 2022). The H I, He II, and N III emission lines present in the early-time spectrum of SN 2020tlf are similar to those found in most other objects. SN 2020tlf differs slightly from SN 2013fs in that it does not contain high-ionization lines such as O IV–VI, which indicates a more extended CSM and thus lower ionization temperature for SN 2020tlf (Dessart et al. 2017). SNe 2013fs and 2014G also do not have the detectable N III unlike SN 2020tlf, SN 1998S, 2020pni and 2017ahn, which have clear N III emission in the double-peaked N III + He II feature. Furthermore, SN 2020tlf does not have significant C IV or N IV emission like most other objects, with the exception of SN 2013fs.

We also compare the mid-time spectra ($\delta t = +40 - 60$ days since peak) of this sample to the second spectrum of SN 2020tlf at +76 days since $B-$band peak, which was obtained once the SN was visible to ground-based observatories (Figure 5.11a). At this phase, the SN is in its recombination phase, with strong signatures of line blanketing by metals in the H-rich ejecta and a red spectrum. Overall, SN 2020tlf has similar ions to other events e.g., strong Balmer series, Fe-group, O I and Ca II profiles. However, absorption profiles in SN 2020tlf are noticeably narrower than other objects, which could be due to the later phase and/or larger $R_\star$ or lower E_k/M_{ej}. The SN 2020tlf spectrum is still photospheric at +76 days (+95 days since explosion) and contains a bluer continuum with weaker line blanketing compared to SNe II at similar epochs. This could indicate persistent energy injection from a more extended envelope or additional CSM interaction powering the SN at this phase. Additionally, we compare the IR spectrum of SN 2020tlf at +127 days post-peak to IR spectra of SNe 1998S, 2013ej, 2017eaw at a similar phase in Figure 5.12. All four SNe show similar ions at this phase such as prominent H emission, Fe-group elements and Mg I. Additionally, the IR spectrum of SN 2020tlf appears to show evidence for CO emission, similar to that confirmed in SN 2017eaw by Rho et al. (2018).

We present the late-time spectra of SN 2020tlf in Figure 5.5(b) over a phase range of $\delta t = 153 - 277$ days since first light. At these phases, SN 2020tlf displays strong emission lines such as Hα, [O I] $\lambda\lambda$ 6300, 6364 [Ca II] $\lambda\lambda$ 7291, 7323 emission. The SN appears to not be fully nebular by the +277 days post-explosion as it still shows Hα and Fe-group element absorption profiles. However, some of these line transitions are optically thick and can exhibit a P-Cygni profile during the nebular phase when the continuum optical depth is low.

To constrain the zero age main sequence (ZAMS) mass of the SN 2020tlf progenitor, we compare the late-time spectra to nebular-phase radiative transfer models that have, in other SN II studies, shown that the [O I] emission profile is a direct tracer of progenitor mass. In Figure 5.15(a), we compare the nebular-phase models from Jerkstrand et al. (2014) for 12-19 $M_\odot$ progenitors to SN 2020tlf at +250 days post-explosion. We find that at this phase, the 12 $M_\odot$ model best reproduces the nebular transitions observed in SN 2020tlf. We also compare the +277 day spectrum of SN 2020tlf to the nebular models from Dessart et al. (2021) that are generated from 9.5-15 $M_\odot$ progenitors at +350 days post explosion and find

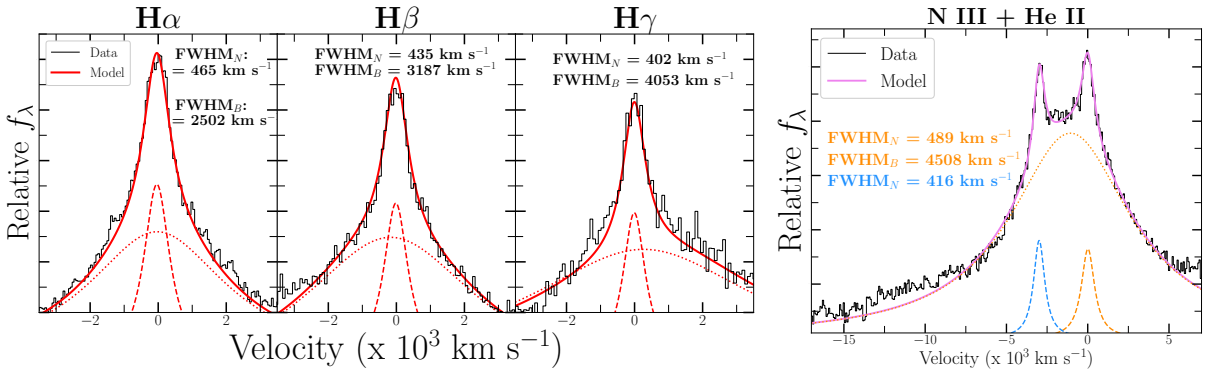

Figure 5.9 (a) Balmer emission features (black) from the LRIS photo-ionization spectrum with respect to multi-component Lorentzian models (red). The true velocities of the narrow component are unknown due to spectral resolution. (b) N III + He II feature (black) with complete Lorentzian emission model shown in violet. N III emission model presented in blue and He II model shown in orange.

that the 10 $M_\odot$ model is the most consistent with the data. We therefore conclude that the progenitor of SN 2020tlf had a ZAMS of $\sim$ 10-12 $M_\odot$. The estimated SN 2020tlf progenitor mass is comparable to that derived from nebular emission in sample studies of SNe II-P ($\sim$ 12-15 $M_\odot$; Silverman et al. 2017), but lower than that of other SNe II with photo-ionization spectra e.g., SN 2014G had an estimated progenitor ZAMS mass of 15-19 $M_\odot$ (Terreran et al. 2016). We note that we cannot completely rule out the possibility that the progenitor of SN 2020tlf was a low-mass ($\sim$ 9 $M_\odot$) super-asymptotic giant branch star, as proposed to be the progenitors of electron-capture SN candidates (e.g., see Hiramatsu et al. 2021). However, based on the observed bolometric light curve evolution and total synthesized ^{56}Ni mass, it is unlikely that SN 2020tlf was an electron-capture SN from such a progenitor star.

5.6.4 Precursor Emission

SN 2020tlf is the first SN with typical SN II-P/L-like spectral and light curve behavior that has a confirmed detection of precursor flux. Precursor emission was also identified $\sim$ 60 years prior to SN II, iPTF14hls in archival imaging (Arcavi et al. 2017b). However, while the spectral evolution of iPTF14hls resembles a normal SN II, the extremely long-lasting and time variable light curve evolution indicated that this event, as well as its progenitor star, were very different than standard SN II explosions. The pre-explosion light curve, presented in Figure 5.3(a), shows $> 3\sigma$ detections in PS1 riz-bands starting from $\delta t = -130$ days and persisting with a consistent flux until first SN light. The lack of precursor detections in bluer bands such as PS1/ZTF $g-$band or ATLAS $c-$band suggests a moderately cool emission or an extended, low-temperature emitting surface of whatever physical mechanism

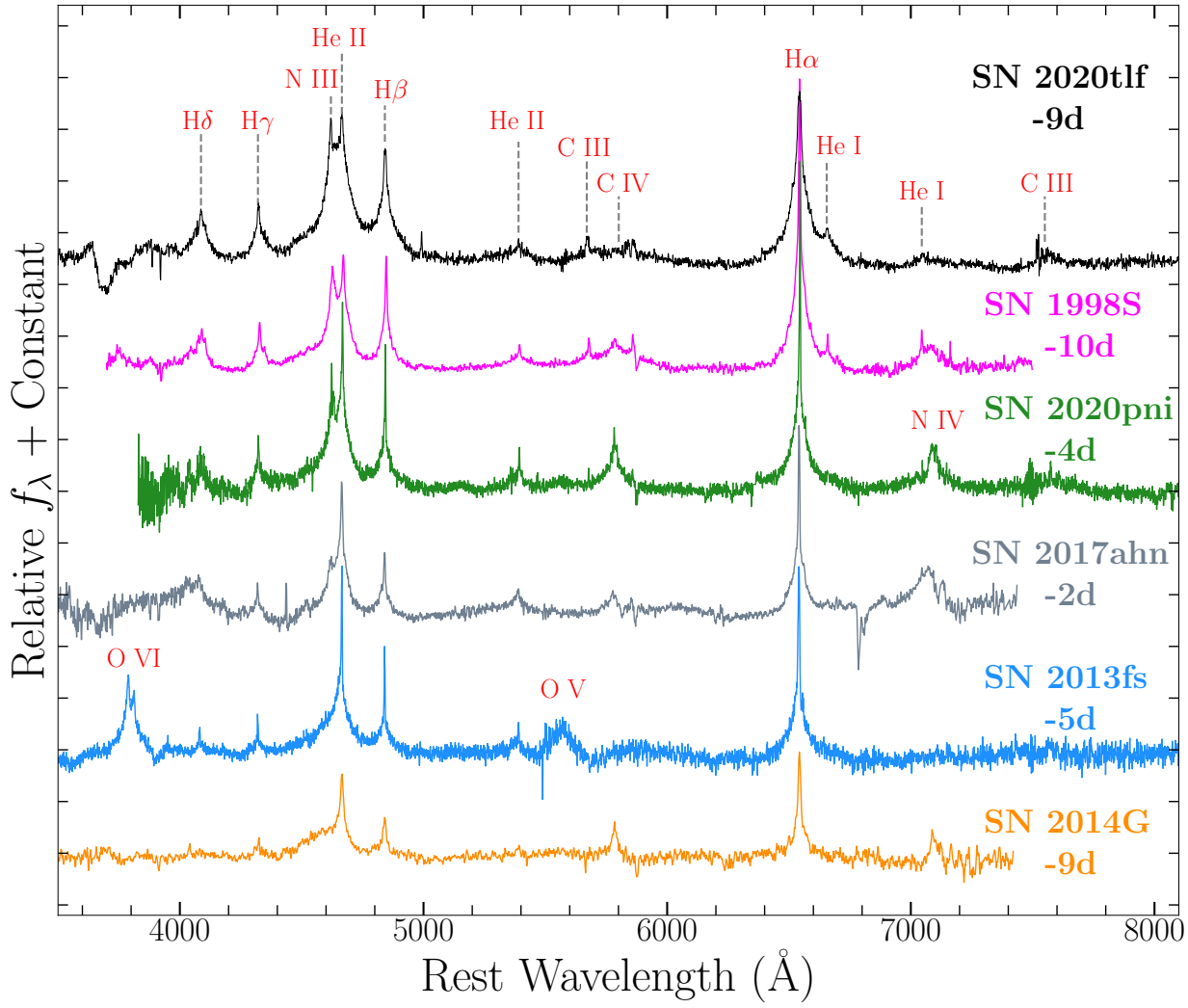

Figure 5.10 Early-time, continuum-subtracted spectral comparison of SNe II, 2020tlf (black), 1998S (magenta; Fassia et al. 2001), 2020pni (green; Terreran et al. 2022), 2017ahn (grey; Tartaglia et al. 2021), 2013fs (blue; Yaron et al. 2017) and 2014G (orange; Terreran et al. 2016). Common photo-ionization ions labeled in red; phases relative to $B-$band maximum. Early-time spectrum of SN 2020tlf shows nearly identical photo-ionization features to SNe 1998S and 2020pni, indicating a similar ionization temperature and CSM extent.

caused this pre-explosion flux. We construct a pre-explosion bolometric light curve, as well as temperatures and radii, by modeling the SED containing 3σ $riz-$band detections and $g-$band upper limits with a blackbody model, same as that used in §5.2. We show the pre-explosion bolometric light curve, blackbody temperatures and radii in Figure 5.13(b). It should be noted that the pre-SN bolometric light curve relies on only 3 optical/NIR bands and thus contributions from undetected parts of the blueward (or IR) ends of SED could cause variations from what is observed. Furthermore, the presence of spectral emission lines during the precursor (e.g., Hα) could lead to increased flux in $r-$band, for example, relative to other bands. We find that the precursor has a bolometric luminosity of $\sim 10^{40}$ erg s^{-1} ($\sim 2 \times 10^6$ L$_\odot$), and has an average blackbody temperature and radius of ~ 5000 K and $\sim 10^{14}$ cm (~ 1500 R$_\odot$), respectively. For reference, we also plot the predicted luminosity, surface temperature and radius evolution of a 15 M$_\odot$ RSG progenitor undergoing wave-driven mass loss as presented in Fuller (2017). This model has a consistent emitting radius to the SN 2020tlf precursor emission, but has significantly lower luminosities and temperatures at phases where pre-explosion emission is detected.

The pre-SN activity prior to SN 2020tlf is considerably fainter than other SNe with confirmed precursor emission. In Figure 5.14, we compare the multi-color SN 2020tlf pre-explosion detections to popular SNe IIn, 2009ip, 2010mc and 2016bhu, all of which had confirmed precursor emission prior to explosion. As shown in the plot, the SN 2020tlf precursor only reaches ~ -11.5 mag in all bands, while the plotted SNe IIn precursors have absolute r-band magnitudes ranging from -13 mag to -15.5 mag. Precursor emission from the SN 2020tlf progenitor system is also fainter than the average absolute magnitude of -13 mag found in the sample of ZTF-observed SNe IIn with pre-explosion outbursts presented by Strotjohann et al. (2021). However, as shown in Figure 5.14, because the limiting magnitude of ZTF (<20.5 mag; Bellm et al. 2019; Graham et al. 2019) is ∼1 mag shallower than YSE (<21.5 mag; Jones et al. 2021), pre-explosion emission in SNe II-like events would not have been detected at the flux level of the precursor of SN 2020tlf. Nevertheless, searches for pre-SN emission from SN II progenitors at closer distances (e.g., $\lesssim 50$ Mpc) in transient survey archival data (e.g., ZTF, ATLAS, YSE, etc) will allow us to determine whether more 20tlf-like precursor events are possible.

Integrating the pre-explosion bolometric light curve yields a total radiated energy of $\sim 10^{47}$ erg over the ~ 130 day precursor event. Coincidentally, this derived radiated energy is approximately the binding energy of a H-rich envelope in a typical RSG (Dessart et al. 2010). We explore potential power sources for the precursor emission in the form of CSM interaction-powered and wind-driven emission. For the former, the precursor emission would result from interaction between material ejected in a progenitor outburst and CSM from a previous outburst and/or steady-state wind-driven mass loss, causing a fraction of the kinetic energy to be converted in radiative energy. In this process, the relation between radiated and kinetic energy, as well as CSM properties, goes as:

$$E_{\rm rad} = \frac{\epsilon}{2} M_{\rm pre} v_{\rm pre}^2 \tag{5.1}$$

where ϵ is the fraction of converted kinetic energy, $M_{\rm pre}$ is mass ejected in the precursor

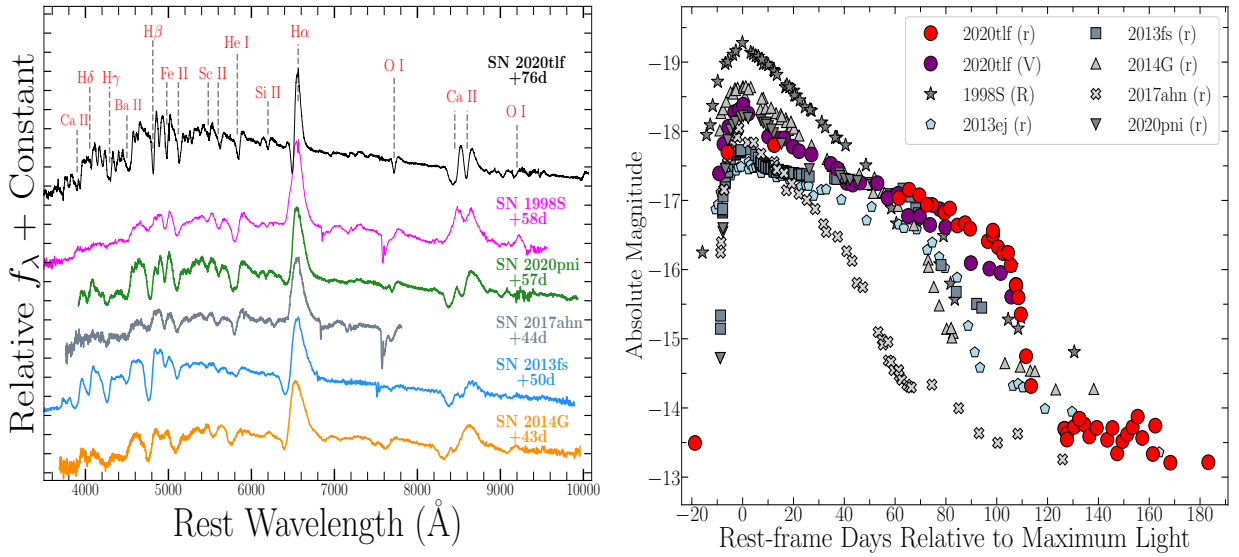

(a) (b)

Figure 5.11 (a) Spectral comparison of SN 2020tlf (black) and other SNe II discovered with photo-ionization spectra at approximately the same phase relative to $B-$band maximum (Fassia et al. 2001; Terreran et al. 2016; Yaron et al. 2017; Tartaglia et al. 2021; Terreran et al. 2022). Common ions are marked by grey lines. (b) Early-time $r/V-$band light curve comparison of SN 2020tlf (red/purple circles) and known SNe II with photo-ionization spectral features (shades of gray) plus SN 2013ej (light blue), which was a SN II discovered very young but without spectroscopic evidence of CSM photo-ionization.

and $v_{\rm pre}$ is the velocity of that material. For the observed precursor radiated energy of $E_{\rm rad} \approx 10^{47}$ erg, efficiency $\epsilon = 1$, and velocities discussed in §8.4.2 (e.g., $v_w = 50{-}200$ km s^{-1}), the total mass ejected in the precursor is $M_{\rm pre} \approx 4.3{-}0.27$ M$_\odot$, respectively. However, if CSM interaction is the mechanism for precursor emission, the conversion efficiency is definitely much less than 100% (Smith et al. 2010) and therefore the derived $M_{\rm pre}$ is at least $\gtrsim$ M$_\odot$ for the largest $v_{\rm pre}$ that is consistent with observations. Furthermore, it should be noted that a material ejected in a precursor that then collides with pre-existing CSM may lead to to formation of a semi-static CSM shell of constant density (i.e., $s = 0$), which is different than the wind-like density CSM that is typically invoked to model events with photo-ionization spectra (e.g., see §8.5).

If the precursor emission from the SN 2020tlf progenitor was instead from a super-Eddington, continuum-driven wind, we follow the mass loss prescription outlined in Shaviv (2001b) that goes as:

$$E_{\rm rad} \approx \frac{1}{W} M_{\rm CSM} c_s c \tag{5.2}$$

where W is an empirical factor found to be ~ 5, c_s is the speed of sound at the base of the optically thick wind (e.g., ~ 60 km s^{-1}; Shaviv 2001a), and c is the speed of light. For $E_{\rm rad} \approx 10^{47}$ erg, we derive a total amount of material lost in a potential super-Eddington wind to be $M_{\rm CSM} \approx 2 \times 10^{-3}$ M$_\odot$. However, it should be noted that this formalism is designed for SN IIn progenitors such as LBVs. Furthermore, a super-Eddington wind is likely unphysical for a 10-12 M$_\odot$ progenitor mass range as derived from the nebular spectra of SN 2020tlf.

Another possible mechanism to explain the pre-SN activity in SN 2020tlf is stellar interaction between the primary RSG progenitor and a smaller binary companion star. This can manifest as a "common envelope" phase in the progenitor's evolution (Sana et al. 2012), which can result in the merging of primary and binary companions, the result of which is a slightly luminous, short-lived transient (Kochanek et al. 2014). While this scenario has been invoked as an explanation for Luminous Red Novae (LRN) or Intermediate Luminosity Optical Transients (ILOT), the resulting luminosity produced by this physical mechanism appears to be too faint ($\sim 10^{2-4}$ L$_\odot$; Pejcha et al. 2017) to match the pre-explosion luminsoty in SN 2020tlf ($\sim 10^6$ L$_\odot$). Therefore, it is more likely that an eruption from the primary progenitor alone is the most likely cause of the pre-SN activity observed in SN 2020tlf.

5.7 Light Curve and Spectral Modeling

We performed non-LTE, radiative transfer modeling of the complete light curve and spectral evolution of SN 2020tlf in order to derive properties of the progenitor and its CSM. Our modeling approach was similar to that presented in Dessart et al. (2017), both in terms of initial conditions for the ejecta and CSM, the simulations of the interaction with the radiation-hydrodynamics code `HERACLES` (González et al. 2007; Vaytet et al. 2011; Dessart et al. 2015), and the post-processing with the non-LTE radiative-transfer code `CMFGEN`. For

the progenitor star, we considered three models of RSGs produced by three different choices of mixing length parameter $\alpha_{\rm MLT}$. A greater $\alpha_{\rm MLT}$ boosts the convective energy transport in the H-rich envelope and produces a more "compact" progenitor. This choice is generally required to match the color evolution of standard (i.e., non-interacting) Type II SNe (see discussion in Dessart & Hillier 2011; Dessart et al. 2013) since more extended RSGs yield SNe II-P that both recombine and turn red too late in their evolution. The progenitor with increased radius may be more compatible with the pre-SN properties of SN 2020tlf given the evidence for an inflated progenitor star prior to explosion (e.g., Fig. 5.13).

In practice, we employed model m15mlt3 ($R_\star = 501$ R$_\odot$), m15 ($R_\star = 768$ R$_\odot$), and m15mlt1 ($R_\star = 1107$ R$_\odot$) from Dessart et al. (2013). Taking these models at a time of a few 1000 s before shock breakout, we stitch a cold, dense, and extended material from the progenitor photosphere out to some large radius. For simplicity, this material corresponds to a constant velocity wind ($v_w = 50\,{\rm km\,s^{-1}}$), a temperature of 2000 K, and a composition set to the surface mixture of the progenitor (Davies & Dessart 2019). We note that only a wind-like density profile (e.g., $s = 2$) is considered in our simultions and not a shell-like profile of constant density (e.g., $s = 0$). The former has proved to be the most realistic CSM structure for modeling similar events (Shivvers et al. 2015; Dessart et al. 2017; Terreran et al. 2022) and the latter could be considered in future modeling. Nonetheless, we choose to adopt a CSM with a non-homogeneous density profile given that the most local CSM around massive stars appears to have complex CSM structure i.e., not constant density or shell-like.

We consider wind mass loss rates of 0.01 and 0.03 M$_\odot$ yr^{-1} from the progenitor surface out to a distance of order 10^{15} cm, beyond which the wind density is forced to smoothly decrease to 10^{-6} M$_\odot$ yr^{-1} at 6 or 8×10^{15} cm. These specific mass loss rates were chosen because simulations with these values, combined with a range of CSM extents, are most consistent with the observed SN properties e.g., early-time light curve evolution, peak luminosity and spectral features. A higher/lower $\dot{M}$ value outside of our adopted range is likely more inconsistent with our observations given the dependence of mass loss with increasing/decreasing the light curve rise time and peak luminosity, for example (Dessart et al. 2017; Moriya et al. 2017a). The dense part of the CSM is limited in extent to reflect the temporary boost in luminosity observed in SN 2020tlf. That is, by increasing (decreasing) the radius that bounds the dense part of the CSM, one can lengthen (shorten) the duration over which the luminosity is boosted as a result of the change in diffusion time through the CSM and the amount of shock/ejecta energy trapped by the CSM.

The interaction configurations described above are used as initial conditions for the multi-group radiation-hydrodynamics simulations with the code `HERACLES`. For simplicity, we assume spherical symmetry and perform all simulations in 1-D; an asymmetric explosion could cause variations in the observed light curve and/or spectral evolution such as an extended SBO or slower evolving early-time light curve evolution. We use eight groups that cover from the ultraviolet to the far infrared: one group for the entire Lyman continuum, two groups for the Balmer continuum, two for the Paschen continuum, and three groups for the Brackett continuum and beyond. We also compute gray variants for some of the calculations: these tend to yield a shorter and brighter initial luminosity peak because the gray opacity under-

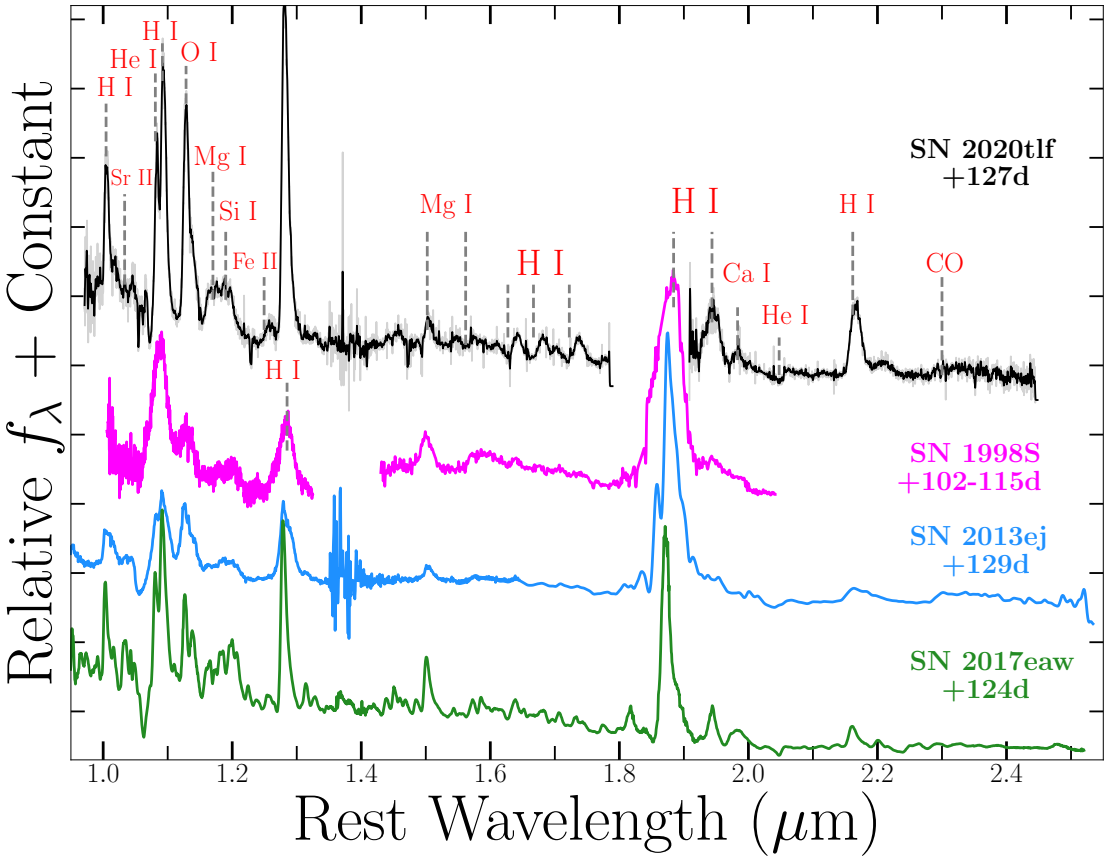

Figure 5.12 Infrared spectral comparison of SNe 2020tlf, 1998S and 2013ej. Common ions marked by grey lines; phases relative to $B-$band maximum. SN 2020tlf has identical IR spectral features to SNe II, 1998S and 2013ej but overall lower photospheric velocities based on the line profiles. Line profile widths are smaller in SN 2020tlf than in other SNe II, which is compatible with a larger $R_\star$ and lower E_k/M_{ej}.

estimates the true opacity of a cold CSM crossed by high-energy radiation (see Dessart et al. 2015 for discussion). The difference between multi-group and gray transport is, however, modest because of the relative small CSM mass and extent. We adopt a simple equation of state that treats the gas as ideal with adiabatic index of $\gamma = 5/3$.

From the `HERACLES` simulations, we extract the total luminosity crossing the outer grid radius as a function of time (the time origin for our light curves is usually set when the total luminosity recorded first exceeds $10^{41}\,\mathrm{erg\,s^{-1}}$). We also extract the hydrodynamical quantities (radius, velocity, density, and temperature) at selected epochs to post-process with the non-monotonic velocity solver in the non-LTE code `CMFGEN` (e.g., see Dessart et al. 2015) and compute the emergent spectrum from the ultraviolet to the infrared. This approach captures the relative contributions from the fast ejecta, the dense shell at the interface between the ejecta and the CSM, the unshocked ionized CSM, as well as the outer cooler unshocked

CSM. One limitation with this version of CMFGEN is the use of the Sobolev approximation (line transfer is therefore simplistic and line blanketing is underestimated) and the necessity to fix the temperature, which results from the hydrodynamics solution and the influence of the shock. This temperature from HERACLES is not very accurate since the radiation hydrodynamics code treats the gas in a simplistic manner (the kinetic equations are not solved for). The composition adopted in our CMFGEN calculations at early times is homogeneous and corresponds to mass fractions of $X_{\rm He} = 0.34$, $X_{\rm C} = 1.28 \times 10^{-3}$, $X_{\rm N} = 3.29 \times 10^{-3}$, $X_{\rm O} = 4.67 \times 10^{-3}$ (and other metals at their solar metallicity value; $X_{\rm H} = 1\text{-}X_{\rm all}$), which are the values predicted for a 15 $M_\odot$ star (Davies & Dessart 2019). The model atoms used in CMFGEN differ for early and late post-explosion times. At early times, we include H I, He I/II, C I–IV, N I–IV, O II–VI, Mg II, Si II, S II, Ca II, Cr II–III, Fe I–IV, Co II–III, and Ni II–III. At later times, we drop the high ionization stages and add the atoms or ions Na I, Mg I, Si I, S I, Ca I, Sc I–III, Ti II–III.

All model characteristics are presented in Table A3 and the CSM structure of most consistent models are plotted in Figure 5.16. Furthermore, in Figure 5.17, we show how early-time CMFGEN spectral models are influenced by both the extent of the CSM and the progenitor mass loss rate. We show that for $\dot{M} = 0.03$ $M_\odot$ yr^{-1} at a phase of +10 days since explosion, models with more extended CSM radii (e.g., $4 - 8 \times 10^{15}$ cm) have wider, more prominent emission profiles from CSM interaction than models with less extended CSM (e.g., $1 - 2 \times 10^{15}$ cm). We also show that for a model with $\dot{M} = 0.01$ $M_\odot$ yr^{-1} and CSM radius of 10^{15} cm, narrow emission lines are less prominent and shorter lived than other models with larger CSM radii and mass loss rates. Furthermore, the more compact the CSM, the higher the ionization, which influences the spectral features present because a smaller optically thick volume leads to a higher radiation temperature and consequently a higher gas temperature.

In Figure 5.18, we present the most consistent bolometric HERACLES models and multi-band CMFGEN models with respect to SN 2020tlf observations. We find that an extended progenitor radius of ~ 1100 $R_\odot$ (dotted line in Fig. 5.18a) is the most consistent with the long-lived and very luminous plateau phase in SN 2020tlf. Additionally, the early light curve of SN 2020tlf, which is strongly influenced by the interaction of the ejecta with the CSM, is best modeled by a mass loss rate of $\dot{M} = 10^{-2}$ $M_\odot$ yr^{-1} ($v_w = 50$ km s^{-1}) and a dense CSM that extends out to a radius of $r_{\rm CSM} = 10^{15}$ cm – the influence of the more tenuous CSM beyond that radius is modest and eventually naught (i.e., at >40 days). As shown in Figure 5.18(b), the light curve model matches the multi-band early-time photometry in most optical/NIR bands, but it over-predicts the UV peak in *Swift* filters by ~ 1 mag. There are many possible reasons for this inconsistency given the simplicity of our assumptions. For example, one possible cause is that there is additional host extinction near the explosion site that was not able to be measured through typical reddening estimates (e.g., see §8.3.2). Additionally, while the model light curves are consistent with the peak bolometric luminosity and decline rate, they cannot reproduce the long rise-time observed in SN 2020tlf following the pre-SN activity. However, model first light is defined when the simulation bolometric light curve rises above 10^{41} erg s^{-1} and thus the two bolometric light curve points in Figure 5.18(a) would not be reproduced by the models given their low luminosities. Nonetheless,

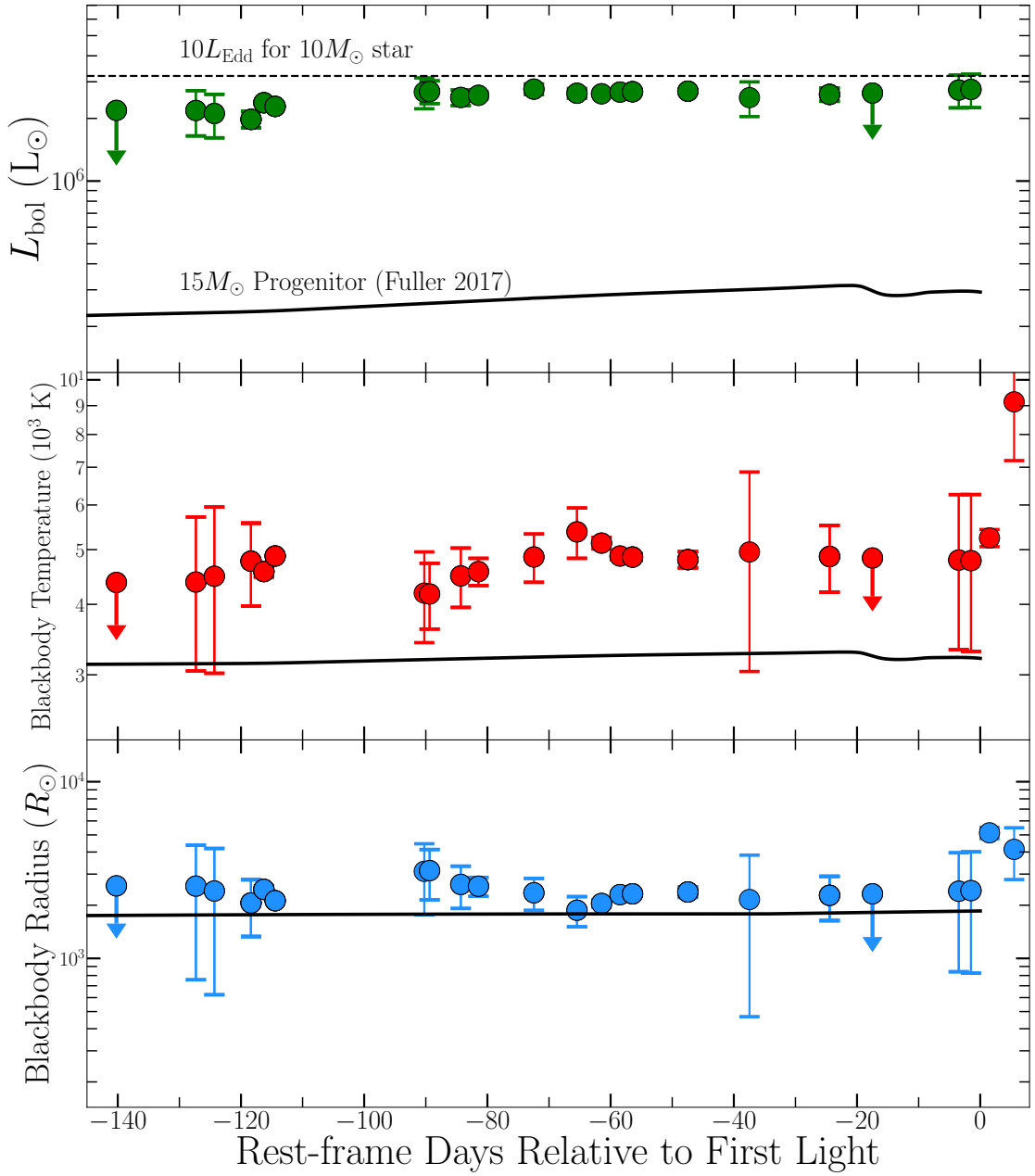

Figure 5.13 Pre-explosion bolometric light curve (top), blackbody temperatures (middle) and radii (bottom) from SED modeling of multi-band photometry associated with $\geq 3\sigma$ flux excesses. Shown in black is a progenitor model from Fuller (2017) of a 15 $M_\odot$ RSG undergoing wave-driven mass loss.

it is worth noting that the model light curves predict a faster rise ($t_{\rm exp} \approx 59108$ MJD) than our estimate based on the earliest photometry ($t_{\rm exp} \approx 59098.7$ MJD). If the former is the true time of explosion, the earliest detections may represent additional precursor activity or SBO emission from an asymmetric explosion or CSM.

In Figure 5.19(a), we present the most consistent `CMFGEN` model with respect to the first spectrum of SN 2020tlf. The model spectrum is a consistent match to the widths and strengths of emission features such as H I, He I–II, and C III–IV, as well as the continuum shape and temperature. Despite the presence of N in the model CSM composition, the most consistent model cannot perfectly reproduce the N III emission feature on the bluewards side of the N III + He II feature. Alternative `CMFGEN` model procedures that include a static wind structure (e.g., see Shivvers et al. 2015; Boian & Groh 2020; Terreran et al. 2022) reproduce this N III line but employ a strong N enrichment, incompatible with the 10-12 $M_\odot$ progenitor mass inferred for SN 2020tlf (e.g., see §8.4.2). Furthermore, the most consistent early-time spectral model is for a phase of +4 days after explosion, therefore indicating a time of first light of MJD 59105, which is between the estimates derived from either early-time photometry or light curve modeling. We also present a late-time `CMFGEN` model at +80 days with respect to the +95 day spectrum in Figure 5.19(b). This model accurately matches most features and line profiles, as well as the boosted continuum at blueward wavelengths that could be the result of persistent CSM interaction.

The modeling of SN 2020tlf's light curve and early-time spectrum suggests similar CSM properties and progenitor mass loss to other SNe II with `CMFGEN` modeling of early-time spectra. Compared to the sample of `CMFGEN`-modeled interacting SNe II presented by Boian & Groh (2020) and expanded by Terreran et al. (2022), the SN 2020tlf progenitor mass loss rate of 10^{-2} $M_\odot$ yr^{-1} is consistent but slightly greater than that of some events with early photo-ionization signatures such as SNe 1998S, 2017ahn, 2013fs and 2020pni ($\dot{M} \approx 5 - 8 \times 10^{-3}$ $M_\odot$ yr^{-1}, $v_w = 40 - 200$ km s^{-1}), and is lower than SNe 2013fr, 2014G, and 2018zd ($\dot{M} \approx 0.04 - 0.2$ $M_\odot$ yr^{-1}, $v_w = 500 - 800$ km s^{-1}). The mass loss derived for SN 2020tlf is also very similar to SN IIn 2010mc ($v_w = 300$ km s^{-1}) that also had confirmed precursor emission but whose narrow emission lines persisted for all of the SN evolution. In terms of the disappearance of narrow emission features in these events, SN 2020tlf cannot be constrained as well as other SNe II with higher cadence early-time spectral coverage, but does have a lower limit on this timescale of $t \geq 10.3$ days since first light. Compared to the SN sample presented in Figure 14 of Terreran et al. (2022), the time of narrow line disappearance in SN 2020tlf is most likely greater than all other presented events besides SN 1998S, whose narrow features persisted until ~ 30 days since first light. This indicates a much more extended CSM in the case of SNe 1998S and, to a lesser degree, 2020tlf, than other events where the observed narrow features persisted for $\lesssim 12$ days since first light.

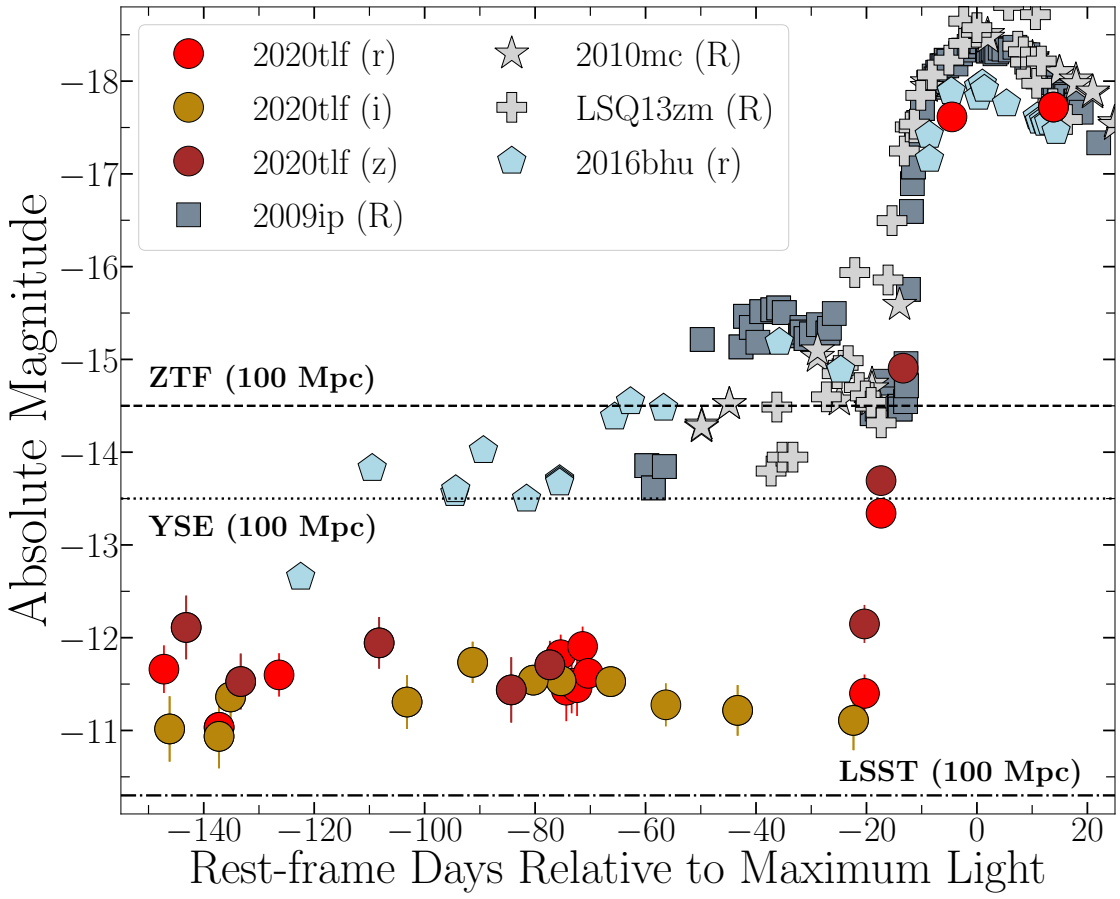

Figure 5.14 Light curve comparison of SN 2020tlf (circles) and SNe IIn with confirmed precursor emission. SN 2009ip $R-$band shown as squares, SN 2010mc $R-$band shown as stars, LSQ13zm $R-$band as plus signs, and SN 2016bhu $r-$band shown as pentagons. Limiting magnitudes at $D < 100$ Mpc for ZTF, YSE and LSST surveys shown as black lines. These limits represent detection magnitudes for single epoch, pre-SN observations whose detection is dependent on relatively deep template imaging that can then be applied in difference imaging.

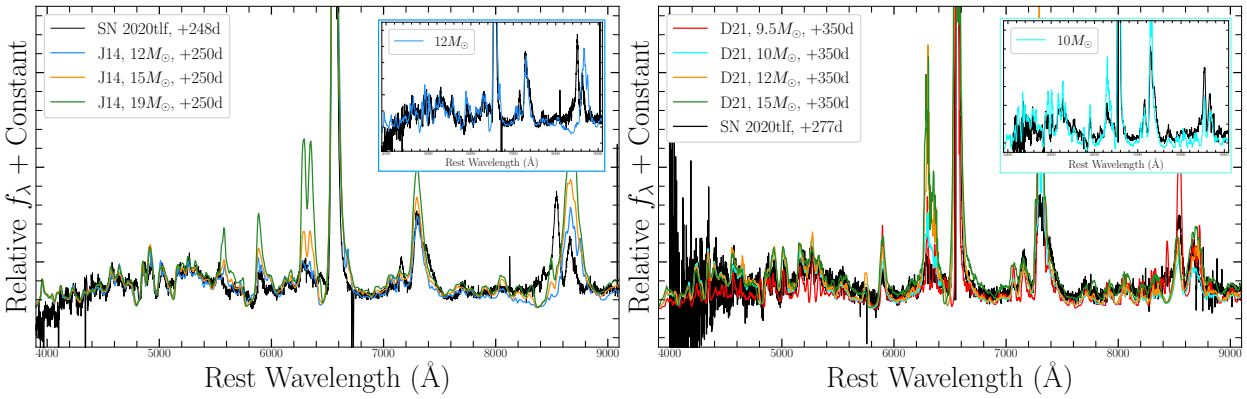

Figure 5.15 *Left:* Nebular spectrum of SN 2020tlf at +248 days post-explosion (black) compared to nebular spectral models at a similar phase from Jerkstrand et al. (2014) for varying progenitor ZAMS masses: 12 $M_\odot$ (blue), 15 $M_\odot$ (orange) and 19 $M_\odot$ (green). The 12 $M_\odot$ ZAMS mass model, shown in upper right panel, is the best match to the nebular SN 2020tlf spectrum at +248 days. *Right:* Nebular models from Dessart et al. (2021) for 9.5 $M_\odot$ (red), 10 $M_\odot$ (cyan), 12 $M_\odot$ (orange) and 15 $M_\odot$ (green) progenitor ZAMS masses with respect to SN 2020tlf at +277 days post-explosion. Here, the 10 $M_\odot$ ZAMS mass model, shown in upper right panel, is the best match to the nebular SN 2020tlf spectrum.

5.8 CSM Constraints from X-ray/Radio Emission

The shock interaction with a dense CSM is a well-known source of X-ray emission (e.g, Chevalier & Fransson 2006). To constrain the parameter space of CSM densities that are consistent with the lack of evidence for X-ray emission at the location of SN2020tlf ($\delta t = 11.0$ – 23.0 days since first light; §5.4.3), we start by generating a grid of intrinsic $n_{\rm H,host}$ values. We then assumed an absorbed bremsstrahlung spectrum with $T = 20$ keV, in analogy to other strongly interacting SNe (e.g. 2014C, Margutti et al. 2017) with different levels of $n_{\rm H,host}$ and converted the upper limit on the observed count-rate into an upper limit on the observed flux F_x using `XSPEC`. The resulting luminosity limits are derived as $L_x = 4\pi D^2 F_x$. We then compare the grid of L_X upper limits to the X-ray luminosities from the analytic formalism presented in Chevalier & Fransson (2006) for free-free emission from reverse-shocked CSM:

$$L_{\rm ff} = 3 \times 10^{35} \frac{(n-3)(n-4)^2}{4(n-2)} \beta^{1/2} \zeta_2^{-1} A_\star^2 t_{10}^{-1} \text{ erg s}^{-1} \tag{5.3}$$

where n is the index of the progenitor outer density profile $\rho(r) \propto r^{-n}$, β is the ratio of electron to equilibrium temperatures (e.g., $T_e/T_{\rm eq}$), ζ is a chemical composition parameter and $\zeta = 1$ for H-rich material, $A_\star$ is a mass loss parameter calibration such that $A_\star = 1$ for $\dot{M} = 10^{-5}$ $M_\odot$ yr^{-1} and $v_w = 1000$ km s^{-1}, and $t_{10} = (t_{\rm exp}/10$ days). For this model, we use $n = 15$ as expected for extended progenitor stars, $\beta = 1$ (equilibrium), and $t_{10} = 2$ (at maximum light) (Chevalier & Fransson 2006). For a given n_H, allowed model X-ray

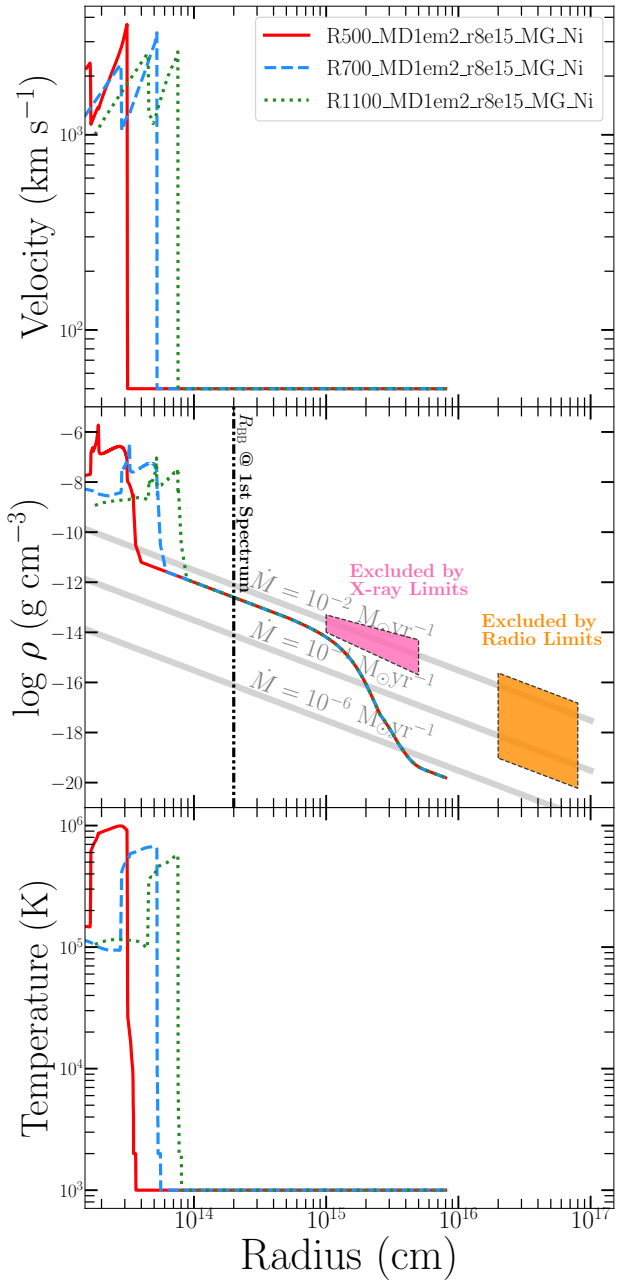

Figure 5.16 Initial stellar structure and circumstellar environment at a few 1000s before shock breakout for the three most consistent models: 500 $R_\odot$ (solid red line), 700 $R_\odot$ (dashed blue line) and 1100 $R_\odot$ (dotted green line). In middle panel, lines of constant mass loss are shown for $v_w = 50$ km s^{-1}. Regions of density parameter space excluded by X-ray and radio limits shown in pink and orange, respectively. Blackbody radius as derived from first spectrum shown as black line.

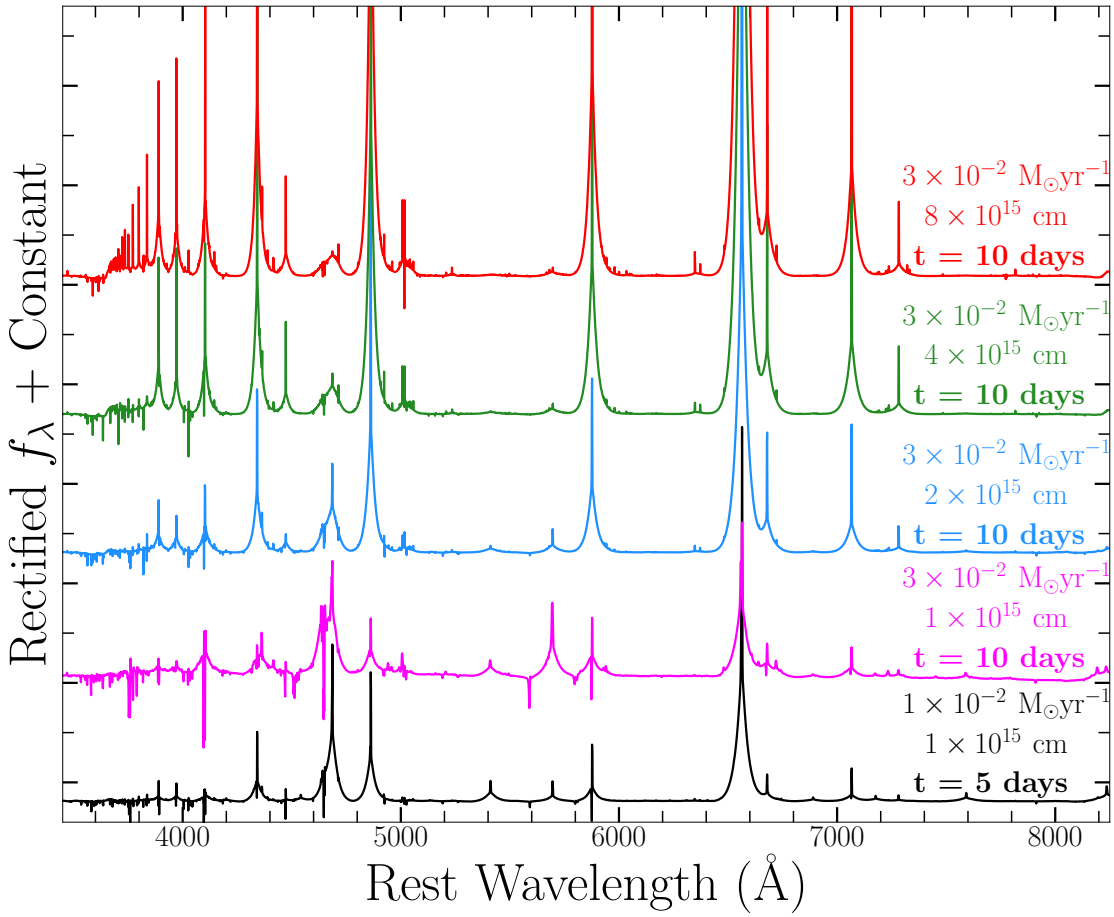

Figure 5.17 Comparison of early-time `CMFGEN` model spectra for varying CSM radius extent and wind mass loss rates. Spectra shown in red ($r_{\rm CSM} = 8 \times 10^{15}$ cm), green ($r_{\rm CSM} = 4 \times 10^{15}$ cm), blue ($r_{\rm CSM} = 2 \times 10^{15}$ cm), and magenta ($r_{\rm CSM} = 1 \times 10^{15}$ cm) include a mass loss rate of $\dot{M} = 0.03$ M$_\odot$ yr^{-1} and phase of +10 day. Model shown in black includes $\dot{M} = 0.01$ M$_\odot$ yr^{-1} and $r_{\rm CSM} = 1 \times 10^{15}$ cm at a phase of +5 day.

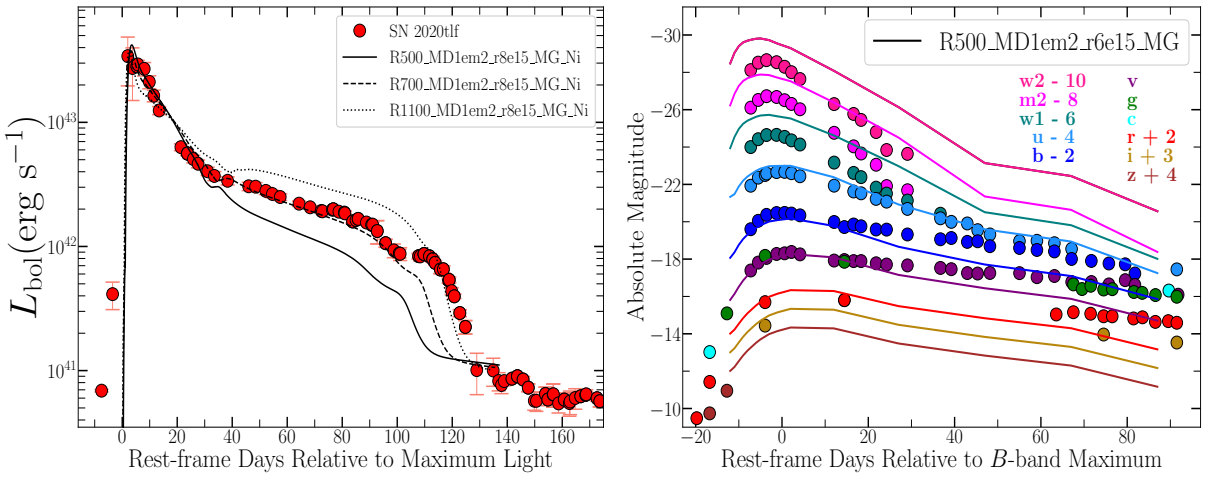

(a) (b)

Figure 5.18 (a) Bolometric light curve models shown in black for CSM that extends to $r = 8 \times 10^{15}$ cm around 15 $M_\odot$ progenitor ($\dot{M} = 0.01$ $M_\odot$ yr^{-1}) of varying envelope radii: 501 $R_\odot$ (solid line), 768 $R_\odot$ (dashed line) and 1107 $R_\odot$ (dotted line). Despite the imperfect match to the complete bolometric evolution, the most extended progenitor model ($R_\star = 1107$ $R_\odot$) is the only simulation that can reproduce the elongated light curve plateau observed in SN 2020tlf. (b) Multi-band, early-time light curve model for extended CSM ($r = 6 \times 10^{15}$ cm) and mass loss rate of $\dot{M} = 0.01$ $M_\odot$ yr^{-1}. Models do not extend in time to the phases of the earliest SN 2020tlf photometry given the low luminosity of multi-band SN detections show above (e.g., $\delta < -15$ days relative to maximum).

model luminosities must be less than the flux limit derived from the stacked XRT image and the specific n_H value must be less than that derived from the model $A_\star$ value e.g., $n_H = 1000 \cdot A_\star/(4\pi R v_w^2 m_p)$ for $R = (1-5) \times 10^{15}$ cm and $v_w = 50$ km s^{-1}. All X-ray luminosities that satisfy these conditions are used to find the resulting $A_\star$ values that are then converted into a range of $\dot{M}$ that are permitted by the observed luminosity limit. We then find an allowed range of progenitor mass loss rates of $\dot{M} < 0.001$ $M_\odot$ yr^{-1} or $\dot{M} > 0.02 - 0.08$ $M_\odot$ yr^{-1}, for $v_w = 50$ km s^{-1}. Furthermore, we convert these mass loss limits into limits on the CSM density at radius $r \approx (1-5) \times 10^{15}$ cm (positions of shock at peak, traveling at $\sim 0.03 - 0.1c$) and present them in Figure 5.16.

We interpret the radio upper limits of §5.4.4 ($\delta t = 146 - 320$ days since first light) in the context of synchrotron emission from electrons accelerated to relativistic speeds at the explosion's forward shock, as the SN shock expands into the medium. We adopt the synchrotron self-absorption (SSA) formalism by Chevalier (1998) and we self-consistently account for free-free absorption (FFA) following Weiler et al. (2002). For the calculation of the free-free optical depth $\tau_{\rm ff}(\nu)$, we adopt a wind-like density profile $\rho_{\rm csm} \propto r^{-2}$ in front of the shock, and we conservatively assume a gas temperature $T = 10^4$ K (higher gas temperatures would lead

to tighter density constraints). The resulting SSA+FFA synchrotron spectral energy distribution depends on the radius of the emitting region, the magnetic field, the environment density and on the shock microphysical parameters ϵ_B and ϵ_e (i.e. the fraction of post-shock energy density in magnetic fields and relativistic electrons, respectively). Additional details on these calculations can be found in the Appendix of Terreran et al. (2022).

We find that for a typical shock velocity of $\sim 0.1c$ (Chevalier & Fransson 2006) and microphysical parameters $\epsilon_B = 0.1$ and $\epsilon_e = 0.1$, the lack of detectable radio emission is consistent with either a low-density medium with density corresponding to $\dot{M} < 1.3 \times 10^{-5}\,\mathrm{M_\odot\,yr^{-1}}$, or a higher density medium with $\dot{M} > 0.032\,\mathrm{M_\odot\,yr^{-1}}$ that would absorb the emission (e.g., $\rho = \dot{M} R_{\rm CSM} v_w^{-1} V^{-1}$). However, this high density limit is excluded based on the optical photometry and spectroscopy. These $\dot{M}$ values are for a wind velocity $v_w = 50\,\mathrm{km\,s^{-1}}$ and CSM radii of $r_w = (2-8) \times 10^{16}$ cm. We present these limits as excluded regions of the SN 2020tlf CSM density parameter space in Figure 5.16. These derived mass loss rates suggest a confined, dense CSM around the SN 2020tlf progenitor star from enhanced mass loss in the final months-to-year before explosion, as well as more diffuse, lower density material extending out to large radii, suggestive of a steady-state RSG wind. The $\dot{M}$ values inferred from radio and X-ray observations are also consistent with other photo-ionization events with multi-wavelength observations e.g., SNe 2013fs (Yaron et al. 2017) and 2020pni (Terreran et al. 2022).

5.9 Discussion

5.9.1 A Physical Progenitor Model

Pre- and post-explosion panchromatic observations have provided an unprecedented picture of the SN 2020tlf progenitor system. In Figure 5.20, we attempt to combine inferences made from observation and modeling to create a visualization of the explosion and surrounding progenitor environment. Our model is a snapshot of the SN at the time of first light and contains physical scales and parameters such as distance, velocity and composition estimates. The illustration also includes progenitor properties derived from precursor emission in the ∼130 days leading up to SBO.

As discussed in §8.5, `CMFGEN` modeling of the SN 2020tlf light curve and photo-ionization spectrum indicate that the 10-12 $\mathrm{M_\odot}$ (ZAMS e.g., see §8.4.2) progenitor star had radius of ∼1100 $\mathrm{R_\odot}$ and was losing mass at an enhanced rate of $\dot{M} = 10^{-2}\,\mathrm{M_\odot\,yr^{-1}}$ in the final months before explosion, leading to the creation of dense CSM (shown in sea foam green; Fig. 5.20) at distances $r \lesssim 10^{15}$ cm; lower density CSM extended out to $r \approx 8 \times 10^{15}$ cm. These models suggest that the SN 2020tlf progenitor star had a total CSM mass of $\sim 0.05 - 0.07$ $\mathrm{M_\odot}$ in the local environment at the time of explosion. At the time of the photo-ionization spectrum ($\delta t \approx 10$ days post-explosion), SN 2020tlf had a blackbody temperature $T \approx 3.7 \times 10^4$ K at the thermalization depth and an emitting radius of $\sim 2 \times 10^{14}$ cm (shown in light blue; Fig. 5.20). The identification of narrow emission lines from photo-ionized material in the earliest

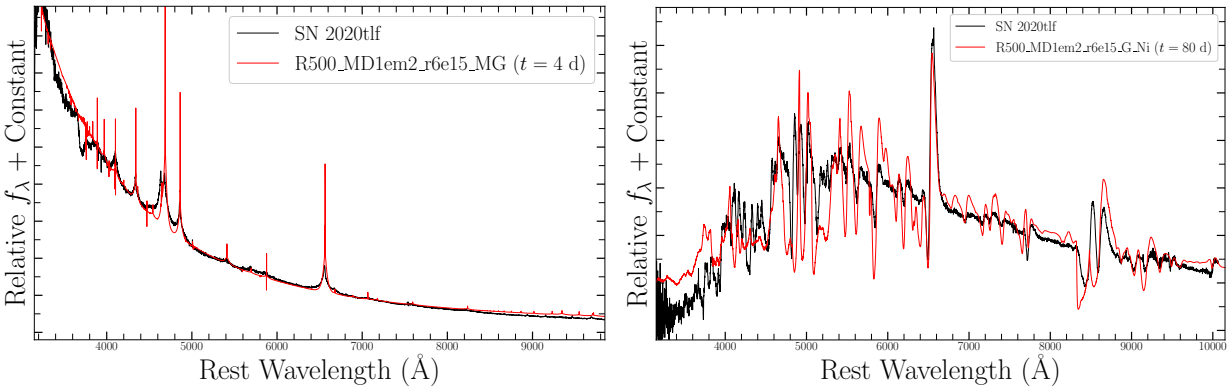

(a) (b)

Figure 5.19 (a) Early-time, LRIS photo-ionization spectrum of SN 2020tlf (black) compared to CMFGEN CSM interaction model (red) at +4 days after model first light. Model CSM that extends to $r = 6 \times 10^{15}$ cm around 15 $M_\odot$ progenitor ($\dot{M} = 0.01$ $M_\odot$ yr^{-1}). (b) Mid-time CMFGEN model spectrum at +80 days after model first light with gray variant solver and with ^{56}Ni included.

spectrum confirms that the CSM was comprised of high-ionization species such as He II, N III and C III–IV, as well as lower ionization species such as H I and He I. As observed in the photo-ionization spectrum, the wind velocity of the CSM is likely $v_w \approx 50 - 200$ km s^{-1}.

Prior to explosion, the SN 2020tlf progenitor star produced detectable precursor emission for ∼130 days prior to SBO. The observed emission is relatively constant leading up to explosion ($\sim 10^{40}$ erg s^{-1}), with an average emission radius and temperature of $\sim 10^{14}$ cm and ∼5000 K, respectively (shown in red; Fig. 5.20). Because the blackbody radius rate of change during the pre-SN activity is ~ 1000 $R_\odot$ over a timescale of ~ 30 days, it is likely that the observed pre-SN emission is not derived from the stellar surface; the Kelvin-Helmholtz timescale for a ~ 10 $M_\odot$ progenitor to change in radius at this rate is $\tau_{th} \gtrsim 200$ days. As discussed in §5.6.4, this precursor emission could have resulted from the ejection, and subsequent CSM interaction, of > 0.3 $M_\odot$ of stellar material that was most local to the progenitor star (shown in dark blue; Fig. 5.20). However, this estimated mass of precursor material is larger than the CSM mass of $\sim 0.05 - 0.07$ $M_\odot$ in the most consistent CMFGEN models. There is also a possibility that the precursor emission arose from a super-Eddington wind that drove off $> 10^{-3}$ $M_\odot$. However, this mass loss mechanism may be unphysical for the low mass progenitor of SN 2020tlf.

An open question in understanding the pre-explosion activity of the SN 2020tlf progenitor star is whether material ejected in the detected precursor is the same CSM responsible for the photo-ionization spectrum at ~ 10 days post-explosion. The validity of this conclusion is dependent on what wind velocity we adopt in the range of possible CSM velocities ($\sim 50 - 200$ km s^{-1}) derived in §8.4.2. If the precursor material was ejected with a velocity of $v_w \approx 50 - 200$ km s^{-1}, that specific CSM could reach radii of $r \approx (0.6 - 2.4) \times 10^{14}$ cm in

the $\sim$ 140 days before the photo-ionization spectrum was obtained. However, if the material was driven off from the surface of a progenitor star with an extended radius of $\sim$1100 $R_\odot$, the distance reached by this material in $\sim$ 140 days increases to $r \approx (1.4 - 3.2) \times 10^{14}$ cm. These distances are consistent with the blackbody radius of $\sim 2 \times 10^{14}$ cm at the time of the photo-ionization spectrum. Therefore, unless the wind velocities are < 50 km s^{-1}, it is feasible that the material driven off to cause the precursor emission is the same CSM material that was photo-ionized by the SN shock wave, resulting in the narrow emission lines present in the early-time spectrum.

5.9.2 Progenitor Mass Loss Mechanisms

The detection of precursor emission, combined with the presence of dense CSM (e.g., see §8.5) around the $\sim$10-12 $M_\odot$ progenitor of SN 2020tlf necessitates a physical mechanism for enhanced mass loss and luminosity, together with a likely structural change to the stellar envelope (inflation), in the final year to months before core collapse. As shown in §5.6.4, powering the precursor emission would require > 0.3 $M_\odot$ of material through CSM interaction and $> 10^{-3}$ $M_\odot$ of material via a super-Eddington wind, the latter of which is much smaller than the CSM mass derived from light curve and spectral modeling (e.g., §8.5). However, a super-Eddington wind is most likely unphysical given the small progenitor ZAMS mass derived from the nebular spectra; it will also lead to larger CSM densities than those derived from modeling (§8.5). Therefore, in the final $\sim$year of stellar evolution, a physical mechanism is needed to produce enhanced mass loss (e.g., 0.01 $M_\odot$ yr^{-1} derived from modeling) and detectable precursor flux.

As discussed initially in §5.6.4, wave-driven mass loss is one process that occurs in late stage stellar evolution that could lead to the ejection of material from the progenitor surface, also resulting in detectable pre-explosion emission. The excitation of gravity waves by oxygen or neon burning in the final years before SN can allow for the injection of energy (e.g., $\sim 10^{46-48}$ erg) into the outer stellar layers, resulting in an inflated envelope and/or eruptive mass loss episodes (Meakin & Arnett 2007; Arnett et al. 2009; Quataert & Shiode 2012; Shiode & Quataert 2014; Fuller 2017; Wu & Fuller 2021). While this mass loss mechanism is a potential explanation for the precursor activity in SN 2020tlf, there are currently no wave-driven models that can match the observed pre-explosion activity. As shown in Figure 5.13(b), the model for a 15$M_\odot$ RSG undergoing wave-driven mass loss by Fuller (2017) does not reproduce the bolometric luminosities of the SN 2020tlf precursor, but is consistent in radius in the final $\sim$130 days before core-collapse. In an updated study of wave-driven models, Wu & Fuller (2021) show that pronounced pre-SN outbursts could occur in progenitor stars of similar mass to that of SN 2020tlf (e.g., < 14 $M_\odot$). However, the timescales of these mass loss episodes are inconsistent with relatively constant emission observed in the SN 2020tlf precursor in the final $\sim$ 130 days before explosion.

A related, promising explanation for enhanced mass loss is the sudden deposition of energy into the internal layers of a massive star outlined by Dessart et al. (2010). Agnostic to the mechanism for energy injection, these models show that a release of energy ($E_{\rm dep}$)

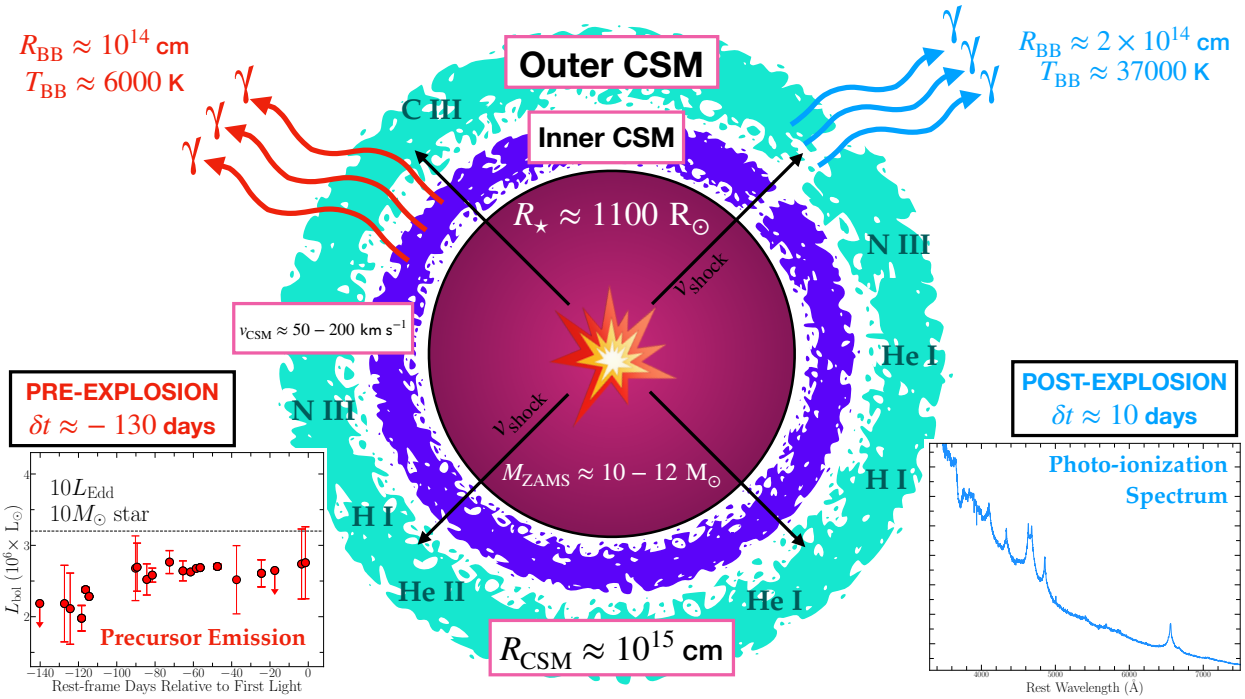

Figure 5.20 Visual representation of SN 2020tlf's progenitor system at the time of explosion (§5.9.1). Here, the SN shock breaks out from an extended H-rich envelope of a 10-12 $M_\odot$ RSG progenitor star and collides with dense CSM ($r \sim 10^{15}$ cm, $v_w \approx 50 - 200$ km s^{-1}), inducing photo-ionized spectral lines observed in the earliest SN spectrum (shown in blue). Precursor emission was detected for ~ 130 days prior to explosion (shown in red) due to the ejection of stellar material. For slower wind velocities ($v - w \lesssim 50$ km s^{-1}), outer CSM (cyan circle) represents the material ejected prior to the precursor ejection of inner CSM (dark blue circle). However, material driven off in the pre-SN activity could be the same material as is visible in the photo-ionization spectrum for wind velocities of $v_w \approx 50 - 200$ km s^{-1}.

that is on the order of the binding energy of the stellar envelope ($E_{\rm bind}$) will create a shock front that will propagate outwards, causing a partial ejection of the stellar envelope. As shown in Figures 8 & 9 in Dessart et al. (2010) for an 11 $M_\odot$ progenitor, energy injection of $E_{\rm dep} \sim E_{\rm bind}$ will produce a detectable pre-SN outburst that is continuous for hundreds of days and matches the observable in the SN 2020tlf precursor e.g., $L \approx 10^6$ $L_\odot$, $T \approx 5000$ K and $R \approx 1500$ $R_\odot$. Possible causes for such energy release could be gravity waves from neon/oxygen burning or even a silicon-flash in the final 100-200 days before explosion. For the latter, Woosley & Heger (2015) show that low mass progenitors (9-11 $M_\odot$) can produce precursor emission in the final $\sim$ year before explosion as a result of silicon deflagration in their cores. Specifically, the 10.0C progenitor model listed in Table 3 of Woosley & Heger (2015) has consistent pre-SN properties to that observed in the SN 2020tlf precursor e.g., $L \approx 10^{40}$ erg s^{-1}, $R \approx 10^{14}$ cm. Overall, the simulations from both of these studies are promising scenarios to explain the enhanced mass loss observed in SN 2020tlf.

5.9.3 Pre-Explosion Variability in SN II Progenitors

SN 2020tlf represents the first instance of a SN II where significant variability has been detected in the RSG progenitor star prior to explosion. These observations reveal a clear disjuncture from the findings by other studies that examined the pre-SN activity of SN II progenitors in the final years before core-collapse. For example, the progenitor behavior prior to SN II-P, 2017eaw has been studied extensively using pre-explosion UV/optical/IR imaging in the final decades before explosion (Kilpatrick & Foley 2018; Rui et al. 2019; Tinyanont et al. 2019; Van Dyk et al. 2019). However, the $\sim 11-13$ $M_\odot$ RSG progenitor of SN 2017eaw only reached a luminosity of ~ 4.7 $L_\odot$ prior to explosion (Kilpatrick & Foley 2018), with IR variability estimated to be at most $\Delta\nu L_\nu \approx 5000$ $L_\odot$ (Tinyanont et al. 2019); both of these progenitor luminosity estimates being orders of magnitude lower than the precursor recorded prior to SN 2020tlf. Similar quiescent behavior is also observed in sample studies on the long-term variability of SN II progenitors by Johnson et al. (2018) as well as the single object study of SN II-P, ASASSN-16fq by Kochanek et al. (2017). Based on the findings of the former, the SN 2020tlf progenitor lies in the $< 37\%$ of RSGs that exhibit extended outbursts after O ignition i.e., $\sim 1000-100$ days before explosion, depending on the progenitor mass. Furthermore, Kochanek et al. (2017) and Johnson et al. (2018) both find that these SN II progenitors show very little variability (e.g., $\Delta\nu L_\nu \lesssim 3000$ $L_\odot$) for years-to-days before core-collapse. Interesting, none of these SNe II showed spectroscopic evidence of interaction with CSM shed by the progenitor during episodes of enhanced mass loss, as detected directly in the earliest spectrum of SN 2020tlf. This may indicate that only RSG progenitors with CSM that is dense enough to be detectable in early-time spectra of young SNe II are also able to produce luminous precursor emission of $\sim 10^6$ $L_\odot$, as observed prior to SN 2020tlf.

5.10 Conclusions

In this paper we have presented pre- and post-explosion (-130 to +300 days) panchromatic observations of the nearby SN II, 2020tlf located in the star-forming SAcd-type galaxy NGC 5731 at $d \approx 36.8$ Mpc. Our observations and modeling cover the electromagnetic spectrum from the X-rays to the radio band, specifically high cadence coverage in UV/optical/NIR. Future studies (e.g., "Final Moments II–") will focus on samples of 20tlf-like events in order to constrain the late-stage evolution of RSG progenitors through pre-SN emission and "flash" spectroscopy. Below we summarize the primary observational findings that make SN 2020tlf one of the most intriguing SNe II to date:

- SN 2020tlf is the first normal SN II-P/L with confirmed precursor emission for $\sim$ 130 days prior to first light. Pre-explosion activity was detected in riz-band YSE/PS1 filters, which showed an average pre-SN bolometric luminosity, blackbody radius and temperature of $\sim 10^{40}$ erg s^{-1} ($\sim 2 \times 10^6$ L$_\odot$), $\sim 10^{14}$ cm (~ 1500 R$_\odot$), and ~ 5000 K, respectively.

- The early-time optical spectrum of SN 2020tlf is nearly identical to the earliest spectra of SN 1998S and includes most of the same narrow, IIn-like emission features. Following classification, SN 2020tlf evolved into a normal SN II-P/L with an extended and luminous plateau light curve phase and strong P-Cygni Hα emission in its spectra.

- Early-time spectroscopic observations of SN 2020tlf revealed prominent narrow emission lines from the photo-ionization of dense CSM shed in enhanced mass loss episodes in the final months before explosion.

- The nebular spectrum of SN 2020tlf is compatible with a 10-12 M$_\odot$ ZAMS mass RSG star. The weak [O I] λ6300 line flux robustly rejects a higher mass progenitor.

- Early-time ($\delta t < 10$ days) *Swift*-XRT non-detections in SN 2020tlf suggest complete absorption of thermal bremsstrahlung X-ray emission by the most local CSM. At larger radii of $r \approx (1-5) \times 10^{15}$ cm, X-ray limits indicate a low density medium ($\rho \lesssim (4-0.2) \times 10^{-15}$ g cm^{-3}, respectively) incapable of producing detectable X-ray emission. For more distant CSM at $r = (2-8) \times 10^{16}$ cm, radio non-detections reveal a limit on the progenitor mass loss rate of $\dot{M} < 1.3 \times 10^{-5}$ M$_\odot$ yr^{-1}.

- Light curve and spectral modeling with `CMFGEN` supports an extended progenitor star at the time of explosion with radius $R_\star \approx 1100$ R$_\odot$, a mass loss rate of $\dot{M} = 0.01$ M$_\odot$ yr^{-1} ($v_w = 50$ km s^{-1}) resulting in dense CSM confined within $r < 10^{15}$ cm. Because of the pre-SN activity, this large progenitor radius may reflect a phase of inflation or expansion prior to core-collapse, concomitant with the phase of enhanced mass loss.

- Given the progenitor mass range derived from nebular spectra, it is likely that the enhanced mass loss and precursor emission is the result of instabilities deeply rooted

in the stellar interior, most likely associated with the final nuclear burning stages. Energy deposition from either gravity waves generated in neon/oxygen burning stages or a silicon flash in the progenitor's final ∼130 days could have ejected stellar material that was then detected in both pre-explosion flux and the early-time SN spectrum.

Based on the novel detection of precursor flux prior to SN 2020tlf, pre-SN emission should be common in SNe II-P/L and has eluded detection until now simply because it is very faint (i.e., below the detection level of most surveys). This statement is supported by the relatively common presence of bright UV emission that dominates the energy release in SNe IIP at early times. As Figure 5.14 shows, LSST, with its improved sensitivity, is uniquely equipped to test our hypothesis and detect pre-SN emission at the level of the pre-SN 2020tlf outburst in newly discovered SNe IIP at $D \lesssim 200$ Mpc.

5.11 Acknowledgements

Research at Northwestern University and CIERA is conducted on the stolen land of the Council of Three Fires, the Ojibwe, Potawatomi, and Odawa people, as well as the Menominee, Miami and Ho-Chunk nations. Research at UC Berkeley is conducted on the territory of Huichin, the ancestral and unceded land of the Chochenyo speaking Ohlone people, the successors of the sovereign Verona Band of Alameda County. Keck I/II, ATLAS, and PS1 observations were conducted on the stolen land of the kānaka ʻōiwi people. We stand in solidarity with the Pu'uhonua o Pu'uhuluhulu Maunakea in their effort to preserve these sacred spaces for native Hawaiʻians. MMT observations were conducted on the stolen land of the Tohono O'odham and Hia-Ced O'odham nations; the Ak-Chin Indian Community, and Hohokam people. ZTF observations were conducted on the stolen land of the Pauma and Cupeño tribes; the Kumeyaay Nation and the Payómkawichum (Luiseño) people. Shane 3-m observations were conducted on the stolen land of the Ohlone (Costanoans), Tamyen and Muwekma Ohlone tribes. VLA observations were conducted on the stolen land of the Chiricahua and Mescalero Apache tribes, and the Pueblo people.

The Young Supernova Experiment and its research infrastructure is supported by the European Research Council under the European Union's Horizon 2020 research and innovation programme (ERC Grant Agreement No. 101002652, PI K. Mandel), the Heising-Simons Foundation (2018-0913, PI R. Foley; 2018-0911, PI R. Margutti), NASA (NNG17PX03C, PI R. Foley), NSF (AST-1720756, AST-1815935, PI R. Foley; AST-1909796, AST-1944985, PI R. Margutti), the David & Lucille Packard Foundation (PI R. Foley), VILLUM FONDEN (project number 16599, PI J. Hjorth), and the Center for AstroPhysical Surveys (CAPS) at the National Center for Supercomputing Applications (NCSA) and the University of Illinois Urbana-Champaign.

We thank Jim Fuller and Samantha Wu for stimulating discussion and RSG models. W.J-G is supported by the National Science Foundation Graduate Research Fellowship Program under Grant No. DGE-1842165 and the IDEAS Fellowship Program at Northwestern University. W.J-G acknowledges support through NASA grants in support of *Hubble Space*

Telescope programs GO-16075 and GO-16500. This research was supported in part by the National Science Foundation under Grant No. NSF PHY-1748958. The Margutti team at UC Berkeley and Northwestern is supported in part by the National Science Foundation under Grant No. AST-1909796 and AST-1944985, by NASA through Award Number 80NSSC20K1575 and by the Heising-Simons Foundation under grant # 2018-0911 (PI: Margutti). Raffaella Margutti is a CIFAR Azrieli Global Scholar in the Gravity & the Extreme Universe Program 2019, and a Sloan Fellow in Physics, 2019.

This work was granted access to the HPC resources of CINES under the allocation 2019 – A0070410554 and 2020 – A0090410554 made by GENCI, France.

MRD acknowledges support from the NSERC through grant RGPIN-2019-06186, the Canada Research Chairs Program, the Canadian Institute for Advanced Research (CIFAR), and the Dunlap Institute at the University of Toronto.

D. A. Coulter acknowledges support from the National Science Foundation Graduate Research Fellowship under Grant DGE1339067. Q.W. acknowledges financial support provided by the STScI Director's Discretionary Fund. M. R. S. is supported by the National Science Foundation Graduate Research Fellowship Program Under Grant No. 1842400. A.G. is supported by the National Science Foundation Graduate Research Fellowship Program under Grant No. DGE–1746047. A.G. also acknowledges funding from the Center for Astrophysical Surveys Fellowship at UIUC/NCSA and the Illinois Distinguished Fellowship. D.O.J is supported by NASA through the NASA Hubble Fellowship grant HF2-51462.001 awarded by the Space Telescope Science Institute, which is operated by the Association of Universities for Research in Astronomy, Inc., for NASA, under contract NAS5-26555. This work was supported by a VILLUM FONDEN Young Investigator Grant to C.G. (project number 25501).

Parts of this research were supported by the Australian Research Council Centre of Excellence for All Sky Astrophysics in 3 Dimensions (ASTRO 3D), through project number CE170100013. This work was supported by a VILLUM FONDEN Investigator grant to J.H. (project number 16599).

The ZTF forced-photometry service was funded under the Heising-Simons Foundation grant #12540303 (PI: Graham).

IRAF is distributed by NOAO, which is operated by AURA, Inc., under cooperative agreement with the National Science Foundation (NSF).

The UCSC team is supported in part by NASA grant 80NSSC20K0953, NSF grant AST-1815935, the Gordon & Betty Moore Foundation, the Heising-Simons Foundation, and by a fellowship from the David and Lucile Packard Foundation to R.J.F.

Some of the data presented herein were obtained at the W. M. Keck Observatory, which is operated as a scientific partnership among the California Institute of Technology, the University of California, and NASA. The Observatory was made possible by the generous financial support of the W. M. Keck Foundation. The authors wish to recognize and acknowledge the very significant cultural role and reverence that the summit of Maunakea has always had within the indigenous Hawaiian community. We are most fortunate to have the opportunity to conduct observations from this mountain. We recognize the destructive

history of colonialism endured by native Hawaiians as we strive to hear the voice of those whose sacred land we continue to utilize for scientific gain.

A major upgrade of the Kast spectrograph on the Shane 3 m telescope at Lick Observatory was made possible through generous gifts from the Heising-Simons Foundation as well as William and Marina Kast. Research at Lick Observatory is partially supported by a generous gift from Google.

The National Radio Astronomy Observatory is a facility of the National Science Foundation operated under cooperative agreement by Associated Universities, Inc.

This work makes use of observations from the Las Cumbres Observatory global telescope network following the approved NOIRLab programs 2020B-0250 and 2021A-0239. Las Cumbres Observatory telescope time was granted by NOIRLab through the Mid-Scale Innovations Program (MSIP). MSIP is funded by NSF.

W. M. Keck Observatory access was supported by Northwestern University and the Center for Interdisciplinary Exploration and Research in Astrophysics (CIERA).

Based in part on observations obtained with the Samuel Oschin 48-inch Telescope at the Palomar Observatory as part of the Zwicky Transient Facility project. ZTF is supported by the NSF under grant AST-1440341 and a collaboration including Caltech, IPAC, the Weizmann Institute for Science, the Oskar Klein Center at Stockholm University, the University of Maryland, the University of Washington, Deutsches Elektronen-Synchrotron and Humboldt University, Los Alamos National Laboratories, the TANGO Consortium of Taiwan, the University of Wisconsin at Milwaukee, and the Lawrence Berkeley National Laboratory. Operations are conducted by the Caltech Optical Observatories (COO), the Infrared Processing and Analysis Center (IPAC), and the University of Washington (UW).

This work has made use of data from the Asteroid Terrestrial-impact Last Alert System (ATLAS) project. The Asteroid Terrestrial-impact Last Alert System (ATLAS) project is primarily funded to search for near earth asteroids through NASA grants NN12AR55G, 80NSSC18K0284, and 80NSSC18K1575; byproducts of the NEO search include images and catalogs from the survey area. This work was partially funded by Kepler/K2 grant J1944/80NSSC19K0112 and HST GO-15889, and STFC grants ST/T000198/1 and ST/S006109/1. The ATLAS science products have been made possible through the contributions of the University of Hawaii Institute for Astronomy, the Queen's University Belfast, the Space Telescope Science Institute, the South African Astronomical Observatory, and The Millennium Institute of Astrophysics (MAS), Chile.

The Pan-STARRS1 Surveys (PS1) and the PS1 public science archive have been made possible through contributions by the Institute for Astronomy, the University of Hawaii, the Pan-STARRS Project Office, the Max-Planck Society and its participating institutes, the Max Planck Institute for Astronomy, Heidelberg and the Max Planck Institute for Extraterrestrial Physics, Garching, The Johns Hopkins University, Durham University, the University of Edinburgh, the Queen's University Belfast, the Harvard-Smithsonian Center for Astrophysics, the Las Cumbres Observatory Global Telescope Network Incorporated, the National Central University of Taiwan, STScI, NASA under grant NNX08AR22G issued through the Planetary Science Division of the NASA Science Mission Directorate, NSF

grant AST-1238877, the University of Maryland, Eotvos Lorand University (ELTE), the Los Alamos National Laboratory, and the Gordon and Betty Moore Foundation.

This publication has made use of data collected at Lulin Observatory, partly supported by MoST grant 108-2112-M-008-001.

5.12 Appendix

5.12.1 Refinement of Pre-SN Detection Algorithm

Here we present an updated procedure for detecting pre-SN emission in Pan-STARRS images taken through the YSE transient survey. This process has been employed successfully in recent and forthcoming publications (e.g., Ransome et al. 2024; Taggart et al. 2024, in prep). Similar to the procedure described in §5.3.1, we construct control light curves of the host-galaxy emission, this time placing apertures along an isophotal contour rather than just an isophotal ellipse, avoiding the SN location itself. Photometry is then calculated in each difference image at each background aperture location and the SN position. We then perform an idealized fake source injection where increasing amounts of discrete counts are added to the photometric measurement of each chosen aperture until the flux to error ratio is greater than three (i.e., 3σ detection). We use the fraction of apertures where the injected source is recovered at $> 3\sigma$ significance to estimate the recovery fraction as a function of the injected source flux. We note that this injection method yields consistent results to more robust fake source injection within the science images during the `Photpipe` reduction (see Section 2.1 of Ransome et al. 2024 for a more detailed discussion of the routine). However, the injection of fake sources during the photometric reduction itself is significantly slower and computationally intensive. Therefore, because it yields very similar limits on the pre-SN emission, we adopt the idealized fake-source injection procedure for our analysis.

In order to determine if a measurement at the SN location is a true detection, we compared the derived limiting magnitude to photometric measurement from `Photpipe` at the SN location and label detection as real if the latter is brighter than the former. We calculate the limiting magnitude based on the flux associated with an 80% recovery fraction in the chosen background apertures i.e., the flux at which $> 80\%$ of the injected sources are recovered at $> 3\sigma$ significance. An 80% recovery level is chosen because this is the point at which we do not generate false positive detections that are expected statistically in standard photometry. The *griz*-band pre-SN light curves of SN 2020tlf, with detections and limiting magnitudes are shown in Figure 5.21. For completeness, we also show pre-SN light curves with 50 and 100 day binning in Figures 5.22 & 5.23, respectively. Difference images of the pre-explosion source at $> 50\%$ and $> 80\%$ detection levels are shown for *griz* bands in Figures 5.25-5.28.

Compared to the initial detection method presented in §5.3.1, the above procedure also recovers detections in *riz*-bands at $\delta t > -100$ days at $> 80\%$ recovery level: 5 in *i*-band, 1 in *r*-band, and 3 in *z*-band. However, the marginal detections at only a 50% recovery level in the updated analysis were originally reported as detections at $\delta t > -130$ days: 4 in *i*-band, 1

in r-band, and 4 in z-band. The photometry derived in this updated method also translates to pre-explosion absolute magnitudes of $M \approx -11.5$ to -12 mag. Similar to the analysis done in §5.6.4, we model the SED of detections and limiting fluxes from the 50 day phase bins using a blackbody model. As shown in Figure 5.24, the pre-explosion ($\delta t > -100$ days) bolometric luminosity is $\sim 10^{40}$ erg s^{-1}, in addition to blackbody radii and temperatures of $\sim 10^{14}$ cm and $\sim 4000-5000$ K, all similar to what is presented in Figure 5.13. Interestingly, the blackbody parameters derived from the SED in the $\delta t = -150$ to -100 day bin suggest a higher bolometric luminosity ($\sim 2 \times 10^{40}$ erg s^{-1} and blackbody radius ($\sim 10^{15}$ cm), but lower temperature (~ 2200 K). However, this model is only constructed during phases with less significant detections and fewer constraints from the r-band flux. Nevertheless, similar to the analysis presented in §5.6.4, the updated analysis confirm rising pre-explosion flux in SN 2020tlf within the last ~ 100 days prior to first light.

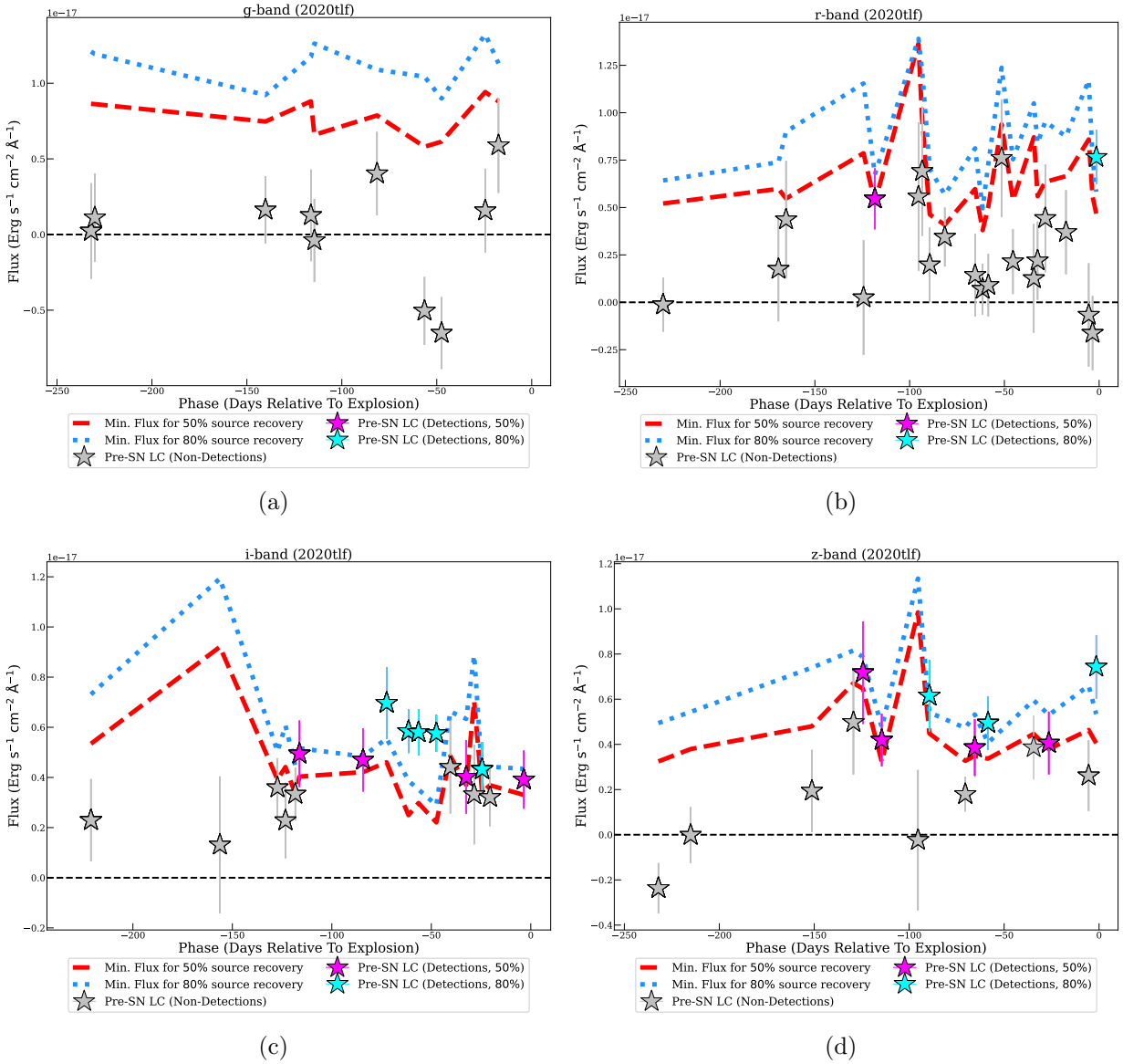

Figure 5.21 Pre-explosion *griz*-band light curve of SN 2020tlf. Detections above 80% and 50% recovery levels shown as cyan and magenta stars, respectively. Calculated flux at the SN location that is below these recovery levels is shown as grey stars. Minimum fluxes for 80% and 50% injected source recovery shown as blue dotted and red dashed lines, respectively.

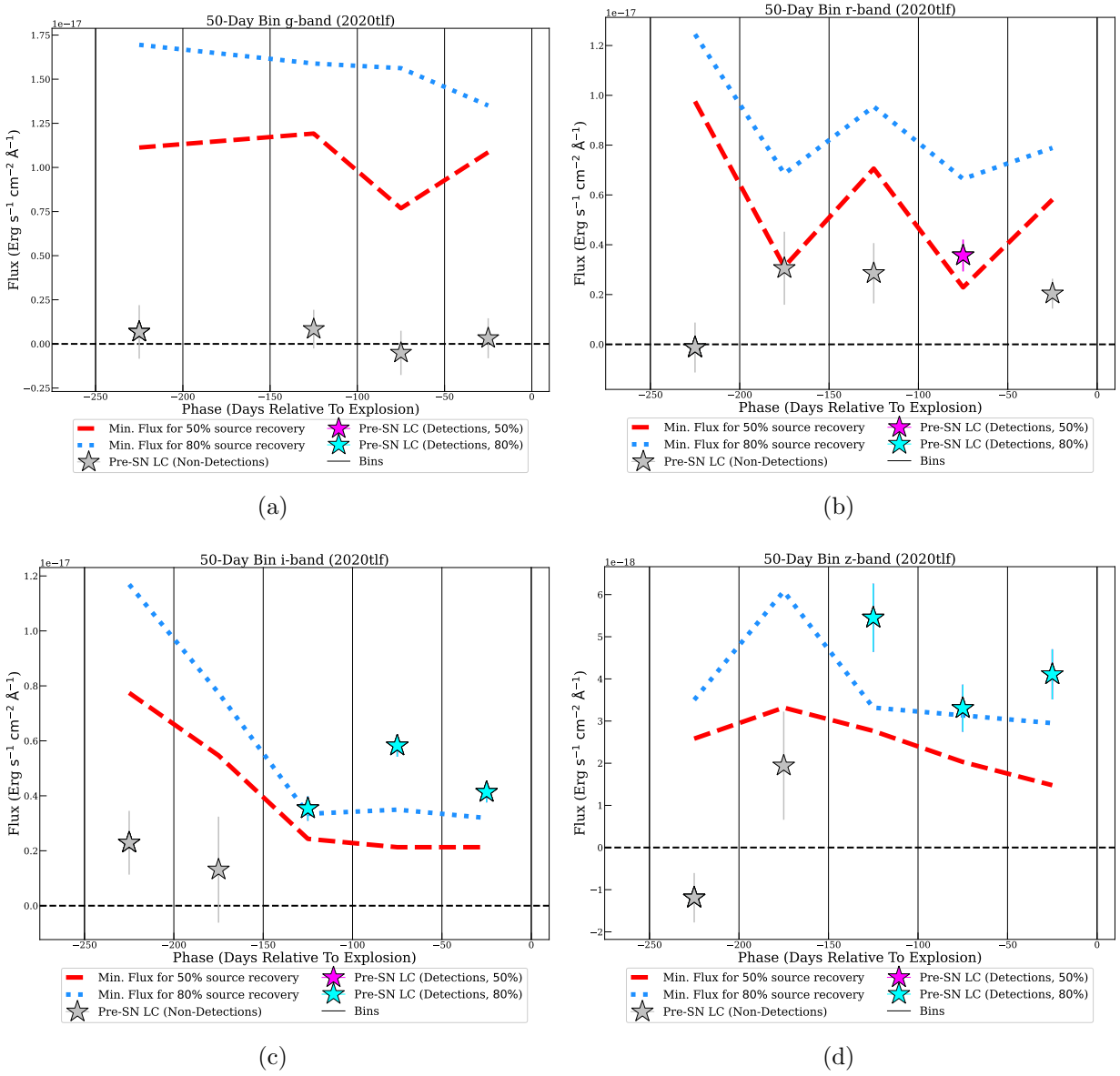

Figure 5.22 Pre-explosion *griz*-band light curve of SN 2020tlf where the flux has been stacked in 50 day bins. Detections above 80% and 50% recovery levels shown as cyan and magenta stars, respectively. Calculated flux at the SN location that is below these recovery levels is shown as grey stars. Minimum fluxes for 80% and 50% injected source recovery shown as blue dotted and red dashed lines, respectively.

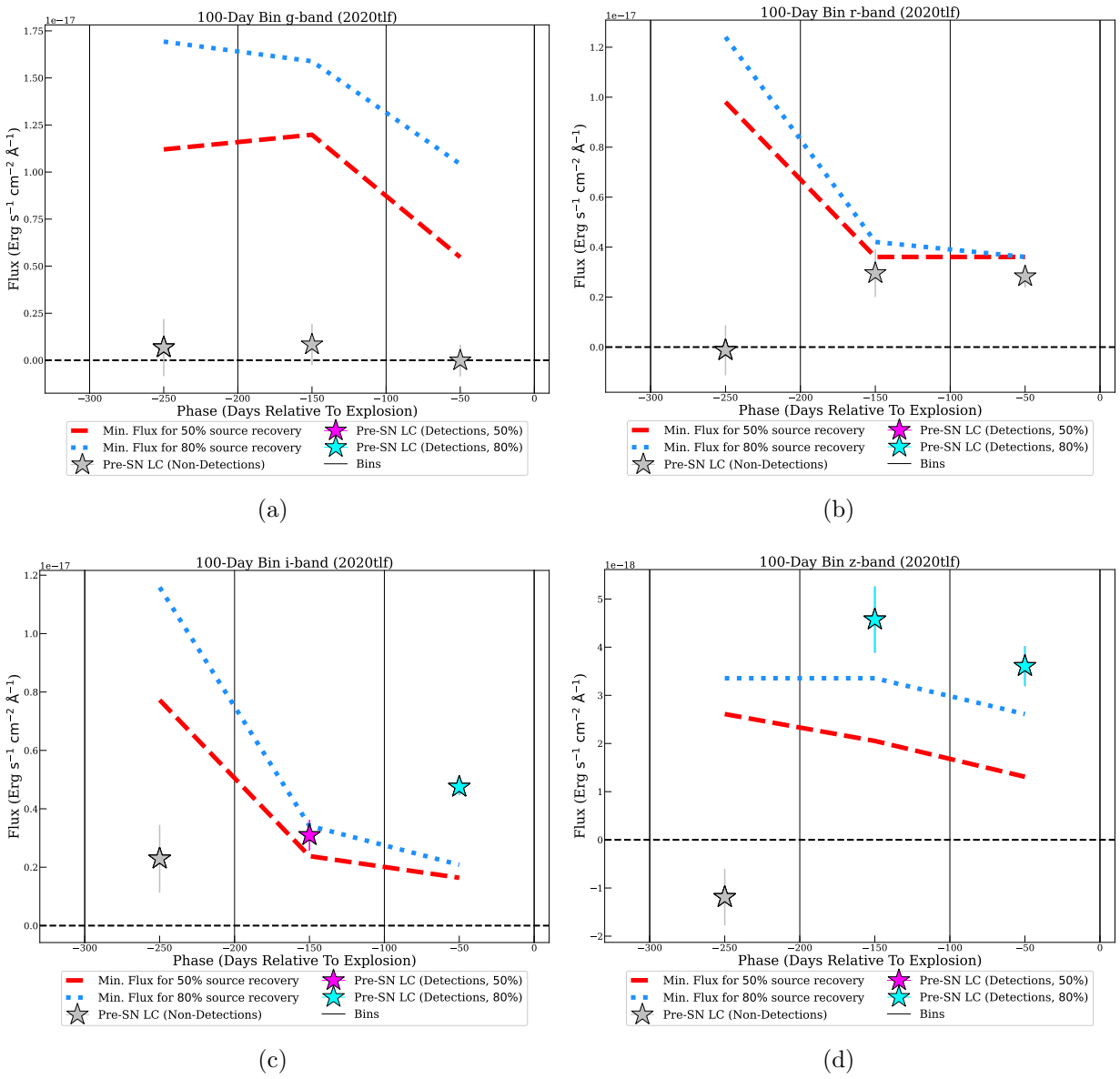

Figure 5.23 Pre-explosion *griz*-band light curve of SN 2020tlf where the flux has been stacked in 100 day bins. Detections above 80% and 50% recovery levels shown as cyan and magenta stars, respectively. Calculated flux at the SN location that is below these recovery levels is shown as grey stars. Minimum fluxes for 80% and 50% injected source recovery shown as blue dotted and red dashed lines, respectively.

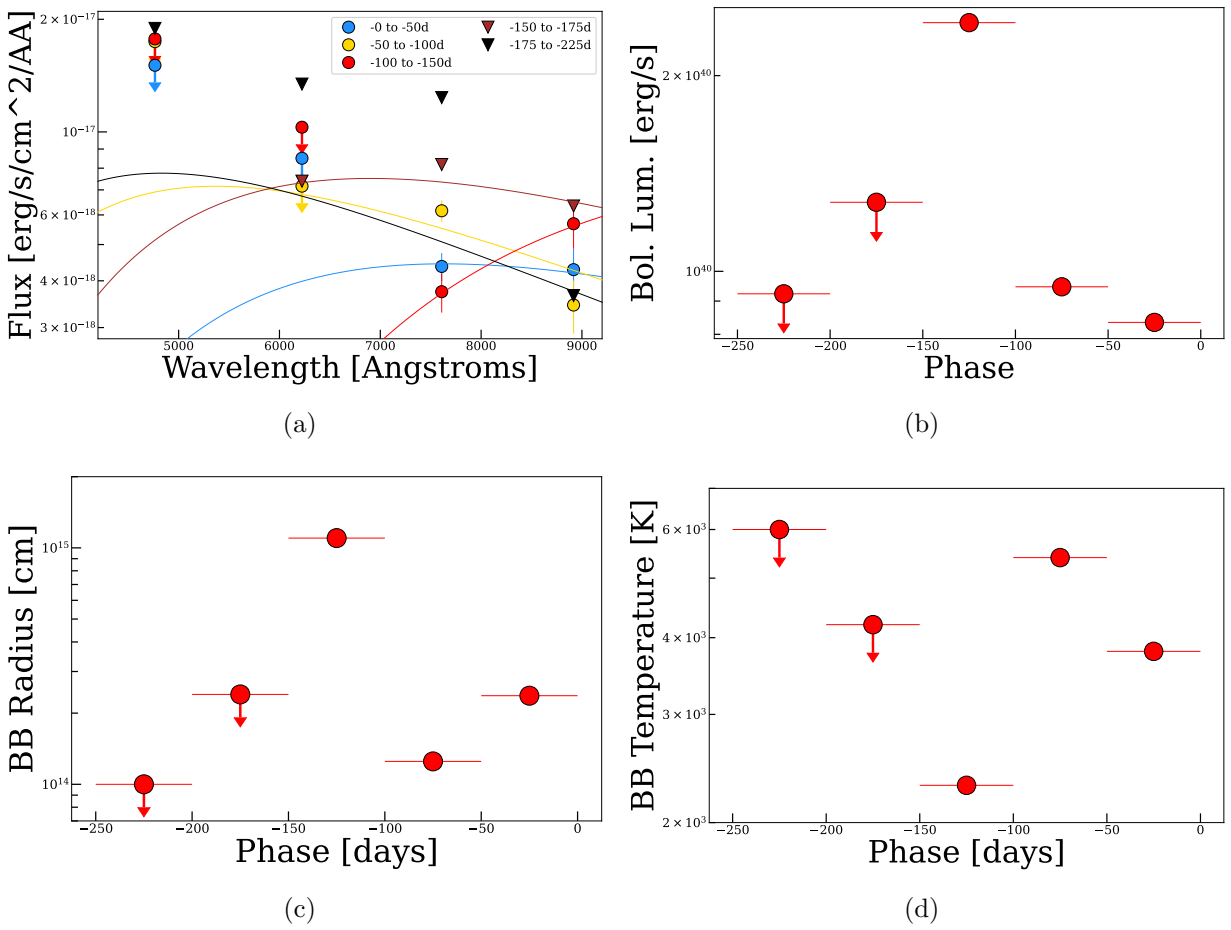

Figure 5.24 (a) Spectral energy distribution using *griz*-band limits and detections in 50 day pre-SN light curve bins. Best-fitting blackbody models shown as solid lines. Pre-explosion (a) bolometric luminosity, (b) blackbody radius, and (c) blackbody temperature as a function of phase. These parameters were derived from blackbody model fits to the 50 day binned SED.

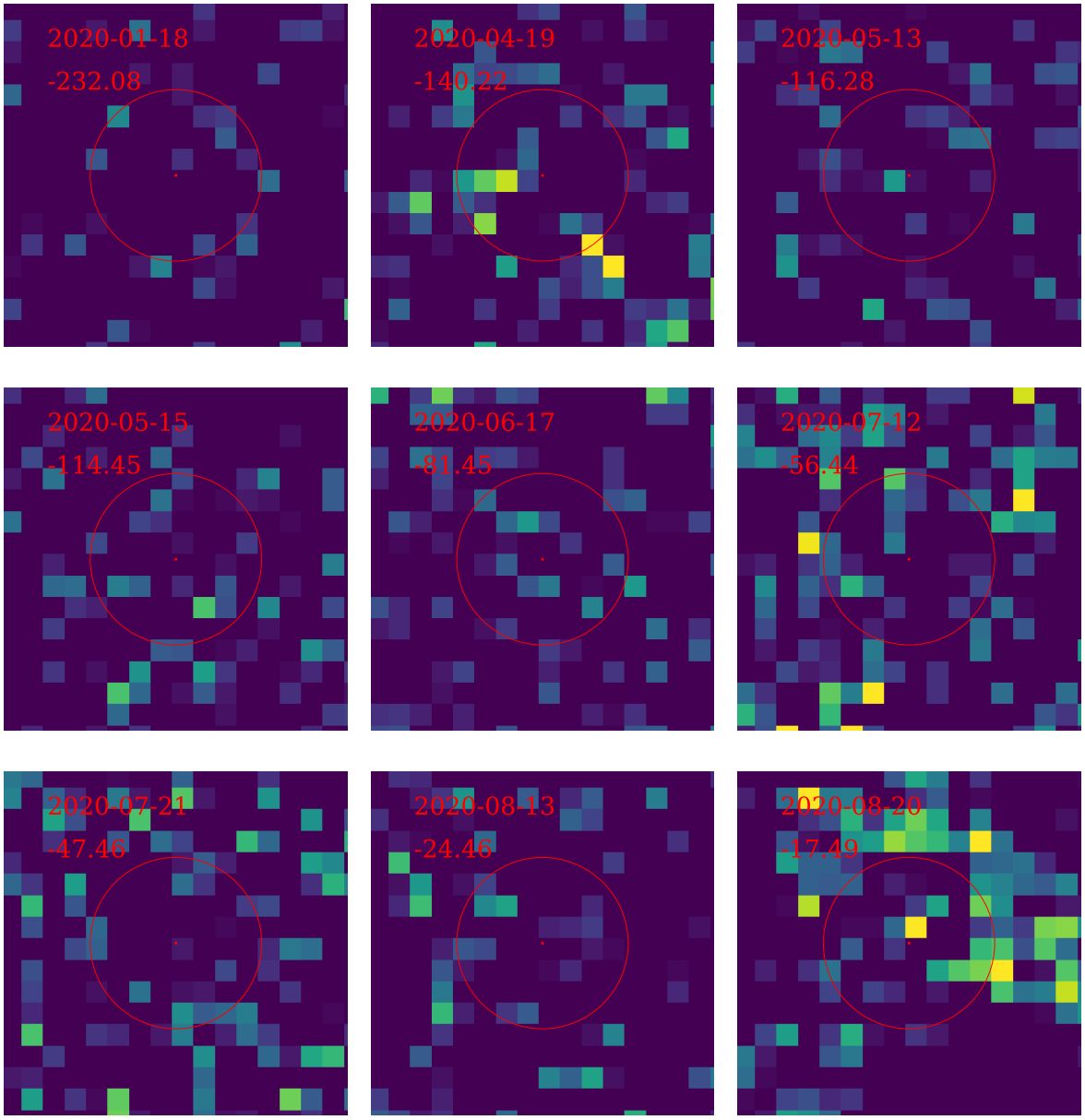

Figure 5.25 Pan-STARRS g-band pre-explosion images of SN 2020tlf. Images with pre-SN emission detected at above 80 and 50% recovery levels labeled with cyan and magenta, respectively.

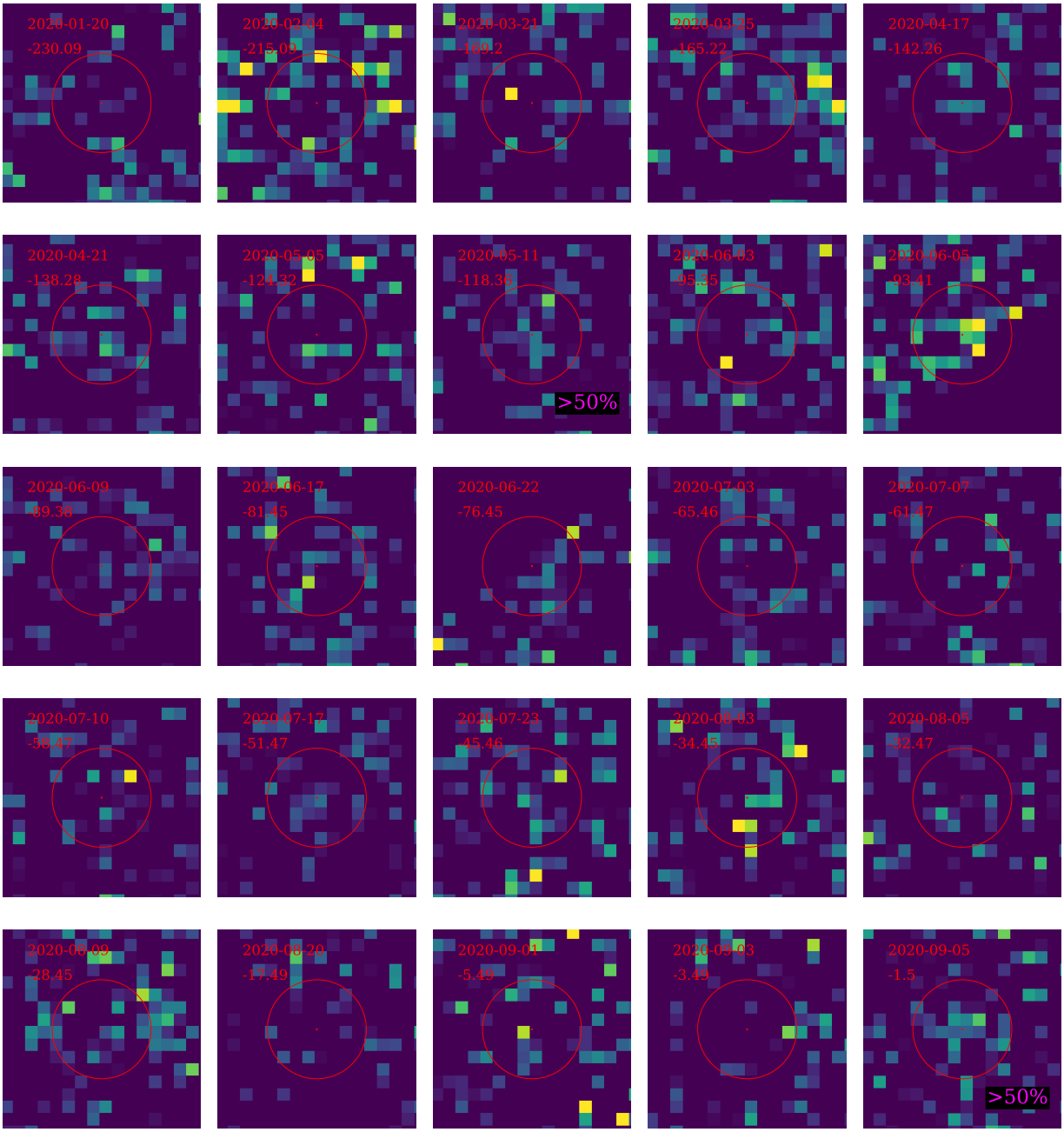

Figure 5.26 Pan-STARRS r-band pre-explosion images of SN 2020tlf. Images with pre-SN emission detected at above 80 and 50% recovery levels labeled with cyan and magenta, respectively.

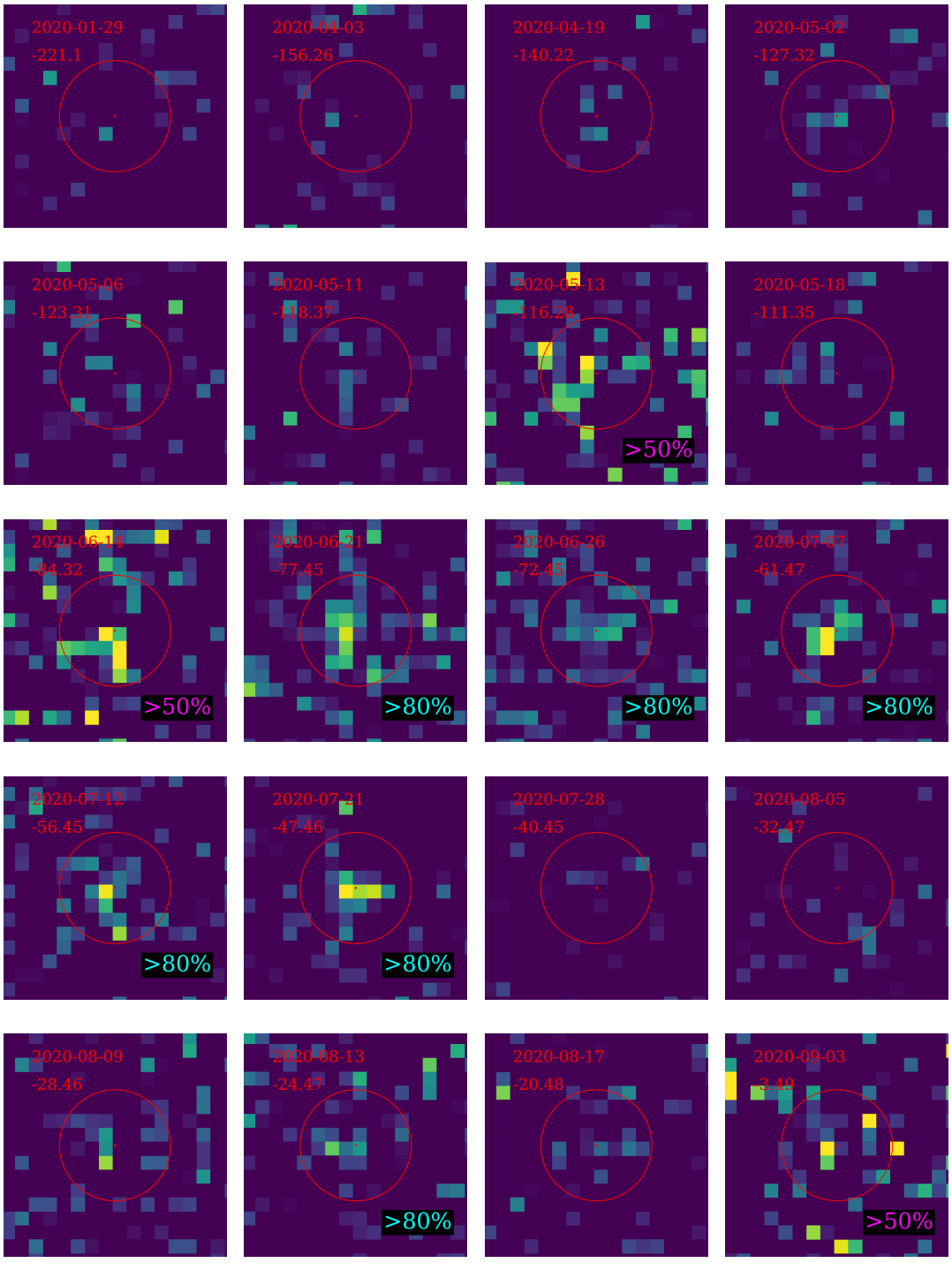

Figure 5.27 Pan-STARRS i-band pre-explosion images of SN 2020tlf. Images with pre-SN emission detected at above 80 and 50% recovery levels labeled with cyan and magenta, respectively.

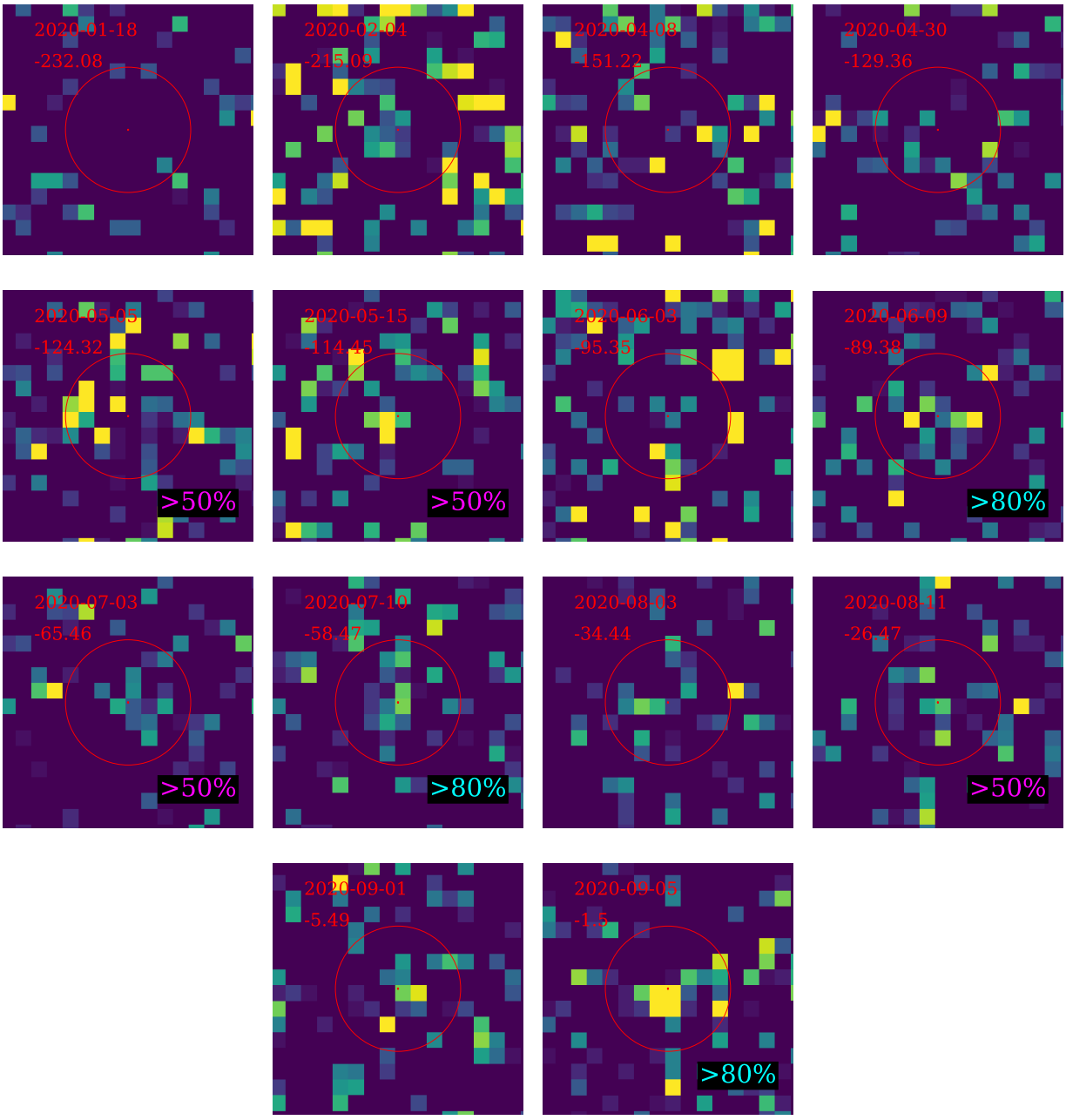

Figure 5.28 Pan-STARRS z-band pre-explosion images of SN 2020tlf. Images with pre-SN emission detected at above 80 and 50% recovery levels labeled with cyan and magenta, respectively.

Table A1. Optical Spectroscopy of SN 2020tlf

UT Date	MJD	Phase[a] (days)	Telescope	Instrument	Wavelength Range (Å)
2020-09-17	59109.0	−8.6	Keck I	LRIS	3200–10800
2020-09-17	59109.1	−8.5	APO 3.5m	DIS	3650–9830
2020-12-11	59194.0	+76.4	Keck I	LRIS	3200–10800
2021-01-11	59225.5	+107.9	Shane	Kast	4000–9200
2021-01-31	59245.0	+127.4	Keck II	NIRES	9500–24500
2021-02-06	59251.5	+133.9	Shane	Kast	4000–9200
2021-04-09	59313.0	+195.4	MMT	Binospec	4000–9200
2021-05-09	59343.0	+225.4	MMT	Binospec	4000–9200
2021-06-10	59375.0	+257.4	Keck II	DEIMOS	3400–10200

[a]Relative to B-band maximum (MJD 59117.6)

Table A2. VLA radio observations of SN 2020tlf (Project SD1096, PI Margutti)

Start Date (UT)	Time[a] (days)	Frequency (GHz)	Bandwidth (GHz)	Flux Density[b] (μJy/beam)
21-Feb-19 12:11:48UT	+146.4	10	4.096	≤ 12
21-May-12 03:27:16UT	+228.7	10	4.096	≤ 72
21-Aug-12 02:11:59UT	+320.7	10	4.096	≤ 42

[a]Relative to $B-$band maximum (MJD 59117.6)

[b]Upper-limits are quoted at 3σ.

Table A3. `CMFGEN` Models

Model Name	ZAMS Mass ($M_\odot$)	Radius ($R_\odot$)	$\dot{M}$ ($M_\odot$ yr^{-1})	$M_{\rm CSM}$ ($M_\odot$)	$r_{\rm CSM}$ (cm)	$M(^{56}{\rm Ni})$ ($M_\odot$)	Gray/Multi-Group
R500_MD1em2_r6e15_MG	15	501	10^{-2}	0.052	6×10^{15}	–	Multi-Group
R500_MD1em2_r6e15_MG_Ni	15	501	10^{-2}	0.052	6×10^{15}	0.02	Multi-Group
R500_MD1em2_r6e15_G_Ni	15	501	10^{-2}	0.052	6×10^{15}	0.02	Gray
R500_MD1em2_r8e15_MG_Ni	15	501	10^{-2}	0.073	8×10^{15}	0.02	Multi-Group
R700_MD1em2_r8e15_MG_Ni	15	768	10^{-2}	0.073	8×10^{15}	0.02	Multi-Group
R1100_MD1em2_r8e15_MG_Ni	15	1107	10^{-2}	0.073	8×10^{15}	0.02	Multi-Group

Note. — Most consistent model to observations includes mass loss of $\dot{M} = 0.01$ $M_\odot$ yr^{-1} and progenitor radius of $R_\star = 1107$ $R_\odot$. Distinction between multi-group and gray variant solvers is discussed in §8.5.

Table A4. Optical Photometry of SN 2020tlf

MJD	Phase[a]	Filter	Magnitude	Uncertainty	Instrument
59104.24	-13.36	g	17.84	0.01	PS1
59220.66	+103.06	g	17.45	0.01	PS1
59226.63	+109.03	g	18.08	0.02	PS1
59236.66	+119.06	g	19.88	0.09	PS1
59257.57	+139.97	g	20.52	0.10	PS1
59261.63	+144.03	g	20.87	0.13	PS1
59313.53	+195.93	g	20.94	0.15	PS1
58980.38	-137.22	r	21.78	0.32	PS1
59097.24	-20.36	r	21.41	0.20	PS1
59100.24	-17.36	r	19.47	0.04	PS1
59226.63	+109.03	r	17.13	0.01	PS1
59242.64	+125.04	r	19.24	0.10	PS1
59244.62	+127.02	r	18.93	0.08	PS1
59245.66	+128.06	r	19.23	0.06	PS1
59246.64	+129.04	r	19.17	0.06	PS1
59261.63	+144.03	r	19.29	0.03	PS1
59270.58	+152.98	r	19.34	0.09	PS1
59298.51	+180.91	r	19.72	0.07	PS1
59304.51	+186.91	r	19.90	0.11	PS1
59313.53	+195.93	r	19.91	0.08	PS1
59328.46	+210.86	r	20.09	0.19	PS1
59331.40	+213.80	r	20.57	0.25	PS1
59333.43	+215.83	r	19.94	0.07	PS1
58971.42	-146.18	i	21.79	0.35	PS1
58980.37	-137.23	i	21.87	0.34	PS1
58982.46	-135.14	i	21.45	0.29	PS1
59014.42	-103.18	i	21.50	0.29	PS1
59026.29	-91.31	i	21.08	0.22	PS1
59037.27	-80.33	i	21.27	0.16	PS1
59042.29	-75.31	i	21.27	0.17	PS1
59051.28	-66.32	i	21.28	0.14	PS1
59061.28	-56.32	i	21.53	0.23	PS1
59074.27	-43.33	i	21.59	0.27	PS1
59095.25	-22.35	i	21.70	0.32	PS1

Table A4 (cont'd)

MJD	Phase[a]	Filter	Magnitude	Uncertainty	Instrument
59236.66	+119.06	i	19.34	0.06	PS1
59242.64	+125.04	i	19.51	0.11	PS1
59245.66	+128.06	i	19.38	0.06	PS1
59257.57	+139.97	i	19.52	0.04	PS1
59270.58	+152.98	i	19.73	0.11	PS1
59303.53	+185.93	i	20.05	0.13	PS1
59317.49	+199.89	i	19.99	0.09	PS1
59326.40	+208.80	i	20.44	0.21	PS1
59351.37	+233.77	i	21.07	0.29	PS1
59391.30	+273.70	i	21.19	0.19	PS1
59398.30	+280.70	i	21.04	0.29	PS1
58974.42	-143.18	z	20.70	0.34	PS1
58984.29	-133.31	z	21.28	0.30	PS1
59009.36	-108.24	z	20.87	0.28	PS1
59033.28	-84.32	z	21.37	0.35	PS1
59040.27	-77.33	z	21.10	0.26	PS1
59097.24	-20.36	z	20.66	0.20	PS1
59100.24	-17.36	z	19.12	0.06	PS1
59104.24	-13.36	z	17.91	0.02	PS1
59220.66	+103.06	z	16.48	0.01	PS1
59246.65	+129.05	z	18.75	0.05	PS1
59298.50	+180.90	z	19.43	0.14	PS1
59304.51	+186.91	z	19.48	0.07	PS1
59328.46	+210.86	z	20.07	0.20	PS1
59333.43	+215.83	z	19.89	0.10	PS1
59382.27	+264.67	z	20.83	0.18	PS1
59184.53	+66.93	g	16.28	0.01	ZTF
59186.53	+68.93	g	16.53	0.02	ZTF
59188.55	+70.95	g	16.36	0.01	ZTF
59193.55	+75.95	g	16.54	0.01	ZTF
59198.55	+80.95	g	16.69	0.01	ZTF
59200.48	+82.88	g	16.74	0.03	ZTF
59203.55	+85.95	g	16.86	0.01	ZTF
59215.57	+97.97	g	17.29	0.02	ZTF

Table A4 (cont'd)

MJD	Phase[a]	Filter	Magnitude	Uncertainty	Instrument
59217.55	+99.95	g	17.26	0.02	ZTF
59219.45	+101.85	g	17.42	0.02	ZTF
59221.52	+103.92	g	17.49	0.01	ZTF
59224.53	+106.93	g	17.79	0.02	ZTF
59226.53	+108.93	g	18.05	0.02	ZTF
59228.51	+110.91	g	18.58	0.03	ZTF
59230.50	+112.90	g	19.24	0.06	ZTF
59232.53	+114.93	g	19.69	0.06	ZTF
59249.45	+131.85	g	20.52	0.26	ZTF
59251.44	+133.84	g	20.49	0.16	ZTF
59253.53	+135.93	g	20.15	0.09	ZTF
59255.39	+137.79	g	20.36	0.15	ZTF
59262.51	+144.91	g	20.68	0.18	ZTF
59264.41	+146.81	g	20.42	0.13	ZTF
59268.50	+150.90	g	20.81	0.16	ZTF
59276.45	+158.85	g	20.58	0.25	ZTF
59280.39	+162.79	g	20.54	0.19	ZTF
59291.50	+173.90	g	20.56	0.16	ZTF
59294.26	+176.66	g	20.68	0.34	ZTF
59297.31	+179.71	g	20.48	0.32	ZTF
59307.33	+189.73	g	20.53	0.13	ZTF
59309.33	+191.73	g	20.63	0.16	ZTF
59311.37	+193.77	g	21.10	0.20	ZTF
59313.29	+195.69	g	21.23	0.35	ZTF
59317.29	+199.69	g	20.67	0.14	ZTF
59321.37	+203.77	g	20.80	0.17	ZTF
59323.30	+205.70	g	20.80	0.22	ZTF
59325.37	+207.77	g	21.08	0.32	ZTF
59329.35	+211.75	g	20.50	0.31	ZTF
59335.29	+217.69	g	20.98	0.25	ZTF
59342.36	+224.76	g	20.89	0.17	ZTF
59345.37	+227.77	g	20.81	0.19	ZTF
59349.24	+231.64	g	21.18	0.23	ZTF
59368.20	+250.60	g	21.42	0.31	ZTF

Table A4 (cont'd)

MJD	Phase[a]	Filter	Magnitude	Uncertainty	Instrument
59377.32	+259.72	g	20.94	0.20	ZTF
58970.39	-147.21	r	21.15	0.26	ZTF
58991.23	-126.37	r	21.21	0.23	ZTF
59042.23	-75.37	r	20.99	0.22	ZTF
59043.24	-74.36	r	21.38	0.33	ZTF
59044.22	-73.38	r	21.30	0.32	ZTF
59045.20	-72.40	r	21.35	0.31	ZTF
59046.20	-71.40	r	20.91	0.21	ZTF
59047.22	-70.38	r	21.19	0.26	ZTF
59180.55	+62.95	r	15.86	0.01	ZTF
59184.52	+66.92	r	15.74	0.01	ZTF
59188.52	+70.92	r	15.82	0.01	ZTF
59193.53	+75.93	r	15.96	0.01	ZTF
59198.46	+80.86	r	16.07	0.01	ZTF
59200.54	+82.94	r	16.01	0.01	ZTF
59203.51	+85.91	r	16.25	0.01	ZTF
59206.52	+88.92	r	16.21	0.02	ZTF
59215.53	+97.93	r	16.48	0.01	ZTF
59217.49	+99.89	r	16.40	0.01	ZTF
59219.51	+101.91	r	16.57	0.01	ZTF
59221.55	+103.95	r	16.65	0.05	ZTF
59224.51	+106.91	r	16.83	0.01	ZTF
59226.49	+108.89	r	17.12	0.01	ZTF
59228.49	+110.89	r	17.54	0.01	ZTF
59230.53	+112.93	r	18.14	0.02	ZTF
59232.51	+114.91	r	18.57	0.03	ZTF
59249.49	+131.89	r	19.16	0.06	ZTF
59251.47	+133.87	r	19.05	0.05	ZTF
59253.50	+135.90	r	19.13	0.05	ZTF
59255.43	+137.83	r	19.30	0.05	ZTF
59258.35	+140.75	r	19.18	0.06	ZTF
59262.50	+144.90	r	19.35	0.06	ZTF
59264.52	+146.92	r	19.18	0.05	ZTF
59266.39	+148.79	r	19.55	0.13	ZTF

Table A4 (cont'd)

MJD	Phase[a]	Filter	Magnitude	Uncertainty	Instrument
59268.47	+150.87	r	19.37	0.06	ZTF
59270.34	+152.74	r	19.27	0.11	ZTF
59272.45	+154.85	r	19.17	0.12	ZTF
59280.43	+162.83	r	19.56	0.10	ZTF
59291.37	+173.77	r	19.50	0.07	ZTF
59297.41	+179.81	r	19.50	0.09	ZTF
59300.41	+182.81	r	19.54	0.17	ZTF
59302.40	+184.80	r	19.81	0.16	ZTF
59305.35	+187.75	r	19.69	0.10	ZTF
59307.35	+189.75	r	19.69	0.07	ZTF
59309.40	+191.80	r	19.64	0.07	ZTF
59311.33	+193.73	r	19.74	0.07	ZTF
59313.35	+195.75	r	19.87	0.10	ZTF
59317.41	+199.81	r	19.91	0.07	ZTF
59321.41	+203.81	r	19.83	0.07	ZTF
59323.35	+205.75	r	19.84	0.09	ZTF
59325.31	+207.71	r	19.87	0.09	ZTF
59329.29	+211.69	r	19.90	0.16	ZTF
59335.33	+217.73	r	19.71	0.20	ZTF
59338.39	+220.79	r	20.09	0.11	ZTF
59340.31	+222.71	r	19.94	0.08	ZTF
59342.41	+224.81	r	20.37	0.12	ZTF
59345.32	+227.72	r	20.22	0.11	ZTF
59349.30	+231.70	r	20.14	0.10	ZTF
59353.32	+235.72	r	20.17	0.12	ZTF
59356.27	+238.67	r	20.62	0.27	ZTF
59359.24	+241.64	r	20.20	0.23	ZTF
59362.27	+244.67	r	20.68	0.27	ZTF
59364.32	+246.72	r	20.46	0.17	ZTF
59366.35	+248.75	r	20.19	0.12	ZTF
59368.30	+250.70	r	20.31	0.11	ZTF
59370.26	+252.66	r	20.74	0.18	ZTF
59375.24	+257.64	r	20.38	0.14	ZTF
59377.24	+259.64	r	20.45	0.13	ZTF

Table A4 (cont'd)

MJD	Phase[a]	Filter	Magnitude	Uncertainty	Instrument
59379.24	+261.64	r	20.53	0.17	ZTF
59385.26	+267.66	r	20.74	0.29	ZTF
59393.22	+275.62	r	20.82	0.18	ZTF
59100.24	-17.36	c	19.89	0.20	ATLAS
59108.22	-9.38	c	15.88	0.04	ATLAS
59206.64	+89.04	c	16.60	0.01	ATLAS
59228.65	+111.05	c	18.22	0.04	ATLAS
59238.61	+121.01	c	20.75	0.31	ATLAS
59256.56	+138.96	c	20.19	0.17	ATLAS
59182.64	+65.04	o	15.79	0.01	ATLAS
59184.65	+67.05	o	15.77	0.01	ATLAS
59190.65	+73.05	o	15.89	0.01	ATLAS
59214.60	+97.00	o	16.42	0.01	ATLAS
59222.67	+105.07	o	16.68	0.03	ATLAS
59242.63	+125.03	o	19.17	0.11	ATLAS
59244.61	+127.01	o	19.28	0.20	ATLAS
59246.61	+129.01	o	19.31	0.12	ATLAS
59250.65	+133.05	o	19.36	0.09	ATLAS
59252.65	+135.05	o	19.34	0.11	ATLAS
59113.08	-3.92	u	14.46	0.02	LCO
59208.49	+91.49	u	19.52	0.21	LCO
59223.42	+106.42	u	20.19	0.13	LCO
59227.53	+110.53	u	20.33	0.23	LCO
59232.40	+115.40	u	20.48	0.24	LCO
59251.48	+134.48	u	20.87	0.26	LCO
59113.08	-3.92	g	14.76	0.01	LCO
59191.52	+74.52	g	16.56	0.03	LCO
59208.49	+91.49	g	16.95	0.02	LCO
59217.47	+100.47	g	17.28	0.02	LCO
59223.42	+106.42	g	17.45	0.03	LCO
59227.54	+110.54	g	17.62	0.04	LCO
59232.40	+115.40	g	17.90	0.11	LCO
59251.49	+134.49	g	19.41	0.05	LCO
59274.46	+157.46	g	20.60	0.20	LCO

Table A4 (cont'd)

MJD	Phase[a]	Filter	Magnitude	Uncertainty	Instrument
59276.28	+159.28	g	20.74	0.26	LCO
59281.39	+164.39	g	20.89	0.24	LCO
59287.33	+170.33	g	20.87	0.26	LCO
59302.27	+185.27	g	20.82	0.30	LCO
59131.46	+14.46	r	15.09	0.01	LCO
59113.08	-3.92	r	15.20	0.02	LCO
59191.53	+74.53	r	15.95	0.02	LCO
59208.50	+91.50	r	16.30	0.02	LCO
59217.48	+100.48	r	16.33	0.02	LCO
59223.43	+106.43	r	16.65	0.02	LCO
59227.54	+110.54	r	17.29	0.03	LCO
59251.49	+134.49	r	19.05	0.05	LCO
59274.46	+157.46	r	19.02	0.19	LCO
59276.28	+159.28	r	19.33	0.15	LCO
59281.39	+164.39	r	19.15	0.18	LCO
59287.33	+170.33	r	19.68	0.18	LCO
59302.27	+185.27	r	19.68	0.18	LCO
59113.08	-3.92	i	15.43	0.02	LCO
59191.53	+74.53	i	15.91	0.02	LCO
59208.50	+91.50	i	16.34	0.03	LCO
59217.48	+100.48	i	16.41	0.02	LCO
59223.43	+106.43	i	16.63	0.03	LCO
59227.54	+110.54	i	17.32	0.04	LCO
59251.49	+134.49	i	19.14	0.14	LCO
59276.28	+159.28	i	19.36	0.17	LCO
59281.39	+164.39	i	19.62	0.19	LCO
59287.33	+170.33	i	19.79	0.19	LCO
59302.27	+185.27	i	19.89	0.26	LCO
59131.45	+14.45	B	15.23	0.01	Lulin
59131.45	+14.45	V	14.96	0.01	Lulin
59131.45	+14.45	g	15.07	0.01	Lulin
59131.46	+14.46	r	15.09	0.01	Lulin
59109.76	-7.24	v	15.52	0.08	*Swift*
59111.48	-5.52	v	15.10	0.06	*Swift*

Table A4 (cont'd)

MJD	Phase[a]	Filter	Magnitude	Uncertainty	Instrument
59113.41	-3.59	v	14.84	0.06	*Swift*
59115.74	-1.26	v	14.63	0.05	*Swift*
59117.60	+0.60	v	14.60	0.06	*Swift*
59119.20	+2.20	v	14.53	0.05	*Swift*
59121.18	+4.18	v	14.65	0.07	*Swift*
59129.08	+12.08	v	14.99	0.07	*Swift*
59133.60	+16.60	v	15.02	0.07	*Swift*
59135.33	+18.33	v	15.01	0.07	*Swift*
59138.81	+21.81	v	15.13	0.07	*Swift*
59141.24	+24.24	v	15.20	0.07	*Swift*
59146.07	+29.07	v	15.25	0.08	*Swift*
59153.72	+36.72	v	15.38	0.10	*Swift*
59156.24	+39.24	v	15.45	0.09	*Swift*
59159.95	+42.95	v	15.66	0.10	*Swift*
59162.34	+45.34	v	15.68	0.10	*Swift*
59165.19	+48.19	v	15.65	0.10	*Swift*
59172.04	+55.04	v	15.66	0.10	*Swift*
59176.08	+59.08	v	15.88	0.12	*Swift*
59180.13	+63.13	v	15.81	0.12	*Swift*
59184.12	+67.12	v	16.13	0.15	*Swift*
59188.70	+71.70	v	16.14	0.15	*Swift*
59192.76	+75.76	v	16.26	0.16	*Swift*
59196.53	+79.53	v	16.04	0.16	*Swift*
59198.79	+81.79	v	16.29	0.19	*Swift*
59208.81	+91.81	v	16.82	0.24	*Swift*
59216.11	+99.11	v	16.90	0.25	*Swift*
59220.56	+103.56	v	16.96	0.26	*Swift*
59224.74	+107.74	v	>17.30	–	*Swift*
59232.85	+115.85	v	>17.31	–	*Swift*
59240.95	+123.95	v	>17.36	–	*Swift*
59246.91	+129.91	v	>17.36	–	*Swift*
59247.79	+130.79	v	>17.29	–	*Swift*
59250.83	+133.83	v	>17.40	–	*Swift*
59263.97	+146.97	v	>17.25	–	*Swift*

Table A4 (cont'd)

MJD	Phase[a]	Filter	Magnitude	Uncertainty	Instrument
59109.75	-7.25	*b*	15.34	0.06	*Swift*
59111.48	-5.52	*b*	14.89	0.05	*Swift*
59113.41	-3.59	*b*	14.57	0.04	*Swift*
59115.74	-1.26	*b*	14.47	0.04	*Swift*
59117.60	+0.60	*b*	14.47	0.04	*Swift*
59119.19	+2.19	*b*	14.50	0.04	*Swift*
59121.18	+4.18	*b*	14.60	0.05	*Swift*
59129.08	+12.08	*b*	14.95	0.05	*Swift*
59133.59	+16.59	*b*	15.09	0.06	*Swift*
59135.33	+18.33	*b*	15.18	0.06	*Swift*
59138.80	+21.80	*b*	15.36	0.06	*Swift*
59141.24	+24.24	*b*	15.36	0.06	*Swift*
59146.07	+29.07	*b*	15.62	0.07	*Swift*
59153.72	+36.72	*b*	15.88	0.09	*Swift*
59156.24	+39.24	*b*	15.81	0.07	*Swift*
59159.94	+42.94	*b*	16.02	0.08	*Swift*
59162.34	+45.34	*b*	15.99	0.08	*Swift*
59165.19	+48.19	*b*	16.25	0.10	*Swift*
59172.03	+55.03	*b*	16.34	0.10	*Swift*
59176.08	+59.08	*b*	16.45	0.12	*Swift*
59180.12	+63.12	*b*	16.53	0.12	*Swift*
59184.11	+67.11	*b*	16.93	0.17	*Swift*
59188.69	+71.69	*b*	17.04	0.19	*Swift*
59192.75	+75.75	*b*	17.18	0.19	*Swift*
59196.53	+79.53	*b*	17.22	0.24	*Swift*
59198.79	+81.79	*b*	17.71	0.35	*Swift*
59208.80	+91.80	*b*	>17.94	–	*Swift*
59216.11	+99.11	*b*	>17.96	–	*Swift*
59220.56	+103.56	*b*	>17.99	–	*Swift*
59224.73	+107.73	*b*	>17.95	–	*Swift*
59232.85	+115.85	*b*	>17.97	–	*Swift*
59240.95	+123.95	*b*	>17.97	–	*Swift*
59246.91	+129.91	*b*	>17.99	–	*Swift*
59247.79	+130.79	*b*	>17.96	–	*Swift*

Table A4 (cont'd)

MJD	Phase[a]	Filter	Magnitude	Uncertainty	Instrument
59250.83	+133.83	*b*	>18.03	–	*Swift*
59253.81	+136.81	*b*	>17.99	–	*Swift*
59257.74	+140.74	*b*	>18.02	–	*Swift*
59263.97	+146.97	*b*	>17.89	–	*Swift*
59109.75	-7.25	*u*	15.04	0.04	*Swift*
59111.48	-5.52	*u*	14.61	0.04	*Swift*
59113.41	-3.59	*u*	14.39	0.04	*Swift*
59115.74	-1.26	*u*	14.31	0.04	*Swift*
59117.60	+0.60	*u*	14.30	0.04	*Swift*
59119.19	+2.19	*u*	14.37	0.04	*Swift*
59121.18	+4.18	*u*	14.53	0.04	*Swift*
59129.08	+12.08	*u*	15.04	0.04	*Swift*
59133.59	+16.59	*u*	15.35	0.05	*Swift*
59135.33	+18.33	*u*	15.45	0.05	*Swift*
59138.80	+21.80	*u*	15.74	0.06	*Swift*
59141.24	+24.24	*u*	15.89	0.06	*Swift*
59146.07	+29.07	*u*	16.28	0.07	*Swift*
59153.72	+36.72	*u*	16.78	0.11	*Swift*
59156.24	+39.24	*u*	16.97	0.11	*Swift*
59159.94	+42.94	*u*	17.06	0.11	*Swift*
59162.34	+45.34	*u*	17.42	0.14	*Swift*
59165.19	+48.19	*u*	17.65	0.18	*Swift*
59172.03	+55.03	*u*	18.01	0.23	*Swift*
59176.08	+59.08	*u*	17.99	0.23	*Swift*
59180.12	+63.12	*u*	18.12	0.26	*Swift*
59184.11	+67.11	*u*	18.42	0.35	*Swift*
59188.69	+71.69	*u*	>18.49	–	*Swift*
59192.75	+75.75	*u*	>18.58	–	*Swift*
59196.53	+79.53	*u*	>18.38	–	*Swift*
59198.79	+81.79	*u*	>18.41	–	*Swift*
59208.80	+91.80	*u*	>18.56	–	*Swift*
59216.11	+99.11	*u*	>18.60	–	*Swift*
59220.55	+103.55	*u*	>18.62	–	*Swift*
59224.73	+107.73	*u*	>18.61	–	*Swift*

Table A4 (cont'd)

MJD	Phase[a]	Filter	Magnitude	Uncertainty	Instrument
59228.67	+111.67	u	>18.04	–	*Swift*
59232.85	+115.85	u	>18.57	–	*Swift*
59240.94	+123.94	u	>18.63	–	*Swift*
59246.91	+129.91	u	>18.58	–	*Swift*
59247.79	+130.79	u	>18.54	–	*Swift*
59250.83	+133.83	u	>18.64	–	*Swift*
59253.81	+136.81	u	>18.59	–	*Swift*
59257.73	+140.73	u	>18.62	–	*Swift*
59263.96	+146.96	u	>18.49	–	*Swift*
59109.75	-7.25	$w1$	15.02	0.04	*Swift*
59111.48	-5.52	$w1$	14.60	0.04	*Swift*
59113.41	-3.59	$w1$	14.38	0.04	*Swift*
59115.73	-1.27	$w1$	14.37	0.04	*Swift*
59117.60	+0.60	$w1$	14.48	0.04	*Swift*
59119.19	+2.19	$w1$	14.66	0.04	*Swift*
59121.18	+4.18	$w1$	14.89	0.04	*Swift*
59129.08	+12.08	$w1$	15.85	0.05	*Swift*
59133.59	+16.59	$w1$	16.41	0.06	*Swift*
59135.33	+18.33	$w1$	16.63	0.06	*Swift*
59138.80	+21.80	$w1$	17.20	0.08	*Swift*
59141.24	+24.24	$w1$	17.51	0.10	*Swift*
59146.07	+29.07	$w1$	17.89	0.13	*Swift*
59153.72	+36.72	$w1$	18.59	0.26	*Swift*
59156.24	+39.24	$w1$	>19.20	–	*Swift*
59159.94	+42.94	$w1$	>19.24	–	*Swift*
59162.34	+45.34	$w1$	>19.23	–	*Swift*
59165.18	+48.18	$w1$	>19.22	–	*Swift*
59172.03	+55.03	$w1$	>19.27	–	*Swift*
59176.08	+59.08	$w1$	>19.26	–	*Swift*
59180.12	+63.12	$w1$	>19.21	–	*Swift*
59184.11	+67.11	$w1$	>19.24	–	*Swift*
59188.69	+71.69	$w1$	>19.24	–	*Swift*
59192.75	+75.75	$w1$	>19.31	–	*Swift*
59196.53	+79.53	$w1$	>19.11	–	*Swift*

Table A4 (cont'd)

MJD	Phase[a]	Filter	Magnitude	Uncertainty	Instrument
59198.79	+81.79	$w1$	>19.14	–	*Swift*
59204.96	+87.96	$w1$	>18.93	–	*Swift*
59208.80	+91.80	$w1$	>19.25	–	*Swift*
59216.11	+99.11	$w1$	>19.25	–	*Swift*
59220.55	+103.55	$w1$	>19.27	–	*Swift*
59224.73	+107.73	$w1$	>19.23	–	*Swift*
59228.67	+111.67	$w1$	>19.20	–	*Swift*
59232.85	+115.85	$w1$	>19.27	–	*Swift*
59240.94	+123.94	$w1$	>19.27	–	*Swift*
59246.91	+129.91	$w1$	>19.24	–	*Swift*
59247.79	+130.79	$w1$	>19.21	–	*Swift*
59250.83	+133.83	$w1$	>19.25	–	*Swift*
59253.81	+136.81	$w1$	>19.27	–	*Swift*
59257.73	+140.73	$w1$	>19.29	–	*Swift*
59263.96	+146.96	$w1$	>19.11	–	*Swift*
59109.76	-7.24	$m2$	15.00	0.04	*Swift*
59111.49	-5.51	$m2$	14.58	0.04	*Swift*
59113.42	-3.58	$m2$	14.38	0.04	*Swift*
59115.74	-1.26	$m2$	14.42	0.04	*Swift*
59117.60	+0.60	$m2$	14.60	0.04	*Swift*
59119.20	+2.20	$m2$	14.79	0.04	*Swift*
59121.18	+4.18	$m2$	15.08	0.04	*Swift*
59129.08	+12.08	$m2$	16.34	0.05	*Swift*
59133.60	+16.60	$m2$	17.07	0.06	*Swift*
59135.34	+18.34	$m2$	17.45	0.07	*Swift*
59138.81	+21.81	$m2$	18.05	0.11	*Swift*
59141.25	+24.25	$m2$	19.19	0.26	*Swift*
59146.08	+29.08	$m2$	19.42	0.32	*Swift*
59153.72	+36.72	$m2$	>19.54	–	*Swift*
59156.25	+39.25	$m2$	>19.64	–	*Swift*
59159.95	+42.95	$m2$	>19.65	–	*Swift*
59162.34	+45.34	$m2$	>19.24	–	*Swift*
59165.19	+48.19	$m2$	>19.67	–	*Swift*
59172.04	+55.04	$m2$	>19.61	–	*Swift*

Table A4 (cont'd)

MJD	Phase[a]	Filter	Magnitude	Uncertainty	Instrument
59176.09	+59.09	$m2$	>19.66	–	*Swift*
59180.13	+63.13	$m2$	>19.68	–	*Swift*
59184.12	+67.12	$m2$	>19.66	–	*Swift*
59188.70	+71.70	$m2$	>19.64	–	*Swift*
59192.76	+75.76	$m2$	>19.70	–	*Swift*
59196.53	+79.53	$m2$	>19.46	–	*Swift*
59198.79	+81.79	$m2$	>19.66	–	*Swift*
59208.81	+91.81	$m2$	>19.65	–	*Swift*
59216.12	+99.12	$m2$	>19.69	–	*Swift*
59220.56	+103.56	$m2$	>19.71	–	*Swift*
59224.74	+107.74	$m2$	>19.63	–	*Swift*
59232.85	+115.85	$m2$	>19.68	–	*Swift*
59240.95	+123.95	$m2$	>19.72	–	*Swift*
59246.92	+129.92	$m2$	>19.64	–	*Swift*
59247.79	+130.79	$m2$	>19.62	–	*Swift*
59250.83	+133.83	$m2$	>19.63	–	*Swift*
59263.97	+146.97	$m2$	>19.54	–	*Swift*
59109.75	-7.25	$w2$	14.95	0.04	*Swift*
59111.48	-5.52	$w2$	14.55	0.04	*Swift*
59113.41	-3.59	$w2$	14.42	0.04	*Swift*
59115.74	-1.26	$w2$	14.53	0.04	*Swift*
59117.60	+0.60	$w2$	14.77	0.04	*Swift*
59119.19	+2.19	$w2$	15.06	0.04	*Swift*
59121.18	+4.18	$w2$	15.43	0.04	*Swift*
59129.08	+12.08	$w2$	16.77	0.06	*Swift*
59133.59	+16.59	$w2$	17.30	0.07	*Swift*
59135.33	+18.33	$w2$	17.62	0.08	*Swift*
59138.81	+21.81	$w2$	18.27	0.12	*Swift*
59141.24	+24.24	$w2$	19.23	0.25	*Swift*
59146.07	+29.07	$w2$	19.43	0.30	*Swift*
59153.72	+36.72	$w2$	>19.55	–	*Swift*
59156.24	+39.24	$w2$	>19.71	–	*Swift*
59159.94	+42.94	$w2$	>19.74	–	*Swift*
59162.34	+45.34	$w2$	>19.73	–	*Swift*

Table A4 (cont'd)

MJD	Phase[a]	Filter	Magnitude	Uncertainty	Instrument
59165.19	+48.19	$w2$	>19.73	–	*Swift*
59172.03	+55.03	$w2$	>19.75	–	*Swift*
59176.08	+59.08	$w2$	>19.74	–	*Swift*
59180.13	+63.13	$w2$	>19.73	–	*Swift*
59184.12	+67.12	$w2$	>19.71	–	*Swift*
59188.69	+71.69	$w2$	>19.70	–	*Swift*
59192.76	+75.76	$w2$	>19.78	–	*Swift*
59196.53	+79.53	$w2$	>19.52	–	*Swift*
59198.79	+81.79	$w2$	>19.68	–	*Swift*
59208.80	+91.80	$w2$	>19.73	–	*Swift*
59216.11	+99.11	$w2$	>19.73	–	*Swift*
59220.56	+103.56	$w2$	>19.78	–	*Swift*
59224.73	+107.73	$w2$	>19.69	–	*Swift*
59232.85	+115.85	$w2$	>19.77	–	*Swift*
59240.95	+123.95	$w2$	>19.75	–	*Swift*
59246.91	+129.91	$w2$	>19.70	–	*Swift*
59247.79	+130.79	$w2$	>19.69	–	*Swift*
59250.83	+133.83	$w2$	>19.72	–	*Swift*
59253.81	+136.81	$w2$	>19.71	–	*Swift*
59257.74	+140.74	$w2$	>19.31	–	*Swift*
59263.97	+146.97	$w2$	>19.59	–	*Swift*

[a]Relative to B-band maximum (MJD 59117.6)

Chapter 6

SN 2023ixf in Messier 101: Photo-ionization of Dense, Close-in Circumstellar Material in a Nearby Type II Supernova

This chapter was previously published as Jacobson-Galán et al., 2023, ApJL, 954, L42

6.1 Abstract

We present UV/optical observations and models of supernova (SN) 2023ixf, a type II SN located in Messier 101 at 6.9 Mpc. Early-time ("flash") spectroscopy of SN 2023ixf, obtained primarily at Lick Observatory, reveals emission lines of H I, He I/II, C IV, and N III/IV/V with a narrow core and broad, symmetric wings arising from the photo-ionization of dense, close-in circumstellar material (CSM) located around the progenitor star prior to shock breakout. These electron-scattering broadened line profiles persist for ∼8 days with respect to first light, at which time Doppler broadened features from the fastest SN ejecta form, suggesting a reduction in CSM density at $r \gtrsim 10^{15}$ cm. The early-time light curve of SN 2023ixf shows peak absolute magnitudes (e.g., $M_u = -18.6$ mag, $M_g = -18.4$ mag) that are $\gtrsim 2$ mag brighter than typical type II supernovae, this photometric boost also being consistent with the shock power supplied from CSM interaction. Comparison of SN 2023ixf to a grid of light curve and multi-epoch spectral models from the non-LTE radiative transfer code `CMFGEN` and the radiation-hydrodynamics code `HERACLES` suggests dense, solar-metallicity, CSM confined to $r = (0.5 - 1) \times 10^{15}$ cm and a progenitor mass-loss rate of $\dot{M} = 10^{-2}$ $M_\odot$ yr^{-1}. For the assumed progenitor wind velocity of $v_w = 50$ km s^{-1}, this corresponds to enhanced mass-loss (i.e., "super-wind" phase) during the last ∼3-6 years before explosion.

6.2 Introduction

A paramount issue in astrophysics is constraining how the lives of red supergiant (RSG) stars end. This avenue of study has a direct impact on the observed diversity of core-collapse supernovae (SNe), compact object formation, and element creation in the Universe. Advancing our understanding of late-stage RSG evolution can be accomplished by probing the composition and structure of the circumstellar medium (CSM) surrounding these stars in the final years before explosion. This CSM is composed of material once located on the RSG surface and is enriched as the progenitor star loses mass via winds and/or violent outbursts (Smith 2014). Understanding the structure of this CSM provides needed constraints on the final stages of stellar evolution before core collapse and the proposed mechanisms for both dynamic (e.g., gravity waves, super-Eddington winds; Owocki et al. 2004, 2017; Quataert & Shiode 2012; Quataert et al. 2016; Fuller 2017; Wu & Fuller 2021) as well as secular (i.e., steady-state wind; Beasor et al. 2020) mass-loss.

Early-time, multi-wavelength observations of young type II SNe (SNe II) are an essential probe of the final stages of stellar evolution; these last months-to-centuries are almost completely unconstrained in stellar evolutionary models. In the era of all-sky transient surveys, "flash" or rapid spectroscopic observations have become a powerful tool in understanding the direct circumstellar environment of SN progenitors in the final months before explosion (e.g., Gal-Yam et al. 2014; Groh 2014; Smith et al. 2015; Khazov et al. 2016; Yaron et al. 2017; Jacobson-Galán et al. 2020b; Bruch et al. 2021b, 2023a; Jacobson-Galán et al. 2022a; Terreran et al. 2022; Tinyanont et al. 2022; Davis et al. 2023b; Wang et al. 2023). Very early-time spectra ($t \lesssim 7$ days) can be used to identify prominent emission lines from the recombination of CSM photo-ionized by the incoming SN radiation at, and following, shock breakout. However, these spectral features are transient, leaving behind broad lines from the fastest ($v_{\rm ej} \approx 10^4$ km s^{-1}) SN ejecta layers (Chugai 2001; Dessart et al. 2017). The strength of the narrow emission features depends on the CSM density and its chemical abundance. This is a robust tracer of the progenitor's chemical composition, identity and recent mass-loss at small distances ($r < 10^{15}$ cm from the explosion; Gal-Yam et al. 2014; Yaron et al. 2017; Dessart et al. 2017; Boian & Groh 2020).

Spectroscopic modeling of CSM-interacting SNe II with non-LTE radiative transfer codes (e.g., `CMFGEN`; Hillier & Dessart 2012; Dessart et al. 2015) has been used to extract quantitative information on the progenitor's radius, chemical composition, wind velocity and mass-loss rate. `CMFGEN` in particular allows for self-consistent post-processing of radiation hydrodynamics simulations, allowing for physically robust constraints on both the SN ejecta and CSM properties (shocked and unshocked) and the creation of accurate synthetic spectra that contain critical information absent from light curves. For example, `CMFGEN` spectral modeling of the prototypical "flash" spectroscopy type II SN 1998S indicated an enhanced RSG mass-loss rate of $\dot{M} \approx (0.6-1) \times 10^{-2}$ M$_\odot$ yr^{-1} ($v_w \approx 50$ km s^{-1}) in the final 15 years before core-collapse (Shivvers et al. 2015; Dessart et al. 2016). This mass-loss rate is significantly larger than that observed in galactic RSGs e.g., $\dot{M} \approx 10^{-6}$ M$_\odot$ yr^{-1} (Beasor et al. 2020). Similarly, modeling of the emission line spectrum in the first days of

SNe 2017ahn and 2020pni (Tartaglia et al. 2021; Terreran et al. 2022) suggested N-rich CSM derived from mass-loss rates of $\dot{M} \approx (3-6) \times 10^{-3}$ $M_\odot$ yr^{-1}. Further diversity was revealed from `CMFGEN` modeling of SN 2013fs (Yaron et al. 2017), observed within hours of explosion, which suggested a compact CSM ($r < 3 \times 10^{14}$ cm) with a lower mass-loss rate of $\dot{M} \approx (3-5) \times 10^{-3}$ $M_\odot$ yr^{-1} (Dessart et al. 2017). Additionally, both UV/optical photometry and the spectral series of SN 2020tlf were accurately modeled by `CMFGEN` simulations involving an inflated RSG progenitor ($R_\star \approx 10^3$ $R_\odot$, which exploded into a dense ($\dot{M} = (1-3) \times 10^{-2}$ $M_\odot$ yr^{-1}, $v_w = 50$ km s^{-1}), extended ($r \approx 10^{15}$ cm) CSM; this scenario is also consistent with the detection of luminous precursor emission before explosion (Jacobson-Galán et al. 2022a).

In this paper we present, analyze, and model photometric and spectroscopic observations of SN 2023ixf, first reported to the Transient Name Server by Koichi Itagaki (Itagaki 2023) on 2023-05-19 (MJD 60083.90). SN 2023ixf was classifed as a Type II SN (Perley et al. 2023) and is located at $\alpha = 14^{\rm h}03^{\rm m}38.56^{\rm s}$, $\delta = +54°18'41.96''$ in host galaxy Messier 101 (NGC 5457). Based on reported pre-discovery images from numerous observations of SN 2023ixf, we adopt a time of first light to be MJD 60082.833 ± 0.020 (Mao et al. 2023) that is based on the average between last non-detection and first detection, but could be earlier given the shallow depth of the last non-detection limit. All phases reported in this paper are with respect to this adopted time of first light. In this paper, we use a redshift-independent host-galaxy distance of 6.85 ± 0.15 Mpc reported by Riess et al. (2022), which is the updated value beyond what is presented in Riess et al. (2016). We adopt a redshift of $z = 0.000804$ (Perley et al. 2023).

Given its close proximity and current relative brightness, SN 2023ixf represents an unparalleled opportunity to study both the very early-time and the long-term evolution of a CSM-interacting SN II in unprecedented detail. In §8.3 we describe UV, optical, and NIR observations of SN 2023ixf. In §8.4 we present analysis, comparisons and modeling of SN 2023ixf's optical photometric and spectroscopic properties. Finally, in §8.6 we discuss the progenitor environment and mass-loss history prior to SN 2023ixf. Conclusions are drawn in §8.7. All uncertainties are quoted at the 68% confidence level (c.l.) unless otherwise stated.

6.3 Observations

6.3.1 Photometric Observations

SN 2023ixf was observed with the Pan-STARRS telescope (PS1/2; Kaiser et al. 2002; Chambers et al. 2017) between 21 May and 2 June 2023 in *grizy*-bands through the Young Supernova Experiment (YSE) (Jones et al. 2021). Data storage/visualization and follow-up coordination was done through the YSE-PZ web broker (Coulter et al. 2022, 2023). The YSE photometric pipeline is based on `photpipe` (Rest et al. 2005), which relies on calibrations from (Magnier et al. 2020; Waters et al. 2020). Each image template was taken from stacked PS1 exposures, with most of the input data from the PS1 3π survey. All images

and templates were resampled and astrometrically aligned to match a skycell in the PS1 sky tessellation. An image zero-point is determined by comparing PSF photometry of the stars to updated stellar catalogs of PS1 observations (Flewelling et al. 2016b). The PS1 templates are convolved with a three-Gaussian kernel to match the PSF of the nightly images, and the convolved templates are subtracted from the nightly images with `HOTPANTS` (Becker 2015). Finally, a flux-weighted centroid is found for the position of the SN in each image and PSF photometry is performed using "forced photometry": the centroid of the PSF is forced to be at the SN position. The nightly zero-point is applied to the photometry to determine the brightness of the SN for that epoch.

We obtained *ugri* imaging of SN 2023ixf with the Las Cumbres Observatory (LCO) 1 m telescopes from 20 May to 1 June 2023 (Programs NSF2023A-011 and NSF2023A-015; PIs Foley and Kilpatrick, respectively). After downloading the `BANZAI`-reduced images from the LCO data archive (McCully et al. 2018), we used `photpipe` (Rest et al. 2005) to perform `DoPhot` PSF photometry (Schechter et al. 1993). All photometry was calibrated using PS1 stellar catalogs described above with additional transformations to SDSS *u*-band derived from Finkbeiner et al. (2016). For additional details on our reductions, see Kilpatrick et al. (2018a). We also obtained photometry using a 0.7 meter Thai Robotic Telescope at Sierra Remote Observatories and the Nickel Telescope at Lick Observatory in the *BVRI* bands. Images are bias subtracted and field flattened. Absolute photometry is obtained using stars in the $10' \times 10'$ field of view.

We also observed SN 2023ixf with the Lulin 1 m telescope in *griz* bands from 21 May to 1 June 2023. Standard calibrations for bias and flat-fielding were performed on the images using `IRAF`, and we reduced the calibrated frames in `photpipe` using the same methods described above for the LCO images.

We also observed SN 2023ixf with the Auburn 10" telescope located in Auburn, AL from 27 May to 3 June 2023 in *BGR* bands. Following standard procedures in `python`, we corrected each frame for bias, dark current, and flat-fielding using image frames obtained in the same instrumental setup. We then registered each frame using *Gaia* DR3 astrometric standard stars (Gaia Collaboration 2022) observed in the same field as each image. Finally, we stacked images in each filter for each night with `swarp` and performed final photometry using `DoPhot` with calibration using Pan-STARRS *gri* standard stars transformed to *BVR* bands[1]. The complete multi-color light curve of SN 2023ixf is presented in Figure 6.1(a)).

The Milky Way (MW) *V*-band extinction and color excess along the SN line of site is $A_V = 0.025$ mag and $E(B\text{-}V) = 0.008$ mag (Schlegel et al. 1998; Schlafly & Finkbeiner 2011), respectively, which we correct for using a standard Fitzpatrick (1999) reddening law ($R_V = 3.1$). In addition to the MW color excess, we estimate the contribution of galaxy extinction in the local SN environment. Using a high resolution Kast spectrum of SN 2023ixf at $\delta t = 2.4$ days, we calculate Na I D2 and D1 equivalent widths (EWs) of 0.16 and 0.12 Å, respectively; these values are consistent with those derived from a Keck Planet

[1]Note that our *G*-band filter is close to Johnson *V*-band, and so we calibrate against Pan-STARRS standard stars transformed into this band. For filter functions, see https://astronomy-imaging-camera.com/product/zwo-lrgb-31mm-filters-2.

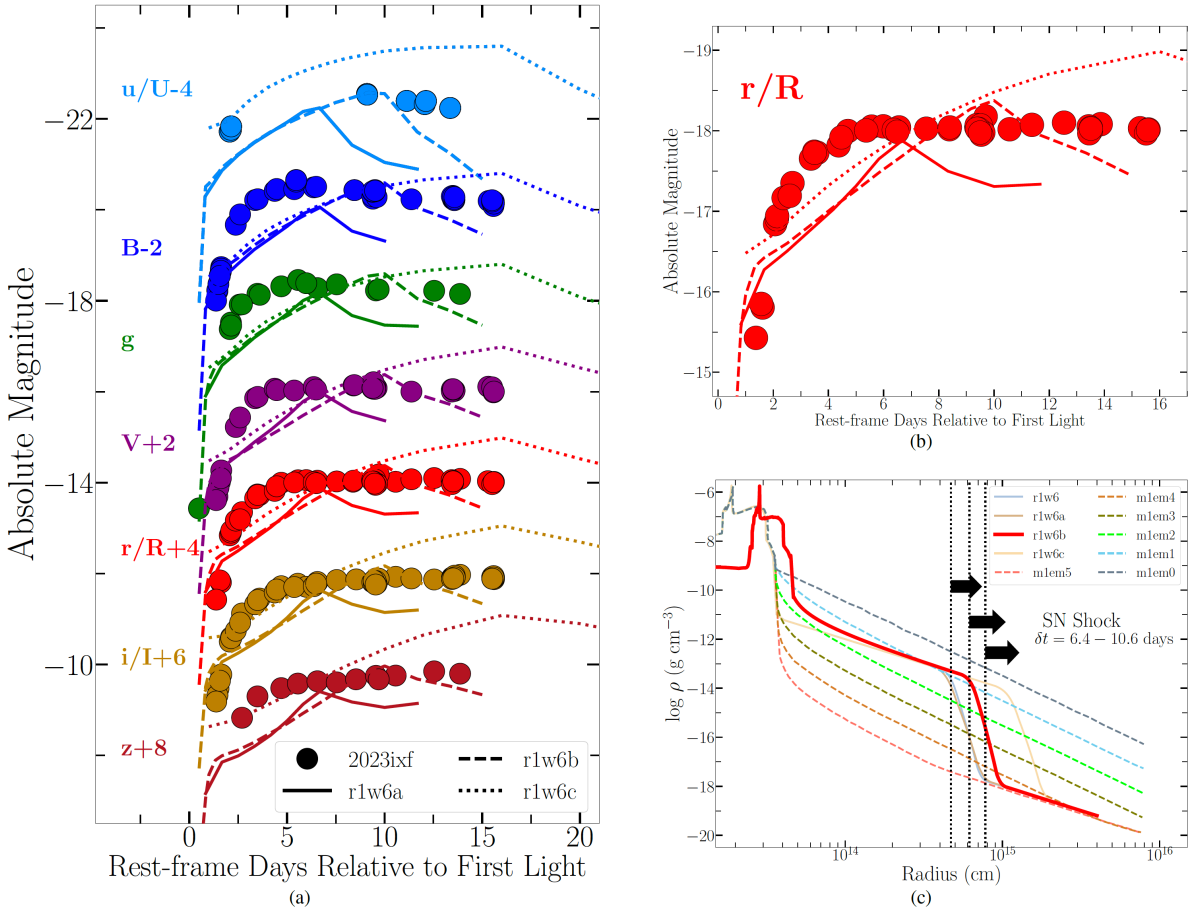

Figure 6.1 (a) Multi-color light curve of SN 2023ixf (circles) with respect to time since first light (MJD 60082.833 ± 0.020) from PS1, LCO, Auburn, TRT, Nickel, and Lulin telescopes. Observed photometry is presented in the AB magnitude system and has been corrected for host galaxy and MW extinction. Light curves of `CMFGEN` models r1w6a ($R_{\rm CSM} = 6 \times 10^{14}$ cm, $\dot{M} = 10^{-2}$ M$_\odot$ yr^{-1}), r1w6b ($R_{\rm CSM} = 8 \times 10^{14}$ cm, $\dot{M} = 10^{-2}$ M$_\odot$ yr^{-1}), and r1w6c ($R_{\rm CSM} = 1 \times 10^{15}$ cm, $\dot{M} = 10^{-2}$ M$_\odot$ yr^{-1}) are plotted as solid, dashed and dotted lines, respectively. (b) Zoom-in of the SN 2023ixf $r/R-$band light curve and `CMFGEN` models, which can reproduce the peak magnitude but are inconsistent with the early-time slope. (c) CSM densities and radii for a subset of the `CMFGEN` model grid (e.g., Table A4) used to find the best fitting model for SN 2023ixf, which is plotted as a solid red line (r1w6b). Dotted black lines represent lower limits on the location of the SN shock at $\delta t = 6.4, 8.4, 10.6$ days, for a lower limit on the SN shock velocity of $\gtrsim 8500$ km s^{-1} (§8.4.2). We expect a decrease of the optical depth to electron-scattering (i.e., $\tau_{\rm ES}$) based on the plotted density profile at around $\sim$8 days, which is consistent with the fading of the IIn-like line profiles observed in SN 2023ixf at these phases.

Finder spectrum (Lundquist et al. 2023). We use Equations 7 & 8 in Poznanski et al. (2012) to convert these EWs to an intrinsic *E(B-V)* and find a host galaxy extinction of $E(B-V)_{\rm host} = 0.033 \pm 0.010$ mag, also corrected for using the Fitzpatrick (1999) reddening law.

6.3.2 Spectroscopic Observations

SN 2023ixf was observed with Shane/Kast (Miller & Stone 1993) between $\delta t = 2.4 - 14.4$ days. For all these spectroscopic observations, standard CCD processing and spectrum extraction were accomplished with IRAF[2]. The data were extracted using the optimal algorithm of Horne (1986). Low-order polynomial fits to calibration-lamp spectra were used to establish the wavelength scale and small adjustments derived from night-sky lines in the object frames were applied. SN 2023ixf spectra were also obtained with the Kitt Peak Ohio State Multi-Object Spectrograph (KOSMOS, Martini et al. 2014) on the Astrophysical Research Consortium (ARC) 3.5-meter Telescope at Apache Point Observatory (APO). The KOSMOS spectra were reduced through the `KOSMOS`[3] pipeline. One optical spectrum (in a red and blue arm) was taken through the Low-Resolution Spectrograph 2 (LRS2) instrument on the Hobby Eberly Telescope (HET) on 2023-05-21 (blue arm) and 2023-05-22 (red arm). The LRS2 data were processed with `Panacea`[4], the HET automated reduction pipeline for LRS2. The initial processing includes bias correction, wavelength calibration, fiber-trace evaluation, fiber normalization, and fiber extraction; moreover, there is an initial flux calibration from default response curves, an estimation of the mirror illumination, as well as the exposure throughput from guider images. After the initial reduction, we use LRS2Multi[5] in order to perform sky subtraction.

In Figure 7.2 we present the complete series of optical spectroscopic observations of SN 2023ixf from $\delta t = 2.4 - 14.4$ days. In this plot, we also show the classification spectrum of SN 2023ixf at +1.1 days from the Liverpool telescope (Perley et al. 2023). However, because we cannot verify the quality of this spectral reduction, we only use these data for narrow line identification. Additionally, we include *Swift* UV grism spectra of SN 2023ixf from $\delta t = +1.8 - 2.8$ days in Appendix Figure 6.7; data were reduced using the techniques outlined in Pan et al. (2020). The complete spectral sequence is shown in Figure 7.2 and the log of spectroscopic observations is presented in Appendix Tables A1.

[2] https://github.com/msiebert1/UCSC_spectral_pipeline
[3] https://github.com/jradavenport/pykosmos
[4] https://github.com/grzeimann/Panacea
[5] https://github.com/grzeimann/LRS2Multi

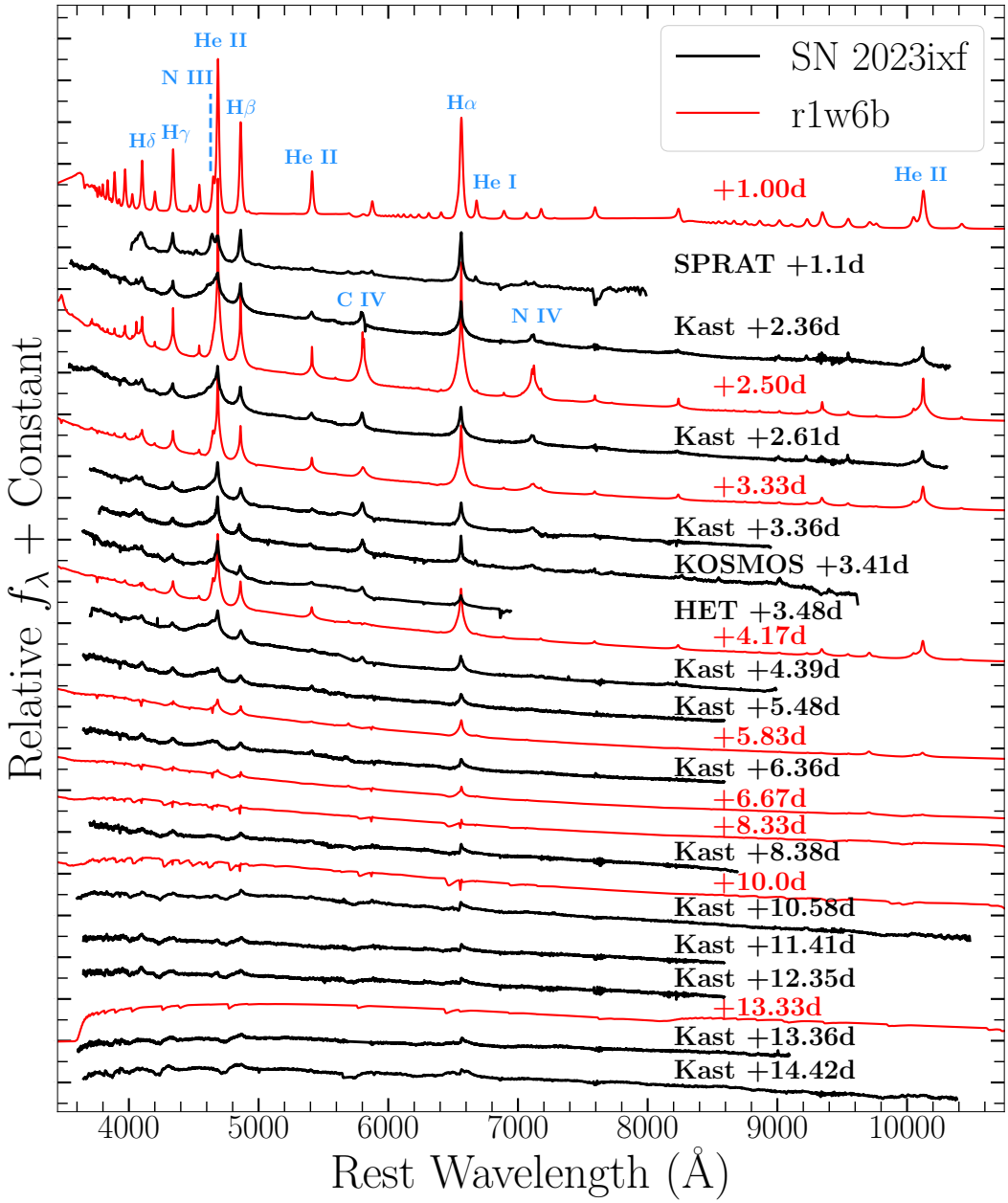

Figure 6.2 Early-time spectral series of SN 2023ixf (black) with respect to `CMFGEN` model r1w6b (red), which is characterized by a wind mass-loss rate of $\dot{M} = 10^{-2}$ $M_\odot$ yr^{-1} that extends to a CSM radius of $R_{\rm CSM} = 8 \times 10^{14}$ cm. Model spectra have been smoothed with a Gaussian kernel to match the spectral resolution of the data. Line identifications shown in blue. The disappearance of He I and N III after the $\delta t = +1.1$ day spectrum indicates a rise in ionization and temperature in SN 2023ixf following the propagation of the shock breakout radiation.

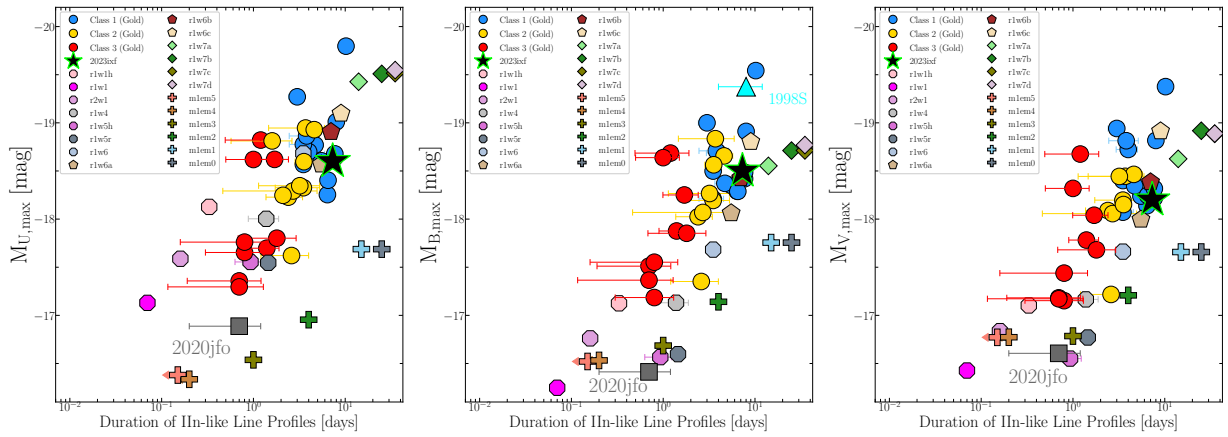

(a) (b) (c)

Figure 6.3 Peak (a) $U-$band, (b) $B-$band, and (c) $V-$band absolute magnitudes versus duration of IIn-like line profiles ($t_{\rm IIn}$) for SN 2023ixf (black star) with respect to CSM-interacting SNe II presented in Jacobson-Galán et al. (2024) shown as circles (color delineation discussed in §8.4.2). SN 2020jfo (Teja et al. 2022) shown as reference canonical SN II without significant CSM interaction (grey square). `CMFGEN` models plotted as colored octagons, polygons, diamonds and plus signs. SN 2023ixf has an observed $t_{\rm IIn}$ and peak absolute magnitude that is consistent with the other gold sample SNe II displaying the strongest signs of CSM interaction e.g., SNe 1998S, 2017ahn, 2020pni, 2020tlf (Leonard et al. 2000; Fassia et al. 2001; Shivvers et al. 2015; Tartaglia et al. 2021; Terreran et al. 2022; Jacobson-Galán et al. 2024)

6.4 Analysis

6.4.1 Photometric Properties

The complete early-time, multi-band light curve of SN 2023ixf is presented in Figure 6.1(a). We fit a 5$^{\rm th}$-order polynomial to the $g-$band light curve to derive a peak absolute $g-$band magnitude of $M_g = -18.4 \pm 0.10$ mag at MJD 60088.61$\pm$0.10, where the uncertainty on peak magnitude is the 1σ error from the fit and the uncertainty on the peak phase is found from adding the uncertainties on both the time of peak magnitude and the time of first light in quadrature. Using the adopted time of first light, this indicates a rise time of $t_r = 5.8 \pm 0.10$ days with respect to g-band maximum. Other filters display similarly bright peak absolute magnitudes e.g., $M_u = -18.6 \pm 0.11$ mag and $M_r = -18.0 \pm 0.09$ mag — this indicates a bolometric boost to the SN brightness rather than a color effect. Following its rise to peak, the multi-color light curve of SN 2023ixf has remained at an approximately constant brightness, indicating that it could be entering a plateau phase (i.e., SN II-P classification). However, at this time, the SN is still very blue, therefore indicating that the recombination phase has yet to be reached. All peak magnitudes and rise-times are presented in Table A1.

In Figure 7.4, we compare the observed peak absolute magnitudes of SN 2023ixf to a sample of SNe II with spectroscopic signatures of CSM-interaction (i.e., IIn-like profiles) (Jacobson-Galán et al. 2024). This gold sample includes most of the known CSM-interacting SNe II that show detectable IIn-like profiles in their early-time spectra and have early-time UV observations with *Swift* UVOT. The color delineation of all presented sample objects is as follows: at phases of $t \sim 2$ days post-explosion, blue colored objects show high ionization emission lines of N III, He II, and C IV (e.g., SNe 1998S, 2017ahn, 2018zd, 2020pni, 2020tlf, etc), yellow colored objects have no N III emission but do show He II, and C IV (e.g., SNe 2014G, 2022jox), and red colored objects only show weaker He II emission (e.g., SNe 2013fs). However, it should be noted that high ionization lines of O V/VI, C V, and N IV are also present in SN 2013fs at $t < 1$ day due to a more compact CSM than other CSM-interacting SNe II (Yaron et al. 2017; Dessart et al. 2017). With respect to other SNe II with evidence for interaction with CSM, SN 2023ixf is ∼0.5 mag brighter in all observed filters than the median peak absolute magnitude observed in the sample. SN 2023ixf has a comparable peak brightness and rise-times to SNe 2017ahn, 2018zd, 2020pni, 2020abjq and 2022ffg (Zhang et al. 2020; Hiramatsu et al. 2021; Tartaglia et al. 2021; Terreran et al. 2022; Jacobson-Galán et al. 2024), all of which have similar early-time spectral morphology and duration of the IIn-like line profiles (§8.4.2). However, the rise-time of SN 2023ixf is significantly shorter than more extreme events such as SNe 1998S, 2019qch, 2020tlf, 2021tyw and 2022pgf, whose rise-times are >12 days. This difference reflects a shorter interaction timescale in a less extended, high-density CSM in SN 2023ixf. Furthermore, SN 2023ixf is distinct from other prototypical SNe II with IIn-like profiles such as SN 2013fs and 2014G (Terreran et al. 2016; Yaron et al. 2017), which have shorter rise-times and lower peak absolute magnitudes. Finally, SN 2023ixf is ∼2 mags brighter in multi-band (i.e., $uBVgriz$) filters than SNe II without IIn-like profiles in their early-time spectra e.g., SN 2020jfo (Teja

et al. 2022; Fig. 7.4) or average values derived from samples of SNe II (Anderson et al. 2014).

6.4.2 Spectroscopic Properties

The complete early-time spectroscopic sequence of SN 2023ixf from $\delta t = +1.1$ to +14.4 days is presented in Figure 7.2, consistent with other spectral sequences released on this object (Stritzinger et al. 2023; Yamanaka et al. 2023). In the earliest spectrum, SN 2023ixf shows narrow, symmetric emission features of H I, He I/II, N III/IV and C IV. A two-component Lorentzian model fit to the Hα profile in the high resolution ($R \approx 3000$) +2.4 d Kast spectrum shows a narrow component full width at half maximum (FWHM) velocity of $<$150 km s^{-1} and broad symmetric component velocity of $\sim$1400 km s^{-1}; the former is ascribed to the progenitor wind while the latter is caused by scattering of recombination line photons by free, thermal electrons in the ionized CSM (Chugai 2001; Dessart et al. 2009; Huang et al. 2018). However, it should be noted that at these phases, there could be radiative acceleration of the CSM that causes the width of the narrow component to be larger than the true velocity of the progenitor wind (Dessart et al. 2015; Tsuna et al. 2023).

SN 2023ixf may be the first SN to exhibit a rapid rise in ionization between the first and second spectrum as shown in Figure 7.2. This is caused initially by the shock breakout pulse and later on by the incoming radiation from the embedded shock. This is witnessed here with the presence of lines of moderately ionized species (i.e. lines of He I or N III) and a moderately blue color at $\delta t = 1.1$ days. At $\delta t = 2.4$ days, the SN 2023ixf spectrum is much bluer, the lines of He I $\lambda\lambda\lambda$5875, 6678, and 7065 have weakened or disappeared, and the spectrum exhibits instead lines of C IV (λ5808) and He II (λ4686). Furthermore, there is emission from N V $\lambda 4604 - 4620$ contributing at wavelengths bluewards of the He II λ4686 line, consistent with heightened ionization at these phases.

The narrow, symmetric line profiles with Lorentzian wings caused by electron-scattering (i.e., IIn-like) continue to persist in SN 2023ixf for the first week of the SN evolution. Then, in the +5.48 d and +6.36 d spectra, the He II emission begins to fade (Fig. 7.5) and the SN develops a broad absorption profile in all Balmer transitions, indicating the escape of photons from the fast moving ejecta and a decrease in CSM density. We therefore define the duration of the IIn-like line profiles as the transition point at which the optical depth to electron-scattering has dropped enough to see the emerging fast-moving SN ejecta. For SN 2023ixf, we estimate that this change occurs at $t_{\rm IIn} \approx 8$ days, which is reflective of the disappearance of the electron-scattering wings in the He II emission line and the development of broad absorption profiles at Balmer series wavelengths. This indicates that the photosphere is first located in the unshocked CSM (far above the shock), then in the swept up material present in the fast moving dense shell (i.e., shocked CSM), and then in the fastest moving SN ejecta below the dense shell. Based on the $T > 10$ keV X-ray spectrum of SN 2023ixf (Grefenstette et al. 2023), there is sufficiently high temperatures for He II to exist, so the decrease in line strength can be attributed to a reduction in particle density as the shock samples CSM at $r > 10^{15}$ cm. As shown in Figure 7.5, the bluest edge of the Hα and Hβ line profiles corresponds to velocities of $\sim$8500 km s^{-1}, which provides a lower limit on the velocities of

the fastest moving H-rich material at the shock front. By two weeks post-explosion, the SN spectra is composed of broad H I absorption profiles, similar to other young SNe II.

The duration of the IIn-like signatures in SN 2023ixf is consistent with other CSM-interacting SNe II with enhanced progenitor mass-loss rates of $\dot{M} > 10^{-2}$ M$_\odot$ yr^{-1} (Figure 7.4). In Figure 7.4, we present peak absolute magnitudes with respect to IIn profile duration for all gold sample CSM-interacting SNe II analyzed in Jacobson-Galán et al. (2024). Intriguingly, there exists a natural trend between peak brightness and IIn-like profile duration amongst these events, which is reflective of a continuum of progenitor mass-loss rate and CSM extent. The observed $t_{\rm IIn}$ in SN 2023ixf is most similar to SNe 2017ahn, 2018zd, 2020pni, 2020tlf and 2022ffg, but is not as large as that observed in 2020tlf, 2021tyw, or 2022pgf, likely due to a more extended dense CSM in those objects. Furthermore, the evolution of SN 2023ixf is unlike other CSM-interacting SNe II with $t_{\rm IIn} < 5$ days post-explosion (e.g., SNe 2013fs or 2014G), which do not show N emission lines at phases > 1 day post-explosion and is caused by a more compact/high density or extended/low density CSM (Dessart et al. 2017). The observed early spectral differences between SN 2023ixf and other CSM-interacting SNe II is illustrated in Figure 6.5. Here it is shown that the line profiles of SN 2023ixf at ~ 2 days post-explosion are most consistent with interaction between SN ejecta and CSM constructed from a high progenitor mass-loss rate ($\dot{M} > 10^{-2}$ M$_\odot$ yr^{-1}; also see Fig. 6.6).

6.4.3 Modeling

In order to quantify the CSM properties of SN 2023ixf, we compared the spectral and photometric properties of SN 2023ixf to a model grid of non-LTE, radiative transfer simulations covering a wide range of progenitor mass-loss rates ($\dot{M} = 10^{-6} - 10^{0}$ M$_\odot$ yr^{-1}; $v_w = 50$ km s^{-1}) and CSM radii ($R = 10^{14} - 10^{16}$ cm), all in spherical symmetry. Simulations of the SN ejecta-CSM interaction were performed with the multi-group radiation-hydrodynamics code `HERACLES` (González et al. 2007; Vaytet et al. 2011; Dessart et al. 2015), which consistently computes the radiation field and hydrodynamics. Then, at selected snapshots in time post-explosion, the hydrodynamical variables are imported into the non-LTE radiative-transfer code `CMFGEN` (Hillier & Dessart 2012; Dessart et al. 2015) for an accurate calculation of the radiative transfer, which includes a complete model atom, $\sim 10^6$ frequency points, and treatment of continuum and line processes as well as electron scattering. For each model, we adopt an explosion energy of 1.2×10^{51} erg, a 15M$_\odot$ progenitor with a radius ranging from $R_\star \approx 500-700$ R$_\odot$, and a CSM composition set to the surface mixture of a RSG progenitor (Davies & Dessart 2019). For the simulations presented in this work, the CSM extent is much greater than $R_\star$ ($\sim$500–1200 R$_\odot$ for a RSG mass range of $\sim$10–20 M$_\odot$) and therefore the progenitor properties have no impact during phases of ejecta-CSM interaction. The progenitor radius plays a more significant role on the light curve evolution during the plateau phase (e.g., see Dessart et al. 2013; Jacobson-Galán et al. 2022a), i.e., once the interaction phase is over and the emission from from the deeper ejecta layers dominate the SN luminosity. Specific methods for each simulation can be found in Dessart et al. (2016, 2017);

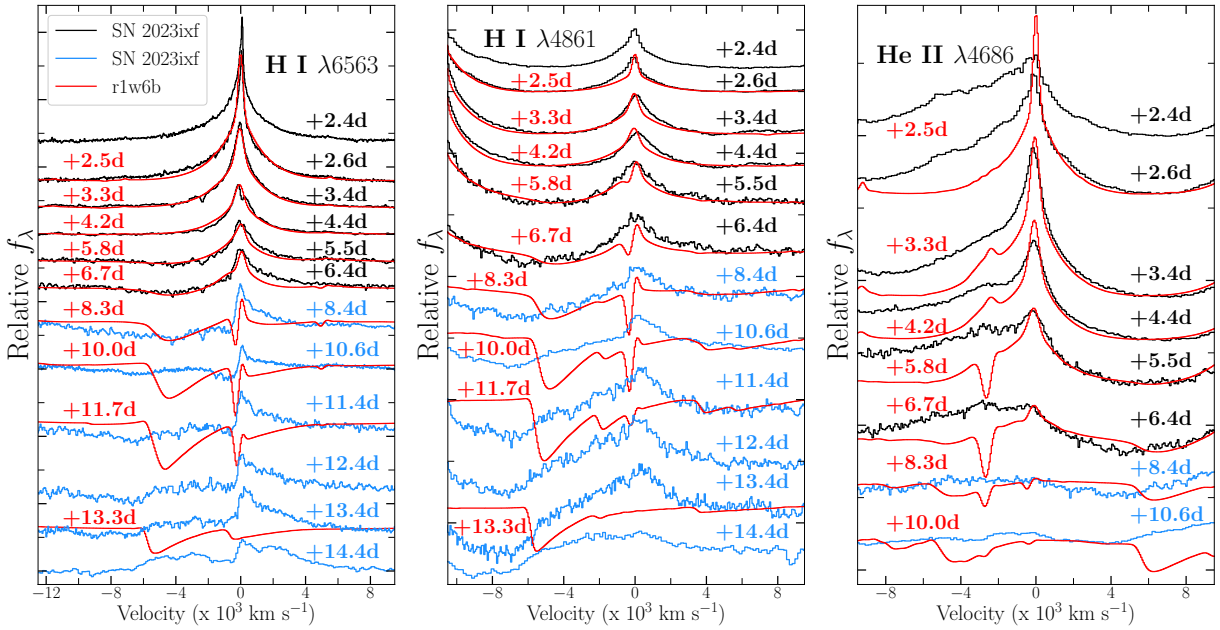

(a) (b) (c)

Figure 6.4 (a) Hα velocity evolution in SN 2023ixf from $\delta t = 2.4 - 14.4$ days with respect to r1w6b model spectra (red), which has been scaled to the emission line peaks of SN 2023ixf and smoothed with a Gaussian filter to better compare with the data. Early-time spectral profiles are shaped by electron-scattering in the dense CSM. The transition shown from black to blue lines ($t_{\rm IIn} \approx 8$ days) marks the emergence of broad absorption features derived from the fastest moving SN ejecta. (b) Hβ velocity evolution, also showing that the electron-scattering line profiles subside after ~ 8 days. (c) He II λ4686 velocity evolution reveals that the electron-scattering profile fades by ~ 8 days, suggesting a significant decrease in CSM density.

Jacobson-Galán et al. (2022a); Dessart & Jacobson-Galán (2023) and all CSM properties of each model are presented in Table A4.

From the CMFGEN model grid, we identify four models (r1w6, r1w6a,b,c) with the smallest residuals between model predictions and both the observed multi-color peak magnitudes and rise-times (§8.4.1) as well as the duration of IIn profiles (§8.4.2). The best matched model peak magnitudes are within ∼0.5 mag of SN 2023ixf in all filters and have a $t_{\rm IIn}$ that is within ±3 days of that observed in SN 2023ixf. The features used for determination of the most consistent model are presented in Figure 7.4. We find that the best-fit models to SN 2023ixf have a mass-loss rate of $\dot{M} = 10^{-2}$ M$_\odot$ yr^{-1}, confined to a radius of $r = (0.5 - 1) \times 10^{15}$ cm and containing a total CSM mass of $M_{\rm CSM} \approx 0.04 - 0.07$ M$_\odot$. Based on model predictions, the mass-loss then decreases to $\dot{M} = 10^{-6}$ M$_\odot$ yr^{-1} (e.g., Fig. 6.1b) at larger distances ($r > 10^{15}$ cm) with a constant wind velocity of $v_w = 50$ km s^{-1}; this geometry is consistent with the changing X-ray absorption observed in SN 2023ixf (Grefenstette et al. 2023). This wind velocity is not derived from spectroscopic observations but the narrow line cores of the higher resolution Kast spectra indicate $v_w \lesssim 150$ km s^{-1}. The spectral time series of the r1w6b model and multi-color light curve of the r1w6a,b,c models are presented in Figures 7.2 and 6.1(a). In Figure 6.6, we present SN 2023ixf spectra with respect to a range of early-time CMFGEN models with varying mass-loss rates and CSM radii to further illustrate the consistencies and inconsistencies between models and observations. In Figure 6.7, we present the UV spectrum of the r1w6b at +2.5 days, which predicts a plethora of high-ionization features (e.g., O IV/VI) in the near-to-far UV spectra of SN 2023ixf. Furthermore, the r1w6b model adequately reproduces the observed IIn-like emission line profiles in SN 2023ixf (e.g., Figs. 6.5 & 6.6) using the 15 M$_\odot$, solar metallicity, RSG progenitor model composition (Dessart et al. 2017; Davies & Dessart 2019).

Unlike the other CSM structures explored in the CMFGEN model grid, the r1w6b model best reproduces both the observed peak absolute magnitudes in $uBgVriz$ filters as well as the duration of IIn-like line profiles observed in SN 2023ixf (Figure 7.4). However, this model cannot match the early light curve slope observed in SN 2023ixf, which is likely a result of the density profile invoked. A better fit to the light curve would require a higher density immediately above $R_\star$ (e.g., through a larger scale height) and a more gradual decline in density at the outer edge of the dense CSM i.e., at $\sim 8 \times 10^{15}$ cm. A more extended CSM, as in model r1w6c, increases the rise time to maximum and is thus not a suitable solution. Furthermore, a larger model kinetic energy will also increase the luminosity at early-times, which would provide more consistency between the model light curve rise and SN 2023ixf.

The evolution of the line profiles in the r1w6b model are consistent with the observed transition from electron-scattering broadened line profiles of Balmer series H I, He II, C IV, and N III/IV ($t < 7$ days) to Doppler broadened absorption profiles of the fastest moving H-rich SN ejecta ($t > 7$ days). Nevertheless, for a consistent continuum slope, the model spectra over-predict the narrow line emission observed in SN 2023ixf (e.g., Fig. 7.2), which is likely caused by a smaller emitting volume of dense CSM in SN 2023ixf than the r1w6b model. The line strengths of SN 2023ixf are well-matched by the r1w6 model, which is characterized by the same $\dot{M}$ but smaller CSM radius (e.g., Fig. 6.5); this model, however, is unable to

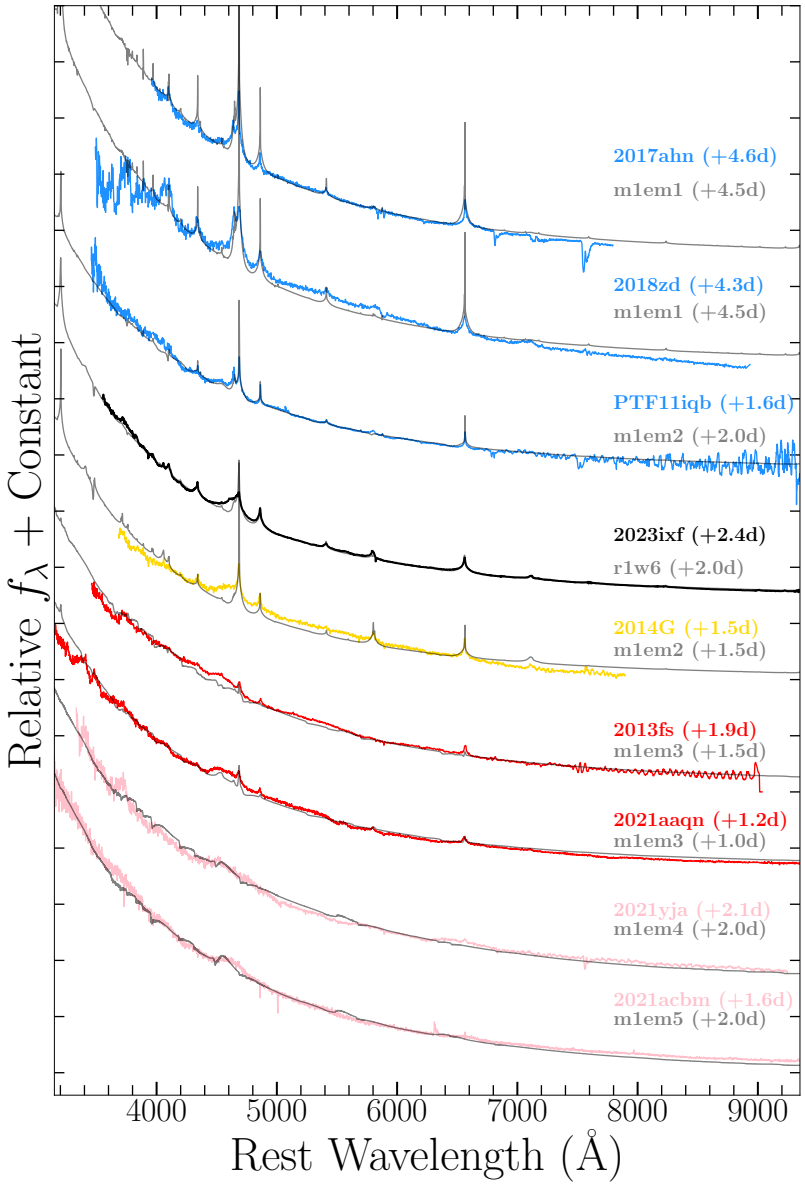

Figure 6.5 Early-time spectra of SNe II with varying degrees of CSM interaction, selected from Jacobson-Galán et al. (2024). Colors delineate differences between duration of IIn-like signatures as well as the presence of different high-ionization species at phases of $t \approx 2$ days (e.g., spectra in blue show N III while others do not). Overplotted in grey are best fitting `CMFGEN` models for high (10^{-1} $M_\odot$ yr^{-1}; top) to low (10^{-5} $M_\odot$ yr^{-1}; bottom) mass-loss rates. SN 2023ixf lies within the continuum of CSM-interacting SNe II and the evolution of its prominent spectral signatures of photo-ionized CSM is consistent with a progenitor mass-loss rate of $\dot{M} = 10^{-2}$ $M_\odot$ yr^{-1}.

Table A1 Main parameters of SN 2023ixf

Host Galaxy	M101
Redshift	0.000804
Distance	6.9 Mpc[6]
Time of First Light (MJD)	60082.83
$E(B-V)_{\rm MW}$	0.008 mag[7]
$E(B-V)_{\rm host}$	0.033 mag[8]
$M_u^{\rm peak}[t_r]$	-18.6 mag[4.9 d]
$M_B^{\rm peak}[t_r]$	-18.5 mag[5.7 d]
$M_g^{\rm peak}[t_r]$	-18.4 mag[5.8 d]
$M_V^{\rm peak}[t_r]$	-18.1 mag[6.0 d]
$M_r^{\rm peak}[t_r]$	-18.0 mag[6.1 d]
$M_i^{\rm peak}[t_r]$	-17.9 mag[7.8 d]
$M_z^{\rm peak}[t_r]$	-17.8 mag[8.2 d]
$\rm R_{CSM}$	$(0.5-1)\times10^{15}$ cm
$\rm M_{CSM}$	$(0.04-0.07)$ $\rm M_\odot$
$\dot{M}[v_w]$[9]	10^{-2} $\rm M_\odot$ $\rm yr^{-1}[50\ km\,s^{-1}]$
CSM Composition	Solar Metallicity[10]
Time of $\dot{M}$	∼3-6 years pre-SN

reproduce the extended duration of the IIn-like features (e.g., see Fig. 7.4). Furthermore, as shown in Figure 7.5(c), the He II λ4686 line profile is not completely reproduced by the model spectrum, which could be due to the fact that these simulations are performed in 1D, assume spherical symmetry of the CSM, or require higher kinetic energies. Additionally, once the IIn-like profiles fade, the model H I ejecta velocities are lower than in SN 2023ixf (e.g., Fig. 7.5). It should also be noted that the narrow Hα P Cygni profile that develops in SN 2023ixf at $t > 8$ days has higher velocities (~ 100 km s^{-1}) than the r1w6b model (~ 50 km s^{-1}), suggesting potential radiative acceleration of the unshocked CSM.

Using the lower limit on the SN shock velocity of $\gtrsim$8500 km s^{-1} as observed at the bluest edge of the Hα absorption profile shown in Figure 7.5, we find that the location of the SN shock at $t = 6.4$ days is $r \gtrsim 5\times10^{14}$ cm, which corresponds to an optical depth to electron-scattering of $\tau \approx 10$ in the r1w6b model. Then, by $t = 10.6$ days, the shock is located at $r \gtrsim 8\times10^{14}$ cm, which in the r1w6b model, is in CSM with an electron-scattering optical depth of $\tau \approx 0.2$. This decrease in $\tau_{\rm ES}$ in the r1w6b model is consistent with the observed fading of IIn-like profiles in SN 2023ixf and reflects a reduction in CSM density at $r > 10^{15}$ cm. However, it should be noted that the shock velocity decreases as the shock crosses the CSM and, therefore, the shock position is not as simplified as $R_{\rm sh} = v_{\rm sh}\times t$. We present the time-series evolution of the r1w6b model luminosity, density, temperature and velocity as a function of radius in Figure 6.8. Furthermore, at +15 days, the r1w6b

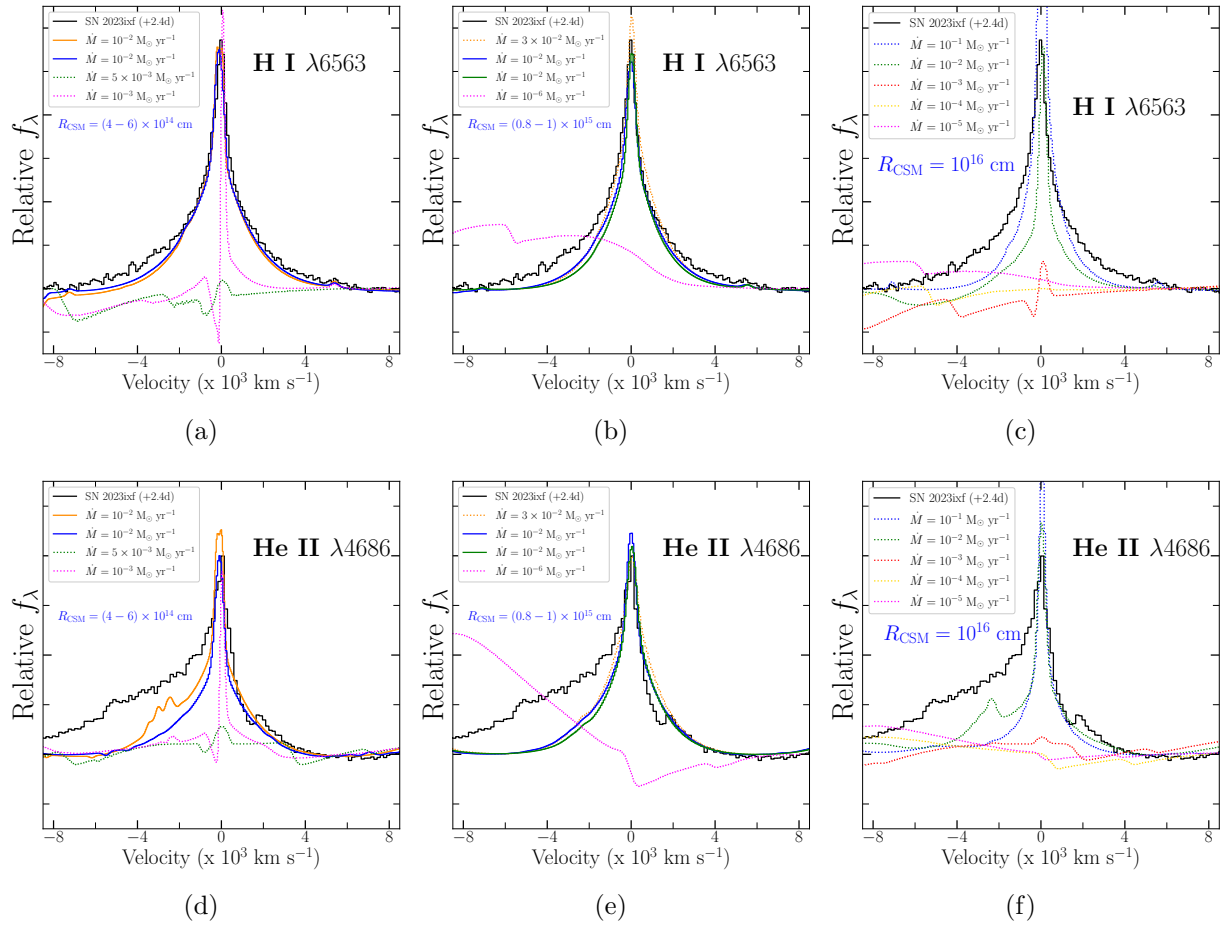

Figure 6.6 Hα velocity of SN 2023ixf at $\delta t = 2.4$ days (black) with respect to `CMFGEN` model spectra at +2 days post-explosion. Best fit models (e.g., §7.4.3) shown as solid lines; additional, inconsistent models plotted as dotted lines. For proper comparison, models are scaled to the continuum of SN 2023ixf and the peak of the presented emission line profile. These models have varying mass-loss rates that are contained within CSM radii of (a) $R_{CSM} = (4-6) \times 10^{14}$ cm, (b) $R_{CSM} = (0.8-1) \times 10^{15}$ cm, and (c) $R_{CSM} = 10^{16}$ cm. (d)/(e)/(f) Same as above, but for He II velocities.

model has a maximum ejecta velocity of $\sim$ 6500 km s^{-1}, which is below the maximum velocities observed in the Hα profile of SN 2023ixf. This may indicate some degree of CSM asymmetry that would cause a deceleration along certain lines of sight while also allowing for typical SN ejecta velocities of $\sim 10^4$ km s^{-1} to be preserved. Also, the weaker Doppler broadened absorption observed in SN 2023ixf compared to the r1w6b model may be the result of persistent CSM interaction that will contribute weak, broad, and boxy Hα emission capable of reducing the absorption profile strength (Dessart & Hillier 2022).

6.5 Discussion

The first 2 weeks of photometric and spectroscopic observations of SN 2023ixf have revealed essential characteristics of the SN progenitor system and the explosion itself. Based on the best fitting `CMFGEN` model, the progenitor of SN 2023ixf was likely a RSG with a mass-loss rate of $\dot{M} \approx 10^{-2}$ M$_\odot$ yr^{-1}, which created dense CSM extending to $r \approx (0.5-1)\times10^{15}$ cm that contained a total mass of $M_{\rm CSM} \approx 0.04 - 0.07$ M$_\odot$. Furthermore, we find that the observed light curve can be fit with standard explosion energy (1.2×10^{51} ergs) and that the IIn-like signatures in SN 2023ixf can be modeled with a CSM composition that matches typical RSG surface abundances with no need for significant N or He enrichment.

For a wind velocity of $\sim$ 50 km s^{-1}, the proposed CSM extent translates to a period of enhanced mass-loss (i.e. "super wind") in the last $\sim$3-6 years years prior to core collapse. This scenario comports with the observed duration of SN 2023ixf's IIn-like line profiles ($\sim$8 days), after which time the optical depth to electron-scattering in the CSM has decreased and SN 2023ixf begins to show absorption profiles from the outer, H-rich ejecta and fast moving dense shell. If the CSM detected in SN 2023ixf represents the only high-density shell of CSM (i.e. only one super wind phase), then the SN shock should continue to sample low-density material ($\dot{M} \approx 10^{-6}$ M$_\odot$ yr^{-1}, $v_w = 50$ km s^{-1}) at larger distances ($r > 10^{15}$ cm). Overall, both the confined high-density CSM shell and the extended low-density wind may have made the RSG progenitor star quite dust obscured prior to explosion (Davies et al. 2022). This is consistent with the findings of Kilpatrick et al. (2023a) who show that the pre-explosion *Hubble* and *Spitzer* imaging of SN 2023ixf indicates a moderately sized ($\sim$11 M$_\odot$) RSG progenitor star enshrouded in a dust shell.

This physical progenitor picture is also consistent with the initial findings of multi-wavelength observations of SN 2023ixf. X-ray observations revealed a 3-30 keV spectrum consistent with bremsstrahlung emission that initially showed significant absorption in the soft part of the spectrum (Grefenstette et al. 2023). These observations are indicative of shock interaction with dense CSM in a confined shell. Furthermore, radio observations have so far produced non-detections at $\nu = 1 - 230$ GHz with SMA, GMRT, and VLA (Berger et al. 2023; Matthews et al. 2023; Chandra et al. 2023), likely caused by large free-free absorption in the optically thick CSM. However, as the SN shock now enters lower density material at larger distances, it is probable that the radio emission in SN 2023ixf will become detectable.

6.6 Conclusions

In this paper we have presented UV/optical observations and models of the nearby SN II, 2023ixf located in nearby spiral host galaxy M101 at $d = 6.9$ Mpc. Below we summarize the primary observational findings of SN 2023ixf:

- The early-time spectra of SN 2023ixf show prominent narrow emission lines of H I, He I/II, N III/IV/V and C IV that result from the photo-ionization of dense, optically thick CSM. These electron-scattering broadened profiles (i.e., IIn-like) last for $t_{\rm IIn} \approx$ 8 days, after which time broad absorption profiles from the fastest H-rich SN ejecta begin to form.

- CSM interaction in SN 2023ixf caused increased peak absolute magnitudes (e.g., $M_u = -18.6$ mag, $M_g = -18.4$ mag) relative to SNe II that occur in a low density circumstellar environment (e.g., $\rho < 10^{-16}$ g cm^{-3}). The observed multi-color peak absolute magnitudes and duration of the IIn-like profiles (i.e., $t_{\rm IIn}$) places SN 2023ixf in the continuum of SNe II with varying degrees of RSG mass-loss before explosion. Compared to the sample of CSM-interacting SNe II compiled in Jacobson-Galán et al. (2024), SN 2023ixf is most similar to SNe 2017ahn, 2018zd, 2020pni and 2022ffg.

- Comparing SN 2023ixf's peak absolute magnitudes and duration of IIn-like profiles to a grid of `CMFGEN` simulations suggests a CSM that has a composition typical of a solar-metallicity RSG, is confined to $r \approx (0.5 - 1) \times 10^{15}$ cm, and is formed from wind corresponding to a progenitor mass-loss rate of $\dot{M} = 10^{-2}$ M$_\odot$ yr^{-1} (i.e., $\rho \approx 10^{-12}$g cm^{-3} at $r = 10^{14}$ cm). Adopting a wind velocity of $v_w = 50$ km s^{-1}, this scenario corresponds to a period of enhanced mass-loss (i.e., "superwind") during the last ∼3-6 years years before core-collapse.

Given its close proximity and present brightness, SN 2023ixf is poised to become the best studied CSM-interacting SN II to date. Future, multi-wavelength observations will, among other things, uncover the density profile of the confined CSM as well as the mass-loss history of the RSG progenitor in its final decades to centuries.

6.7 Acknowledgements

Research at UC Berkeley is conducted on the territory of Huichin, the ancestral and unceded land of the Chochenyo speaking Ohlone people, the successors of the sovereign Verona Band of Alameda County. PS1/2 observations were conducted on the stolen land of the kānaka ʻōiwi people. We stand in solidarity with the Pu'uhonua o Pu'uhuluhulu Maunakea in their effort to preserve these sacred spaces for native Hawaiʻians. Shane 3-m observations were conducted on the stolen land of the Ohlone (Costanoans), Tamyen and Muwekma Ohlone tribes.

We thank Greg Zeimann for help with HET data reduction and Dan Weisz for Kast observations.

The Young Supernova Experiment and its research infrastructure is supported by the European Research Council under the European Union's Horizon 2020 research and innovation programme (ERC Grant Agreement No. 101002652, PI K. Mandel), the Heising-Simons Foundation (2018-0913, PI R. Foley; 2018-0911, PI R. Margutti), NASA (NNG17PX03C, PI R. Foley), NSF (AST-1720756, AST-1815935, PI R. Foley; AST-1909796, AST-1944985, PI R. Margutti), the David & Lucille Packard Foundation (PI R. Foley), VILLUM FONDEN (project number 16599, PI J. Hjorth), and the Center for AstroPhysical Surveys (CAPS) at the National Center for Supercomputing Applications (NCSA) and the University of Illinois Urbana-Champaign.

W.J.-G. is supported by the National Science Foundation Graduate Research Fellowship Program under Grant No. DGE-1842165. W.J.-G. acknowledges support through NASA grants in support of *Hubble Space Telescope* program GO-16075 and 16500. This research was supported in part by the National Science Foundation under Grant No. NSF PHY-1748958. R.M. acknowledges support by the National Science Foundation under Award No. AST-2221789 and AST-2224255. The Margutti team at UC Berkeley is partially funded by the Heising-Simons Foundation under grant # 2018-0911 and #2021-3248 (PI: Margutti).

C.D.K. is partly supported by a CIERA postdoctoral fellowship and a grant in support of NASA program HST-GO-16136. V.A.V. acknowledges support by the National Science Foundation under Award No.AST-2108676. C.R.A. was supported by grants from VILLUM FONDEN (project numbers 16599). Parts of this research were supported by the Australian Research Council Centre of Excellence for All Sky Astrophysics in 3 Dimensions (ASTRO 3D), through project number CE170100013. Y.-C.P. is supported by the National Science and Technology Council (NSTC grant 109-2112-M-008-031-MY3. A.G. is supported by the National Science Foundation Graduate Research Fellowship Program under Grant No. DGE–1746047. A.G. also acknowledges funding from the Center for Astrophysical Surveys Fellowship at UIUC/NCSA and the Illinois Distinguished Fellowship. C.G. is supported by a VILLUM FONDEN Young Investigator Grant (project number 25501). SJS acknowledges funding from STFC grants Ref: ST/T000198/1 and ST/S006109/1. J.H. was supported by a VILLUM FONDEN Investigator grant (project number 16599). D. M. acknowledges NSF support from grants PHY-2209451 and AST-2206532.

The UCSC team is supported in part by NASA grants NNG17PX03C and 80NSSC22K1518, NSF grant AST–1815935, and by a fellowship from the David and Lucile Packard Foundation to R.J.F.

YSE-PZ (Coulter et al. 2023) was developed by the UC Santa Cruz Transients Team with support from NASA grants NNG17PX03C, 80NSSC19K1386, and 80NSSC20K0953; NSF grants AST-1518052, AST-1815935, and AST-1911206; the Gordon & Betty Moore Foundation; the Heising-Simons Foundation; a fellowship from the David and Lucile Packard Foundation to R.J.F.; Gordon and Betty Moore Foundation postdoctoral fellowships and a NASA Einstein fellowship, as administered through the NASA Hubble Fellowship program and grant HST-HF2-51462.001, to D.O.J.; and a National Science Foundation Graduate

Research Fellowship, administered through grant No. DGE-1339067, to D.A.C.

A major upgrade of the Kast spectrograph on the Shane 3 m telescope at Lick Observatory, led by Brad Holden, was made possible through generous gifts from the Heising-Simons Foundation, William and Marina Kast, and the University of California Observatories. Research at Lick Observatory is partially supported by a generous gift from Google.

This research was supported by the Munich Institute for Astro-, Particle and BioPhysics (MIAPbP) which is funded by the Deutsche Forschungsgemeinschaft (DFG, German Research Foundation) under Germany´s Excellence Strategy – EXC-2094 – 390783311.

The Pan-STARRS1 Surveys (PS1) and the PS1 public science archive have been made possible through contributions by the Institute for Astronomy, the University of Hawaii, the Pan-STARRS Project Office, the Max-Planck Society and its participating institutes, the Max Planck Institute for Astronomy, Heidelberg and the Max Planck Institute for Extraterrestrial Physics, Garching, The Johns Hopkins University, Durham University, the University of Edinburgh, the Queen's University Belfast, the Harvard-Smithsonian Center for Astrophysics, the Las Cumbres Observatory Global Telescope Network Incorporated, the National Central University of Taiwan, STScI, NASA under grant NNX08AR22G issued through the Planetary Science Division of the NASA Science Mission Directorate, NSF grant AST–1238877, the University of Maryland, Eotvos Lorand University (ELTE), the Los Alamos National Laboratory, and the Gordon and Betty Moore Foundation.

IRAF is distributed by NOAO, which is operated by AURA, Inc., under cooperative agreement with the National Science Foundation (NSF).

6.8 Appendix

Here we present a log of optical spectroscopic observations of SN 2023ixf in Table A1 and a list of model properties for all `CMFGEN` simulations in Table A4. Figure 6.7 presents *Swift* UVOT grism spectra of SN 2023ixf and model predictions for FUV spectral features. Figure 6.8 shows the time-series evolution of luminosity, density, temperature and velocity as a function of radius in the r1w6b model.

Table A1. Optical Spectroscopy of SN 2023ixf

UT Date	MJD	Phase[a] (days)	Telescope	Instrument	Wavelength Range (Å)
2023-05-21	60085.20	2.36	Shane	Kast	3600–10800
2023-05-21	60085.21	2.37	Shane	Kast	5600–7254
2023-05-21	60085.44	2.61	Shane	Kast	3600–10800
2023-05-21	60085.46	2.63	Shane	Kast	5600–7254
2023-05-22	60086.20	3.36	Shane	Kast	3600–9000
2023-05-22	60086.24	3.41	APO	KOSMOS	3600–10800
2023-05-22	60086.31	3.48	HET	LRS	3600–7000
2023-05-23	60087.23	4.39	Shane	Kast	3600–9000
2023-05-24	60088.31	5.48	Shane	Kast	3600–9000
2023-05-25	60089.20	6.36	Shane	Kast	3600–9000
2023-05-27	60091.21	8.38	Shane	Kast	3600–9000
2023-05-29	60093.41	10.58	Shane	Kast	3600–10800
2023-05-29	60093.42	10.59	Shane	Kast	5600–7254
2023-05-30	60094.25	11.41	Shane	Kast	3600–9000
2023-05-31	60095.19	12.35	Shane	Kast	3600–9000
2023-06-02	60097.26	14.43	Shane	Kast	3600–10800

[a]Relative to first light (MJD 60082.83)

Table A2. Model Properties

Name	$t_{\rm IIn}$ (days)	$\dot{M}$ ($M_\odot$ yr^{-1})	$\rho_{\rm CSM,14}$[a] (g cm^{-3})	$R_{\rm CSM}$ (cm)	Reference
r1w1h	< 0.3	1.0e-06	2.7e-12	3×10^{14}	Dessart et al. (2017)
r1w1	< 0.1	1.0e-06	1.0e-16	1×10^{15}	Dessart et al. (2017)
r2w1	< 0.2	1.0e-06	9.0e-16	1×10^{14}	Dessart et al. (2017)
r1w4	1.4	1.0e-03	1.0e-13	5×10^{14}	Dessart et al. (2017)
r1w5h	0.9	3.0e-03	5.0e-13	3×10^{14}	Dessart et al. (2017)
r1w5r	1.4	5.0e-03	5.0e-13	4×10^{14}	Dessart et al. (2017)
r1w6	3.5	1.0e-02	1.0e-12	5×10^{14}	Dessart et al. (2017)
r1w6a	5.5	1.0e-02	1.0e-12	6×10^{14}	This work
r1w6b	7.0	1.0e-02	1.0e-12	8×10^{14}	This work
r1w6c	9.0	1.0e-02	1.0e-12	1×10^{15}	Jacobson-Galán et al. (2022a)
r1w7a	14.0	3.0e-02	3.0e-12	1×10^{15}	Jacobson-Galán et al. (2022a)
r1w7b	25.0	3.0e-02	3.0e-12	2×10^{15}	Jacobson-Galán et al. (2022a)
r1w7c	35.0	3.0e-02	3.0e-12	4×10^{15}	Jacobson-Galán et al. (2022a)
r1w7d	35.0	3.0e-02	3.0e-12	8×10^{15}	Jacobson-Galán et al. (2022a)
m1em5	< 0.1	1.0e-05	6.1e-16	1×10^{16}	Dessart & Jacobson-Galán (2023)
m1em4	< 0.2	1.0e-04	5.2e-15	1×10^{16}	Dessart & Jacobson-Galán (2023)
m1em3	1.0	1.0e-03	5.4e-14	1×10^{16}	Dessart & Jacobson-Galán (2023)
m1em2	4.0	1.0e-02	1.3e-12	1×10^{16}	Dessart & Jacobson-Galán (2023)
m1em1	15.0	1.0e-01	1.4e-11	1×10^{16}	Dessart & Jacobson-Galán (2023)
m1em0	25.0	1.0e+00	7.3e-11	1×10^{16}	Dessart & Jacobson-Galán (2023)

[a]Density at 10^{14} cm

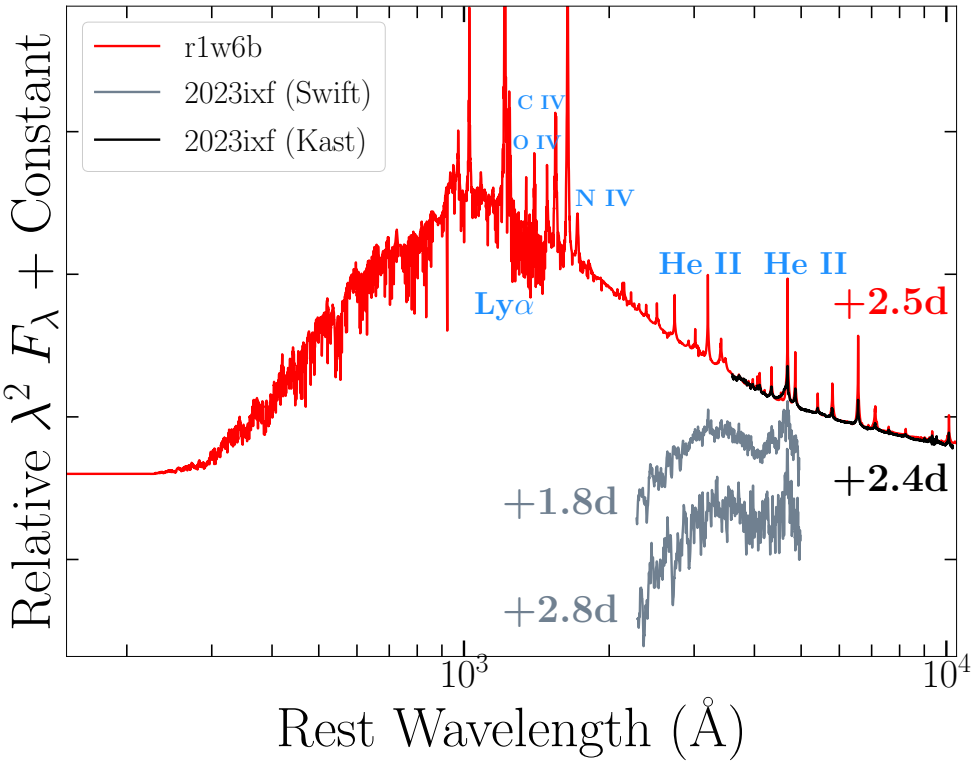

Figure 6.7 *Swift* UV grism spectra (grey) with respect to best fitting `CMFGEN` model (red); y-axis is in units of λ^2 F_λ. The *Swift* UV grism response function below $\sim$ 3200 Å is not reflective of the true slope of the SN SED. The r1w6b model shows that the NUV and FUV spectra of SN 2023ixf likely contains a plethora of narrow, high-ionization emission lines (e.g., He II, C IV, N IV/V, and O IV) derived from CSM interaction.

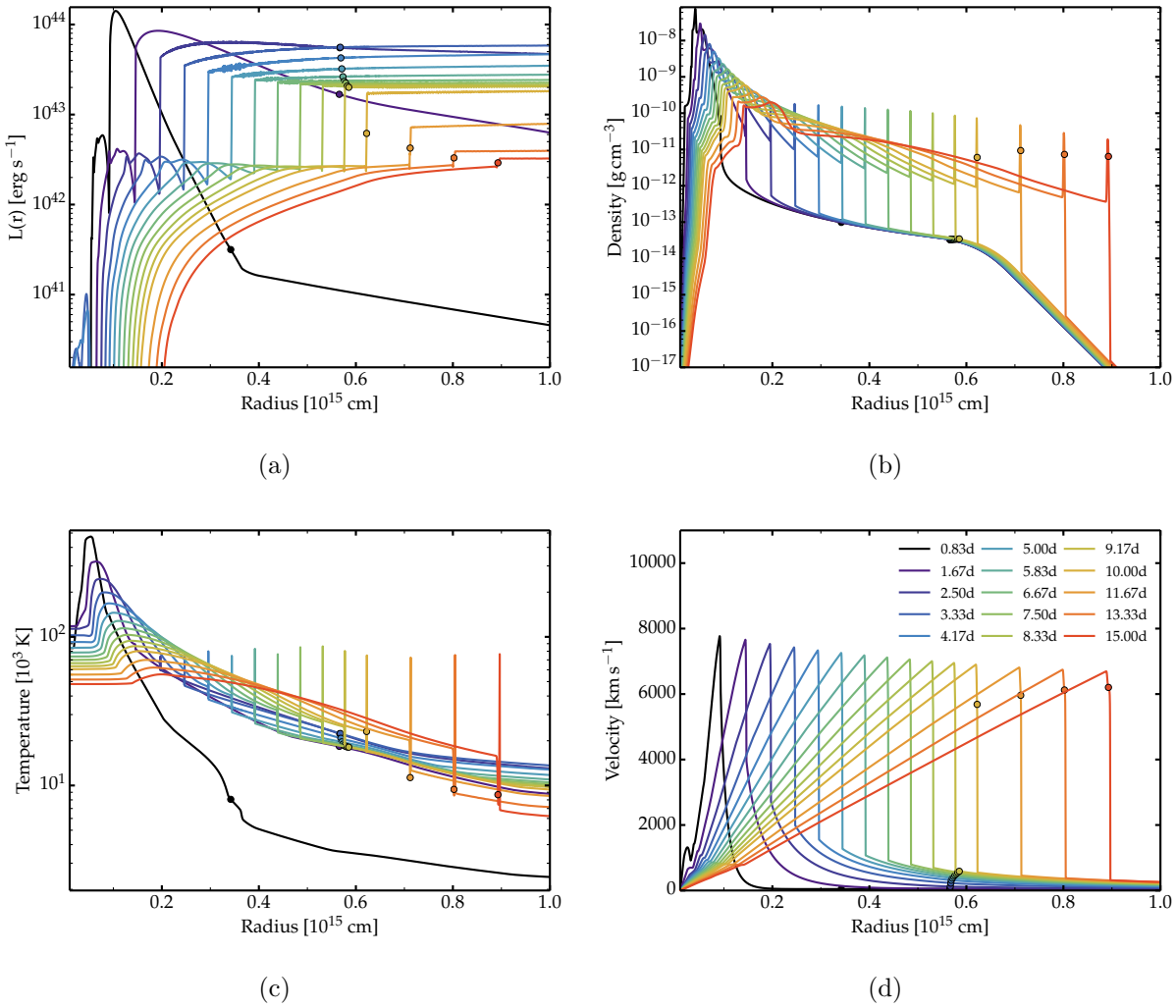

Figure 6.8 Time-series of the (a) luminosity, (b) density, (c) temperature, and (d) velocity versus radius for best fitting `CMFGEN` model r1w6b. Circles show the location of the photosphere, which resides in the slow moving CSM until $\sim$ 8 days and after which recedes into the fast moving dense shell. The model phases begin at the onset of the radiation hydrodyanmics simulation, which is $\sim$1 hr before the shock crosses the progenitor radius (as given in the progenitor stellar model, i.e. without CSM).

Chapter 7

SN 2024ggi in NGC 3621: Rising Ionization in a Nearby, CSM-Interacting Type II Supernova

This chapter is currently being published as Jacobson-Galán et al., 2024b, ApJ, accepted

7.1 Abstract

We present UV/optical/NIR observations and modeling of supernova (SN) 2024ggi, a type II supernova (SN II) located in NGC 3621 at 7.2 Mpc. Early-time ("flash") spectroscopy of SN 2024ggi within +0.8 days of discovery shows emission lines of H I, He I, C III, and N III with a narrow core and broad, symmetric wings (i.e., IIn-like) arising from the photoionized, optically-thick, unshocked circumstellar material (CSM) that surrounded the progenitor star at shock breakout. By the next spectral epoch at +1.5 days, SN 2024ggi showed a rise in ionization as emission lines of He II, C IV, N IV/V and O V became visible. This phenomenon is temporally consistent with a blueward shift in the UV/optical colors, both likely the result of shock breakout in an extended, dense CSM. The IIn-like features in SN 2024ggi persist on a timescale of $t_{\rm IIn} = 3.8 \pm 1.6$ days at which time a reduction in CSM density allows the detection of Doppler broadened features from the fastest SN material. SN 2024ggi has peak UV/optical absolute magnitudes of $M_{\rm w2} = -18.7$ mag and $M_{\rm g} = -18.1$ mag that are consistent with the known population of CSM-interacting SNe II. Comparison of SN 2024ggi with a grid of radiation hydrodynamics and non-local thermodynamic equilibrium (nLTE) radiative-transfer simulations suggests a progenitor mass-loss rate of $\dot{M} = 10^{-2}$ M$_\odot$ yr^{-1} ($v_w = 50$ km s^{-1}), confined to a distance of $r < 5 \times 10^{14}$ cm. Assuming a wind velocity of $v_w = 50$ km s^{-1}, the progenitor star underwent an enhanced mass-loss episode in the last ~ 3 years before explosion.

7.2 Introduction

Shock breakout (SBO) from a red supergiant (RSG) star is characterized by an optical depth of $\tau \approx c/v_{\rm sh}$, where c is the speed of light and $v_{\rm sh}$ is the shock velocity. Consequently, the location and timescale of SBO photon escape is highly dependent on the density and extent of circumstellar material (CSM) that borders the RSG prior to explosion. In addition to light travel effects during SBO (Waxman & Katz 2017; Goldberg et al. 2022), the SBO signal can be significantly enhanced and elongated by the presence of high density CSM directly above the stellar surface (Chevalier & Irwin 2011; Dessart et al. 2017; Haynie & Piro 2021). Once the shock has "broken out," the associated burst of high-energy radiation will "flash ionize" the surrounding medium – observationally this manifests as a hot supernova (SN) continuum riddled with recombination lines from ionization CSM. However, to overcome the recombination timescale of the "flash ionized CSM" ($t_{\rm rec} \propto 1/n_e \approx$ hours-days for $n \approx 10^{7-10}$ cm^{-3}, $\rho \approx 10^{-14} - 10^{-17}$ g cm^{-3} at $r < 2R_\star$, where $R_\star$ is progenitor radius), SN ejecta interaction with dense CSM provides continuous photoionization of the medium for sufficiently large CSM densities (e.g., $\rho \gtrsim 10^{-14}$ g cm^{-3}).

For type II supernovae (SNe II) interacting with such dense CSM, high-energy photons will be emitted from the shock front as the post-shock gas cools primarily through free-free emission ($T_{\rm sh} \approx 10^{5-8}$ K; Chevalier & Irwin 2012; Chevalier & Fransson 2017). This process then prolongs the formation of high-ionization recombination lines (e.g., He II, N III/IV/V, C III/IV) present during the "flash ionization" phase. Intriguingly, as recombination line photons try to exit the CSM, they electron-scatter off of free electrons in the ionized gas, which broadens the observed emission lines that will then appear as the combination of a narrow core and Lorentzian wings (i.e., "IIn-like features"; Chugai 2001; Dessart et al. 2009; Huang & Chevalier 2018). However, as the CSM density and optical depth to electron-scattering drops, these electron-scattering profiles will fade on a characteristic timescale ($t_{\rm IIn}$), with the SN photosphere then revealing the fastest moving SN material (Dessart et al. 2017; Dessart & Jacobson-Galán 2023; Jacobson-Galán et al. 2023, 2024).

Given the rapid evolution of CSM-interacting SNe II in their first hours-to-days, ultra-rapid ("flash") spectroscopy is essential to both capture the SBO signal and persistent photo-ionization of dense CSM, but also to constrain the composition and mass-loss history of the progenitor star in its final year(s) before collapse (Gal-Yam et al. 2014; Khazov et al. 2016; Yaron et al. 2017; Terreran et al. 2022; Jacobson-Galán et al. 2023). To date, all-sky transient surveys have allowed for systematic discovery of SNe II within days of first light. Through modeling of early-time SN II spectra showing IIn-like features with non-LTE radiative transfer codes (e.g., `CMFGEN`; Hillier & Dessart 2012; Dessart et al. 2015), numerous single-object studies indicate enhanced RSG mass-loss ($\dot{M} \approx 10^{-3}$– 10^{-2} M$_\odot$ yr^{-1}, $v_w \approx 50$–100 km s^{-1}) in the final years before explosion (e.g., PTF11iqb, Smith et al. 2015; SN 2013fs, Yaron et al. 2017; Dessart et al. 2017; SN 2014G, Terreran et al. 2016; SN 2016bkv, Hosseinzadeh et al. 2018; Nakaoka et al. 2018; SN 2017ahn, Tartaglia et al. 2021; SN 2018zd, Zhang et al. 2020; Hiramatsu et al. 2021; SN 2019nyk, Dastidar et al. 2024; SN 2020pni, Terreran et al. 2022; SN 2020tlf, Jacobson-Galán et al. 2022a; SN 2022jox, Andrews et al.

2023; SN 2023ixf, Jacobson-Galán et al. 2023; Bostroem et al. 2023; Teja et al. 2023; Smith et al. 2023; Zimmerman et al. 2024). Furthermore, sample studies suggest that >40% of SNe II discovered within 2 days of first light show IIn-like features from interaction with dense CSM (Bruch et al. 2021b, 2023a). Additionally, relative to standard SNe II, events with early-time IIn-like features are incredibly bright in the ultraviolet (Irani et al. 2023; Jacobson-Galán et al. 2024).

In this paper we present, analyze, and model photometric and spectroscopic observations of SN 2024ggi, first discovered by the Asteroid Terrestrial-impact Last Alert System (ATLAS) (Srivastav et al. 2024; Tonry et al. 2024; Chen et al. 2024) on 2024-04-11 (MJD 60411.14). SN 2024ggi was classified as a Type II SN (Hoogendam et al. 2024; Zhai et al. 2024) and is located at $\alpha = 11^{\rm h}18^{\rm m}22.09^{\rm s}$, $\delta = -32°50'15.26''$ in host galaxy NGC 3621. We adopt a time of first light of MJD 60410.80 ± 0.34 days, which is based on the average between the times of last non-detection ($m_L = 19.5$ mag) and first detection $m_o = 18.9$ mag. To validate this estimate of first light, we first fit the ATLAS o-band light curve with a two-component power-law in the `REDBACK` software package (Sarin et al. 2023) and derive a time of first light of MJD 60411.07 ± 0.01. Additionally, using a uniform prior distribution derived from the last ATLAS non-detection on MJD 60410.45, we fit the bolometric light curve of SN 2024ggi to a suite of hydrodynamical models (e.g., see Moriya et al. 2023; Subrayan et al. 2023) which constrains the time of first light to be MJD $60410.56^{+0.07}_{-0.12}$. Both methods yield consistent explosion epochs to that derived above from the phases of last non-detection and first detection. All phases reported in this paper are with respect to this adopted time of first light (δt). In this paper, we use a redshift-independent host-galaxy distance of 7.24 ± 0.20 Mpc (Saha et al. 2006) and adopt a redshift of $z = 0.002215$ based on Na I D absorption in high-resolution spectra of SN 2024ggi obtained with the NEID Spectrograph on the WIYN Telescope (private communication).

Given detection and classification during its infancy, SN 2024ggi represents an incredible opportunity to study the SBO phase of a CSM-interacting SN II in unprecedented detail. In §8.3 we describe UV, optical, and NIR observations of SN 2024ggi. In §8.4 we present analysis, comparisons and modeling of SN 2024ggi's optical photometric and spectroscopic properties. Finally, in §8.6 we discuss the progenitor environment and mass-loss history prior to SN 2024ggi. Conclusions are drawn in §8.7. All uncertainties are quoted at the 68% confidence level (c.l.) unless otherwise stated.

7.3 Observations

7.3.1 Photometric Observations

The Ultraviolet Optical Telescope (UVOT; Roming et al. 2005) onboard the Neil Gehrels *Swift* Observatory (Gehrels et al. 2004) started observing SN 2024ggi on 11 April 2024 ($\delta t = 0.79$ days). We performed aperture photometry with a 5″ region radius with `uvotsource` within HEAsoft v6.33 (Nasa High Energy Astrophysics Science Archive Research Center

(Heasarc) 2014)[1], following the standard guidelines from Brown et al. (2014)[2]. In order to remove contamination from the host galaxy, we employed pre-explosion images to subtract the measured count rate at the location of the SN from the count rates in the SN images and corrected for point-spread-function (PSF) losses following the prescriptions of Brown et al. (2014). We note that not all early-time UVOT observations are included in this analysis given the degree of saturation.

We obtained *ugri* imaging of SN 2024ggi with the Las Cumbres Observatory (LCO) 1 m telescopes from 12 April to 26 April 2024 (Program ANU2024A-004). After downloading the `BANZAI`-reduced images from the LCO data archive (McCully et al. 2018), we used `photpipe` (Rest et al. 2005) to perform `DoPhot` PSF photometry (Schechter et al. 1993). All photometry was calibrated using PS1 stellar catalogs described above with additional transformations to SDSS *u*-band derived from Finkbeiner et al. (2016). For additional details on our reductions, see Kilpatrick et al. (2018a). We also obtained photometry using a 0.7 meter Thai Robotic Telescope at Cerro Tololo Inter-American Observatory in the *ugriz* bands. Images are bias subtracted and field flattened. Absolute photometry is obtained using stars in the $10' \times 10'$ field of view. We also observed SN 2024ggi with the Lulin 1 m telescope in *griz* bands. Standard calibrations for bias and flat-fielding were performed on the images using `IRAF`, and we reduced the calibrated frames in `photpipe` using the same methods described above for the LCO images.

We also observed SN 2024ggi in *grizH*-bands with the Rapid Eye Mount (REM; Antonelli et al. 2003) telescope located in La Silla, Chile. REM is equipped with two cameras, which can observe simultaneously the same field of view (10'×10') in the optical and near-IR. Single images have been initially corrected for dark and flat frames observed each night. Then, images obtained with the same setup have been stacked and finally corrected for cosmic rays, all using a dedicated pipeline written in Python. Magnitudes were measured with aperture photometry, with a variable aperture size according to the seeing of the night, and calibrated against selected field stars from the Skymapper DR4 (Onken et al. 2024) that also have 2MASS *JHK*-band photometry. We also obtained *ugriz* imaging of SN 2024ggi with the 0.8 m T80S telescope at Cerro Tololo Inter-american Observatory, Chile. These were processed using the S-PLUS Transient Extension Program pipeline (Santos et al. 2024), including non-linearity to recover detections of SN 2024ggi close to the saturation level. Additionally, we include *o*-band photometry by ATLAS that was downloaded from the forced photometry server (Smith et al. 2020). The complete multi-color light curve of SN 2024ggi is presented in Figure 7.1.

The Milky Way (MW) *V*-band extinction and color excess along the SN line of sight is $A_V = 0.22$ mag and $E(B\text{-}V) = 0.07$ mag (Schlegel et al. 1998; Schlafly & Finkbeiner 2011), respectively, which we correct for using a standard Fitzpatrick (1999) reddening law ($R_V = 3.1$). In addition to the MW color excess, we estimate the contribution of galaxy extinction in the local SN environment. Using a high-resolution Kast spectrum of SN 2024ggi at $\delta t = 5.5$ days, we calculate Na I D2 and D1 equivalent widths (EWs) of 0.18 and 0.13 Å,

[1]We used the most recent calibration database (CALDB) version.

[2]https://github.com/gterreran/Swift_host_subtraction

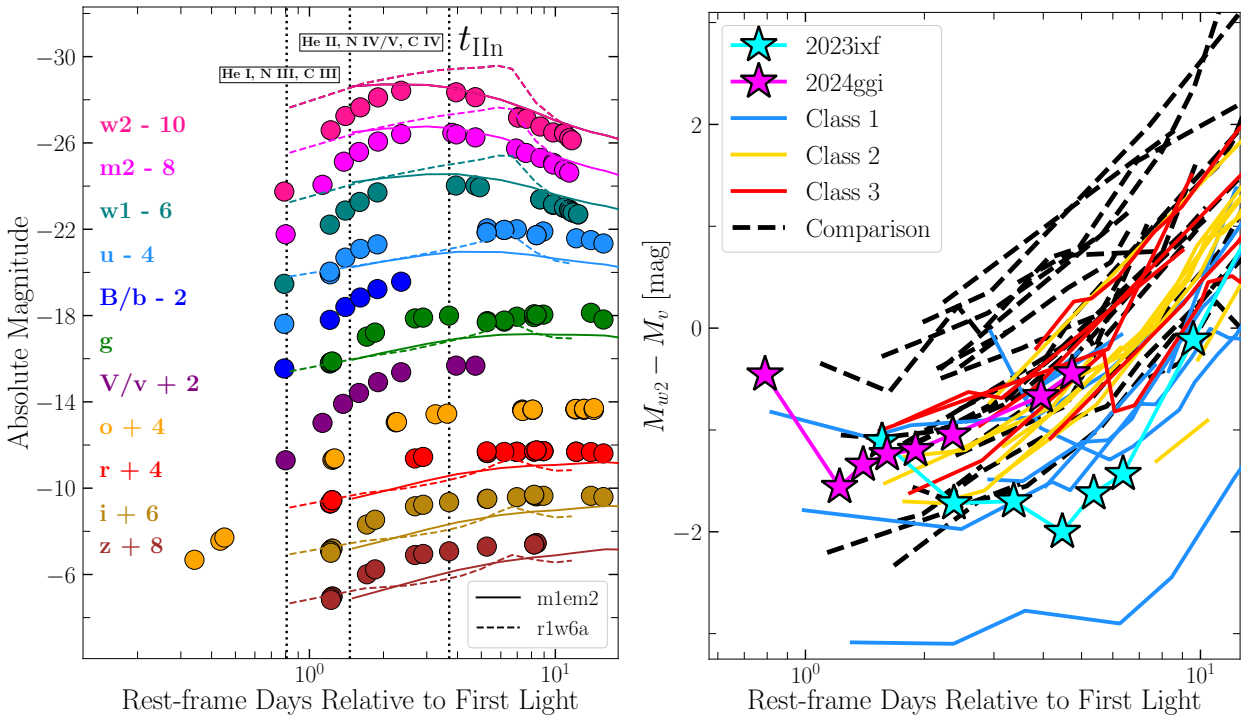

Figure 7.1 *Left:* Multi-color light curve of SN 2024ggi (circles) with respect to time since first light (MJD 60410.80 ± 0.34) from *Swift*, ATLAS, LCO, TRT, REM, T80s, and Lulin telescopes. Observed photometry is presented in the AB magnitude system and has been corrected for host galaxy and MW extinction. `CMFGEN` m1em2 and r1w6a model light curves are shown as solid and dashed lines, respectively. *Right:* Early-time, reddening-corrected $W2-V$ color plot for SN 2024ggi (magenta stars) and SN 2023ixf (cyan stars) with respect to gold/silver-sample objects (red, yellow, blue lines) and comparison sample objects (black dashed lines) (Jacobson-Galán et al. 2024). SN 2024ggi shows a blueward shift in color within the first ∼day since first light that is consistent with a rise in temperature and ionization (e.g., Fig. 7.2).

respectively; these values are confirmed in a follow-up high resolution Gemini spectrum at $\delta t = 9.2$ days. We use $A_V^{\rm host} = (0.78 \pm 0.15)$ mag $\times$ (EW$_{\rm NaID}$/Å) from Stritzinger et al. (2018) to convert these EWs to an intrinsic host-galaxy $E(B-V)$ and find a host galaxy extinction of $E(B-V)_{\rm host} = 0.084 \pm 0.018$ mag, also corrected for using the Fitzpatrick (1999) reddening law.

7.3.2 Spectroscopic Observations

SN 2024ggi was observed with Shane/Kast (Miller & Stone 1993) and the Goodman spectrograph (Clemens et al. 2004) at the Southern Astrophysical Research (SOAR) telescope between $\delta t = 1.5 - 9.3$ days. For all these spectroscopic observations, standard CCD processing and spectrum extraction were accomplished with IRAF[3]. The data were extracted using the optimal algorithm of Horne (1986). Low-order polynomial fits to calibration-lamp spectra were used to establish the wavelength scale and small adjustments derived from night-sky lines in the object frames were applied. SN 2024ggi spectra were also obtained Gemini Multi-Object Spectrograph (GMOS) at Gemini South Observatory at $\delta t = 9.2$ days and reduced with the Data Reduction for Astronomy from Gemini Observatory North and South (DRAGONS) pipeline (Labrie et al. 2023). Spectra were also obtained with the TripleSpec4.1 NIR Imaging Spectrograph (TSpec) at the SOAR telescope, and reduced using a modified version of `Spextool` (Cushing et al. 2004b). Telluric corrections were applied using `xtellcor` presented in Vacca et al. (2003). Additional modifications to calibrations are described in Kirkpatrick et al. (2011).

In Figure 7.2 we present the complete series of optical spectroscopic observations of SN 2024ggi from $\delta t = 0.8 - 9.3$ days. In this plot, we also show the classification spectrum of SN 2024ggi at +0.8 days from the Lijiang 2.4m telescope (Zhai et al. 2024), which we only use for narrow line identification. The complete optical/NIR spectral sequence is shown in Figures 7.2 & 7.3 and the log of spectroscopic observations is presented in Appendix Table A1.

7.4 Analysis

7.4.1 Photometric Properties

We present the complete early-time, multi-band light curve of SN 2024ggi in Figure 7.1. Given the estimated time of first light, SN 2024ggi was first detected by ATLAS at $\delta t = 0.3$ days with absolute magnitude of $M_o = -10.7$ mag and then quickly increased in luminosity to $M_o = -15.3$ mag by $\delta t = 1.2$ days. We fit high-order polynomials to $w2, m2, w1, u, g, r, i$-band light curves in order to estimate the peak luminosity and rise-time of SN 2024ggi. All measurements are reported in Table A1, with the uncertainty in peak magnitude being the 1σ error from the fit and the uncertainty in the peak phase being

[3] https://github.com/msiebert1/UCSC_spectral_pipeline

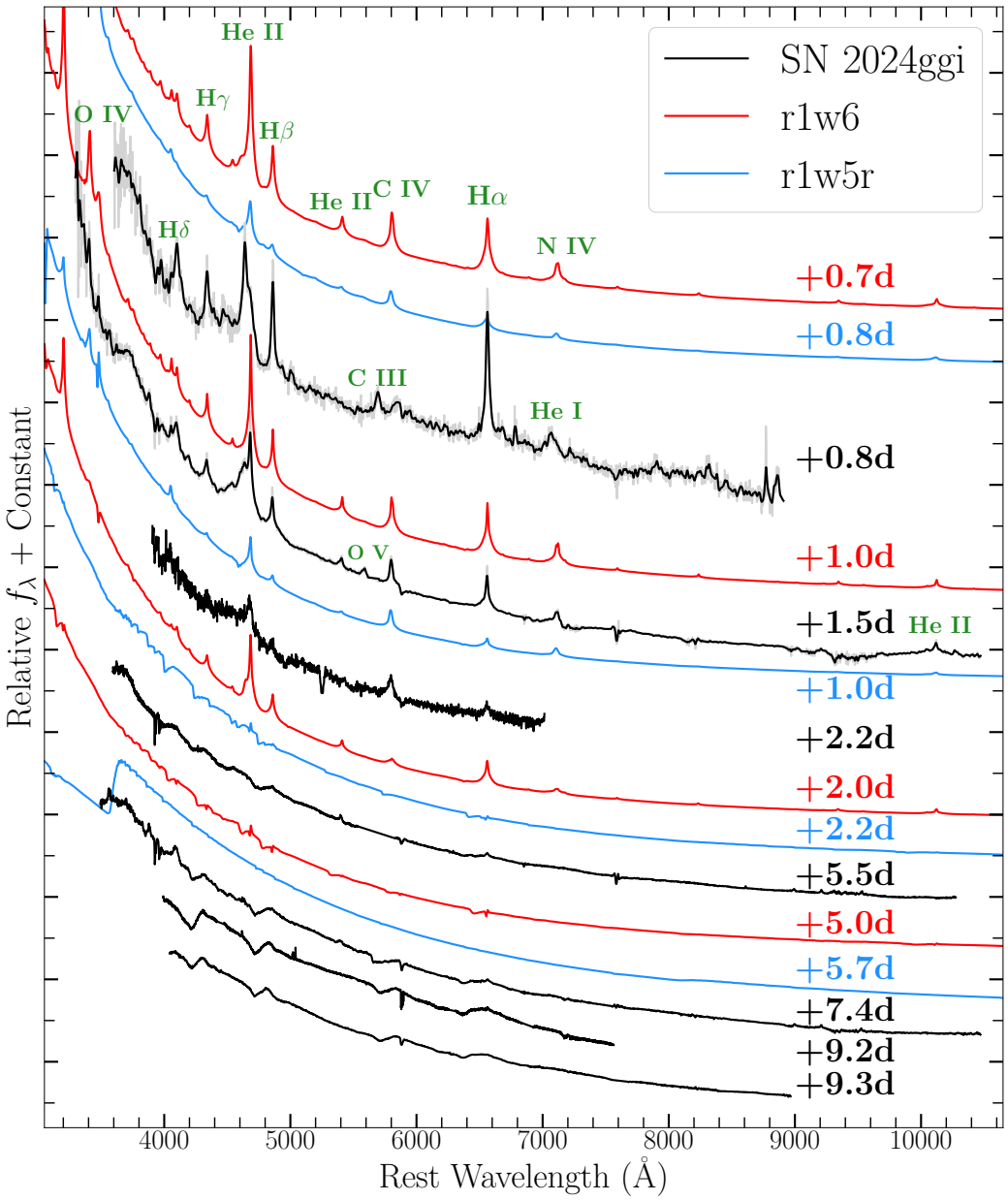

Figure 7.2 Early-time optical spectral series of SN 2024ggi (black) together with r1w6 (red) and r1w5r (blue) models from Dessart et al. (2017). The r1w6 and r1w5r models are characterized by wind mass-loss rates of $\dot{M} = (0.5 - 1) \times 10^{-2}$ $M_\odot$ yr^{-1} that extends to a CSM radius of $R_{\rm CSM} = (2 - 5) \times 10^{14}$ cm. Model spectra have been smoothed with a Gaussian kernel to match the spectral resolution of the data. Line identifications shown in green. The appearance of He II, C IV, N IV/V and O V after the $\delta t = +0.8$ day spectrum indicates a rise in ionization and temperature in SN 2024ggi as the breakout pulse and the subsequent continuous release of radiation from the shock diffuses through the CSM.

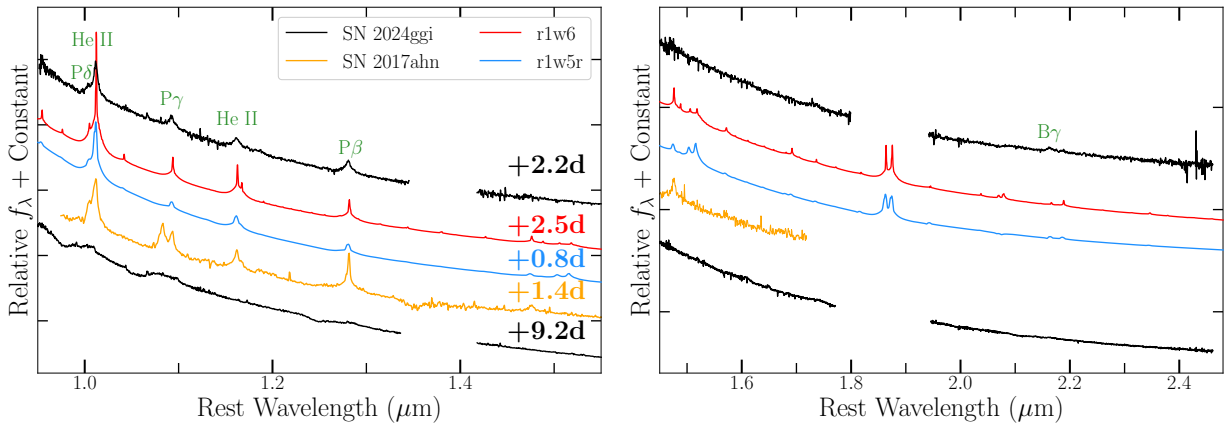

Figure 7.3 *Left/Right:* NIR spectra of SN 2024ggi (black) and SN 2017ahn (orange) compared to r1w5r (blue) and r1w6 (red) models from Dessart et al. (2017). Line identifications shown in green.

found from adding the uncertainties in both the time of peak magnitude and the time of first light in quadrature. We find that SN 2024ggi has UV and optical peak absolute magnitudes of $M_{w2} = -18.7 \pm 0.07$ mag and $M_g = -18.1 \pm 0.06$ mag, respectively. Using the adopted time of first light, we estimate UV and optical rise-times of $t_{w2} = 3.0 \pm 0.3$ days and $t_g = 6.5 \pm 0.9$ days.

In Figure 7.4, we compare the observed peak absolute magnitudes of SN 2024ggi to a sample of 74 SNe II from Jacobson-Galán et al. (2024). This sample includes 39 SNe II with detected IIn-like features in their early-time spectra: "gold-sample" objects have spectra at $\delta t < 2$ days and "silver-sample" objects only have spectra obtained at $\delta t > 2$ days. As discussed in Jacobson-Galán et al. (2024) and delineated by color in Figure 7.4, the gold/silver-sample objects are classifed in three main groups: "Class 1" (blue) show emission lines of N III, He II, and C IV (e.g., SNe 1998S, 2017ahn, 2018zd, 2020pni, 2020tlf, 2023ixf), "Class 2" (yellow) have no N III emission but do show He II and C IV (e.g., SNe 2014G, 2022jox), and "Class 3" (red) only show weaker, narrow He II emission superimposed with a blueshifted, Doppler-broadened He II (e.g., SN 2013fs, 2020xua). However, this classification scheme is epoch dependent because emission lines of O V/VI and N IV/V are also present in some objects such as SN 2013fs at $t < 1$ day owing to a more compact CSM than other CSM-interacting SNe II (Yaron et al. 2017; Dessart et al. 2017). Additionally, we present the comparison sample of 35 SNe II with spectra obtained at $\delta t < 2$ days but no detected IIn-like features.

As shown in Figure 7.4, SN 2024ggi is more luminous than most in the comparison sample SNe II without IIn-like features in all UV/optical filters. Furthermore, SN 2024ggi has a longer rise-time in UV filters than comparison sample objects but comparable rise-times in optical filters. However, SN 2024ggi shows consistent UV/optical luminosities and rise-times to gold/silver-sample objects such as iPTF11iqb (Smith et al. 2015) and SN 2014G (Terreran

et al. 2016). Additionally, SN 2024ggi has a comparable optical luminosity to SN 2023ixf but is less luminous in the UV by ∼0.7 mags. In the right panel of Figure 7.1, we also compare the early-time ($\delta t < 10$ days) $w2-v$ colors of SN 2024ggi to gold, silver and comparison objects. Interestingly, SN 2024ggi shows a dramatic red-to-blue $w2-v$ color evolution of -0.46 mag to -1.56 mag between $\delta t = 0.8-1.2$ days, followed by consistently blue colors as it evolves redward in its first week. This unusual color evolution is also observed in other SNe II with IIn-like features such as SN 2023ixf (Hosseinzadeh et al. 2023; Hiramatsu et al. 2023; Li et al. 2024; Zimmerman et al. 2024), which was proposed as evidence for SBO in an extended dense CSM. This phenomenon is a product of the breakout pulse and the subsequent continuous release of radiation from the shock diffusing through the CSM (Dessart et al. 2017) and also corresponds to the phase during which the photosphere moves outward, initially at $R_\star$ and then out to the location of the electron scattering photosphere ($R_{\tau=1}$; Dessart & Jacobson-Galán 2023). We also fit a blackbody model to the SN 2024ggi UV/optical SED and find blackbody temperature[radii] during this red-to-blue color evolution of ∼20 kK[5.3×10^{13} cm] at $\delta t = 0.8$ days and ∼23 kK[1.1×10^{14} cm] at $\delta t = 1.2$ days. Furthermore, we find that the blackbody temperature of SN 2024ggi peaks at ∼34 kK on $\delta t = 1.4$ days. This is a similar peak blackbody temperature to the 34.3 kK found for SN 2023ixf at $\delta t = 3.51$ days (Zimmerman et al. 2024). However, we note that these blackbody temperatures correspond to the temperature at the thermalization depth and that the blackbody radius is not equivalent to the location of the photosphere (i.e., $R_{\rm BB} << R_{\rm phot}$).

7.4.2 Spectroscopic Properties

We present our sample of optical observations for SN 2024ggi spanning from $\delta t = +0.8$ to +9.3 days in Figure 7.2. In the earliest spectrum at $\delta t = +0.8$ days, SN 2024ggi shows IIn-like features of H I ($\chi = 13.6$ eV), He I ($\chi = 24.6$ eV), N III ($\chi = 47.4$ eV) and C III ($\chi = 47.9$ eV). However, by the next spectral observation at $\delta t = +1.5$ days, SN 2024ggi shows prominent emission lines of He II ($\chi = 54.5$ eV), N III/IV/V ($\chi = 47.4/77.5/97.9$ eV), C IV ($\chi = 64.5$ eV) and O V ($\chi = 113.9$ eV), indicating a dramatic rise in ionization and temperature within ∼14 hours that is temporally consistent with the blueward evolution in $w2-v$ colors (e.g., Fig. 7.1). There may also be a detection of O IV λ3410 but the lower S/N in that spectral region makes the line identification uncertain. Interestingly, the detection of O IV/V has only been confirmed in one other SN II, 2013fs, and in that object the timescale of this emission was < 0.5 days (Yaron et al. 2017). Notably, the shift in ionization seen in SN 2024ggi was also observed in SN 2023ixf but at later phases of $+1.1-2.4$ days (Jacobson-Galán et al. 2023). A two-component Lorentzian model fit to the Hα profile in the +1.5 d Kast spectrum shows a narrow component full width at half maximum (FWHM) velocity of <270 km s^{-1} that traces the unshocked CSM combined with a broad symmetric component with velocity of ∼1320 km s^{-1} that is caused by scattering of recombination line photons by free, thermal electrons in the ionized CSM (Chugai 2001; Dessart et al. 2009; Huang et al. 2018). However, the narrow component is likely affected by radiative acceleration of the CSM that causes the width of the narrow component to be larger than the true velocity of

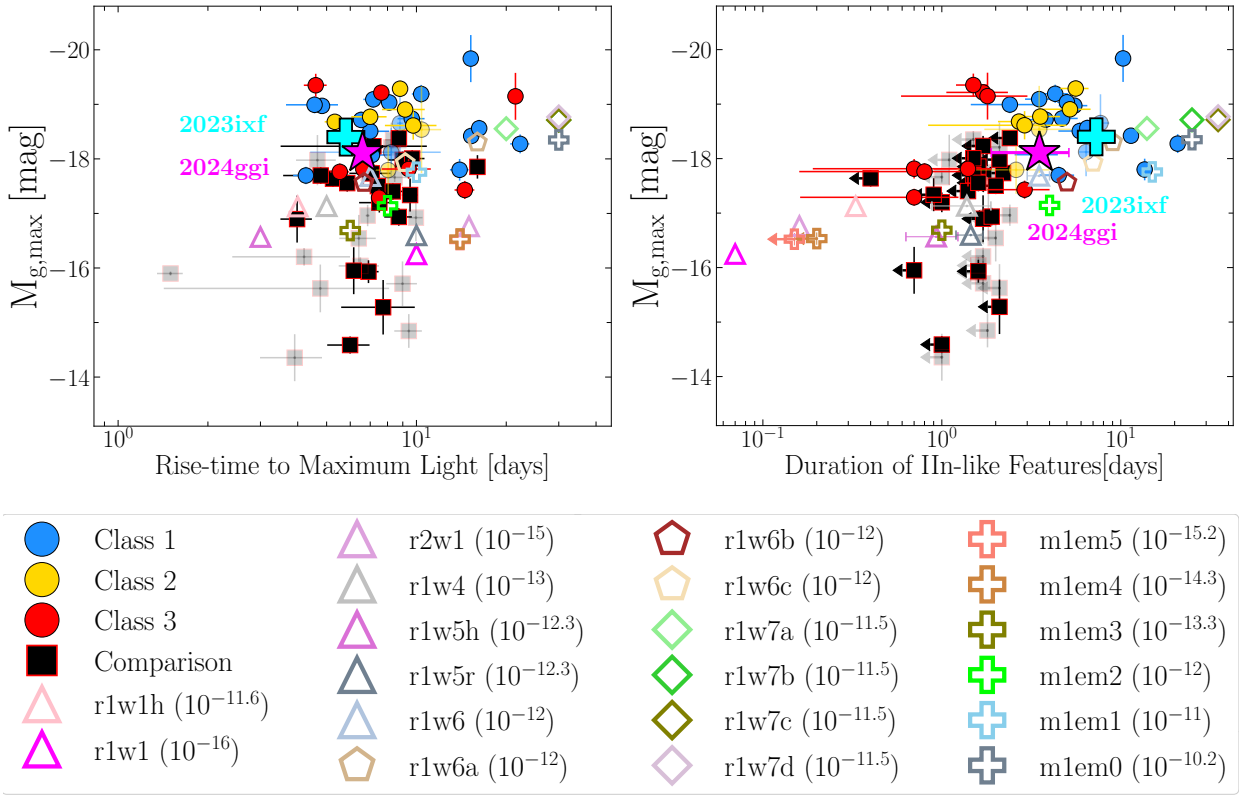

Figure 7.4 *Left:* Peak g-band absolute magnitude versus rise time (Left) and duration of IIn-like features (Right). Gold/silver samples shown as blue/yellow/red circles and the comparison sample is shown as black squares. Solid colored points represent the subsample of objects at $D > 40$ Mpc. Parameters from the `CMFGEN` model grid (§7.4.3) are plotted as colored stars, polygons, diamonds and plus signs with the CSM densities at 10^{14} cm (in g cm^{-3}) for each model displayed in parentheses. SNe 2024ggi and 2023ixf are shown as a magenta star and a cyan cross, respectively.

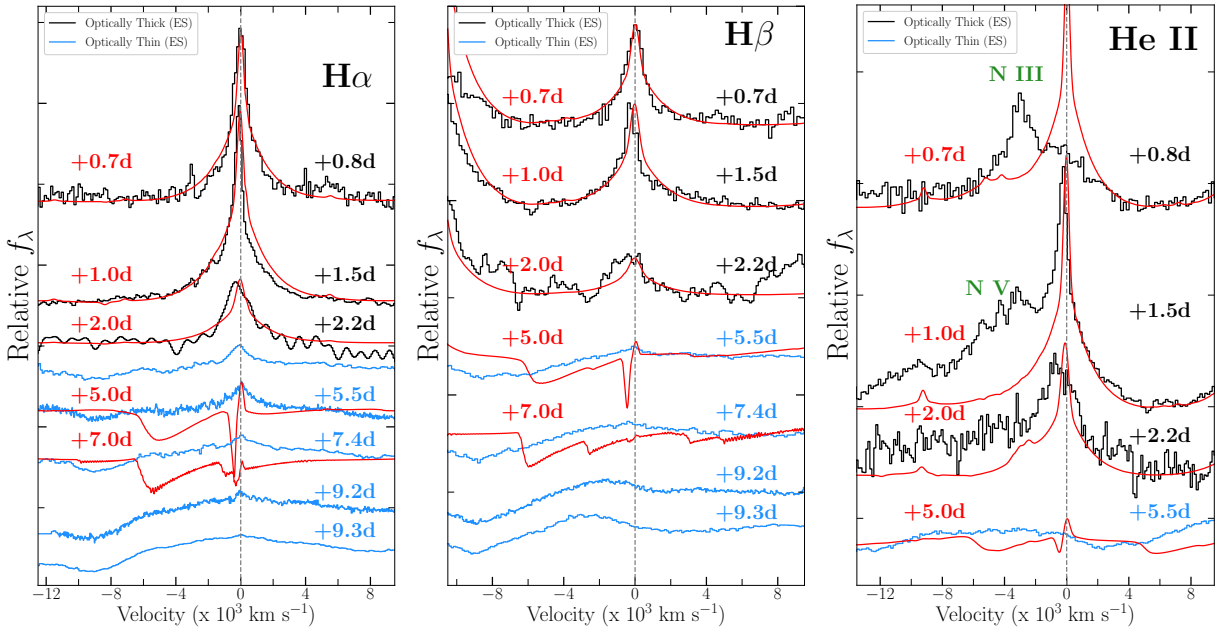

Figure 7.5 *Left:* Hα velocity evolution in SN 2024ggi (black) from $\delta t = 0.8 - 9.3$ days with respect to r1w6 model spectra (red), which has been scaled to the emission line peaks of SN 2024ggi and smoothed with a Gaussian filter to better compare with the data. Early-time spectral profiles are shaped by electron-scattering in the dense CSM. The transition shown from black to blue lines ($t_{\rm IIn} = 3.7 \pm 1.8$ days) marks the emergence of broad absorption features derived from the fastest moving SN ejecta. *Middle:* Hβ velocity evolution, also showing that the electron-scattering line profiles subside by ~ 5.5 days. *Right:* He II λ4686 velocity evolution reveals that the electron-scattering profile fades by ~ 5.5 days, suggesting a significant decrease in CSM density.

the progenitor wind (Dessart et al. 2015, 2017; Tsuna et al. 2023).

In addition to optical spectroscopy, we present NIR spectra of SN 2024ggi in Figure 7.3 that extend from $0.9-2.4$ μm. The first spectrum at $\delta t = 2.2$ days shows IIn-like features of He II as well as Hydrogen Paschen and Brackett transitions of P δ, P γ, P β and B γ. We then compare this spectrum to SN II 2017ahn (Tartaglia et al. 2021), one of the only SN with IIn-like features to have a NIR spectrum during the dense CSM-interaction phase. Overall, the NIR spectrum of SN 2024ggi at $\delta t = 2.2$ days shows similar narrow emission lines to SN 2017ahn with the exception being that SN 2017ahn shows prominent He I emission while SN 2024ggi only shows He II.

As shown in Figure 7.5, the IIn-like features in SN 2024ggi are already fading by the +2.2 day epoch, with possible blue-shifted, Doppler-broadened He II emission as the fastest moving ejecta and/or the dense shell starts to become visible given a decrease in optical depth. Then, by $\delta t = 5.5$ days, the IIn-like features have vanished and SN 2024ggi shows a broad, blueshifted absorption profile in all Balmer transitions as well as a blue-shifted He II profile extending out to $\sim (10-12) \times 10^4$ km s^{-1} (i.e., "ledge feature"; Dessart et al. 2016; Hosseinzadeh et al. 2022; Pearson et al. 2023; Chugai & Utrobin 2023; Shrestha et al. 2024). Based on this evolution, we estimate the duration of the IIn-like line profiles to be $t_{\rm IIn} = 3.8 \pm 1.6$ days, which marks the transition point at which the optical depth to electron-scattering has dropped enough to see the emerging fast-moving SN ejecta. At $\delta t > 5$ days, we observe broad absorption profiles in the Hα and Hβ transitions that extend to ~ 12000 km s^{-1}, which provides a decent estimate of the velocities of the fastest moving H-rich material at the shock front. Using the estimated $t_{\rm IIn}$ and a shock velocity of $v_{\rm sh} = 12000$ km s^{-1}, the transition to lower density CSM likely occurs at a radius of $r = R_\star + v_{\rm sh} \times t_{\rm IIn} = (4.3 \pm 1.7) \times 10^{14}$ cm (for $R_\star = 500$ R$_\odot$) and at a CSM density of $\rho = (\kappa_{\rm T} \times t_{\rm IIn} \times v_{\rm sh})^{-1} = (7.4 \pm 3.1) \times 10^{-15}$ g cm^{-3}, for $\tau = 1$ and Thompson opacity of $\kappa_{\rm T} = 0.34$ cm^2 g^{-1}. This likely indicates a more confined CSM and/or lower mass-loss rate for SN 2024ggi than Class 1 gold/silver sample SNe II that have $t_{\rm IIn} > 5$ days e.g., SNe 2017ahn, 2018zd, 2020pni, 2020tlf, 2023ixf. However, as shown in Figure 7.4, the duration of IIn-like features in SN 2024ggi is similar to Class 2/3 objects, which reveals that if earlier time spectra (e.g., $\delta t < 1$ day) had been obtained for these objects, they may have shown N III emission like Class 1 objects and SN 2024ggi at $\delta t < 1$ day.

7.4.3 Model Matching

In order to quantify the CSM properties of SN 2024ggi, we compared the spectral and photometric properties of SN 2024ggi to a model grid of radiation hydrodynamics and non-LTE radiative transfer simulations covering a wide range of progenitor mass-loss rates ($\dot{M} = 10^{-6} - 10^{0}$ M$_\odot$ yr^{-1}; $v_w = 50$ km s^{-1}) and CSM radii ($R = 10^{14} - 10^{16}$ cm), all in spherical symmetry. Density profiles for a representative set of models are present in Figure 7.6. Simulations of the SN ejecta-CSM interaction were performed with the multi-group radiation-hydrodynamics code `HERACLES` (González et al. 2007; Vaytet et al. 2011; Dessart et al. 2015), which consistently computes the radiation field and hydrodynamics. Then, at selected

snapshots in time post-explosion, the hydrodynamical variables are imported into the non-LTE radiative-transfer code `CMFGEN` (Hillier & Dessart 2012; Dessart et al. 2015) for an accurate calculation of the radiative transfer, which includes a complete model atom, $\sim 10^6$ frequency points, and treatment of continuum and line processes as well as non-coherent electron scattering. For each model, we adopt an explosion energy of 1.2×10^{51} erg, a $15 M_\odot$ progenitor with a radius ranging from $R_\star \approx 500 - 700$ $R_\odot$, and a CSM composition set to the surface mixture of a RSG progenitor (Dessart et al. 2017). For the simulations presented in this work, the CSM extent is much greater than $R_\star$ ($\sim$500–1200 $R_\odot$ for a RSG mass range of $\sim$10–20 $M_\odot$) and $R_\star$ has little impact during phases of ejecta-CSM interaction. The progenitor radius plays a more significant role on the light curve evolution during the plateau phase (e.g., see Dessart et al. 2013; Jacobson-Galán et al. 2022a), i.e., once the interaction phase is over and the emission from the deeper ejecta layers dominate the SN luminosity. Specific methods for each simulation can be found in Dessart et al. (2016, 2017); Jacobson-Galán et al. (2022a); Dessart & Jacobson-Galán (2023).

We determine the best-matched model to SN 2024ggi through direct spectral matching and peak/rise-time in all available UV/optical filters (see Jacobson-Galán et al. 2024 for specifics of the model matching procedure). As shown in Figure 7.2, the early-time evolution of SN 2024ggi is most consistent with the r1w6 model, suggesting a mass-loss rate of $\dot{M} = 10^{-2}$ $M_\odot$ yr^{-1}and a dense CSM (i.e., optically thick to electron scattering) that extends to $\sim 5 \times 10^{14}$ cm. In Figure 7.5 we show that the line profiles in SN 2024ggi during the first few days of SN 2024ggi are decently matched by the r1w6 model and that a lower mass-loss rate model (e.g., $\dot{M} = 5 \times 10^{-3}$ $M_\odot$ yr^{-1}; r1w5r) cannot match the duration of the IIn-like features. However, notable differences include the lack of N III and the strong He II at +0.8 days that is not present in SN 2024ggi and inability of the r1w6 model to adequately reproduce the complete N III/He II complex i.e., the model profile is too narrow as was observed in SN 2023ixf (Jacobson-Galán et al. 2023), which could be due to the fact that these simulations assume spherical symmetry and/or require higher kinetic energies. After $t_{\rm IIn}$, the r1w6 model spectra show a narrow P-Cygni profile combined with broad absorption that extends to $\sim$ 7000 km s^{-1} in Balmer transitions. However, while this is qualitatively the behavior observed in SN 2024ggi, there is no narrow P Cygni observed until the +9.3 day spectra and the absorption profiles in SN 2024ggi extend to much larger velocities of $\sim$ 12000 km s^{-1}. This mismatch is likely due to increased ejecta deceleration in the models that is not present in SN 2024ggi and/or the CSM of SN 2024ggi is asymmetric, allowing for some parts of the SN ejecta that only encounter low density CSM to retain higher velocities. Asymmetric CSM has been proposed for similar events such as SNe 1998S and 2023ixf (Leonard et al. 2000; Vasylyev et al. 2023) based on spectropolarimetry. Similar to SN 2023ixf, CSM asymmetry may need to be invoked if the densities inferred from X-ray detections (Margutti & Grefenstette 2024; Zhang et al. 2024) deviate from those inferred from the early-time UV/optical light curve and spectra. Furthermore, it is expected that the dense shell formed from post-shock gas should break up, even for a spherical explosion and spherical CSM, which would lead to a much more complicated structure than is obtained when spherical symmetry is imposed.

Table A1 Main parameters of SN 2024ggi

Host Galaxy	NGC 3621
Redshift	0.002215
Distance	7.2 ± 0.2 Mpc[4]
Time of First Light (MJD)	60410.80 ± 0.34
$E(B-V)_{\rm MW}$	0.07 mag[5]
$E(B-V)_{\rm host}$	0.084 ± 0.018 mag[6]
$M_{w2}^{\rm peak}[t_r]$	-18.7 ± 0.07 mag[3.0 ± 0.3 d]
$M_{m2}^{\rm peak}[t_r]$	-18.7 ± 0.07 mag[3.1 ± 0.3 d]
$M_{w1}^{\rm peak}[t_r]$	-18.4 ± 0.07 mag[3.2 ± 0.3 d]
$M_{u}^{\rm peak}[t_r]$	-18.2 ± 0.06 mag[3.5 ± 0.3 d]
$M_{g}^{\rm peak}[t_r]$	-18.1 ± 0.06 mag[6.5 ± 0.9 d]
$M_{r}^{\rm peak}[t_r]$	-17.8 ± 0.14 mag[8.6 ± 1.4 d]
$M_{i}^{\rm peak}[t_r]$	-17.7 ± 0.09 mag[8.5 ± 2.6 d]
$\rm R_{CSM}$	$\sim 5 \times 10^{14}$ cm
$\rm M_{CSM}$	$(0.02 - 0.04)$ $\rm M_\odot$
$\dot{M}$[7]	10^{-2} $\rm M_\odot$ $\rm yr^{-1}$
v_w	50 $\rm km\,s^{-1}$
CSM Composition	Solar Metallicity[8]
Time of $\dot{M}$	~3 years pre-SN

In addition to direct spectral comparison, we also use the peak absolute magnitudes and rise-times in all UV/optical filters to determine the best-matched models from the `CMFGEN` grid. Using the residuals between the model predictions and observables, we find that SN 2024ggi is best matched by the r1w4, m1em2, r1w6 and r1w6b models, which have a mass-loss range of $\dot{M} = (0.1 - 1) \times 10^{-2}$ $\rm M_\odot$ $\rm yr^{-1}$and radii of dense CSM that ranges from $r = 4 - 8 \times 10^{14}$ cm. We note that the m1em2 model (Dessart & Jacobson-Galán 2023) does not have a confined shell of dense CSM but rather has a continuous r^{-3} density profile that extends to 10^{16} cm (e.g., see Fig. 7.6). Furthermore, the r1w4 model ($\dot{M} = 10^{-3}$ $\rm M_\odot$ $\rm yr^{-1}$) cannot reproduce the spectral evolution of SN 2024ggi because the IIn-like features are not sustained for a long enough timescale. Additionally, matching the observed $t_{\rm IIn}$ in SN 2024ggi to the model grid produces only three consistent models: m1em2, r1w6, r1w6a, all with $\dot{M} = 10^{-2}$ $\rm M_\odot$ $\rm yr^{-1}$. As shown in Figure 7.1, the complete m1em2 and r1w6a model light curves provide a decent match to the multi-band SN 2024ggi light curve at maximum light but cannot capture the steep rise to peak. This inconsistency is likely the result of the CSM density profile immediately beyond $R_\star$ and/or the limitations of the simulations at very early phases (e.g., $\delta t < 1$ day) e.g., light travel time effects which are considered in the radiation hydrodynamics simulations but are not included in the computation of the resulting spectrum.

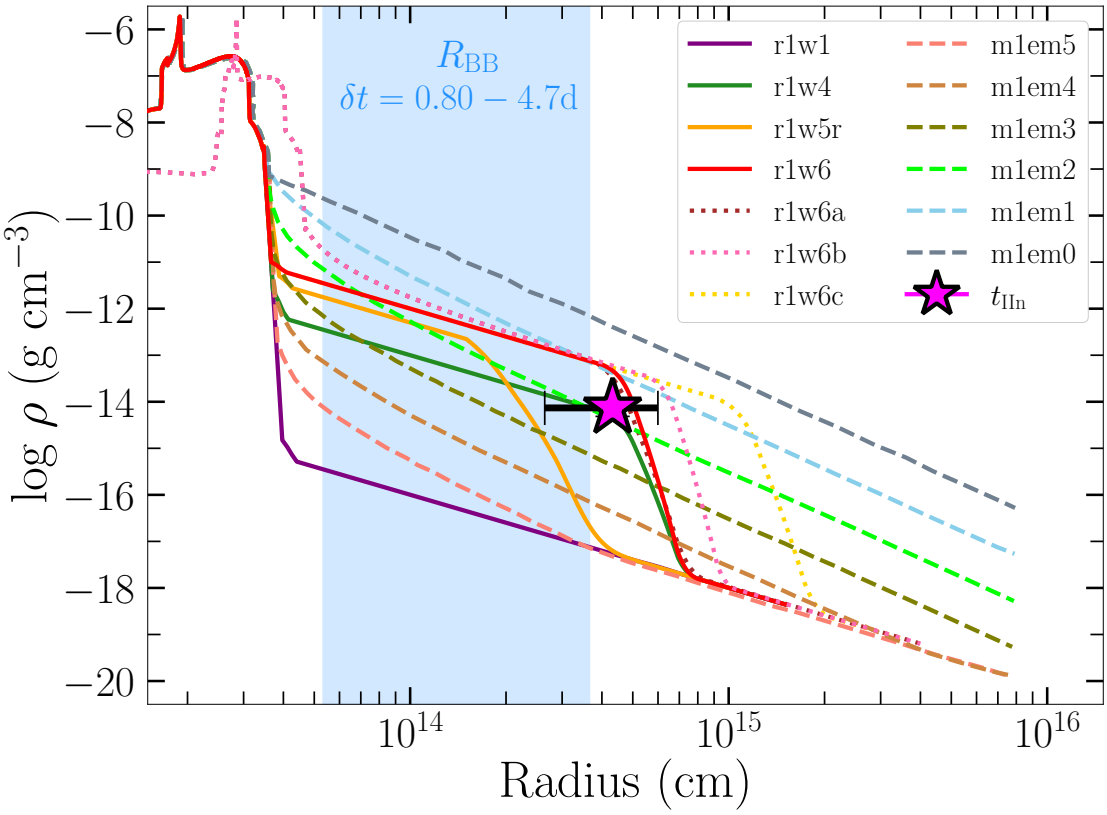

Figure 7.6 CSM densities and radii for a subset of the `CMFGEN` model grid used in Jacobson-Galán et al. (2024). Best-matched models to SN 2024ggi (§7.4.3) are r1w6 (solid red line), m1em2 (dashed limegreen line), r1w4 (solid dark green line) and r1w5r (solid orange line). Blackbody radii between $\delta t = 0.8 - 4.7$ days shown in light blue shaded region. Transition point where the CSM goes from optically thick to thin to electron scattering shown as magenta star (§8.4.2).

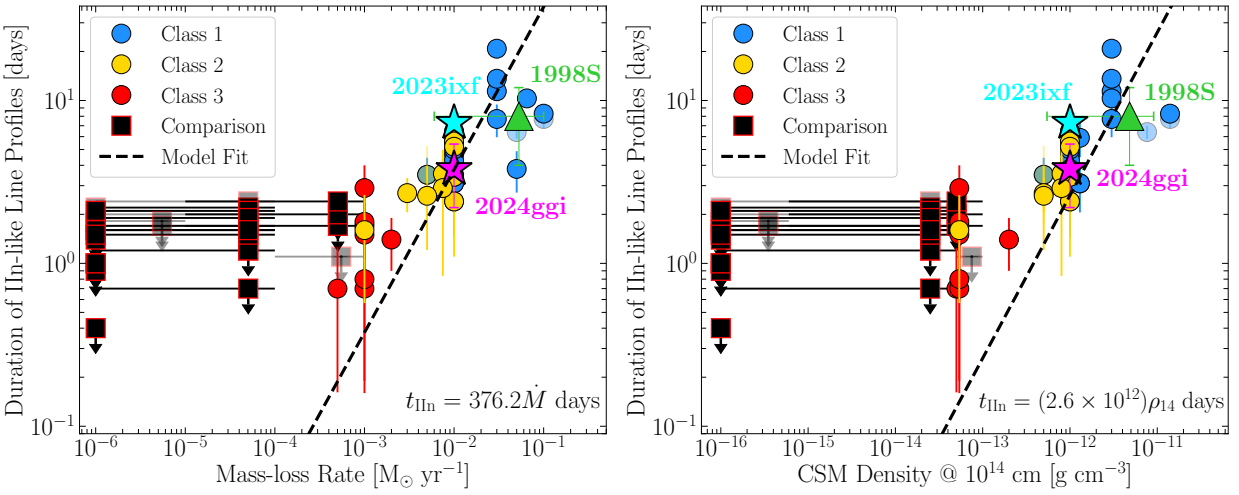

Figure 7.7 Duration of IIn-like features versus mass-loss rates *(left)* and CSM densities at $r = 10^{14}$ cm *(right)* derived from direct spectral matching for gold/silver- (blue, yellow and red circles) and comparison- (black squares) sample objects presented in Jacobson-Galán et al. (2024). Solid colored points represent the subsample of objects at $D > 40$ Mpc. Best-matched mass-loss rate and CSM densities at $r = 10^{14}$ cm for SN 2024ggi from spectral matching (§7.4.3) shown as magenta star. SNe 1998S and 2023ixf are shown for reference as a green triangle and cyan star, respectively.

7.5 Discussion

Observations of SN 2024ggi for 2 weeks after first light have helped to constrain both the explosion dynamics/physics as well as progenitor activity prior to core-collapse. Specifically, the observed change in ionization present in the $\sim 0.8 - 1.5$ day spectra (Fig. 7.5) and the rise in temperature shown by the red-to-blue color evolution (Fig. 7.1) suggests that we caught the SN as the shock broke out of the optically-thick envelope and into the extended, dense, and initially cold CSM. Rather than a prompt rise in temperature to $\sim 10^5$ K, the CSM heats up to a lower temperature and becomes progressively more ionized (e.g., He I/II, C III/IV, or N III/IV/V) on a $\sim 1 - 2$ day timescale as the radiative precursor, and then the radiation from the shock/ejecta, diffuses through the CSM. Furthermore, comparison of the spectral series, $t_{\rm IIn}$, peak luminosities and rise-times to a grid of `CMFGEN` models indicates that the progenitor of SN 2024ggi was likely a RSG with a mass-loss rate of $\dot{M} \approx 10^{-2}$ $M_\odot$ yr^{-1}, which created dense CSM extending to $r \approx 5 \times 10^{14}$ cm that contained a total mass of $M_{\rm CSM} \approx 0.02 - 0.04$ $M_\odot$. This range of CSM masses is consistent with simulations of RSG mass-loss through energy injection within convective RSG envelopes (Tsang et al. 2022), pre-SN outbursts (Takei et al. 2022), and RSG "boil-off" (Fuller & Tsuna 2024). We also find that the observed light curve can be matched with standard explosion energy (1.2×10^{51} erg) and that the IIn-like signatures in SN 2024ggi can be modeled with a CSM composition that matches typical RSG surface abundances, which suggests that significant N or He enrichment

to the CSM may not be required.

For a wind velocity of $\sim$ 50 km s^{-1}, the proposed CSM extent translates to a period of enhanced mass-loss in the last $\sim$3 years years prior to core-collapse. Similarly, for the observed $t_{\rm IIn}$ and a shock velocity of $v_{\rm sh}$ = 12000 km s^{-1}, the dense CSM would extend to $r \approx (4.3 \pm 1.7) \times 10^{14}$ cm and would indicate enhanced mass-loss in the final $\sim 1.4-3.6$ years before first light, for a progenitor wind velocity of 50 km s^{-1}. However, it should be noted that this timescale may not be accurate for enhanced wind scenarios (e.g., Davies et al. 2022) because the timescales for wind acceleration to a terminal velocity can take longer than the above pre-SN timescale. From the spectral evolution of SN 2024ggi in its first two weeks, it is clear that a reduction in CSM density did occur at $\sim$ 3.8 days because as the CSM optical depth to electron-scattering drops below unity, the Lorentzian wings of the IIn-like features disappear and absorption profiles from the fastest moving material become visible. However, the open question is whether the CSM detected in SN 2024ggi represents the only high-density shell of CSM (i.e. only one phase of enhanced mass-loss) that extends to $r < 5 \times 10^{14}$ cm (e.g., r1w6 model density profile) or if SN 2024ggi sustained enhanced mass-loss for several decades before explosion (e.g., m1em2 model density profile). As was done for SN 2023ixf, future multi-wavelength monitoring will be able to determine the CSM density at larger scales as the SN shock samples material that was liberated from the progenitor star years-to-decades before explosion (Grefenstette et al. 2023; Berger et al. 2023; Chandra et al. 2024a; Panjkov et al. 2023, Nayana et al., in prep). Overall, both the confined high-density CSM shell and the extended low-density wind may have made the RSG progenitor star quite dust-obscured prior to explosion (Davies et al. 2022), similar to what was revealed by pre-explosion imaging of the SN 2023ixf RSG progenitor (Kilpatrick et al. 2023a; Jencson et al. 2023; Qin et al. 2023; Soraisam et al. 2023; Van Dyk et al. 2023; Niu et al. 2023).

As shown in Figures 7.4 & 7.7, the observables and best-matched CSM properties of SN 2024ggi reside naturally within the continuum of SNe II, both with and without spectroscopic signatures of interaction with dense CSM. SN 2024ggi's best-matched $\dot{M}$ and CSM density at 10^{14} cm is lower than that inferred for more extreme Class 1 events such as SNe 1998S, 2017ahn, 2018zd, 2020tlf, 2020pni and 2023ixf, all of which likely have higher mass-loss rates, and/or dense CSM that extends to larger radii. Nonetheless, SN 2024ggi's evolution requires a progenitor mass-loss rate that is significantly higher than what is inferred for standard SNe II as well as what is measured in local RSGs (Beasor et al. 2020). Overall, this continues to point towards a phase of enhanced mass-loss in the final years before explosion for some significant fraction of RSGs.

7.6 Conclusions

In this paper we have presented UV/optical/NIR observations of the nearby SN II, 2024ggi located in nearby spiral host galaxy NGC 3621 at D = 7.2 Mpc. Below we summarize the primary observational findings of SN 2024ggi:

- The first optical spectrum of SN 2024ggi shows prominent narrow emission lines of H I, He I, N III and C III that result from the photo-ionization of dense, optically thick CSM. Between $\delta t = 0.8 - 1.5$ days, SN 2024ggi exhibits a detectable rise in temperature and ionization that manifests as the appearance of higher ionization species such as He II, N IV/V, C IV, and O V. This spectral evolution is temporally consistent with a dramatic red-to-blue evolution in $w2 - v$ colors and an increasing blackbody temperature. These phenomena suggest that SN 2024ggi was observed during the initial precursor associated with shock breakout inside dense CSM.

- SN 2024ggi displayed electron-scattering broadened profiles (i.e., IIn-like) that persist on a characteristic timescale of $t_{\rm IIn} = 3.8 \pm 1.6$ days, after which time a decrease in optical depth to electron scattering due to a reduction in CSM density allows for the detection of broad absorption profiles from the fastest H-rich SN ejecta.

- Interaction of the SN 2024ggi ejecta with dense, confined CSM yielded peak UV/optical absolute magnitudes (e.g., $M_{\rm w2} = -18.7$ mag, $M_{\rm g} = -18.1$ mag) that are consistent with other SNe II with IIn-like features presented in sample studies (e.g., Jacobson-Galán et al. 2024).

- Comparison of SN 2024ggi's spectral evolution, peak absolute magnitudes, rise-times and duration of IIn-like profiles to a grid of `CMFGEN` simulations suggests a CSM that has a composition typical of a solar-metallicity RSG, confined to $r < 5 \times 10^{14}$ cm, and that is formed from a progenitor mass-loss rate of $\dot{M} = 10^{-2}$ M$_\odot$ yr^{-1} (i.e., $\rho \approx 10^{-12}$ g cm^{-3} at $r = 10^{14}$ cm). Adopting a wind velocity of $v_w = 50$ km s^{-1}, this scenario corresponds to a period of enhanced mass-loss during the last $\sim$3 years years before core-collapse.

- SN 2024ggi is similar to SN 2023ixf in its rise in ionization within $\sim$days of first light and the high-ionization species present in its early-time spectra, both objects likely observed during shock breakout within dense CSM. However, SN 2024ggi has a shorter timescale of IIn-like features ($\sim$ 4 days vs. $\sim$ 7 days) and a more compact CSM ($< 5 \times 10^{14}$ cm vs $(0.5 - 1) \times 10^{15}$ cm) despite a similar mass-loss rate and CSM density at 10^{14} cm.

Like SN 2023ixf, SN 2024ggi represents a unique opportunity to study the long-term, multi-wavelength evolution of a SN II that interact with dense, confined CSM in exquisite detail. Future studies and multi-wavelength observations will probe the nature and late-stage evolution of the progenitor star as well as uncover the properties of the large-scale circumstellar environment, both of which tracing an unconstrained period of RSG evolution before core-collapse.

7.7 Acknowledgements

Research at UC Berkeley is conducted on the territory of Huichin, the ancestral and unceded land of the Chochenyo speaking Ohlone people, the successors of the sovereign

Verona Band of Alameda County. Shane 3-m observations were conducted on the land of the Ohlone (Costanoans), Tamyen and Muwekma Ohlone tribes.

W.J.-G. is supported by the National Science Foundation Graduate Research Fellowship Program under Grant No. DGE-1842165. W.J.-G. acknowledges support through NASA grants in support of *Hubble Space Telescope* program GO-16075 and 16500. This research was supported in part by the National Science Foundation under Grant No. NSF PHY-1748958. R.M. acknowledges support by the National Science Foundation under Award No. AST-2221789 and AST-2224255. The Margutti team at UC Berkeley is partially funded by the Heising-Simons Foundation under grant # 2018-0911 and #2021-3248 (PI: Margutti).

MRD acknowledges support from the NSERC through grant RGPIN-2019-06186, the Canada Research Chairs Program, and the Dunlap Institute at the University of Toronto. Parts of this research were supported by the Australian Research Council Discovery Early Career Researcher Award (DECRA) through project number DE230101069. Y.-C.P. is supported by the National Science and Technology Council (NSTC grant 109-2112-M-008-031-MY3. CG is supported by a VILLUM FONDEN Young Investigator Grant (project number 25501). D.M. acknowledges NSF support from grants PHY-2209451 and AST-2206532. A.S. acknowledges the financial support from CNPq (402577/2022-1). G.D. is supported by the H2020 European Research Council grant no.758638. CRB acknowledges the financial support from CNPq (316072/2021-4) and from FAPERJ (grants 201.456/2022 and 210.330/2022) and the FINEP contract 01.22.0505.00 (ref. 1891/22). This research is based on observations made with the Thai Robotic Telescope under program ID TRTC11B006, which is operated by the National Astronomical Research Institute of Thailand (Public Organization). Part of the data were obtained with the REM telescope, located in Chile and operated by the d'REM team for INAF. This work is supported by the National Science Foundation under Cooperative Agreement PHY-2019786 (The NSF AI Institute for Artificial Intelligence and Fundamental Interactions, http://iaifi.org/).

The UCSC team is supported in part by NASA grants NNG17PX03C and 80NSSC22K1518, NSF grant AST–1815935, and by a fellowship from the David and Lucile Packard Foundation to R.J.F.

YSE-PZ (Coulter et al. 2023) was developed by the UC Santa Cruz Transients Team with support from NASA grants NNG17PX03C, 80NSSC19K1386, and 80NSSC20K0953; NSF grants AST-1518052, AST-1815935, and AST-1911206; the Gordon & Betty Moore Foundation; the Heising-Simons Foundation; a fellowship from the David and Lucile Packard Foundation to R.J.F.; Gordon and Betty Moore Foundation postdoctoral fellowships and a NASA Einstein fellowship, as administered through the NASA Hubble Fellowship program and grant HST-HF2-51462.001, to D.O.J.; and a National Science Foundation Graduate Research Fellowship, administered through grant No. DGE-1339067, to D.A.C.

A major upgrade of the Kast spectrograph on the Shane 3 m telescope at Lick Observatory, led by Brad Holden, was made possible through generous gifts from the Heising-Simons Foundation, William and Marina Kast, and the University of California Observatories. Research at Lick Observatory is partially supported by a generous gift from Google.

This work has made use of data from the Asteroid Terrestrial-impact Last Alert System

(ATLAS) project. The Asteroid Terrestrial-impact Last Alert System (ATLAS) project is primarily funded to search for near earth asteroids through NASA grants NN12AR55G, 80NSSC18K0284, and 80NSSC18K1575; byproducts of the NEO search include images and catalogs from the survey area. This work was partially funded by Kepler/K2 grant J1944/80NSSC19K0112 and HST GO-15889, and STFC grants ST/T000198/1 and ST/S006109/1. The ATLAS science products have been made possible through the contributions of the University of Hawaii Institute for Astronomy, the Queen's University Belfast, the Space Telescope Science Institute, the South African Astronomical Observatory, and The Millennium Institute of Astrophysics (MAS), Chile.

This research was supported by the Munich Institute for Astro-, Particle and BioPhysics (MIAPbP) which is funded by the Deutsche Forschungsgemeinschaft (DFG, German Research Foundation) under Germany's Excellence Strategy – EXC-2094 – 390783311.

IRAF is distributed by NOAO, which is operated by AURA, Inc., under cooperative agreement with the National Science Foundation (NSF).

Table A1. Optical Spectroscopy of SN 2024ggi

UT Date	MJD	Phase[a] (days)	Telescope	Instrument	Wavelength Range (Å)
2024-04-12T06:10:08.92	60412.26	1.46	Shane	Kast	3254–10495
2024-04-13T00:00:05.88	60413.00	2.20	SOAR	TripleSpec	8243.4–24667.1
2024-04-13T00:41:21.57	60413.03	2.22	SOAR	Goodman	3816–7030
2024-04-16 06:21:35.01	60416.26	5.46	Shane	Kast	3603–10293
2024-04-16T06:34:06.69	60416.27	5.47	Shane	Kast	5800–7000
2024-04-18T05:49:43.62	60418.24	7.44	Shane	Kast	3253–10494
2024-04-19T23:41:17.00	60419.99	9.19	Gemini-S	GMOS	4000–7580
2024-04-20T01:32:39.64	60420.06	9.26	SOAR	TripleSpec	8243.0–24667.5
2024-04-20T02:19:26.89	60420.10	9.30	SOAR	Goodman	3854–8986

[a]Relative to first light (MJD 60410.80)

7.8 Appendix

Here we present a log of optical spectroscopic observations of SN 2024ggi in Table A1.

Chapter 8

Observational Properties and Physical Modeling of CSM-Interacting Type II Supernovae

This chapter is has been published as Jacobson-Galán et al., 2024a, ApJ, 970, 189

8.1 Abstract

We present ultraviolet/optical/near-infrared observations and modeling of Type II supernovae (SNe II) whose early-time ($\delta t < 2$ days) spectra show transient, narrow emission lines from shock ionization of confined ($r < 10^{15}$ cm) circumstellar material (CSM). The observed electron-scattering broadened line profiles (i.e., IIn-like) of H I, He I/II, C IV, and N III/IV/V from the CSM persist on a characteristic timescale ($t_{\rm IIn}$) that marks a transition to a lower-density CSM and the emergence of Doppler-broadened features from the fast-moving SN ejecta. Our sample, the largest to date, consists of 39 SNe with early-time IIn-like features in addition to 35 "comparison" SNe with no evidence of early-time IIn-like features, all with ultraviolet observations. The total sample includes 50 unpublished objects with a total of 474 previously unpublished spectra and 50 multiband light curves, collected primarily through the Young Supernova Experiment and Global Supernova Project collaborations. For all sample objects, we find a significant correlation between peak ultraviolet brightness and both $t_{\rm IIn}$ and the rise time, as well as evidence for enhanced peak luminosities in SNe II with IIn-like features. We quantify mass-loss rates and CSM density for the sample through matching of peak multiband absolute magnitudes, rise times, $t_{\rm IIn}$ and optical SN spectra with a grid of radiation hydrodynamics and non-local thermodynamic equilibrium (nLTE) radiative-transfer simulations. For our grid of models, all with the same underlying explosion, there is a trend between the duration of the electron-scattering broadened line profiles and inferred mass-loss rate: $t_{\rm IIn} \approx 3.8[\dot{M}/(0.01\ {\rm M}_\odot\ {\rm yr}^{-1})]$ days.

8.2 Introduction

Shock breakout (SBO) from a red supergiant (RSG) premieres as a burst of luminous ultraviolet (UV) and X-ray radiation that lasts several hours (Waxman & Katz 2017; Goldberg et al. 2022). The breakout photons escape from a characteristic optical depth ($\tau \approx c/v_{\rm sh}$, where c is the speed of light and $v_{\rm sh}$ is the shock velocity), which could occur either in the outer RSG envelope or inside of high-density circumstellar material (CSM) surrounding the star at the time of first light (Chevalier & Irwin 2011; Haynie & Piro 2021). Following first light at the characteristic optical depth, the photons emitted at SBO will "flash ionize" the CSM, leading to narrow emission lines in the early-time spectra of highly ionized elements such as He II, C IV, O VI, and N III/IV/V. However, without the presence of a continuous ionizing source in the CSM after SBO, the CSM will quickly recombine and the "flash ionization" phase will conclude within minutes to hours after SBO ($t_{\rm rec} \propto 1/n_e$, where n_e is number density of free electrons) given the densities typical of RSG environments (e.g., $n \approx 10^{7-10}$ cm^{-3}, $\rho \approx 10^{-14} - 10^{-17}$ g cm^{-3} at $r < 2R_\star$).

For Type II supernovae (SNe II) propagating in a low-density environment ($\rho < 10^{-15}$ g cm^{-3} at $r \approx 10^{14-15}$ cm), the fast-moving SN ejecta will then sweep up low-density, optically thin CSM and the Doppler-broadened spectral features of SN ejecta will be visible within hours-to-days after first light. For higher densities associated with some SN II environments (e.g., $\rho \gtrsim 10^{-14}$ g cm^{-3}), radiative cooling of the shocked regions will result in the formation of a cold dense shell (CDS) even at early times (Chevalier & Fransson 1994, 2017). Consequently, SNe II in dense CSM ($\rho \gtrsim 10^{-14}$ g cm^{-3} at $r \approx 10^{14-15}$ cm) present a unique opportunity to probe more extreme RSG mass-loss histories through ultrarapid ("flash") spectroscopy during the explosion's first days (Gal-Yam et al. 2014; Khazov et al. 2016; Yaron et al. 2017; Terreran et al. 2022; Jacobson-Galán et al. 2023).

Following SN ejecta-CSM interaction, the forward-shock kinetic luminosity goes as $L_{\rm sh} = \dot{M} v_{\rm sh}^3 / 2 v_w$, where $v_{\rm sh}$ is the shock velocity, v_w is the wind velocity, and $\dot{M}$ is the mass-loss rate (e.g., $\dot{M} = 4\pi\rho r^2 v_w$). Consequently, in high-density CSM, the SN shock power is quite high ($> 10^{41}$ erg s^{-1} for $\dot{M} > 10^{-4}$ M$_\odot$ yr^{-1}, $v_{\rm sh} \approx 10^4$ km s^{-1}) and for typical post-shock temperatures ($T_{\rm sh} \approx 10^{5-8}$ K), the gas will cool primarily via free-free emission, as well as line emission (Chevalier & Fransson 2017). High-energy photons emitted at the shock front will continue to ionize the intervening CSM, prolonging the formation of high-ionization recombination lines present during the "flash ionization" phase. During this "photoionization" phase, recombination photons inside the CSM will encounter a large number density of free electrons and consequently participate in multiple scatterings before they exit the CSM. Observationally, this manifests as spectral line profiles that contain a combination of a narrow core and Lorentzian wings (i.e., IIn-like), the former tracing the expansion velocities in the wind/CSM while the latter resulting from the photon's frequency shift following electron scattering (Chugai 2001; Dessart et al. 2009; Huang & Chevalier 2018). In the single-scattering limit, the observed emission line will map the thermal velocity of the free electrons ($v_e \approx 10^3 (T/10^{4.5}\ {\rm K})^{1/2}$ km s^{-1}), but with sufficiently large electron-scattering optical depths ($\tau \approx$ 3–10) the resulting line profiles can extend to thousands of km s^{-1}.

However, as the shock samples lower density CSM at large radii (assuming a wind-like profile or CSM shell), these electron-scattering profiles will vanish within days-to-weeks of first light, with the SN photosphere then revealing the CDS, if present, and subsequently the fast moving SN ejecta (Dessart et al. 2017). However, departures from CSM spherical symmetry and/or homogeneous density may blur the transition between these three phases; for example, Doppler-broadened line profiles can appear while spectral signatures of unshocked optically-thick CSM are still present in the early-time spectra.

Given the transient nature of these spectral features, high-cadence "flash" spectroscopy during the first days post-SBO is essential to map the densities, kinematics, and progenitor chemical composition in the pre-explosion environment at radii of $r < 10^{15}$ cm. Consequently, such observations provide a window into the largely unconstrained stages of stellar evolution in the final years-to-months before core collapse. Enabled by the advent of high-cadence surveys in the past decade, the study of SNe II with such photoionization spectral features has revealed enhanced, late-stage mass-loss rates in RSG progenitor systems. Interestingly, one of the first records of this phenomenon was in SN 1983K (Niemela et al. 1985), but garnered the most attention through observations of SN 1998S (Fassia et al. 2000; Leonard et al. 2000), which showed high-ionization features at early-times ($\delta t < 7$ days) and then transitioned to a Type IIL supernova (SN IIL) at later phases ($\delta t > 7$ days) as the IIn-like features disappeared. Spectroscopic and photometric modeling of SN 1998S suggested significant mass loss of $\dot{M} \approx 10^{-2}$ M$_\odot$ yr^{-1}for $v_w \approx 50 - 100$ km s^{-1} (Shivvers et al. 2015; Dessart et al. 2016), capable of producing transient IIn-like features and an overluminous light curve, placing it as extreme compared to normal SNe II, but not quite placing it in the Type IIn SN subclass.

Since SN 1998S, a number of SNe II have been discovered with photoionization spectral features from SN ejecta-CSM interaction at early times. Modeling of the photoionized spectra continues to point toward confined ($r < 10^{15}$ cm), high-density ($\dot{M} \approx 10^{-3}$– 10^{-2} M$_\odot$ yr^{-1}, $v_w \approx 50$–100 km s^{-1}) CSM created in the final years before explosion (e.g., PTF11iqb, Smith et al. 2015; SN 2013fs, Yaron et al. 2017; Dessart et al. 2017; SN 2014G, Terreran et al. 2016; SN 2016bkv, Hosseinzadeh et al. 2018; Nakaoka et al. 2018; SN 2017ahn, Tartaglia et al. 2021; SN 2018zd, Zhang et al. 2020; Hiramatsu et al. 2021; SN 2020pni, Terreran et al. 2022; SN 2020tlf, Jacobson-Galán et al. 2022a; SN 2023ixf, Jacobson-Galán et al. 2023; Bostroem et al. 2023; Smith et al. 2023; Zimmerman et al. 2024; Fig. 11 of Brethauer et al. 2022). Sample studies have sought to uncover the rates of such events, the most recent estimate being $> 40\%$ for all SN II discovered within 2 days of first light (Bruch et al. 2021b, 2023b). Intriguingly, mass-loss rates derived for individual explosions stand in contradiction with observations of weak, steady-state mass loss (e.g., 10^{-6} M$_\odot$ yr^{-1}) in observed RSGs (Beasor et al. 2020) as well as the quiescent behavior of SN II progenitor stars in pre-explosion imaging (Kochanek et al. 2017). However, this could be related to the pre-explosion timescales that each method is probing. Furthermore, beyond H-rich SNe, "flash spectroscopy" has aided in significant breakthroughs in our understanding of H-poor SN progenitor identity and late-stage evolution e.g., Type IIb, Type Ibc, and calcium-rich (e.g., Gal-Yam et al. 2014; Pastorello et al. 2015; Jacobson-Galán et al. 2020b; Davis et al. 2023b; Wang et al. 2023).

However, it is also evident that some massive stars undergo enhanced mass loss even before their final years (e.g., $t \approx 10$–1000 yr) and therefore X-ray/radio observations as well as long-term UV/optical monitoring is essential to reconstruct a more complete mass-loss history (e.g., Chevalier 1998; Fransson et al. 1996; Chevalier & Fransson 2006; Weiler et al. 2002; Wellons et al. 2012; Milisavljevic et al. 2015; Chevalier & Fransson 2017; Margutti et al. 2017; Brethauer et al. 2022; DeMarchi et al. 2022; Stroh et al. 2021; Dessart et al. 2023; Shahbandeh et al. 2023; Grefenstette et al. 2023; Berger et al. 2023; Panjkov et al. 2023).

In this study, we present observations and modeling of the largest sample to date of SNe II with early-time ($\delta t < 2$ days) spectroscopic signatures of CSM interaction. This sample consists of 27 unpublished SNe with photoionization emission features, which includes 293 new spectra as well as 27 UV/optical/near-infrared (NIR) light curves. In Section 2 we define the sample and present the spectroscopic and photometric observations. Section 3 presents an analysis of the bolometric and multiband light curves as well as early-time and photospheric-phase spectra. In Section 4 we present the `HERACLES`/`CMFGEN` model grid and the derived mass-loss rates and CSM densities based on model comparisons to the sample data. Our results are discussed in Section 5 and our conclusions are in Section 6.

All phases reported in this paper are with respect to the adopted time of first light (Table A1) and are in rest-frame days. The time of first light (δt) and its uncertainty are calculated from the average phase between the last deep non-detection and the first detection using forced photometry from the survey that initially imaged the SN (e.g., ZTF, ATLAS, YSE, DLT40). However, we note that the first-light phase could be earlier in some instances given a shallow depth of the last non-detection limit. Furthermore, "first light" in this case only refers to when photons are first detected from the SN, which is unlikely to reflect the first emission from the explosion. When available for a given sample object, we adopt the time of first light reported in a previously published study and confirm that this phase is consistent with first detection and last non-detection using forced photometry. When possible, we use redshift-independent host-galaxy distances and adopt standard ΛCDM cosmology ($H_0 = 70$ km s^{-1} Mpc^{-1}, $\Omega_M = 0.27$, $\Omega_\Lambda = 0.73$) if only redshift information is available for a given object.

8.3 Observations

8.3.1 Sample Definition

Our total sample consists of 74 SNe II, 39 of which show spectroscopic evidence for CSM interaction at early times ($\delta t < 10$ days) through the detection of transient IIn-like features. Gold-sample objects have a spectrum obtained at $\delta t < 2$ days while silver-sample objects only have spectra obtained at $\delta t > 2$ days. Additionally, we include 35 SNe II with "flash spectroscopy" (i.e., spectra at $\delta t < 2$ days) but no detection of IIn-like features (the comparison sample). For the gold and comparison samples, we require that the uncertainty in the time of first light be < 1 day. To construct the total sample, we first query the Transient

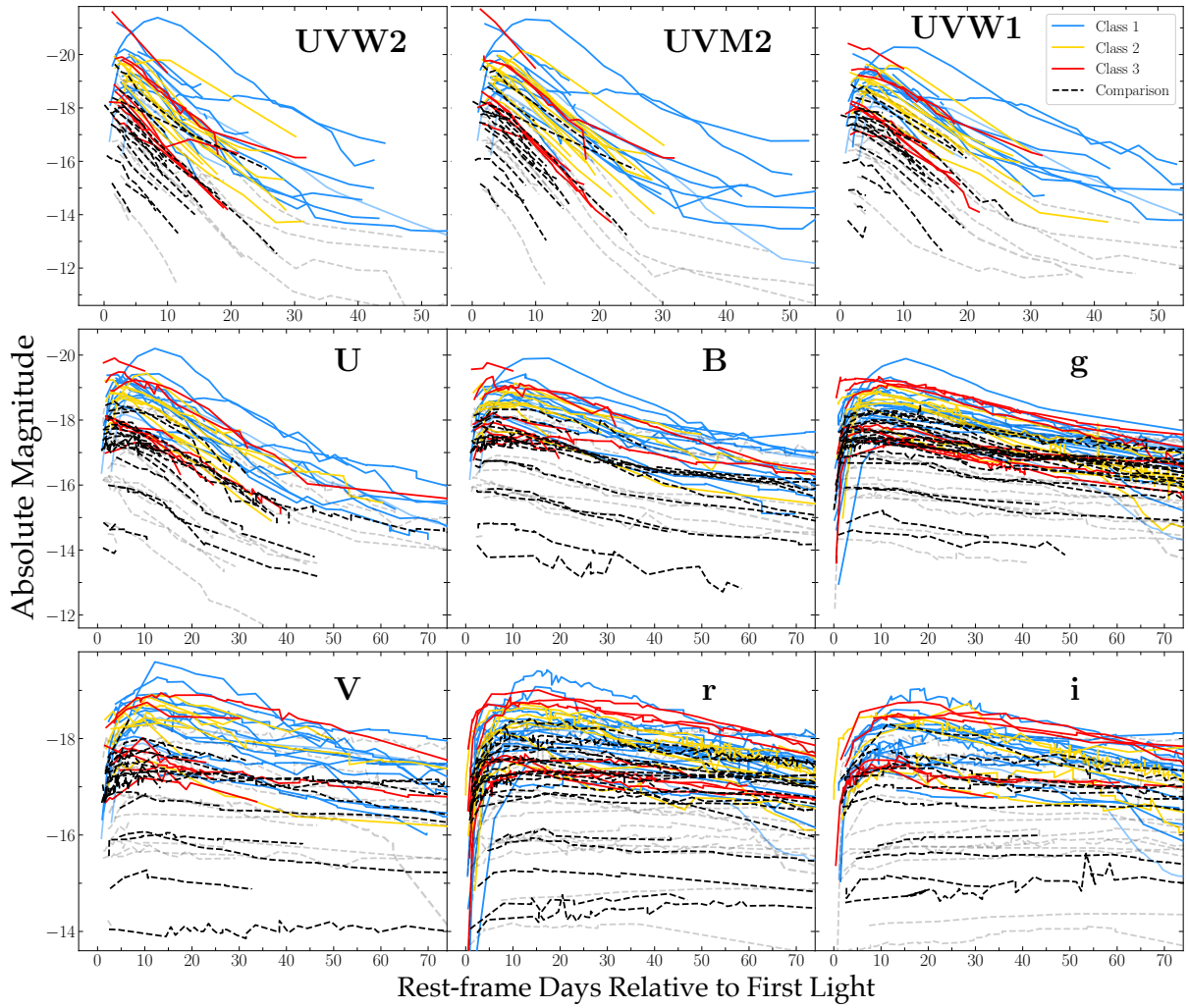

Figure 8.1 *Left to tight, top to bottom:* Early-time, extinction corrected *w2*-, *m2*-, *w1*-, *U/u*-, *B/b*-, *V/v*-, *g*-, *r*-, and *i*-band light curves of SNe II with IIn-like profiles in their early spectra. No K-corrections have been applied. Gold and silver samples shown in blue, yellow, and red; comparison sample plotted as black dashed lines. Solid colored curves represent the subsample of objects at $D > 40$ Mpc. Compared to SNe II without IIn-like features (i.e., comparison sample), objects with confirmed IIn-like signatures have notably more luminous and longer-lasting UV emission at early times. Furthermore, Class 1 objects that show longer lived IIn-like profiles of He II and N III are typically brighter than other gold-sample objects with shorter-lived IIn-like features. The variance of the total sample decreases with increasing wavelength, with the least luminous objects being those in the comparison sample.

Name Server (TNS)[1] for every transient discovered between 2004-11-20 and 2022-08-01 and then select only objects with Type II-like classification (e.g., SN II, SN IIP, SN IIL, SN IIn, SN II-pec) at redshifts $z < 0.05$, which returns 1697 SNe. For those SNe II, we keep objects having spectra within 3 days of discovery, which returns 428 objects. Next, we query the *Swift*-UVOT data archive and record how many total observations of the SN location exist within 10 days of discovery. We then keep objects with > 2 *Swift*-UVOT observations at < 10 days post-discovery, which returns 114 total objects, after cutting SNe IIn. This exercise is repeated using the Weizmann Interactive Supernova Data Repository (WISeREP)[2], finding 48 total objects, both with and without IAU names, that meet the sample selection criteria listed above. We are then left with 137 total SNe II after removing duplicate objects. Lastly, we cut all SNe II with no IIn-like features that do not have a spectrum at $\delta t < 2$ days and/or uncertainty in the time of first light of > 1 day. Furthermore, we cut all objects that do not have $\Delta m > 1$ mag between last non-detection and first detection, in the same filter, and/or $\Delta M > 3$ mag between first detection and peak brightness. Consequently, our total sample contains 74 objects: 20 gold, 19 silver, and 35 comparison-sample SNe II. In this data release, we also include multicolor light curves and spectra of five additional SNe II with IIn-like features: 2018cvn, 2018khh, 2019ofc, 2019nyk, 2021ulv. These objects are not used in our analysis given the lack of UV photometry.

The gold/silver samples contain 12 previously published objects with a total of 208 spectra and 12 UV/optical light curves, in addition to 27 unpublished objects with a total of 293 spectra and 27 UV/optical light curves. The comparison sample contains 12 previously published and 23 unpublished objects, with a total of 464 spectra. As shown in Figure 8.23, peak absolute magnitude as a function of SN distance reveals a trend consistent with a Malmquist bias i.e., only higher luminosity objects can be detected at further distances. An examination of peak apparent magnitude before extinction corrections are applied shows that the sample extends to low luminosities, with the majority of nearby ($D < 20$ Mpc) events being in the comparison sample. The lack of nearby gold/silver sample objects may be the result of selection effects and/or the intrinsic rarity of SNe II with IIn-like features. Furthermore, the difference in redshift distribution (top-left panel of Fig. 8.23) implies that the gold and comparison samples may not arise from the same parent distribution. We account for this difference by applying a distance cut in our comparison of observables in each sub-sample in §8.4.1. Additionally, we note the lack of highly reddened SNe ($A_V > 3$ mag; Jencson et al. 2019) in our sample, which represents a selection effect in our sample because these objects are unlikely to have associated *Swift*-UVOT observations.

Within both subsamples, the color delineation (e.g., Figures 8.1 and 8.3) is as follows: at phases of $t \approx 2$ days post-first light, blue-colored objects ("Class 1") show high-ionization emission lines of N III, He II, and C IV (e.g., SNe 1998S, 2017ahn, 2018zd, 2020pni, 2020tlf), yellow-colored objects ("Class 2") have no N III emission but do show He II and C IV (e.g., SNe 2014G, 2022jox), and red-colored objects ("Class 3") only show weaker, narrow He II emission superimposed with a blueshifted, Doppler-broadened He II (e.g., SN 2013fs,

[1] https://www.wis-tns.org/
[2] https://www.wiserep.org/

2020xua). However, it should be noted that high-ionization lines of O V/VI, C V, and N IV are also present in SN 2013fs at $t < 1$ day owing to a more compact CSM than other CSM-interacting SNe II (Yaron et al. 2017; Dessart et al. 2017), thus, the color delineation is epoch dependent.

All targets were selected from private collaborations/surveys as well as all public/published studies on SNe II with prominent or potential IIn-like features in their early-time spectra (Tables A1 and A2). We emphasize that while the SNe in our sample may show IIn-like line profiles at early times, they are not prototypical SNe IIn that show relatively narrow line profiles from CSM interaction for weeks-to-months following explosion (e.g., SNe 2005ip, 2010jl; Smith et al. 2009; Taddia et al. 2013; Gall et al. 2014; Fransson et al. 2014; Dessart et al. 2015). The IIn-like profiles in our sample objects fade within days to a week after first light and the explosion proceeds to evolve photometrically and spectroscopically as a standard RSG explosion — a light-curve plateau or linear (in magnitudes) decline where hydrogen recombination mitigates the release of stored radiative energy and the photospheric spectra are dominated by P Cygni profiles formed from H, He, and Fe-group elements in the SN ejecta.

8.3.2 Photometric Observations

All gold-, silver- and comparison-sample objects were observed during their evolution with the Ultraviolet Optical Telescope (UVOT; Roming et al. 2005) onboard the *Neil Gehrels Swift Observatory* (Gehrels et al. 2004). We performed aperture photometry with a 5″ region radius with `uvotsource` within HEAsoft v6.26[3], following the standard guidelines from Brown et al. (2014)[4]. In order to remove contamination from the host galaxy, we employed images acquired at $\delta t > 1$ yr, assuming that the SN contribution is negligible at this phase. This is supported by visual inspection in which we found no flux at the SN location. We subtracted the measured count rate at the location of the SN from the count rates in the SN images and corrected for point-spread-function (PSF) losses following the prescriptions of Brown et al. (2014). We also note that the $w2$ filter has a known red leak (Brown et al. 2010), which could impact post-peak observations when the SN is significantly cooler.

For the total sample, optical/NIR photometry was obtained from a variety of collaborations and telescopes. Pan-STARRS telescope (PS1/2; Kaiser et al. 2002; Chambers et al. 2017) imaging in the *grizy* bands was obtained through the Young Supernova Experiment (YSE; Jones et al. 2021). Data storage/visualization and follow-up coordination was done through the YSE-PZ web broker (Coulter et al. 2022, 2023). The YSE photometric pipeline is based on `photpipe` (Rest et al. 2005), which relies on calibrations from Magnier et al. (2020) and Waters et al. (2020). Each image template was taken from stacked PS1 exposures, with most of the input data from the PS1 3π survey. All images and templates were resampled and astrometrically aligned to match a skycell in the PS1 sky tessellation. An

[3]We used the calibration database (CALDB) version 20201008.

[4]`https://github.com/gterreran/Swift_host_subtraction`

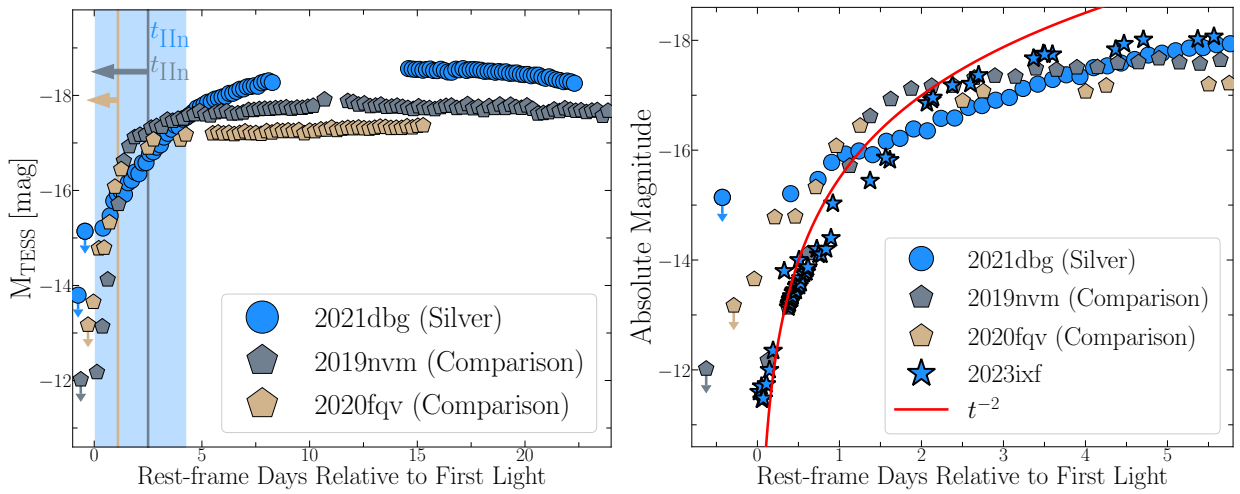

Figure 8.2 *Top:* *TESS* ($\lambda_{\rm eff}$ = 7453 Å) light curves (binned) for silver-sample object SN 2021dbg (blue circles) and comparison-sample objects SNe 2019nvm (gray polygons) and 2020fqv (tan polygons). SN 2021dbg shows IIn-like signatures for $\sim$ 4 days after first light (blue shaded region), consistent with an increased rise time and peak absolute magnitude. Conversely, the persistence of IIn-like features in SNe 2019nvm and 2020fqv is constrained to $<$ 2.6 and $<$ 1.1 days, respectively. These SN light curves are likely consistent with shock-cooling emission from confined ($< 2R_\star$), high-density stellar material and/or SN ejecta interaction with lower density CSM that extends out to larger distances, neither scenario being able to form IIn-like features. *Bottom:* Zoom-in of the first 5 days of the *TESS* light curves for SNe 2021dbg, 2020fqv, and 2019nvm compared to ground-based photometry in optical clear- and r-band filters of the nearby CSM-interacting SN II 2023ixf (Hosseinzadeh et al. 2023).

image zero-point is determined by comparing PSF photometry of the stars to updated stellar catalogs of PS1 observations (Flewelling et al. 2016b). The PS1 templates are convolved with a three-Gaussian kernel to match the PSF of the nightly images, and the convolved templates are subtracted from the nightly images with `HOTPANTS` (Becker 2015). Finally, a flux-weighted centroid is found for the position of the SN in each image and PSF photometry is performed using "forced photometry": the centroid of the PSF is forced to be at the SN position. The nightly zero-point is applied to the photometry to determine the brightness of the SN for that epoch.

We obtained $uUBVgriz$ imaging with the Las Cumbres Observatory (LCO) 1 m telescopes through the Global Supernova Project (GSP) and YSE. After downloading the `BANZAI`-reduced images from the Las Cumbres Observatory data archive (McCully et al. 2018), we used `photpipe` (Rest et al. 2005) to perform `DoPhot` PSF photometry (Schechter et al. 1993). All photometry was calibrated using PS1 stellar catalogs described above with additional transformations to the SDSS u band derived from Finkbeiner et al. (2016). For additional details on our reductions, see Kilpatrick et al. (2018a). We also obtained photometry using a 0.7 m Thai Robotic Telescope at Sierra Remote Observatories and the 1 m Nickel telescope at Lick Observatory in the $BVRI$ bands. Images are bias subtracted and field flattened. Absolute photometry is obtained using stars in the $10' \times 10'$ field of view. We also observed objects with the Lulin 1 m telescope in $griz$ bands and the Swope 1 m telescope in $uBVgri$. Standard calibrations for bias and flat-fielding were performed on the images using `IRAF`, and we reduced the calibrated frames in `photpipe` using the methods described above for the Las Cumbres Observatory images.

Sample objects were also observed with ATLAS, a twin 0.5 m telescope system installed on Haleakala and Maunaloa in the Hawai'ian islands that robotically surveys the sky in cyan (c) and orange (o) filters (Tonry et al. 2018a). The survey images are processed as described by Tonry et al. (2018a) and photometrically and astrometrically calibrated immediately (using the RefCat2 catalogue; Tonry et al. 2018c). Template generation, image-subtraction procedures, and identification of transient objects are described by Smith et al. (2020). PSF photometry is carried out on the difference images and all detections more significant than 5σ are recorded and go through an automatic validation process that removes spurious objects (Smith et al. 2020). Photometry on the difference images (both forced and non-forced) is obtained from automated PSF fitting as documented by Tonry et al. (2018a). The photometry presented here is derived from the weighted averages of the nightly individual 30 s exposures, carried out with forced photometry at the position of each SN. In addition to our observations, we include gri-band photometry from the Zwicky Transient Facility (ZTF; Bellm et al. 2019; Graham et al. 2019) forced-photometry service (Masci et al. 2019).

In Figure 8.2, we present new *Transiting Exoplanet Survey Satellite* (*TESS*; Ricker et al. 2015) light curves of SNe 2019nvm and 2021dbg, reduced using the `TESSreduce` package (Ridden-Harper et al. 2021), compared to previously published *TESS* light curve of SN 2020fqv (Tinyanont et al. 2022). These observations have been binned to a 6 hr cadence and are able to constrain the uncertainty in the time of first light to a few hours. To our knowledge, SN 2021dbg represents the first SN II with IIn-like features to have a complete

TESS light curve.

For all SNe, the Milky Way (MW) V-band extinction and color excess along the SN line of sight is inferred using a standard Fitzpatrick (1999) reddening law ($R_V = 3.1$). In addition to the MW color excess, we estimate the contribution of host-galaxy extinction in the local SN environment using Na I D absorption lines for all gold-, silver-, and comparison-sample objects. To determine if Na I D is detected, we fit the continuum in a region around the transition based on the spectral resolution and calculate the residuals between the continuum fit and the spectral data. We then integrate the residual flux and confirm that it is greater than or equal to three times the residual flux uncertainty in order to claim a "detection." We calculate the Na I D equivalent width (EW) and use $A_V^{\rm host} = (0.78 \pm 0.15)$ mag $\times$ (EW$_{\rm NaID}$/Å) from Stritzinger et al. (2018) to convert these EWs to an intrinsic host-galaxy $E(B-V)$, also using the Fitzpatrick (1999) reddening law. A visualization of this method is shown in Figure 8.20. For non-detections, we calculate an upper limit on the EW and host reddening using the fitted continuum flux. We present a detailed discussion of the host extinction uncertainties in Appendix Section A. We do not apply alternative methods for estimating host extinction such as using the diffuse interstellar band (DIB) at 5780 Å (Phillips et al. 2013), which has been shown to yield consistent extinction values to Na I D EW for other SNe (Hosseinzadeh et al. 2022). We test whether the reddening values of the gold and comparison samples come from the sample parent distribution by applying a logrank test and finding a 35% chance probability that the gold and comparison sample reddening come from the same distribution. Therefore, there is no statistical evidence that the extinction correction affects the two sub-samples differently and is thus is not a source of differences between the luminosity distribution of each sub-samples (see §8.4.1). We present cumulative distributions of the gold, silver and comparison sample host extinction in Figure 8.20 and, in Appendix §8.10, we discuss the use of colors as a metric for host galaxy reddening.

All adopted extinction (MW and host), redshift, distance, and first light date values are reported for gold-, silver-, and comparison-sample objects in Tables A1, A2, and A3, respectively. Complete, multiband light curves are shown in Figure 8.1. All photometric data/logs will be publicly available in an online data repository.[5]

8.3.3 Spectroscopic Observations

We obtained spectra for sample objects with the Kast spectrograph on the 3 m Shane telescope at Lick Observatory (Miller & Stone 1993) and Keck/LRIS (Oke et al. 1995). For all of these spectroscopic observations, standard CCD processing and spectrum extraction were accomplished with IRAF[6]. The data were extracted using the optimal algorithm of Horne (1986). Low-order polynomial fits to calibration-lamp spectra were used to establish the wavelength scale and small adjustments derived from night-sky lines in the object frames were applied.

[5] https://github.com/wynnjacobson-galan/Flash_Spectra_Sample

[6] https://github.com/msiebert1/UCSC_spectral_pipeline

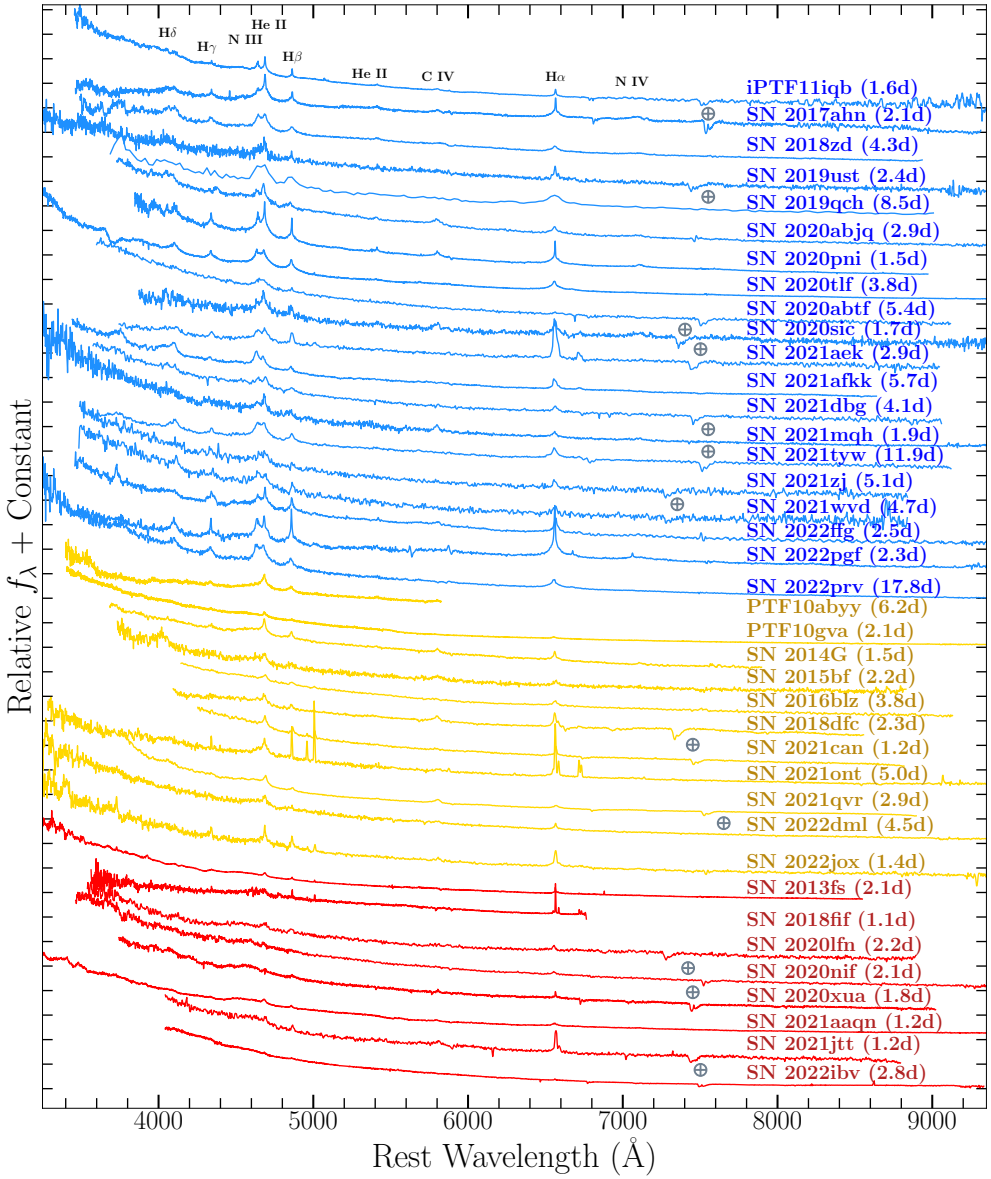

Figure 8.3 Early-time ("flash") spectra of all gold- and silver-sample SNe II (e.g., §8.3.1); phases are relative to time of first light. All plotted SNe show transient, IIn-like (i.e., electron-scattering broadened) line profiles formed from persistent photoionization of dense, slow, unshocked CSM. Objects in blue ("Class 1") show prominent He II and N III emission, objects in yellow ("Class 2") exhibit only prominent He II emission, and objects in red ("Class 3") have weak He II emission. Gray circles with a plus indicate telluric absorption. We note that because a number of spectra were obtained from public databases, there has not been a consistent flux calibration applied and therefore the relative continuum shapes should be interpreted with caution.

Las Cumbres Observatory optical spectra were taken with the FLOYDS spectrographs (Brown et al. 2013) mounted on the 2 m Faulkes Telescope North and South at Haleakala (USA) and Siding Spring (Australia), respectively, through the Global Supernova Project. A 2″ slit was placed on the target at the parallactic angle (Filippenko 1982). One-dimensional spectra were extracted, reduced, and calibrated following standard procedures using the FLOYDS pipeline[7] (Valenti et al. 2014b).

Spectra were also obtained with the Alhambra Faint Object Spectrograph (ALFOSC) on The Nordic Optical Telescope (NOT), the Goodman spectrograph (Clemens et al. 2004) at the Southern Astrophysical Research (SOAR) telescope, Gemini Multi-Object Spectrographs (GMOS), Wide-Field Spectrograph (WiFeS) at Siding Spring, Binospec on the MMT (Fabricant et al. 2019b), Lijiang 2.4-m telescope (+YFOSC) (Fan et al. 2015), and SpeX (Rayner et al. 2003) at the NASA Infrared Telescope Facility (IRTF). All of the spectra were reduced using standard techniques, which included correction for bias, overscan, and flat-field. Spectra of comparison lamps and standard stars acquired during the same night and with the same instrumental setting have been used for the wavelength and flux calibrations, respectively. When possible, we further removed the telluric bands using standard stars. Given the various instruments employed, the data-reduction steps described above have been applied using several instrument-specific routines. We used standard IRAF commands to extract all spectra.

Sample spectral data were also collected using EFOSC2 (Buzzoni et al. 1984) at the 3.58 m ESO New Technology Telescope (NTT) through the ePESSTO+ program (Smartt et al. 2015). Standard data-reduction processes were performed using the PESSTO pipeline (Smartt et al. 2015)[8]. The reduced spectrum was then extracted, and calibrated in wavelength and flux. In some instances, public classification spectra from TNS as well as published data stored in WISeREP were used in the presented sample. Early-time spectra for the gold and silver samples are presented in Figure 8.3, with comparison-sample spectra shown in Figure 8.19. In total, this study includes 491 published and 474 previously unpublished spectra of SNe II. All spectroscopic data/logs will be publicly available in an online data repository.[9]

8.4 Analysis

8.4.1 Photometric Properties

We present extinction-corrected $w2, m2, w1, u, b, v, g, r$ light curves of gold-, silver-, and comparison-sample objects in Figure 8.1. Given that the redshift/distance distributions of the gold and comparison samples are not the same, we divide sample objects based on a distance cut of $D > 40$ Mpc; this distance being the threshold when the distance distributions

[7] https://github.com/svalenti/FLOYDS_pipeline
[8] https://github.com/svalenti/pessto
[9] https://github.com/wynnjacobson-galan/Flash_Spectra_Sample

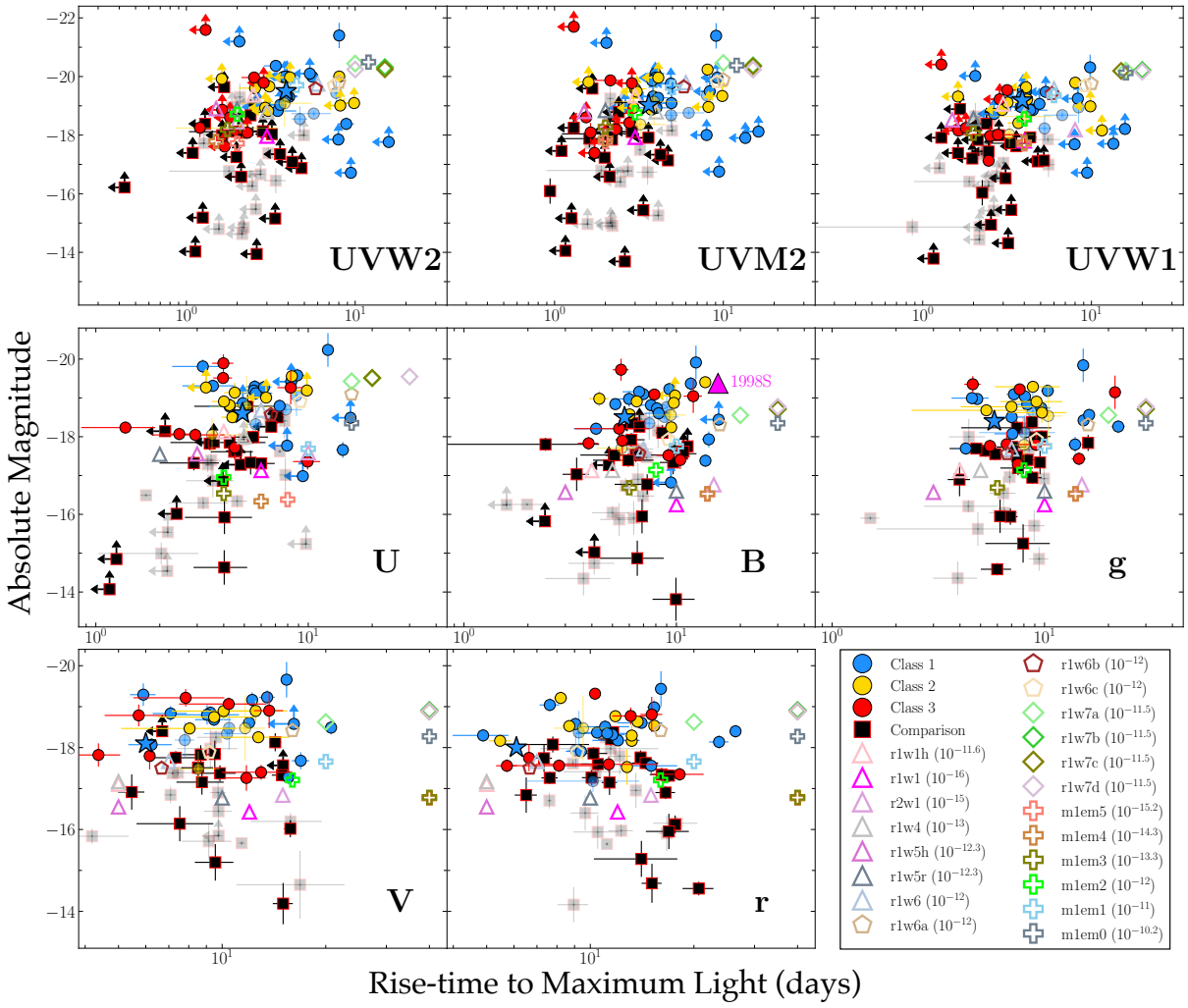

Figure 8.4 *Left to right, top to bottom:* Peak absolute magnitude versus rise time in the *w2*, *m2*, *w1*, *u*, *B/b*, *V/v*, *g*, and *r* bands. Gold/silver samples shown as blue/yellow/red circles and the comparison sample is shown as black squares. Solid colored points represent the subsample of objects at $D > 40$ Mpc. Parameters from the `CMFGEN` model grid (§8.5.1) are plotted as colored stars, polygons, diamonds and plus signs with the CSM densities at 10^{14} cm (in g cm^{-3}) for each model displayed in parentheses. SNe 1998S and 2023ixf are shown for reference as a magenta triangle and blue star, respectively. We note that the model parameters do not cover the dynamical range of the observations, which will influence the derivation of CSM properties for some objects (§8.5). Furthermore, in the UV bands, the data show significantly larger variance than the models, which follow a well-defined trend. This likely indicates a dependence on a variable not included in the models.

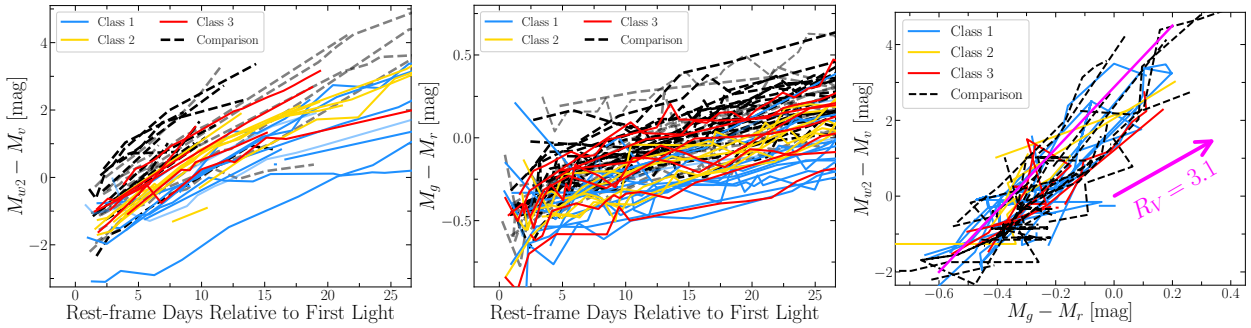

Figure 8.5 *Left:* Early-time, reddening-corrected $W2-V$ color plot for gold- and silver-sample objects (red, yellow, blue lines) compared to comparison sample objects (black dashed lines). Solid colored curves represent the subsample of objects at $D > 40$ Mpc. Gold- and silver-sample objects, in particular the Class 1 objects, show significantly bluer colors than Class 2/3 or comparison-sample objects, which is indicative of increased temperatures from persistent CSM interaction. *Middle:* Early-time, reddening-corrected $g - r$ color plot shows a less clear delineation between objects/classes with varying signatures of CSM interaction, suggesting that the UV colors are the most sensitive metric for confirming ejecta-CSM interaction. *Right:* $W2 - V$ vs. $g - r$ colors for gold- and comparison-sample objects. The reddening vector for $R_V = 3.1$ using the Fitzpatrick (1999) reddening law is shown as a magenta arrow.

of both sub-samples are consistent. In order to quantify the differences between the gold-sample classes and the comparison sample, we fit high-order polynomials to all light curves to derive a peak absolute magnitude and a rise time in all eight filters. These values are reported in Jacobson-Galán et al. (2024), with the uncertainty in peak magnitude being the 1σ error from the fit and the uncertainty in the peak phase being found from adding the uncertainties in both the time of peak magnitude and the time of first light in quadrature. We note that the pre-peak evolution in the UV filters of some sample objects is unconstrained (e.g., Fig. 8.1). For those objects with no constrained rise, we report the peak absolute magnitude and rise time as lower and upper limits, respectively.

As shown in Figure 8.4, we identify moderate positive trends between $M_{\rm peak}$ and $t_{\rm rise}$ in $w2, m2, w1, u$-band filters, and we find that while such trends are not as significant in b, g, v, r filters, there is still a difference between gold/silver and comparison samples in optical filters. Amongst gold-sample SNe, Class 1 objects display the brightest peak absolute magnitudes and longest rise times compared to Class 3 and comparison-sample objects. On average, gold-sample objects are > 2 mag brighter in the UV bands than comparison-sample objects (e.g., $M^{\rm W2}_{\rm avg} = -19.5$ mag versus $M^{\rm W2}_{\rm avg} = -17.1$ mag), even after a distance cut is applied, suggesting a significant luminosity boost from CSM interaction at early times. Furthermore, the $w2 - v$ and $g - r$ colors plotted in Figure 8.5 show that gold-sample objects, in particular Class 1 SNe, are bluer at earlier times than comparison-sample objects. Additionally, most Class 1/2 objects sustain blue colors ($g - r < 0$) longer than the comparison sample,

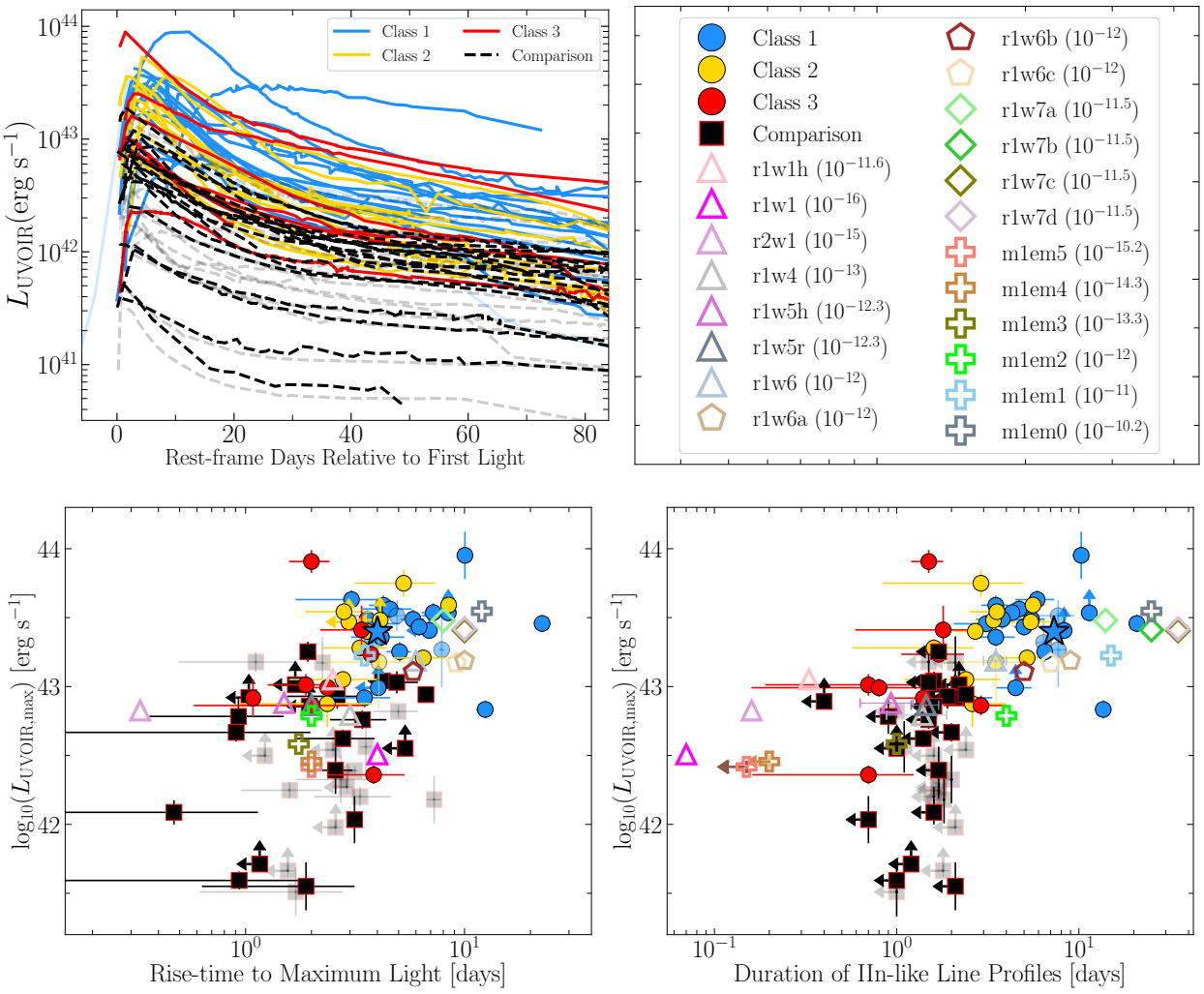

Figure 8.6 *Top left:* Pseudo-bolometric (i.e., UVOIR) light curves of gold/silver samples (blue/yellow/red solid lines) and the comparison sample (dashed black lines). Solid colored points/curves represent the subsample of objects at $D > 40$ Mpc. The CSM interaction present in SNe II with IIn signatures can create more than an order of magnitude luminosity excess beyond SNe II in low-density CSM. The light curve of gold-sample object SN 2020tlf (blue) extends before first light because of detected precursor emission (Jacobson-Galán et al. 2022a). *Top right:* Legend with all models. *Bottom left:* Peak bolometric luminosity versus rise time for gold-, silver-, and comparison-sample objects, compared to `CMFGEN` model grid. *Bottom right:* Peak bolometric luminosity versus duration of IIn-like features ($t_{\rm IIn}$) also shows a clear positive trend (§8.4.2). SN 2023ixf is shown for reference as a blue star.

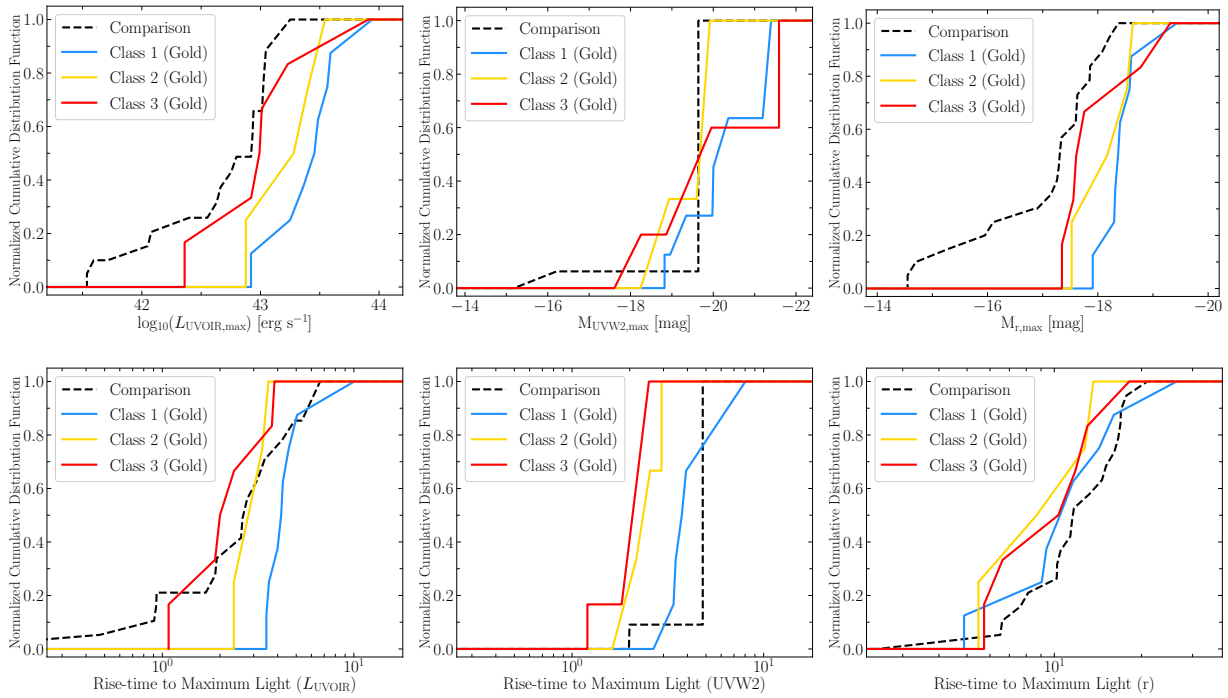

Figure 8.7 *Left to right, top to bottom:* Cumulative distributions of peak UVOIR luminosities, peak $w2$-band absolute magnitudes, peak r-band absolute magnitudes, UVOIR rise times, $w2$-band rise times, and r-band rise times for Class 1, 2, 3 gold-sample (blue, yellow, red lines) and comparison-sample (black dashed lines) objects after a distance cut ($D > 40$ Mpc) is applied. Distinct distributions are present in the peak bolometric and optical luminosities for gold-sample objects compared to the comparison-sample SNe, which is most likely due to the effects of CSM interaction on the early-time light curves.

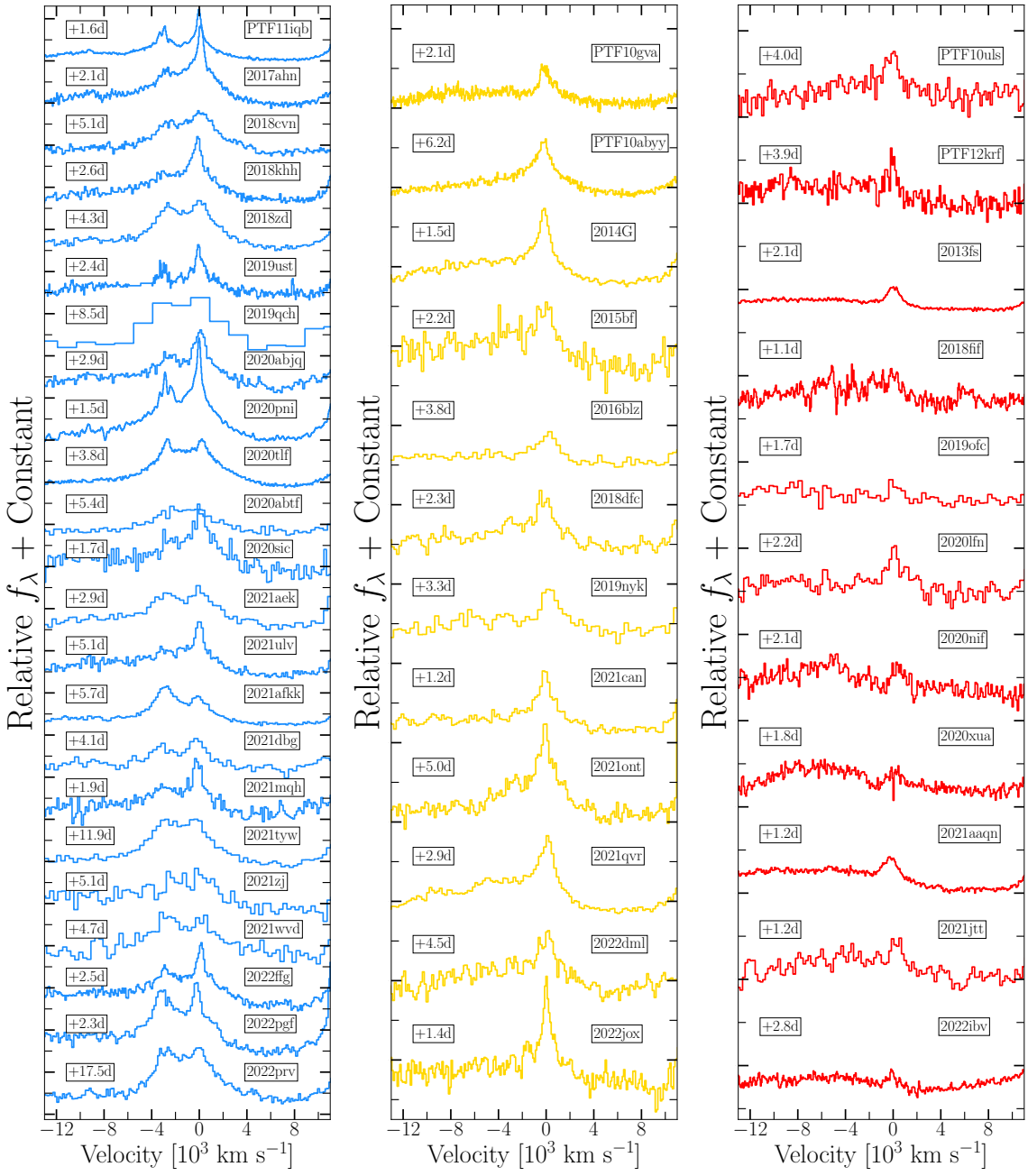

Figure 8.8 He II emission-line profiles for gold- and silver-sample objects. *Left:* SNe with visible, narrow N III emission are shown in blue (Class 1). *Middle/right:* Objects plotted in yellow (Class 2) and red (Class 3) show only narrow He II emission lines, the latter possessing the weakest emission superimposed on top of the broad He II profile from the fastest moving SN ejecta.

suggesting continued interaction with more distant CSM that is at higher densities than a typical RSG wind. Similarly, the plateau luminosities of Class 1/2 objects remains higher than the control sample, also indicating long-lived interaction power.

In Figure 8.6 we present pseudo-bolometric UV/optical/NIR (UVOIR) light curves of the gold/silver- and comparison-sample objects generated using the `superbol`[10] code. For all SNe, we extrapolate between light-curve data points using a low-order polynomial spline in regions without complete color information. Repeating the analysis used for the multiband light curves, we calculate peak pseudo-bolometric luminosities and rise times; these values are presented in Jacobson-Galán et al. (2024). For objects without a constrained rise to peak in all UV filters (i.e., $w2, m2, w1$), we report peak luminosities and rise times as lower and upper limits, respectively. As shown in Figure 8.6, we find a significant trend between peak UVOIR luminosities and rise time to maximum light; this is similar to UV filters discussed above and indicates that the majority of the flux at early times is focused in the UV bands, especially with the presence of ejecta-CSM interaction. Furthermore, we find that gold/silver-sample objects can be more than one order of magnitude more luminous at peak than comparison-sample SNe, also suggesting excess luminosity from CSM interaction.

In Figure 8.7, we present the cumulative distributions of maximum brightness and rise times for the pseudo-bolometric, $w2$-band, and r-band light curves of the gold/silver and comparison samples that are constructed using Kaplan-Meier estimation for all objects at $D > 40$ Mpc. To test our null hypothesis of whether these sample observables come from the same parent distribution, we apply a logrank test for (i) gold vs. comparison samples, (ii) gold-sample Classes 1 & 2 vs. 3, and (iii) gold-sample Classes 1 vs. 3. Limits on peak luminosity and rise time are accounted for using survival statistics. For (i), the chance probability that peak-brightness values of the gold and comparison samples come from the same distribution is 0.1% for $L_{\rm max}$, 80.0% for $M_{w2,\rm max}$, and 3×10^{-3}% for $M_{r,\rm max}$. We find that the pseudo-bolometric, UV, and r-band rise times between samples do belong to the same distribution at the 60.6%, 7.1%, and 55.6% levels, respectively. For (ii), the null-hypothesis probability for pseudo-bolometric, UV, and r-band peak brightness (rise time) is 23.1(1.67)%, 73.3(1.9)%, and 69.4(83.3)%, respectively. For (iii), the null hypothesis probability for pseudo-bolometric, UV, and r-band peak brightness (rise-time) is 17.3(0.24)%, 92.6(1.51)%, and 46.6(60.1)%, respectively. Therefore, we conclude that the gold sample is significantly more luminous than the comparison sample in bolometric and optical light curves, but luminosity differences within the classes of the gold sample are not statistically significant. Given the large number of limits present in the $w2$-band light curves, peak UV luminosity differences between gold and comparison samples cannot be claimed as significant. Furthermore, there is evidence that the differences in bolometric and UV rise-times between Class 1 & 2 vs 3, as well as Class 1 vs. 3, are statistically significant. However, differences in the rise time between all other groups are not statistically significant.

[10] https://github.com/mnicholl/superbol

8.4.2 Spectroscopic Properties

We present single epoch, "flash" spectroscopy of the gold/silver and comparison samples in Figures 8.3 and 8.19, respectively, with complete spectral series shown for each object in the supplementary, online-only text. As discussed in Section 8.3.1, the blue (Class 1), yellow (Class 2), and red (Class 3) color delineation is based on the structure of the He II λ4686 line, which is shown in detail for all gold/silver-sample objects in Figure 8.8. As illustrated in Figure 8.10, the IIn-like features of semi-isolated (i.e., unblended) transitions such as Hα can be modeled with a two-component Lorentzian, which includes a narrow component that provides an upper limit on the CSM velocity (due to likely radiative acceleration) and a broad component that forms from electron scattering of recombination-line photons in the optically thick unshocked CSM. The physical origin of the He II λ4686 profile is slightly more complex and can be modeled with a high-velocity, blueshifted, full width at half-maximum intensity (FWHM) $\approx 10^4$ km s^{-1} component representing fast-moving material in the CDS and/or outer ejecta, plus a narrow, and possibly electron-scattering broadened, emission at the central wavelength for Class 2 and 3 objects (e.g., 2014G and 2013fs; Fig. 8.10). However, Class 1 objects (e.g., 2020pni; 8.10) require multiple narrow and electron-scattering emission components of He II and N III, which may be superimposed on an underlying, blueshifted He II profile, the same as Classes 2 & 3 (e.g., see Dessart et al. 2017)

As confirmed by our sample, the narrow, symmetric line profiles with Lorentzian wings caused by electron scattering (i.e., IIn-like) can persist for days after first light. After these phases, the SNe develop broad P-Cygni profiles in all Balmer transitions as a result of the escape of photons from the fast-moving ejecta and a decrease in CSM density. We therefore define the duration of the IIn-like features (i.e., $t_{\rm IIn}$) as the transition point at which the unshocked CSM optical depth to electron scattering has dropped enough to see the emerging fast-moving SN ejecta (Dessart & Jacobson-Galán 2023; Jacobson-Galán et al. 2023). This evolution is shown in Figure 8.9 for gold-sample SNe 2013fs, 2017ahn, and 2018zd, all of which have high enough spectral cadence to allow for a precise observation of the fading of the IIn-like features. We use this transition to calculate $t_{\rm IIn}$ and its uncertainty, which is derived from the cadence of the spectral observations. For gold/silver-sample objects without sufficiently high spectral cadence to confidently estimate $t_{\rm IIn}$, we use spectral comparisons to SNe 2013fs, 2017ahn, and 2018zd to derive a IIn-like feature duration timescale by extrapolating phase measurements and assuming that the spectral evolution is consistent with the SNe used for reference. The uncertainty of $t_{\rm IIn}$ from spectral comparison is added in quadrature with the uncertainty in the time of first light for each sample object. For comparison-sample objects, which do not show IIn-like features, we take the phase of their earliest spectrum to be an upper limit on $t_{\rm IIn}$. All $t_{\rm IIn}$ values are presented in Jacobson-Galán et al. (2024).

In Figures 8.6 and 8.12, we plot $t_{\rm IIn}$ with respect to peak luminosity for all UV, optical, and pseudo-bolometric light curves. We find a moderate positive trend between between peak luminosity and $t_{\rm IIn}$ in $w2, m2, w1, u, b$-band filters, which is similar to the rise-time trends shown in Figure 8.4. While the peak absolute magnitude in optical v, g, r-band filters reveal a more obvious trend with $t_{\rm IIn}$ than $t_{\rm rise}$, their correlation can only be claimed as tentative. A

similar trend is found in Bruch et al. (2023b) between the duration of narrow He II emission and g-band peak magnitude. Furthermore, as shown in Figure 8.6, peak pseudo-bolometric luminosities and the duration of IIn-like features are moderately correlated. Amongst the gold/silver samples, Class 1 objects consistently show the highest peak luminosities across wavelengths, coupled with a longer duration of observed IIn-like features, indicating ejecta-CSM interaction with denser, and likely more extended, CSM than Class 2/3 objects (e.g., see Figs. 8.7 and 8.13).

As the IIn-like features fade, all gold/silver-sample objects transition into standard SNe II with Doppler broadened, blueshifted P Cygni features of the fast-moving, H-rich ejecta. In Figure 8.11, we present photospheric velocities calculated from the absorption minima of Hα and Fe II λ5169 transitions for gold-, silver-, and comparison-sample objects. Overall, there is some spread in Hα velocities amongst gold/silver-sample objects with a few Class 1 SNe displaying slower velocities ($v \approx 5000$–8000 km s^{-1}) than Classes 2/3 ($v > 10^4$ km s^{-1}). However, in general, we find little difference in the Hα and Fe II velocities found in the absorption minima between gold/silver and comparison sample from $\delta t \approx 10$–100 days.

8.5 Modeling

8.5.1 HERACLES/CMFGEN Model Grid

In order to quantify the CSM properties in our gold, silver, and comparison samples, we compared the spectral and photometric properties of all SNe to a model grid of radiation hydrodynamics and non-LTE, radiative-transfer simulations covering a wide range of progenitor mass-loss rates ($\dot{M} = 10^{-6}$–10^{0} M$_\odot$ yr^{-1}; $v_w = 50$ km s^{-1}), maximum radii of dense CSM ($R = 10^{14}$–10^{16} cm), and CSM densities at 10^{14} cm ($\rho_{14} = 10^{-16}$–7.3×10^{-11} g cm^{-3}), all in spherical symmetry. Simulations of the SN ejecta-CSM interaction were performed with the multigroup radiation-hydrodynamics code HERACLES (González et al. 2007; Vaytet et al. 2011; Dessart et al. 2015), which consistently computes the radiation field and hydrodynamics. Then, at selected snapshots in time post-explosion, the hydrodynamical variables are imported into the non-LTE radiative-transfer code CMFGEN (Hillier & Dessart 2012; Dessart et al. 2015) for an accurate calculation of the radiative transfer, which includes a complete model atom, $\sim 10^6$ frequency points, a proper handling of the complex, nonmonotonic velocity field, and treatment of continuum and line processes as well as electron scattering. For each model, we adopt an explosion energy of 1.2×10^{51} erg, a 15 M$_\odot$ progenitor with a radius in the range $R_\star \approx 500$–700 R$_\odot$, and a CSM composition set to the surface mixture of an RSG progenitor (Davies & Dessart 2019).

For the simulations presented in this work, the CSM extent is much greater than $R_\star$ ($\sim$ 500–1200 R$_\odot$ for an RSG mass range of $\sim$ 10–20 M$_\odot$), and therefore we have found that the progenitor properties have little impact during phases of ejecta-CSM interaction. The progenitor radius plays a more significant role on the light-curve evolution during the plateau phase (e.g., see Dessart et al. 2013; Hiramatsu et al. 2021; Jacobson-Galán et al.

2022a), once the interaction phase is over and the emission from the deeper ejecta layers dominate the SN luminosity. However, in scenarios with weak CSM interaction, the explosion energy will greatly influence the total luminosity, which could be contributing to the brighter pseudo-bolometric and UV luminosities in comparison-sample events (e.g., Figs. 8.1 and 8.6). Specific methods for each simulation are given by Dessart et al. (2016, 2017), Jacobson-Galán et al. (2022a), Dessart & Jacobson-Galán (2023), and Jacobson-Galán et al. (2023); all CSM properties of each model are presented in Table A4. CSM densities for all models are shown in Figure 8.14, which primarily differ at radii above the stellar surface, $r > 4 \times 10^{13}$ cm.

In order to identify a best-matched $\dot{M}$ and ρ_{14} for all sample objects, we employ three independent methods of matching observables to the model grid. (1) We use the rise times, peak absolute magnitudes, and $t_{\rm IIn}$ to construct a 3-dimensional root-mean-square (RMS) between each model for all eight UV/optical filters and the pseudo-bolometric light curve. We then select the best-matched model for a given filter (as well as pseudo-bolometric) based on the lowest resulting RMS, $[((M_{\rm data} - M_{\rm model})/M_{\rm model})^2 + ((t_{\rm r,data} - t_{\rm r,model})/t_{\rm r,model})^2 + ((t_{\rm IIn,data} - t_{\rm IIn,model})/t_{\rm IIn,model})^2]^{0.5}$. This method results in $N + 1$ mass-loss inferences: N filters plus the pseudo-bolometric light curve. The range of mass-loss rates and CSM densities for all filters are presented in Jacobson-Galán et al. (2024) and plotted in the left panels of Figure 8.15. For this method, we do not incorporate the relative uncertainties in peak luminosities and rise times, but instead report the range of best-matched model parameters as the uncertainty in the derived $\dot{M}$ and ρ_{14}. However, as discussed in §8.4.1, the peak absolute magnitude and rise times, especially in UV filters, are unconstrained in some sample objects, which will influence the best-matched model parameters. For such objects, we use upper limit or the ill-constrained peak and rise-time values reported in Jacobson-Galán et al. (2024) in the above RMS relation, but note that the output model parameters may only represent limits on the true CSM properties in these SNe. (2) We minimize the residuals between only $t_{\rm IIn}$ estimates for each object in order to find the best-matched model in the grid, which is plotted in the middle panels of Figure 8.15 with error bars on mass-loss/density estimates coming from uncertainties in the given $t_{\rm IIn}$ values. (3) We perform direct spectral matching of `CMFGEN` synthetic spectra to gold-, silver-, and comparison-sample objects in order to estimate the most consistent mass-loss rates and CSM densities. To do this, we degrade the synthetic spectrum to the resolution of the SN spectrum and scale the average flux of each model spectrum to the observations over the wavelength range of the optical spectrum, and calculate the residuals in flux density between model and data in the wavelength ranges that cover emission lines of the H I Balmer series, He II $\lambda\lambda$4686, 5412, N III λ4641, N IV λ7112, and C IV λ5801. For each sample object, we estimate a best-matched mass-loss rate and CSM density (right panels of Figures 8.15) by selecting the model with the smallest average residual (i.e., $\overline{\Delta}_{\rm IIn}$) between model and SN spectra in all IIn-like feature wavelength ranges. However, we note that the best-matched model spectrum may not reproduce the intrinsic continuum flux of the SN data despite overall consistency with the observed IIn-like features. Similarly, the best-matched model using method 1 may not match the SN light-curve shape on the rise despite consistency with peak brightness and rise time. We discuss inconsistencies between model-matching methods below as well as future improvements to the grid in §8.6.2.

Below, we discuss the resulting mass-loss rates and CSM densities derived for each model-matching method. We find that gold/silver-sample objects with visible IIn-like features reside in a parameter space of progenitor CSM densities of $\sim 10^{-16}$–10^{-11} g cm^{-3} ($\dot{M} \approx 10^{-6}$–10^{-1} M$_\odot$ yr^{-1}, $v_w = 50$ km s^{-1}) when comparing rise times, peak absolute magnitudes, and $t_{\rm IIn}$ to the model grid (i.e., Methods 1 and 2). However, this parameter space becomes more constrained to $\sim 5 \times 10^{-14}$–10^{-11} g cm^{-3} ($\dot{M} \approx 10^{-3}$–10^{-1} M$_\odot$ yr^{-1}, $v_w = 50$ km s^{-1}) when using a direct spectral matching method (i.e., Method 3). With regards to subdivisions of the gold and silver samples, the Class 1 objects show the highest mass-loss rates of $\dot{M} \approx 5 \times 10^{-3}$–$10^{-1}$ M$_\odot$ yr^{-1}, Class 2 objects showing low to intermediate mass-loss rates of $\dot{M} \approx 10^{-6}$–10^{-2} M$_\odot$ yr^{-1}, and Class 3 objects displaying generally lower mass-loss rates of $\dot{M} \approx 10^{-6}$–10^{-3} M$_\odot$ yr^{-1}. Furthermore, comparison-sample objects that have no detected IIn-like features at $\delta t < 2$ days are consistent with overall low mass-loss rates of $\dot{M} \approx 10^{-6}$–10^{-3} M$_\odot$ yr^{-1}. Across all three model-matching methods, the average $\dot{M}$ derived is consistent to within an order of magnitude (e.g., see Fig. 8.24). However, there are instances where mass-loss rates derived from some peak magnitudes or rise times in Method 1 are inconsistent with what would be inferred from Methods 2 and 3 involving $t_{\rm IIn}$ and direct spectral matching. For example, many of the Class 3 objects have $\dot{M}$ ranges of $\sim 10^{-6}$–$10^{-2.3}$ M$_\odot$ yr^{-1} based on Method 1, but have more constrained estimates of $\sim 10^{-3}$–$10^{-2.3}$ M$_\odot$ yr^{-1} based on Methods 2 and 3 that are inconsistent with the lower $\dot{M}$ values. This is caused by similar peak absolute magnitudes and/or rise times across models in optical filters as well as the low resolution of the model grid in general. With future grids, the incorporation of additional explosion parameters such as a variable kinetic energy will provide more self-consistent results between model-matching methods.

As shown in Figure 8.15, there is a clear trend between the $t_{\rm IIn}$ parameter and derived mass-loss rates or CSM densities for both gold/silver- and comparison-sample objects. We then fit a linear function to the mass-loss rates and $t_{\rm IIn}$ from the model grid and overplot the function as black dashed lines in Figure 8.15. This relation between the duration of the electron-scattering line profiles and the inferred mass-loss rate, in units of M$_\odot$ yr^{-1}, goes as $t_{\rm IIn} \approx 3.8[\dot{M}/(0.01$ M$_\odot$ yr$^{-1})]$ days. We note that this correlation is valid for the chosen explosion and progenitor parameters.

Additionally, we calculate the velocities of the fastest moving H-rich ejecta that we can detect at $\delta t = 50$ days by examination of the bluest (reddest) edge of the absorption (emission) profiles in Hα. However, we note that there is likely faster, optically thin H-rich material that we cannot detect in these spectra and, therefore, these estimates provide a lower limit on velocity of the fastest ejecta. We then compare to model predictions from Dessart & Jacobson-Galán (2023) for the deceleration of ejecta as a function of total mass in the CDS, which is also connected to the mass-loss rate. From comparison to the models, the slow moving ejecta of some Class 1/2 objects would indicate enhanced mass-loss rates of $\dot{M} = 10^{-3}$–10^{0} M$_\odot$ yr^{-1}, while the velocities observed in other Class 1/2 and all Class 3 objects suggest low mass-loss rates of $\dot{M} < 10^{-5}$ M$_\odot$ yr^{-1}; these values are presented Figure 8.16. However, many of the Class 1, as well as all of the Class 2 & 3, mass-loss rates inferred for gold/silver-sample objects from direct spectral matching are larger than those that are

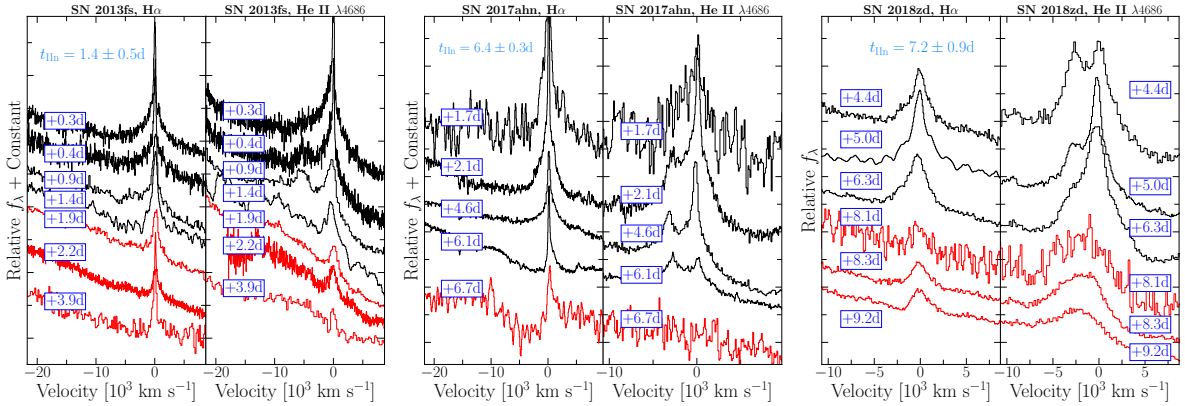

Figure 8.9 *Left:* SN 2013fs spectral series of Hα *(left panel)* and He II λ4686 *(right panel)* velocities during the CSM interaction phase. Spectra in black represent phases when the CSM remains optically thick to electron scattering (e.g., Lorentzian line profiles). The transition shown from black to red lines marks the emergence of broad absorption features derived from the fastest moving SN ejecta. The transition between these two phases is the basis for calculating the $t_{\rm IIn}$ parameter. *Middle/right:* Same plot but for SNe 2017ahn and 2018zd, respectively, which show longer-lived IIn profiles.

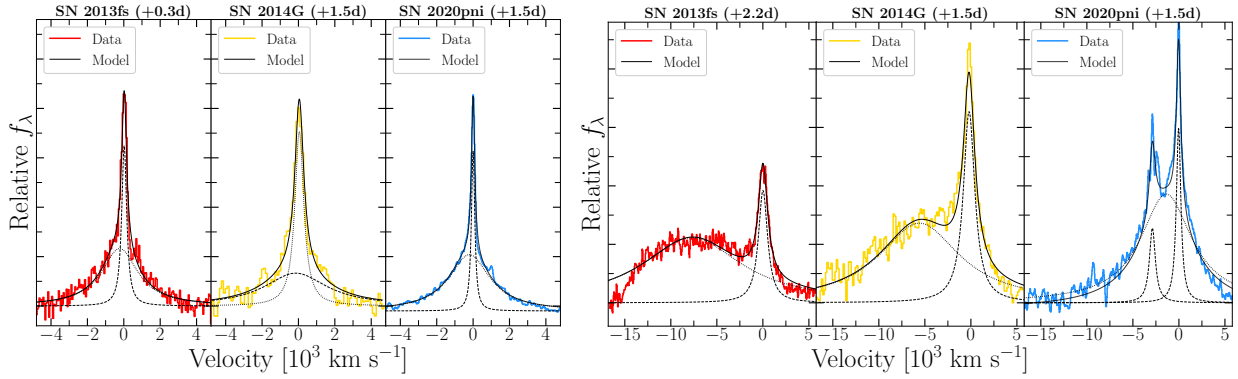

Figure 8.10 Hα (*left*) and He II λ4686 (*right*) emission lines modeled with multicomponent Lorentzian profiles during the CSM interaction phase. Class 1 objects (shown in blue) possess longer-lived (days-to-weeks) high-ionization species of He II and N III. Class 2 (shown in yellow) and Class 3 (shown in red) objects show only He II emission, with the former having stronger emission lines that last longer. Class 3 objects may represent transitional SNe between the comparison and gold/silver samples given their weak narrow He II emission superimposed on a blueshifted He II profile, the latter being seen in comparison-sample objects (e.g., Fig. 8.19).

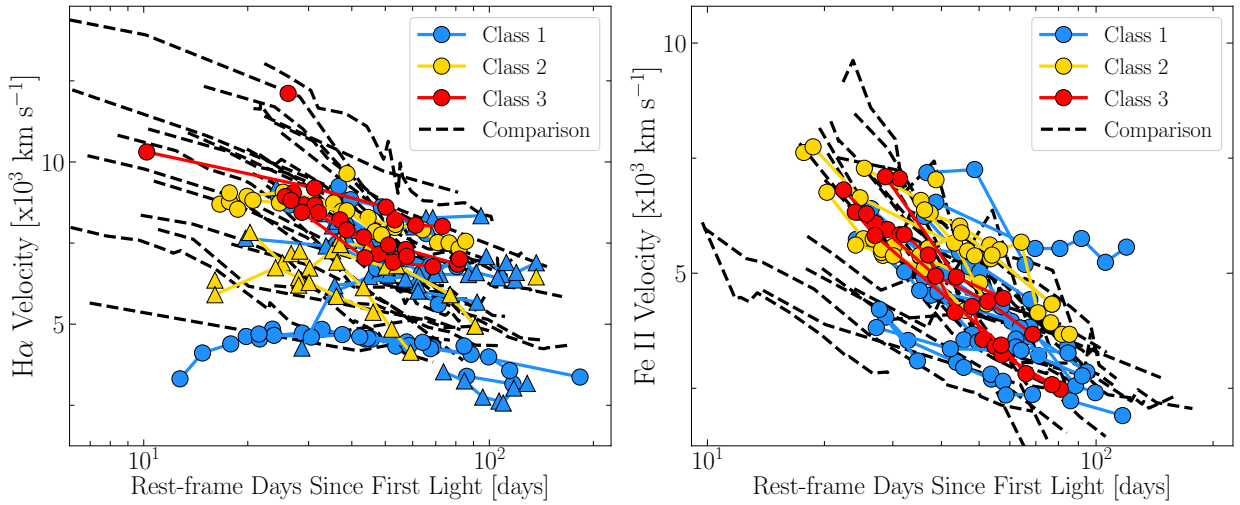

Figure 8.11 Photospheric-phase velocities for gold/silver- (blue, yellow, red lines) and comparison- (black dashed lines) sample objects calculated from absorption minimum (circles) or emission FWHM (triangles) of Hα (*left*) and Fe II λ5169 (*right*) line profiles. While some gold-sample objects with more persistent CSM interaction show slower ejecta velocities than the comparison sample, overall both samples possess a consistent evolution in their photospheric velocities.

estimated from the fastest moving ejecta. This potentially suggests a degree of CSM asymmetry that would keep some fraction of the ejecta from being decelerated by dense CSM at early times, as is predicted by `CMFGEN` models for spherically symmetric CSM.

8.5.2 Additional Model Grids

In order to better explore the parameter space of ejecta-CSM interaction in SNe II, we perform the same spectral matching analysis as above but with the public[11] grid of `CMFGEN` models presented by Boian & Groh (2020). This model grid consists of 137 synthetic spectra with varying CSM compositions (e.g., solar metallicity, CNO-enriched, He-rich), mass-loss rates ($\dot{M}$ = 10^{-3}–10^{-2} M$_\odot$ yr^{-1}), inner radii of the interaction region ($R_{\rm in}$ = 8×10^{13}–3.2×10^{14} cm), and SN luminosity ($L_{\rm SN}$ = 1.9×10^{8}–2.5×10^{10} L$_\odot$). These models impose an optically thick wind in radiative equilibrium, assume steady state, and have an input luminosity, CSM radius, and mass-loss rate at a given time step. Furthermore, these models contain no radiation hydrodynamics and all of the CSM remains unshocked/unaccelerated at all phases. Similar to our presented model grid, we scale each model spectrum to the observations over the wavelength range of the optical spectrum and calculate the minimum average residual in wavelength regions of IIn-like features (i.e., $\overline{\Delta}_{\rm IIn}$). An example of this matching process is shown for SN 2020abjq in Figure 8.17, and all best-matched model

[11] https://www.wiserep.org/object/14764

parameters for gold and silver samples are listed in Jacobson-Galán et al. (2024) and plotted in Figure 8.17.

We find rough agreement between the mass-loss rates derived from the Boian & Groh (2020) grid and our own: 20/39 objects having mass-loss rates that are consistent to within 50%. However, the Boian & Groh (2020) grid does not explore a sufficiently large range of CSM properties (e.g., $\dot{M} > 10^{-2}$ $M_\odot$ yr^{-1}, $\dot{M} < 10^{-3}$ $M_\odot$ yr^{-1}, $R_{CSM} > 3\times10^{14}$ cm), so these mass-loss estimates may be more biased by the model grid. Furthermore, the Boian & Groh (2020) model spectra only cover the phases of $\delta t = 1.0$–3.7 days (assuming a shock velocity of 10^4 km s^{-1}) and also do not create synthetic multiband and bolometric light curves to compare with the sample photometry. Nonetheless, the advantage of this model grid is the variety of CSM compositions explored.

In addition to the Boian & Groh (2020) spectral models, we also apply a grid of synthetic light curves for shock breakout from dense CSM presented by Haynie & Piro (2021). The model grid contains 168 multiband light curves created with the LTE, Lagrangian radiative-transfer code `SNEC` (Morozova et al. 2015) for varying mass-loading parameter $D_\star = \dot{M}/(4\pi v_w) = 8 \times 10^{16}$–$10^{18}$ g cm^{-1}, explosion energy ($E_k = (0.3$–$3.0) \times 10^{51}$ erg), and CSM radius ($R_{CSM} = 1500$–2700 $R_\odot$). For all objects in the gold/silver and comparison samples, we find the most consistent model by minimizing the residuals between the synthetic light curves and the observed UV/optical/NIR photometry at $\delta t < 20$ days. First light in these models is assumed to be when the synthetic absolute magnitude rises above -12 mag. Furthermore, we note that the uncertainty in the time of first light associated with each sample object could lead to uncertainties in the model parameters derived from the best-matched model light curves. However, these uncertainties are not large enough to impact the overall model trend observed in Figure 8.18. An example of a best-match light-curve model to Class 2 gold-sample object SN 2022jox is shown in the left panel of Figure 8.18; all derived model parameters are listed in Jacobson-Galán et al. (2024).

As shown in Figure 8.18, the CSM properties inferred from the best-matched `SNEC` light curves are inconsistent with those derived from both `CMFGEN` model grids. For example, the best-matched light-curve model from Haynie & Piro (2021) implies $D_\star[R_{CSM}] = 10^{18}$ g cm^{-1}[1900 $R_\odot$] for SN 2013fs, similar to what was found in Morozova et al. (2017), which is several orders of magnitude higher than the most consistent `CMFGEN` model for this SN (e.g., $D_\star \approx 10^{15}$ g cm^{-1}). Similarly, the distribution of $D_\star$ values derived for the comparison sample is consistent with the distribution of $D_\star$ values found by Morozova et al. (2018) (e.g., $\sim 10^{17-18}$ g cm^{-1}) when modeling the light curves of normal SNe II with `SNEC`. However, the large densities derived from `SNEC` models ($\rho_{14} \approx 10^{-10}$ g cm^{-3}) would imply mean free paths of $l_{mfp} \approx 3 \times 10^{10}$ cm for close-in CSM, $\sim 2R_\star$. Such mean free paths are much smaller than the size of extended CSM ($\sim 10^{14}$–10^{15} cm); therefore, electron-scattered photons created from photoionized gas would never escape the CSM to create the IIn-like features observed in the optical spectra while the shock wave is inside of this part of the CSM. Furthermore, at these densities the ionization parameter will be > 10 (i.e., $\xi = L_{sh}/nr^2$), indicating that the gas will be completely ionized (Lundqvist & Fransson 1996; Chevalier & Irwin 2012). As shown by Dessart & Jacobson-Galán (2023), SBO into CSM densities this

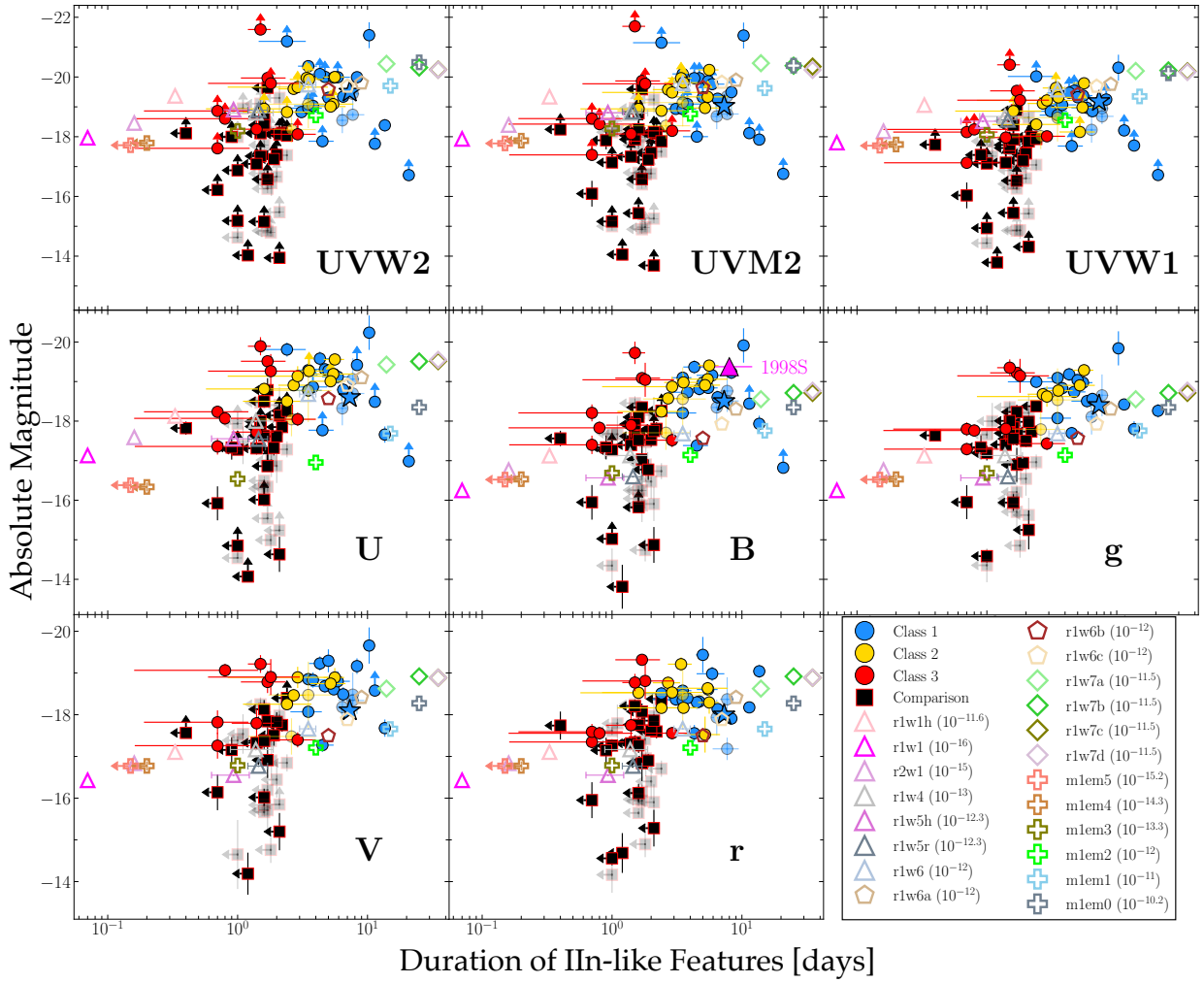

Figure 8.12 *Left to right, top to bottom:* Peak absolute magnitude in the *w2*, *m2*, *w1*, *u*, *B/b*, *V/v*, *g*, and *r* bands versus duration of IIn-like features. Gold and silver samples shown as blue/yellow/red circles and comparison sample shown as black squares. Solid colored points represent the subsample of objects at $D > 40$ Mpc. Parameters from the `CMFGEN` model grid (§8.5.1) are plotted as colored stars, polygons, diamonds, and plus signs. SNe 1998S and 2023ixf are shown for reference as a solid magenta triangle and solid blue star, respectively.

large will trap the photons stored in the wake of the radiation-dominated shock until the shock has exited the edge of the densest material; the shock front will propagate adiabatically and will not extract kinetic energy that can be used to boost the overall luminosity, as is the case for lower density CSM. Consequently, SBO from such high-density material may provide additional luminosity to early-time light curves, but lower density ($\rho \approx 10^{-12}$–10^{-14} g cm^{-3}) material at larger distances ($r \approx 10^{14-15}$ cm) is needed to create IIn-like features observed in gold/silver-sample objects.

8.6 Discussion

8.6.1 A Continuum of RSG Mass-Loss Rates

In §8.5.1, we presented three independent model-matching methods used to derive mass-loss rates and CSM densities for 39 SNe II (gold/silver samples) with IIn-like features as well as for 35 SNe II without such spectral signatures. In the total sample, we find significant diversity amongst the mass-loss rates and CSM densities in SNe II, which is intrinsically tied to the distributions of observables between gold/silver and comparison samples such as peak brightness and rise times in their pseudo-bolometric/UV/optical light curves as well as the duration of the IIn-like features. Assuming that all gold-, silver-, and comparison-sample objects arise from the explosion of RSGs, this suggests a continuum of mass-loss histories in the final years-to-months before explosion: Class 1/2 objects (e.g., SNe 20tlf-like, 20pni-like, 98S-like, 14G-like) being associated with RSGs having enhanced mass-loss rates of $\dot{M} \approx 10^{-3}$–10^{-1} M$_\odot$ yr^{-1}and potentially extended dense CSM ($r \approx 10^{15}$–10^{16} cm), while Class 3 objects (e.g., SN 2013fs-like) may be the result of RSG explosions with lower density ($\dot{M} \approx 10^{-3}$–10^{-4} M$_\odot$ yr^{-1}), possibly compact ($r < 5 \times 10^{14}$ cm) CSM. Given the lack of IIn-like features at very early-time phases in comparison-sample objects, these SNe need to arise from RSGs with similar or lower mass-loss rates than Class 3 objects ($\dot{M} < 10^{-4}$ M$_\odot$ yr^{-1}), which may make them more consistent with the weak, steady-state mass-loss rates of Galactic RSGs (e.g., $\dot{M} < 10^{-6}$ M$_\odot$ yr^{-1}; Beasor et al. 2020) or highly confined CSM (i.e., $< 10^{14}$ cm) at the time of explosion. Nonetheless, the presence of high-density material directly above the RSG surface may be a universal property of SN II progenitors in order to explain fast-rising light curves (e.g., Morozova et al. 2017).

8.6.2 Future Improvements to `HERACLES/CMFGEN` Grids

While the differences in $t_{\rm IIn}$, as well as possibly UV $M_{\rm peak}$, are physically linked to differences in CSM density between the gold/silver and comparison samples, the extraction of $\dot{M}$ and ρ_{14} estimates from comparison to the `HERACLES/CMFGEN` model grid comes with some assumptions about the physics of the explosion and CSM structure/origin. For the former, this present grid only explores one progenitor mass/radius and explosion energy, which could have an effect on observables such as $t_{\rm rise}$ and $M_{\rm peak}$; future `HERACLES/CMFGEN` grids will explore this parameter space in more detail. For the latter, some models in the

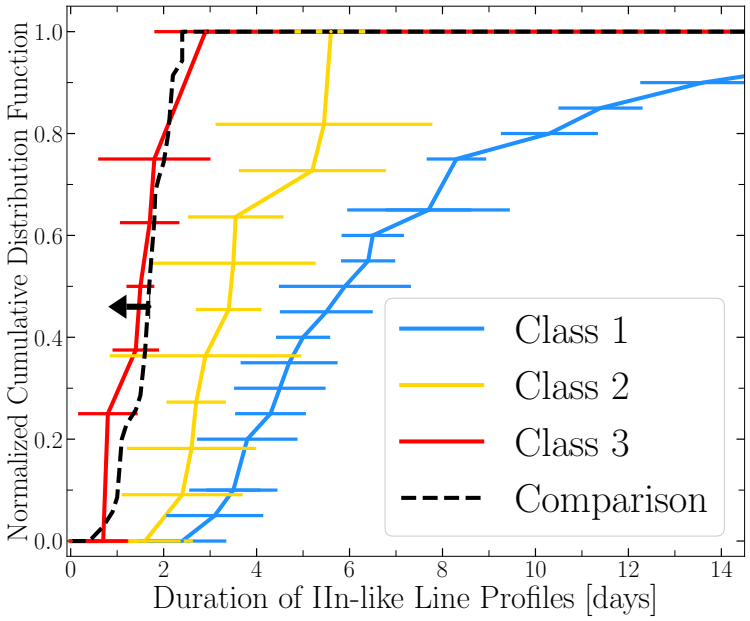

Figure 8.13 Cumulative distribution of $t_{\rm IIn}$ values in Class 1 (blue), 2 (yellow), and 3 (red) gold- and silver-sample objects, as well as upper limits from the comparison sample. Overall, Class 1 objects have longer durations of observed IIn-like features, indicating higher density, and possibly more extended, CSM.

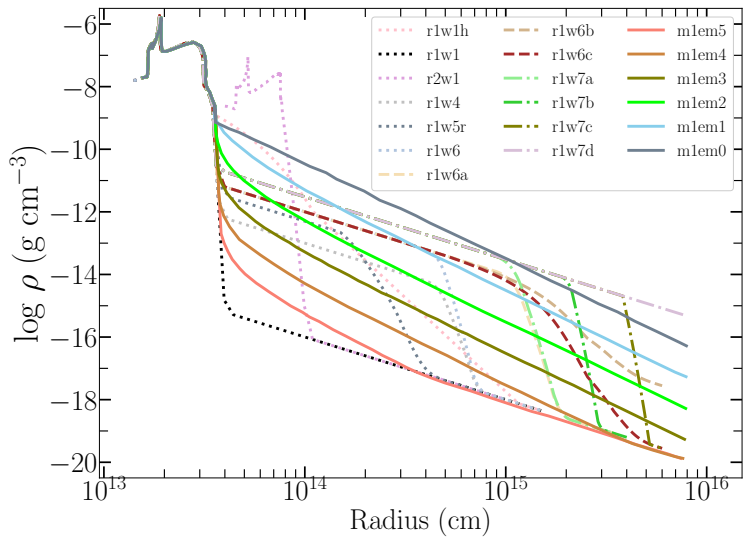

Figure 8.14 CSM densities and radii for complete `CMFGEN` model grid (e.g., Table A4) used to find the best-matched model for gold-, silver-, and comparison-sample objects. A description of the model setup is provided in §8.5.1.

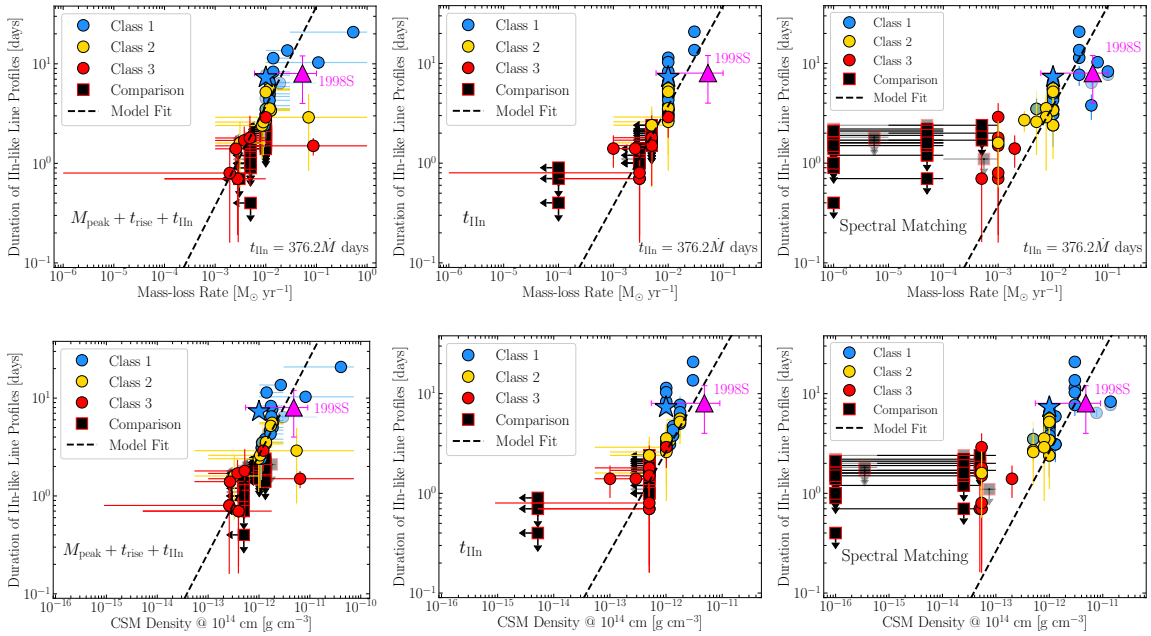

Figure 8.15 Duration of IIn-like features versus best-matched mass-loss rates *(top panel)* and CSM densities at $r = 10^{14}$ cm *(bottom panel)* for all gold/silver- (blue, yellow and red circles) and comparison- (black squares) sample objects. Solid colored points represent the subsample of objects at $D > 40$ Mpc. SNe 1998S and 2023ixf are shown for reference as a magenta triangle and blue star, respectively. Mass-loss rates were estimated for each object based on comparison of (*left*) multiband photometry and $t_{\rm IIn}$, (*middle*) only $t_{\rm IIn}$, and (*right*) early-time spectra, to the `CMFGEN` model grid. Specifics of feature matching and selection of the best model are presented in §8.5.1. A linear relation between $t_{\rm IIn}$ and $\dot{M}$ (black dashed line) is derived from fitting model parameters used in the `CMFGEN` grid (i.e., the correlations shown are built into our model grid).

present grid assume a homogeneous, spherically symmetric CSM with a wind-like density profile, all of which could be potential sources of uncertainty in extracting true mass-loss rates from the present sample. However, some models (e.g., from Dessart et al. 2023) have varying CSM scale heights as well as different degrees of CSM acceleration. Additionally, the present model grid uses a CSM composition typical of 15 $M_\odot$ RSGs (Davies & Dessart 2019, which could be varied in future models.

We are also aware of CSM asymmetries from polarization measurements of SNe II during the photoionization phase (e.g., SN 1998S, Leonard et al. 2000; SN 2023ixf, Vasylyev et al. 2023), which suggest that there the CSM is denser along certain lines of sight. Such a physical picture could account for discrepancies between the mass-loss rates inferred from the fastest detectable Hα velocities (e.g., Fig. 8.11) and those estimated from the model grid for Class 1/2 objects in the gold/silver samples. In this case, high mass-loss rates (e.g., $\sim 10^{-2}$ $M_\odot$ yr^{-1}) could still be inferred from electron scattering of recombination photons in dense parts of CSM, while lower density material along different lines of sight would still allow typical ejecta velocities of $\sim 10^4$ km s^{-1}, with little to no deceleration by dense CSM. This physical picture may also be able to explain the discrepancies in the derived mass-loss rates between UV/optical vs. X-ray/radio observations of SN 2023ixf (Berger et al. 2023; Chandra et al. 2024b; Grefenstette et al. 2023; Jacobson-Galán et al. 2023; Matthews et al. 2023; Nayana et al. 2024, in prep.). Furthermore, a deviation from a steady-state CSM density profile ($\rho \propto r^{-2}$) in these models may be necessary to adequately match the early-time light-curve slope (e.g., SN 2023ixf; Jacobson-Galán et al. 2023; Hiramatsu et al. 2023). For example, SBO from close-in ($r < 10^{14}$ cm) high-density CSM as in the `SNEC` model grid (e.g., §8.5.2) followed by interaction with lower density material would yield both the fast-rising, luminous light curves and the observation of IIn-like features in some SNe II.

8.6.3 Implications of Photometry-Only Modeling

As shown in Figure 8.18, the extraction of SN II mass-loss-rate information can yield discrepant results if photometric information is used independently from early-time spectroscopic observations. Here, CSM densities inferred from light-curve matching using a grid of `SNEC` models (Haynie & Piro 2021) are too high to allow for the escape of recombination-line photons in the CSM and the formation of IIn-like features. Consequently, without early-time spectroscopy, calculated mass-loss rates and densities close-in to the RSG progenitor (e.g., $< 10^{15}$ cm) may be inconsistent with the presence of narrow emission lines in CSM-interacting SNe II. Similarly, some studies invoke large CSM masses of ~ 0.1–0.5 $M_\odot$, confined to $< 10^{14}$ cm, in order to match model light curves to early-time SNe II observations (Morozova et al. 2017; Tinyanont et al. 2022; Subrayan et al. 2023). However, as shown by Dessart & Jacobson-Galán (2023), reproducing the enhanced peak UV/optical luminosity in some early-time SN II light curves can also be accomplished with ∼10% of these CSM masses. Nevertheless, the early-time light curves of some SNe II may be influenced by high-density, extended mass, but such explosions can only display IIn-like features during these phases if there are also regions of lower density material via CSM asymmetry or inhomogeneity.

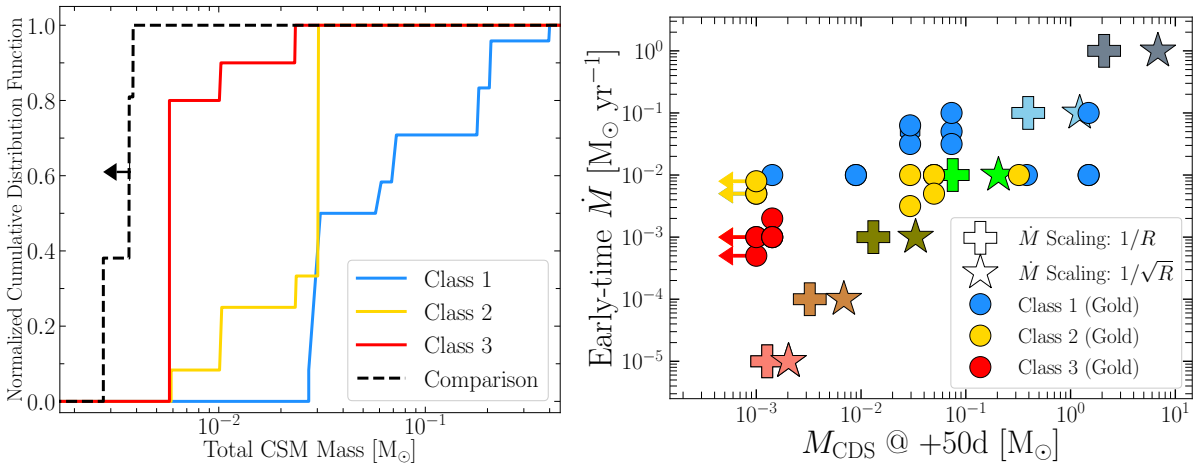

Figure 8.16 *Left:* Histogram of total CSM mass derived from direct spectral matching of the `CMFGEN` grid to Class 1 (blue), 2 (yellow), and 3 (red) gold/silver samples, as well as comparison-sample (black) objects, after a distance cut ($D > 40$ Mpc) is applied. *Right:* CDS mass (abscissa) derived from the maximum velocity of gold- and silver-sample objects as measured from the bluest edge of the Hα absorption profile at $\delta t \approx 50$ days post-first light using the model trend found by Dessart & Jacobson-Galán (2023) for `CMFGEN` models of varying mass loss; models shown as plus sign and stars. CDS mass is compared to mass-loss rate (ordinate) derived from comparison of early-time observations to `CMFGEN` model grid.

It is likely that there is a combination of effects present: (1) SBO from extended envelope and/or high-density CSM located at $< 2R_\star$ (e.g., Haynie & Piro 2021), and (2) interaction with lower density CSM that results in the formation of IIn-like features and increased luminosity. A similar picture is proposed in Irani et al. (2023) from the light curve modeling of SNe II with and without IIn-like features, the former requiring larger breakout radii and the latter. Furthermore, it is worth noting that large amounts of spherically symmetric CSM will cause significant deceleration to the fastest moving SN ejecta; this is an observable that could confirm the existence of such CSM properties (Hillier & Dessart 2019). Overall, the combination of photometric and spectroscopic modeling is essential in order to probe both high- and low-density components of CSM in SNe II.

8.7 Conclusions

In this paper we have presented UV/optical/NIR observations and modeling of the largest sample to date of SNe II with spectroscopic evidence for CSM interaction. Below we summarize the primary observational findings from our sample analysis.

- Our sample consists of 39 SNe II whose early-time ("flash") spectroscopy shows transient, narrow emission lines with electron-scattering wings (i.e., IIn-like) from the photoionization of dense, confined CSM. The total gold/silver sample contains 39 SNe II, 27 of which are unpublished, and includes 501 total spectra (293 previously unpublished) and 39 UV/optical/NIR light curves (27 previously unpublished). The IIn-like features persist on a characteristic timescale ($t_{\rm IIn}$), which signals a transition in CSM density and the emergence of Doppler-broadened features from the fast-moving SN ejecta.

- Within the total 74 objects, the "gold" sample contains 20 SNe with both early-time IIn-like features, complete UV coverage with *Swift*-UVOT and spectral observations at $\delta t < 2$ days. The "silver" sample contains 19 SNe that have detectable IIn-like features, complete UV coverage with *Swift*-UVOT, and spectral observations only at $\delta t > 2$ days. We divide the gold/silver samples into three classes based on their early-time ($t < 3$ days) spectra: Class 1 shows high-ionization lines of He II, N III, and C IV (e.g., SNe 1998S, 2020pni, 2020tlf, 2023ixf, etc), Class 2 shows high-ionization lines He II and C IV but not N III (e.g., SNe 2014G, 2022jox), and Class 3 shows only weak He II (e.g., SN 2013fs). Additionally, we include a "comparison" sample of 35 SNe II that have optical spectra at $t < 2$ days with no IIn-like features as well as a complete UV/optical light curve. Furthermore, Class 1 objects show the longest IIn-like feature timescales (i.e., $t_{\rm IIn} \approx$ 2–14 days), while Class 2 and 3 objects displayed shorter-lived emission lines of $t_{\rm IIn} < 4$ days and $t_{\rm IIn} < 2$ days, respectively. We interpret this diversity as arising from variations in CSM extent and density: Class 1 objects arise from RSGs with more extended, higher density CSM than Class 2/3 or the comparison samples.

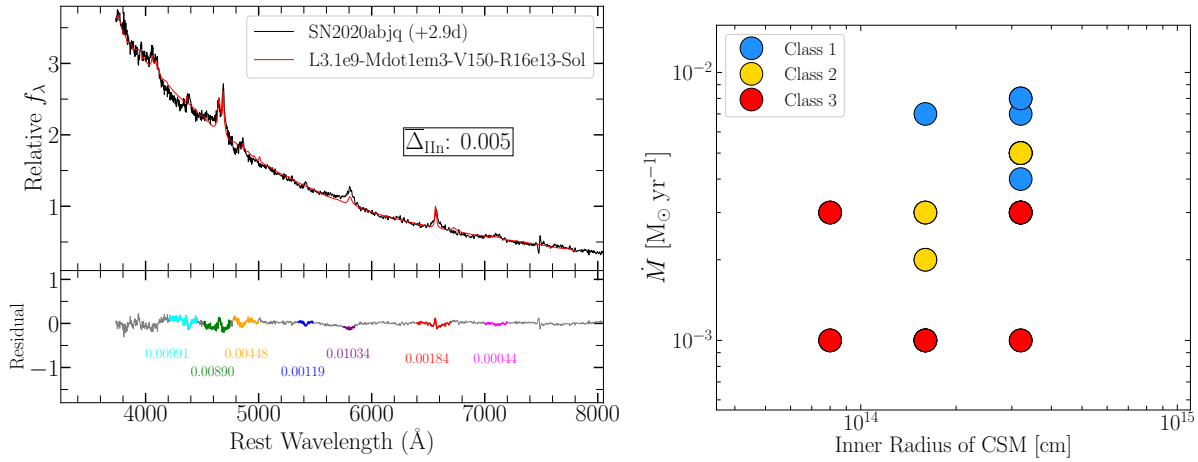

Figure 8.17 *Left:* Early-time optical spectra of Class 1 gold-sample object SN 2020abjq is shown with respect to the best-matched `CMFGEN` model from the Boian & Groh (2020) model grid. Specifics of model matching for the complete sample are presented in §8.5.2. Numbers in the bottom panel are the residuals between data and model spectra in the wavelength ranges of IIn-like features ($\Delta_{\rm IIn}$). *Right:* Best-matching mass-loss rate and inner CSM radius calculated from direct comparison of gold- and silver-sample object spectra to the Boian & Groh (2020) `CMFGEN` model grid. Some key differences between this grid and that presented in this paper are the lack of spectral time series, multiband photometry, or wider coverage of CSM densities and radii in the former that are present in the latter grid.

- We find a significant contrast between the peak optical and pseudo-bolometric luminosities in the gold versus comparison samples. We also identify clear correlations between peak UV/optical luminosity and both rise time and $t_{\rm IIn}$. Furthermore, as discussed in §8.4.1, logrank tests on these observables reveal that the peak pseudo-bolometric and optical luminosities of both samples are likely derived from separate distributions. The difference between sub-samples remains statistically significant after a distance cut ($D > 40$ Mpc) is applied.

- We apply a grid of ejecta/CSM interaction models, generated with the `CMFGEN` and `HERACLES` codes, to extract best-matching mass-loss rates and CSM densities for the gold, silver, and comparison samples. Based on three independent model-matching procedures, we find a continuum of RSG mass-loss rates that extends from $\sim 10^{-6}$ to 10^{-1} M$_\odot$ yr^{-1}. From this model set, we derive an approximate relation between the duration of the electron-scattering broadened line profiles and inferred mass-loss rate: $t_{\rm IIn} \approx 3.8[\dot{M}/(0.01\ {\rm M}_\odot\ {\rm yr}^{-1})]$ days.

Beyond the early-time data presented in this work, future studies (e.g., "Final Moments III-") will explore the progenitor and explosion properties of this sample through modeling of their late-time photometric and spectroscopic evolution, as well as multi-wavelength

(e.g., X-ray/radio) observations. Now that a sample of SNe II with IIn-like features has been compiled and examined in detail, it is essential to create new, high-resolution grids of `HERACLES`/`CMFGEN` simulations that can be used together to constrain the CSM properties of such events. Future model grids will provide a more accurate coverage of the CSM interaction parameter space and uncover deficiencies in our model approach (e.g., asymmetries, multidimensional effects, etc.). Furthermore, it is important to build spectroscopically complete, volume-limited surveys that will include systematically discover and classify SNe II within days of first light, therefore reducing biases in follow-up observations and subsequent modeling of certain events. Such discovery efforts will enable volumetric rate measurements of enhanced mass loss in the final years of RSG evolution.

8.8 Acknowledgements

Research at UC Berkeley is conducted on the territory of Huichin, the ancestral and unceded land of the Chochenyo speaking Ohlone people, the successors of the sovereign Verona Band of Alameda County. Keck I/II, ATLAS, and PS1 observations were conducted on the stolen land of the kānaka ʻōiwi people. We stand in solidarity with the Pu'uhonua o Pu'uhuluhulu Maunakea in their effort to preserve these sacred spaces for native Hawaiʻians. MMT observations were conducted on the stolen land of the Tohono O'odham and Hia-Ced O'odham nations; the Ak-Chin Indian Community, and Hohokam people. ZTF observations were conducted on the stolen land of the Pauma and Cupeño tribes; the Kumeyaay Nation and the Payómkawichum (Luiseño) people. Shane 3 m observations were conducted on the stolen land of the Ohlone (Costanoans), Tamyen and Muwekma Ohlone tribes.

We thank Nathan Smith, David Sand and Avishay Gal-Yam for valuable discussions, and Viktoriya Morozova for providing the initial `SNEC` models. IRAF is distributed by NOAO, which is operated by AURA, Inc., under cooperative agreement with the NSF.

The Young Supernova Experiment and its research infrastructure is supported by the European Research Council under the European Union's Horizon 2020 research and innovation programme (ERC Grant Agreement No. 101002652, PI K. Mandel), the Heising-Simons Foundation (2018-0913, PI R. Foley; 2018-0911, PI R. Margutti), NASA (NNG17PX03C, PI R. Foley), NSF (AST-1720756, AST-1815935, PI R. Foley), the David & Lucille Packard Foundation (PI R. Foley), VILLUM FONDEN (project number 16599, PI J. Hjorth), and the Center for AstroPhysical Surveys (CAPS) at NCSA and the University of Illinois Urbana-Champaign.

W.J.-G. is supported by the National Science Foundation (NSF) Graduate Research Fellowship Program under grant DGE-1842165. W.J.-G. acknowledges NASA grants in support of *Hubble Space Telescope* programs GO-16075 and GO-16500. This research was supported in part by the NSF under grant PHY-1748958. The Margutti team at UC Berkeley is partially funded by the Heising-Simons Foundation under grants #2018-0911 and #2021-3248 (PI R. Margutti). R.C. acknowledges support from NASA *Swift* grant 80NSSC22K0946.

C.D.K. is partly supported by a CIERA postdoctoral fellowship. A. Haynie is supported

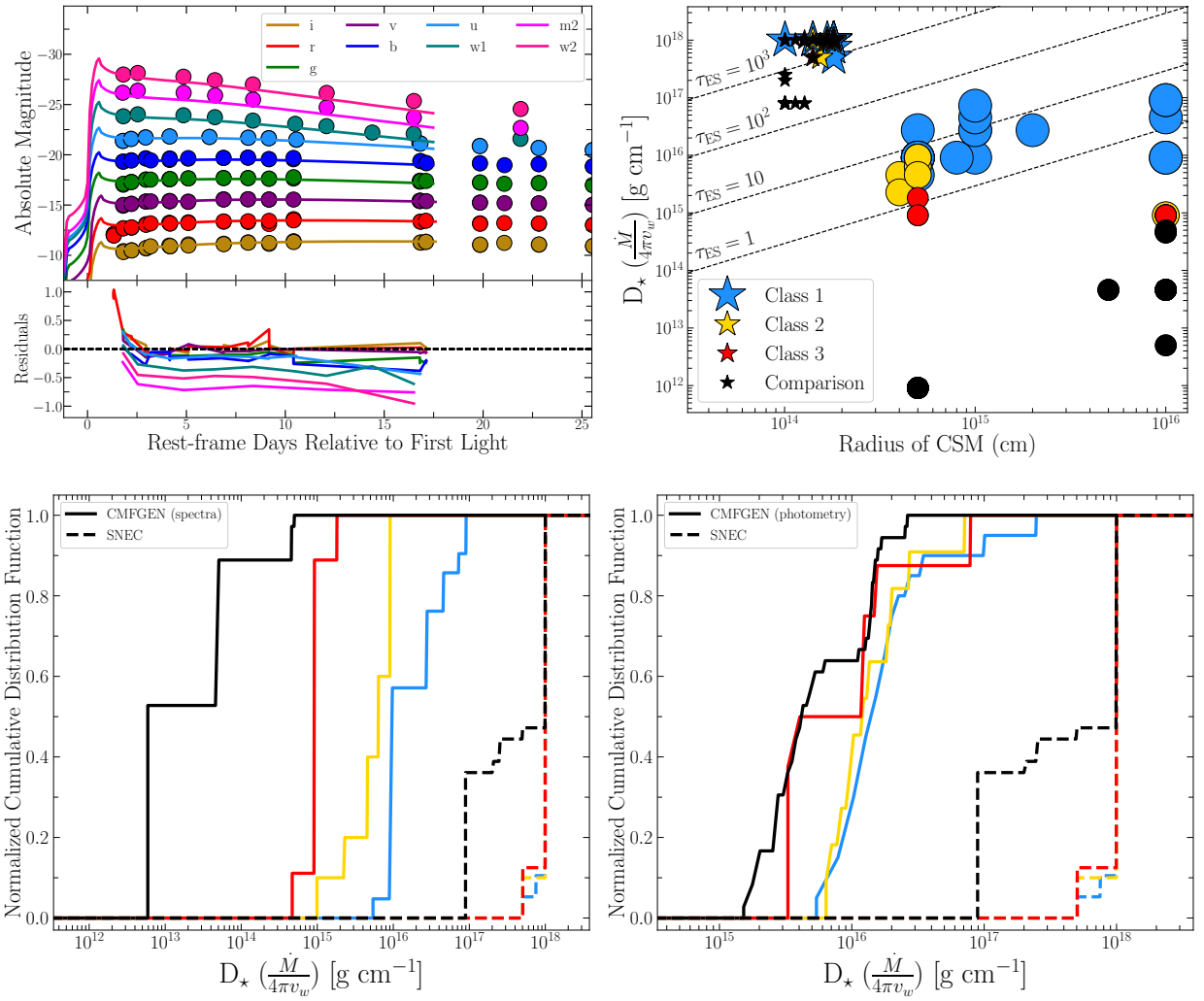

Figure 8.18 *Top left:* Multiband photometry of Class 2 gold-sample object SN 2022jox compared to the most consistent CSM interaction model from the grid presented by Haynie & Piro (2021). Despite the overall match to the photometry, the high CSM densities (e.g., $\rho_{14} \approx 10^{-10}$ g cm^{-3}) required by this model would not allow for the formation of the IIn-like features observed in SN 2022jox. Specifics of model matching for the complete sample are presented in §8.5.2. *Top right:* Mass-loading parameter ($D_\star$) versus CSM radius from the best-matched Haynie & Piro (2021) model for all gold/silver- (blue, yellow and red stars) and comparison- (black stars) sample objects. Shown as circles are the best-matching `CMFGEN` models for the gold and comparison samples, which can reproduce both the high peak luminosities and the formation of IIn-like features in the optical spectra. Electron-scattering optical depths shown as dashed lines. *Bottom left:* Cumulative distribution of $D_\star$ values derived from `SNEC` photometric (dashed lines) and `CMFGEN` spectral (solid lines) model matching. *Bottom right:* Cumulative distribution of $D_\star$ values derived from `SNEC` (dashed lines) and `CMFGEN` (solid lines) model matching to photometry only.

by the USC-Carnegie Graduate Fellowship. D.L. was supported by a VILLUM FONDEN Investigator grant (project number 16599). C.G. is supported by a VILLUM FONDEN Young Investigator Grant (project number 25501). This work was funded by ANID, Millennium Science Initiative, ICN12_009. The work of X.W. is supported by the National Natural Science Foundation of China (NSFC grants 12288102 and 12033003) and the New Cornerstone Science Foundation through the XPLORER PRIZE. This work was granted access to the HPC resources of TGCC under the allocation 2021 – A0110410554 and 2022 – A0130410554 made by GENCI, France. This research was supported by the Munich Institute for Astro-, Particle and BioPhysics (MIAPbP) which is funded by the Deutsche Forschungsgemeinschaft (DFG, German Research Foundation) under Germany's Excellence Strategy – EXC-2094 – 390783311. K.A.B. is supported by an LSSTC Catalyst Fellowship; this publication was thus made possible through the support of Grant 62192 from the John Templeton Foundation to LSSTC. The opinions expressed in this publication are those of the authors and do not necessarily reflect the views of LSSTC or the John Templeton Foundation.

A.V.F.'s research group at UC Berkeley acknowledges financial assistance from the Christopher R. Redlich Fund, as well as donations from Gary and Cynthia Bengier, Clark and Sharon Winslow, Alan Eustace, William Draper, Timothy and Melissa Draper, Briggs and Kathleen Wood, and Sanford Robertson (W.Z. is a Bengier-Winslow-Eustace Specialist in Astronomy, T.G.B. is a Draper-Wood-Robertson Specialist in Astronomy, Y.Y. was a Bengier-Winslow-Robertson Fellow in Astronomy). Numerous other donors to his group and/or research at Lick Observatory include Michael and Evelyn Antin, Shawn Atkisson, Charles Baxter and Jinee Tao, Duncan and Catherine Beardsley, Marc and Cristina Bensadoun, Frank and Roberta Bliss, Ann and Gordon Brown, Tina and Greg Butler, Alan and Jane Chew, Curt Covey, Byron and Allison Deeter, Arthur and Cindy Folker, Peter and Robin Frazier, Ellen Fujikawa, Heidi Gerster, Harvey Glasser, John Gnuse, George and Allison Good, Charles and Gretchen Gooding, Thomas and Dana Grogan, Alan Gould and Diane Tokugawa, Timothy and Judi Hachman, Michael and Virginia Halloran, Robert and Tina Hinckley, Alan and Gladys Hoefer, Jeff and Allison Holland, Jerry and Patti Hume, the Hugh Stuart Center Charitable Trust, James and Zem Joaquin, Joel Krajweski, Walter and Karen Loewenstern, Gregory Losito and Veronica Bayduza, Art and Rita Levinson, Jesse Levinson, Herbert Masters III, Bruce and Judith Moorad, Rand Morimoto and Ana Henderson, James and Marie O'Brient, Douglas and Emily Ogden, Jim Ostendorf, Garry Parton, Edward and Ellin Purdom, Jonathan and Susan Reiter, Margaret Renn, Paul Robinson, Catherine Rondeau, Eric Rudney, Stanley and Miriam Schiffman, Thomas and Alison Schneider, Ajay Shah and Lata Krishnan, Bruce and Debby Smith, Hans Spiller Justin and Seana Stephens, Charles and Darla Stevens, David and Joanne Turner, Rolf Weber, Gerald and Virginia Weiss, Byron and Nancy Wood, Weldon Wood, Richard Wylie, David and Angie Yancey, and Thomas Zdeblick.

The TReX team at UC Berkeley is supported in part by the NSF under grants AST-2221789 and AST-2224255, and by the Heising-Simons Foundation under grant #2021-3248 (PI R. Margutti).

M.R.D. acknowledges support from the NSERC through grant RGPIN-2019-06186, the

Canada Research Chairs Program, and the Dunlap Institute at the University of Toronto. This research was supported by the Munich Institute for Astro-, Particle and BioPhysics (MIAPbP) which is funded by the Deutsche Forschungsgemeinschaft (DFG, German Research Foundation) under Germany´s Excellence Strategy – EXC-2094 – 390783311. V.A.V. acknowledges support by the NSF under grant AST-2108676. C.R.A. was supported by grants from VILLUM FONDEN (project numbers 16599 and 25501). Parts of this research were supported by the Australian Research Council Centre of Excellence for All Sky Astrophysics in 3 Dimensions (ASTRO 3D), through project number CE170100013. The UCSC team is supported in part by NASA grant 80NSSC20K0953, NSF grant AST–1815935, the Gordon & Betty Moore Foundation, the Heising-Simons Foundation, and by a fellowship from the David and Lucile Packard Foundation to R.J.F.

Based in part on observations made with the Nordic Optical Telescope, owned in collaboration by the University of Turku and Aarhus University, and operated jointly by Aarhus University, the University of Turku and the University of Oslo, representing Denmark, Finland and Norway, the University of Iceland and Stockholm University at the Observatorio del Roque de los Muchachos, La Palma, Spain, of the Instituto de Astrofisica de Canarias. Observations were obtained under program P62-507 (PI: Angus).

This work includes data obtained with the Swope telescope at Las Campanas Observatory, Chile, as part of the Swope Time Domain Key Project (PI A. Piro; CoIs Coulter, Drout, Phillips, Holoien, French, Cowperthwaite, Burns, Madore, Foley, Kilpatrick, Rojas-Bravo, Dimitriadis, Hsiao). We thank Abdo Campillay, Yilin Kong-Riveros, Piera Soto-King, and Natalie Ulloa for observations on the Swope telescope.

Some of the data presented herein were obtained at the W. M. Keck Observatory, which is operated as a scientific partnership among the California Institute of Technology, the University of California, and NASA. The Observatory was made possible by the generous financial support of the W. M. Keck Foundation. The authors wish to recognize and acknowledge the very significant cultural role and reverence that the summit of Maunakea has always had within the indigenous Hawaiian community. We are most fortunate to have the opportunity to conduct observations from this mountain. A major upgrade of the Kast spectrograph on the Shane 3 m telescope at Lick Observatory, led by Brad Holden, was made possible through generous gifts from the Heising-Simons Foundation, William and Marina Kast, and the University of California Observatories. Research at Lick Observatory is partially supported by a generous gift from Google.

Based in part on observations obtained with the Samuel Oschin 48-inch Telescope at the Palomar Observatory as part of the Zwicky Transient Facility project. ZTF is supported by the NSF under grant AST-1440341 and a collaboration including Caltech, IPAC, the Weizmann Institute for Science, the Oskar Klein Center at Stockholm University, the University of Maryland, the University of Washington, Deutsches Elektronen-Synchrotron and Humboldt University, Los Alamos National Laboratories, the TANGO Consortium of Taiwan, the University of Wisconsin at Milwaukee, and the Lawrence Berkeley National Laboratory. Operations are conducted by the Caltech Optical Observatories (COO), the Infrared Processing and Analysis Center (IPAC), and the University of Washington (UW).

The Pan-STARRS1 Surveys (PS1) and the PS1 public science archive have been made possible through contributions by the Institute for Astronomy, the University of Hawaii, the Pan-STARRS Project Office, the Max-Planck Society and its participating institutes, the Max Planck Institute for Astronomy, Heidelberg and the Max Planck Institute for Extraterrestrial Physics, Garching, The Johns Hopkins University, Durham University, the University of Edinburgh, the Queen's University Belfast, the Harvard-Smithsonian Center for Astrophysics, the Las Cumbres Observatory Global Telescope Network Incorporated, the National Central University of Taiwan, STScI, NASA under grant NNX08AR22G issued through the Planetary Science Division of the NASA Science Mission Directorate, NSF grant AST-1238877, the University of Maryland, Eotvos Lorand University (ELTE), the Los Alamos National Laboratory, and the Gordon and Betty Moore Foundation.

This work makes use of observations taken by the Las Cumbres Observatory global telescope network. The Las Cumbres Observatory Group is funded by NSF grants AST-1911225 and AST-1911151. The new SALT data presented here were obtained through Rutgers University program 2022-1-MLT-004 (PI S. Jha). Funding for the Lijiang 2.4 m telescope has been provided by the CAS and the People's Government of Yunnan Province.

We are grateful to the staffs at the various observatories where data were obtained. We thank S. Bradley Cenko, Thomas de Jaeger, Ori Fox, Melissa Graham, Goni Halevi, Michael Kandrashoff, Patrick Kelly, Io Kleiser, Jon Mauerhan, Adam Miller, Sarafina Nance, Kishore Patra, Neil Pichay, Anthony Rodriguez, Isaac Shivvers, Jeffrey Silverman, Benjamin Stahl, Erika Strasburger, Heechan Yuk, and Sameen Yunus for assistance with some of the Lick/Shane/Kast observations or reductions. The following U.C. Berkeley undergraduate students helped with the Lick/Nickel observations: Raphael Baer-Way, Sanyum Channa, Teagan Chapman, Nick Choksi, Maxime de Kouchkovsky, Nachiket Girish, Goni Halevy, Andrew Halle, Romain Hardy, Andrew Hoffman, Benjamin Jeffers, Connor Jennings, Sahana Kumar, Evelyn Liu, Emma McGinness, Jeffrey Molloy, Yukei Murakami, Andrew Rikhter, Timothy Ross, Jackson Sipple, Samantha Stegman, Haynes Stephens, James Sunseri, Kevin Tang, and Sameen Yunus.

8.9 Appendix

Here we present SN properties for all gold-, silver-, and comparison-sample objects in Tables A1, A2, and A3, respectively. Model properties for all `HERACLES`/`CMFGEN` simulations are listed in Table A4. Logs of optical/NIR spectroscopic observations of all unpublished gold-, silver-, and comparison-sample objects are provided in Table A5. All multicolor/bolometric light curves, spectral sequences, and best-matching light-curve and spectral models are shown for each gold-, silver-, and comparison-sample object as supplementary pages in Chapter 9.

8.10 Host-Galaxy Extinction Uncertainty

Host-galaxy extinction for sample objects is estimated by measuring the EW of the Na I D line and converting it to a host $E(B-V)$ using the relation derived by Stritzinger et al. (2018). We also test the relations between EW and host extinction from Poznanski et al. (2012) and find that for the total sample, that relation returns average[min,max] $E(B-V)_{\rm host}$ values of 2.3[0.014, 87.0] compared to 0.19[0.018, 0.81] when using Stritzinger et al. (2018). We choose to adopt the Stritzinger et al. (2018) relation given the large scatter associated with the Poznanski et al. (2012) relations (e.g., see Phillips et al. 2013) and inaccuracy of the latter at large EWs due to limited number of objects used in their fitting procedure. In Figure 8.20, we present the cumulative distributions of the host $E(B-V)$ values as well as the observed $g-r$ color versus Na I D EW. For the latter, we note that there is a large scatter relative to the Stritzinger et al. (2018) relation i.e., gold/silver sample objects are bluer than comparison sample objects for similar EW. Consequently, it appears that Na I D and/or colors are likely limited measures of reddening in SNe II, especially for large EWs and reddened colors. Additionally, in the top panel of Figure 8.21, we compare peak UV/optical magnitudes to host extinction derived from Na I D for all subsamples. We note that there is clearly a lack of highly-reddened objects in the sample (e.g., lower-right panel of Fig. 8.20). Also, there appears to be a correlation present in this host extinction correction method that traces the reddening vector at larger reddening values (e.g., >0.3 mag) indicating inaccuracy in using Na I D as a tracer of reddening. Nonetheless, when looking at the distribution of peak UV magnitudes for objects without large host reddening, there remains a contrast in absolute magnitude between gold- and comparison-sample objects, most likely the result of CSM interaction. Furthermore, we note that using Na I D absorption as a probe of host extinction is dependent on the resolution of the spectrograph used to observe each SN in our sample. However, most of the spectra obtained for this study have resolutions of $R>500$, which corresponds to $\Delta\lambda \lesssim 12$ Å for a combination of both the Na I D1 & D2 transitions. Reliable detections of this transition only become problematic with very low resolution (e.g., $R<100$, $\Delta\lambda>60$ Å) spectrographs for the typical signal-to-noise ratio of our SN spectra.

In Figure 8.20, we compare our host reddening distribution to SN II samples from Anderson et al. (2014) and Irani et al. (2023), where the former derives host extinction from the Na I D EW using Poznanski et al. (2012) and the latter derives it using shock-cooling modeling. Overall, our host reddening distributions contain larger values than both the Anderson et al. (2014) and Irani et al. (2023) samples. We note that for some objects that are in both our sample and that of Irani et al. (2023) (e.g., SNe 2020pni, 2019nvm, 2018dfc, 2019ust), the derived host-galaxy $E(B-V)$ is larger by $\sim$ 0.1–0.2 mag when using the Na I D EW. However, Irani et al. (2023) also fit for an R_V value while we apply a consistent $R_V=3.1$ with a Fitzpatrick (1999) reddening law; the choice of both the R_V and the reddening law could lead to bias in the host extinction correction.

We test whether the enhanced UV/optical luminosities observed in the gold sample are a product of the explosion and not uncertainty in the host extinction by first comparing the reddening vector for $R_V=3.1$ in the Fitzpatrick (1999) reddening law to the $w2-v$ vs. $g-r$

color evolution, as shown in Figure 8.5. The reddening vector has a slope of ~ 4.3, which is inconsistent with a slope of ~ 8.1 measured in the color-color evolution of the gold and comparison samples. This implies that extinction correction alone is not able to make all of these SNe have the sample peak absolute magnitude. Additionally, we apply a synthetic host extinction correction to the $g-r$ colors of the gold/comparison samples until the colors of each object are consistent with the bluest object in the sample at $\delta t = 5$ days, prior to any host reddening correction (e.g., see Figures 8.5 and 8.22). We find that an average of 0.21 mag of host reddening is needed, which translates to ~ 1.9 mag of UV extinction. However, even this amount of reddening cannot account for an average difference > 3 mag observed between gold and comparison-sample UV luminosities, further indicating that this observed phenomenon is not a result of host-galaxy extinction. Furthermore, even after this relative host reddening is applied based on colors, there remains a difference between the peak UV/optical luminosities of many comparison objects relative to those in the gold sample (e.g., see Fig. 8.21).

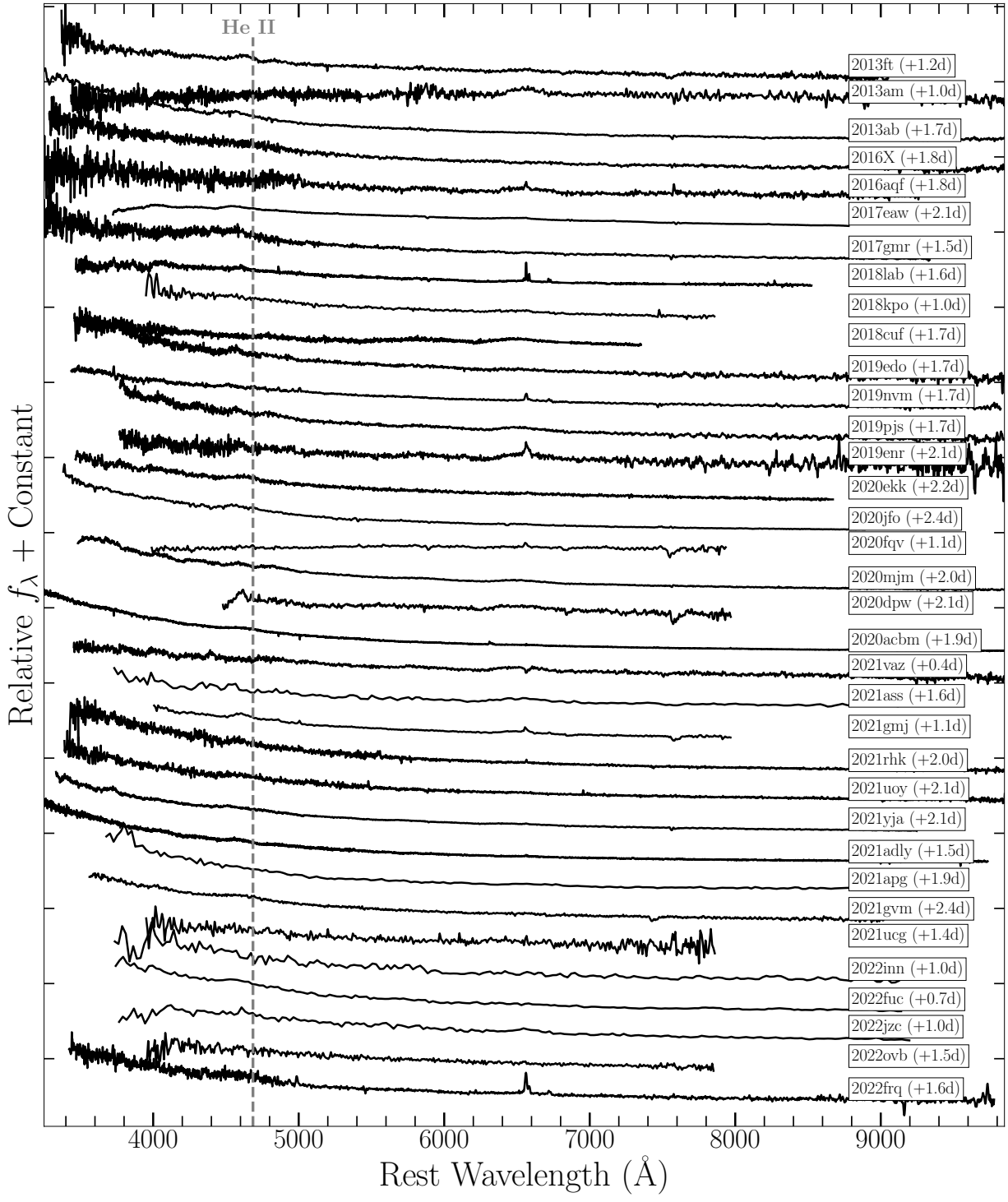

Figure 8.19 Comparison-sample spectra obtained at $t \lesssim 2$ days post-first light. These SNe II do not show prominent spectroscopic evidence for CSM interaction but do have complete UV photometry for comparison to the gold-sample objects.

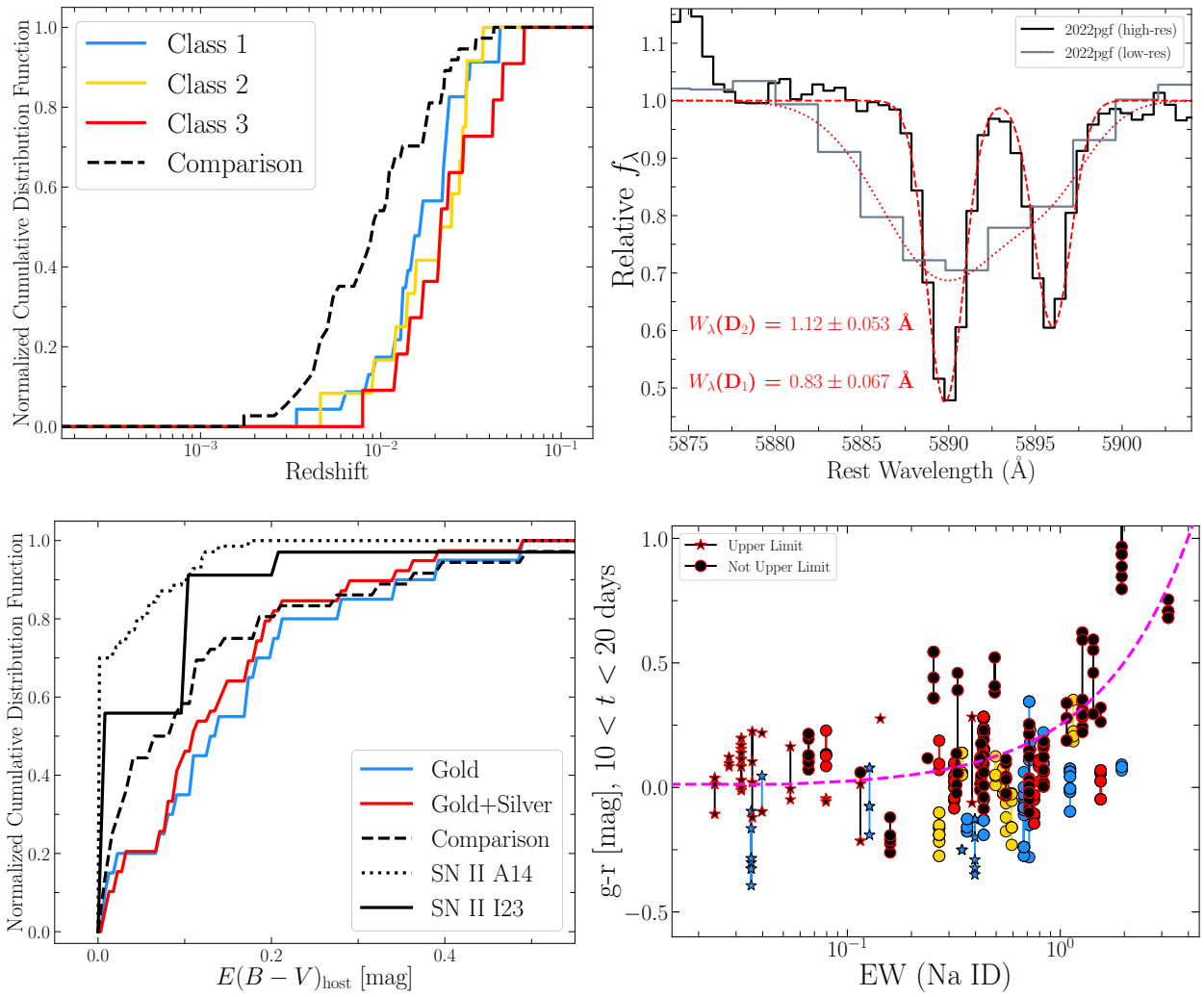

Figure 8.20 *Top left:* Redshift distribution of gold/silver Class 1 (blue), 2 (yellow), 3 (red) sample compared to comparison sample (black dashed lines). *Top right:* Visualization of host-galaxy extinction calculation using EWs of Na I D1 and D2 transitions and applying the relation from Stritzinger et al. (2018). *Bottom left:* Cumulative distribution of host-galaxy extinction for gold-, silver-, and comparison-sample objects. Host-galaxy extinction distribution from SN II sample by Anderson et al. (2014) shown as a black dotted line and by Irani et al. (2023) as a black solid line. *Bottom right:* Observed $g-r$ colors at $10 < \delta t < 20$ days versus equivalent width of Na I D. Relation from Stritzinger et al. (2018) shown as dashed magenta line. Notably, gold-sample objects tend to reside below the reddening relation, implying that they are intrinsically bluer than the inferred host extinction.

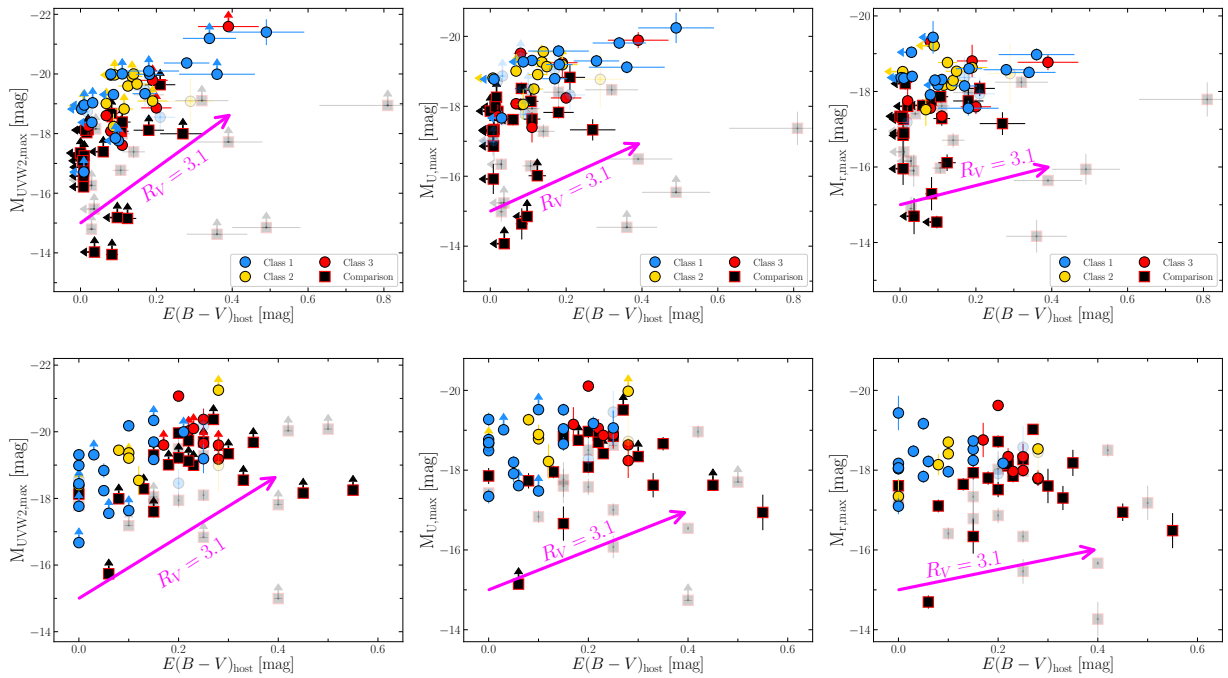

Figure 8.21 *Top panel:* Comparison of host-galaxy extinction versus extinction-corrected peak $w2$-, u-, and r-band absolute magnitudes for all of the sample objects. Host-extinction correction based on Na I D EW. Solid colored points represent the subsample of objects at $D > 40$ Mpc. We note that the highest luminosity objects ($M_{w2} < -21$ mag) also have some of the largest host extinction values, suggesting that Na I D is a limited measure of host reddening. This is further supported by the lack of objects with similarly high luminosities at low $E(B-V)_{host}$ values. *Bottom panel:* Peak $w2$-, u-, and r-band absolute magnitudes versus host-extinction correction using $g-r$ colors.

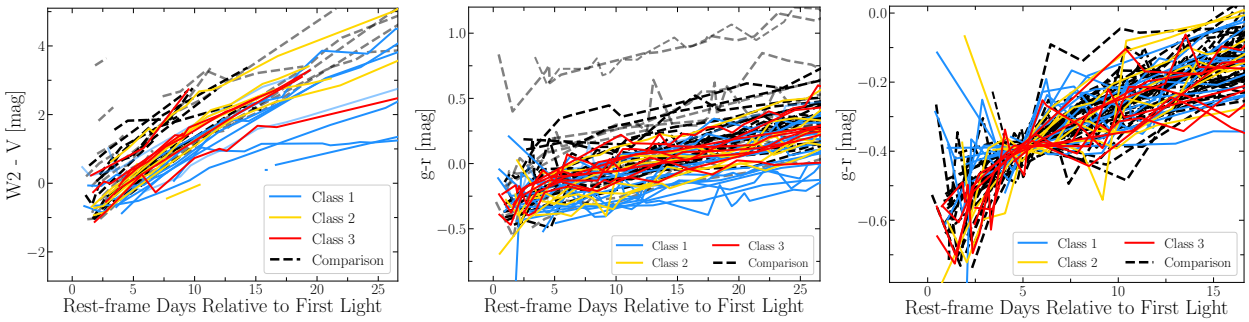

Figure 8.22 Observed $W2-V$ *(left)* and $g-r$ *(middle)* colors before host-extinction correction is applied. The reddest objects are comparison-sample objects 2013am and 2020fqv. As discussed in Appendix Section A, host reddening is unlikely to cause the contrast observed between the gold and comparison samples. Class 1 objects remain the bluest objects for all phases, suggesting continued CSM interaction. *Right:* $g-r$ colors after applying synthetic host extinction correction until all objects have the same color as the bluest object in the sample at $\delta t = 5$ days.

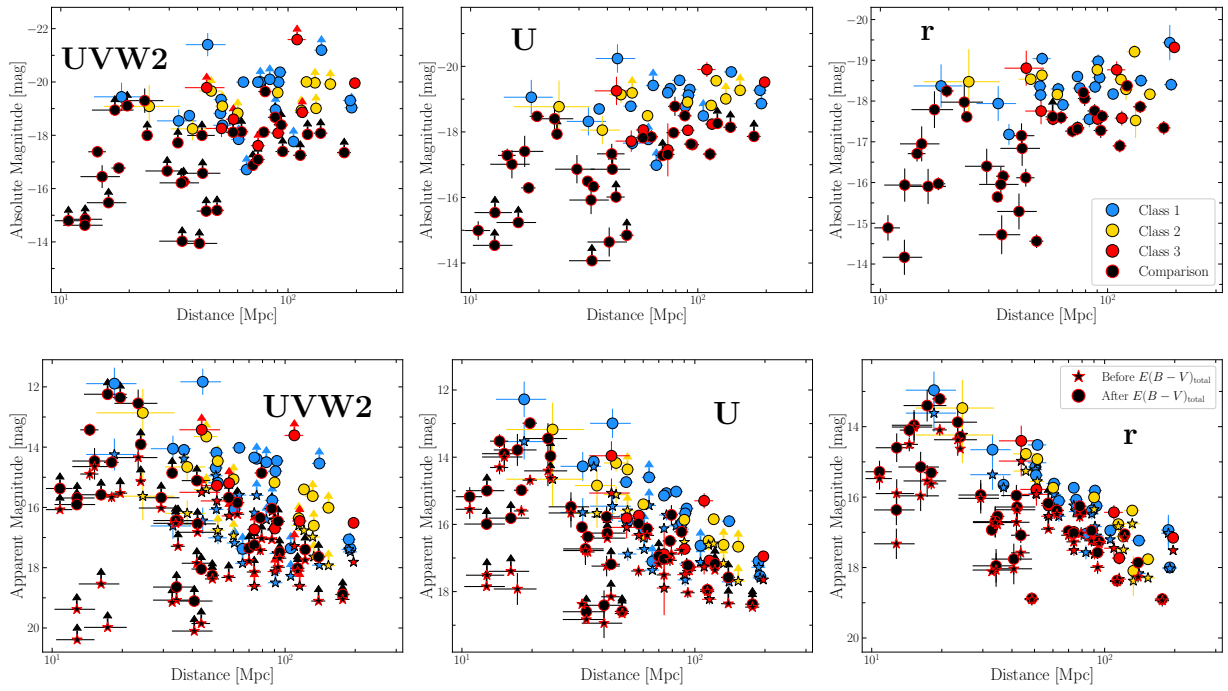

Figure 8.23 *Top:* Peak $w2$- (left), u- (middle), and r-band (right) absolute magnitudes versus distance for gold/silver (blue, yellow, red circles/stars) and comparison (black circles/stars) samples. Plotted stars (circles) represent peak magnitudes before (after) host extinction is applied using the Na I D EW. *Bottom:* Peak $w2$- (left), u- (middle), and r-band (right) apparent magnitude versus distance.

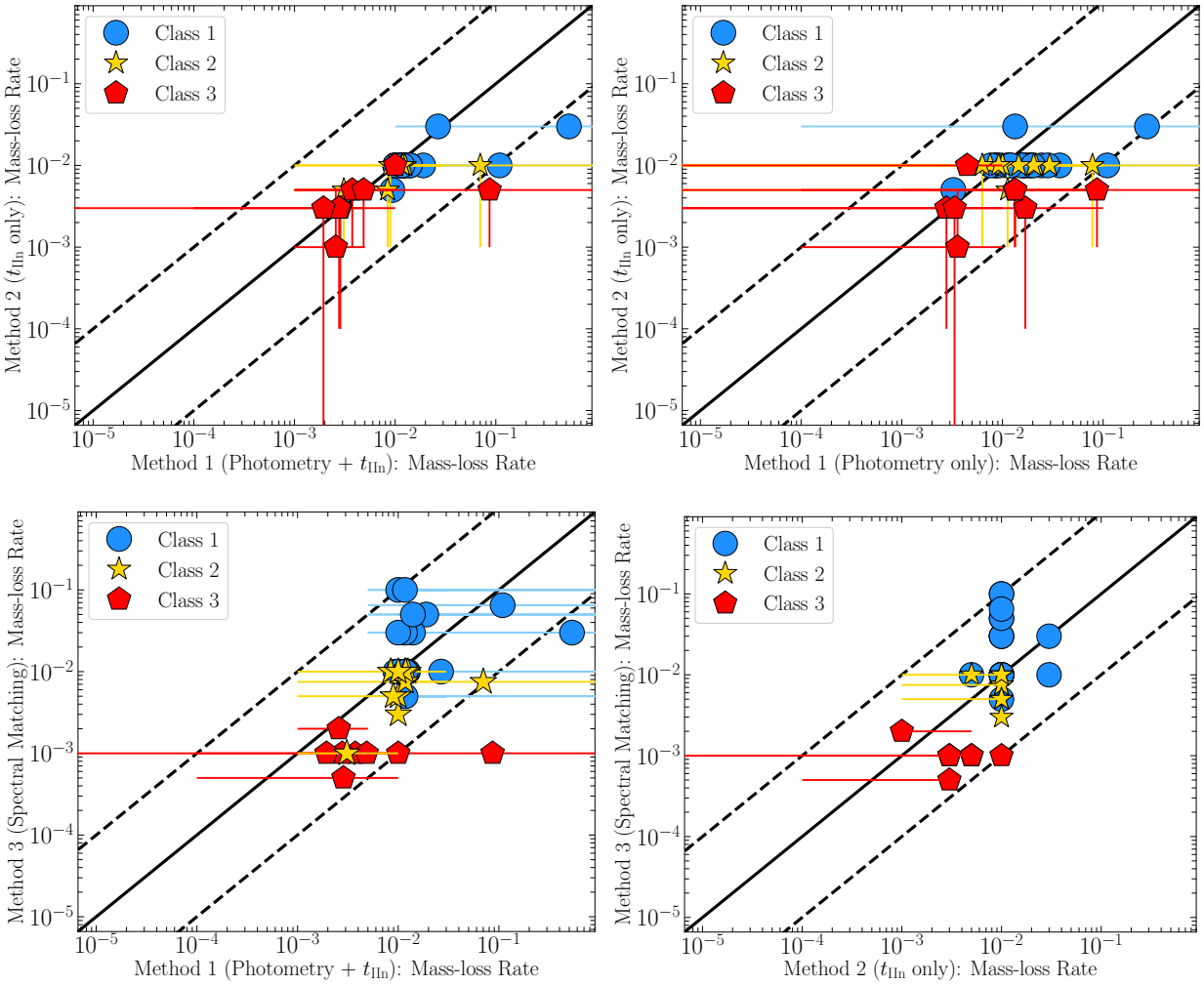

Figure 8.24 Comparison of model-matching methods (§8.5.1): *Top left:* Multicolor/bolometric light-curve properties plus $t_{\rm IIn}$ versus $t_{\rm IIn}$ only. *Top right:* Multicolor/bolometric light-curve properties versus $t_{\rm IIn}$. *Bottom left:* multicolor/bolometric light-curve properties plus $t_{\rm IIn}$ versus direct spectral matching. *Bottom right:* $t_{\rm IIn}$ versus direct spectral matching. The plotted points represent the average mass-loss rates derived from each method and the error bars represent the range of model parameters that are consistent with the observations (e.g., see §8.5.1).

Table A1. Gold-Sample Objects

Name	Time of First Light (MJD)	Host Galaxy	Redshift z	Distance (Mpc)	$E(B-V)_{\rm MW}$ (mag)	$E(B-V)_{\rm host}$ (mag)
PTF10gva	55320.3 ± 0.9	SDSS	0.028	114.5 ± 8.0^c	0.026	< 0.007
PTF11iqb	55764.4 ± 1.0	NGC 151	0.013	50.4 ± 3.5^d	0.028	< 0.003
2013fs	56571.11 ± 0.02	NGC 7610	0.012	50.6 ± 0.9^c	0.035	0.02 ± 0.004
2017ahn	57791.8 ± 0.5	NGC 3318	0.0090	33.0 ± 6.5^d	0.068	0.21 ± 0.04
2018zd	58178.4 ± 0.2	NGC 2146	0.0030	18.4 ± 4.5^d	0.085	0.17 ± 0.03
2018fif	58350.3 ± 0.2	UGC 00085	0.017	73.8 ± 5.2^c	0.094	0.18 ± 0.04
2018dfc	58302.3 ± 0.9	SDSS	0.037	153.5 ± 10.7^c	0.072	0.14 ± 0.03
2019ust	58799.8 ± 0.5	UGC 00548	0.022	92.2 ± 6.5^c	0.053	0.28 ± 0.06
2020pni	59045.8 ± 0.1	UGC 09684	0.017	73.7 ± 1.3^c	0.017	0.18 ± 0.04
2020sic	59092.2 ± 0.9	NGC 6001	0.033	140.3 ± 9.8^c	0.026	0.34 ± 0.07
2020abjq	59183.4 ± 1.0	UGC 00678	0.018	75.5 ± 5.3^c	0.022	0.11 ± 0.02
2020lfn	58995.8 ± 0.4	SDSS	0.044	196.8 ± 4.6^c	0.061	0.08 ± 0.02
2021can	59251.8 ± 0.4	SDSS	0.0207	90.1 ± 2.3^c	0.010	0.13 ± 0.03
2021jtt	59318.7 ± 0.4	NGC 2955	0.023	109.6 ± 10.1^c	0.009	0.39 ± 0.08
2021mqh	59351.3 ± 0.9	MCG-01-30-021	0.021	88.1 ± 6.2^c	0.039	< 0.01
2021aaqn	59492.9 ± 0.5	UGC 02119	0.028	115.5 ± 8.1^c	0.034	0.20 ± 0.04
2022ffg	59663.8 ± 0.6	CGCG 093-074	0.012	50.7 ± 3.6^c	0.034	0.17 ± 0.03
2022ibv	59690.5 ± 0.4	ESO 437-G064	0.014	57.5 ± 4.1^c	0.05	0.07 ± 0.02
2022jox	59706.9 ± 1.3	ESO 435-G014	0.0089	38.0 ± 7.5^d	0.08	0.09 ± 0.02
2022pgf	59782.0 ± 0.3	NGC 5894	0.0082	44.3 ± 8.8^d	0.01	0.49 ± 0.10

[c]Distance derived from redshift with peculiar-velocity uncertainties included.

[d]Redshift-independent distance.

Table A2. Silver-Sample Objects

Name	Time of First Light (MJD)	Host Galaxy	Redshift z	Distance (Mpc)	$E(B-V)_{\rm MW}$ (mag)	$E(B-V)_{\rm host}$ (mag)
PTF10abyy	55532.0 ± 0.5	WISEA	0.030	123.6 ± 8.6^{c}	0.150	< 0.09
2014G	56669.6 ± 1.7	NGC 3448	0.0043	24.5 ± 9.0^{d}	0.01	0.29 ± 0.06
2015bf	57367.8 ± 1.2	NGC 7653	0.014	60.1 ± 1.4^{d}	0.059	0.19 ± 0.04
2016blz	57485.5 ± 3.0	ECO 0866	0.012	51.4 ± 3.6^{c}	0.09	0.12 ± 0.024
2019qch	58739.0 ± 0.1	WISEA	0.024	105.7 ± 4.5^{c}	0.1	< 0.1
2020abtf	59184.9 ± 0.4	SDSS	0.014	61.2 ± 4.4^{c}	0.029	0.09 ± 0.02
2020xua	59142.3 ± 1.1	UGC 12218	0.021	90.4 ± 6.3^{c}	0.075	0.08 ± 0.02
2020tlf	59098.7 ± 1.5^{b}	NGC 5731	0.0084	36.8 ± 1.3^{c}	0.014	0.02 ± 0.01
2020nif	59022.3 ± 1.1	NGC 4939	0.010	43.85 ± 8.7^{d}	0.035	0.19 ± 0.04
2021wvd	59448.3 ± 0.5	CGCG 077-028	0.045	187.8 ± 13.1^{c}	0.036	< 0.087
2021zj	59222.4 ± 0.6	SDSS	0.046	190.5 ± 13.3^{c}	0.036	< 0.032
2021aek	59226.5 ± 1.1	I SZ 091	0.022	90.9 ± 6.4^{c}	0.041	0.36 ± 0.10
2021dbg	59257.1 ± 0.7	MCG-01-24-014	0.020	83.1 ± 5.9^{c}	0.027	0.18 ± 0.08
2021ont	59364.4 ± 0.1	WISE	0.028	120.5 ± 8.4^{c}	0.008	0.14 ± 0.03
2021qvr	59385.6 ± 1.9	NGC 7678	0.012	45.9 ± 5.3^{d}	0.042	0.15 ± 0.03
2021tyw	59413.4 ± 1.0	UGC 12354	0.013	51.5 ± 4.7^{d}	0.198	< 0.03
2021afkk	59540.9 ± 0.4	UGC 01971	0.014	63.6 ± 4.5^{c}	0.09	0.08 ± 0.02
2022dml	59634.0 ± 1.5	WISEA	0.03	132.8 ± 4.5^{c}	0.044	0.07 ± 0.01
2022prv	59780.8 ± 1.5	IC 1132	0.015	65.7 ± 4.6^{c}	0.052	<0.009

[b]Based on photometric detection. Time of first light used throughout is MJD 59108 based on modeling.

[c]Distance derived from redshift with peculiar-velocity uncertainties included.

[d]Redshift-independent distance.

Table A3. Comparison-Sample Objects

Name	Time of First Light (MJD)	Host Galaxy	Redshift z	Distance (Mpc)	$E(B-V)_{\rm MW}$ (mag)	$E(B-V)_{\rm host}$ (mag)
2013ft	56546.8 ± 1.0	NGC 7732	0.0096	34.2 ± 7.1^{g}	0.047	<0.037
2013ab	56339.5 ± 1.0	NGC 5669	0.0046	24.0 ± 0.9^{g}	0.023	0.11 ± 0.020
2013am	56371.5 ± 1.0	M65	0.0030	12.8 ± 2.4^{g}	0.02	0.49 ± 0.090
2016X	57405.9 ± 0.5	UGC 08041	0.0044	15.2 ± 3.0^{g}	0.02	< 0.007
2016aqf	57443.6 ± 1.0	NGC 2101	0.004	10.8 ± 1.4^{g}	0.047	0.03 ± 0.006
2017eaw	57885.7 ± 0.1	NGC 6946	0.0013	6.70 ± 0.15^{g}	0.30	0.04 ± 0.01
2017gmr	57999.1 ± 0.5	NGC 988	0.0050	19.6 ± 1.4^{g}	0.024	0.32 ± 0.070
2018lab	58480.4 ± 0.1	IC 2163	0.0089	32.8 ± 0.4^{g}	0.075	0.39 ± 0.09
2018kpo	58475.96 ± 0.4	MCG-01-10-019	0.0175	70.0 ± 4.9^{f}	0.047	<0.009
2018cuf	58291.8 ± 0.6	IC 5092	0.011	41.8 ± 5.8^{f}	0.027	0.27 ± 0.06
2019edo	58599.8 ± 0.5	NGC 4162	0.0086	42.1 ± 8.3^{f}	0.030	<0.01
2019nvm	58713.7 ± 0.4	UGC 10858	0.018	79.3 ± 5.3^{f}	0.026	0.21 ± 0.040
2019pjs	58729.7 ± 0.5	UGC 11105	0.007	34.7 ± 2.4^{f}	0.092	<0.029
2019enr	58606.3 ± 1.0	NGC 2919	0.0082	40.7 ± 8.1^{f}	0.025	0.083 ± 0.016
2020ekk	58918.7 ± 1.0	UGC 10528	0.011	62.4 ± 4.4^{f}	0.041	<0.02
2020fqv	58938.9 ± 0.2	NGC 4568	0.0075	17.3 ± 3.6^{g}	0.029	0.81 ± 0.18
2020jfo	58973.7 ± 0.1	M61	0.0052	14.5 ± 1.3^{g}	0.019	0.14 ± 0.030
2020mjm	59011.3 ± 0.9	UGC 09299	0.005	29.4 ± 5.8^{g}	0.037	<0.008
2020dpw	58904.8 ± 0.7	NGC 6951	0.0048	16.2 ± 3.2^{g}	0.32	<0.036
2020acbm	59192.4 ± 0.5	LSBC F831-08	0.022	87.7 ± 6.1^{f}	0.029	0.08 ± 0.02
2021vaz	59432.2 ± 0.4	NGC 1961	0.013	57.3 ± 4.0^{f}	0.107	0.18 ± 0.04
2021ass	59230.7 ± 0.6	NGC 0684	0.0118	43.7 ± 4.0^{g}	0.072	0.12 ± 0.023
2021gmj	59292.2 ± 1.0	NGC 3310	0.0034	18.0 ± 1.3^{g}	0.019	0.11 ± 0.020
2021rhk	59395.3 ± 1.0	ECO 01022	0.022515	94.7 ± 6.6^{f}	0.021	< 0.06
2021uoy	59427.4 ± 1.0	CGCG 453-026	0.0335	139.2 ± 9.7^{f}	0.052	0.11 ± 0.02

Table A3 (cont'd)

Name	Time of First Light (MJD)	Host Galaxy	Redshift z	Distance (Mpc)	$E(B-V)_{\rm MW}$ (mag)	$E(B-V)_{\rm host}$ (mag)
2021yja	59464.4 ± 0.1	NGC 1325	0.0057	23.4 ± 4.9^{g}	0.015	0.18 ± 0.040
2021adly	59522.5 ± 1.0	WISE	0.042	176.7 ± 12.4^{f}	0.018	< 0.05
2021apg	59230.5 ± 0.9	UGC 08661	0.027	113.2 ± 7.9^{f}	0.01	< 0.01
2021gvm	59293.9 ± 0.4	NGC 5185	0.0246	121.9 ± 4.5^{g}	0.021	0.017 ± 0.003
2021ucg	59419.6 ± 0.9	UGC 12188	0.0172	73.7 ± 5.2^{f}	0.097	<0.0056
2022inn	59695.3 ± 0.9	UGC 06365	0.0108	48.7 ± 3.4^{f}	0.013	<0.097
2022fuc	59671.4 ± 0.03	NGC 4545	0.0091	33.9 ± 6.7^{g}	0.01	<0.008
2022jzc	59714.3 ± 0.9	NGC 4088	0.0029	12.8 ± 2.5^{g}	0.017	0.36 ± 0.08
2022ovb	59773.5 ± 0.9	UGC 12005	0.0183	78.2 ± 5.5^{f}	0.117	<0.014
2022frq	59670.9 ± 0.5	MCG-02-34-054	0.0226	93.3 ± 6.5^{f}	0.055	0.11 ± 0.022

[f]Distance derived from redshift with peculiar-velocity uncertainties included.

[g]Redshift-independent distance.

Table A4. Model Properties

Name	$t_{\rm IIn}$ (days)	$\log_{10}(\dot{M})$ ($M_\odot$ yr^{-1})	$\log_{10}(\rho_{\rm CSM,14})^a$ (g cm^{-3})	$\log_{10}(R_{\rm CSM})$ (cm)	$M_{\rm CSM}$ ($M_\odot$)	Reference
r1w1h	< 0.3	-6.0	-11.6	14.5	0.016	Dessart et al. (2017)
r1w1	< 0.1	-6.0	-16.0	15.0	0.0028	Dessart et al. (2017)
r2w1	< 0.2	-6.0	-15.0	14.0	0.061	Dessart et al. (2017)
r1w4	1.4	-3.0	-13.0	14.7	0.0056	Dessart et al. (2017)
r1w5h	0.9	-2.5	-12.3	14.5	0.036	Dessart et al. (2017)
r1w5r	1.4	-2.3	-12.3	14.6	0.010	Dessart et al. (2017)
r1w6	3.5	-2.0	-12.0	14.7	0.030	Dessart et al. (2017)
r1w6a	5.5	-2.0	-12.0	14.8	0.044	Jacobson-Galán et al. (2023)
r1w6b	7.0	-2.0	-12.0	14.9	0.059	Jacobson-Galán et al. (2023)
r1w6c	9.0	-2.0	-12.0	15.0	0.072	Jacobson-Galán et al. (2022a)
r1w7a	14.0	-1.5	-12.5	15.0	0.21	Jacobson-Galán et al. (2022a)
r1w7b	25.0	-1.5	-12.5	15.3	0.40	Jacobson-Galán et al. (2022a)
r1w7c	35.0	-1.5	-12.5	15.6	0.75	Jacobson-Galán et al. (2022a)
r1w7d	35.0	-1.5	-12.5	15.9	1.5	Jacobson-Galán et al. (2022a)
m1em5	< 0.1	-5.0	-15.2	16.0	0.0037	Dessart & Jacobson-Galán (2023)
m1em4	< 0.2	-4.0	-14.3	16.0	0.0039	Dessart & Jacobson-Galán (2023)
m1em3	1.0	-3.0	-13.3	16.0	0.0056	Dessart & Jacobson-Galán (2023)
m1em2	4.0	-2.0	-11.9	16.0	0.024	Dessart & Jacobson-Galán (2023)
m1em1	15.0	-1.0	-10.9	16.0	0.18	Dessart & Jacobson-Galán (2023)
m1em0	25.0	1.0	-10.1	16.0	1.21	Dessart & Jacobson-Galán (2023)

[a]Density at 10^{14} cm.

Table A5. Optical/NIR Spectroscopy

SN Name	UT Date	MJD	Phase[a] (days)	Telescope	Instrument	Wavelength Range (Å)	Data Source
2018cvn	2018-06-29T09:21:36	58298.4	5.1	SOAR	Goodman	4057-8021	Cartier
2018cvn	2018-12-22T02:38:24	58474.1	180.8	SOAR	Goodman	3833-7779	Cartier
2018cvn	2019-01-14T01:40:48	58497.1	203.8	SOAR	Goodman	3899-7765	Cartier
2018khh	2018-12-21T02:09:36	58473.1	2.6	SOAR	Goodman	3892-7760	Cartier
2018khh	2018-12-22T01:26:24	58474.1	3.6	SOAR	Goodman	3331-9000	Cartier
2018khh	2019-01-14T00:43:12	58497.0	26.5	SOAR	Goodman	3793-7756	Cartier
2018khh	2019-04-18T02:09:36	58591.1	120.6	SOAR	Goodman	3302-9001	Cartier
2018khh	2019-05-17T08:38:24	58620.4	149.9	SOAR	Goodman	3813-7779	Cartier
2018kpo	2018-12-25T00:00:00	58477.0	1.0	LT	SPRAT	4020-7994	TNS
2018kpo	2018-12-30T01:53:55	58482.1	6.1	P60	SEDM	3777-9223	TNS
2018kpo	2018-12-30T02:56:21	58482.1	6.2	NTT	EFOSC2	3338-7458	TNS
2018kpo	2018-12-30T03:30:14	58482.1	6.2	NTT	EFOSC2	3338-7458	TNS
2018kpo	2018-12-30T04:06:53	58482.2	6.2	NTT	EFOSC2	5994-9993	TNS
2018kpo	2019-01-08T04:36:45	58491.2	15.2	NTT	EFOSC2	3637-9235	TNS
2018kpo	2019-02-01T01:44:16	58515.1	39.1	NTT	EFOSC2	3637-9235	TNS
2018kpo	2019-03-08T00:23:45	58550.0	74.1	NTT	EFOSC2	3633-9229	TNS
2018lab	2019-01-04T08:00:00	58487.3	6.7	Lick	Kast	3614-10586	Filippenko
2019edo	2019-04-28T11:34:15	58601.5	1.7	Faulkes-South	FLOYDS	3799-10001	GSP
2019edo	2019-04-29T11:47:23	58602.5	2.7	Faulkes-South	FLOYDS	3800-10000	GSP
2019edo	2019-05-04T05:00:00	58607.2	7.4	Shane	Kast	3616-10714	Filippenko
2019edo	2019-05-07T07:48:06	58610.3	10.5	Faulkes-North	FLOYDS	3500-9999	GSP
2019edo	2019-05-09T05:00:00	58612.2	12.4	Shane	Kast	3616-10716	Filippenko
2019edo	2019-05-10T09:47:16	58613.4	13.6	Faulkes-North	FLOYDS	3500-10000	GSP
2019edo	2019-05-17T11:08:22	58620.5	20.6	Faulkes-South	FLOYDS	3800-10001	GSP
2019edo	2019-05-22T08:58:07	58625.4	25.5	Faulkes-North	FLOYDS	3500-10000	GSP

Table A5 (cont'd)

SN Name	UT Date	MJD	Phase[a] (days)	Telescope	Instrument	Wavelength Range (Å)	Data Source
2019edo	2019-05-28T10:24:44	58631.4	31.6	Faulkes-South	FLOYDS	3800-10001	GSP
2019edo	2019-06-08T08:48:52	58642.4	42.5	Faulkes-North	FLOYDS	3500-9999	GSP
2019edo	2019-06-20T06:20:00	58654.3	54.4	Faulkes-North	FLOYDS	3499-10000	GSP
2019edo	2019-07-14T06:11:51	58678.3	78.4	Faulkes-North	FLOYDS	3500-10001	GSP
2019enr	2019-05-05T09:18:41	58608.4	2.1	Faulkes-South	FLOYDS	3800-10000	GSP
2019enr	2019-05-06T10:09:07	58609.4	3.1	Faulkes-South	FLOYDS	3500-10000	GSP
2019enr	2019-05-06T13:32:36	58609.6	3.2	Xinglong	BFOSC	4093-8812	X.Wang
2019nvm	2019-08-20T08:38:36	58715.4	1.7	Faulkes-North	FLOYDS	3499-10000	GSP
2019nvm	2019-08-22T22:14:56	58717.9	4.2	P60	SEDM	3777-9223	TNS
2019nvm	2019-08-26T04:06:09	58721.2	7.5	Shane	Kast	3503-9896	YSE
2019nvm	2019-09-01T05:14:53	58727.2	13.5	Shane	Kast	3503-9994	YSE
2019nvm	2019-09-09T05:05:20	58735.2	21.5	Shane	Kast	3503-10096	YSE
2019nvm	2019-10-06T03:34:14	58762.1	48.4	Shane	Kast	3504-9994	YSE
2019nvm	2019-11-07T02:13:31	58794.1	80.4	Shane	Kast	3554-10194	YSE
2019nyk	2019-08-21T05:29:23	58716.2	3.3	NTT	EFOSC2	3645-9237	ePESSTO
2019nyk	2019-08-26T08:35:16	58721.4	8.4	Shane	Kast	3504-9895	YSE
2019nyk	2019-08-27T07:13:42	58722.3	9.4	P60	SEDM	3777-9223	TNS
2019nyk	2019-09-01T07:31:53	58727.3	14.4	Shane	Kast	3503-9996	YSE
2019nyk	2019-09-09T06:32:30	58735.3	22.4	Shane	Kast	3503-9993	YSE
2019nyk	2019-10-06T05:42:43	58762.2	49.3	Shane	Kast	3503-9894	YSE
2019nyk	2019-10-30T07:41:21	58786.3	73.4	Shane	Kast	3353-9993	YSE
2019pjs	2019-09-04T07:38:00	58730.3	0.7	Shane	Kast	3626-10702	Filippenko
2019pjs	2019-09-05T03:50:00	58731.2	1.5	Shane	Kast	3626-10710	Filippenko
2019pjs	2019-09-05T09:22:38	58731.4	1.7	Faulkes-South	FLOYDS	3799-9999	GSP
2019pjs	2019-09-10T07:17:14	58736.3	6.7	P60	SEDM	3777-9223	TNS

Table A5 (cont'd)

SN Name	UT Date	MJD	Phase[a] (days)	Telescope	Instrument	Wavelength Range (Å)	Data Source
2019pjs	2019-09-10T09:47:56	58736.4	6.8	Faulkes-South	FLOYDS	3800-10001	GSP
2019pjs	2019-09-14T08:13:45	58740.3	10.7	Faulkes-North	FLOYDS	3501-10000	GSP
2019pjs	2019-09-23T08:59:47	58749.4	19.7	Faulkes-South	FLOYDS	3801-10001	GSP
2019pjs	2019-09-25T11:22:60	58751.5	21.8	Xinglong	BFOSC	3623-8796	X.Wang
2019pjs	2019-10-03T03:50:00	58759.2	29.5	Shane	Kast	3616-10710	Filippenko
2019pjs	2019-10-03T07:03:54	58759.3	29.6	Faulkes-North	FLOYDS	3500-9999	GSP
2019pjs	2019-10-08T11:54:06	58764.5	34.8	Xinglong	BFOSC	3842-8800	X.Wang
2019pjs	2019-10-19T04:49:47	58775.2	45.6	Faulkes-North	FLOYDS	3500-10000	GSP
2019pjs	2019-10-31T03:50:00	58787.2	57.5	Shane	Kast	3616-10702	Filippenko
2019pjs	2019-11-03T10:16:45	58790.4	60.8	Xinglong	BFOSC	3259-8788	X.Wang
2019pjs	2019-11-04T04:41:24	58791.2	61.5	Faulkes-North	FLOYDS	3499-10001	GSP
2019ofc	2019-08-23T06:39:17	58718.3	1.7	NTT	EFOSC2	3644-9241	ePESSTO
2019qch	2019-09-21T04:19:12	58747.18	8.5	Palomar	SEDM	3800–9000	TNS
2019ust	2019-11-14T12:01:50	58801.5	1.7	Gemini-North	GMOS	3709-6861	TNS
2019ust	2019-11-15T05:38:44	58802.2	2.4	Faulkes-North	FLOYDS	3202-10500	YSE
2019ust	2019-11-17T09:59:26	58804.4	4.6	Faulkes-North	FLOYDS	3500-10001	GSP
2019ust	2019-11-24T09:52:29	58811.4	11.6	Faulkes-North	FLOYDS	3500-10000	GSP
2019ust	2019-11-27T09:57:41	58814.4	14.6	Faulkes-North	FLOYDS	3500-10000	GSP
2019ust	2019-12-03T09:17:43	58820.4	20.6	Faulkes-North	FLOYDS	3500-10000	GSP
2019ust	2019-12-09T05:34:58	58826.2	26.4	Faulkes-North	FLOYDS	3501-10000	GSP
2019ust	2019-12-19T06:38:00	58836.3	36.5	Faulkes-North	FLOYDS	3499-9999	GSP
2019ust	2019-12-30T04:49:29	58847.2	47.4	Faulkes-North	FLOYDS	3500-10000	GSP
2019ust	2020-01-02T06:07:10	58850.3	50.4	Faulkes-North	FLOYDS	3499-10000	GSP
2019ust	2020-01-23T05:56:06	58871.2	71.4	Faulkes-North	FLOYDS	3499-10000	GSP
2020dpw	2020-02-27T19:12:00	58906.8	2.1	Seimei	KOOLS	4501-8008	TNS

Table A5 (cont'd)

SN Name	UT Date	MJD	Phase[a] (days)	Telescope	Instrument	Wavelength Range (Å)	Data Source
2020dpw	2020-03-02T13:12:00	58910.6	5.8	Shane	Kast	3614-10708	Filippenko
2020dpw	2020-03-03T13:08:08	58911.5	6.8	Shane	Kast	3503-9995	YSE
2020dpw	2020-05-27T11:11:31	58996.5	91.7	Shane	Kast	3504-10494	YSE
2020ekk	2020-03-12T20:24:00	58920.8	2.2	Lijiang	YFOSC	3504-8767	TNS
2020ekk	2020-03-17T17:33:26	58925.7	7.1	Faulkes-South	FLOYDS	3501-9999	GSP
2020ekk	2020-03-21T17:05:40	58929.7	11.0	Faulkes-South	FLOYDS	3499-9999	GSP
2020ekk	2020-03-23T11:16:24	58931.5	12.8	Faulkes-North	FLOYDS	3501-10001	GSP
2020ekk	2020-04-03T12:52:00	58942.5	23.9	Faulkes-North	FLOYDS	3500-9999	GSP
2020ekk	2020-04-10T15:44:13	58949.7	31.0	Faulkes-South	FLOYDS	3800-10000	GSP
2020ekk	2020-04-16T13:05:53	58955.5	36.9	Faulkes-North	FLOYDS	3500-10000	GSP
2020ekk	2020-04-20T12:39:43	58959.5	40.9	Faulkes-North	FLOYDS	3500-10001	GSP
2020ekk	2020-04-26T13:53:18	58965.6	46.9	Faulkes-North	FLOYDS	3499-9999	GSP
2020ekk	2020-05-16T07:16:56	58985.3	66.6	Faulkes-North	FLOYDS	3501-10000	GSP
2020ekk	2020-05-26T09:02:08	58995.4	76.7	Faulkes-North	FLOYDS	3500-10000	GSP
2020ekk	2020-06-09T12:59:10	59009.5	90.9	Faulkes-North	FLOYDS	3500-10000	GSP
2020ekk	2020-06-24T11:29:08	59024.5	105.8	Faulkes-North	FLOYDS	3499-10000	GSP
2020lfn	2020-05-29T00:00:00	58998.0	2.2	NOT	ALFOSC	3700-9294	TNS
2020lfn	2020-07-19T07:11:26	59049.3	53.5	Shane	Kast	3255-10892	YSE
2020mjm	2020-06-13T08:03:16	59013.3	2.0	Faulkes-North	FLOYDS	3500-10000	GSP
2020mjm	2020-06-16T12:59:39	59016.5	5.2	Faulkes-South	FLOYDS	3499-10000	GSP
2020mjm	2020-06-19T08:37:52	59019.4	8.1	Faulkes-North	FLOYDS	3500-10001	GSP
2020mjm	2020-06-27T06:07:30	59027.3	16.0	Faulkes-North	FLOYDS	3500-10000	GSP
2020mjm	2020-07-03T10:32:57	59033.4	22.1	Faulkes-South	FLOYDS	3501-10000	GSP
2020mjm	2020-07-13T07:45:27	59043.3	32.0	Faulkes-North	FLOYDS	3500-10000	GSP
2020mjm	2020-07-24T06:09:03	59054.3	43.0	Faulkes-North	FLOYDS	3499-10001	GSP

Table A5 (cont'd)

SN Name	UT Date	MJD	Phase[a] (days)	Telescope	Instrument	Wavelength Range (Å)	Data Source
2020mjm	2020-08-11T05:51:12	59072.2	60.9	Faulkes-North	FLOYDS	3499-10001	GSP
2020mjm	2020-08-27T09:07:18	59088.4	77.1	Faulkes-South	FLOYDS	3501-9999	GSP
2020nif	2020-06-24T08:28:14	59024.4	2.1	Faulkes-North	FLOYDS	3501-9999	GSP
2020nif	2020-06-26T07:20:12	59026.3	4.0	Faulkes-North	FLOYDS	3297-10178	YSE
2020nif	2020-06-27T11:32:53	59027.5	5.2	Faulkes-North	FLOYDS	3300-10181	YSE
2020nif	2020-07-19T04:38:09	59049.2	26.9	Shane	Kast	3254-10896	YSE
2020sic	2020-09-01T20:52:48	59093.87	1.7	NOT	ALFOSC	3800–9300	TNS
2020xua	2020-10-22T03:04:59	59144.1	1.8	MMT	Binospec	3824-9214	TNS
2020xua	2020-10-24T08:53:31	59146.4	4.0	Faulkes-North	FLOYDS	3500-10000	GSP
2020xua	2020-10-26T07:58:15	59148.3	6.0	Faulkes-North	FLOYDS	3500-10001	GSP
2020xua	2020-10-31T07:17:55	59153.3	11.0	Faulkes-North	FLOYDS	3501-10001	GSP
2020xua	2020-11-01T08:27:43	59154.4	12.0	Faulkes-North	FLOYDS	3500-10000	GSP
2020xua	2020-11-03T05:45:27	59156.2	13.9	Faulkes-North	FLOYDS	3800-10001	GSP
2020xua	2020-11-05T08:17:30	59158.3	16.0	Shane	Kast	3854-10094	YSE
2020xua	2020-11-06T07:21:24	59159.3	17.0	Faulkes-North	FLOYDS	3799-9999	GSP
2020xua	2020-11-08T05:47:20	59161.2	18.9	Faulkes-North	FLOYDS	3500-10000	GSP
2020xua	2020-11-15T05:14:26	59168.2	25.9	Shane	Kast	3254-10893	YSE
2020xua	2020-11-16T07:30:53	59169.3	27.0	Faulkes-North	FLOYDS	3500-10000	GSP
2020xua	2020-11-28T05:57:47	59181.2	38.9	Faulkes-North	FLOYDS	3501-9999	GSP
2020xua	2020-12-12T06:37:45	59195.3	52.9	Faulkes-North	FLOYDS	3500-10001	GSP
2020xua	2020-12-28T04:48:21	59211.2	68.9	Faulkes-North	FLOYDS	3799-9999	GSP
2020abjq	2020-12-03T08:11:34	59186.3	2.9	Faulkes-North	FLOYDS	3799-10000	GSP
2020abjq	2020-12-04T08:09:04	59187.3	3.9	Faulkes-North	FLOYDS	3501-10000	GSP
2020abjq	2020-12-07T08:02:13	59190.3	6.9	Shane	Kast	3354-9994	YSE
2020abjq	2020-12-09T11:37:20	59192.5	9.0	Faulkes-South	FLOYDS	3800-10001	GSP

Table A5 (cont'd)

SN Name	UT Date	MJD	Phase[a] (days)	Telescope	Instrument	Wavelength Range (Å)	Data Source
2020abjq	2020-12-11T04:31:21	59194.2	10.7	Keck	LRIS	3162-10147	YSE
2020abjq	2020-12-11T07:43:04	59194.3	10.9	Faulkes-North	FLOYDS	3500-10001	GSP
2020abjq	2020-12-15T04:42:45	59198.2	14.7	Faulkes-North	FLOYDS	3499-10001	GSP
2020abjq	2020-12-22T03:36:10	59205.2	21.7	Shane	Kast	3254-10894	YSE
2020abjq	2021-01-06T02:30:04	59220.1	36.7	Shane	Kast	3255-10894	YSE
2020abjq	2021-01-14T05:36:33	59228.2	44.8	Faulkes-North	FLOYDS	3500-10000	GSP
2020abjq	2021-02-06T03:26:54	59251.1	67.7	Shane	Kast	3254-10894	YSE
2020abjq	2021-02-19T03:21:57	59264.1	80.7	Shane	Kast	3254-10894	YSE
2020abtf	2020-12-07T07:48:00	59190.3	5.4	NTT	EFOSC2	3650-9245	TNS
2020abtf	2020-12-08T14:18:11	59191.6	6.7	Faulkes-North	FLOYDS	3499-10000	GSP
2020abtf	2020-12-09T16:19:36	59192.7	7.8	Faulkes-South	FLOYDS	3800-10000	GSP
2020abtf	2020-12-11T09:36:56	59194.4	9.5	Faulkes-North	FLOYDS	3499-10001	GSP
2020abtf	2020-12-24T08:03:43	59207.3	22.4	Faulkes-North	FLOYDS	3499-9999	GSP
2020abtf	2021-01-02T07:31:27	59216.3	31.4	Faulkes-North	FLOYDS	3500-10001	GSP
2020abtf	2021-01-09T11:09:59	59223.5	38.6	Faulkes-North	FLOYDS	3499-10000	GSP
2020abtf	2021-01-16T13:05:57	59230.5	45.6	Faulkes-South	FLOYDS	3501-10000	GSP
2020abtf	2021-02-08T11:22:09	59253.5	68.6	Faulkes-South	FLOYDS	3500-10000	GSP
2020abtf	2021-03-01T11:38:37	59274.5	89.6	Faulkes-South	FLOYDS	3499-9999	GSP
2020abtf	2021-03-12T11:40:32	59285.5	100.6	Faulkes-South	FLOYDS	4851-8794	GSP
2020abtf	2021-03-27T11:05:15	59300.5	115.6	Faulkes-South	FLOYDS	3799-10000	GSP
2020acbm	2020-12-11T07:50:47	59194.3	1.9	Keck	LRIS	3162-10146	YSE
2020acbm	2020-12-15T03:27:54	59198.1	5.7	NTT	ESFOSC2	3648-9247	ePESSTO
2020acbm	2020-12-22T04:10:39	59205.2	12.8	Shane	Kast	3254-10892	YSE
2021zj	2021-01-13T08:49:37	59227.4	5.1	NTT	EFOSC2	3650-9245	TNS
2021zj	2021-01-15T13:27:46	59229.6	7.3	Faulkes-North	FLOYDS	3501-10000	GSP

Table A5 (cont'd)

SN Name	UT Date	MJD	Phase[a] (days)	Telescope	Instrument	Wavelength Range (Å)	Data Source
2021zj	2021-02-10T11:29:17	59255.5	33.2	Faulkes-North	FLOYDS	3500-9999	GSP
2021zj	2021-02-16T08:16:56	59261.3	39.0	Faulkes-North	FLOYDS	3500-10000	GSP
2021zj	2021-03-19T06:36:26	59292.3	70.0	Faulkes-North	FLOYDS	3500-10000	GSP
2021zj	2021-03-30T09:46:30	59303.4	81.1	Faulkes-North	FLOYDS	4001-10000	GSP
2021zj	2021-04-10T10:07:26	59314.4	92.1	Faulkes-North	FLOYDS	3500-10001	GSP
2021zj	2021-04-24T07:26:28	59328.3	106.0	Faulkes-North	FLOYDS	3500-9999	GSP
2021zj	2021-05-07T00:00:00	59341.0	118.7	NOT	ALFOSC	5680-8580	YSE
2021zj	2021-05-08T07:10:58	59342.3	120.0	Faulkes-North	FLOYDS	3499-9999	GSP
2021zj	2021-05-25T06:46:01	59359.3	137.0	Faulkes-North	FLOYDS	3500-10000	GSP
2021zj	2021-06-11T05:49:43	59376.2	153.9	Shane	Kast	3254-10496	YSE
2021zj	2021-06-16T00:00:00	59381.0	158.7	NOT	ALFOSC	5680-8580	YSE
2021aek	2021-01-15T08:31:37	59229.4	2.9	NTT	EFOSC2	3829-9247	TNS
2021aek	2021-01-24T13:23:40	59238.6	12.1	Faulkes-South	FLOYDS	3499-10000	GSP
2021aek	2021-01-25T15:15:54	59239.6	13.1	Faulkes-South	FLOYDS	3800-10000	GSP
2021aek	2021-03-12T15:53:20	59285.7	59.2	Faulkes-South	FLOYDS	3500-10000	GSP
2021aek	2021-03-27T13:23:21	59300.6	74.1	Faulkes-South	FLOYDS	3800-9999	GSP
2021aek	2021-04-07T08:10:51	59311.3	84.8	Faulkes-North	FLOYDS	3499-9999	GSP
2021apg	2021-01-18T08:42:55	59232.4	1.9	P60	SEDM	3777-9223	TNS
2021apg	2021-01-18T13:54:00	59232.6	2.1	Shane	Kast	3622-10700	Filippenko
2021apg	2021-01-19T08:19:50	59233.3	2.8	NTT	EFOSC2	3650-9243	ePESSTO
2021ass	2021-01-18T05:08:10	59232.2	1.5	Shane	Kast	3622-10700	Filippenko
2021ass	2021-01-18T06:20:36	59232.3	1.6	Palomar	SEDM	3777-9223	TNS
2021ass	2021-01-28T06:57:12	59242.3	11.6	Faulkes-North	FLOYDS	3499-10000	GSP
2021ass	2021-02-10T05:47:35	59255.2	24.6	Faulkes-North	FLOYDS	3500-9999	GSP
2021can	2021-02-08T00:00:00	59253.0	1.2	NOT	ALFOSC	4003-9000	YSE

Table A5 (cont'd)

SN Name	UT Date	MJD	Phase[a] (days)	Telescope	Instrument	Wavelength Range (Å)	Data Source
2021can	2021-02-11T10:39:00	59256.4	4.6	Faulkes-North	FLOYDS	3499-10000	GSP
2021can	2021-02-12T15:41:02	59257.7	5.9	Keck	LRIS	3161-7820	YSE
2021can	2021-02-13T13:58:37	59258.6	6.8	Faulkes-North	FLOYDS	3501-10000	GSP
2021can	2021-02-16T12:58:22	59261.5	9.7	Faulkes-North	FLOYDS	3500-10001	GSP
2021can	2021-02-18T12:41:02	59263.5	11.7	Shane	Kast	3632-10742	Filippenko
2021can	2021-03-15T14:16:02	59288.6	36.8	Faulkes-North	FLOYDS	3499-9999	GSP
2021can	2021-03-22T13:10:21	59295.5	43.7	Faulkes-North	FLOYDS	3500-10000	GSP
2021can	2021-03-31T10:44:20	59304.4	52.6	Faulkes-North	FLOYDS	3500-10000	GSP
2021can	2021-04-06T06:33:34	59310.3	58.5	Shane	Kast	3255-10894	YSE
2021can	2021-04-07T12:50:19	59311.5	59.7	Faulkes-North	FLOYDS	3499-10000	GSP
2021dbg	2021-02-16T04:05:44	59261.2	4.1	NTT	EFOSC2	3650-9245	TNS
2021dbg	2021-02-17T11:41:10	59262.5	5.5	Faulkes-North	FLOYDS	3500-10000	GSP
2021dbg	2021-02-19T06:47:30	59264.3	7.3	Shane	Kast	3255-10893	YSE
2021dbg	2021-02-23T09:06:46	59268.4	11.4	Faulkes-North	FLOYDS	3295-10174	YSE
2021dbg	2021-02-25T10:46:47	59270.4	13.4	Faulkes-North	FLOYDS	3500-10000	GSP
2021dbg	2021-03-08T00:00:00	59281.0	23.6	Xinglong	BFOSC	3865-8825	X.Wang
2021dbg	2021-03-21T02:06:24	59294.1	37.1	Shane	Kast	4002-6964	YSE
2021dbg	2021-03-24T12:07:30	59297.5	40.5	Faulkes-South	FLOYDS	3800-10000	GSP
2021dbg	2021-04-02T05:31:56	59306.2	49.2	Faulkes-North	FLOYDS	3499-10001	GSP
2021dbg	2021-04-19T05:08:46	59323.2	66.2	Shane	Kast	3254-10896	YSE
2021gmj	2021-03-20T20:35:50	59293.9	1.6	LT	SPRAT	4020-7994	TNS
2021gmj	2021-03-21T01:22:39	59294.1	1.8	NOT	AFOSC	3383-8174	TNS
2021gmj	2021-03-21T05:00:00	59294.2	2.0	IRTF	SpeX	6905-25708	YSE
2021gmj	2021-03-22T00:00:00	59295.0	2.8	Shane	Kast	3404-10497	YSE
2021gmj	2021-04-06T03:32:00	59310.1	17.9	Shane	Kast	3506-9994	YSE

Table A5 (cont'd)

SN Name	UT Date	MJD	Phase[a] (days)	Telescope	Instrument	Wavelength Range (Å)	Data Source
2021gmj	2021-04-10T05:00:00	59314.2	22.0	IRTF	SpeX	6906-25709	YSE
2021gmj	2021-04-19T03:46:53	59323.2	30.9	Shane	Kast	3266-10896	YSE
2021gmj	2021-05-09T05:26:51	59343.2	51.0	IRTF	SpeX	6905-25708	YSE
2021gmj	2021-05-10T04:06:27	59344.2	52.0	Shane	Kast	3255-10894	YSE
2021gmj	2021-06-11T04:24:09	59376.2	84.0	Shane	Kast	3256-10892	YSE
2021gvm	2021-03-23T06:07:18	59296.3	2.4	NTT	EFOSC2	3650-9245	TNS
2021gvm	2021-04-03T02:28:20	59307.1	13.2	LT	SPRAT	4020-7994	TNS
2021jtt	2021-04-15T22:00:00	59319.9	1.2	NOT	ALFOSC	3800-9000	YSE
2021jtt	2021-04-16T09:42:52	59320.4	1.7	Faulkes-North	FLOYDS	3499-10001	GSP
2021jtt	2021-04-23T07:17:09	59327.3	8.6	Faulkes-North	FLOYDS	3500-9999	GSP
2021jtt	2021-04-29T04:34:17	59333.2	14.5	P60	SEDM	3777-9223	TNS
2021jtt	2021-05-03T07:06:33	59337.3	18.6	Faulkes-North	FLOYDS	3500-10000	GSP
2021jtt	2021-05-12T07:25:21	59346.3	27.6	Faulkes-North	FLOYDS	3500-10001	GSP
2021jtt	2021-05-27T06:10:43	59361.3	42.6	Faulkes-North	FLOYDS	3499-10001	GSP
2021jtt	2021-06-10T06:02:37	59375.3	56.6	Faulkes-North	FLOYDS	3500-10000	GSP
2021mqh	2021-05-19T04:56:05	59353.2	1.9	Shane	Kast	3254-10895	YSE
2021mqh	2021-05-20T10:47:01	59354.4	3.1	Faulkes-South	FLOYDS	3800-10000	GSP
2021mqh	2021-05-23T11:05:06	59357.5	6.2	Faulkes-South	FLOYDS	3800-9999	GSP
2021mqh	2021-05-29T11:35:06	59363.5	12.2	Faulkes-South	FLOYDS	3801-10001	GSP
2021mqh	2021-06-04T04:59:31	59369.2	17.9	Shane	Kast	3255-10896	YSE
2021mqh	2021-06-06T08:45:33	59371.4	20.1	Faulkes-South	FLOYDS	3501-10001	GSP
2021mqh	2021-06-20T08:51:12	59385.4	34.1	Faulkes-South	FLOYDS	3501-10000	GSP
2021ont	2021-06-04T10:23:14	59369.4	5.0	Shane	Kast	3378-10893	YSE
2021ont	2021-06-05T10:28:00	59370.4	6.0	Shane	Kast	3622-10754	Filippenko
2021ont	2021-06-06T23:25:23	59372.0	7.6	LT	SPRAT	4270-7300	TNS

Table A5 (cont'd)

SN Name	UT Date	MJD	Phase[a] (days)	Telescope	Instrument	Wavelength Range (Å)	Data Source
2021ont	2021-06-11T09:44:50	59376.4	12.0	Shane	Kast	3255-10495	YSE
2021ont	2021-06-15T09:59:25	59380.4	16.0	Shane	Kast	3505-10892	YSE
2021ont	2021-07-02T10:30:00	59397.4	33.0	Shane	Kast	3356-10493	YSE
2021ont	2021-07-03T09:22:00	59398.4	34.0	Shane	Kast	3626-10740	Filippenko
2021ont	2021-07-08T00:36:00	59403.0	38.6	NOT	ALFOSC	3503-9590	TNS
2021ont	2021-08-03T05:39:00	59429.2	64.8	Shane	Kast	3254-10894	YSE
2021ont	2021-10-16T04:06:01	59503.2	138.8	Shane	Kast	3255-10493	YSE
2021qvr	2021-06-23T00:00:00	59388.0	2.4	NOT	ALFOSC	3800-9000	YSE
2021qvr	2021-06-23T12:31:47	59388.5	2.9	Faulkes-North	FLOYDS	3500-10000	YSE
2021qvr	2021-06-24T03:21:39	59389.1	3.5	LT	SPRAT	4020-7994	TNS
2021qvr	2021-06-25T00:00:00	59390.0	4.4	NOT	ALFOSC	3800-9000	YSE
2021qvr	2021-06-25T13:32:39	59390.6	5.0	Faulkes-North	FLOYDS	3297-10178	YSE
2021qvr	2021-07-01T08:35:05	59396.4	10.8	SOAR	Goodman	4004-8985	YSE
2021qvr	2021-07-02T19:34:58	59397.8	12.2	Faulkes-South	FLOYDS	3301-10185	YSE
2021qvr	2021-07-02T11:19:30	59397.5	11.9	Shane	Kast	3505-10494	YSE
2021qvr	2021-07-04T00:00:00	59399.0	13.4	Shane	Kast	3404-9997	YSE
2021qvr	2021-07-04T16:15:14	59399.7	14.1	Faulkes-South	FLOYDS	3299-10181	YSE
2021qvr	2021-07-08T11:24:23	59403.5	17.9	Faulkes-North	FLOYDS	3295-10175	YSE
2021qvr	2021-07-08T00:00:00	59403.0	17.4	Keck	LRIS	3162-10148	YSE
2021qvr	2021-07-09T10:49:58	59404.5	18.9	Shane	Kast	3254-10893	YSE
2021qvr	2021-07-11T11:46:23	59406.5	20.9	Faulkes-North	FLOYDS	3294-10172	YSE
2021qvr	2021-07-15T10:18:48	59410.4	24.8	Shane	Kast	3254-10895	YSE
2021qvr	2021-07-29T18:50:42	59424.8	39.2	Faulkes-Soutg	FLOYDS	3296-10177	YSE
2021qvr	2021-08-06T00:00:00	59432.0	46.4	Keck	LRIS	3162-10147	YSE
2021qvr	2021-08-08T05:56:00	59434.2	48.6	Shane	Kast	3356-10693	YSE

Table A5 (cont'd)

SN Name	UT Date	MJD	Phase[a] (days)	Telescope	Instrument	Wavelength Range (Å)	Data Source
2021qvr	2021-08-19T13:11:18	59445.5	59.9	IRTF	SpeX	6883-25422	YSE
2021qvr	2021-09-05T13:07:04	59462.5	76.9	IRTF	SpeX	6882-25421	YSE
2021qvr	2021-09-23T13:37:10	59480.6	95.0	Faulkes-South	FLOYDS	3299-10180	YSE
2021qvr	2021-11-06T00:00:00	59524.0	138.4	Keck	LRIS	3162-10147	YSE
2021rhk	2021-07-02T07:17:59	59397.3	2.0	Shane	Kast	3503-10895	YSE
2021rhk	2021-07-04T07:05:09	59399.3	4.0	Shane	Kast	3254-10894	YSE
2021rhk	2021-07-07T05:04:24	59402.2	6.9	P60	SEDM	3777-9223	TNS
2021rhk	2021-07-09T05:44:00	59404.2	8.9	Shane	Kast	3256-10893	YSE
2021tyw	2021-07-30T06:28:28	59425.3	11.9	NTT	EFOSC2	3644-9239	TNS
2021tyw	2021-07-31T12:37:21	59426.5	13.1	Faulkes-North	FLOYDS	3500-9999	GSP
2021tyw	2021-08-02T11:45:00	59428.5	15.1	Shane	Kast	3624-10760	Filippenko
2021tyw	2021-08-03T13:45:36	59429.6	16.2	Faulkes-North	FLOYDS	3500-10001	GSP
2021tyw	2021-08-03T10:09:28	59429.4	16.0	Shane	Kast	3254-10893	YSE
2021tyw	2021-08-06T13:33:30	59432.6	19.2	Faulkes-North	FLOYDS	3500-10000	GSP
2021tyw	2021-08-09T13:13:02	59435.6	22.2	Faulkes-North	FLOYDS	3500-10000	GSP
2021tyw	2021-08-12T11:45:00	59438.5	25.1	Shane	Kast	3622-7857	Filippenko
2021tyw	2021-08-13T07:45:00	59439.3	25.9	Shane	Kast	3262-10895	YSE
2021tyw	2021-08-14T09:40:51	59440.4	27.0	Faulkes-North	FLOYDS	3500-10001	GSP
2021tyw	2021-08-21T11:56:01	59447.5	34.1	Faulkes-North	FLOYDS	3500-10000	GSP
2021tyw	2021-08-26T13:09:06	59452.5	39.1	Faulkes-North	FLOYDS	3500-10001	GSP
2021tyw	2021-08-26T23:59:00	59453.0	39.6	NOT	ALFOSC	3800-9000	YSE
2021tyw	2021-08-30T11:13:10	59456.5	43.1	Faulkes-North	FLOYDS	3500-10000	GSP
2021tyw	2021-09-05T07:34:59	59462.3	48.9	Faulkes-North	FLOYDS	3799-10001	GSP
2021tyw	2021-09-09T06:34:28	59466.3	52.9	Faulkes-North	FLOYDS	3500-10000	GSP
2021tyw	2021-09-12T14:59:37	59469.6	56.2	Faulkes-South	FLOYDS	3501-9999	GSP

Table A5 (cont'd)

SN Name	UT Date	MJD	Phase[a] (days)	Telescope	Instrument	Wavelength Range (Å)	Data Source
2021tyw	2021-09-22T13:29:57	59479.6	66.2	Faulkes-South	FLOYDS	3501-10000	GSP
2021tyw	2021-10-03T12:06:55	59490.5	77.1	Faulkes-South	FLOYDS	3500-10001	GSP
2021tyw	2021-10-14T10:04:46	59501.4	88.0	Faulkes-South	FLOYDS	3499-10000	GSP
2021tyw	2021-10-25T04:46:24	59512.2	98.8	Faulkes-North	FLOYDS	3799-9999	GSP
2021tyw	2021-11-05T08:51:51	59523.4	110.0	Faulkes-North	FLOYDS	3501-9999	GSP
2021tyw	2021-11-08T07:24:24	59526.3	112.9	Shane	Kast	3405-10294	YSE
2021tyw	2021-11-16T10:23:53	59534.4	121.0	Faulkes-South	FLOYDS	3501-9999	GSP
2021tyw	2021-11-27T05:38:38	59545.2	131.8	Faulkes-North	FLOYDS	3499-10001	GSP
2021tyw	2021-12-11T03:45:00	59559.2	145.8	Shane	Kast	3624-10670	Filippenko
2021ucg	2021-07-25T23:42:40	59421.0	1.4	LT	SPRAT	4020-7994	TNS
2021ucg	2021-07-28T06:27:54	59423.3	3.7	Palomar	SEDM	3777-9223	TNS
2021ucg	2021-08-01T14:10:54	59427.6	8.0	Faulkes-North	FLOYDS	3499-10001	GSP
2021ucg	2021-08-08T11:55:47	59434.5	14.9	Faulkes-North	FLOYDS	3500-9999	GSP
2021ucg	2021-08-17T11:42:40	59443.5	23.9	Faulkes-North	FLOYDS	3500-10001	GSP
2021ucg	2021-08-22T11:49:38	59448.5	28.9	Faulkes-North	FLOYDS	3499-9999	GSP
2021ucg	2021-08-27T13:02:08	59453.5	34.0	Faulkes-North	FLOYDS	3500-10001	GSP
2021ucg	2021-09-04T12:38:07	59461.5	42.0	Faulkes-North	FLOYDS	3800-10001	GSP
2021ucg	2021-09-11T09:42:33	59468.4	48.8	Faulkes-North	FLOYDS	3500-9999	GSP
2021ucg	2021-09-22T11:50:10	59479.5	59.9	Faulkes-North	FLOYDS	3500-10001	GSP
2021ucg	2021-10-03T08:41:31	59490.4	70.8	Faulkes-North	FLOYDS	3500-10000	GSP
2021ucg	2021-10-18T06:32:32	59505.3	85.7	Faulkes-North	FLOYDS	3499-9999	GSP
2021ucg	2021-10-29T06:13:17	59516.3	96.7	Faulkes-North	FLOYDS	3499-10001	GSP
2021ucg	2021-11-03T08:45:52	59521.4	101.8	Faulkes-North	FLOYDS	3500-10001	GSP
2021ucg	2021-11-14T07:36:48	59532.3	112.7	Faulkes-North	FLOYDS	3801-10000	GSP
2021ulv	2021-08-03T06:28:48	59429.3	4.6	UH88	SCAT	3403-9100	TNS

Table A5 (cont'd)

SN Name	UT Date	MJD	Phase[a] (days)	Telescope	Instrument	Wavelength Range (Å)	Data Source
2021ulv	2021-08-03T04:43:07	59429.2	4.5	Shane	Kast	3254-10892	YSE
2021ulv	2021-08-22T00:00:00	59448.0	23.3	NOT	ALFOSC	3800-9000	YSE
2021ulv	2021-09-01T04:13:49	59458.2	33.5	P60	SEDM	3777-9223	TNS
2021uoy	2021-08-03T09:42:01	59429.4	2.1	Shane	Kast	3504-10293	YSE
2021uoy	2021-08-07T00:00:00	59433.0	5.7	Palomar	DBSP	3301-9999	TNS
2021uoy	2021-08-08T10:31:48	59434.4	7.1	Shane	Kast	3504-10295	YSE
2021vaz	2021-08-06T14:34:56	59432.6	0.4	Faukes-North	FLOYDS	3499-10000	GSP
2021vaz	2021-08-08T14:11:54	59434.6	2.4	Faukes-North	FLOYDS	3500-10000	GSP
2021vaz	2021-08-09T14:34:17	59435.6	3.4	Faukes-North	FLOYDS	3499-10000	GSP
2021vaz	2021-08-19T13:58:40	59445.6	13.4	Faukes-North	FLOYDS	3499-10001	GSP
2021vaz	2021-08-25T13:53:28	59451.6	19.4	Faukes-North	FLOYDS	3499-9999	GSP
2021vaz	2021-09-05T11:48:54	59462.5	30.3	Shane	Kast	3355-9994	YSE
2021vaz	2021-09-08T12:26:45	59465.5	33.4	Faukes-North	FLOYDS	3500-9999	GSP
2021vaz	2021-09-15T12:33:37	59472.5	40.4	Faukes-North	FLOYDS	3500-10000	GSP
2021vaz	2021-09-26T12:05:46	59483.5	51.3	Shane	Kast	5451-10299	YSE
2021vaz	2021-09-26T14:16:23	59483.6	51.4	Faukes-North	FLOYDS	3499-10001	GSP
2021vaz	2021-10-11T12:57:01	59498.5	66.4	Faukes-North	FLOYDS	3500-10001	GSP
2021vaz	2021-10-22T12:21:23	59509.5	77.4	Faukes-North	FLOYDS	3500-9999	GSP
2021vaz	2021-11-02T13:45:59	59520.6	88.4	Faukes-North	FLOYDS	3500-9999	GSP
2021vaz	2021-11-16T12:10:56	59534.5	102.3	Faukes-North	FLOYDS	3500-9999	GSP
2021wvd	2021-08-26T05:34:25	59452.2	3.9	IRTF	SpeX	6884-25423	YSE
2021wvd	2021-08-26T23:36:16	59453.0	4.7	NTT	EFOSC2	3642-9237	TNS
2021wvd	2021-08-31T04:00:00	59457.2	8.9	Shane	Kast	3620-10744	Filippenko
2021wvd	2021-09-05T04:06:59	59462.2	13.9	Shane	Kast	3355-10896	YSE
2021aaqn	2021-10-07T00:00:00	59494.0	1.2	Keck	LRIS	3162-10148	YSE

Table A5 (cont'd)

SN Name	UT Date	MJD	Phase[a] (days)	Telescope	Instrument	Wavelength Range (Å)	Data Source
2021aaqn	2021-10-08T19:37:00	59495.8	3.0	Keck	DEIMOS	4550-9775	YSE
2021aaqn	2021-10-10T08:07:11	59497.3	4.5	Shane	Kast	3539-10095	YSE
2021aaqn	2021-10-11T02:16:00	59498.1	5.3	NOT	ALFOSC	3800-9000	YSE
2021aaqn	2021-10-16T11:07:54	59503.5	10.7	Shane	Kast	3504-10496	YSE
2021aaqn	2021-11-06T00:00:00	59524.0	31.2	Keck	LRIS	3162-10147	YSE
2021aaqn	2021-11-25T06:03:59	59543.3	50.5	Shane	Kast	3505-10493	YSE
2021aaqn	2021-12-06T06:42:26	59554.3	61.5	Shane	Kast	3254-10895	YSE
2021aaqn	2021-12-18T03:00:00	59566.1	73.3	SOAR	Goodman	4694-8897	YSE
2021adly	2021-11-06T00:00:00	59524.0	1.5	Keck	LRIS	3162-10148	YSE
2021adly	2021-11-08T11:40:05	59526.5	4.0	Shane	Kast	3504-9994	YSE
2021adly	2021-11-12T11:50:00	59530.5	8.0	Shane	Kast	3624-10620	Filippenko
2021adly	2021-11-13T00:00:00	59531.0	8.5	NOT	ALFOSC	3800-9000	YSE
2021adly	2021-12-06T10:23:38	59554.4	31.9	Shane	Kast	3305-10794	YSE
2021afkk	2021-11-28T14:09:36	59546.6	5.7	LJT	G3	3494-8771	Zhang
2021afkk	2021-12-06T04:52:31	59554.2	13.3	Shane	Kast	3254-10892	YSE
2021afkk	2021-12-08T14:00:00	59556.6	15.7	LJT	G3	3491-8768	Zhang
2021afkk	2021-12-21T14:00:00	59569.6	28.7	LJT	G3	3487-8744	Zhang
2021afkk	2021-12-29T00:00:00	59577.0	36.1	NOT	ALFOSC	3800-9000	YSE
2021afkk	2022-01-10T07:49:33	59589.3	48.4	IRTF	SpeX	6905-25706	YSE
2021afkk	2022-01-26T04:30:07	59605.2	64.3	Shane	Kast	3505-10492	YSE
2022dml	2022-02-28T12:21:35	59638.5	4.5	Shane	Kast	3505-10895	YSE
2022dml	2022-03-01T13:48:54	59639.6	5.6	Faulkes-North	FLOYDS	3500-10000	GSP
2022dml	2022-03-03T14:31:54	59641.6	7.6	Faulkes-North	FLOYDS	3499-10001	GSP
2022dml	2022-03-06T12:02:53	59644.5	10.5	Faulkes-North	FLOYDS	3500-10000	GSP
2022dml	2022-03-10T11:25:15	59648.5	14.5	Faulkes-North	FLOYDS	3500-10001	GSP

Table A5 (cont'd)

SN Name	UT Date	MJD	Phase[a] (days)	Telescope	Instrument	Wavelength Range (Å)	Data Source
2022dml	2022-03-12T14:31:08	59650.6	16.6	Faulkes-North	FLOYDS	3500-10000	GSP
2022dml	2022-03-15T12:20:13	59653.5	19.5	Faulkes-North	FLOYDS	3500-10000	GSP
2022dml	2022-03-19T11:33:50	59657.5	23.5	Faulkes-North	FLOYDS	3500-10000	GSP
2022dml	2022-03-24T10:30:30	59662.4	28.4	Shane	Kast	3620-10752	Filippenko
2022dml	2022-03-25T12:13:21	59663.5	29.5	Shane	Kast	3580-10050	TReX
2022dml	2022-04-02T16:37:27	59671.7	37.7	Faulkes-South	FLOYDS	3500-9999	GSP
2022dml	2022-04-02T09:37:31	59671.4	37.4	Shane	Kast	3907-10295	YSE
2022dml	2022-04-10T14:14:22	59679.6	45.6	Faulkes-North	FLOYDS	3500-10000	GSP
2022dml	2022-04-19T14:00:07	59688.6	54.6	Faulkes-North	FLOYDS	3500-10000	GSP
2022dml	2022-05-12T09:06:25	59711.4	77.4	Faulkes-North	FLOYDS	3500-10000	GSP
2022dml	2022-05-26T14:29:02	59725.6	91.6	Faulkes-South	FLOYDS	3800-9999	GSP
2022ffg	2022-03-28T06:58:51	59666.3	2.5	Faulkes-North	FLOYDS	3500-10000	GSP
2022ffg	2022-03-29T10:33:46	59667.4	3.6	Faulkes-North	FLOYDS	3500-10001	GSP
2022ffg	2022-03-29T00:00:00	59667.0	3.2	NOT	ALFOSC	3800-9000	YSE
2022ffg	2022-03-30T04:50:18	59668.2	4.4	Shane	Kast	3604-10094	YSE
2022ffg	2022-03-31T06:00:00	59669.2	5.4	Keck	LRIS	3063-10296	TReX
2022ffg	2022-04-02T04:06:12	59671.2	7.3	Shane	Kast	3253-10394	YSE
2022ffg	2022-04-04T10:58:01	59673.5	9.6	Faulkes-South	FLOYDS	3500-9999	GSP
2022ffg	2022-04-05T06:28:33	59674.3	10.4	Shane	Kast	3654-10193	TReX
2022ffg	2022-04-05T11:12:37	59674.5	10.6	Faulkes-South	FLOYDS	3500-10000	GSP
2022ffg	2022-04-05T06:02:53	59674.3	10.4	Shane	Kast	5771-7127	TReX
2022ffg	2022-04-07T03:34:25	59676.1	12.3	Shane	Kast	3354-10093	YSE
2022ffg	2022-04-14T09:19:32	59683.4	19.6	Faulkes-North	FLOYDS	3500-9999	GSP
2022ffg	2022-04-17T10:41:49	59686.4	22.6	Faulkes-South	FLOYDS	3750-10001	GSP
2022ffg	2022-04-19T00:00:00	59688.0	24.2	NOT	ALFOSC	3800-9000	YSE

Table A5 (cont'd)

SN Name	UT Date	MJD	Phase[a] (days)	Telescope	Instrument	Wavelength Range (Å)	Data Source
2022ffg	2022-04-20T10:14:39	59689.4	25.6	Faulkes-South	FLOYDS	3500-10000	GSP
2022ffg	2022-04-25T09:21:56	59694.4	30.6	Faulkes-North	FLOYDS	3500-10000	GSP
2022ffg	2022-04-27T04:06:53	59696.2	32.3	Shane	Kast	3409-10194	YSE
2022ffg	2022-04-30T03:55:11	59699.2	35.3	Shane	Kast	3584-10194	TReX
2022ffg	2022-05-01T09:52:25	59700.4	36.6	Faulkes-South	FLOYDS	3499-10000	GSP
2022ffg	2022-05-04T05:41:41	59703.2	39.4	Shane	Kast	3253-9994	YSE
2022ffg	2022-05-22T04:54:25	59721.2	57.4	Shane	Kast	3584-9008	TReX
2022ffg	2022-05-27T04:57:04	59726.2	62.4	Shane	Kast	3453-10094	YSE
2022ffg	2022-05-27T06:10:29	59726.3	62.4	Faulkes-North	FLOYDS	3500-10000	GSP
2022ffg	2022-06-26T04:39:29	59756.2	92.4	Shane	Kast	3578-10096	TReX
2022frq	2022-04-03T10:48:57	59672.5	1.6	Faukes-North	FLOYDS	3500-10000	GSP
2022frq	2022-04-03T11:00:00	59672.5	1.6	Shane	Kast	3620-10744	Filippenko
2022frq	2022-04-04T16:20:12	59673.7	2.8	Faukes-South	FLOYDS	3499-10000	GSP
2022frq	2022-04-07T09:10:55	59676.4	5.5	Faukes-North	FLOYDS	3499-10001	GSP
2022frq	2022-04-08T11:37:40	59677.5	6.6	Faukes-North	FLOYDS	3499-10000	GSP
2022frq	2022-04-11T15:25:02	59680.6	9.7	Faukes-South	FLOYDS	3499-9999	GSP
2022frq	2022-04-18T14:12:11	59687.6	16.7	Faukes-South	FLOYDS	3500-10001	GSP
2022frq	2022-04-23T11:10:40	59692.5	21.6	Faukes-North	FLOYDS	3500-10000	GSP
2022frq	2022-05-02T13:06:38	59701.5	30.6	Faukes-South	FLOYDS	3501-10000	GSP
2022frq	2022-05-10T09:25:04	59709.4	38.5	Faukes-North	FLOYDS	3499-10001	GSP
2022frq	2022-05-21T08:23:38	59720.3	49.4	Faukes-North	FLOYDS	3500-9999	GSP
2022frq	2022-06-14T11:45:41	59744.5	73.6	Faukes-South	FLOYDS	3500-10000	GSP
2022fuc	2022-04-03T03:17:37	59672.1	0.7	Palomar	SEDM	3777-9223	TNS
2022fuc	2022-04-03T06:48:57	59672.3	0.9	Gemini-North	GMOS	3623-6873	TNS
2022fuc	2022-04-05T12:04:22	59674.5	3.1	Shane	Kast	3574-10196	YSE

Table A5 (cont'd)

SN Name	UT Date	MJD	Phase[a] (days)	Telescope	Instrument	Wavelength Range (Å)	Data Source
2022fuc	2022-04-07T06:53:50	59676.3	4.9	Shane	Kast	3511-9994	YSE
2022fuc	2022-04-09T06:35:56	59678.3	6.9	Faukes-North	FLOYDS	3500-10000	GSP
2022fuc	2022-04-12T10:47:50	59681.4	10.0	Faukes-North	FLOYDS	3500-10000	GSP
2022fuc	2022-04-20T11:14:33	59689.5	18.1	Faukes-North	FLOYDS	3500-10000	GSP
2022fuc	2022-04-23T12:19:53	59692.5	21.1	Faukes-North	FLOYDS	3500-10001	GSP
2022fuc	2022-04-30T08:48:51	59699.4	28.0	Shane	Kast	3564-10296	YSE
2022fuc	2022-05-13T10:28:12	59712.4	41.0	Faukes-North	FLOYDS	3500-10000	GSP
2022fuc	2022-05-22T06:59:32	59721.3	49.9	Shane	Kast	3604-10096	TReX
2022fuc	2022-07-04T06:18:02	59764.3	92.9	Shane	Kast	3554-10494	TReX
2022fuc	2022-07-08T07:15:22	59768.3	96.9	Faukes-North	FLOYDS	3500-9999	GSP
2022ibv	2022-04-23T07:55:48	59692.3	1.8	Gemini-North	GMOS	5301-9000	YSE
2022ibv	2022-04-24T08:00:00	59693.3	2.8	Gemini-South	GMOS	4101-9467	YSE
2022ibv	2022-05-03T02:29:57	59702.1	11.6	SOAR	Goodman	3950-6924	YSE
2022inn	2022-04-27T06:57:34	59696.3	1.0	Palomar	SEDM	3777-9223	TNS
2022inn	2022-04-29T00:00:00	59698.0	2.7	Keck	LRIS	3153-7041	Filippenko
2022inn	2022-04-30T07:45:35	59699.3	4.1	Shane	Kast	3564-10192	TReX
2022inn	2022-05-27T04:51:13	59726.2	30.9	Palomar	SEDM	3777-9223	TNS
2022jox	2022-05-09T6:31:12	59708.3	1.4	Faulkes-North	FLOYDS	3201-9999	GSP
2022jox	2022-05-09T20:11:12	59708.8	1.9	SALT	SALT	3496-7256	GSP
2022jox	2022-05-12T20:03:23	59711.8	4.9	SALT	SALT	3495-7255	GSP
2022jox	2022-05-14T6:53:59	59713.3	6.4	Faulkes-North	FLOYDS	3500-10000	GSP
2022jox	2022-05-16T12:38:35	59715.5	8.6	Faulkes-South	FLOYDS	3799-10000	GSP
2022jox	2022-05-18T9:45:21	59717.4	10.5	Faulkes-South	FLOYDS	3500-10001	GSP
2022jox	2022-05-24T1:25:18	59723.1	16.1	SOAR	Goodman	4373-7026	GSP
2022jox	2022-05-24T11:39:50	59723.5	16.6	Faulkes-South	FLOYDS	3500-10000	GSP

Table A5 (cont'd)

SN Name	UT Date	MJD	Phase[a] (days)	Telescope	Instrument	Wavelength Range (Å)	Data Source
2022jox	2022-06-01T18:35:28	59731.8	24.9	SALT	SALT	3495-7254	GSP
2022jox	2022-06-05T18:24:57	59735.8	28.8	SALT	SALT	3495-7254	GSP
2022jox	2022-06-05T23:39:38	59736.0	29.1	SOAR	Goodman	4387-7027	GSP
2022jox	2022-06-07T18:27:05	59737.8	30.8	SALT	SALT	3495-7254	GSP
2022jox	2022-06-13T10:26:57	59743.4	36.5	Faulkes-South	FLOYDS	3500-10001	GSP
2022jox	2022-06-23T9:43:59	59753.4	46.5	Faulkes-South	FLOYDS	3800-10001	GSP
2022jzc	2022-05-16T06:24:59	59715.3	1.0	Palomar	SEDM	3777-9223	TNS
2022jzc	2022-05-17T10:17:10	59716.4	2.1	Faukes-North	FLOYDS	3500-10001	GSP
2022jzc	2022-05-17T00:00:00	59716.0	1.7	Xinglong	BFOSC	3871-8833	X.Wang
2022jzc	2022-05-22T06:21:34	59721.3	7.0	Shane	Kast	3579-10194	TReX
2022jzc	2022-05-23T00:00:00	59722.0	7.7	Xinglong	BFOSC	3895-8844	X.Wang
2022jzc	2022-05-23T08:02:24	59722.3	8.0	Shane	Kast	3632-10734	Filippenko
2022jzc	2022-06-26T05:48:01	59756.2	42.0	Shane	Kast	3603-10194	TReX
2022jzc	2022-07-04T04:37:24	59764.2	49.9	Shane	Kast	3551-5549	TReX
2022jzc	2022-07-08T06:06:53	59768.3	54.0	Faukes-North	FLOYDS	3500-10001	GSP
2022jzc	2022-07-09T06:21:21	59769.3	55.0	Faukes-North	FLOYDS	3501-10000	GSP
2022jzc	2022-07-20T04:50:55	59780.2	65.9	Shane	Kast	3603-10194	TReX
2022jzc	2022-07-31T04:37:17	59791.2	76.9	Shane	Kast	3573-9995	TReX
2022ovb	2022-07-14T23:40:33	59775.0	1.5	LT	SPRAT	4020-7994	TNS
2022ovb	2022-07-18T02:07:33	59778.1	4.6	LT	SPRAT	4020-7994	TNS
2022ovb	2022-08-07T11:10:48	59798.5	25.0	Shane	Kast	3254-10895	YSE
2022ovb	2022-08-27T07:22:06	59818.3	44.9	Shane	Kast	3254-10894	YSE
2022ovb	2022-09-24T06:30:27	59846.3	72.8	Shane	Kast	3353-9995	YSE
2022ovb	2022-11-04T05:50:33	59887.2	113.8	Shane	Kast	5602-9999	YSE
2022pgf	2022-07-23T07:15:29	59783.3	1.3	Shane	Kast	3604-9646	TReX

Table A5 (cont'd)

SN Name	UT Date	MJD	Phase[a] (days)	Telescope	Instrument	Wavelength Range (Å)	Data Source
2022pgf	2022-07-24T07:48:36	59784.3	2.3	Shane	Kast	3254-10742	YSE
2022pgf	2022-07-27T06:30:00	59787.3	5.3	Shane	Kast	3500-11100	Filippenko
2022pgf	2022-07-28T06:31:52	59788.3	6.3	Shane	Kast	3304-10743	YSE
2022pgf	2022-07-29T07:50:00	59789.3	7.3	Shane	Kast	3622-10740	Filippenko
2022pgf	2022-07-31T07:00:00	59791.3	9.3	Shane	Kast	3651-10098	YSE
2022pgf	2022-07-31T07:00:00	59791.3	9.3	Shane	Kast	5582-6940	TReX
2022pgf	2022-08-01T06:50:00	59792.3	10.3	Shane	Kast	3624-10742	Filippenko
2022pgf	2022-08-02T07:38:23	59793.3	11.3	Shane	Kast	3304-10896	YSE
2022pgf	2022-08-05T06:50:00	59796.3	14.3	Shane	Kast	3624-10748	Filippenko
2022pgf	2022-08-06T04:58:59	59797.2	15.2	Shane	Kast	3583-10195	TReX
2022pgf	2022-08-06T05:16:48	59797.2	15.2	Shane	Kast	5585-6942	TReX
2022pgf	2022-08-07T06:59:47	59798.3	16.3	Shane	Kast	3254-10794	YSE
2022pgf	2022-08-18T04:17:18	59809.2	27.2	Shane	Kast	3583-10195	TReX
2022pgf	2022-08-18T04:48:00	59809.2	27.2	Shane	Kast	5591-7264	TReX
2022pgf	2022-08-19T06:50:00	59810.3	28.3	Shane	Kast	3622-10748	Filippenko
2022pgf	2022-08-22T06:50:00	59813.3	31.3	Shane	Kast	3622-10746	Filippenko
2022pgf	2022-09-02T04:01:20	59824.2	42.2	Shane	Kast	3584-10494	TReX
2022pgf	2022-09-24T03:01:01	59846.1	64.1	Shane	Kast	3453-10145	YSE
2022pgf	2022-09-25T03:30:00	59847.1	65.1	Shane	Kast	3622-10754	Filippenko
2022pgf	2022-10-04T03:10:00	59856.1	74.1	Shane	Kast	3620-10762	Filippenko
2022prv	2022-07-28T05:42:59	59788.2	7.5	Shane	Kast	3255-10896	YSE
2022prv	2022-08-02T07:18:11	59793.3	12.6	Shane	Kast	3255-10894	YSE
2022prv	2022-08-07T06:23:52	59798.3	17.5	Shane	Kast	3254-10895	YSE
2022prv	2022-09-24T03:29:34	59846.1	65.4	Shane	Kast	3504-9995	YSE
2022prv	2022-09-28T03:00:00	59850.1	69.4	Shane	Kast	3622-10744	Filippenko

Table A5 (cont'd)

SN Name	UT Date	MJD	Phase[a] (days)	Telescope	Instrument	Wavelength Range (Å)	Data Source
2022prv	2022-10-05T02:42:49	59857.1	76.4	Shane	Kast	3504-10295	YSE

[a]Relative to first light.

Chapter 9

Supplementary Figures

This chapter includes supplementary figures associated with Chapter 8.

9.1 Chapter 8 Supplementary Figures

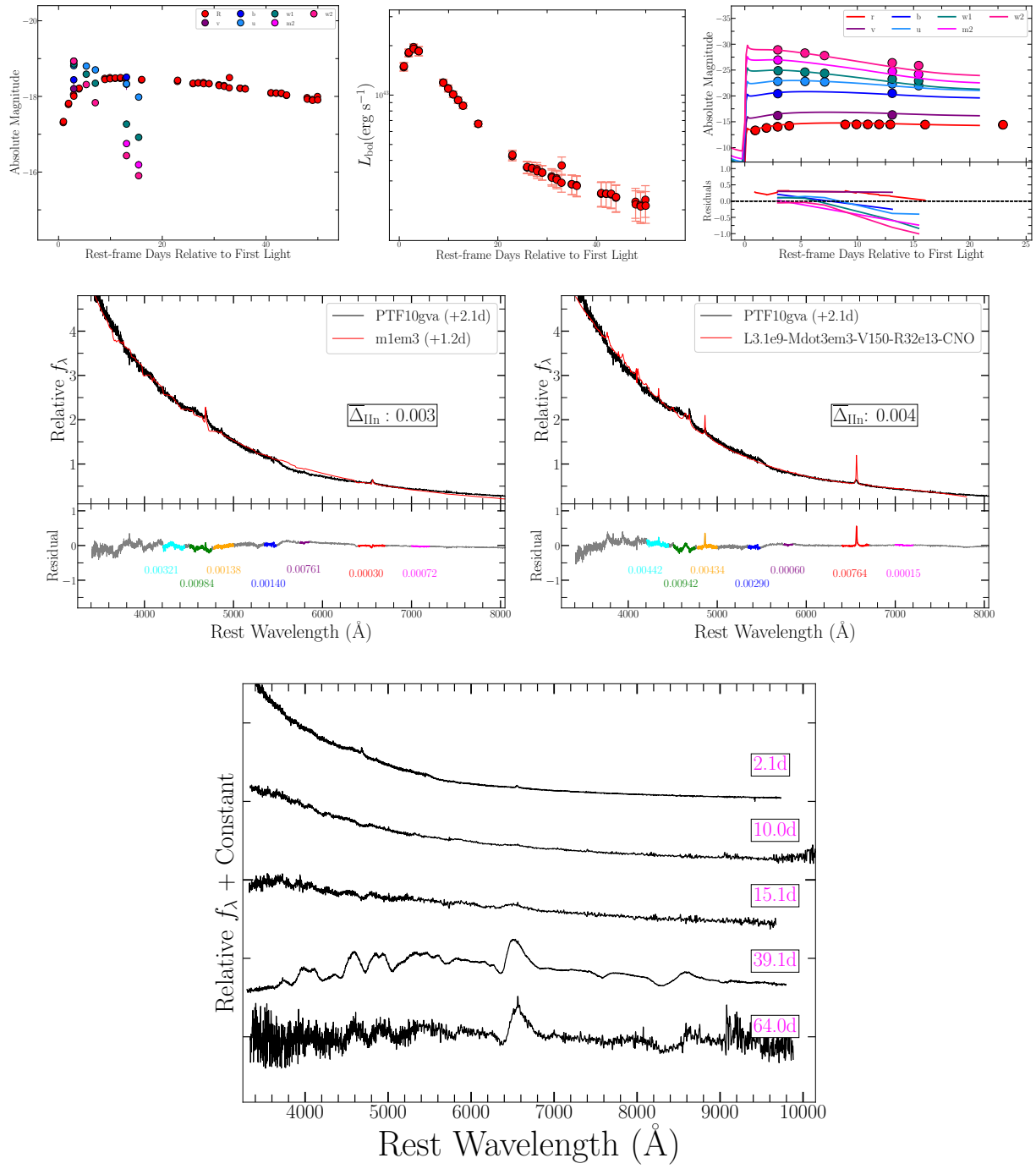

Figure 9.1 (a) PTF10gva (gold): (a) Multi-color light curves, (b) UVOIR bolometric light curve, (c) best fit multi-color light curve model from Haynie & Piro (2021), (d) best fit spectral model from `CMFGEN` grid, (e) best fit spectral model from Boian & Groh (2020) grid, and (f) spectral series. Spectra and optical photometry are from Khazov et al. (2016). UV photometry was re-reduced with template subtraction.

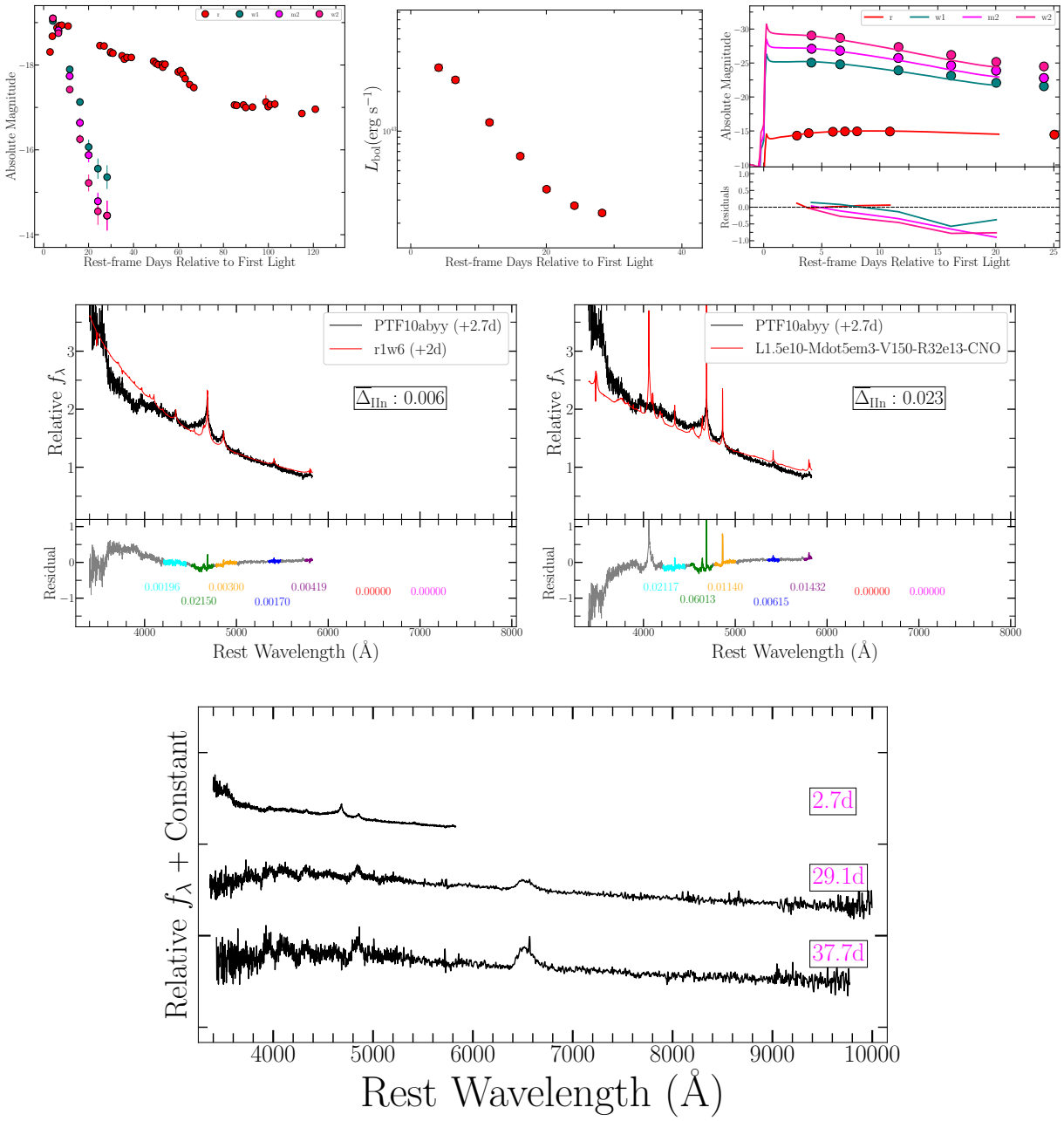

Figure 9.2 PTF10abyy (silver): (a) Multi-color light curves, (b) UVOIR bolometric light curve, (c) best fit multi-color light curve model from Haynie & Piro (2021), (d) best fit spectral model from `CMFGEN` grid, (e) best fit spectral model from Boian & Groh (2020) grid, and (f) spectral series. Spectra and optical photometry are from Khazov et al. (2016). UV photometry was re-reduced with template subtraction.

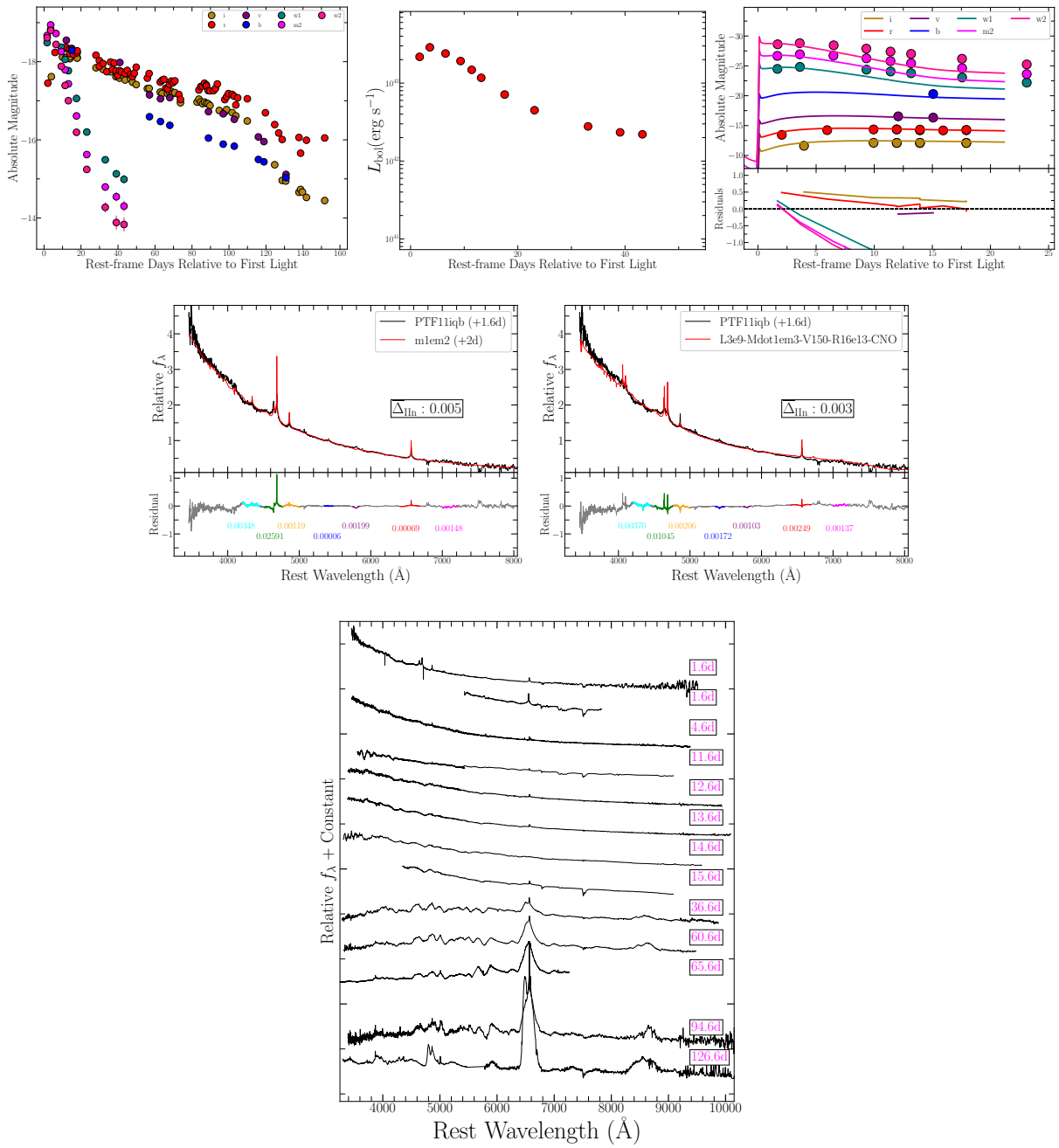

Figure 9.3 (a) PTF11iqb (gold): (a) Multi-color light curves, (b) UVOIR bolometric light curve, (c) best fit multi-color light curve model from Haynie & Piro (2021), (d) best fit spectral model from `CMFGEN` grid, (e) best fit spectral model from Boian & Groh (2020) grid, and (f) spectral series. Spectra and optical photometry are from Smith et al. (2015). UV photometry was re-reduced with template subtraction.

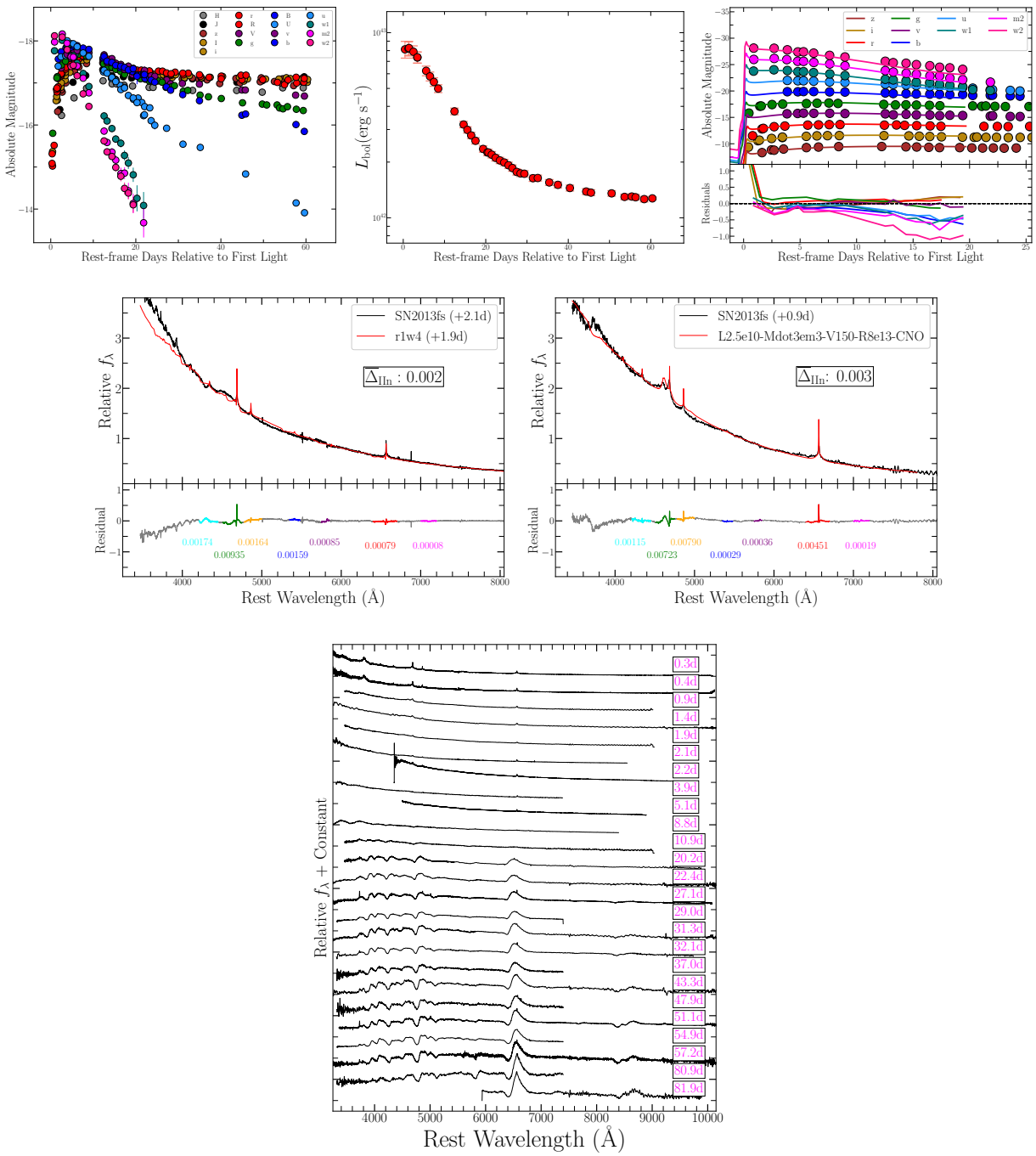

Figure 9.4 (a) SN 2013fs (gold): (a) Multi-color light curves, (b) UVOIR bolometric light curve, (c) best fit multi-color light curve model from Haynie & Piro (2021), (d) best fit spectral model from `CMFGEN` grid, (e) best fit spectral model from Boian & Groh (2020) grid, and (f) spectral series. Spectra and optical photometry are from Yaron et al. (2017). UV photometry was re-reduced with template subtraction.

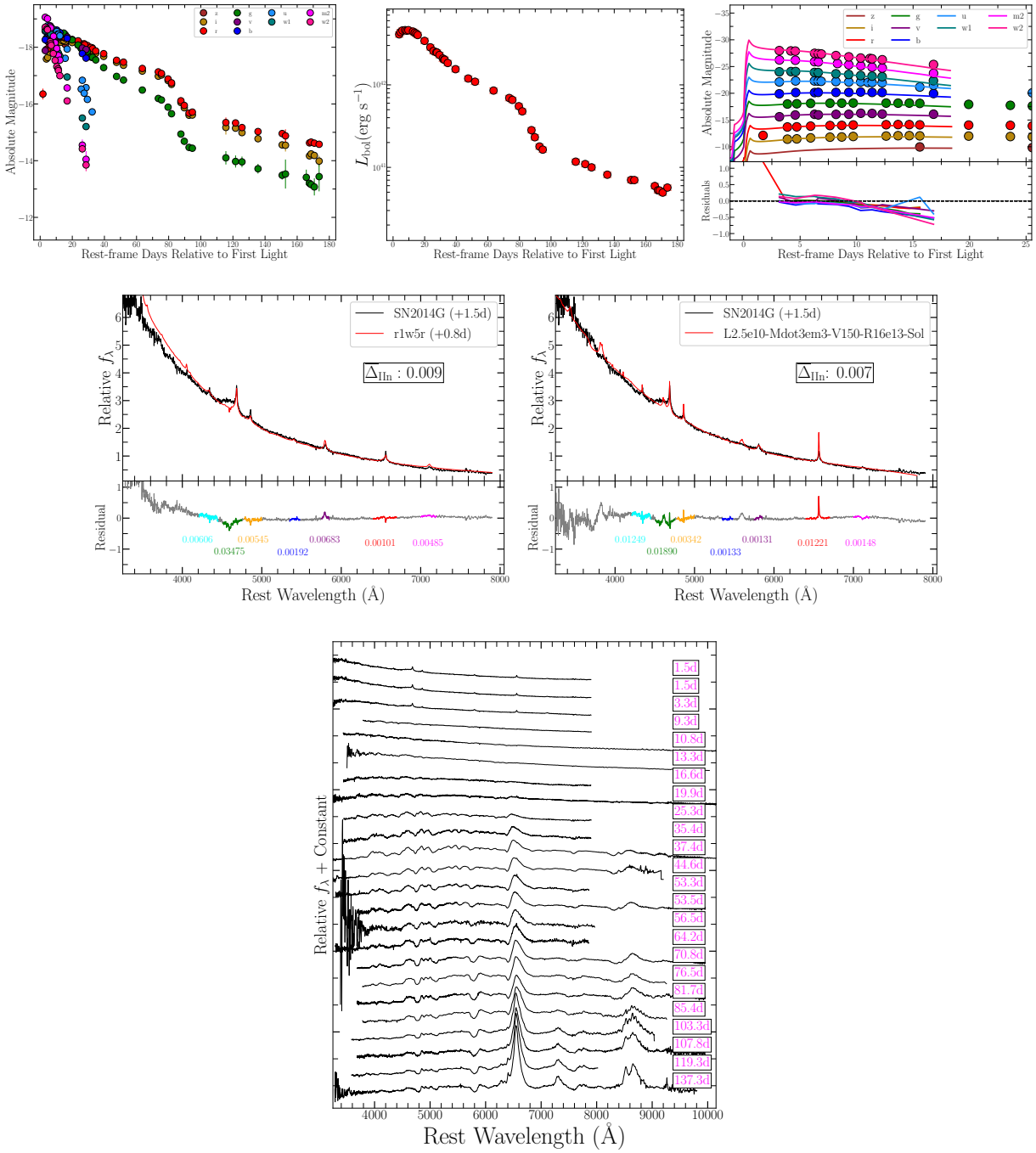

Figure 9.5 (a) SN 2014G (silver): (a) Multi-color light curves, (b) UVOIR bolometric light curve, (c) best fit multi-color light curve model from Haynie & Piro (2021), (d) best fit spectral model from `CMFGEN` grid, (e) best fit spectral model from Boian & Groh (2020) grid, and (f) spectral series. Spectra and optical photometry are from Terreran et al. (2016). UV photometry was re-reduced with template subtraction.

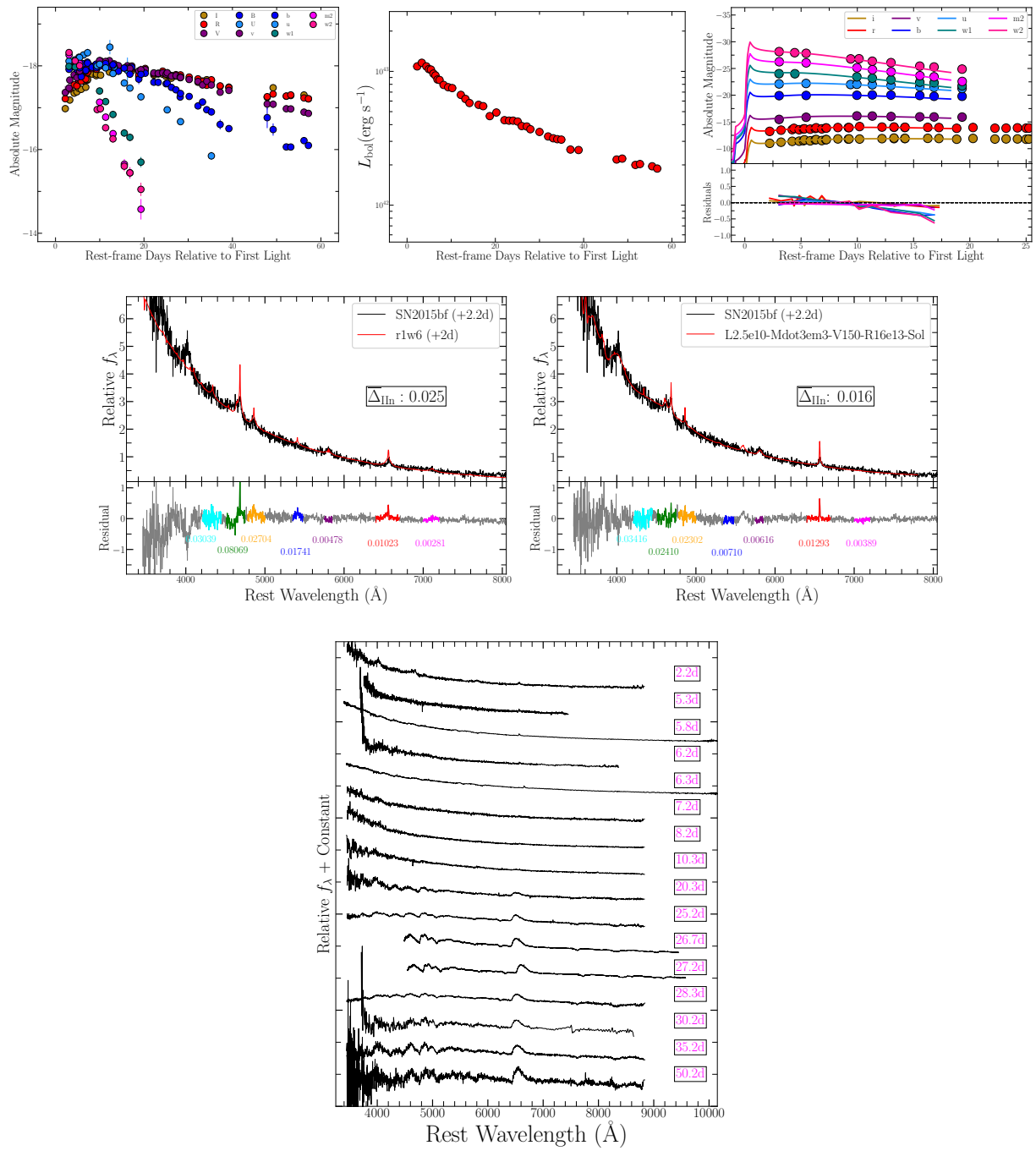

Figure 9.6 (a) SN 2015bf (silver): (a) Multi-color light curves, (b) UVOIR bolometric light curve, (c) best fit multi-color light curve model from Haynie & Piro (2021), (d) best fit spectral model from `CMFGEN` grid, (e) best fit spectral model from Boian & Groh (2020) grid, and (f) spectral series. Spectra and optical photometry are from Lin et al. (2021). UV photometry was re-reduced with template subtraction.

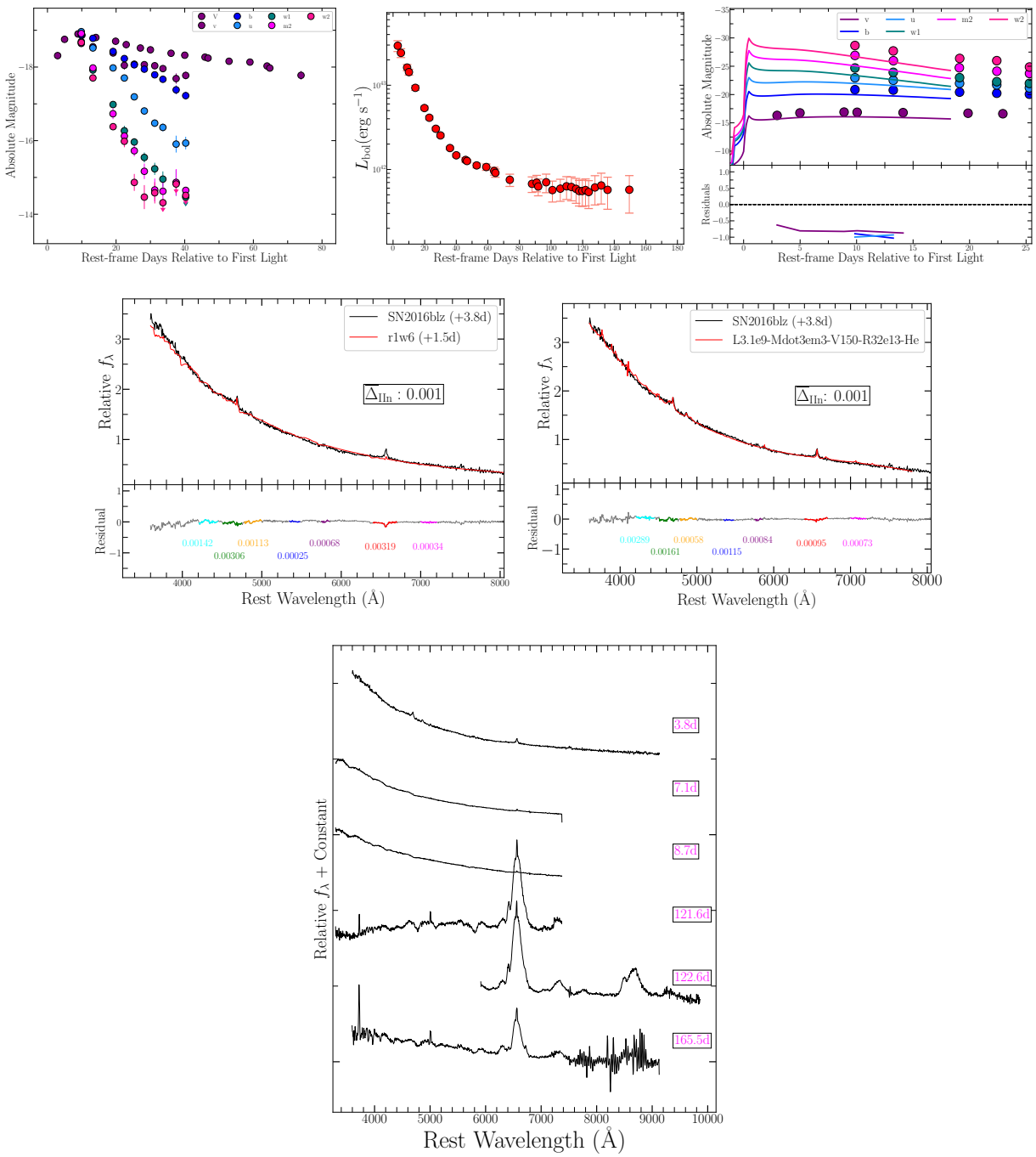

Figure 9.7 (a) SN 2016blz (silver): (a) Multi-color light curves, (b) UVOIR bolometric light curve, (c) best fit multi-color light curve model from Haynie & Piro (2021), (d) best fit spectral model from `CMFGEN` grid, (e) best fit spectral model from Boian & Groh (2020) grid, and (f) spectral series. Spectra and optical photometry are from Lin et al. (2021). UV photometry was re-reduced with template subtraction.

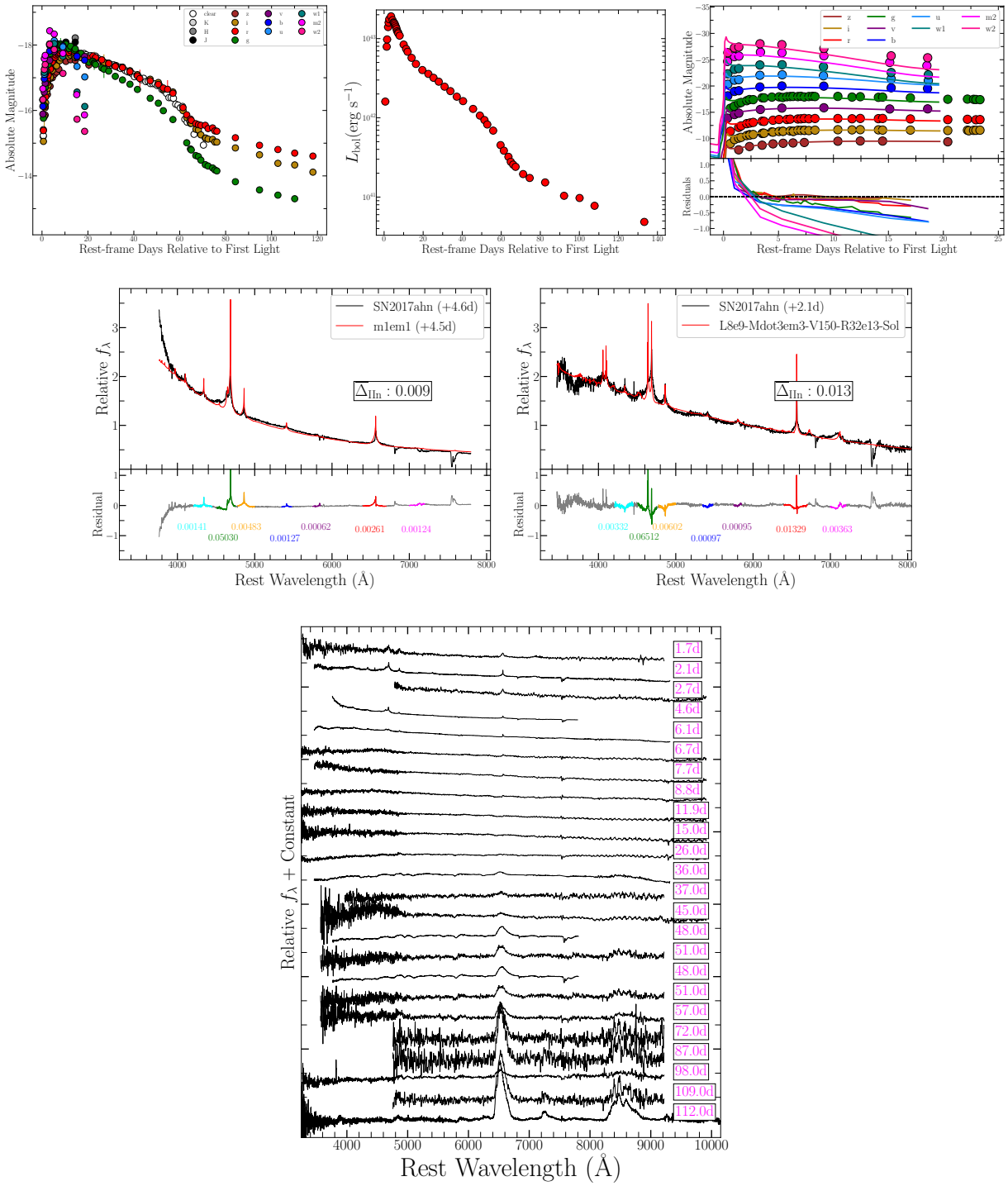

Figure 9.8 (a) SN 2017ahn (gold): (a) Multi-color light curves, (b) UVOIR bolometric light curve, (c) best fit multi-color light curve model from Haynie & Piro (2021), (d) best fit spectral model from `CMFGEN` grid, (e) best fit spectral model from Boian & Groh (2020) grid, and (f) spectral series. Spectra and optical photometry are from Tartaglia et al. (2021). UV photometry was re-reduced with template subtraction.

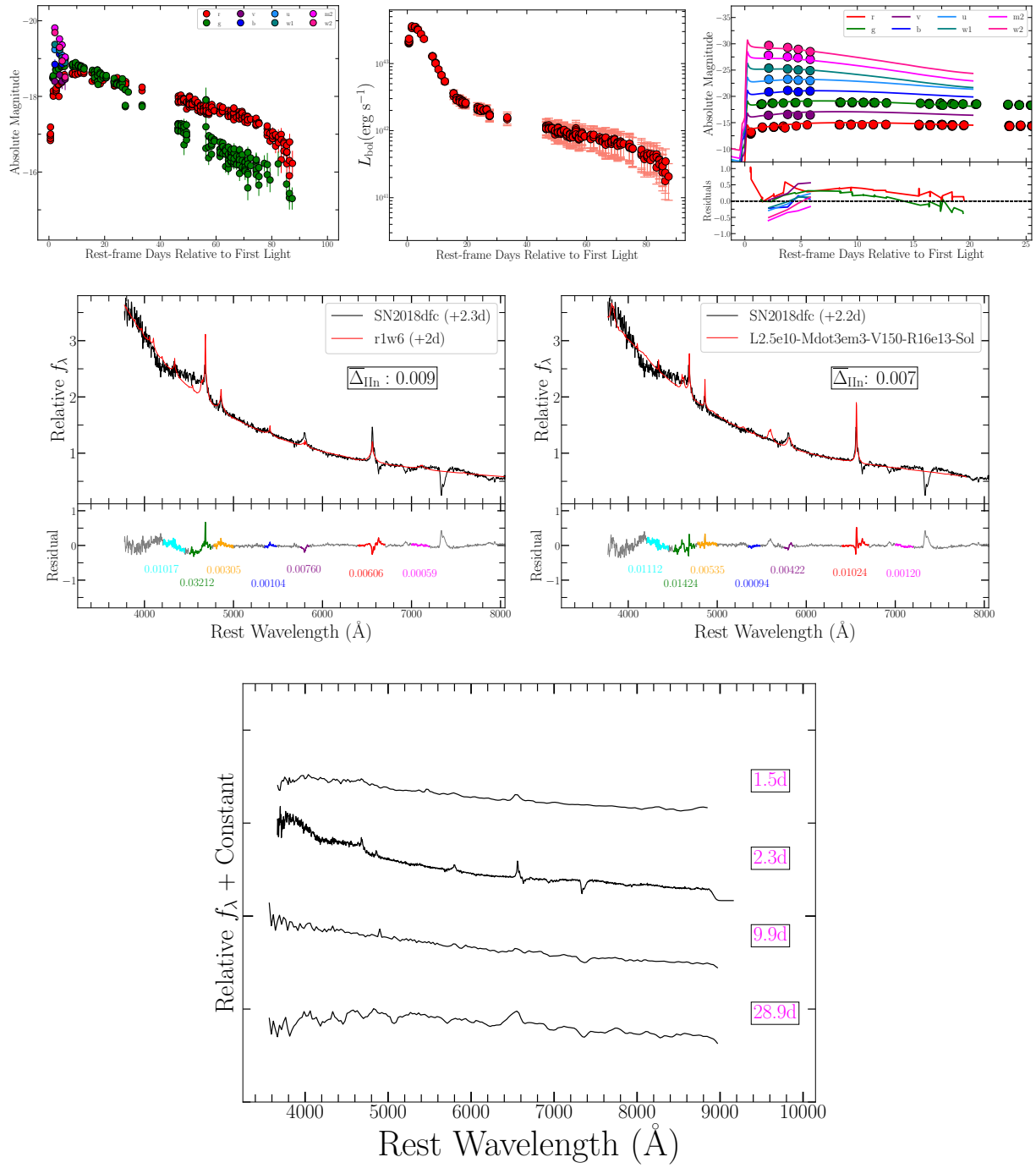

Figure 9.9 (a) SN 2018dfc (gold): (a) Multi-color light curves, (b) UVOIR bolometric light curve, (c) best fit multi-color light curve model from Haynie & Piro (2021), (d) best fit spectral model from `CMFGEN` grid, (e) best fit spectral model from Boian & Groh (2020) grid, and (f) spectral series. Spectra and optical photometry are from Bruch et al. (2021b). UV photometry was re-reduced with template subtraction.

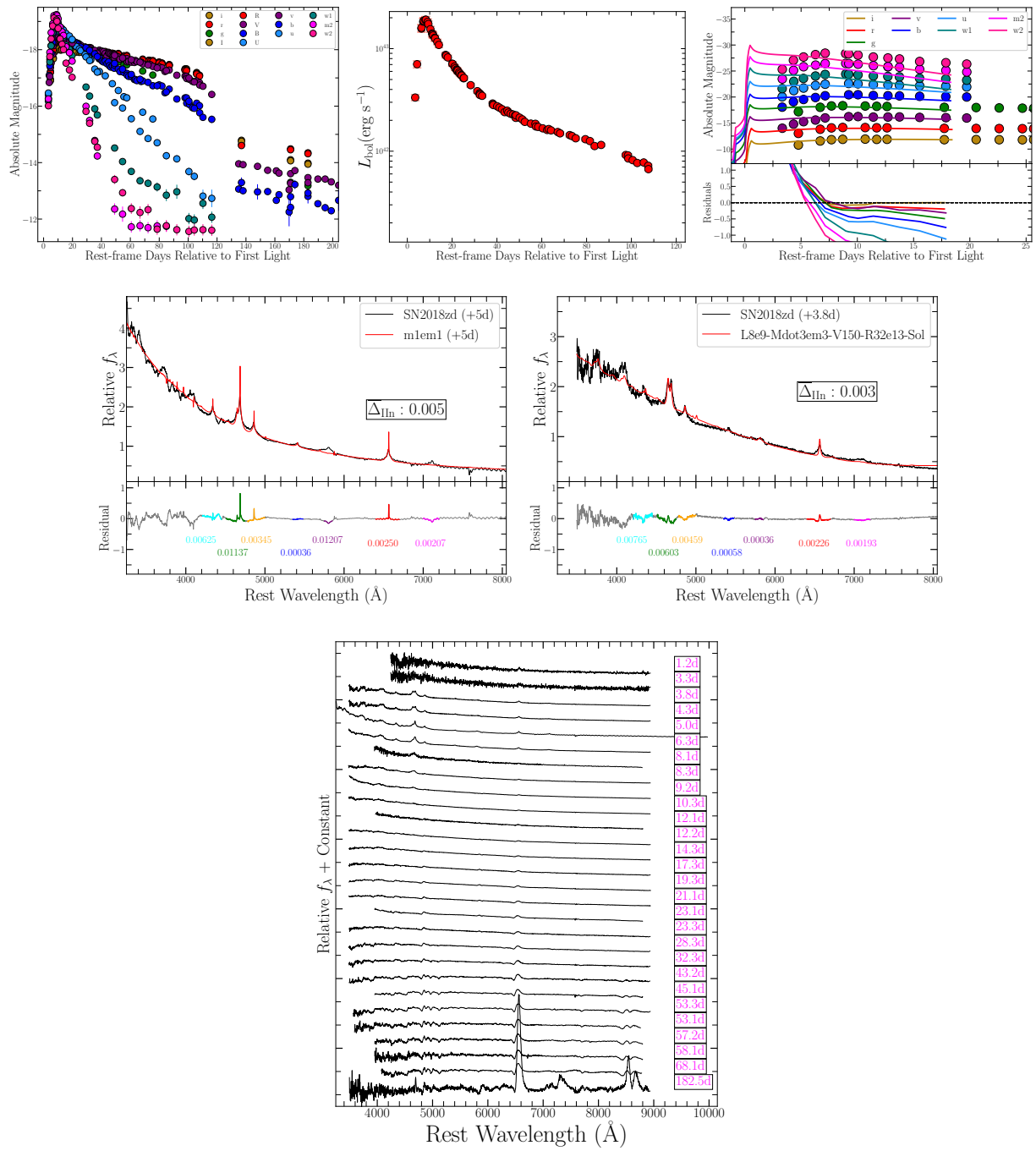

Figure 9.10 (a) SN 2018zd (gold): (a) Multi-color light curves, (b) UVOIR bolometric light curve, (c) best fit multi-color light curve model from Haynie & Piro (2021), (d) best fit spectral model from `CMFGEN` grid, (e) best fit spectral model from Boian & Groh (2020) grid, and (f) spectral series. Spectra and optical photometry are from Zhang et al. (2020). UV photometry was re-reduced with template subtraction.

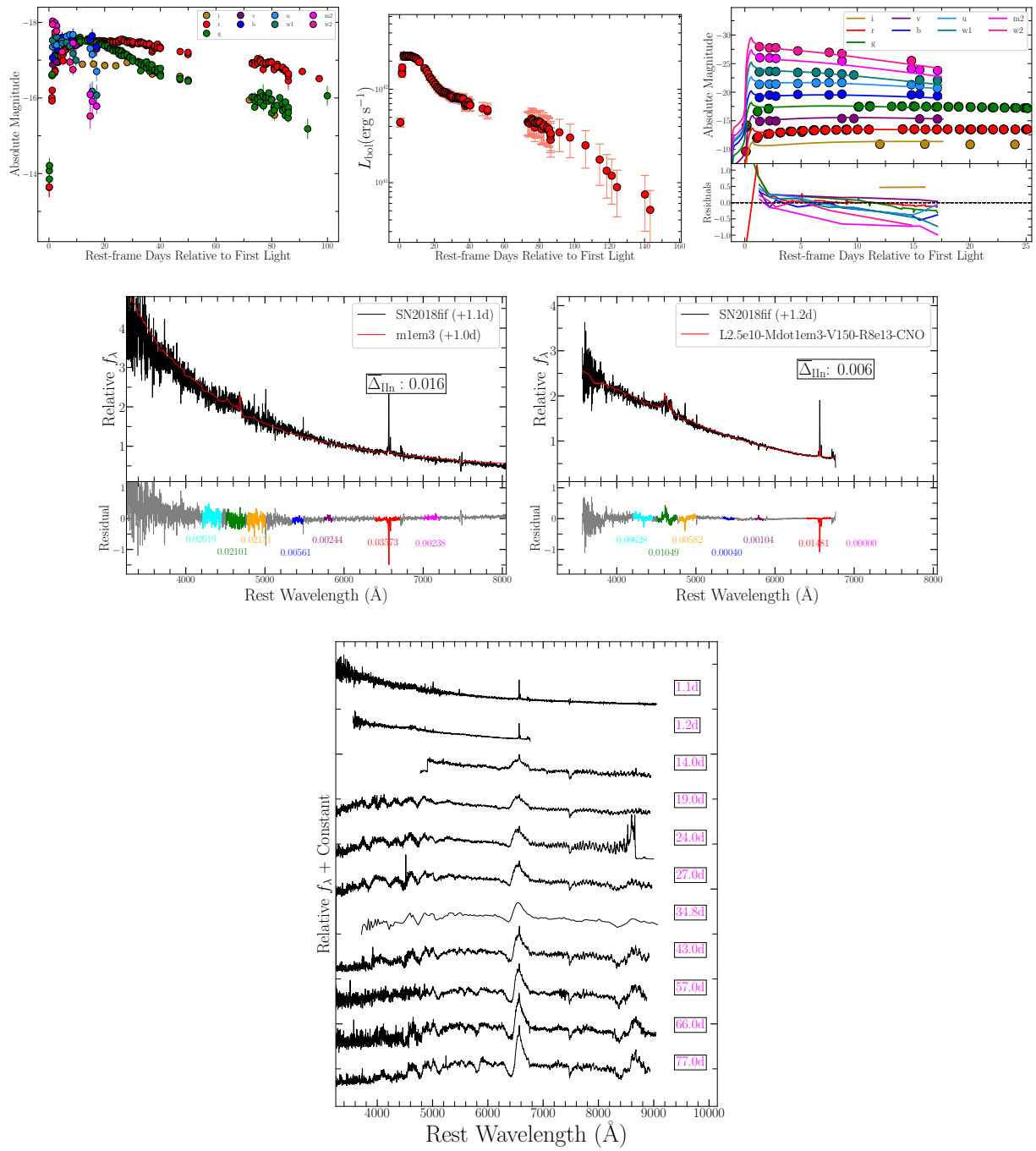

Figure 9.11 (a) SN 2018fif (gold): (a) Multi-color light curves, (b) UVOIR bolometric light curve, (c) best fit multi-color light curve model from Haynie & Piro (2021), (d) best fit spectral model from `CMFGEN` grid, (e) best fit spectral model from Boian & Groh (2020) grid, and (f) spectral series. Spectra and optical photometry are from Soumagnac et al. (2020). UV photometry was re-reduced with template subtraction.

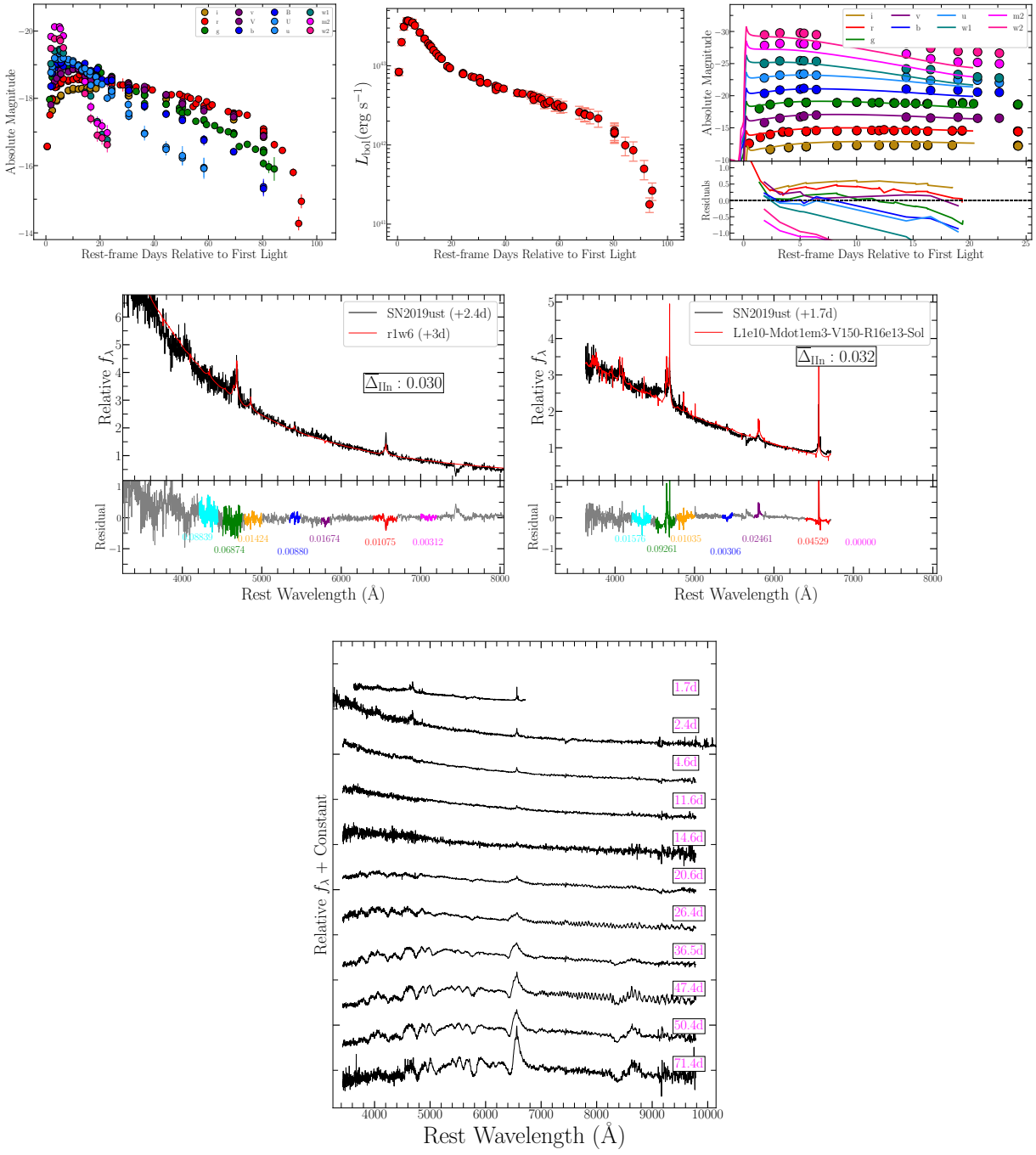

Figure 9.12 (a) SN 2019ust (gold): (a) Multi-color light curves, (b) UVOIR bolometric light curve, (c) best fit multi-color light curve model from Haynie & Piro (2021), (d) best fit spectral model from `CMFGEN` grid, (e) best fit spectral model from Boian & Groh (2020) grid, and (f) spectral series.

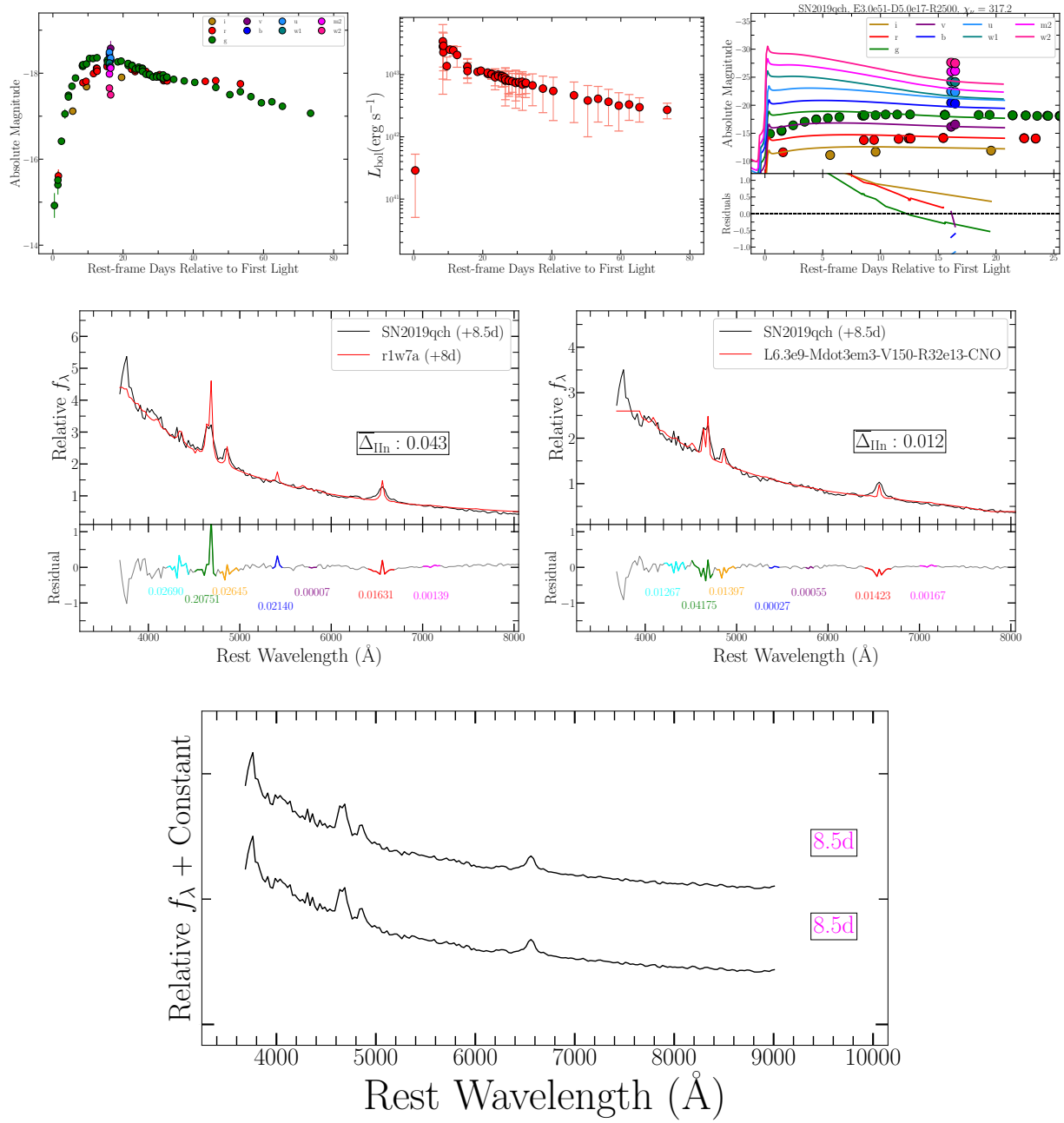

Figure 9.13 (a) SN 2019qch (silver): (a) Multi-color light curves, (b) UVOIR bolometric light curve, (c) best fit multi-color light curve model from Haynie & Piro (2021), (d) best fit spectral model from `CMFGEN` grid, (e) best fit spectral model from Boian & Groh (2020) grid, and (f) spectral series.

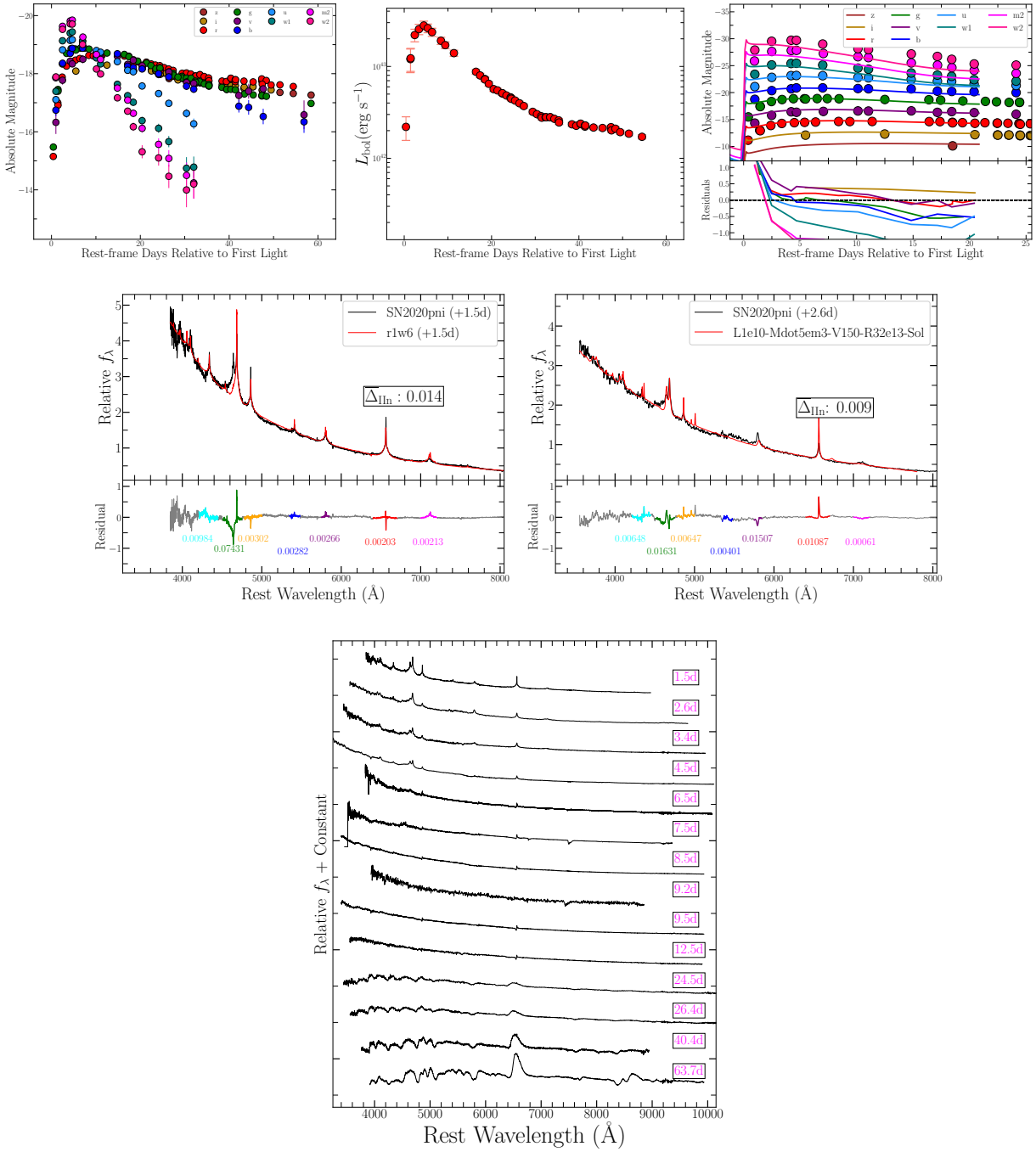

Figure 9.14 (a) SN 2020pni (gold): (a) Multi-color light curves, (b) UVOIR bolometric light curve, (c) best fit multi-color light curve model from Haynie & Piro (2021), (d) best fit spectral model from `CMFGEN` grid, (e) best fit spectral model from Boian & Groh (2020) grid, and (f) spectral series. Spectra and UV/optical photometry are from Terreran et al. (2022).

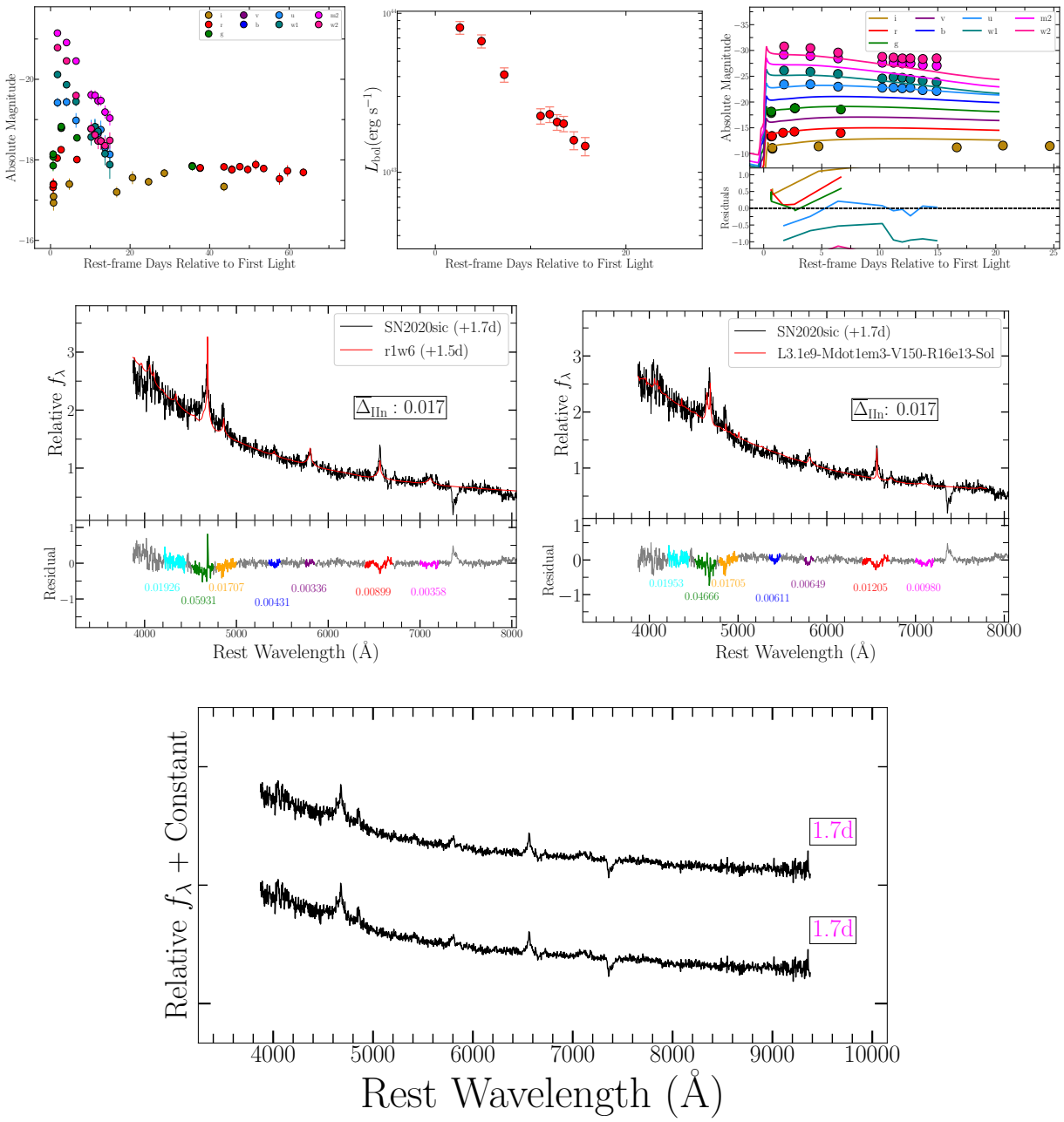

Figure 9.15 (a) SN 2020sic (gold): (a) Multi-color light curves, (b) UVOIR bolometric light curve, (c) best fit multi-color light curve model from Haynie & Piro (2021), (d) best fit spectral model from `CMFGEN` grid, (e) best fit spectral model from Boian & Groh (2020) grid, and (f) spectral series.

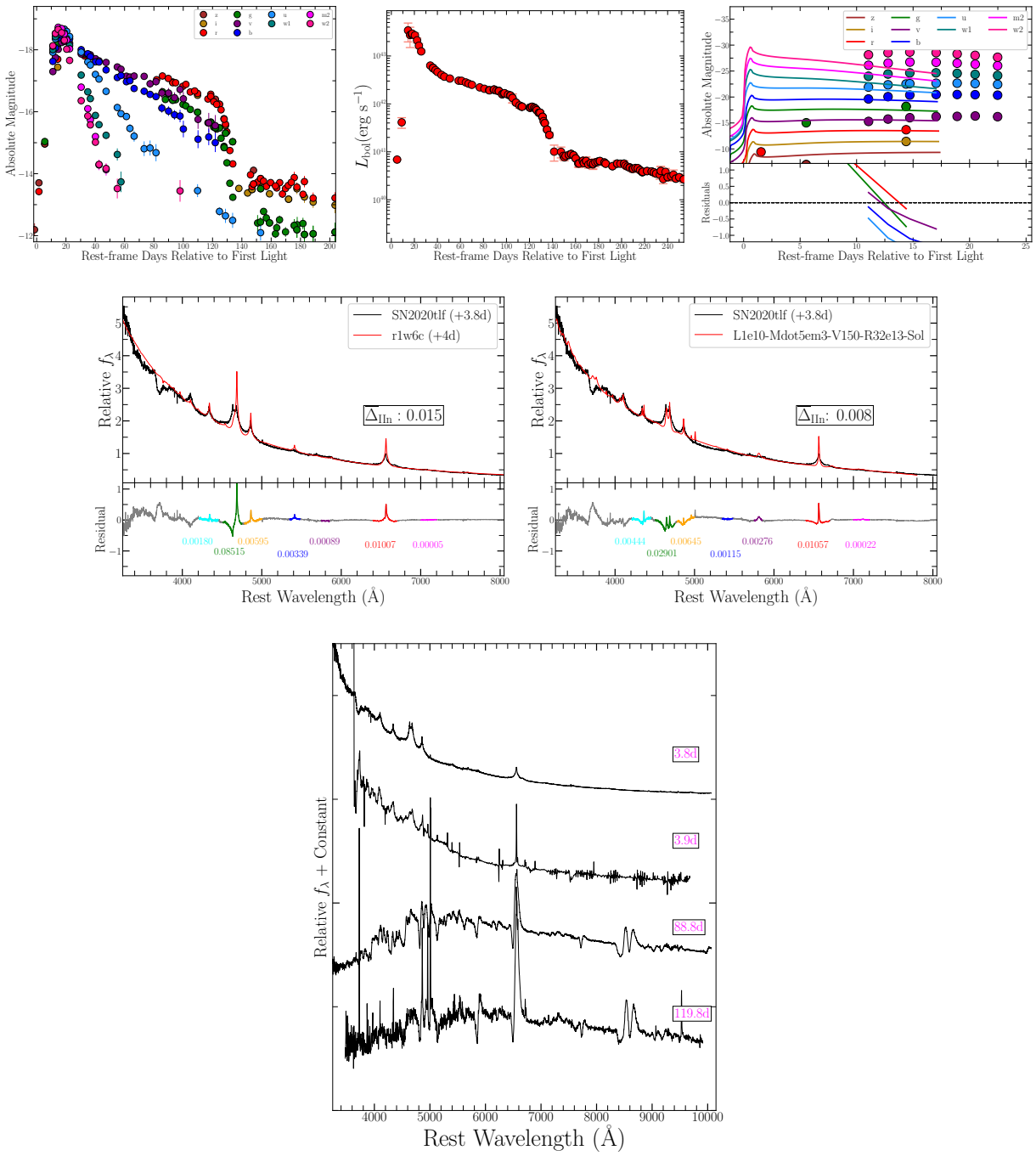

Figure 9.16 (a) SN 2020tlf (silver): (a) Multi-color light curves, (b) UVOIR bolometric light curve, (c) best fit multi-color light curve model from Haynie & Piro (2021), (d) best fit spectral model from `CMFGEN` grid, (e) best fit spectral model from Boian & Groh (2020) grid, and (f) spectral series. Spectra and UV/optical photometry are from Jacobson-Galán et al. (2022a).

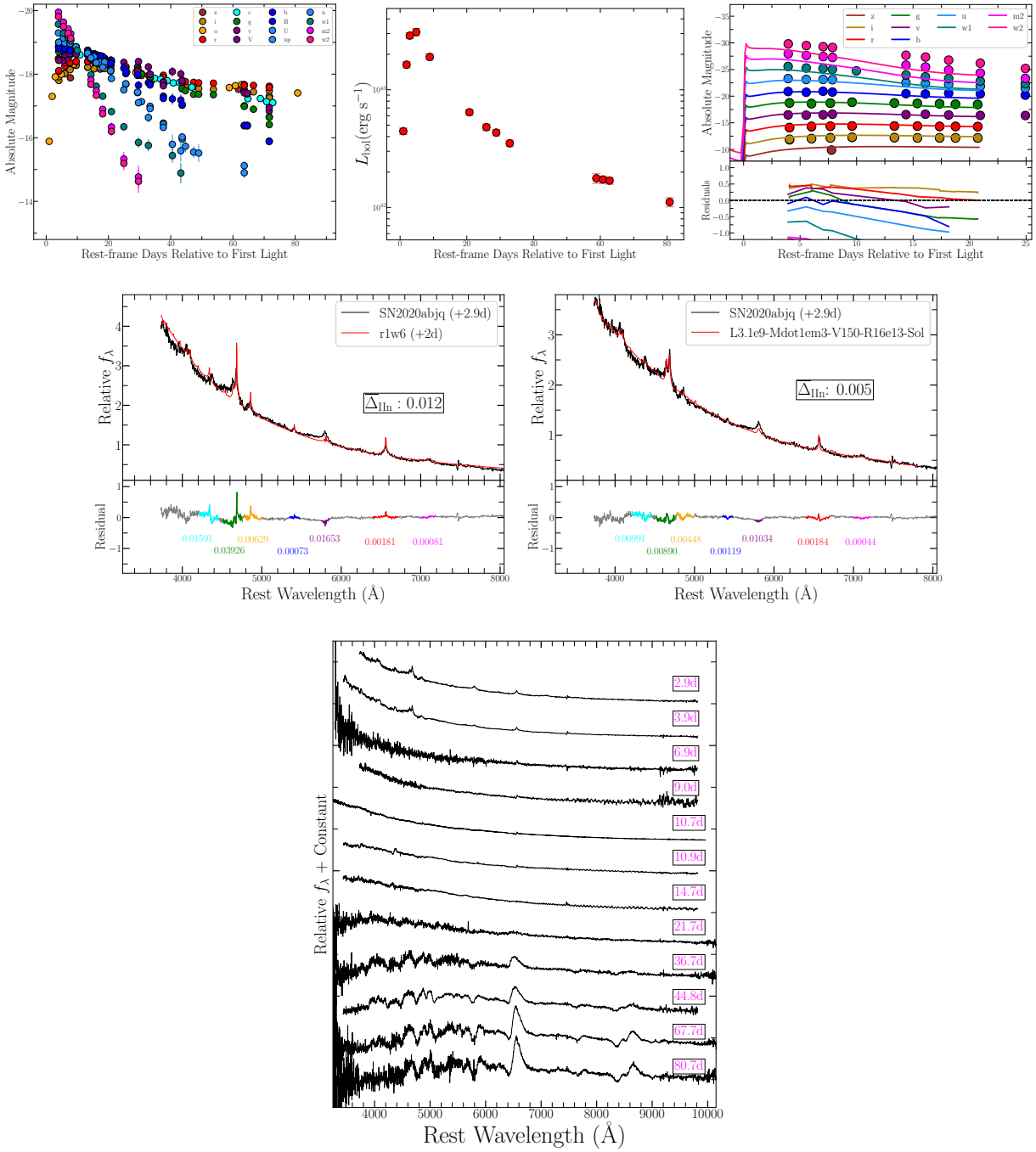

Figure 9.17 (a) SN 2020abjq (gold): (a) Multi-color light curves, (b) UVOIR bolometric light curve, (c) best fit multi-color light curve model from Haynie & Piro (2021), (d) best fit spectral model from `CMFGEN` grid, (e) best fit spectral model from Boian & Groh (2020) grid, and (f) spectral series.

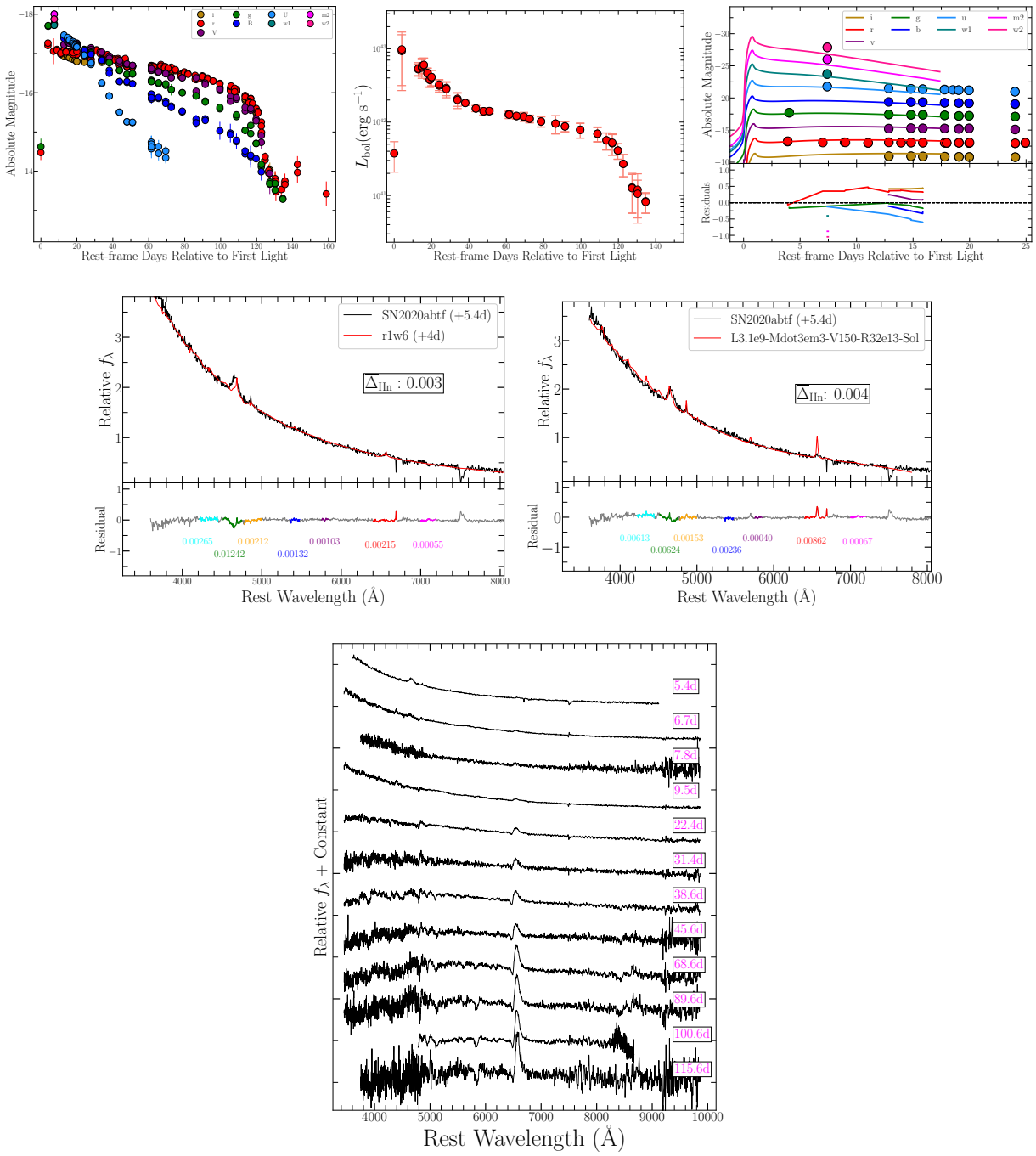

Figure 9.18 (a) SN 2020abtf (silver): (a) Multi-color light curves, (b) UVOIR bolometric light curve, (c) best fit multi-color light curve model from Haynie & Piro (2021), (d) best fit spectral model from `CMFGEN` grid, (e) best fit spectral model from Boian & Groh (2020) grid, and (f) spectral series.

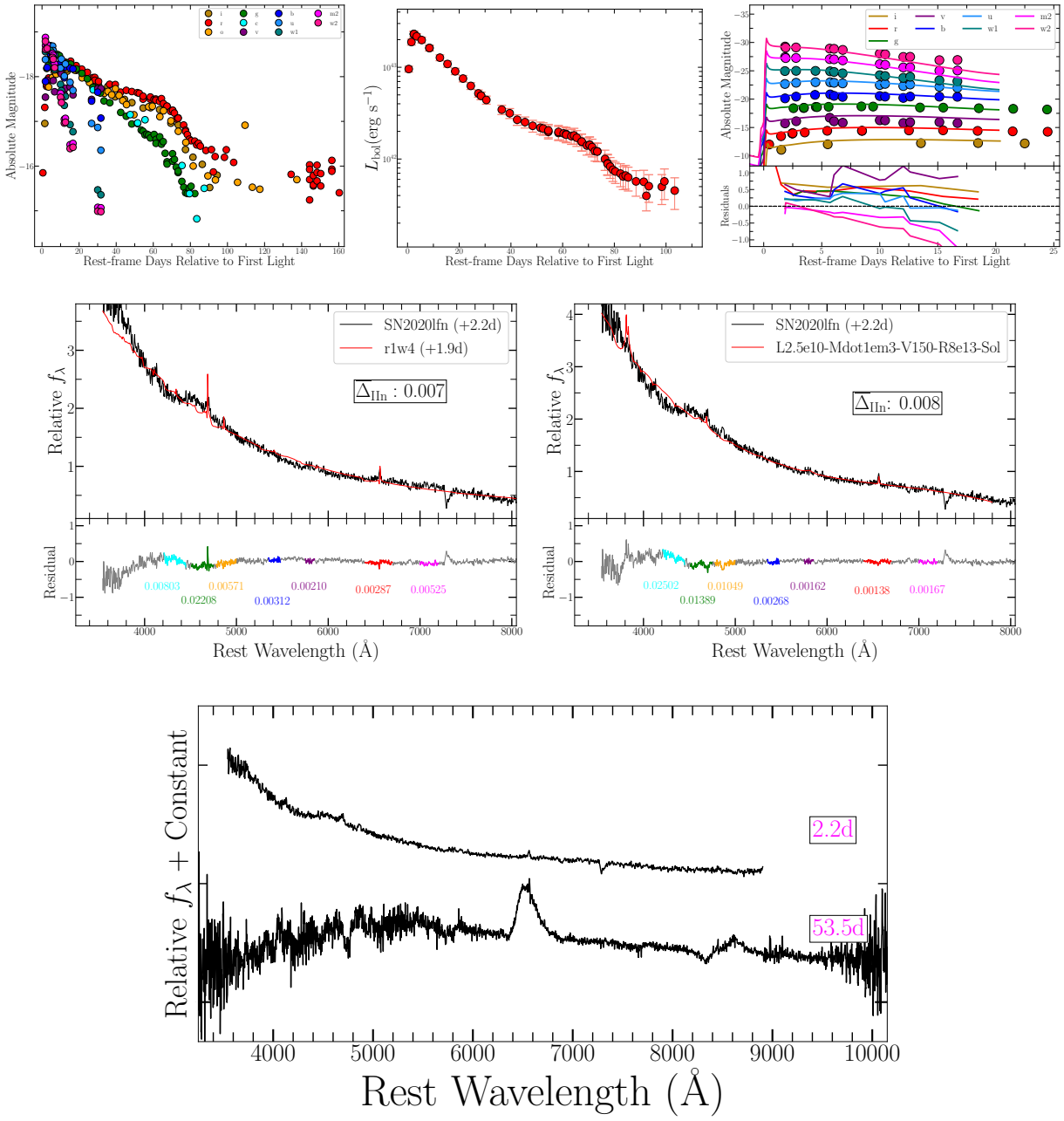

Figure 9.19 (a) SN 2020lfn (gold): (a) Multi-color light curves, (b) UVOIR bolometric light curve, (c) best fit multi-color light curve model from Haynie & Piro (2021), (d) best fit spectral model from `CMFGEN` grid, (e) best fit spectral model from Boian & Groh (2020) grid, and (f) spectral series.

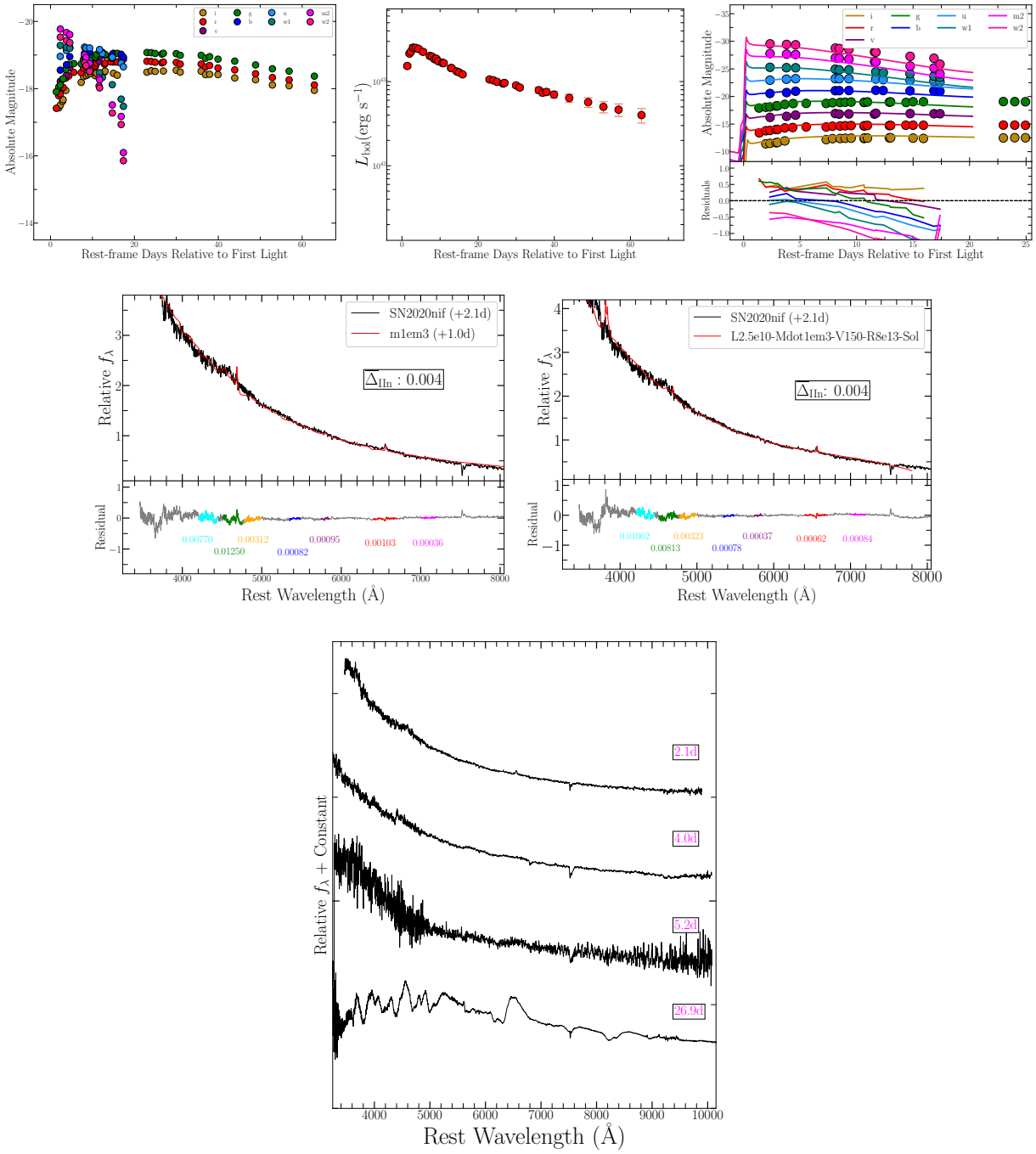

Figure 9.20 (a) SN 2020nif (silver): (a) Multi-color light curves, (b) UVOIR bolometric light curve, (c) best fit multi-color light curve model from Haynie & Piro (2021), (d) best fit spectral model from `CMFGEN` grid, (e) best fit spectral model from Boian & Groh (2020) grid, and (f) spectral series.

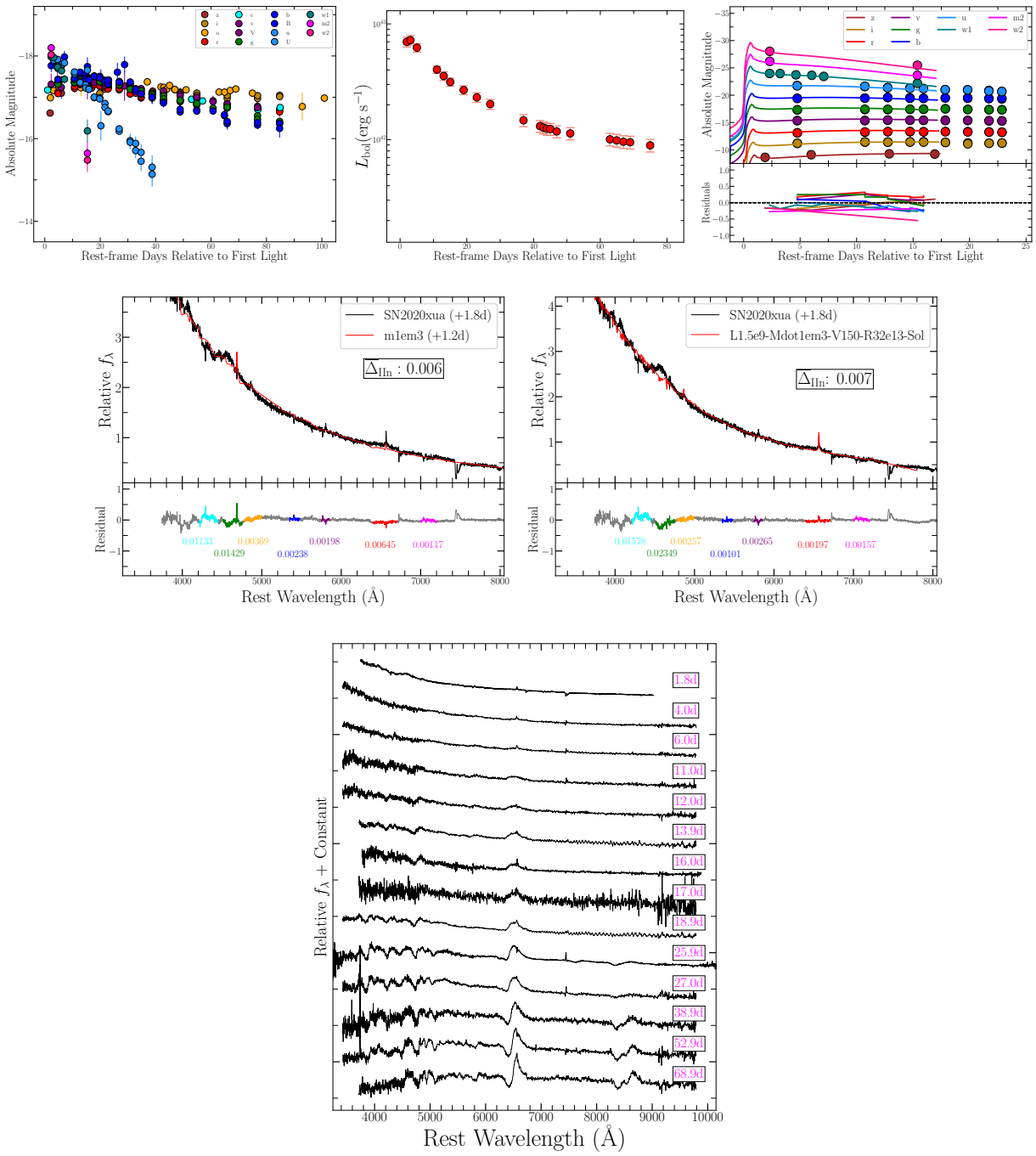

Figure 9.21 (a) SN 2020xua (silver): (a) Multi-color light curves, (b) UVOIR bolometric light curve, (c) best fit multi-color light curve model from Haynie & Piro (2021), (d) best fit spectral model from `CMFGEN` grid, (e) best fit spectral model from Boian & Groh (2020) grid, and (f) spectral series.

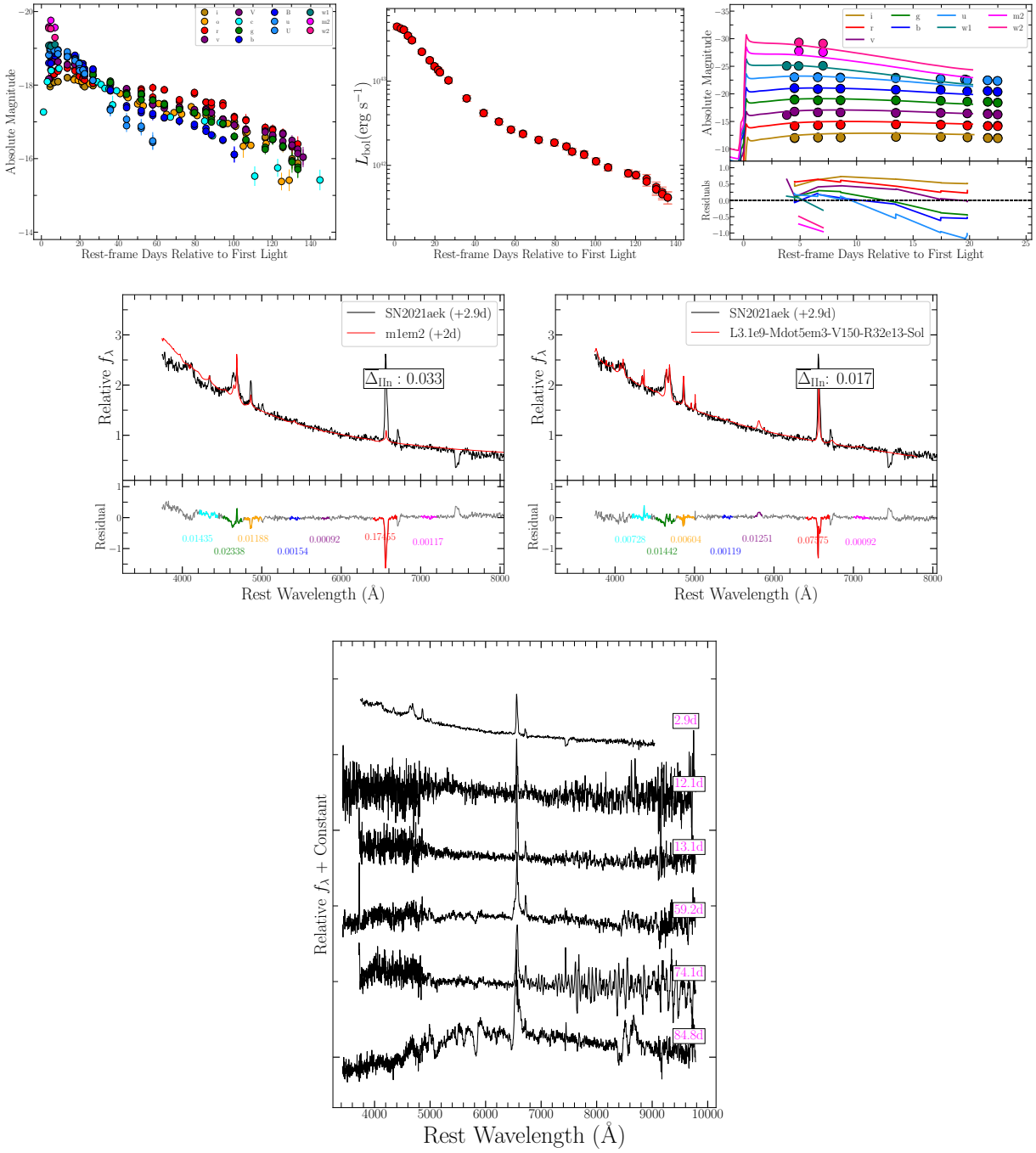

Figure 9.22 (a) SN 2021aek (silver): (a) Multi-color light curves, (b) UVOIR bolometric light curve, (c) best fit multi-color light curve model from Haynie & Piro (2021), (d) best fit spectral model from `CMFGEN` grid, (e) best fit spectral model from Boian & Groh (2020) grid, and (f) spectral series.

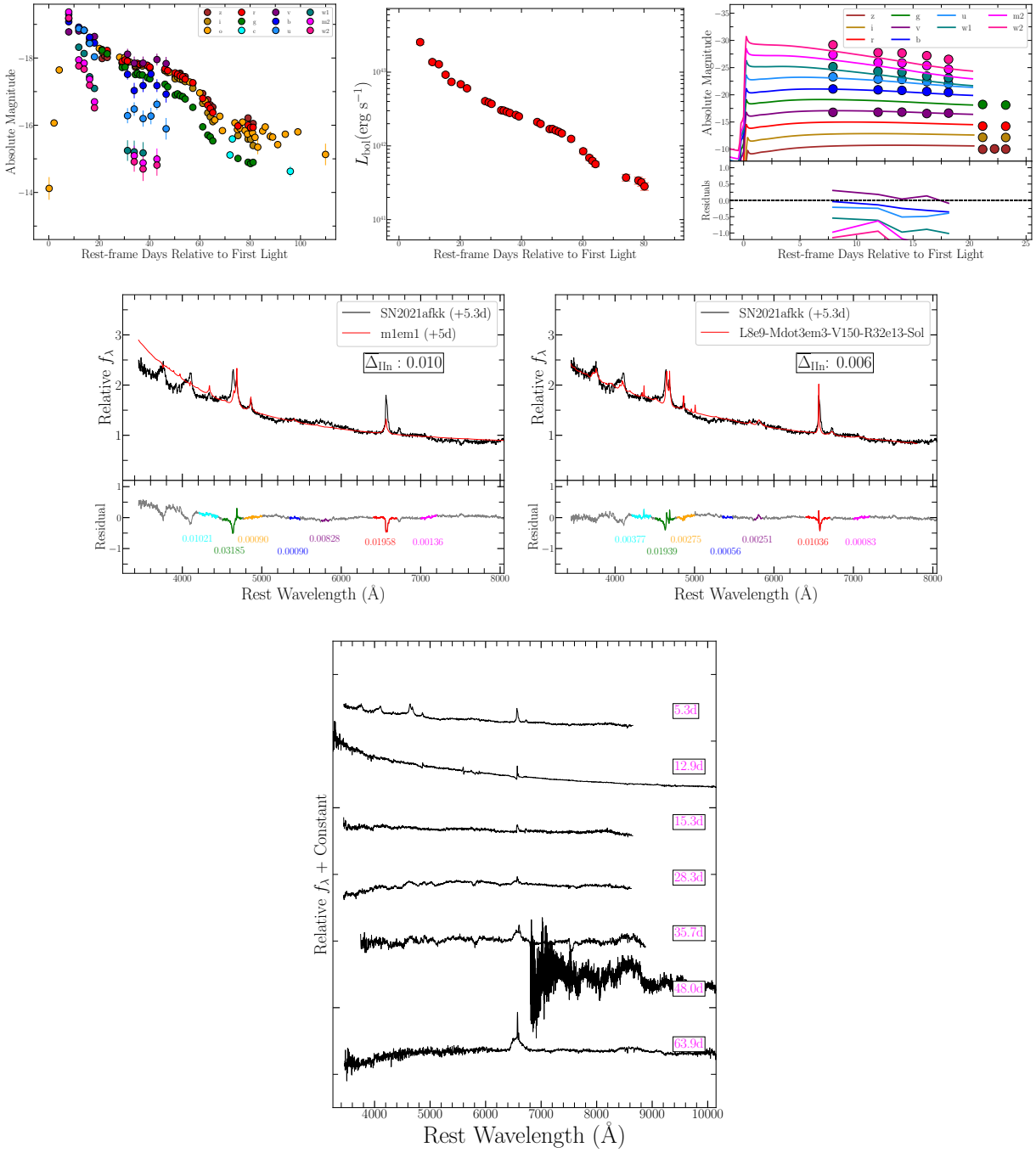

Figure 9.23 (a) SN 2021afkk (silver): (a) Multi-color light curves, (b) UVOIR bolometric light curve, (c) best fit multi-color light curve model from Haynie & Piro (2021), (d) best fit spectral model from `CMFGEN` grid, (e) best fit spectral model from Boian & Groh (2020) grid, and (f) spectral series.

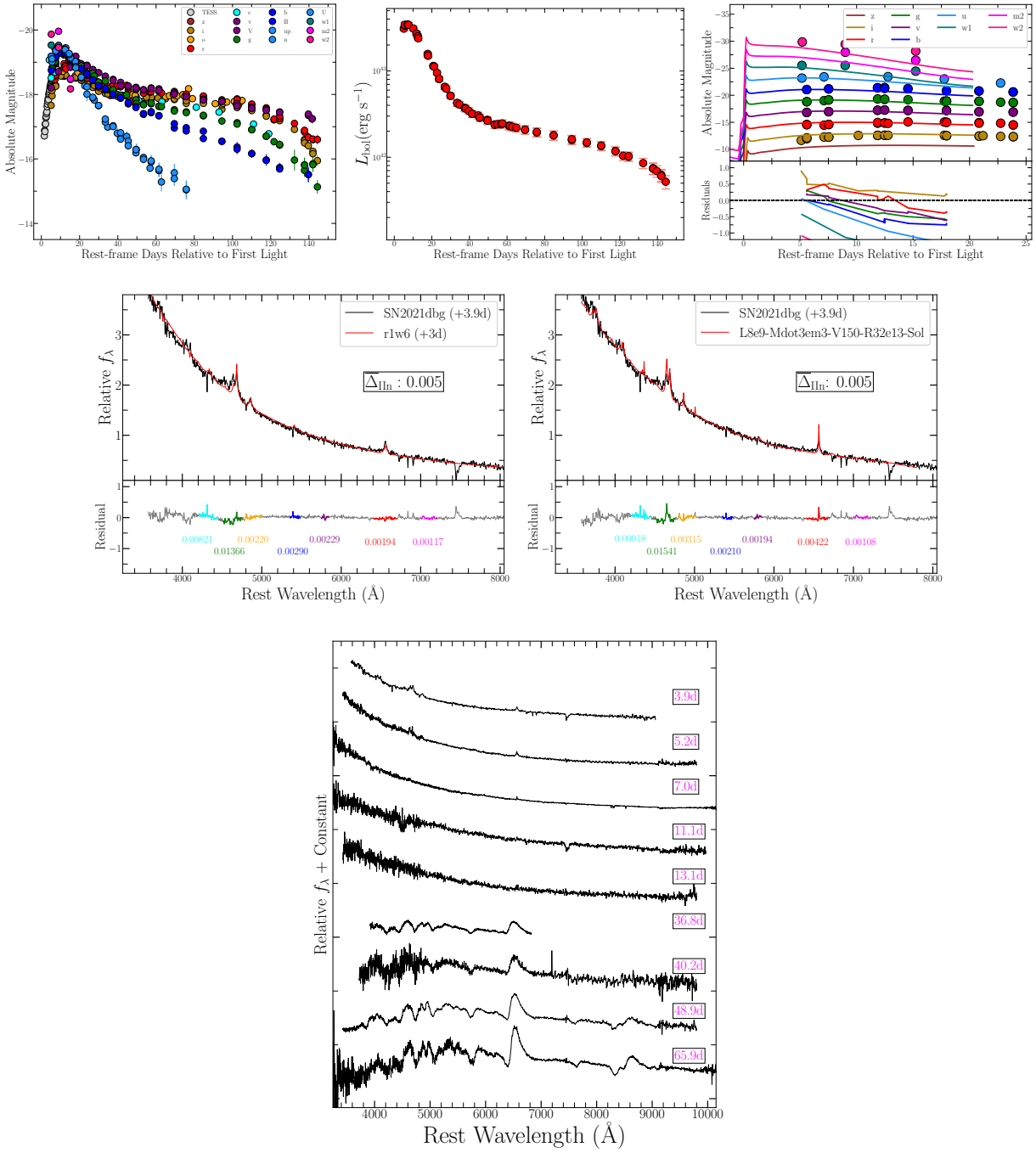

Figure 9.24 (a) SN 2021dbg (silver): (a) Multi-color light curves, (b) UVOIR bolometric light curve, (c) best fit multi-color light curve model from Haynie & Piro (2021), (d) best fit spectral model from `CMFGEN` grid, (e) best fit spectral model from Boian & Groh (2020) grid, and (f) spectral series.

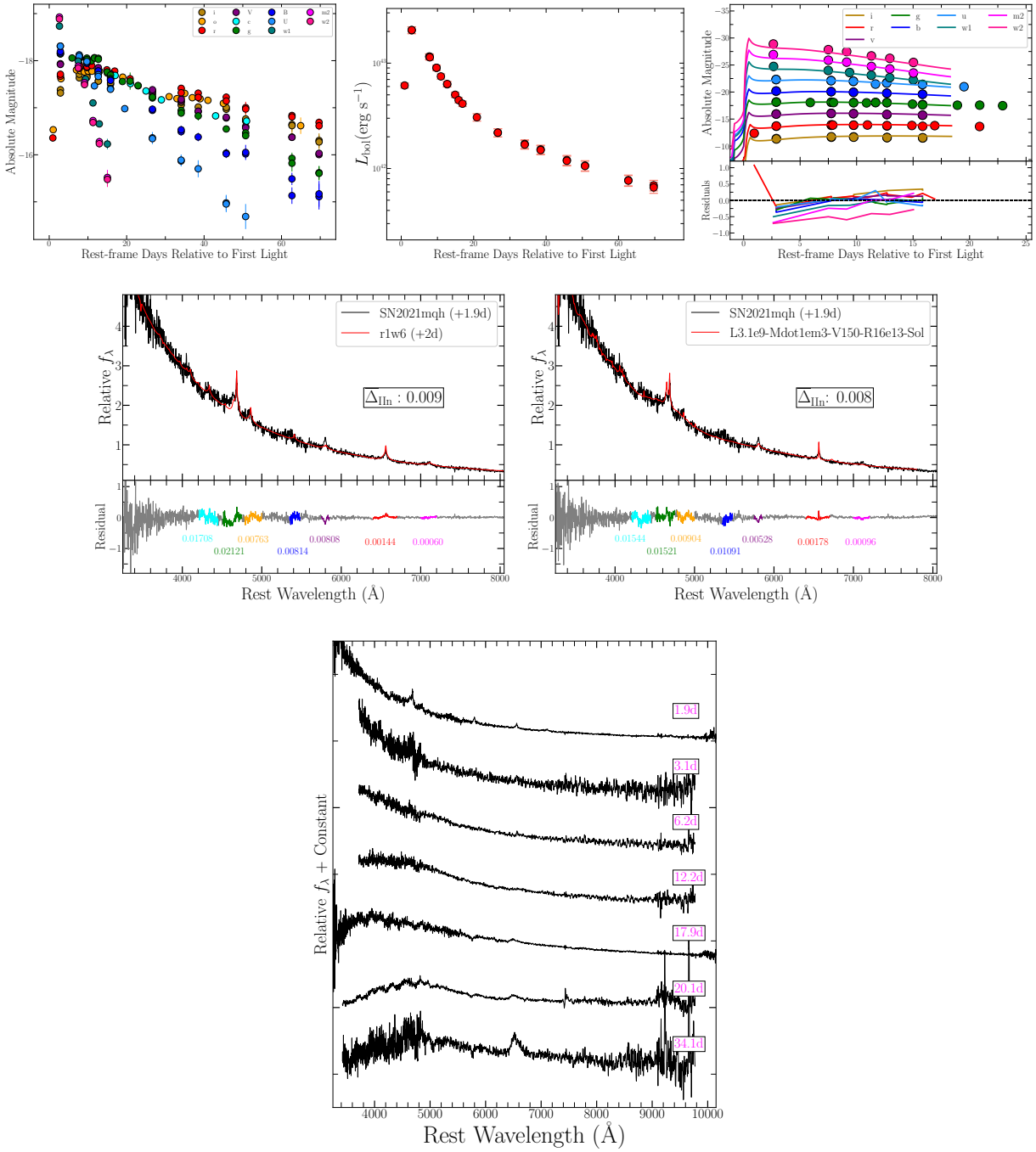

Figure 9.25 (a) SN 2021mqh (gold): (a) Multi-color light curves, (b) UVOIR bolometric light curve, (c) best fit multi-color light curve model from Haynie & Piro (2021), (d) best fit spectral model from `CMFGEN` grid, (e) best fit spectral model from Boian & Groh (2020) grid, and (f) spectral series.

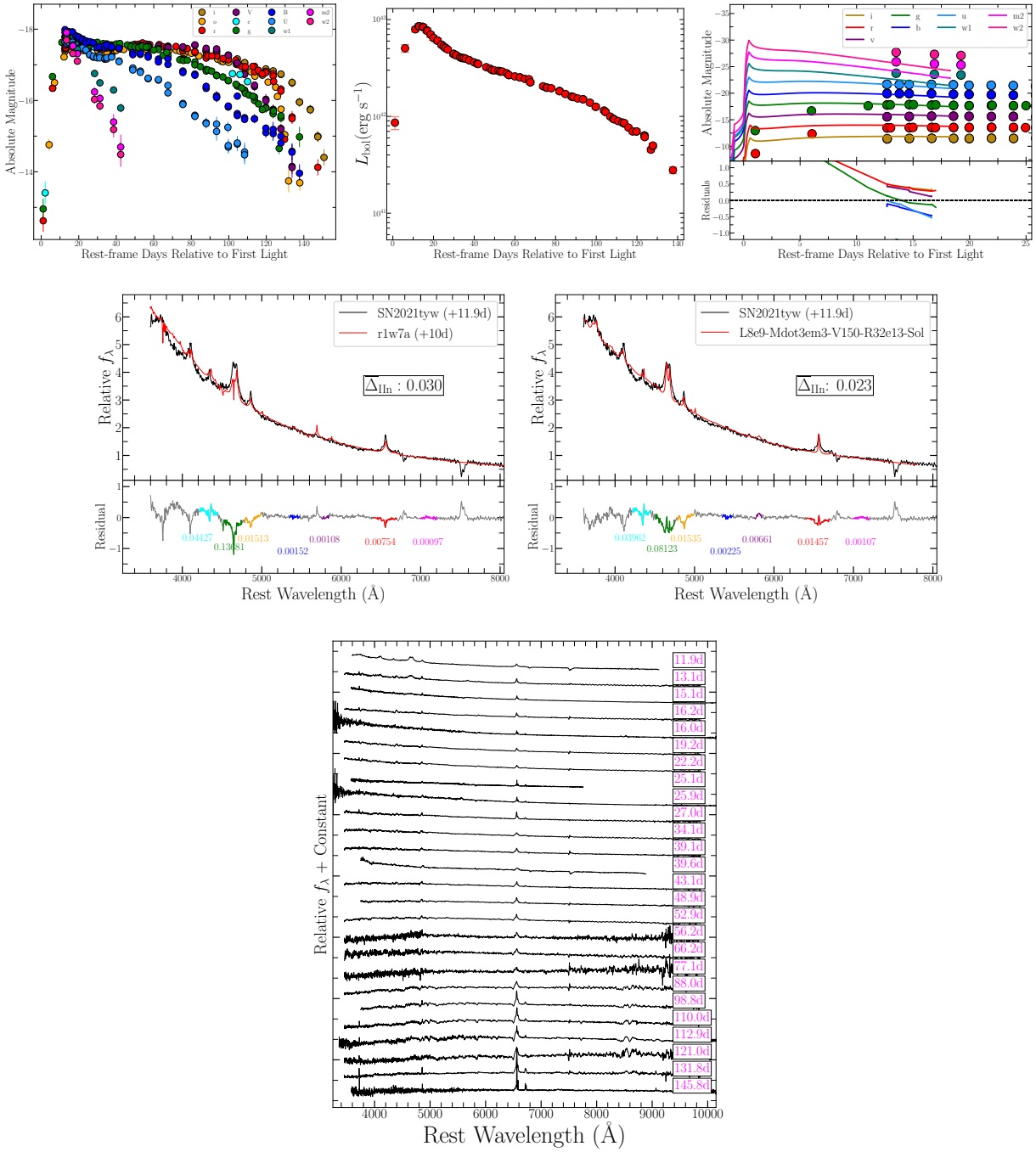

Figure 9.26 (a) SN 2021tyw (silver): (a) Multi-color light curves, (b) UVOIR bolometric light curve, (c) best fit multi-color light curve model from Haynie & Piro (2021), (d) best fit spectral model from `CMFGEN` grid, (e) best fit spectral model from Boian & Groh (2020) grid, and (f) spectral series.

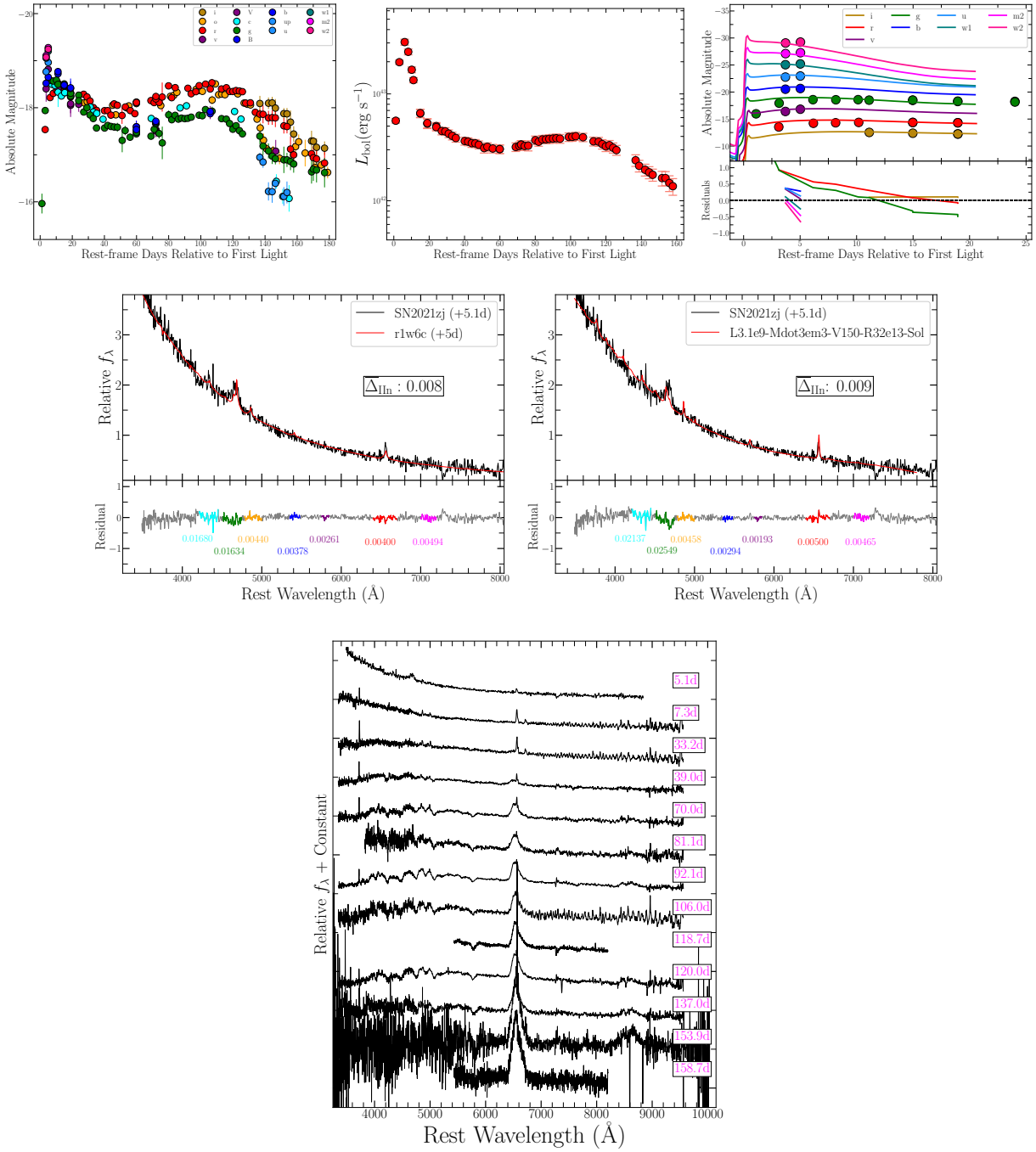

Figure 9.27 (a) SN 2021zj (silver): (a) Multi-color light curves, (b) UVOIR bolometric light curve, (c) best fit multi-color light curve model from Haynie & Piro (2021), (d) best fit spectral model from `CMFGEN` grid, (e) best fit spectral model from Boian & Groh (2020) grid, and (f) spectral series.

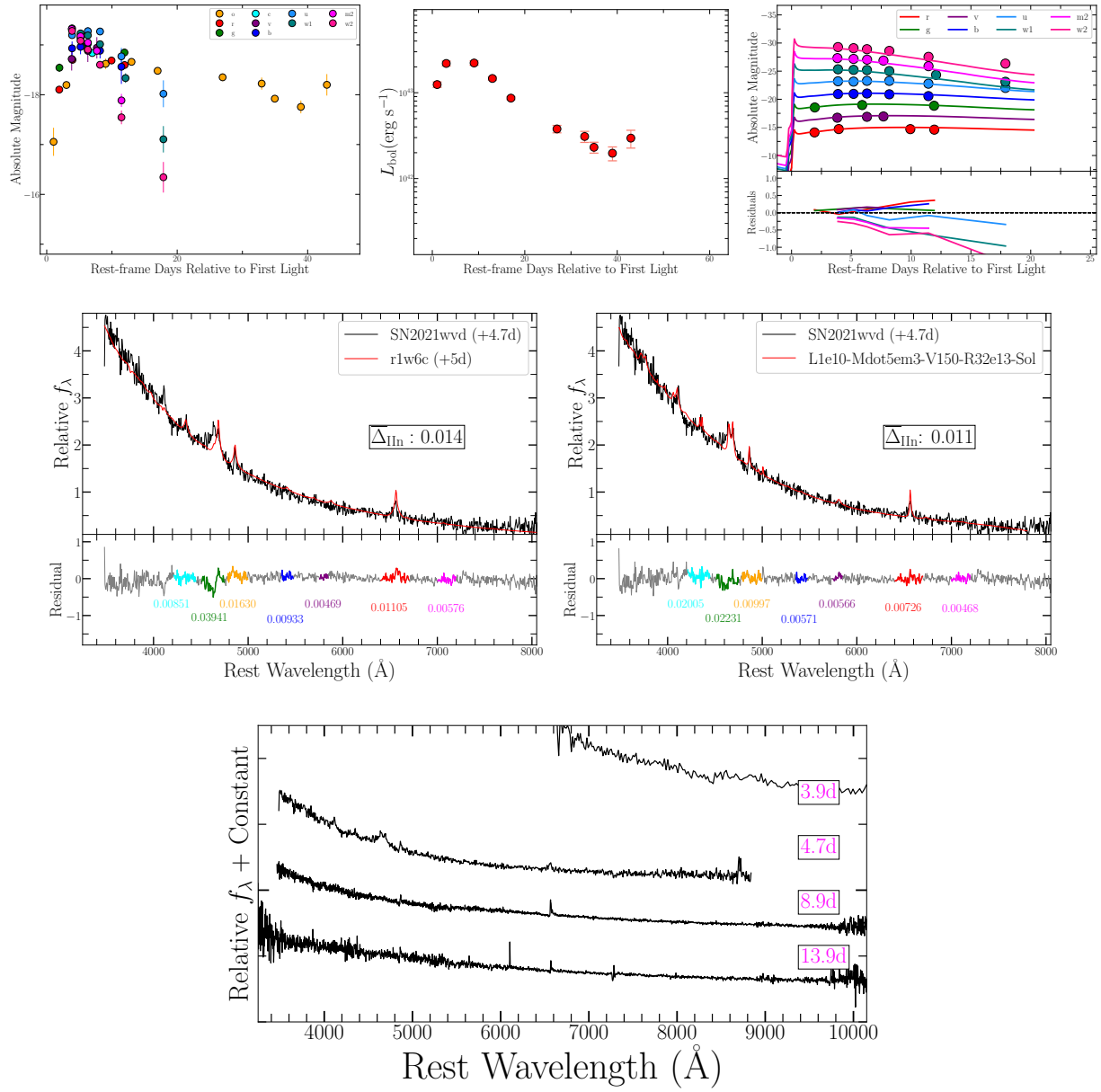

Figure 9.28 (a) SN 2021wvd (silver): (a) Multi-color light curves, (b) UVOIR bolometric light curve, (c) best fit multi-color light curve model from Haynie & Piro (2021), (d) best fit spectral model from `CMFGEN` grid, (e) best fit spectral model from Boian & Groh (2020) grid, and (f) spectral series.

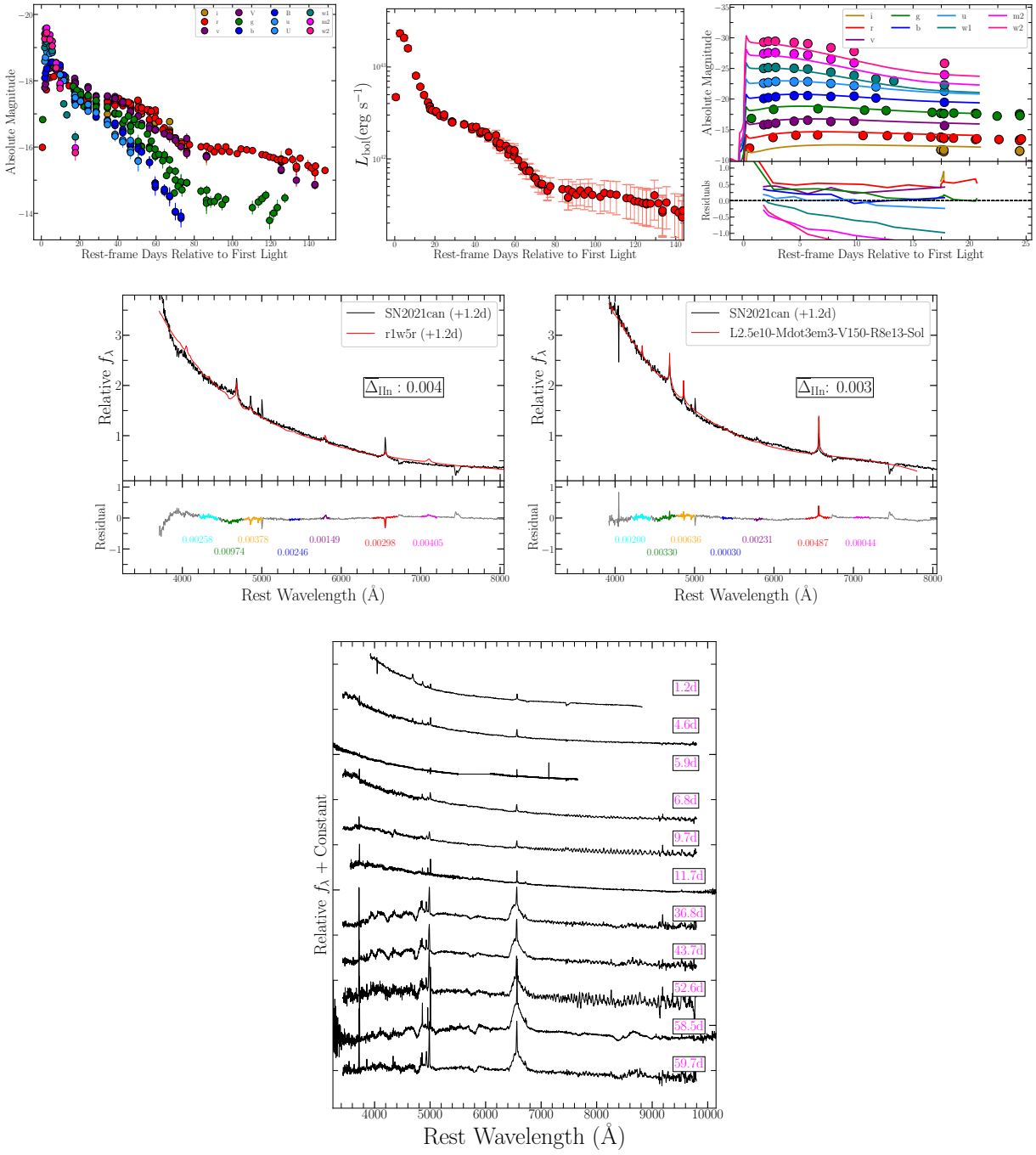

Figure 9.29 (a) SN 2021can (gold): (a) Multi-color light curves, (b) UVOIR bolometric light curve, (c) best fit multi-color light curve model from Haynie & Piro (2021), (d) best fit spectral model from `CMFGEN` grid, (e) best fit spectral model from Boian & Groh (2020) grid, and (f) spectral series.

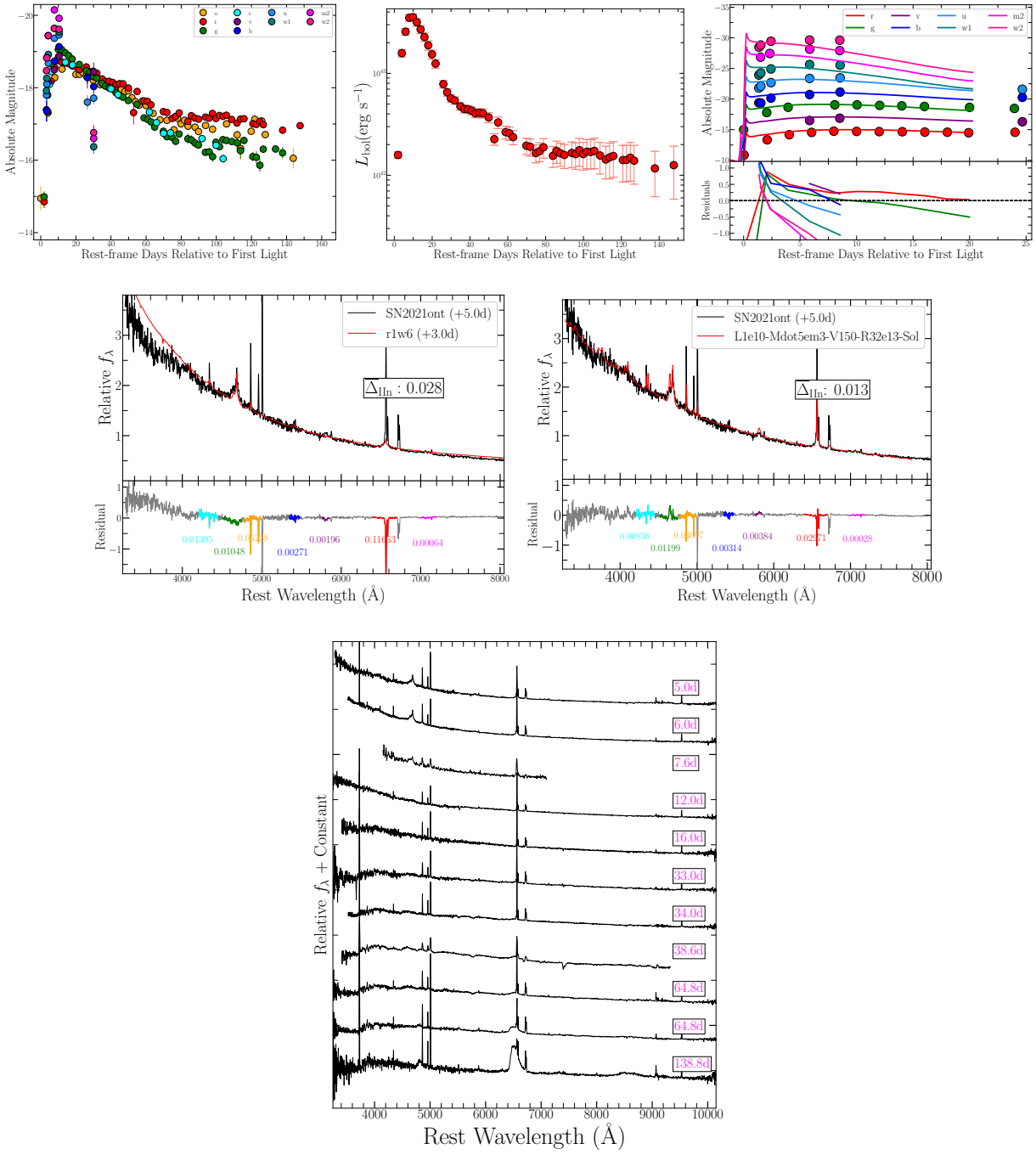

Figure 9.30 (a) SN 2021ont (silver): (a) Multi-color light curves, (b) UVOIR bolometric light curve, (c) best fit multi-color light curve model from Haynie & Piro (2021), (d) best fit spectral model from `CMFGEN` grid, (e) best fit spectral model from Boian & Groh (2020) grid, and (f) spectral series.

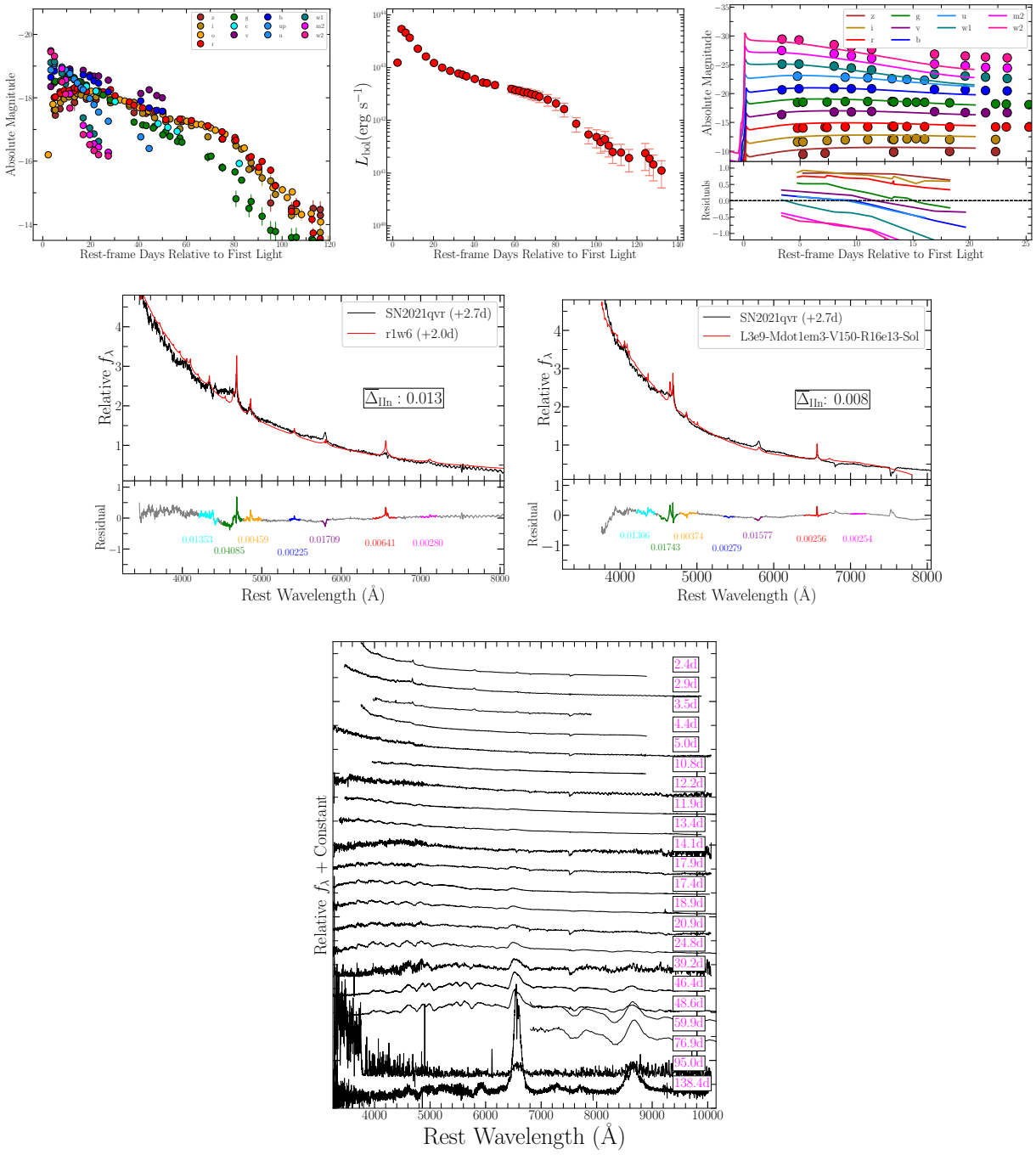

Figure 9.31 (a) SN 2021qvr (silver): (a) Multi-color light curves, (b) UVOIR bolometric light curve, (c) best fit multi-color light curve model from Haynie & Piro (2021), (d) best fit spectral model from `CMFGEN` grid, (e) best fit spectral model from Boian & Groh (2020) grid, and (f) spectral series.

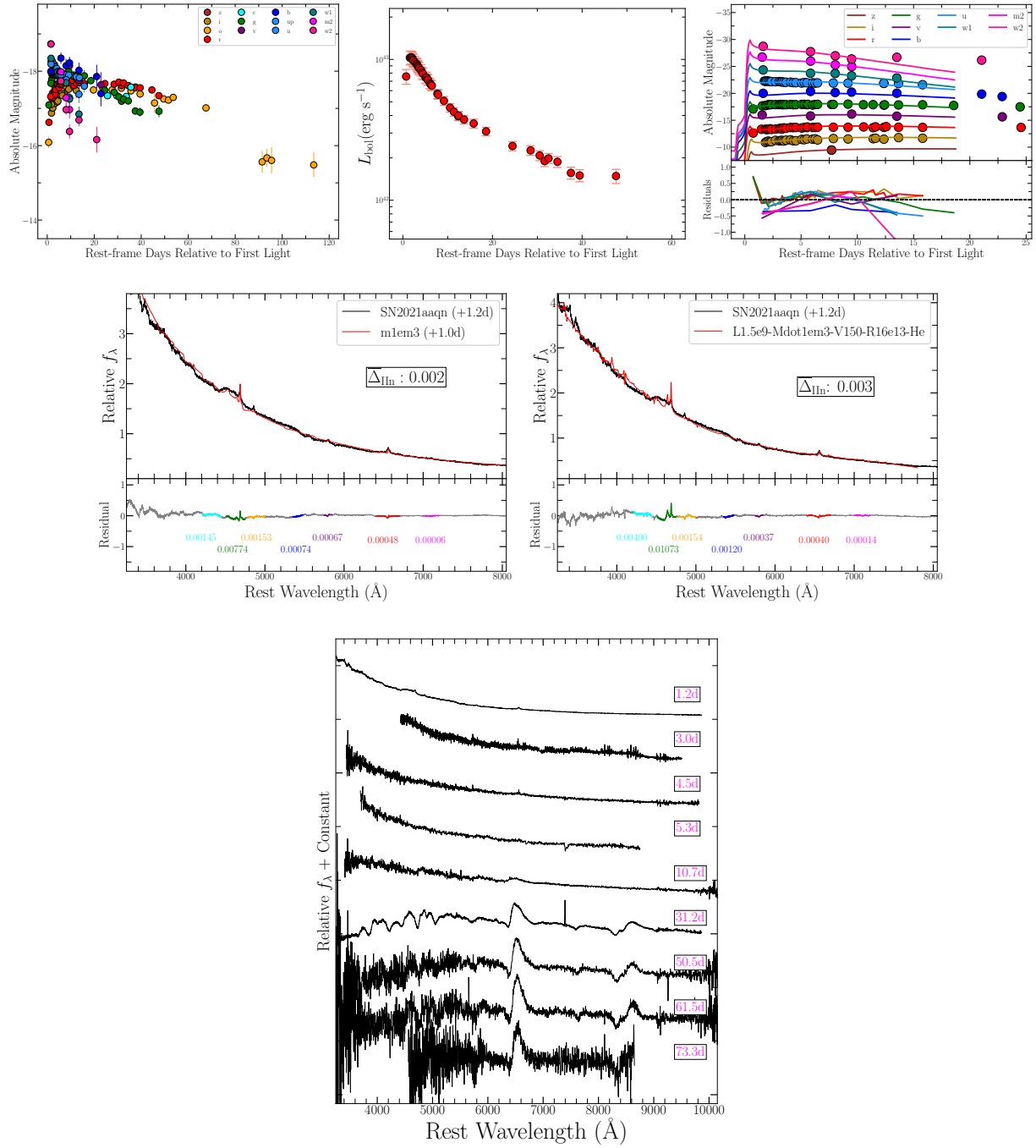

Figure 9.32 (a) SN 2021aaqn (gold): (a) Multi-color light curves, (b) UVOIR bolometric light curve, (c) best fit multi-color light curve model from Haynie & Piro (2021), (d) best fit spectral model from `CMFGEN` grid, (e) best fit spectral model from Boian & Groh (2020) grid, and (f) spectral series.

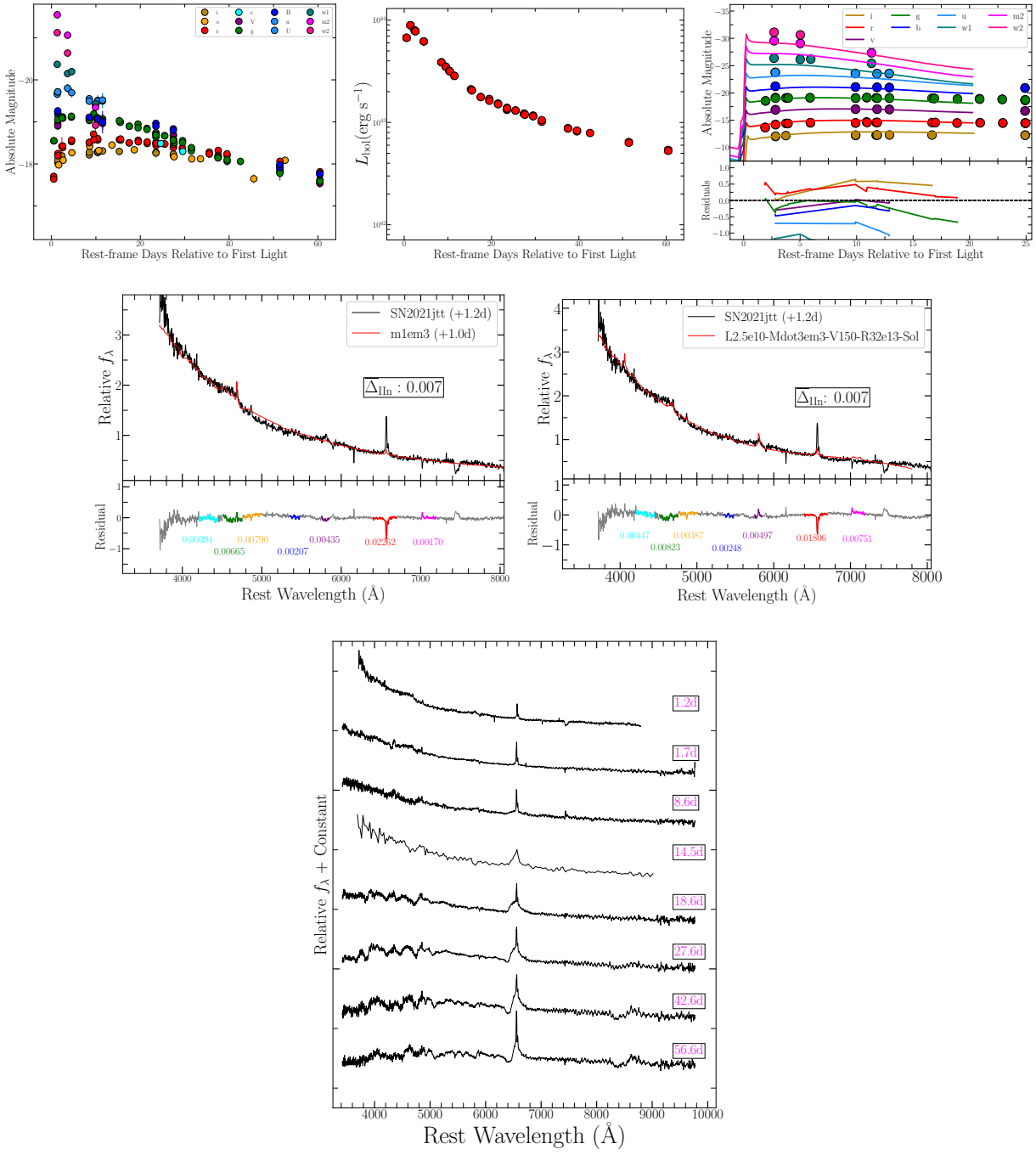

Figure 9.33 (a) SN 2021jtt (gold): (a) Multi-color light curves, (b) UVOIR bolometric light curve, (c) best fit multi-color light curve model from Haynie & Piro (2021), (d) best fit spectral model from `CMFGEN` grid, (e) best fit spectral model from Boian & Groh (2020) grid, and (f) spectral series.

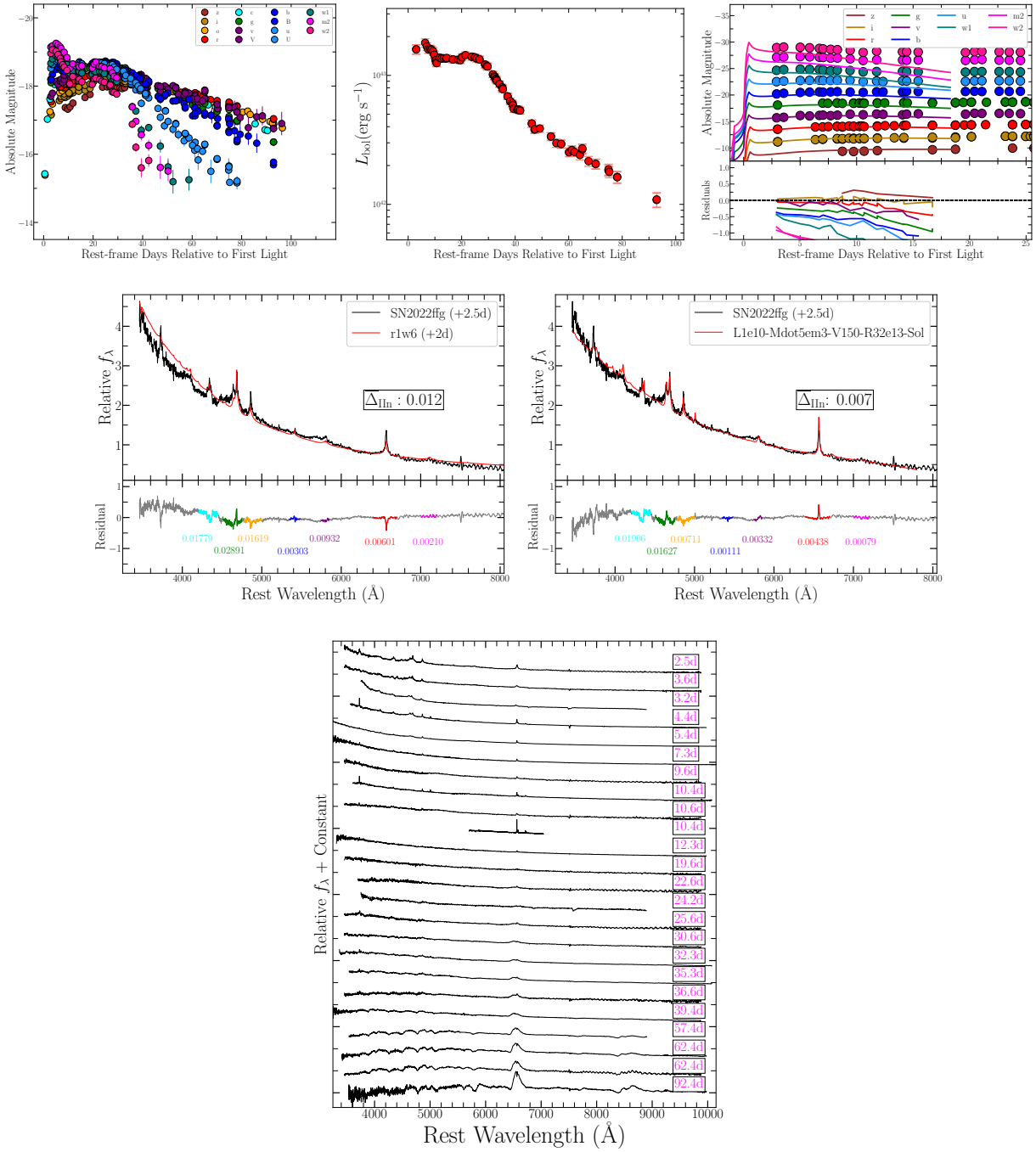

Figure 9.34 (a) SN 2022ffg (gold): (a) Multi-color light curves, (b) UVOIR bolometric light curve, (c) best fit multi-color light curve model from Haynie & Piro (2021), (d) best fit spectral model from `CMFGEN` grid, (e) best fit spectral model from Boian & Groh (2020) grid, and (f) spectral series.

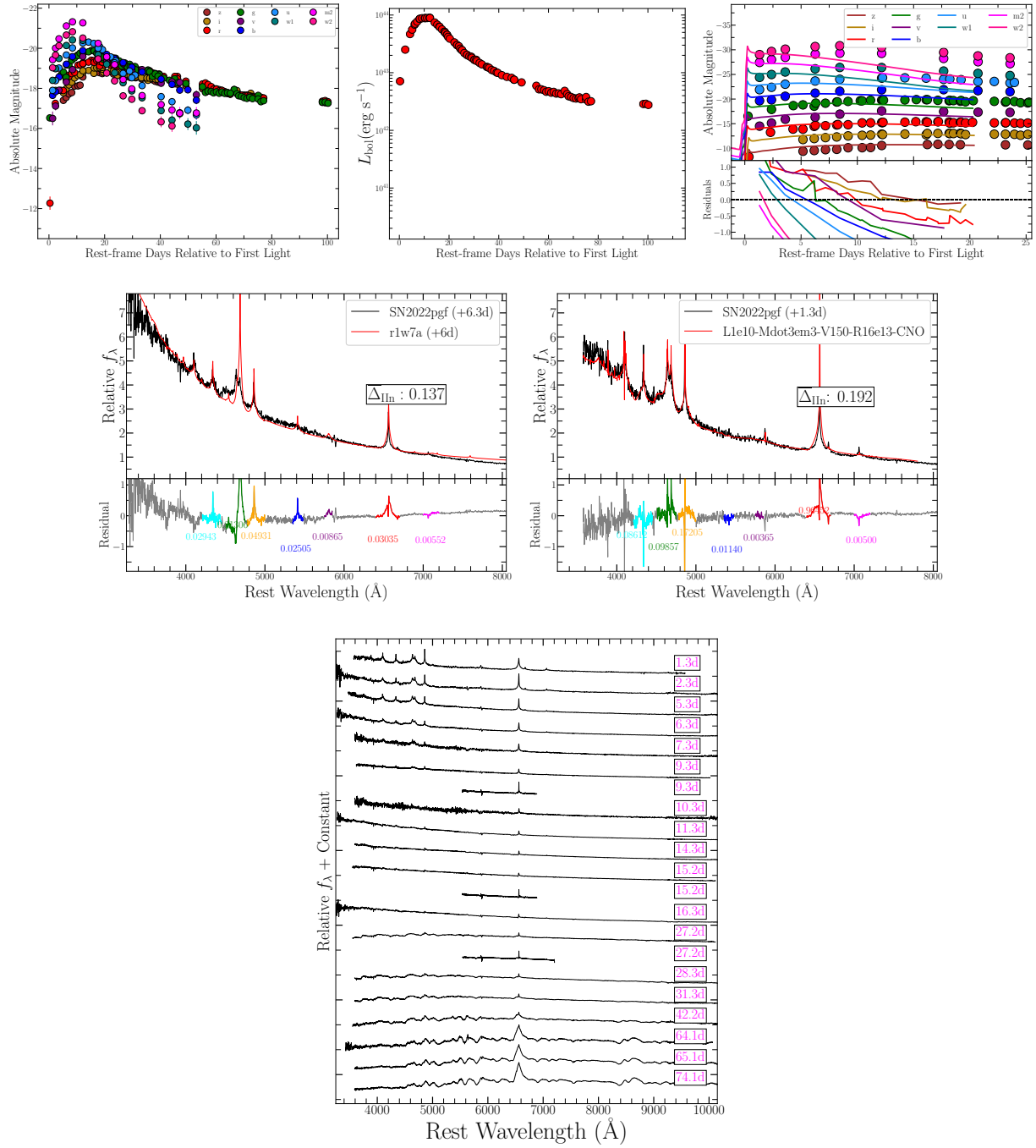

Figure 9.35 (a) SN 2022pgf (gold): (a) Multi-color light curves, (b) UVOIR bolometric light curve, (c) best fit multi-color light curve model from Haynie & Piro (2021), (d) best fit spectral model from `CMFGEN` grid, (e) best fit spectral model from Boian & Groh (2020) grid, and (f) spectral series.

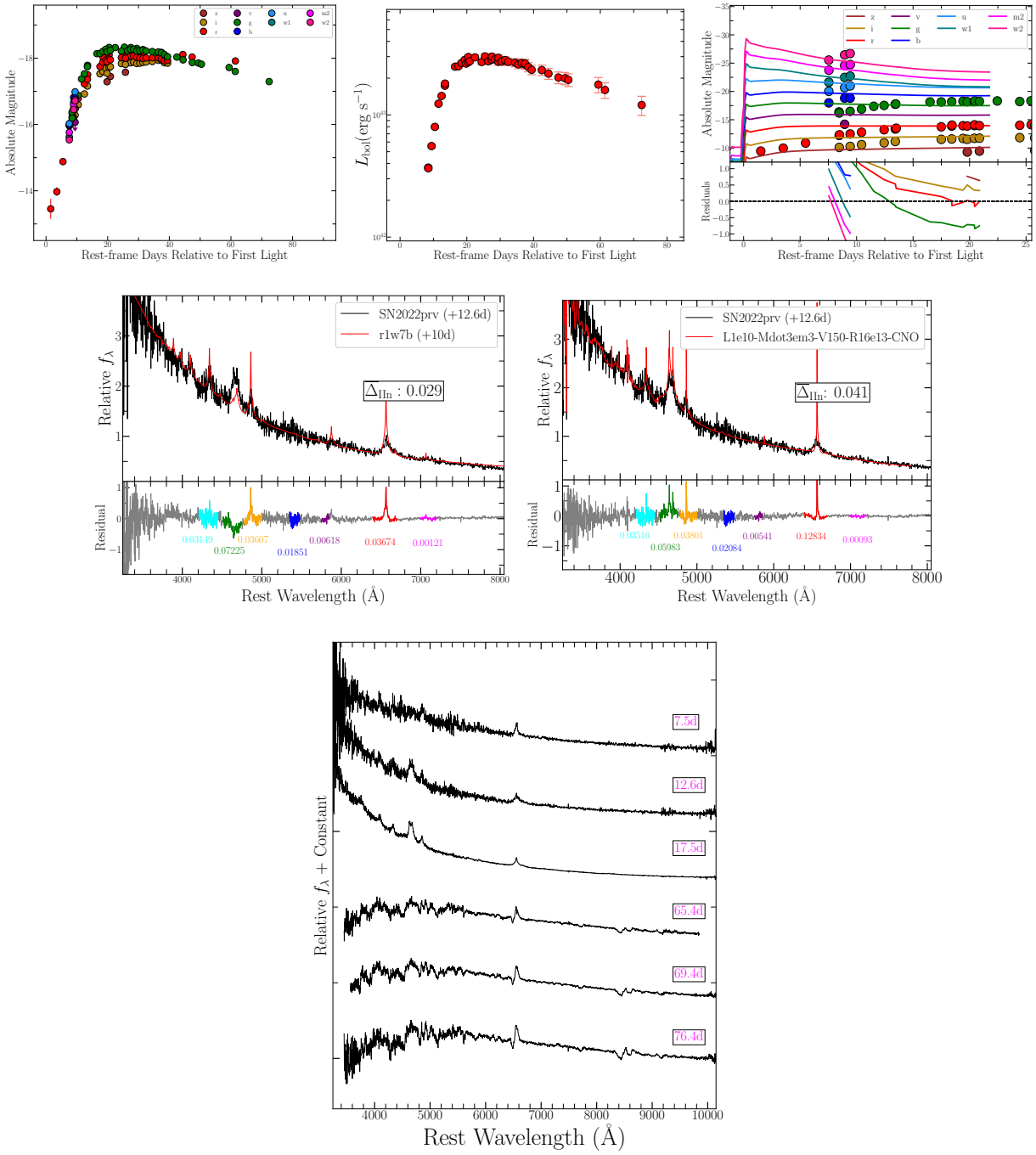

Figure 9.36 (a) SN 2022prv (silver): (a) Multi-color light curves, (b) UVOIR bolometric light curve, (c) best fit multi-color light curve model from Haynie & Piro (2021), (d) best fit spectral model from `CMFGEN` grid, (e) best fit spectral model from Boian & Groh (2020) grid, and (f) spectral series.

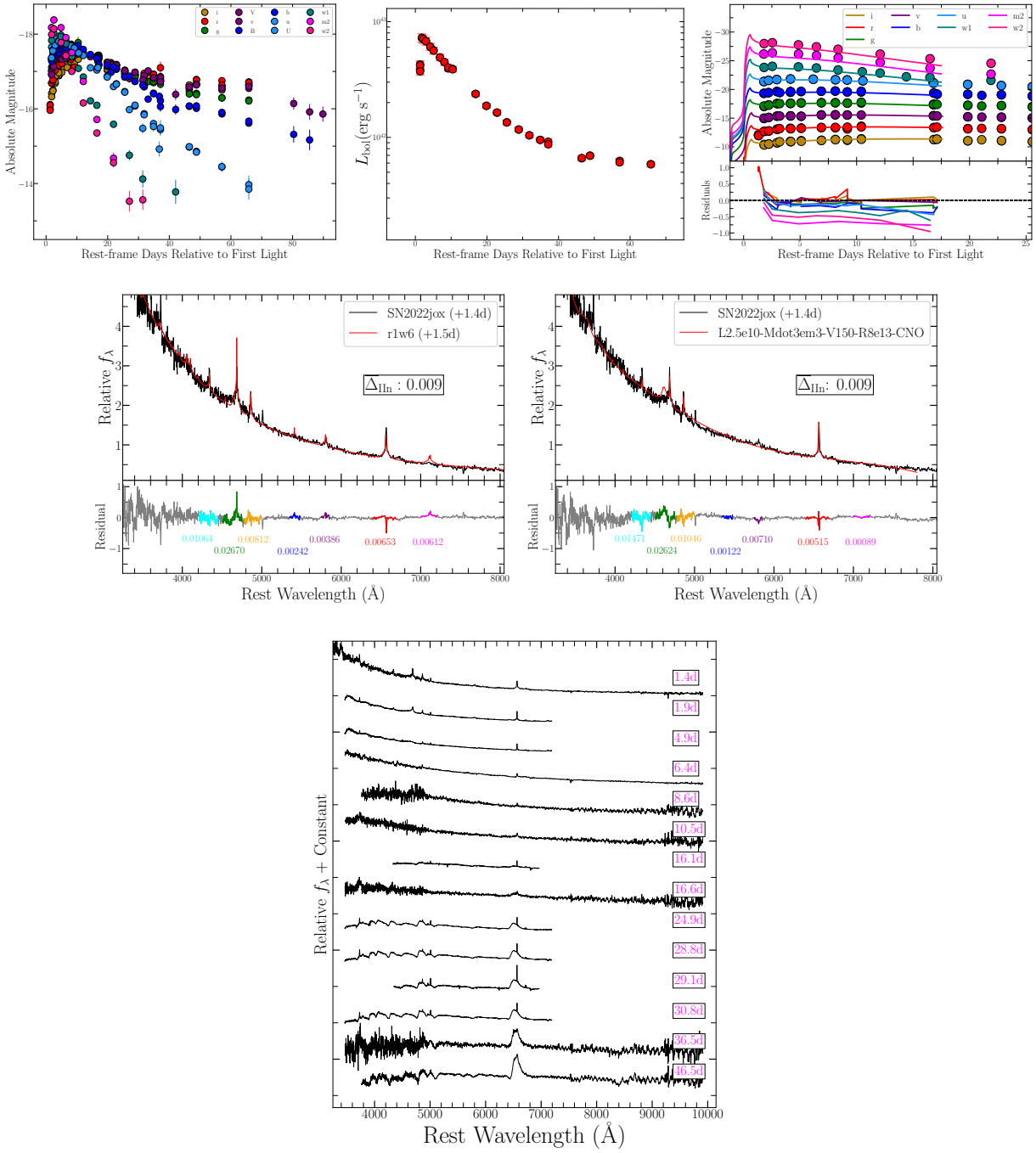

Figure 9.37 (a) SN 2022jox (gold): (a) Multi-color light curves, (b) UVOIR bolometric light curve, (c) best fit multi-color light curve model from Haynie & Piro (2021), (d) best fit spectral model from `CMFGEN` grid, (e) best fit spectral model from Boian & Groh (2020) grid, and (f) spectral series.

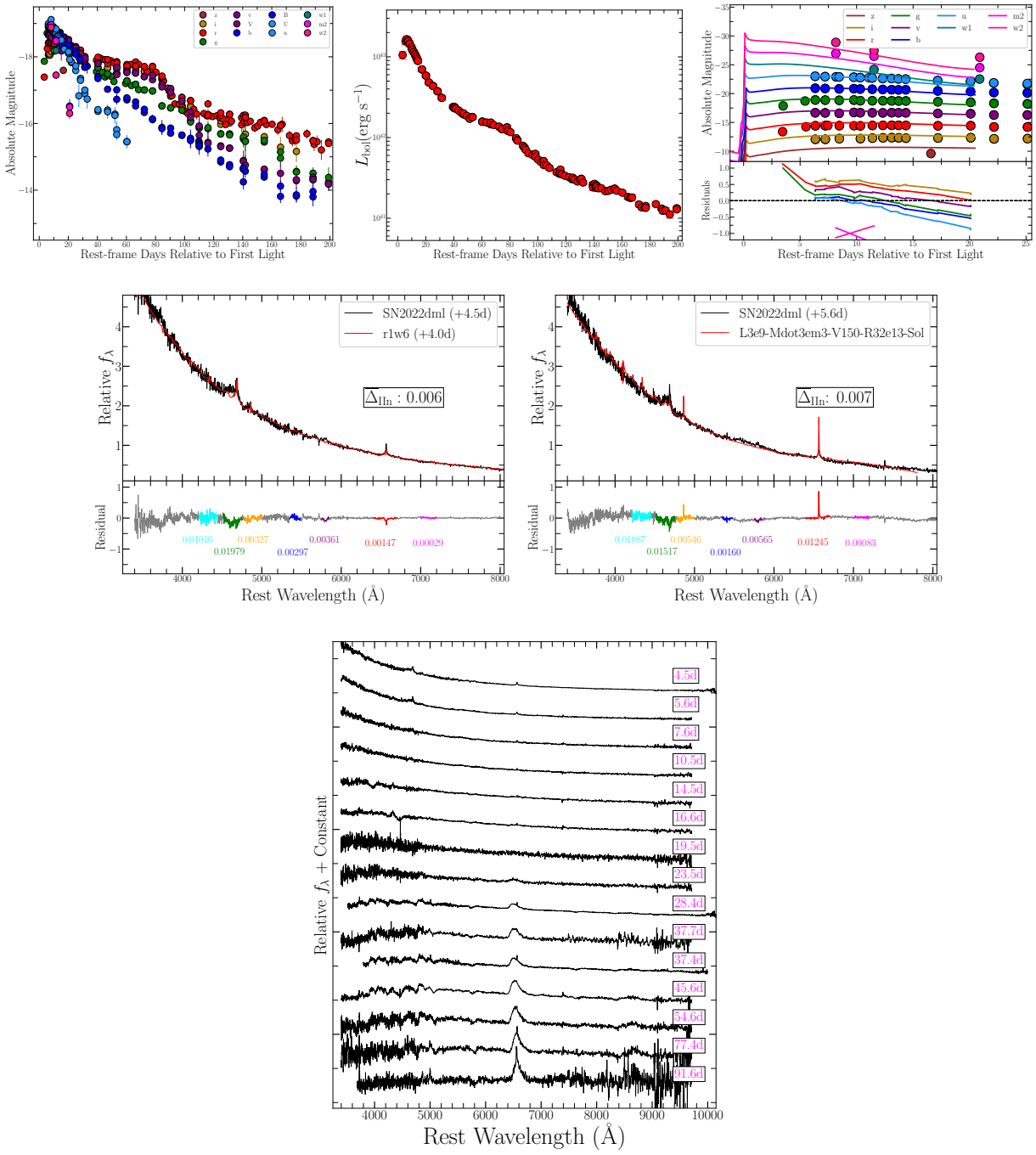

Figure 9.38 (a) SN 2022dml (silver): (a) Multi-color light curves, (b) UVOIR bolometric light curve, (c) best fit multi-color light curve model from Haynie & Piro (2021), (d) best fit spectral model from `CMFGEN` grid, (e) best fit spectral model from Boian & Groh (2020) grid, and (f) spectral series.

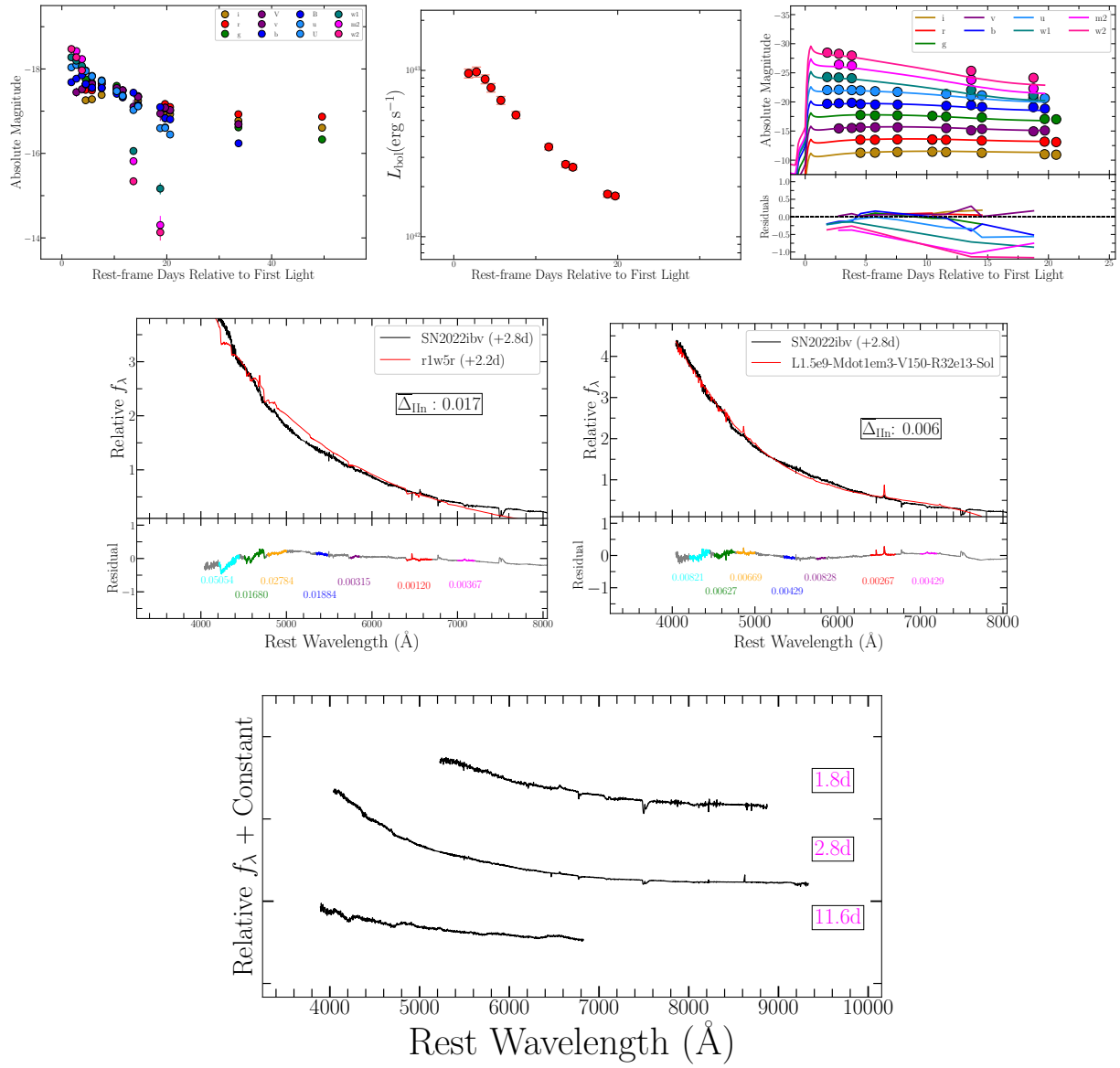

Figure 9.39 (a) SN 2022ibv (gold): (a) Multi-color light curves, (b) UVOIR bolometric light curve, (c) best fit multi-color light curve model from Haynie & Piro (2021), (d) best fit spectral model from `CMFGEN` grid, (e) best fit spectral model from Boian & Groh (2020) grid, and (f) spectral series.

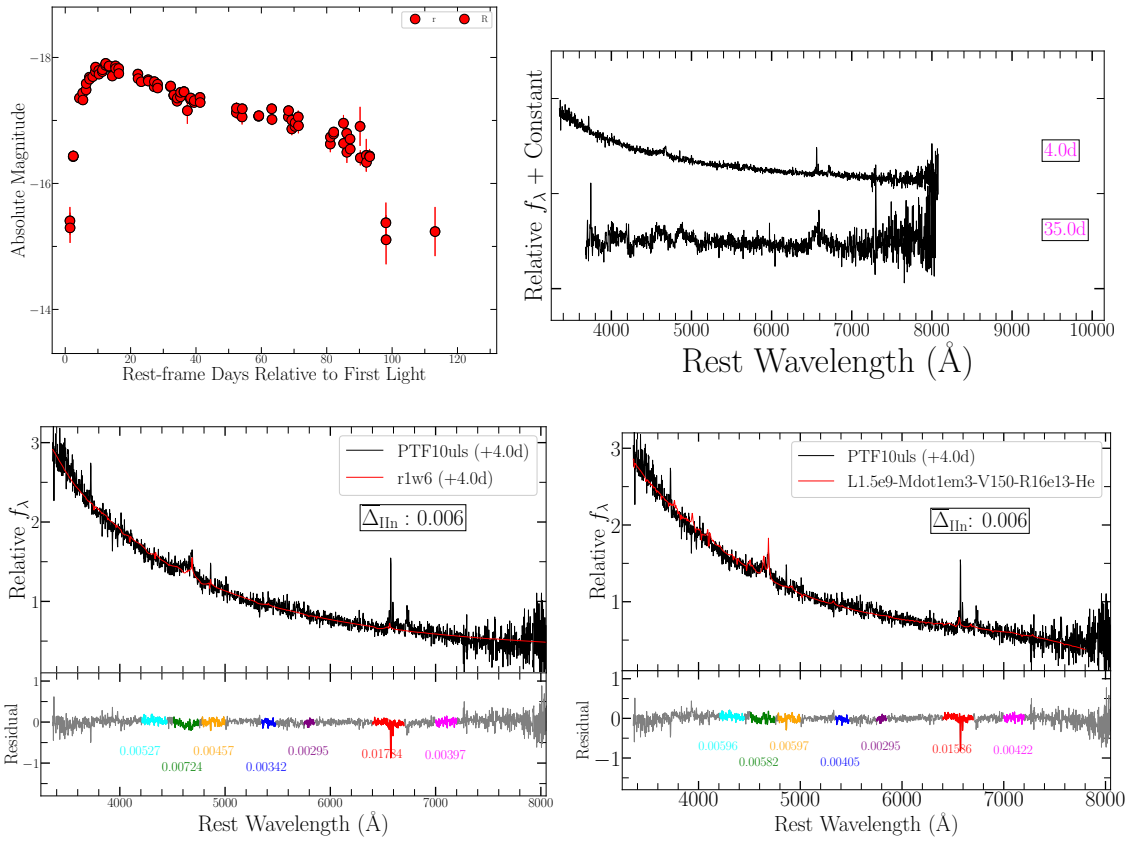

Figure 9.40 (a) PTF10uls (bronze): (a) Multi-color light curves, (b) spectral series, (c) best fit spectral model from `CMFGEN` grid, (d) best fit spectral model from Boian & Groh (2020) grid. Spectra and optical photometry are from Khazov et al. (2016).

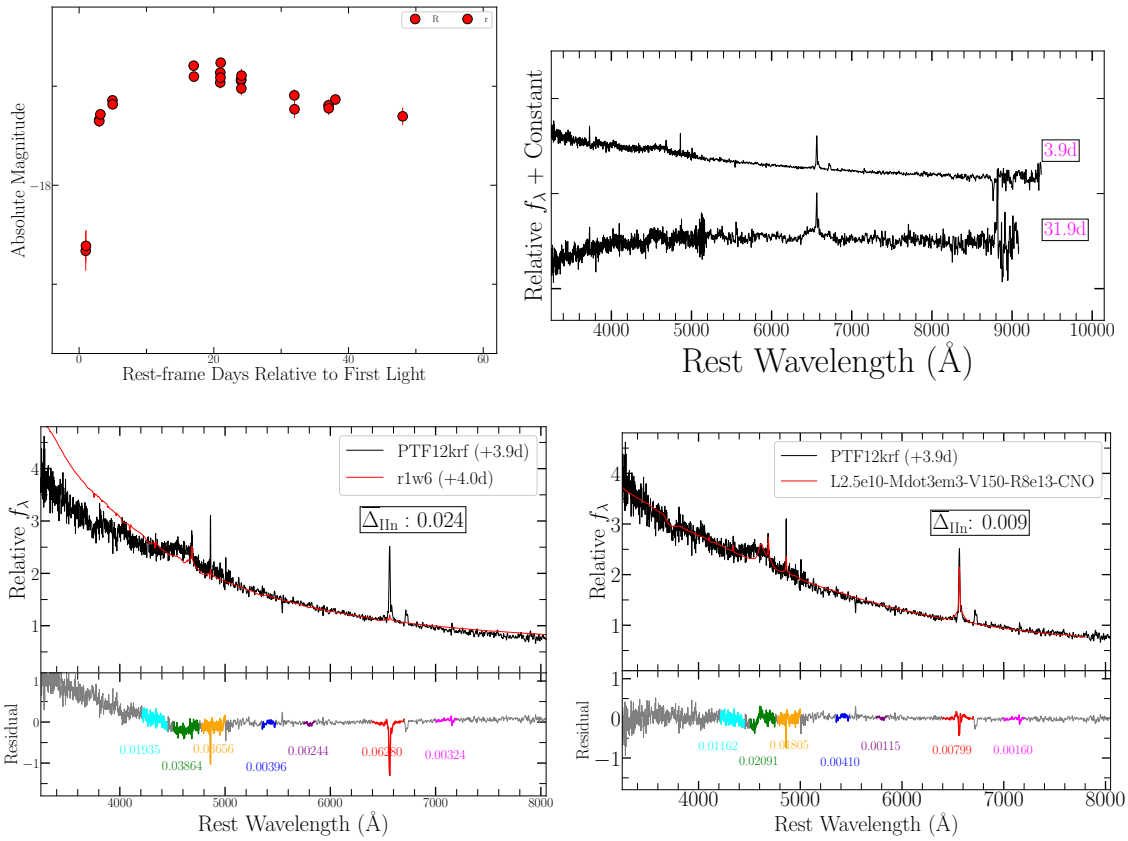

Figure 9.41 (a) PTF12krf (bronze): (a) Multi-color light curves, (b) spectral series, (c) best fit spectral model from `CMFGEN` grid, (d) best fit spectral model from Boian & Groh (2020) grid. Spectra and optical photometry are from Khazov et al. (2016).

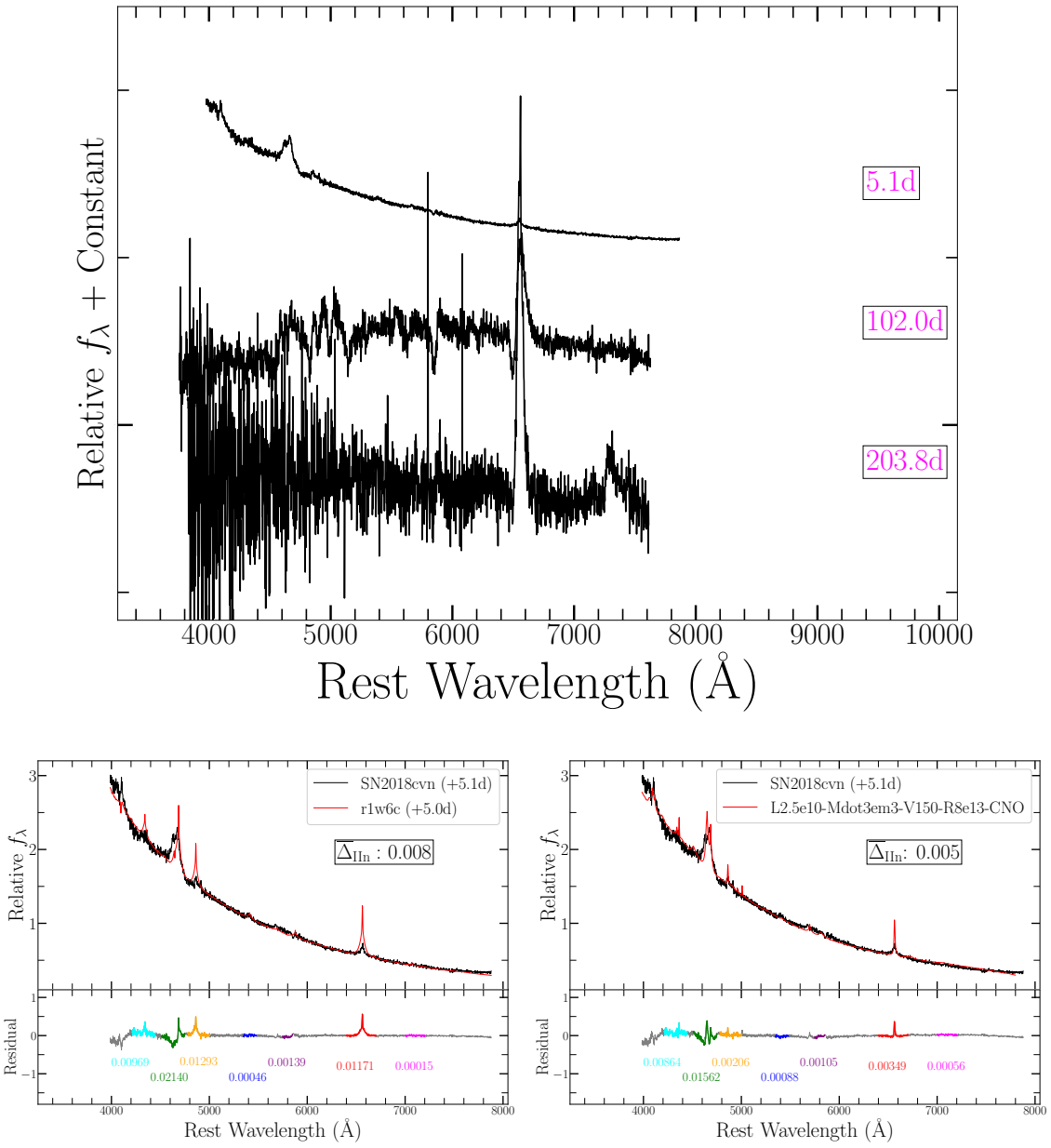

Figure 9.42 (a) SN 2018cvn (bronze): (a) spectral series, (b) best fit spectral model from `CMFGEN` grid, (c) best fit spectral model from Boian & Groh (2020) grid.

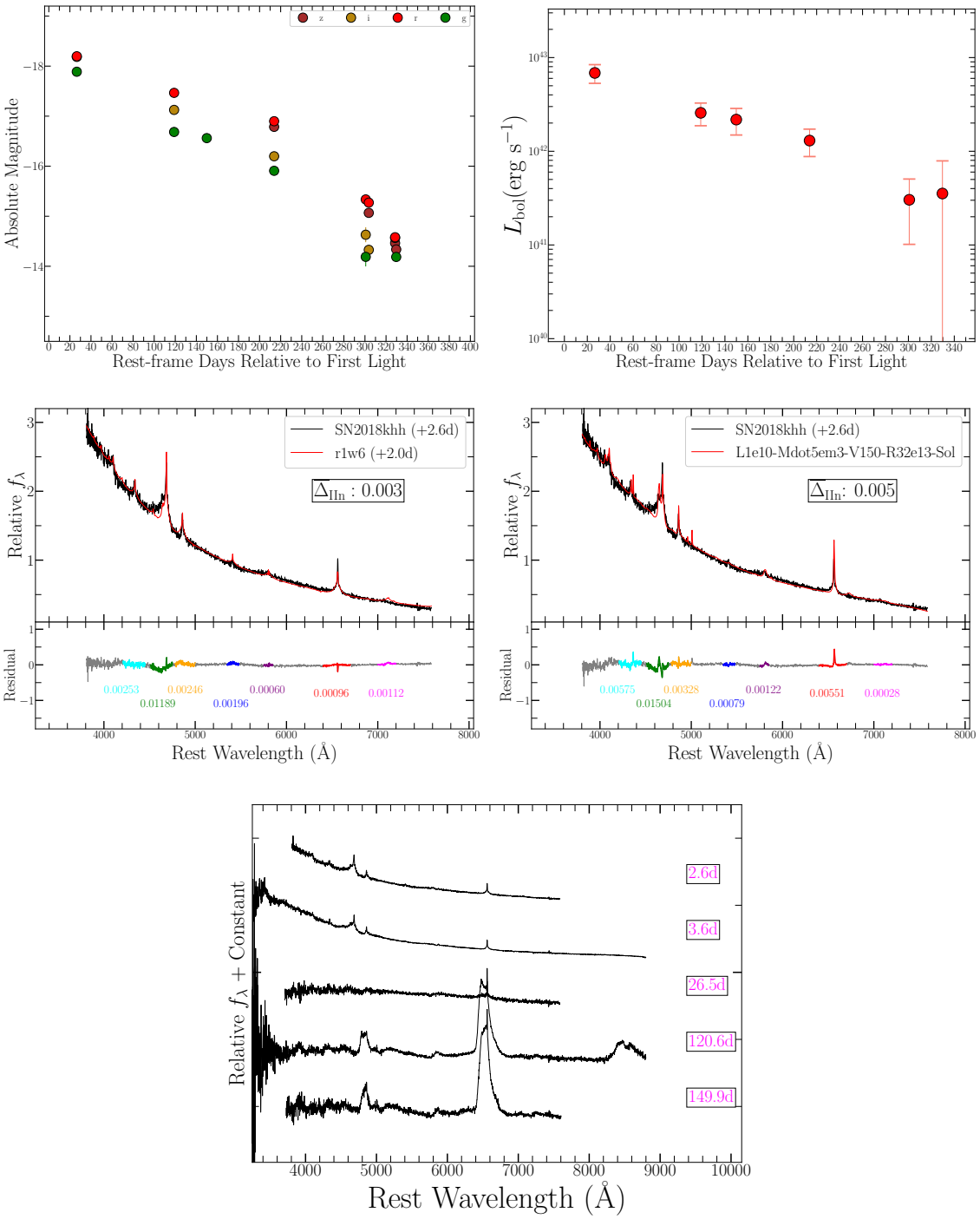

Figure 9.43 (a) SN 2018khh (bronze): (a) Multi-color light curves, (b) spectral series, (c) best fit spectral model from `CMFGEN` grid, (d) best fit spectral model from Boian & Groh (2020) grid.

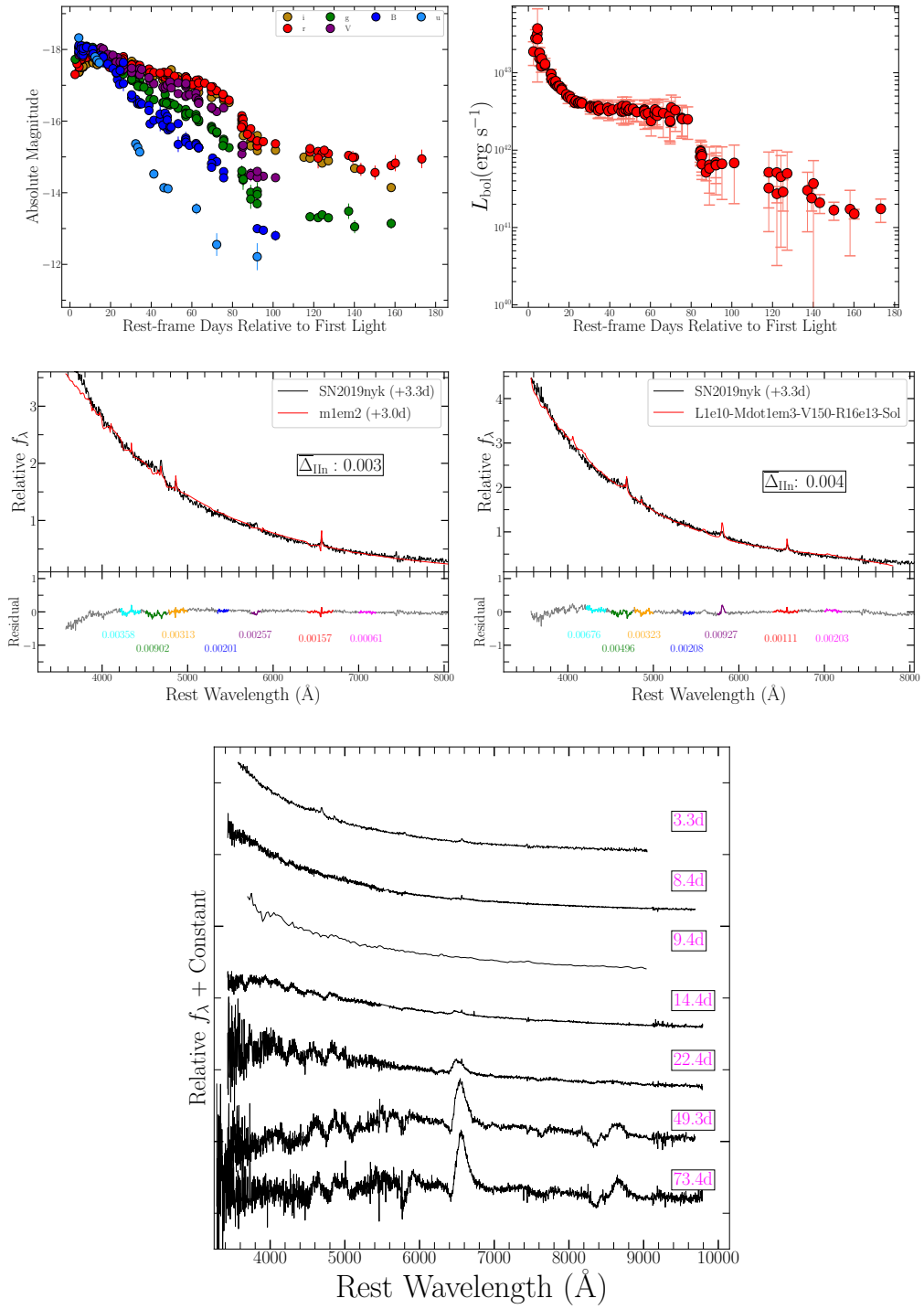

Figure 9.44 (a) SN 2019nyk (bronze): (a) Multi-color light curves, (b) spectral series, (c) best fit spectral model from `CMFGEN` grid, (d) best fit spectral model from Boian & Groh (2020) grid.

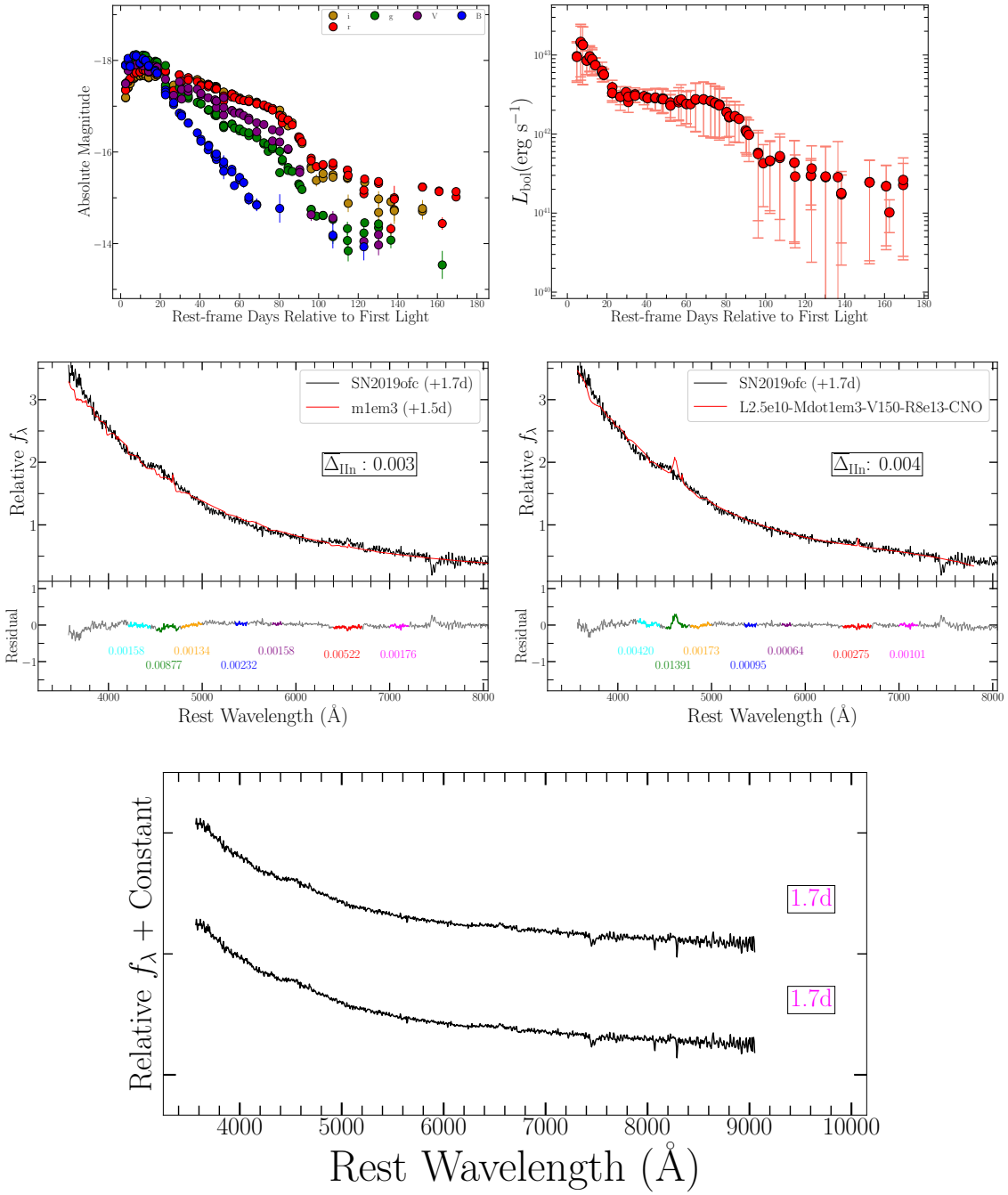

Figure 9.45 (a) SN 2019ofc (bronze): (a) Multi-color light curves, (b) spectral series, (c) best fit spectral model from `CMFGEN` grid, (d) best fit spectral model from Boian & Groh (2020) grid.

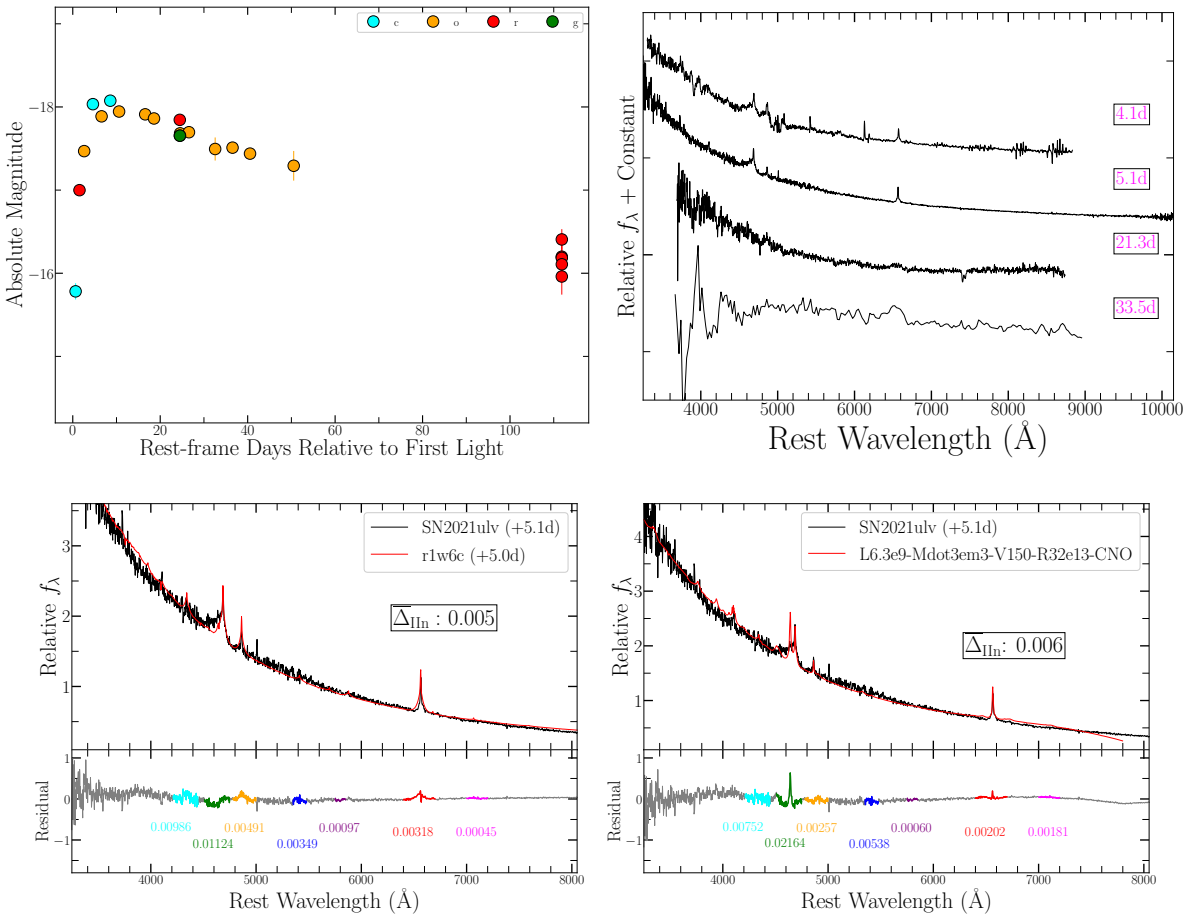

Figure 9.46 (a) SN 2021ulv (bronze): (a) Multi-color light curves, (b) spectral series, (c) best fit spectral model from `CMFGEN` grid, (d) best fit spectral model from Boian & Groh (2020) grid.

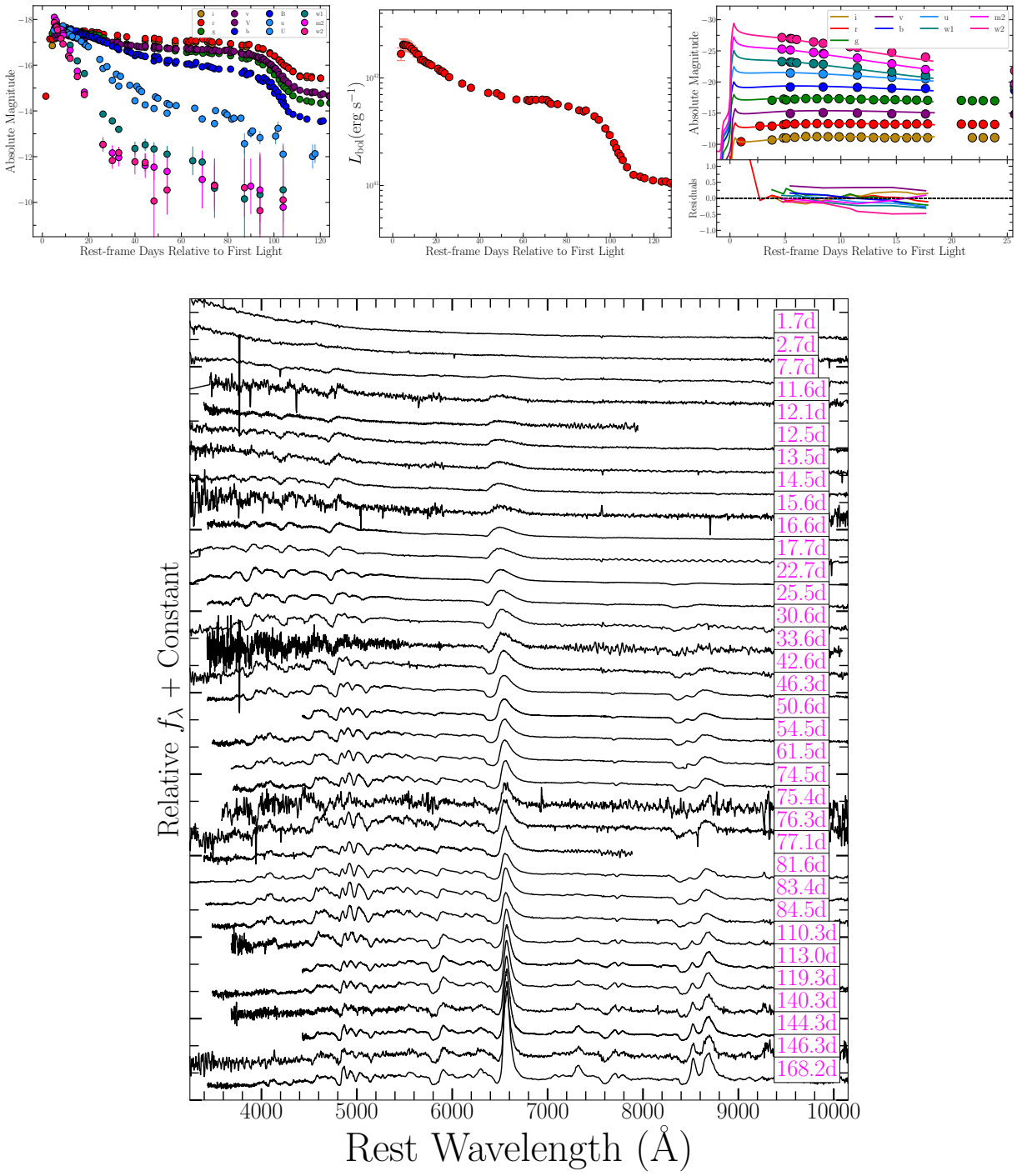

Figure 9.47 (a) SN 2013ab (comparison): (a) Multi-color light curves, (b) UVOIR bolometric light curve, (c) best fit multi-color light curve model from Haynie & Piro (2021), (d) spectral series. Spectra and photometry are from Bose et al. (2015).

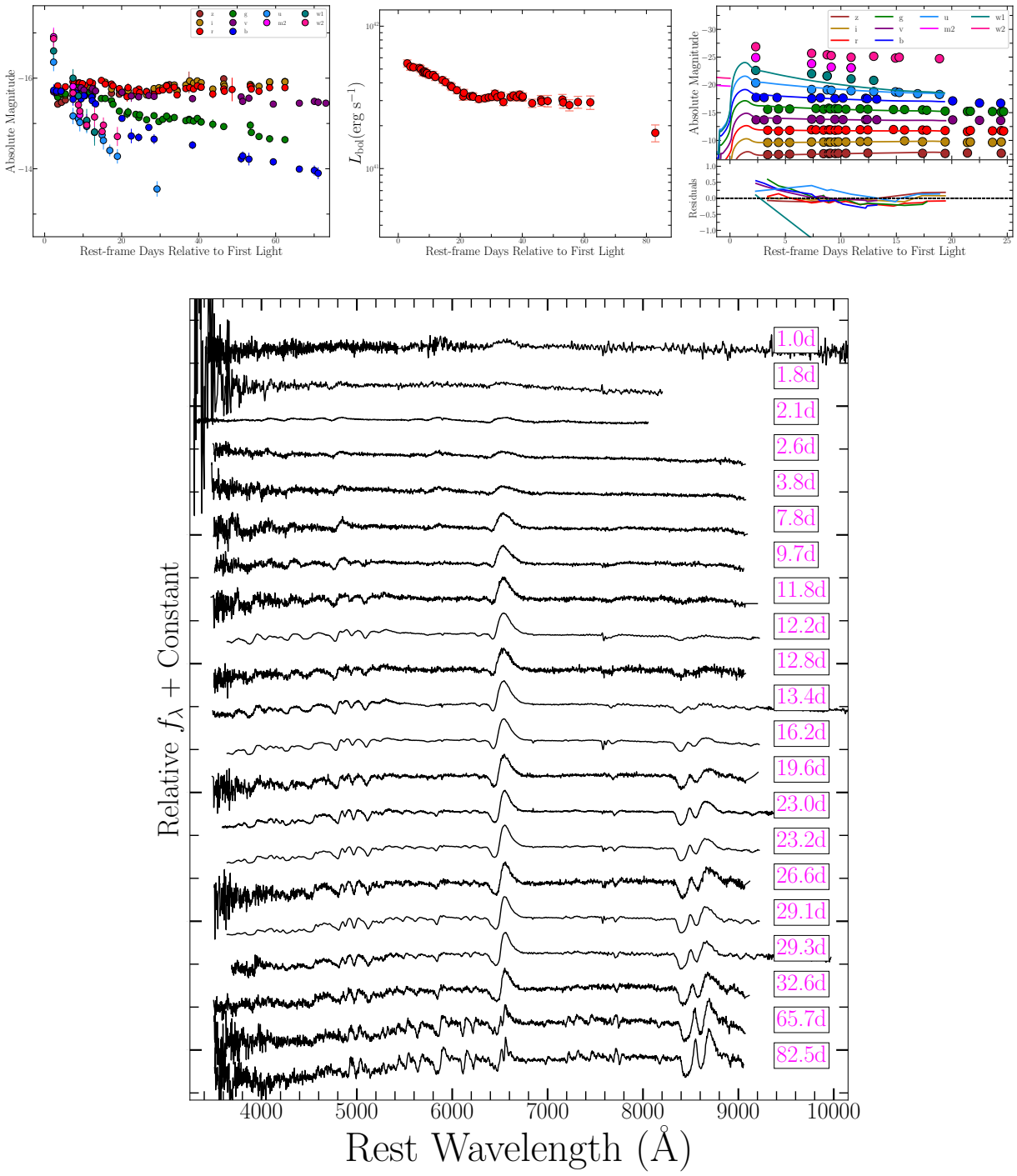

Figure 9.48 (a) SN 2013am (comparison): (a) Multi-color light curves, (b) UVOIR bolometric light curve, (c) best fit multi-color light curve model from Haynie & Piro (2021), (d) spectral series. Spectra and photometry are from Zhang et al. (2014).

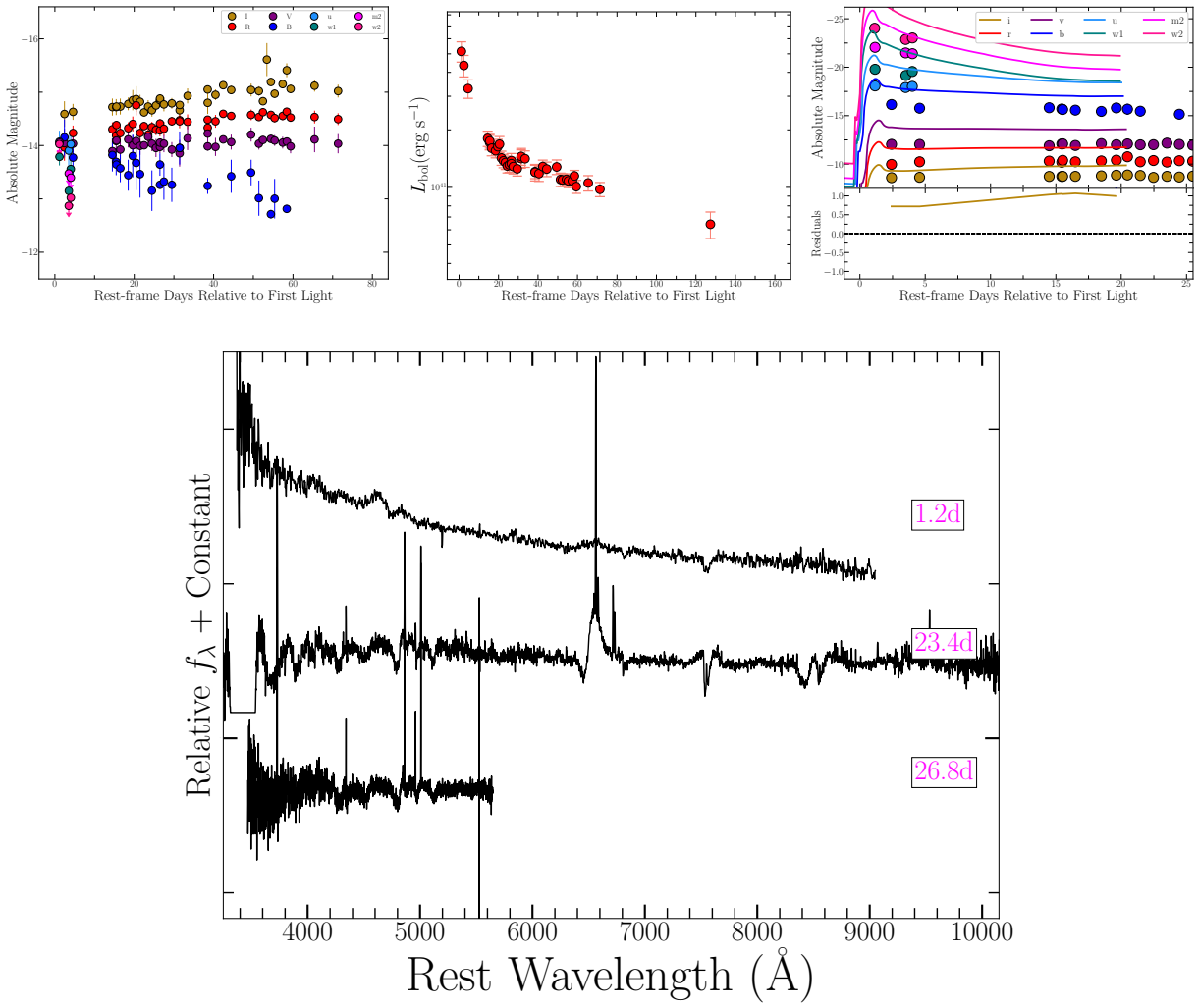

Figure 9.49 (a) SN 2013ft (comparison): (a) Multi-color light curves, (b) UVOIR bolometric light curve, (c) best fit multi-color light curve model from Haynie & Piro (2021), (d) spectral series. Spectra and photometry are from Khazov et al. (2016); de Jaeger et al. (2019).

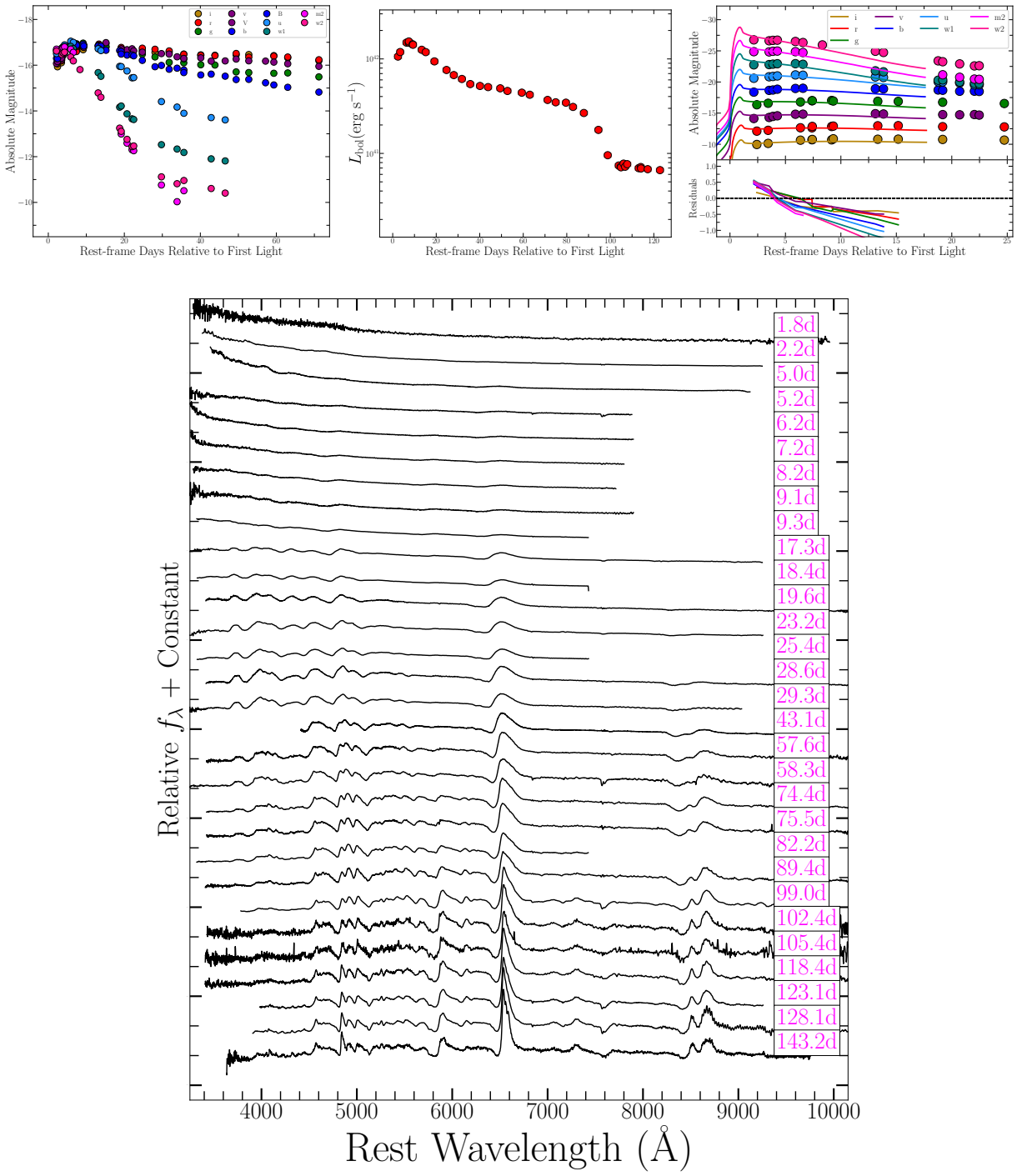

Figure 9.50 (a) SN 2016X (comparison): (a) Multi-color light curves, (b) UVOIR bolometric light curve, (c) best fit multi-color light curve model from Haynie & Piro (2021), (d) spectral series. Spectra and photometry are from Huang et al. (2018).

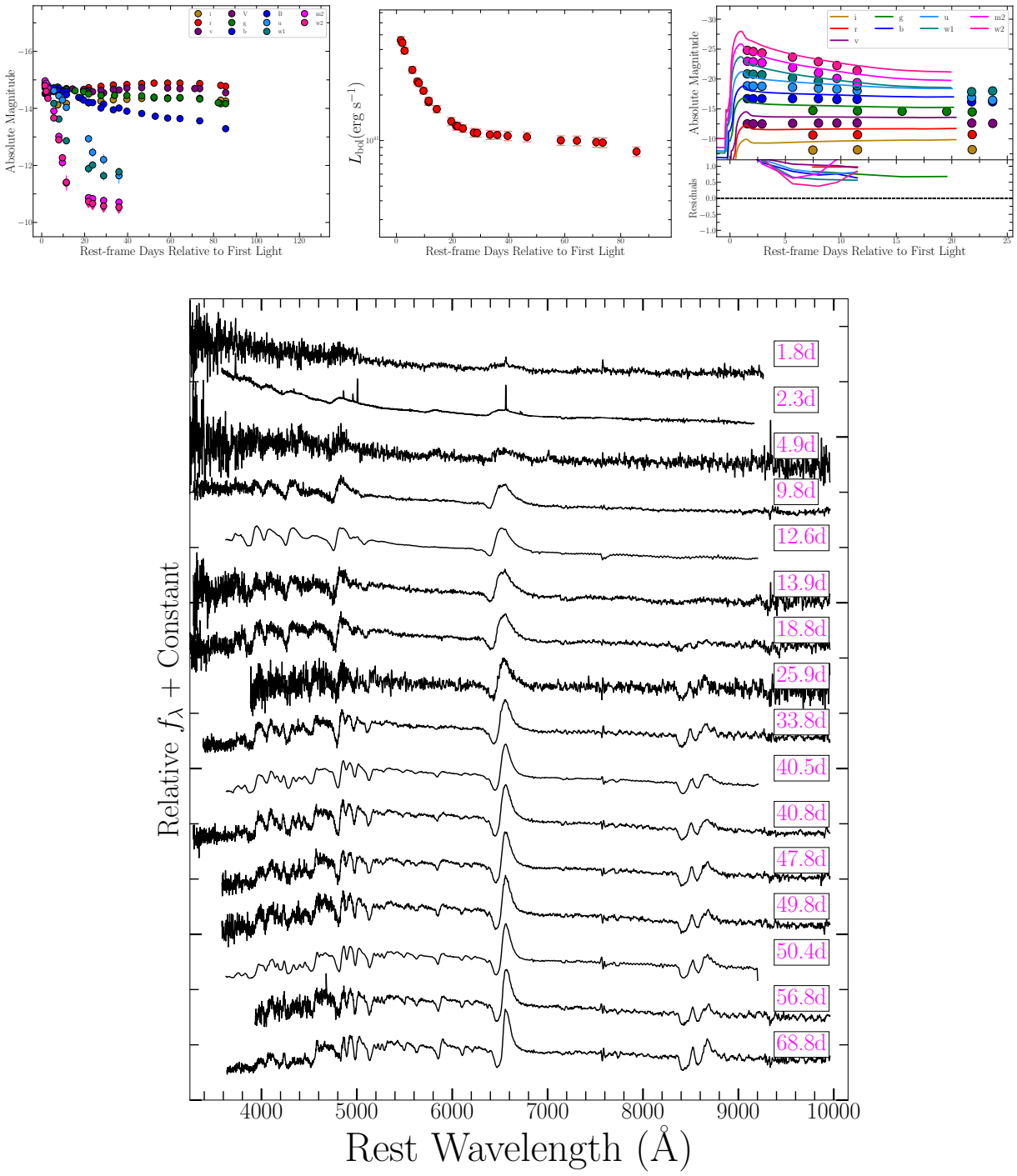

Figure 9.51 (a) SN 2016aqf (comparison): (a) Multi-color light curves, (b) UVOIR bolometric light curve, (c) best fit multi-color light curve model from Haynie & Piro (2021), (d) spectral series. Spectra and photometry are from Müller-Bravo et al. (2020).

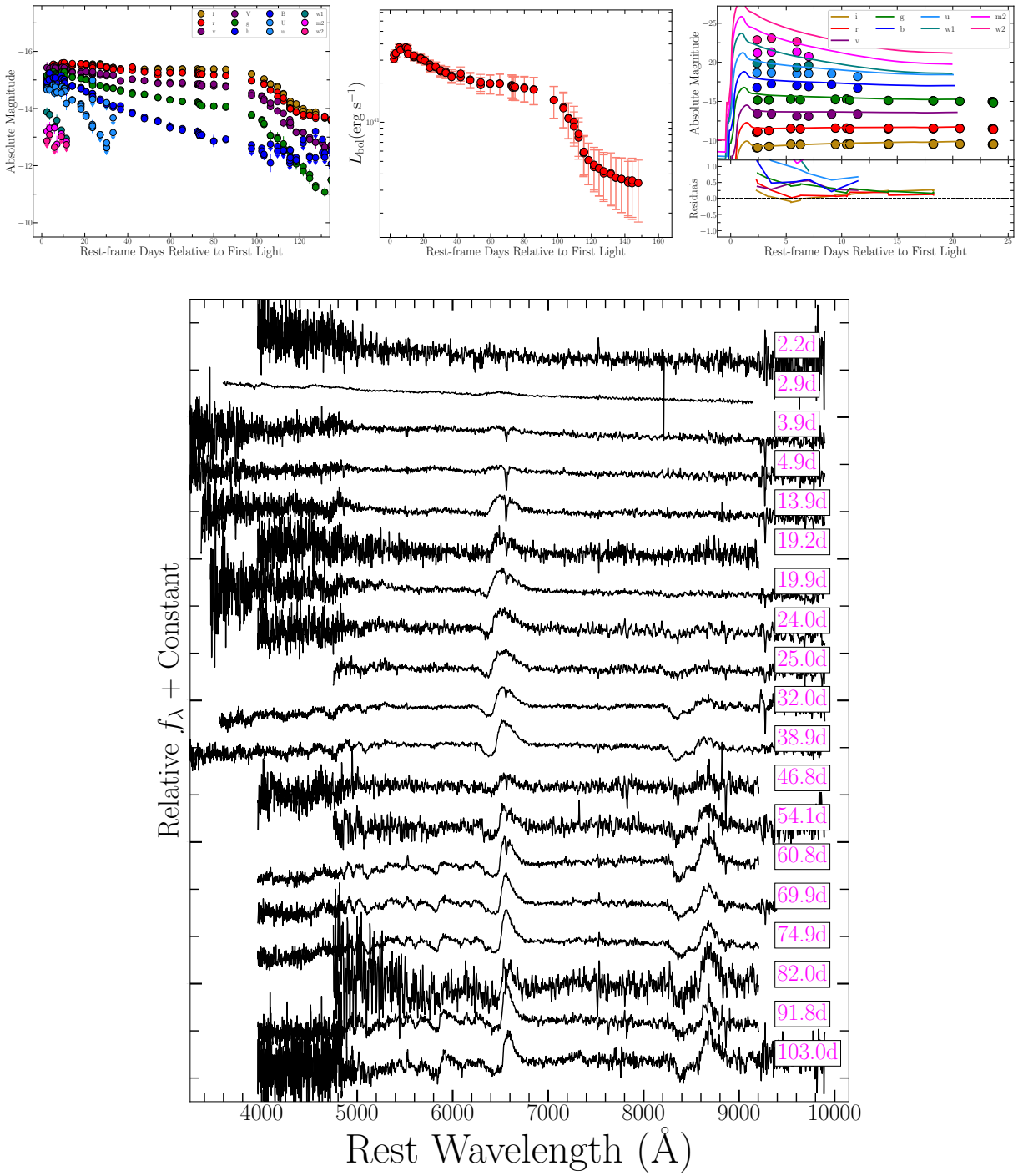

Figure 9.52 (a) SN 2016iyz (comparison): (a) Multi-color light curves, (b) UVOIR bolometric light curve, (c) best fit multi-color light curve model from Haynie & Piro (2021), (d) spectral series.

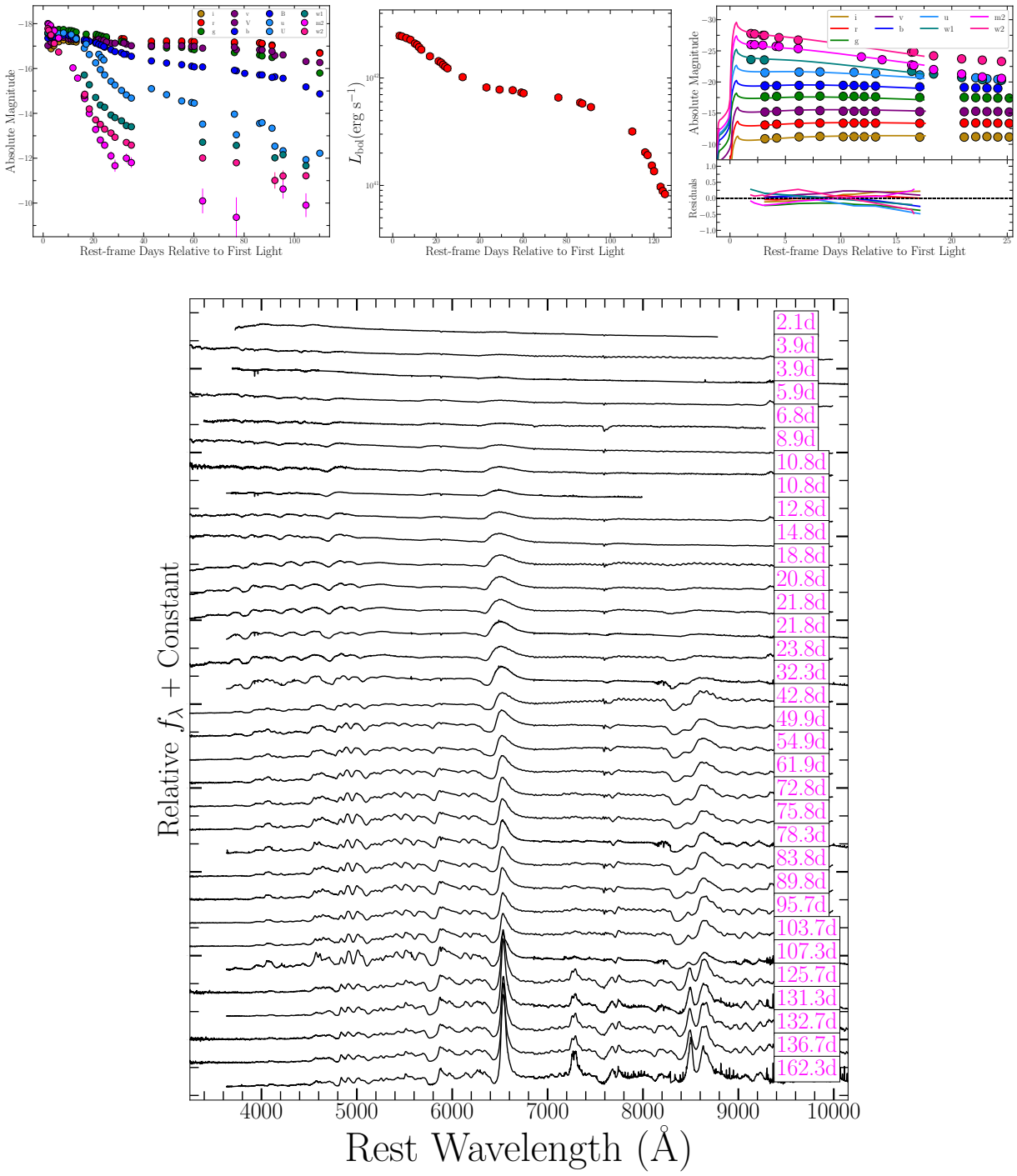

Figure 9.53 (a) SN 2017eaw (comparison): (a) Multi-color light curves, (b) UVOIR bolometric light curve, (c) best fit multi-color light curve model from Haynie & Piro (2021), (d) spectral series. Spectra and photometry are from Szalai et al. (2019).

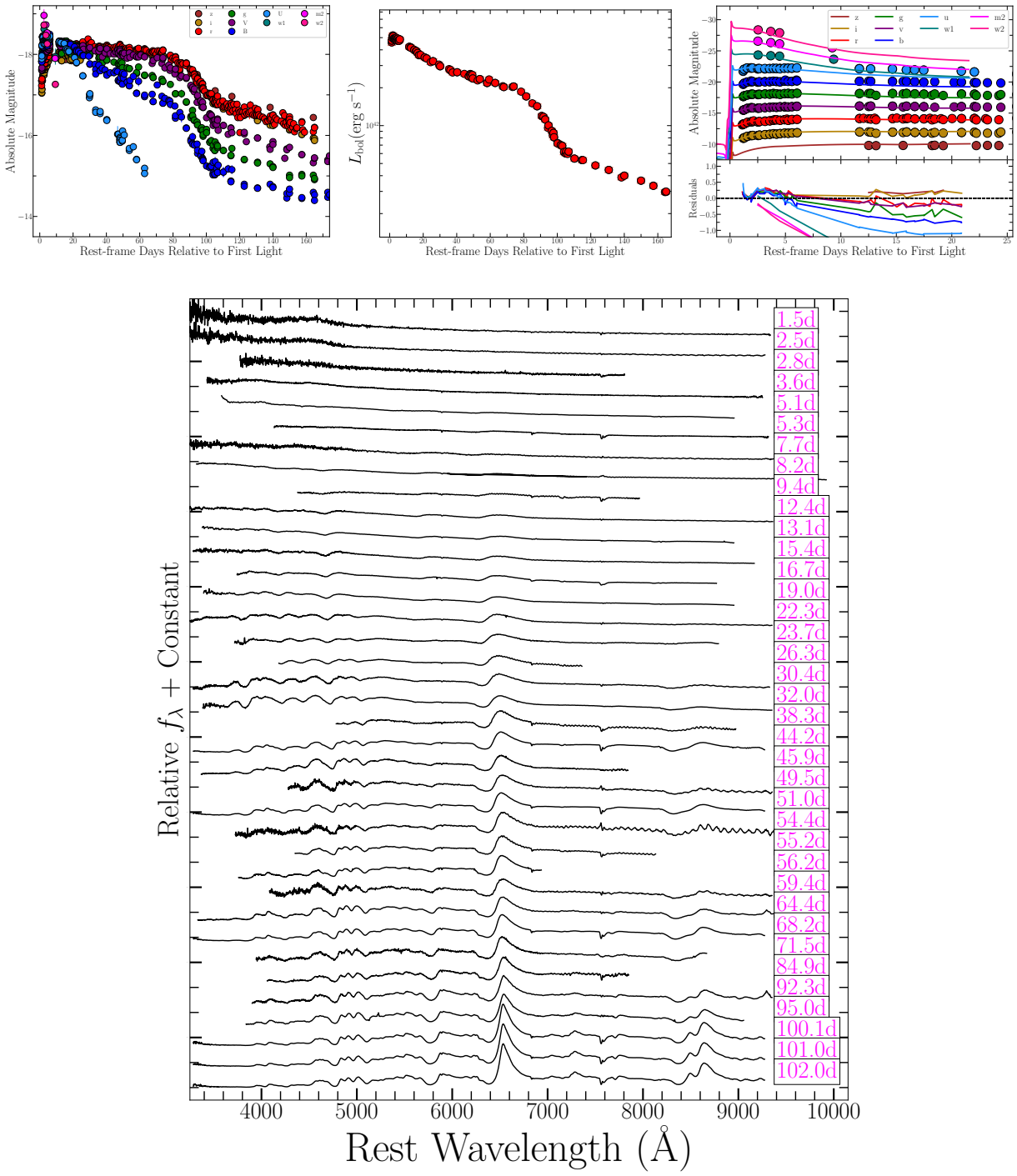

Figure 9.54 (a) SN 2017gmr (comparison): (a) Multi-color light curves, (b) UVOIR bolometric light curve, (c) best fit multi-color light curve model from Haynie & Piro (2021), (d) spectral series. Spectra and photometry are from Andrews et al. (2019).

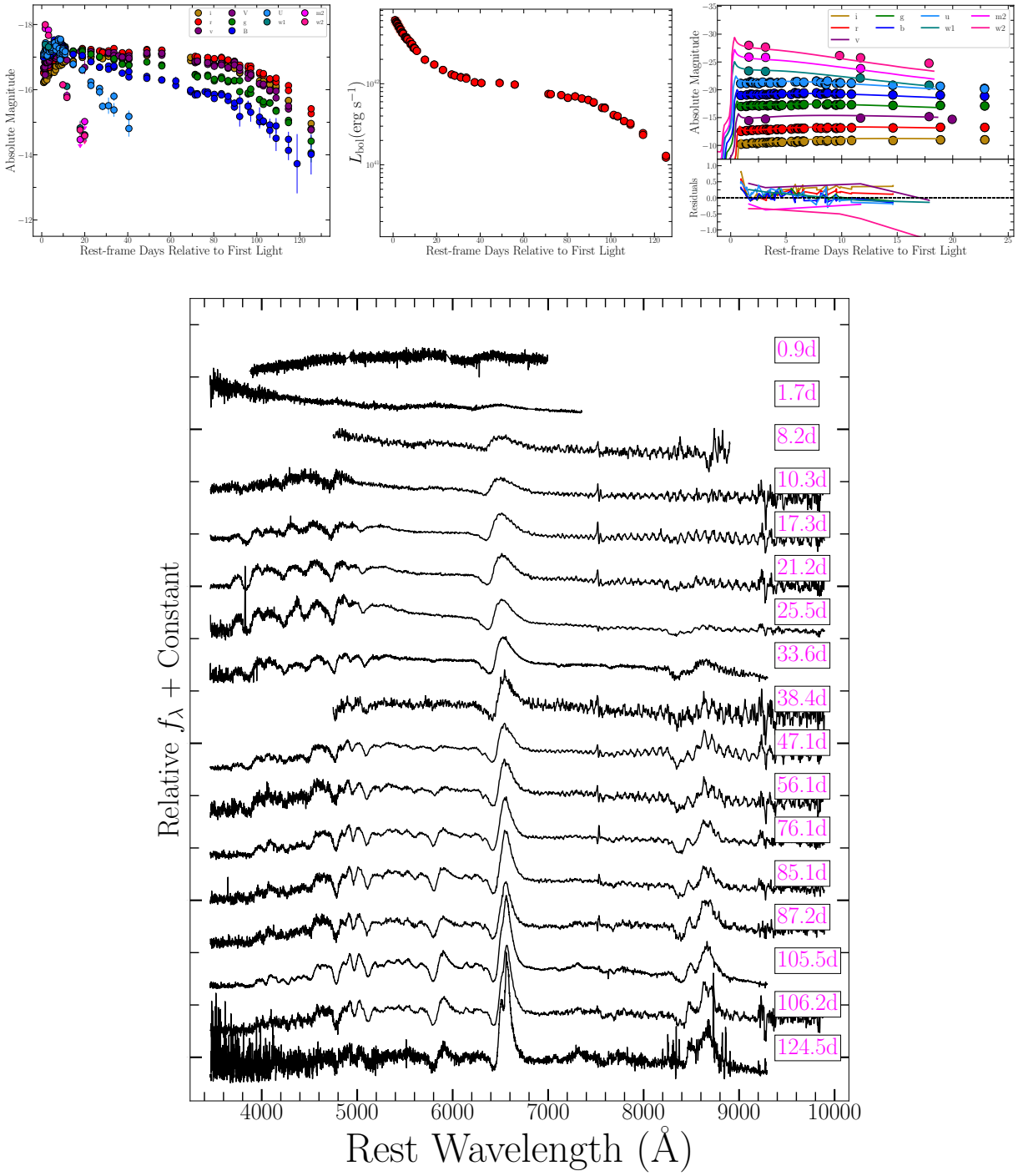

Figure 9.55 (a) SN 2018cuf (comparison): (a) Multi-color light curves, (b) UVOIR bolometric light curve, (c) best fit multi-color light curve model from Haynie & Piro (2021), (d) spectral series. Spectra and photometry are from Dong et al. (2021).

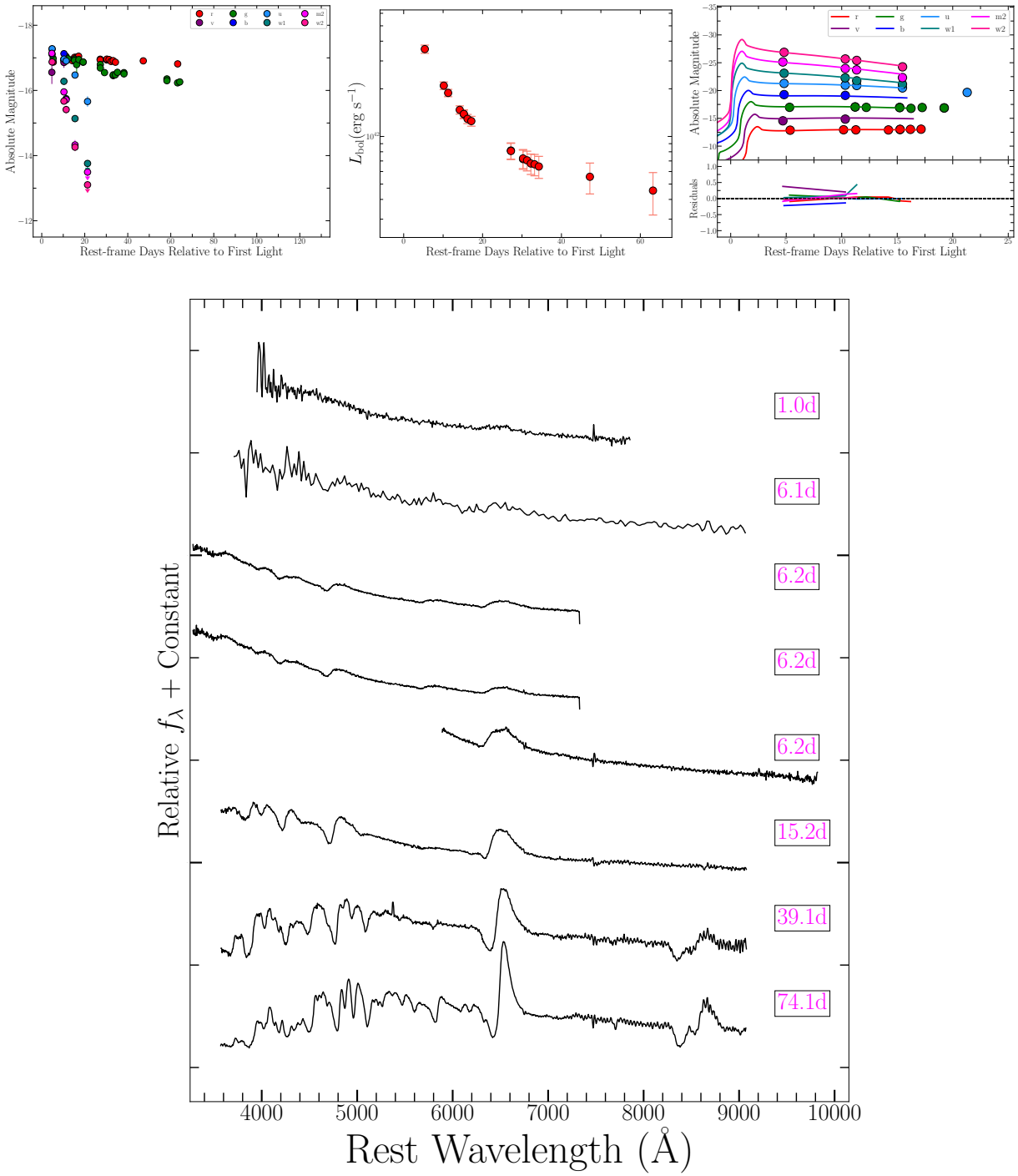

Figure 9.56 (a) SN 2018kpo (comparison): (a) Multi-color light curves, (b) UVOIR bolometric light curve, (c) best fit multi-color light curve model from Haynie & Piro (2021), (d) spectral series.

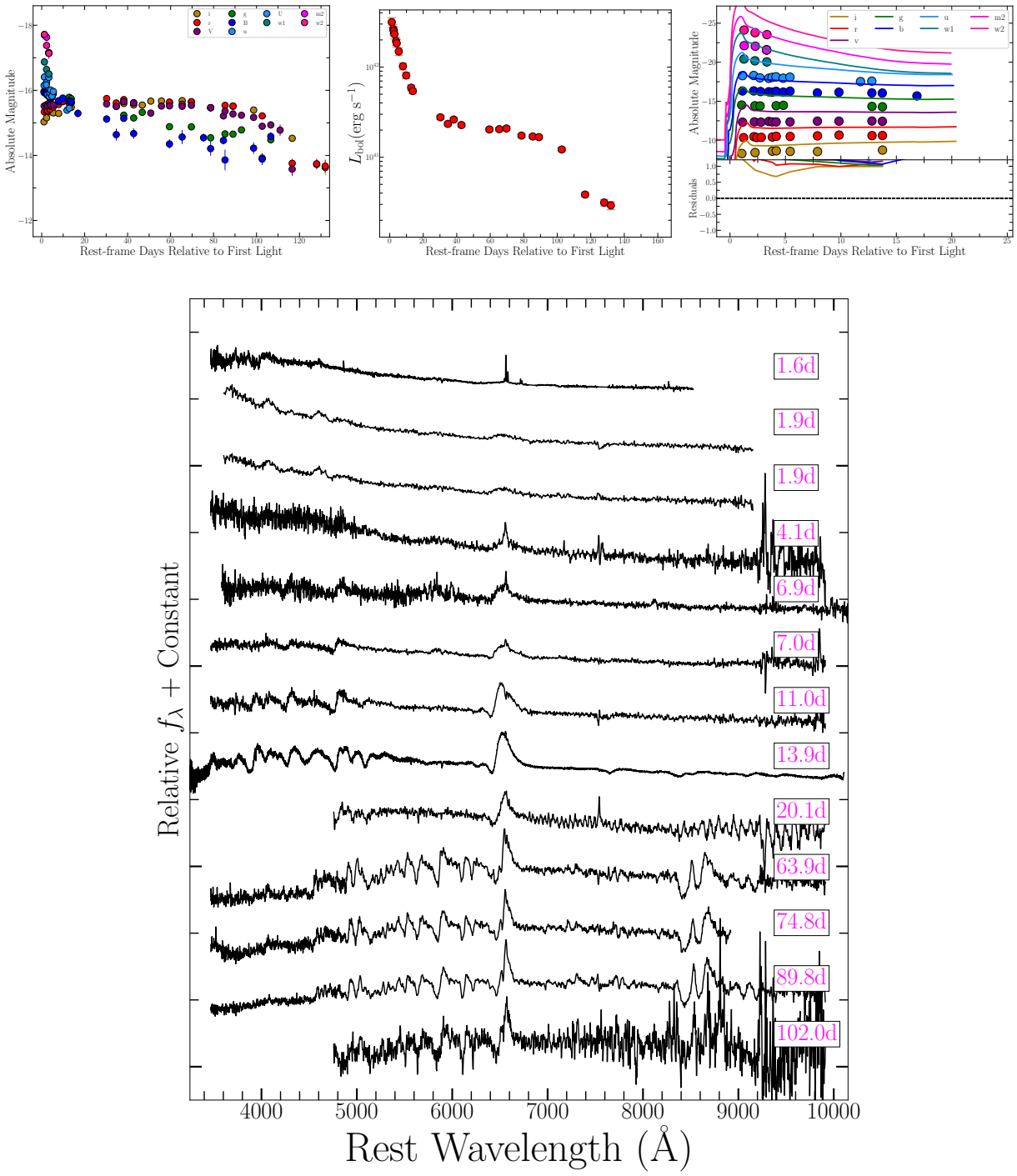

Figure 9.57 (a) SN 2018lab (comparison): (a) Multi-color light curves, (b) UVOIR bolometric light curve, (c) best fit multi-color light curve model from Haynie & Piro (2021), (d) spectral series. Spectra and photometry are from Pearson et al. (2023).

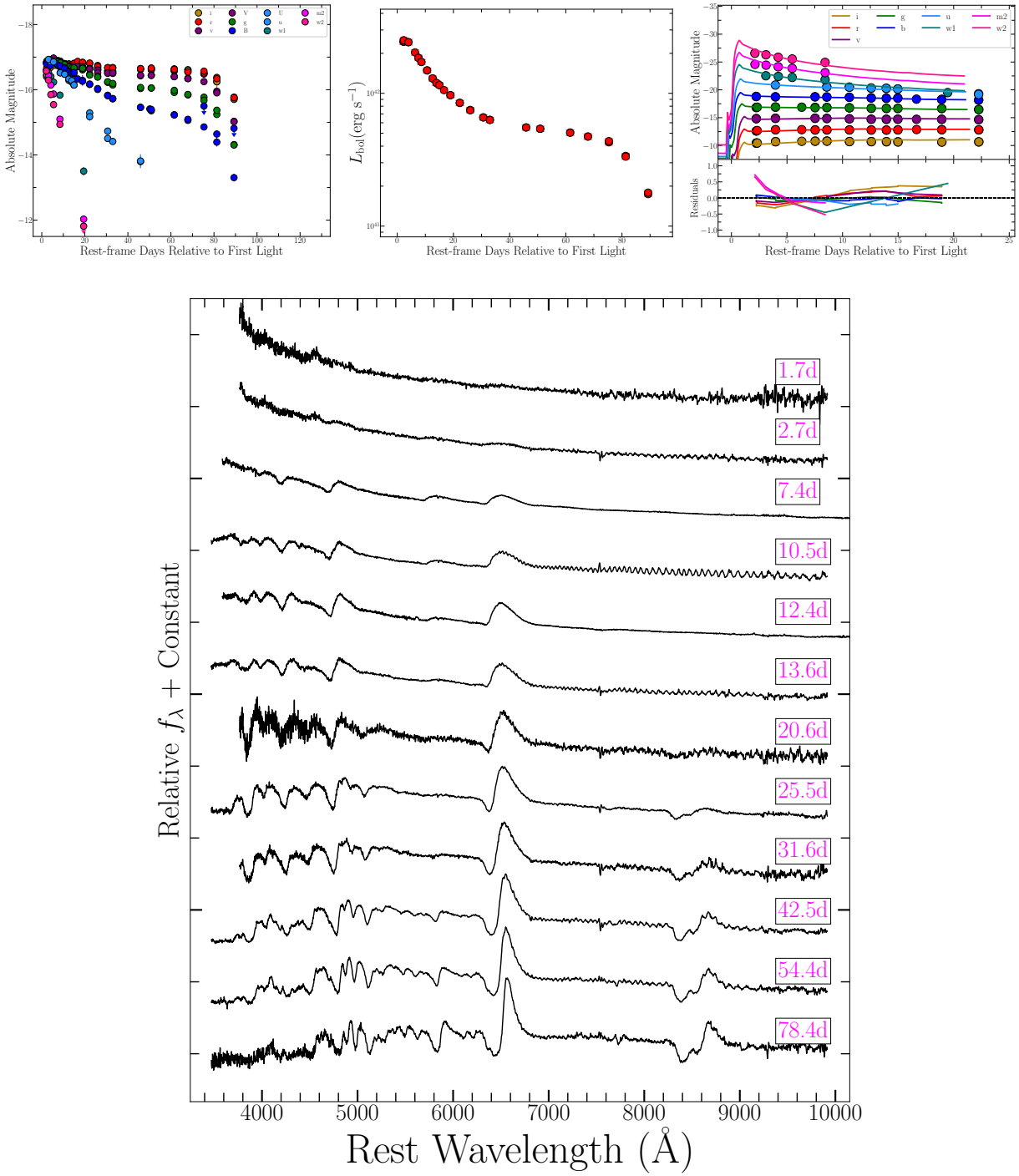

Figure 9.58 (a) SN 2019edo (comparison): (a) Multi-color light curves, (b) UVOIR bolometric light curve, (c) best fit multi-color light curve model from Haynie & Piro (2021), (d) spectral series.

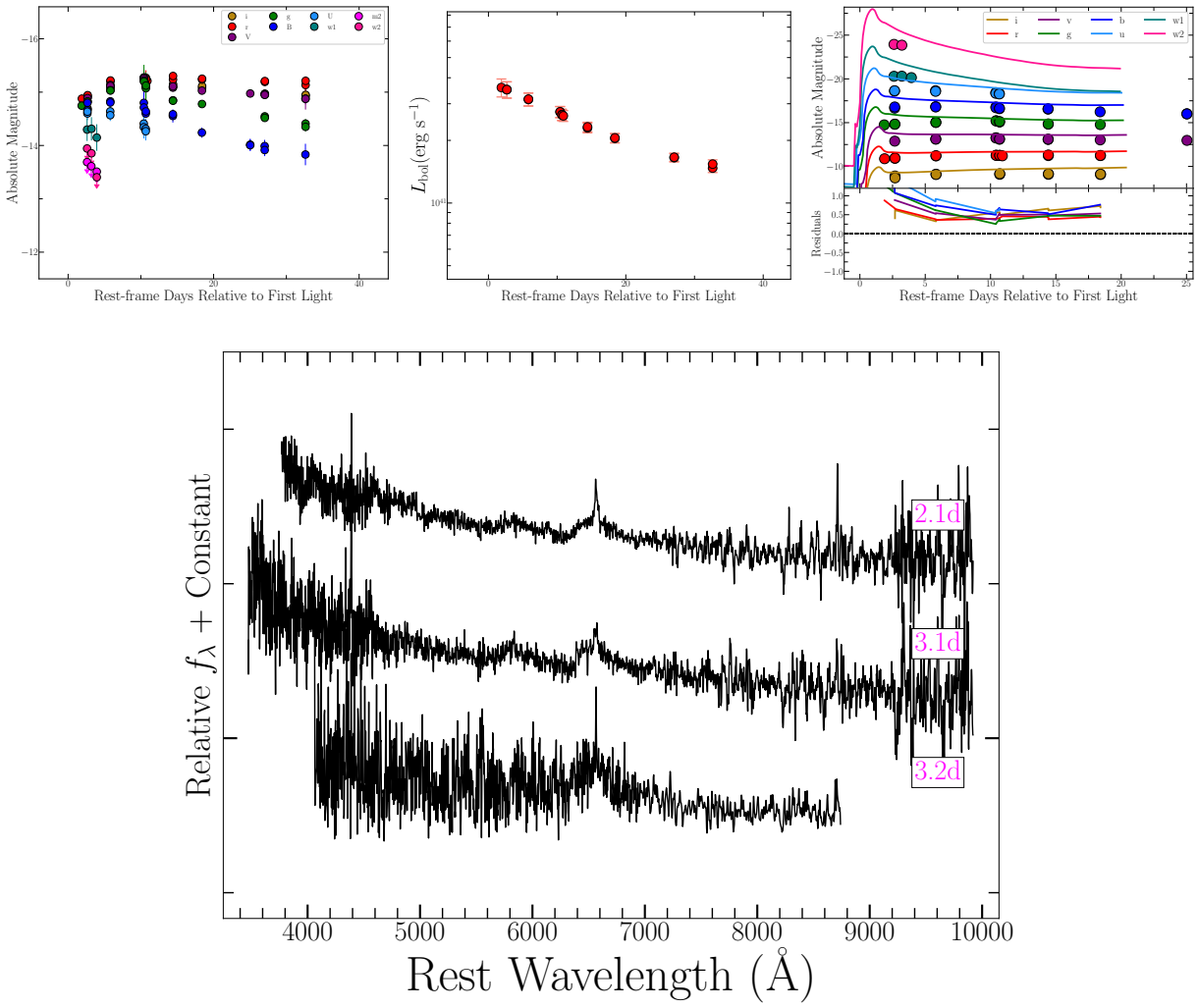

Figure 9.59 (a) SN 2019enr (comparison): (a) Multi-color light curves, (b) UVOIR bolometric light curve, (c) best fit multi-color light curve model from Haynie & Piro (2021), (d) spectral series.

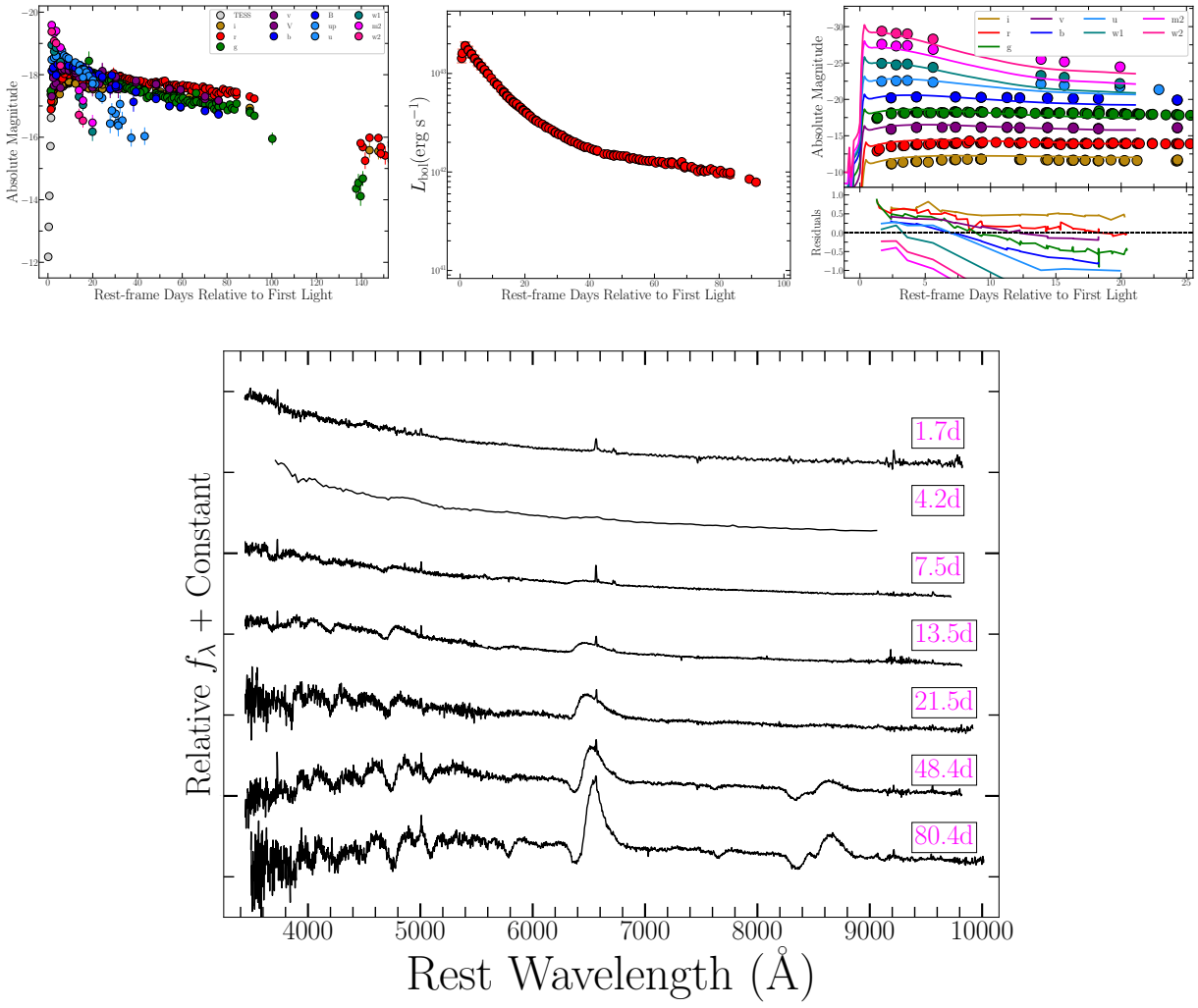

Figure 9.60 (a) SN 2019nvm (comparison): (a) Multi-color light curves, (b) UVOIR bolometric light curve, (c) best fit multi-color light curve model from Haynie & Piro (2021), (d) spectral series.

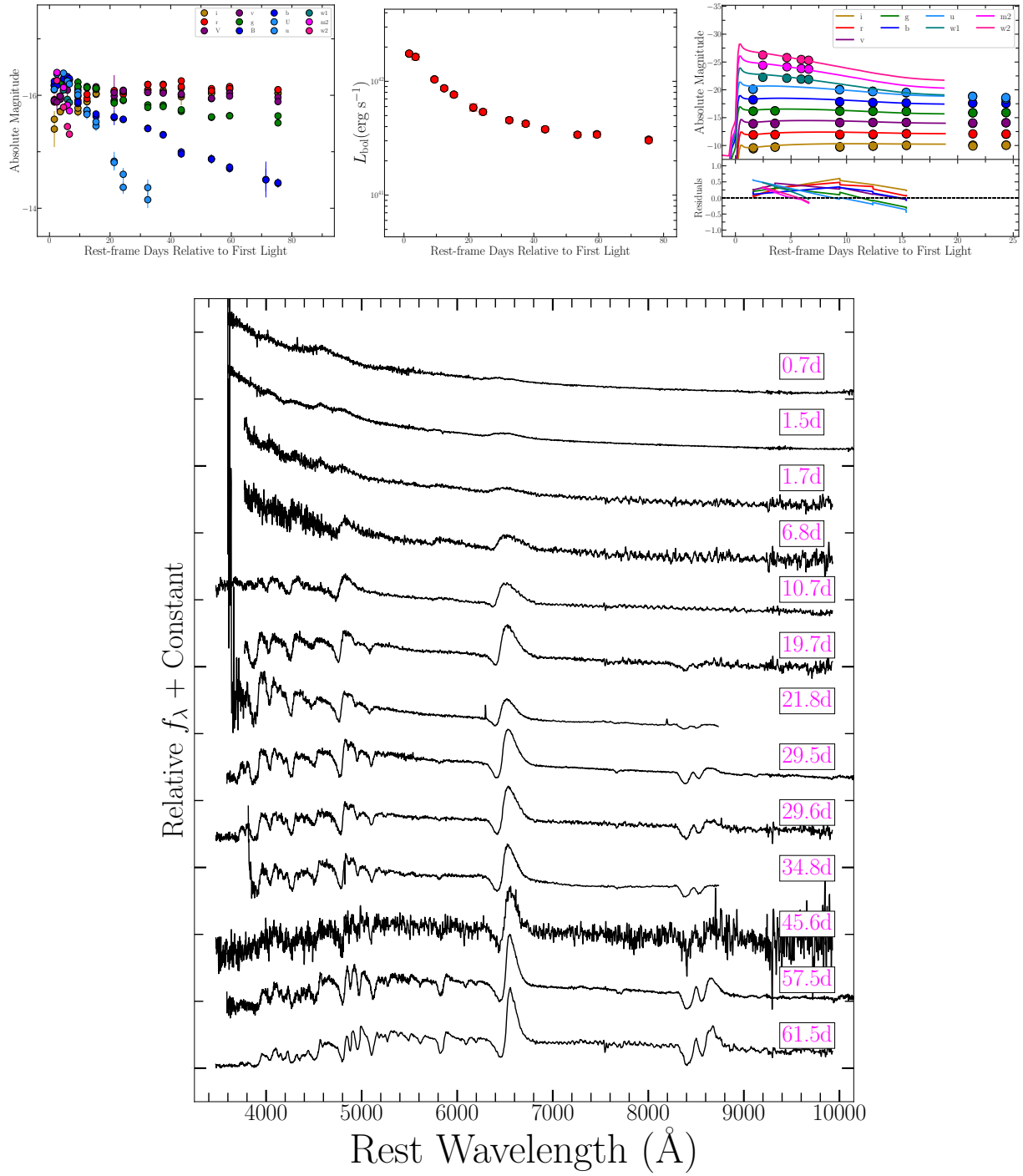

Figure 9.61 (a) SN 2019pjs (comparison): (a) Multi-color light curves, (b) UVOIR bolometric light curve, (c) best fit multi-color light curve model from Haynie & Piro (2021), (d) spectral series.

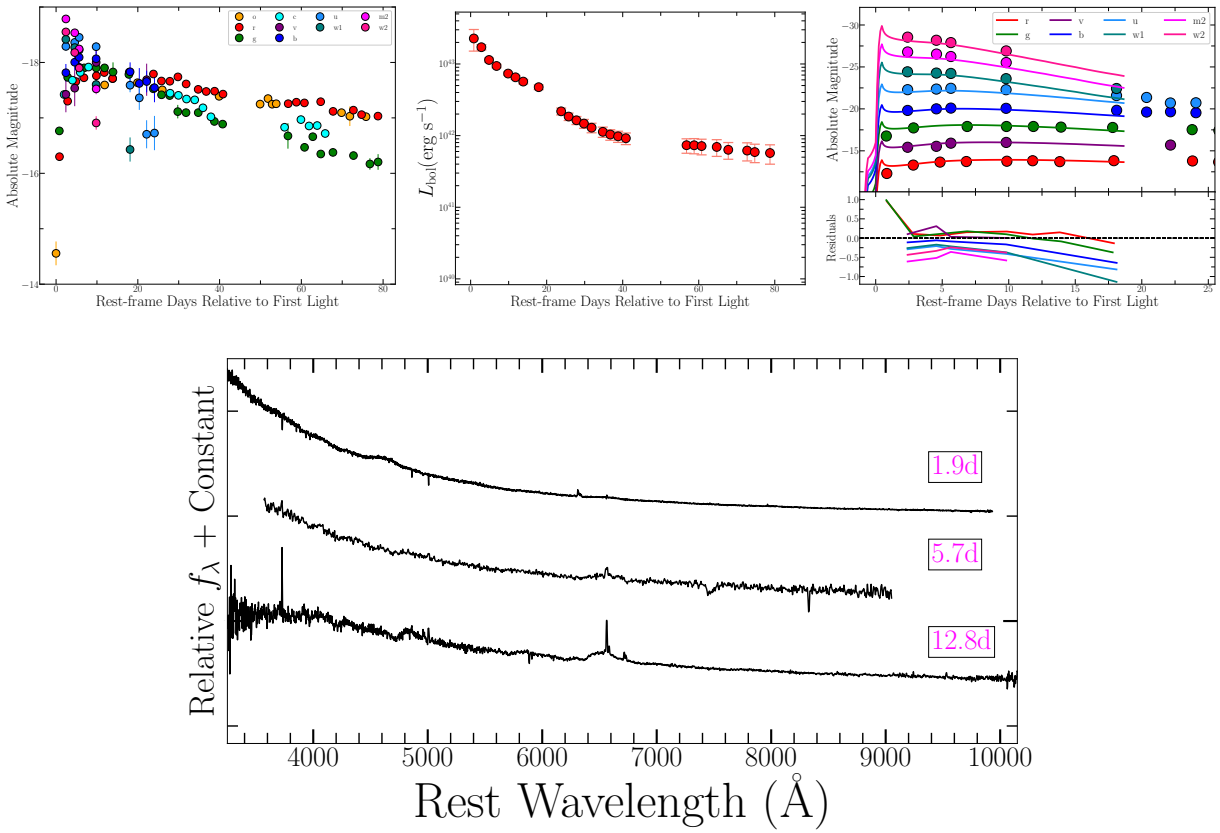

Figure 9.62 (a) SN 2020acbm (comparison): (a) Multi-color light curves, (b) UVOIR bolometric light curve, (c) best fit multi-color light curve model from Haynie & Piro (2021), (d) spectral series.

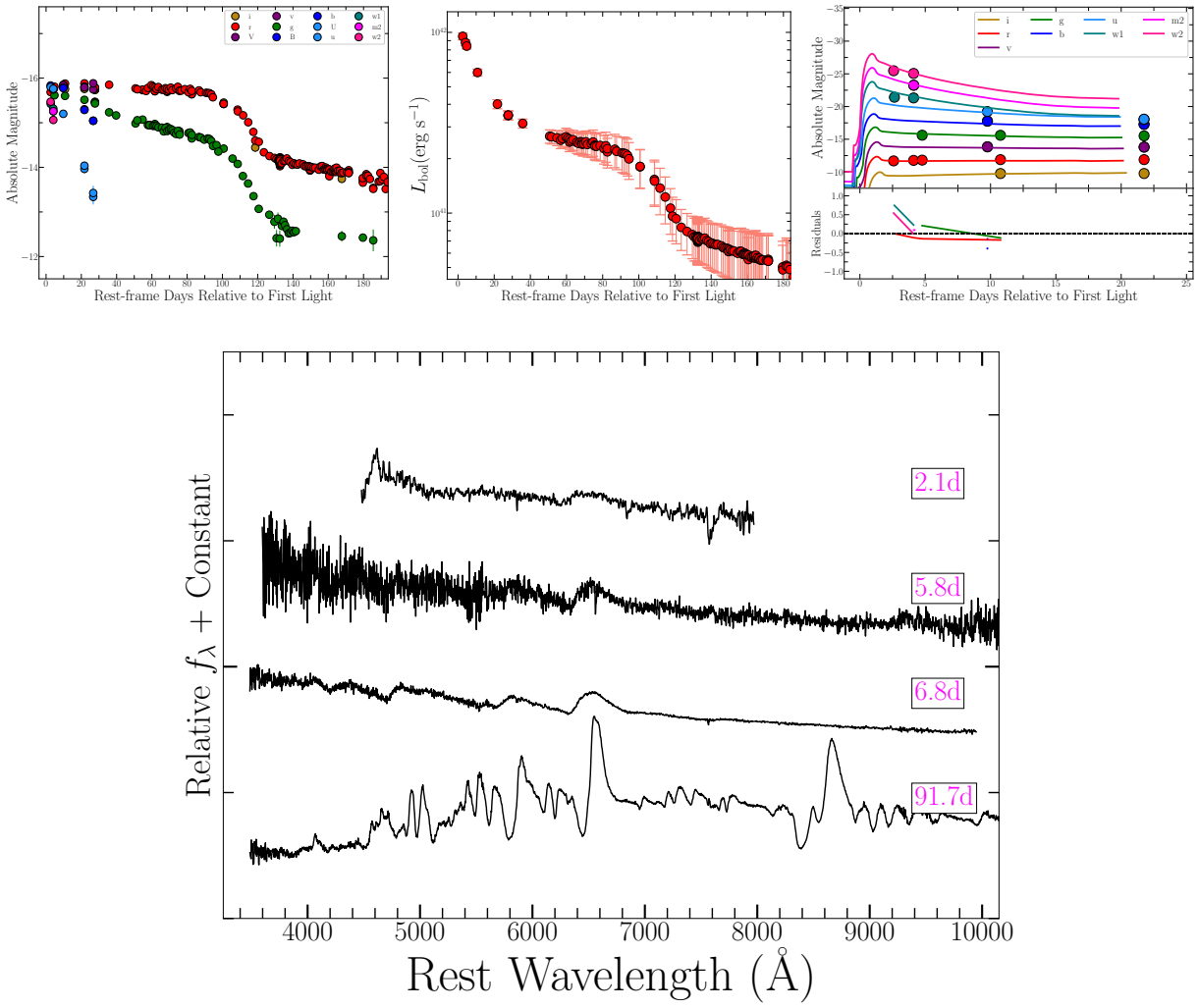

Figure 9.63 (a) SN 2020dpw (comparison): (a) Multi-color light curves, (b) UVOIR bolometric light curve, (c) best fit multi-color light curve model from Haynie & Piro (2021), (d) spectral series.

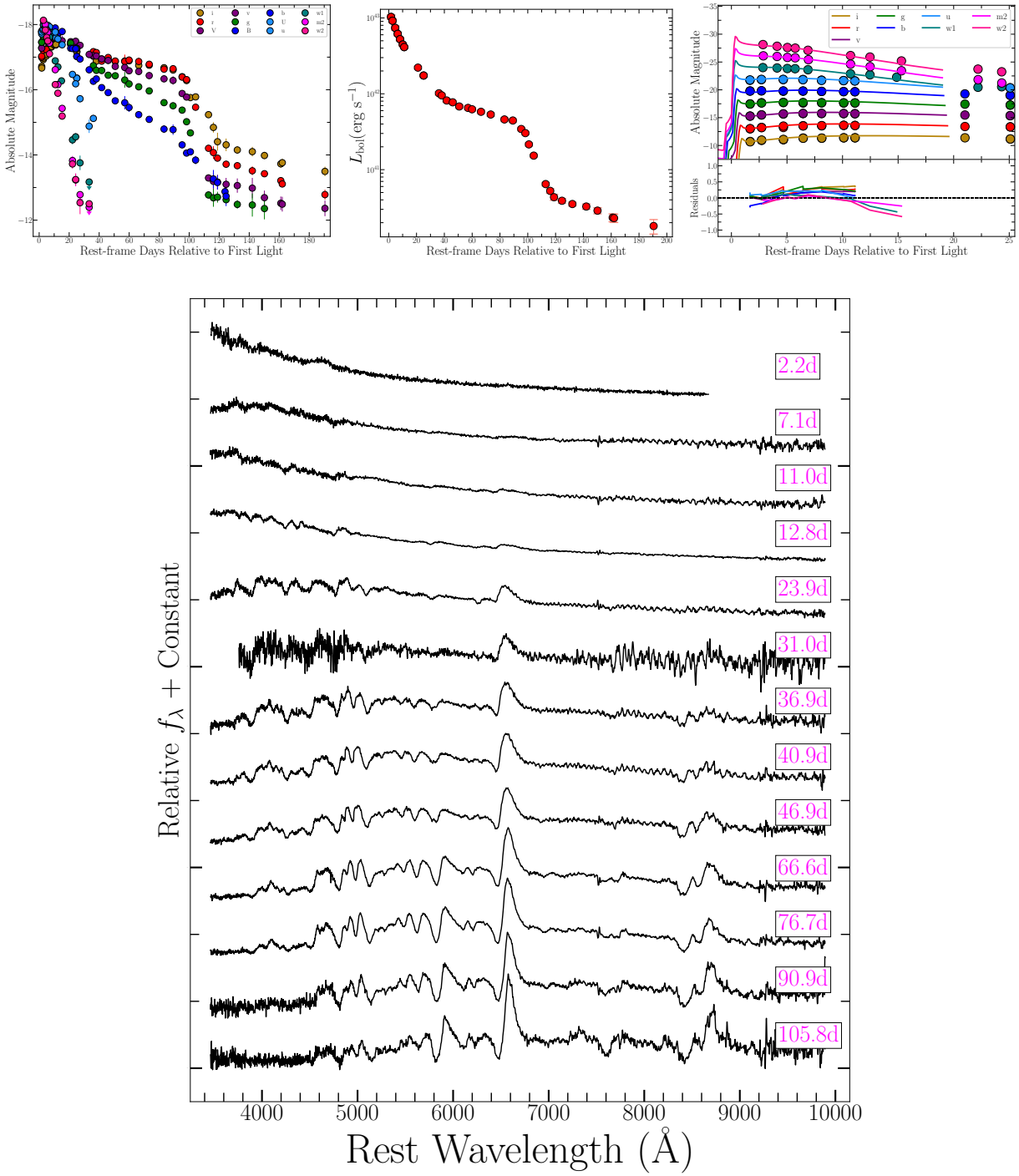

Figure 9.64 (a) SN 2020ekk (comparison): (a) Multi-color light curves, (b) UVOIR bolometric light curve, (c) best fit multi-color light curve model from Haynie & Piro (2021), (d) spectral series.

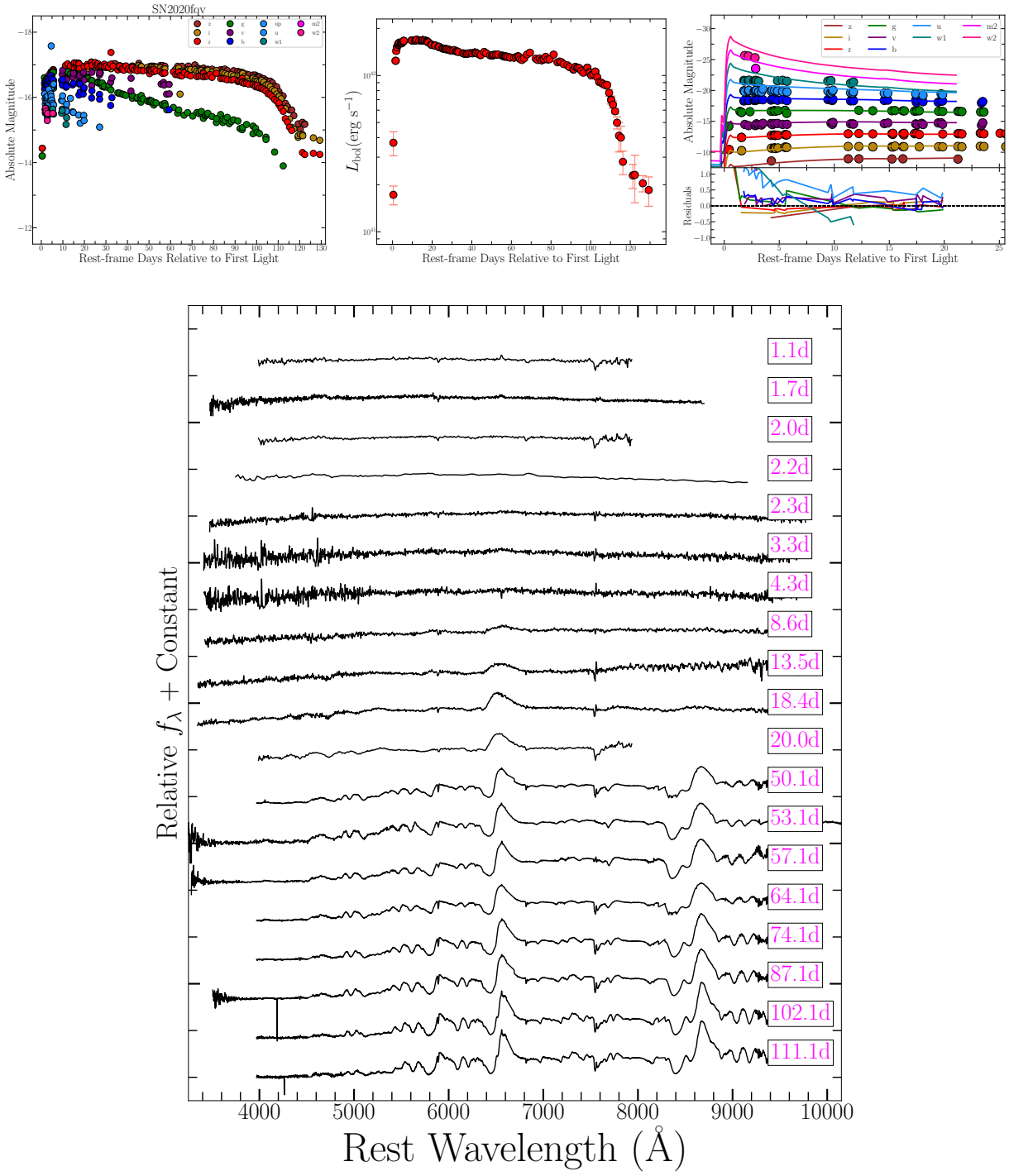

Figure 9.65 (a) SN 2020fqv (comparison): (a) Multi-color light curves, (b) UVOIR bolometric light curve, (c) best fit multi-color light curve model from Haynie & Piro (2021), (d) spectral series. Spectra and photometry are from Tinyanont et al. (2022).

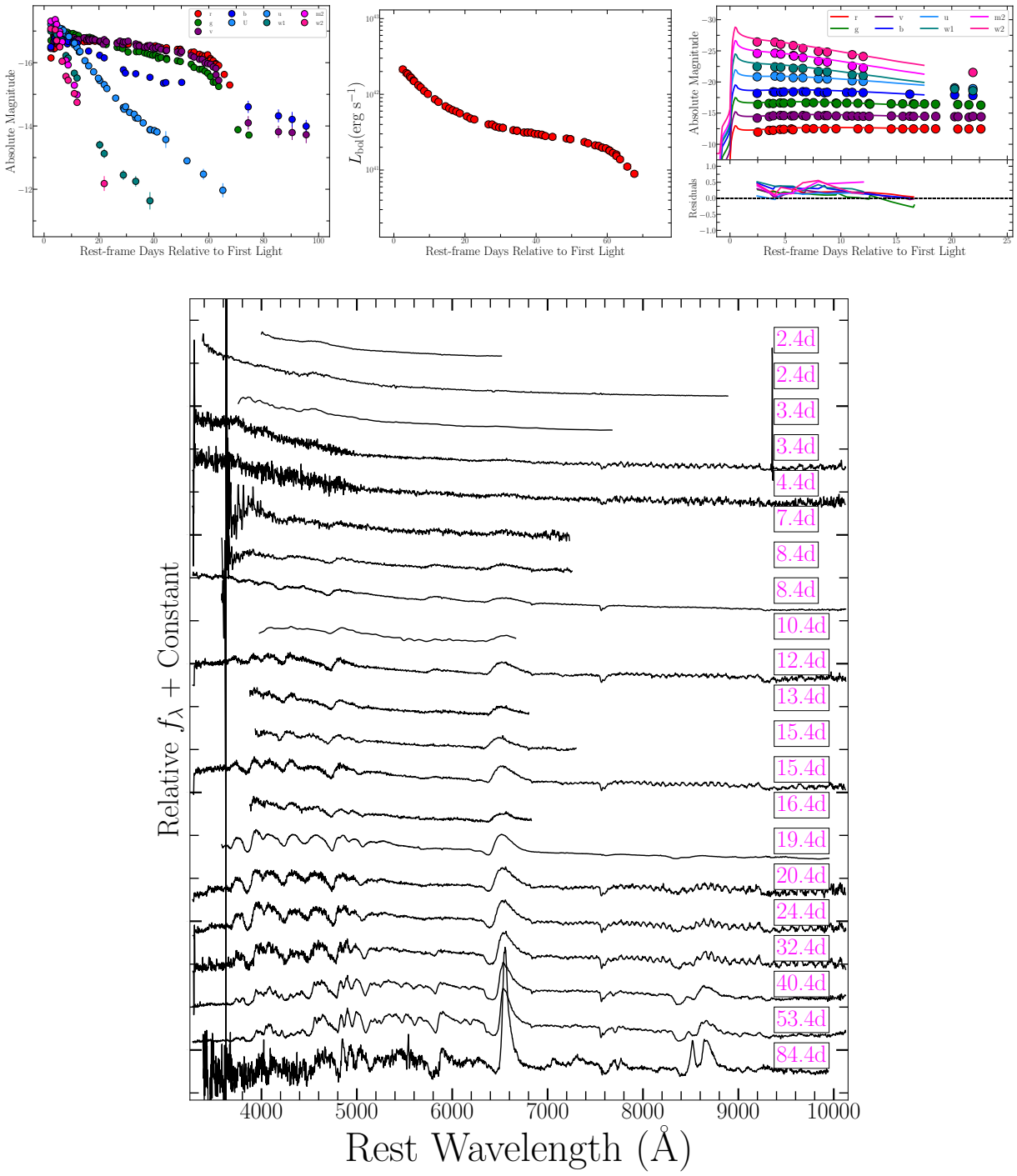

Figure 9.66 (a) SN 2020jfo (comparison): (a) Multi-color light curves, (b) UVOIR bolometric light curve, (c) best fit multi-color light curve model from Haynie & Piro (2021), (d) spectral series. Spectra and photometry are from Kilpatrick et al. (2023b).

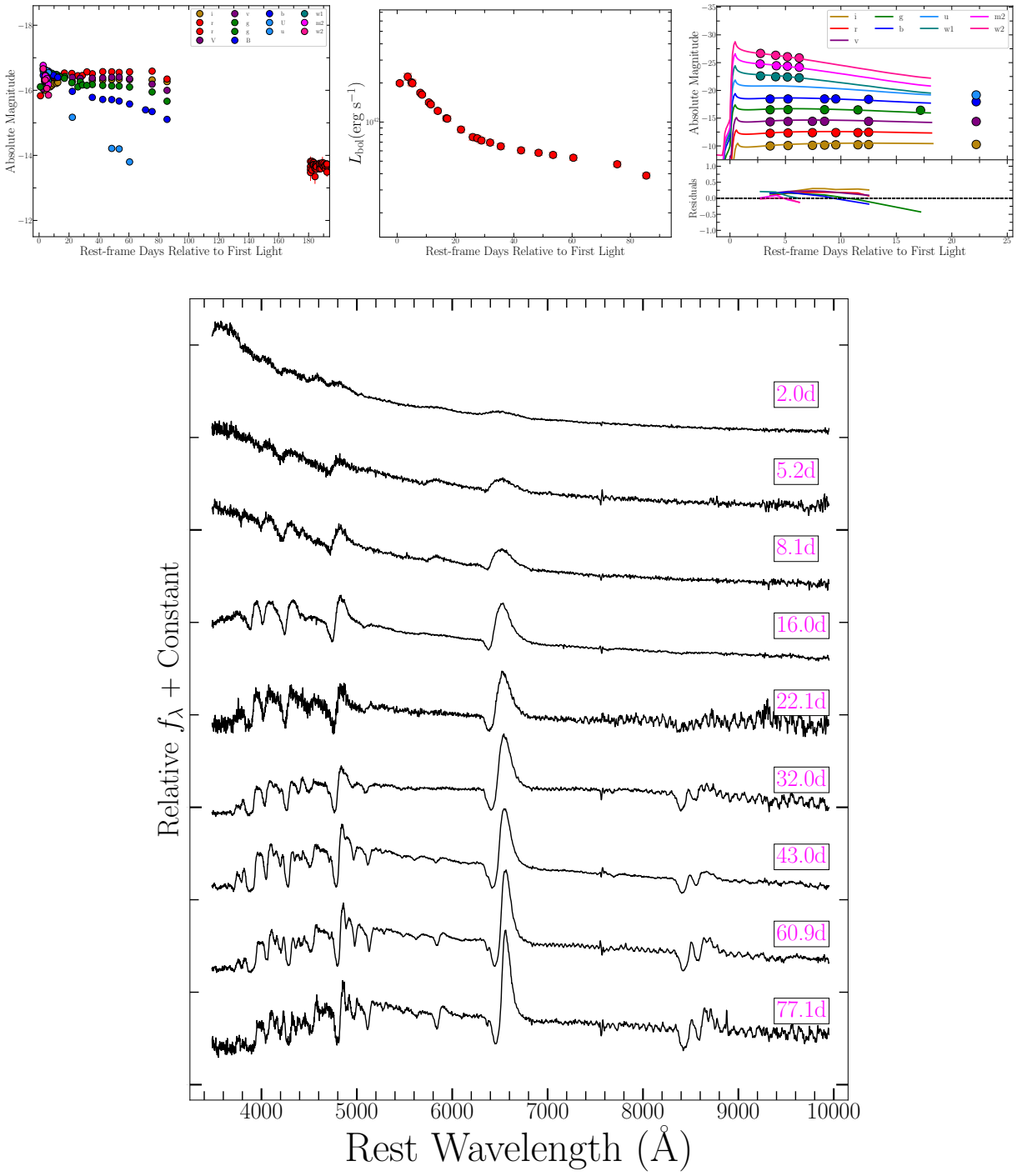

Figure 9.67 (a) SN 2020mjm (comparison): (a) Multi-color light curves, (b) UVOIR bolometric light curve, (c) best fit multi-color light curve model from Haynie & Piro (2021), (d) spectral series.

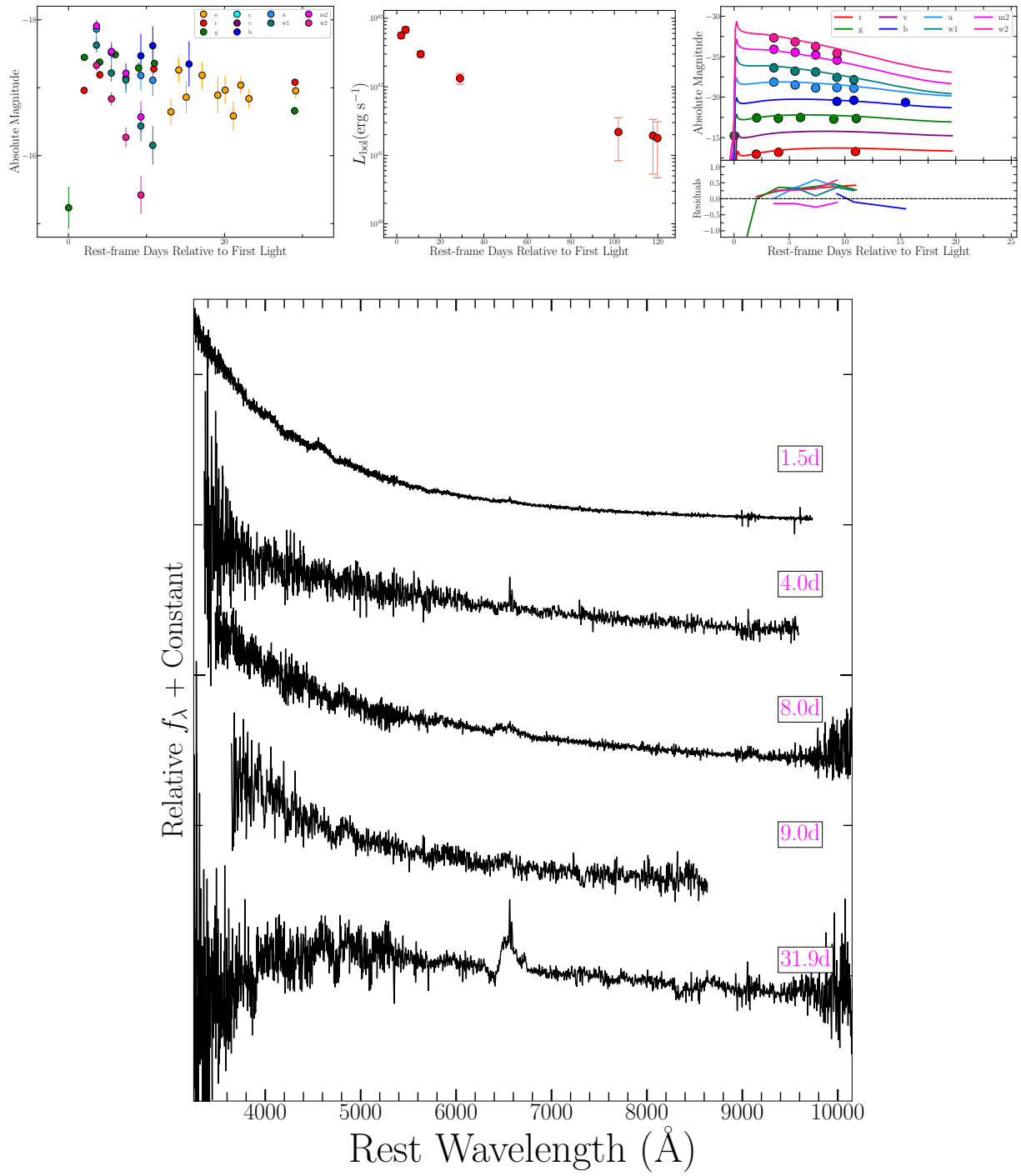

Figure 9.68 (a) SN 2021adly (comparison): (a) Multi-color light curves, (b) UVOIR bolometric light curve, (c) best fit multi-color light curve model from Haynie & Piro (2021), (d) spectral series.

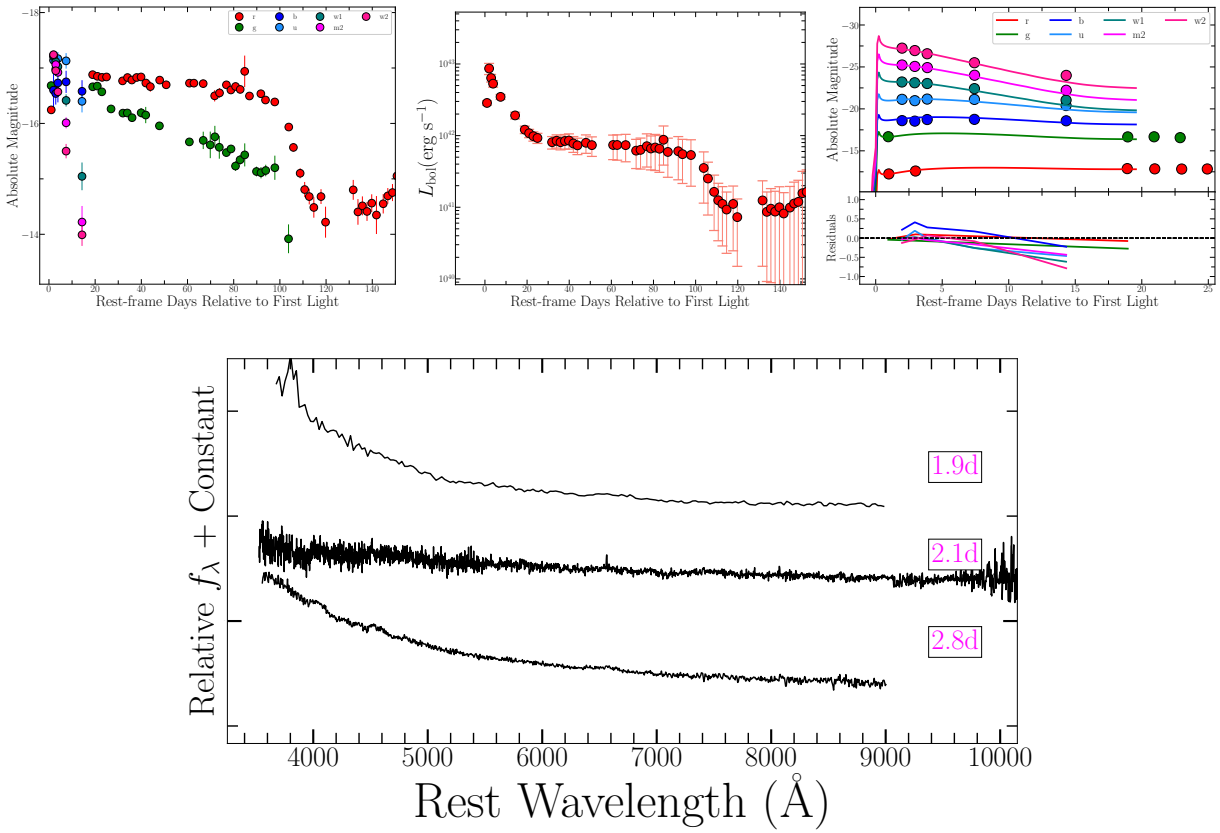

Figure 9.69 (a) SN 2021apg (comparison): (a) Multi-color light curves, (b) UVOIR bolometric light curve, (c) best fit multi-color light curve model from Haynie & Piro (2021), (d) spectral series.

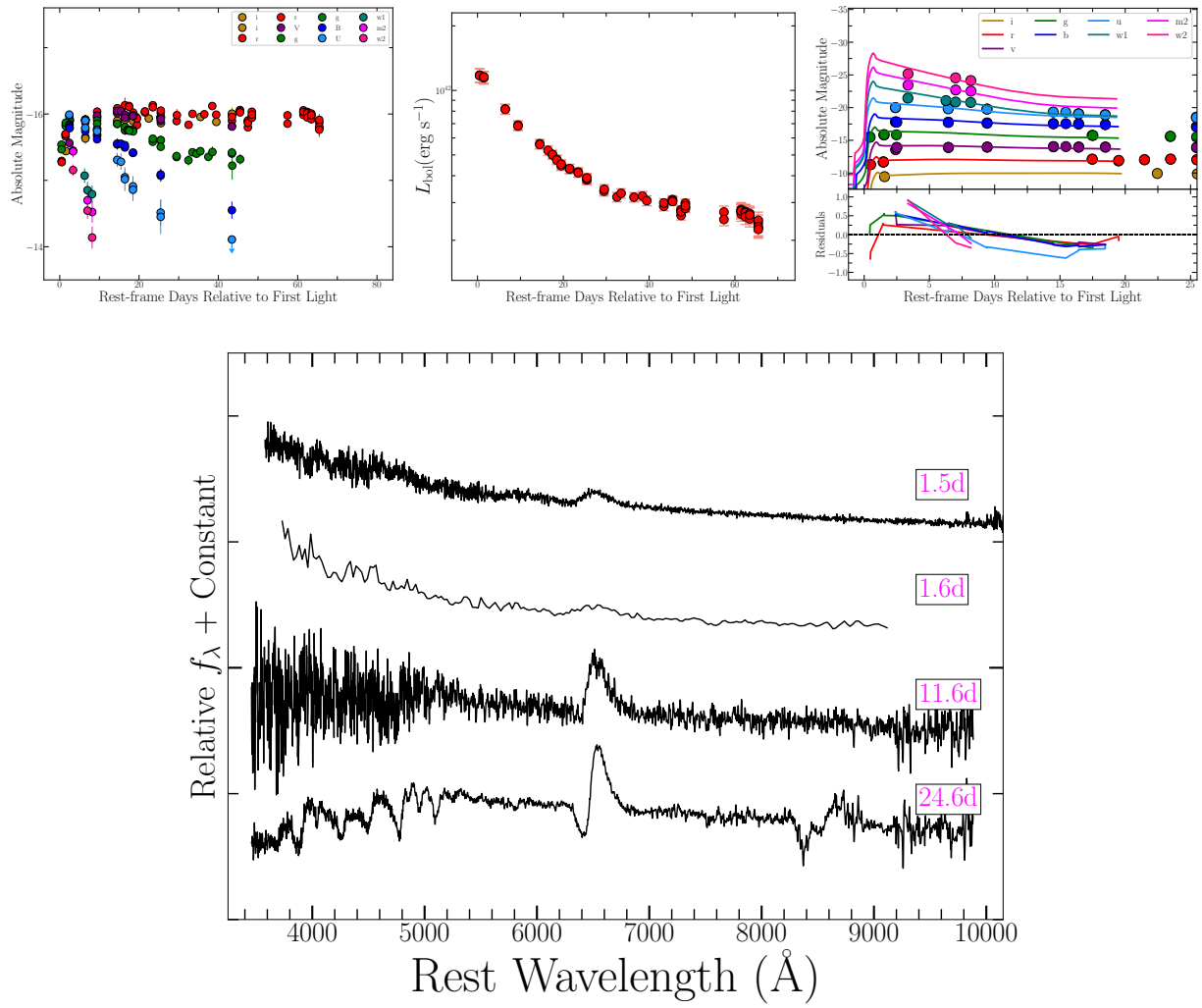

Figure 9.70 (a) SN 2021ass (comparison): (a) Multi-color light curves, (b) UVOIR bolometric light curve, (c) best fit multi-color light curve model from Haynie & Piro (2021), (d) spectral series.

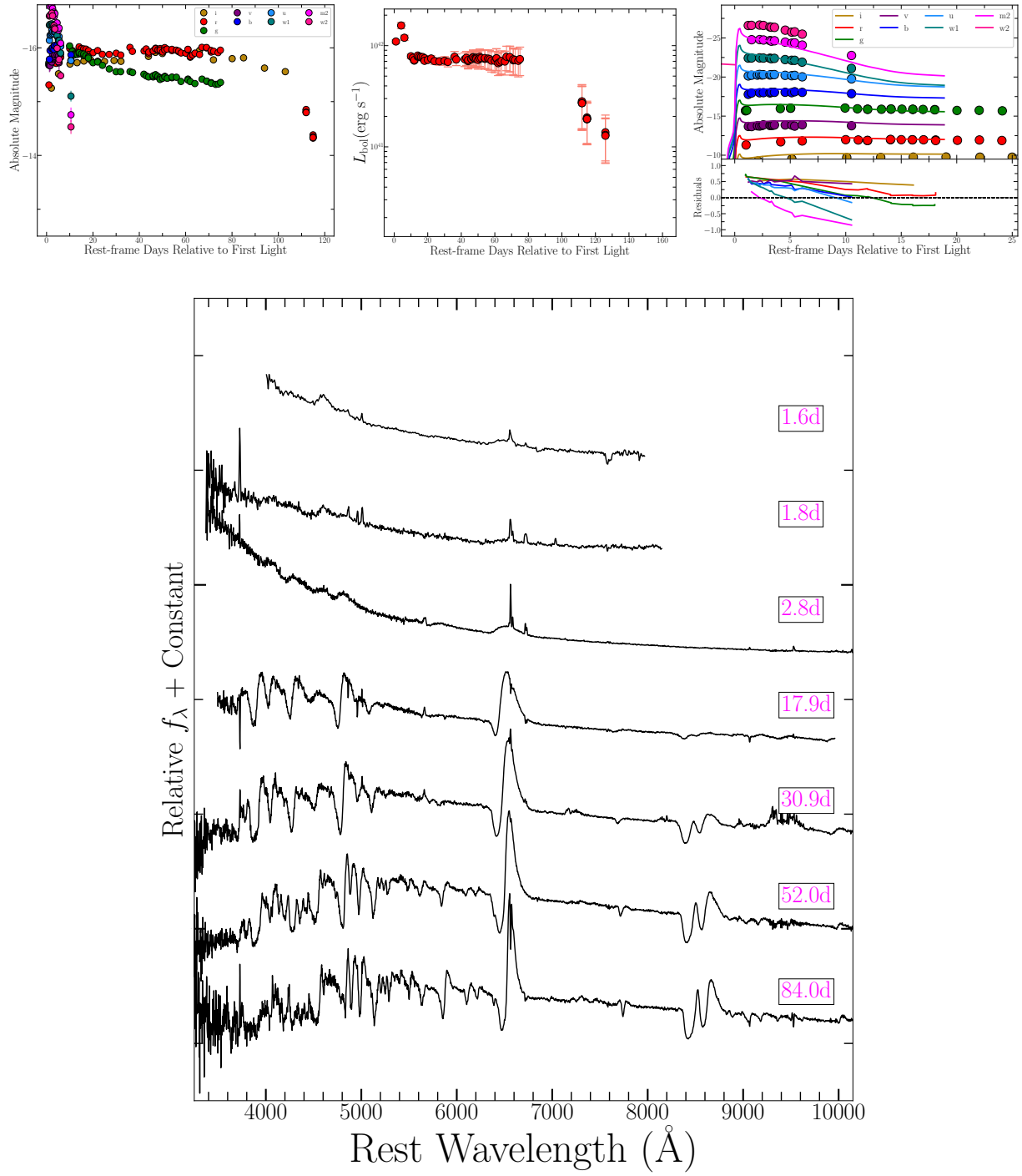

Figure 9.71 (a) SN 2021gmj (comparison): (a) Multi-color light curves, (b) UVOIR bolometric light curve, (c) best fit multi-color light curve model from Haynie & Piro (2021), (d) spectral series.

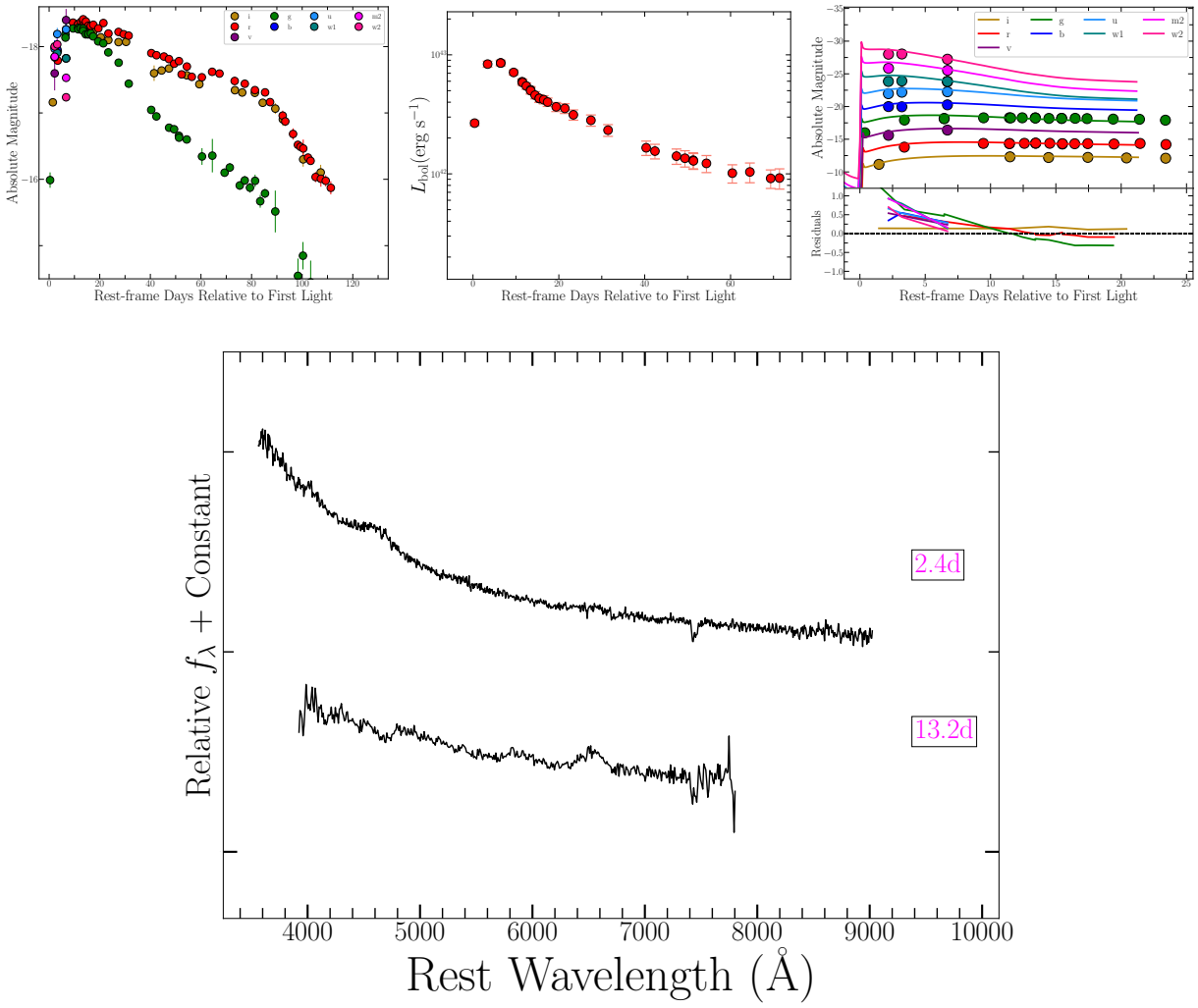

Figure 9.72 (a) SN 2021gvm (comparison): (a) Multi-color light curves, (b) UVOIR bolometric light curve, (c) best fit multi-color light curve model from Haynie & Piro (2021), (d) spectral series.

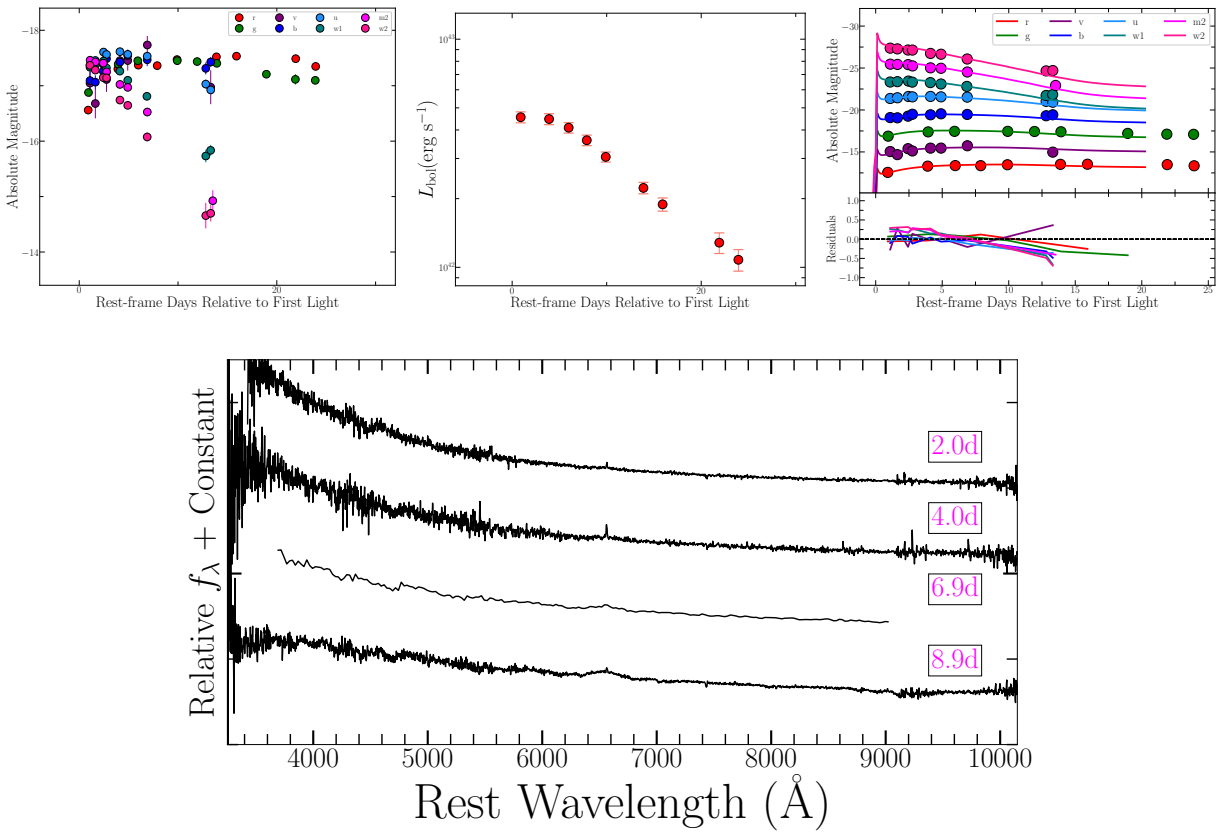

Figure 9.73 (a) SN 2021rhk (comparison): (a) Multi-color light curves, (b) UVOIR bolometric light curve, (c) best fit multi-color light curve model from Haynie & Piro (2021), (d) spectral series.

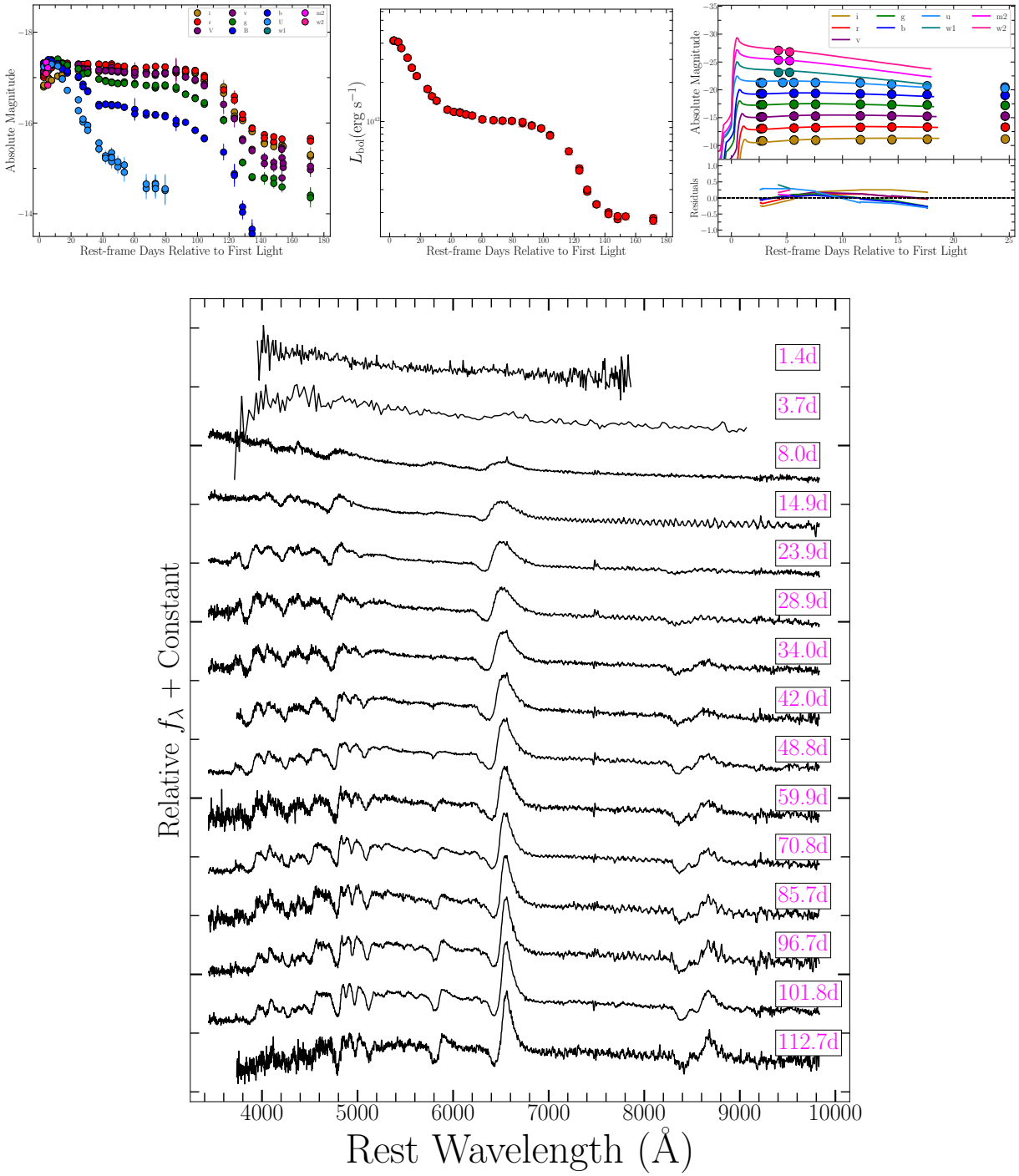

Figure 9.74 (a) SN 2021ucg (comparison): (a) Multi-color light curves, (b) UVOIR bolometric light curve, (c) best fit multi-color light curve model from Haynie & Piro (2021), (d) spectral series.

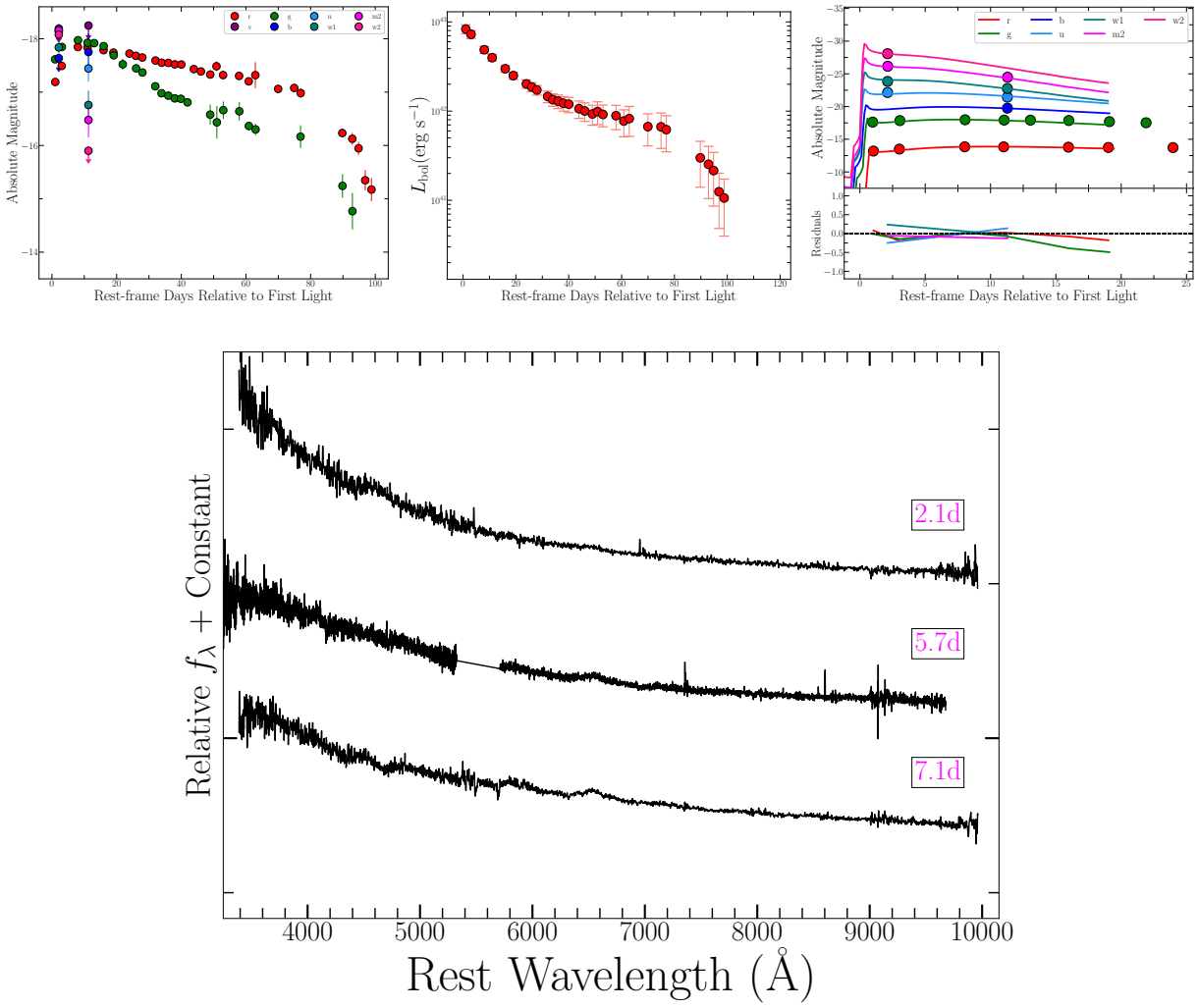

Figure 9.75 (a) SN 2021uoy (comparison): (a) Multi-color light curves, (b) UVOIR bolometric light curve, (c) best fit multi-color light curve model from Haynie & Piro (2021), (d) spectral series.

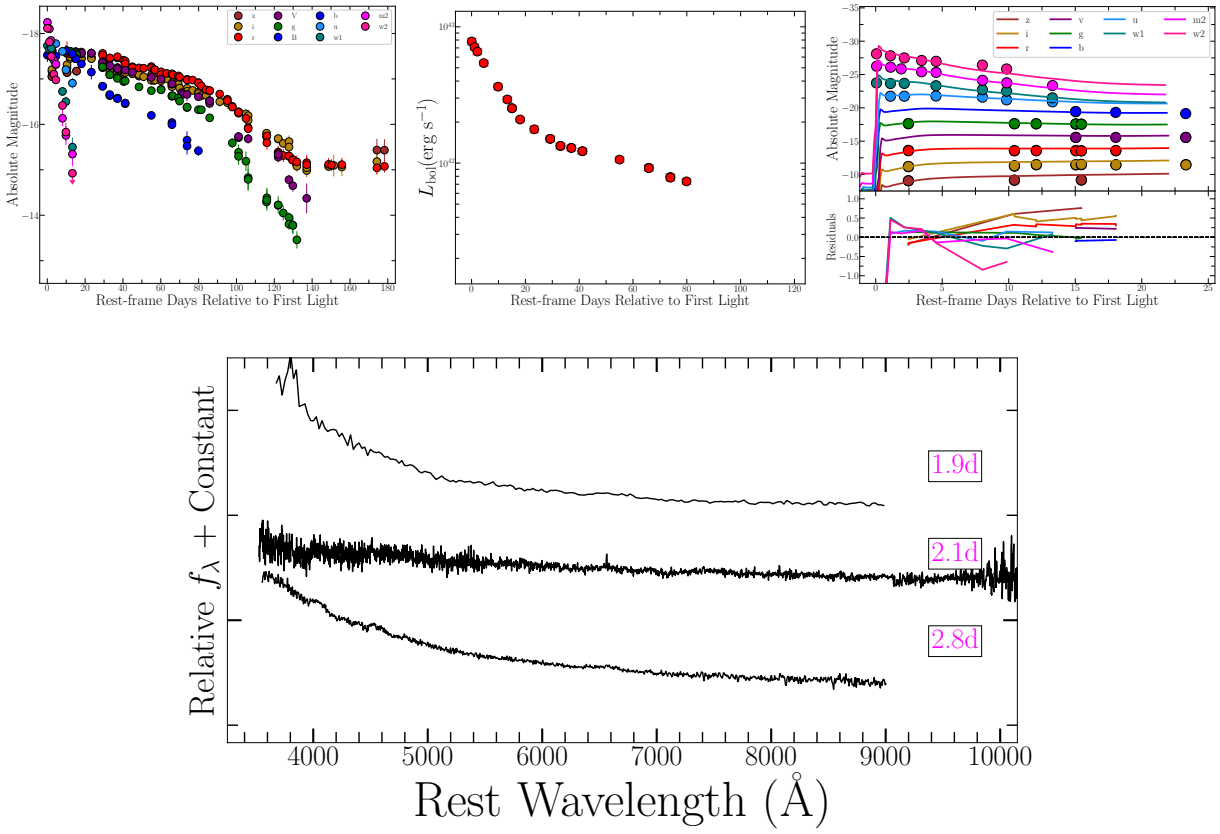

Figure 9.76 (a) SN 2021vaz (comparison): (a) Multi-color light curves, (b) UVOIR bolometric light curve, (c) best fit multi-color light curve model from Haynie & Piro (2021), (d) spectral series.

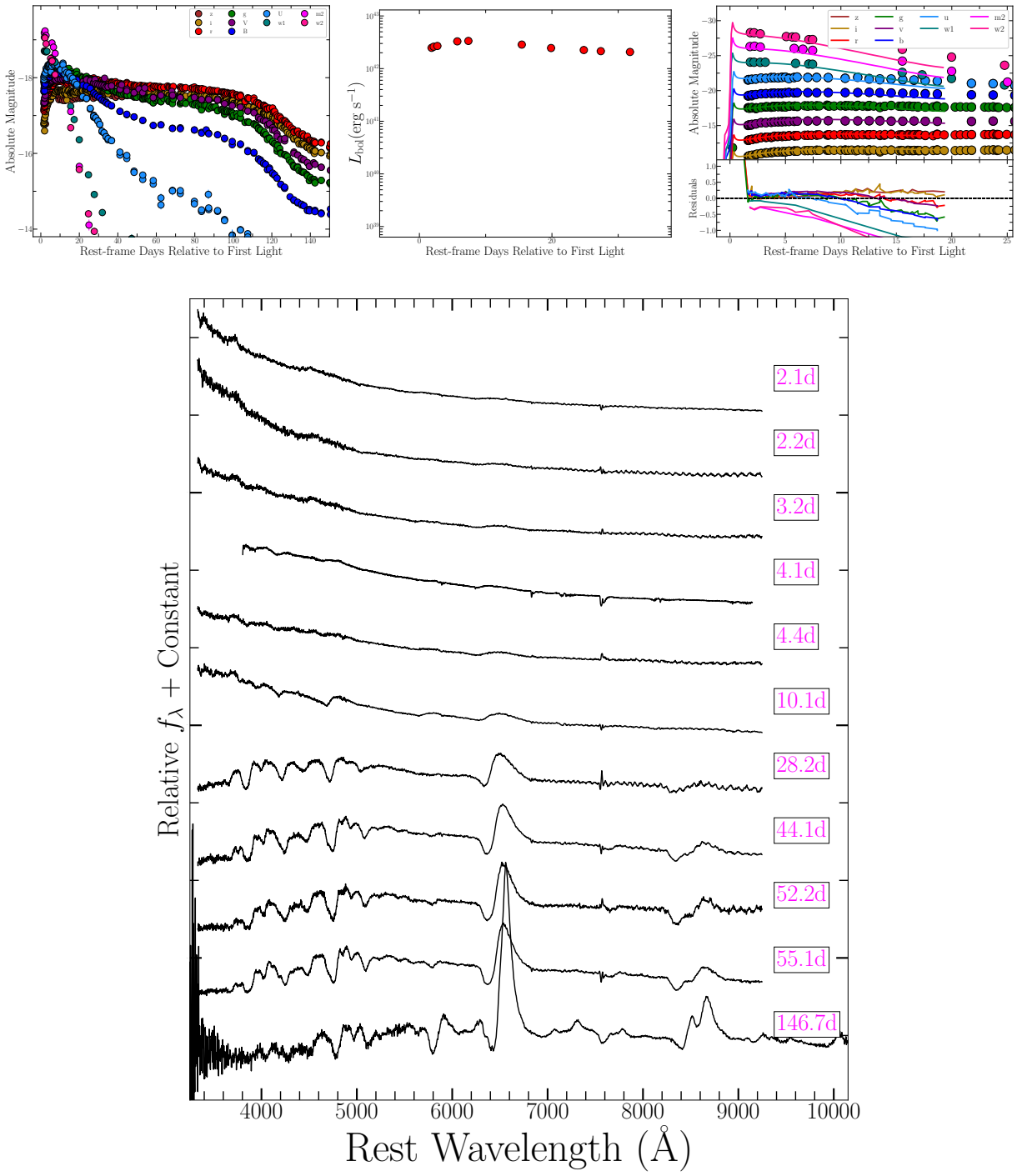

Figure 9.77 (a) SN 2021yja (comparison): (a) Multi-color light curves, (b) UVOIR bolometric light curve, (c) best fit multi-color light curve model from Haynie & Piro (2021), (d) spectral series. Spectra and photometry are from Hosseinzadeh et al. (2022).

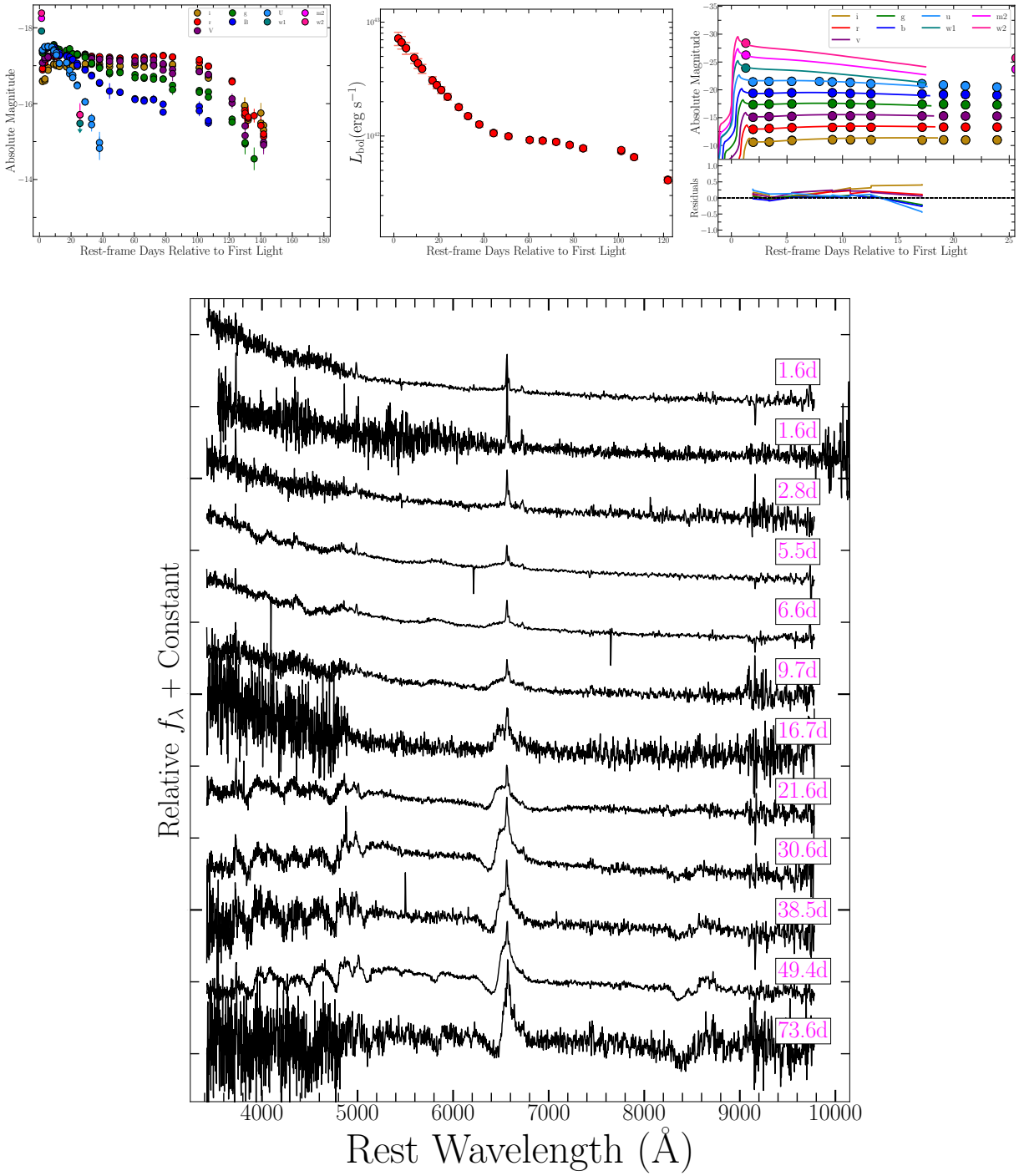

Figure 9.78 (a) SN 2022frq (comparison): (a) Multi-color light curves, (b) UVOIR bolometric light curve, (c) best fit multi-color light curve model from Haynie & Piro (2021), (d) spectral series.

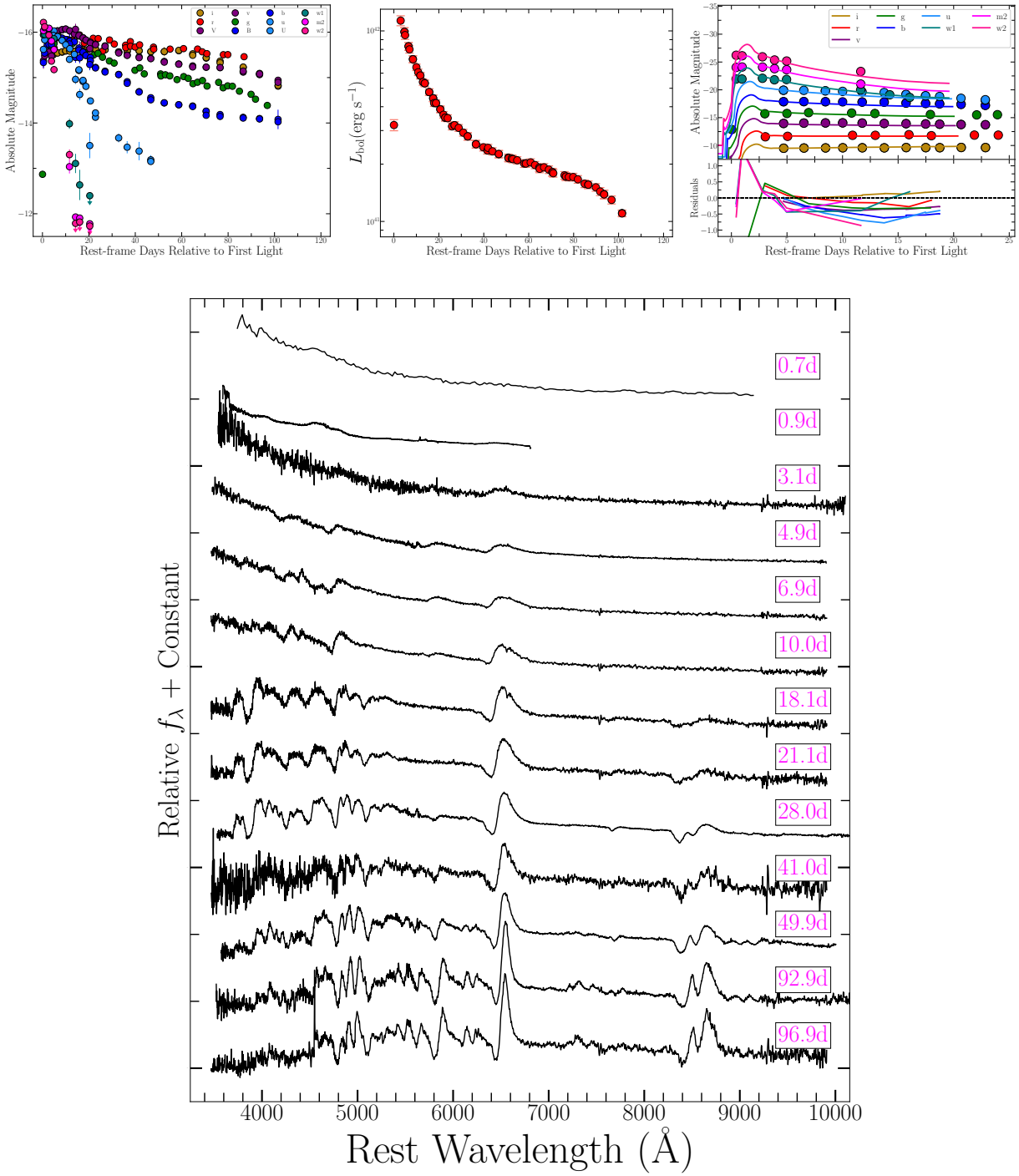

Figure 9.79 (a) SN 2022fuc (comparison): (a) Multi-color light curves, (b) UVOIR bolometric light curve, (c) best fit multi-color light curve model from Haynie & Piro (2021), (d) spectral series.

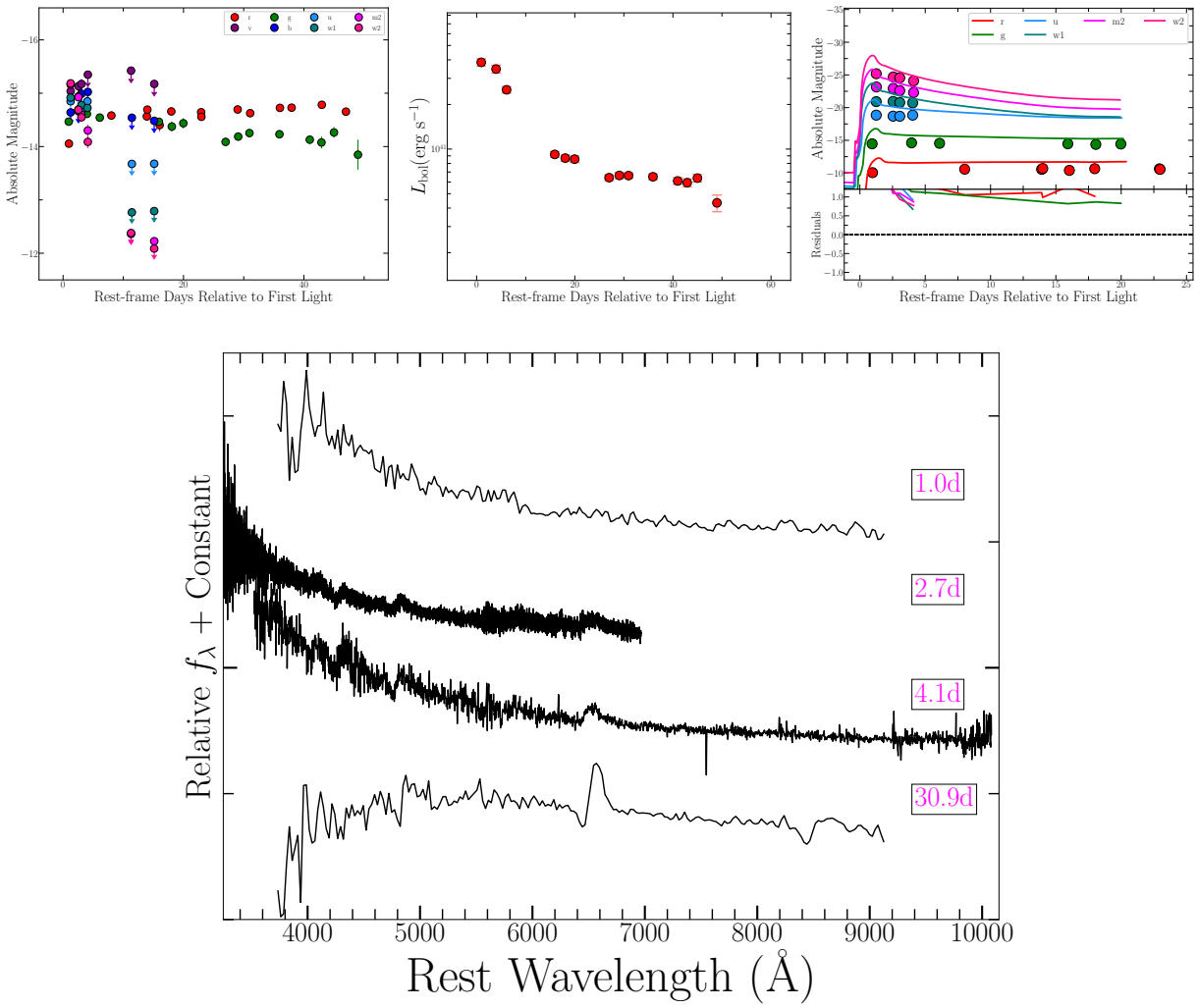

Figure 9.80 (a) SN 2022inn (comparison): (a) Multi-color light curves, (b) UVOIR bolometric light curve, (c) best fit multi-color light curve model from Haynie & Piro (2021), (d) spectral series.

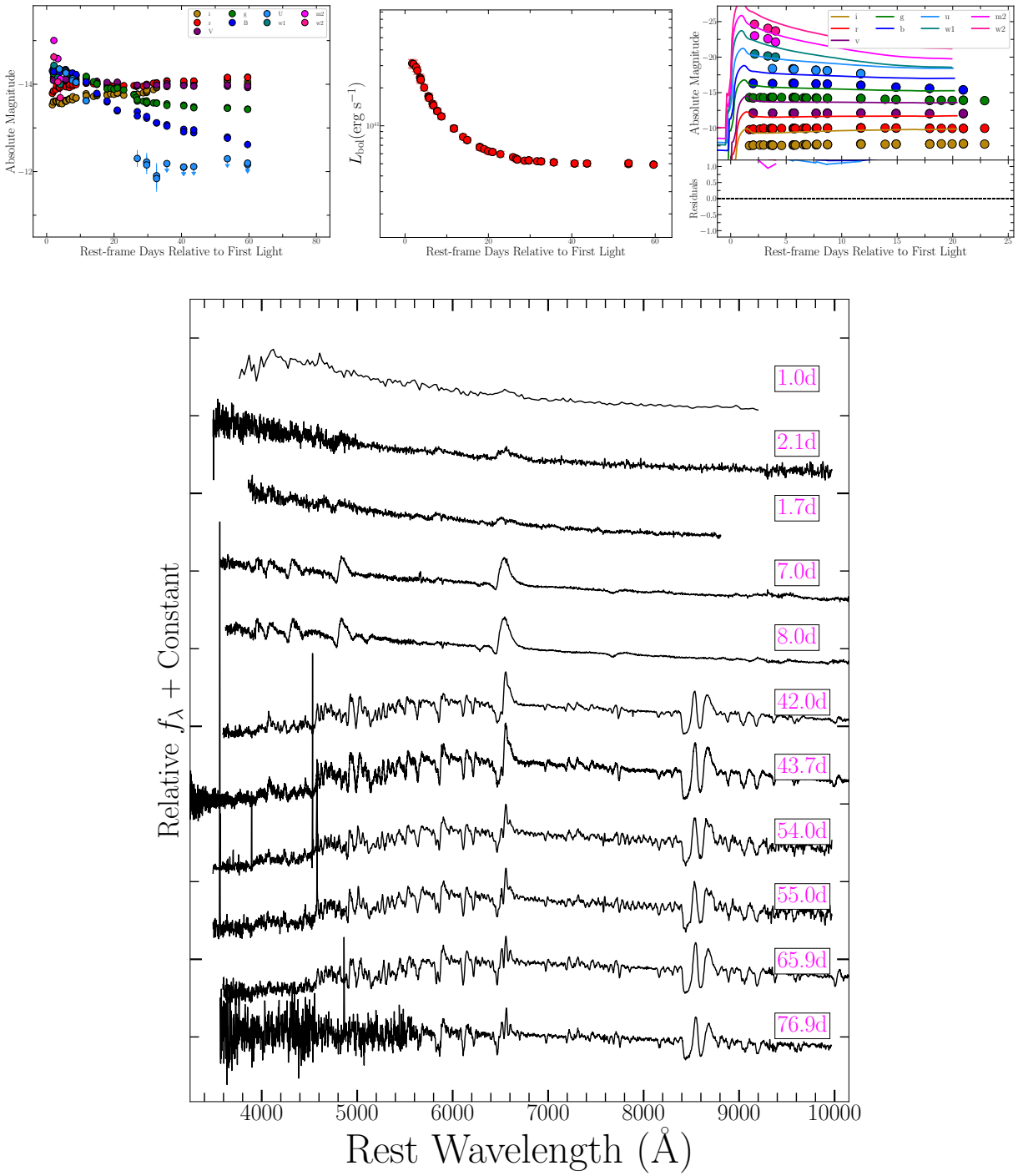

Figure 9.81 (a) SN 2022jzc (comparison): (a) Multi-color light curves, (b) UVOIR bolometric light curve, (c) best fit multi-color light curve model from Haynie & Piro (2021), (d) spectral series.

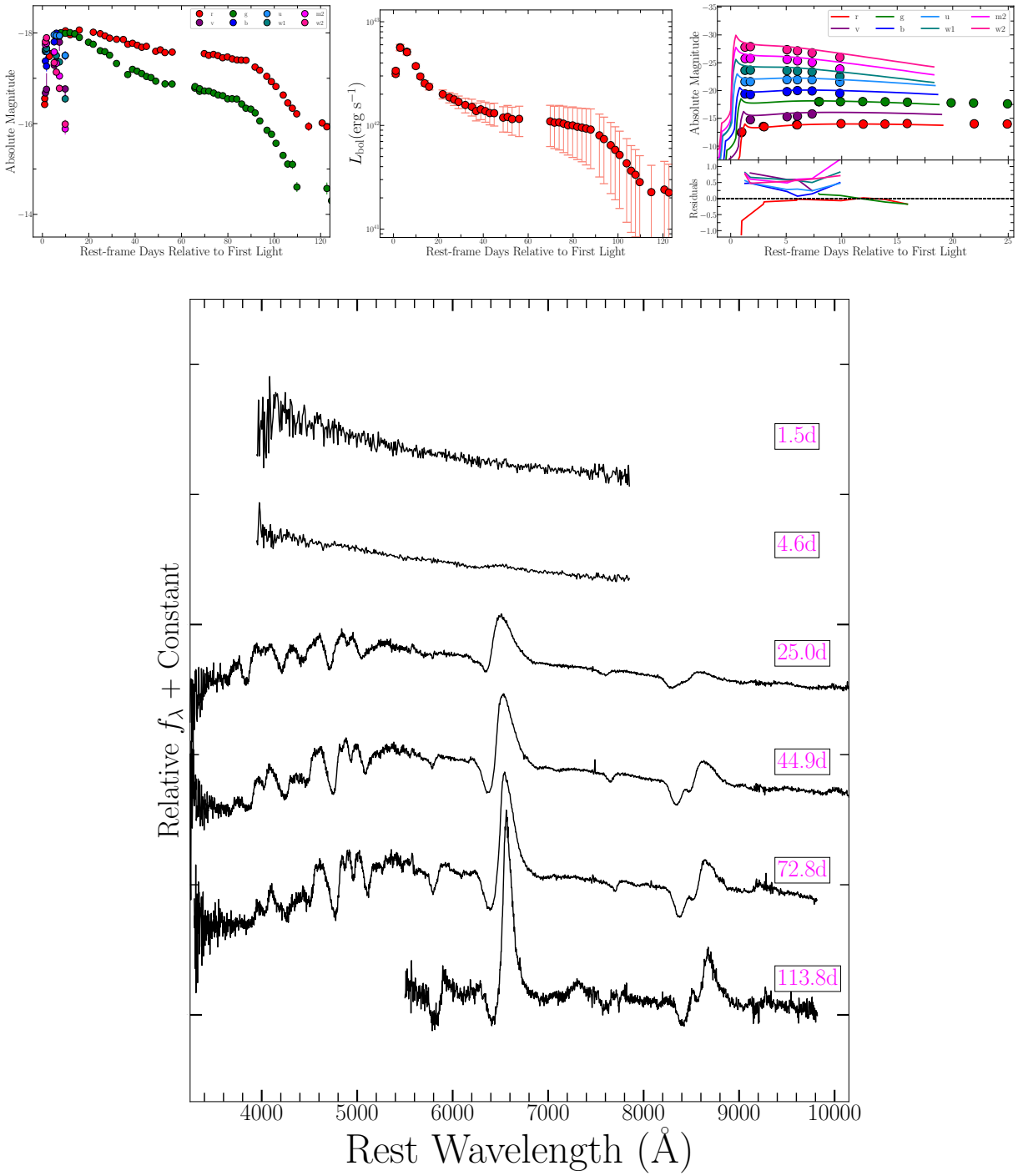

Figure 9.82 (a) SN 2022ovb (comparison): (a) Multi-color light curves, (b) UVOIR bolometric light curve, (c) best fit multi-color light curve model from Haynie & Piro (2021), (d) spectral series.

Chapter 10

Conclusions

Throughout this thesis, I have presented work on the use of early-time, multi-wavelength observations of supernovae (SNe) as a probe of their progenitor circumstellar environment. Through the direct detection of SN ejecta colliding with confined circumstellar material (CSM), we are able to place novel constraints on the progenitor identity and mass-loss history of both core-collapse SNe from massive stars and thermonuclear SN varieties from white dwarf (WD) explosions in binary systems. Below I summarize the main findings presented in this thesis.

10.1 The Circumstellar Environments of Calcium-rich Transients

As presented in Chapters 2 & 4, the discovery of SNe 2019ehk and 2021gno revealed that Calcium-rich supernovae can produce luminous X-ray emission in their first days post-explosion from SN ejecta-CSM interaction. For SN 2019ehk, luminous X-rays were coincident with narrow spectral emission lines of H I and He II from photoionization of local H- and He-rich CSM. The combination of multi-wavelength observations (X-ray to radio) of both SNe allowed for the construction of a pre-explosion CSM density profile ($r \approx 10^{13-16}$ cm) that is most consistent with the model predictions for the disruption of a low-mass C/O WD or a hybrid HeCO WD by another low-mass hybrid WD. This progenitor scenario is further supported for SN 2019ehk by pre-explosion imaging limits and the nucleosythetic yields inferred from modeling of the very late-time light curve (e.g., Ch. 3). Future observations of Calcium-rich transients at very early-times will hopefully allow for more X-ray detections as well as spectroscopic evidence for CSM-interaction.

10.2 Detection of Supernova Precursor Events

As presented in Chaper 5, the Pan-STARRS telescope through the Young Supernova Experiment (YSE) survey was able to detect the pre-SN emission from a normal SN II

for the first time. Prior to explosion, the red supergiant (RSG) progenitor of SN 2020tlf experienced rising pre-SN emission for the last $\sim$ 100 days before core-collapse; such activity was never previously observed in type II SN (SN II) progenitor stars. This work revealed that ground-based sky surveys now have the potential to discover the death throes of even RSGs before explosion; a phase space that had previously been limited to the precursors of type IIn SNe, which likely come from extreme stellar systems such as Hypergiants or Luminous Blue Variables. The precursor activity in SN 2020tlf suggested that its RSG progenitor underwent an extreme eruption during its final stages of nuclear burning, an occurrence that had only ever been considered in some simulations of lower mass RSGs. Future work will explore the phase space of precursor emission in SNe observed during the YSE survey in preparation for the enhanced detection rate of pre-SN emission by the Legacy Survey of Space and Time (LSST).

10.3 Flash Spectroscopy of Red Supergiant Explosions

Early-time, multi-wavelength observations of young SNe II are an essential probe of the final stages of stellar evolution. In the era of all-sky transient surveys, "flash" or rapid spectroscopic observations have become a powerful tool in understanding the circumstellar environment of pre-SN systems in the final years to months before explosion. With this observational technique, we can identify prominent emission lines in very early-time ($t \approx 2$ days) SN spectra from the recombination of photo-ionized CSM after shock breakout. These emission lines are direct evidence of CSM surrounding the RSG progenitor star, comprised of chemical elements ejected during enhanced mass-loss episodes right before explosion. In Chapters 5-8, I presented work on the observational properties and progenitor systems of these unique SNe II through multiple single-object studies, as well as the largest sample study to date, which combined multi-wavelength observations with state-of-the-art non-LTE (local thermodynamic equilibrium) radiative transfer simulations to uncover the mass-loss histories of RSGs during their final stages of evolution.

The presented work on "flash" spectroscopy of SNe II reveals a number of events that challenge observations of quiescent SN II progenitors and the mechanisms for RSG mass-loss explored in stellar evolution simulations. Chapters 5-7 present single-object studies of SNe II 2020tlf, 2023ixf, 2024ggi that were discovered and observed spectroscopically within days of explosion. These SNe showed transient, high-ionization emission lines from shock interaction with dense CSM that was likely created in the last year(s) before their RSG progenitor stars exploded. To quantity the pre-explosion environment of these SNe, I utilized non-LTE radiative transfer code `CMFGEN` (Hillier & Dessart 2012), combined with radiation hydrodynamics code `HERACLES` (González et al. 2007; Dessart et al. 2015), which can accurately predict the spectroscopic and photometric signatures of CSM-interaction in SNe II. For example, light curve and spectral modeling of type II SNe 2020tlf, 2023ixf and 2024ggi revealed increased mass-loss rates of $\sim 10^{-3} - 10^{-2}$ $M_{\odot}$ yr^{-1}, indicating an unprecedented period of enhanced RSG mass-loss in the final year(s) before explosion.

Building on the studies of individual CSM-interacting SNe II, Chapters 8 & 9 present the construction and application of a grid of `CMFGEN/HERACLES` simulations capable of modeling a large sample of these events (Dessart & Jacobson-Galán 2023). This state-of-the-art model grid contains both synthetic time-series spectra and multi-color light curves for SNe II interacting with a variety of mass-loss rates (e.g., $\dot{M} = 10^{-6} - 10^{0}$ $M_{\odot}$ yr^{-1}) and CSM radii (e.g., $r = 10^{14-16}$ cm). These models were applied to the largest sample to date of SNe II with spectroscopic signatures of CSM-interaction (i.e., "flash" spectroscopy); the total sample includes > 700 spectra and > 50 high-cadence ultraviolet/optical/near-infrared light curves. Modeling of all 74 SNe in the sample revealed a continuum of mass-loss rates that extended from "weak" (i.e., 10^{-6} $M_{\odot}$ yr^{-1}) to "enhanced" (i.e., 10^{-2} $M_{\odot}$ yr^{-1}), suggesting significant diversity in the mechanism for mass loss in RSGs during their late-stage evolution. Given the size of the SN sample and model grid, this study represented the first "big data" analysis of CSM-interacting SNe II and will directly inform future studies involving significantly larger samples of such events discovered by future transient surveys.

Bibliography

Albareti, F. D., Allende Prieto, C., Almeida, A., et al. 2017a, ApJS, 233, 25

—. 2017b, ApJS, 233, 25

Almgren, A. S., Beckner, V. E., Bell, J. B., et al. 2010, ApJ, 715, 1221

Anderson, J. P., González-Gaitán, S., Hamuy, M., et al. 2014, ApJ, 786, 67

Anderson, J. P., Gutiérrez, C. P., Dessart, L., et al. 2016, A&A, 589, A110

Andrews, J. E., Sand, D. J., Valenti, S., et al. 2019, ApJ, 885, 43

Andrews, J. E., Pearson, J., Hosseinzadeh, G., et al. 2023, arXiv e-prints, arXiv:2310.16092

Antonelli, L. A., Zerbi, F. M., Chincarini, G., et al. 2003, Mem. Soc. Astron. Italiana, 74, 304

Arcavi, I., Gal-Yam, A., Yaron, O., et al. 2011, ApJ, 742, L18

Arcavi, I., Hosseinzadeh, G., Brown, P. J., et al. 2017a, ApJ, 837, L2

Arcavi, I., Howell, D. A., Kasen, D., et al. 2017b, Nature, 551, 210

Armstrong, P., Tucker, B. E., Rest, A., et al. 2021, MNRAS, 507, 3125

Arnaud, K. A. 1996, in Astronomical Society of the Pacific Conference Series, Vol. 101, Astronomical Data Analysis Software and Systems V, ed. G. H. Jacoby & J. Barnes, 17

Arnett, D., Meakin, C., & Young, P. A. 2009, ApJ, 690, 1715

Arnett, W. D. 1982, ApJ, 253, 785

Balcon, C. 2020, Transient Name Server Classification Report, 2020-2839, 1

Beasor, E. R., Davies, B., Smith, N., et al. 2020, MNRAS, 492, 5994

Beasor, E. R., & Smith, N. 2022, ApJ, 933, 41

Becker, A. 2015, HOTPANTS: High Order Transform of PSF ANd Template Subtraction, Astrophysics Source Code Library, ascl:1504.004

Bellm, E. C., Kulkarni, S. R., Graham, M. J., et al. 2019, PASP, 131, 018002

Benjamin, R. A., Skillman, E. D., & Smits, D. P. 1999, ApJ, 514, 307

Berger, E., Keating, G., Alexander, K., et al. 2023, Transient Name Server AstroNote, 131, 1

Bertin, E. 2010, SWarp: Resampling and Co-adding FITS Images Together

Bertin, E., & Arnouts, S. 1996, A&AS, 117, 393

Bietenholz, M. F., Bartel, N., Argo, M., et al. 2021, ApJ, 908, 75

Bietenholz, M. F., Kamble, A., Margutti, R., Milisavljevic, D., & Soderberg, A. 2018, MNRAS, 475, 1756

Bobrick, A., Davies, M. B., & Church, R. P. 2017, MNRAS, 467, 3556

Bobrick, A., Zenati, Y., Perets, H. B., Davies, M. B., & Church, R. 2022, MNRAS, 510, 3758
Boian, I., & Groh, J. H. 2020, MNRAS, 496, 1325
Bose, S., Valenti, S., Misra, K., et al. 2015, MNRAS, 450, 2373
Bostroem, K. A., Pearson, J., Shrestha, M., et al. 2023, arXiv e-prints, arXiv:2306.10119
Brennan, S. J., Sollerman, J., Irani, I., et al. 2024, A&A, 684, L18
Brethauer, D., Margutti, R., Milisavljevic, D., et al. 2022, ApJ, 939, 105
Brown, P. J., Breeveld, A. A., Holland, S., Kuin, P., & Pritchard, T. 2014, Ap&SS, 354, 89
Brown, P. J., Roming, P. W. A., Milne, P., et al. 2010, ApJ, 721, 1608
Brown, T. M., Baliber, N., Bianco, F. B., et al. 2013, PASP, 125, 1031
Bruch, R., Zimmerman, E., & Johansson, J. 2021a, Transient Name Server Discovery Report, 2021-843, 1
Bruch, R. J., Gal-Yam, A., Schulze, S., et al. 2021b, ApJ, 912, 46
Bruch, R. J., Gal-Yam, A., Yaron, O., et al. 2023a, ApJ, 952, 119
—. 2023b, ApJ, 952, 119
Bruzual, G., & Charlot, S. 2003, MNRAS, 344, 1000
Burrows, D. N., Hill, J. E., Nousek, J. A., et al. 2005, Space Sci. Rev., 120, 165
Buzzoni, B., Delabre, B., Dekker, H., et al. 1984, The Messenger, 38, 9
Cao, Y., Kasliwal, M. M., Arcavi, I., et al. 2013, ApJ, 775, L7
Cappellaro, E., Mazzali, P. A., Benetti, S., et al. 1997, A&A, 328, 203
Caprioli, D. 2023, arXiv e-prints, arXiv:2307.00284
Caprioli, D., & Spitkovsky, A. 2014, ApJ, 783, 91
Castor, J. I., Abbott, D. C., & Klein, R. I. 1975, ApJ, 195, 157
Chabrier, G. 2003, in IAU Symposium, Vol. 221, IAU Symposium, P67
Chambers, K. C., Huber, M. E., Flewelling, H., et al. 2017, Transient Name Server Discovery Report, 2017-324, 1
Chandra, P., Chevalier, R., Nayana, A. J., Maeda, K., & Ray, A. 2023, The Astronomer's Telegram, 16052, 1
Chandra, P., Chevalier, R. A., Chugai, N., Fransson, C., & Soderberg, A. M. 2015, ApJ, 810, 32
Chandra, P., Chevalier, R. A., Maeda, K., Ray, A. K., & Nayana, A. J. 2024a, ApJ, 963, L4
—. 2024b, ApJ, 963, L4
Chatzopoulos, E., Wheeler, J. C., Vinko, J., et al. 2016, ApJ, 828, 94
Chen, T.-W., Yang, S., Srivastav, S., et al. 2024, arXiv e-prints, arXiv:2406.09270
Chen, X., Han, Z., & Tout, C. A. 2011, ApJ, 735, L31
Chevalier, R. A. 1982a, ApJ, 258, 790
—. 1982b, ApJ, 259, 302
—. 1990, ApJ, 359, 463
—. 1998, ApJ, 499, 810
Chevalier, R. A., & Fransson, C. 1994, ApJ, 420, 268
—. 2006, ApJ, 651, 381
—. 2017, in Handbook of Supernovae, ed. A. W. Alsabti & P. Murdin, 875

Chevalier, R. A., & Irwin, C. M. 2011, ApJ, 729, L6
—. 2012, ApJ, 747, L17
Choi, J., Dotter, A., Conroy, C., et al. 2016, ApJ, 823, 102
Chomiuk, L., Soderberg, A. M., Moe, M., et al. 2012, ApJ, 750, 164
Chomiuk, L., Soderberg, A. M., Chevalier, R. A., et al. 2016, ApJ, 821, 119
Chugai, N. N. 2001, MNRAS, 326, 1448
Chugai, N. N., & Utrobin, V. P. 2023, Astronomy Letters, 49, 639
Cid Fernandes, R., Mateus, A., Sodré, L., Stasińska, G., & Gomes, J. M. 2005, MNRAS, 358, 363
Clemens, J. C., Crain, J. A., & Anderson, R. 2004, in Society of Photo-Optical Instrumentation Engineers (SPIE) Conference Series, Vol. 5492, Ground-based Instrumentation for Astronomy, ed. A. F. M. Moorwood & M. Iye, 331
Clocchiatti, A., & Wheeler, J. C. 1997, ApJ, 491, 375
Colgate, S. A., Petschek, A. G., & Kriese, J. T. 1980, ApJ, 237, L81
Conroy, C., Gunn, J. E., & White, M. 2009, ApJ, 699, 486
Contreras, C., Hamuy, M., Phillips, M. M., et al. 2010, AJ, 139, 519
Coulter, D. A., Jones, D. O., McGill, P., et al. 2022, YSE-PZ: An Open-source Target and Observation Management System, Zenodo
—. 2023, PASP, 135, 064501
Crowther, P. A. 2007, ARA&A, 45, 177
Cushing, M. C., Vacca, W. D., & Rayner, J. T. 2004a, PASP, 116, 362
—. 2004b, PASP, 116, 362
Cutri, R. M., Skrutskie, M. F., van Dyk, S., et al. 2003, 2MASS All Sky Catalog of point sources.
Dastidar, R., Pignata, G., Dukiya, N., et al. 2024, arXiv e-prints, arXiv:2403.00927
Davies, B., & Dessart, L. 2019, MNRAS, 483, 887
Davies, B., Plez, B., & Petrault, M. 2022, MNRAS, 517, 1483
Davis, K. W., Taggart, K., Tinyanont, S., et al. 2023a, MNRAS, 523, 2530
—. 2023b, MNRAS, arXiv:2211.05134 [astro-ph.HE]
De, K., Fremling, U. C., Gal-Yam, A., et al. 2021, ApJ, 907, L18
De, K., Kasliwal, M. M., Ofek, E. O., et al. 2018a, Science, 362, 201
De, K., Kasliwal, M. M., Cantwell, T., et al. 2018b, ApJ, 866, 72
De, K., Kasliwal, M. M., Polin, A., et al. 2019, ApJ, 873, L18
De, K., Kasliwal, M. M., Tzanidakis, A., et al. 2020, ApJ, 905, 58
de Jaeger, T., Zheng, W., Stahl, B. E., et al. 2019, MNRAS, 490, 2799
de Vaucouleurs, G., de Vaucouleurs, A., Corwin, Herold G., J., et al. 1991, Third Reference Catalogue of Bright Galaxies
DeMarchi, L., Margutti, R., Dittman, J., et al. 2022, ApJ, 938, 84
Dere, K. P., Landi, E., Mason, H. E., Monsignori Fossi, B. C., & Young, P. R. 1997, A&AS, 125, 149
Dessart, L., Audit, E., & Hillier, D. J. 2015, MNRAS, 449, 4304
Dessart, L., Gutiérrez, C. P., Kuncarayakti, H., Fox, O. D., & Filippenko, A. V. 2023, A&A,

675, A33
Dessart, L., & Hillier, D. J. 2005, A&A, 439, 671
—. 2011, MNRAS, 410, 1739
—. 2022, A&A, 660, L9
Dessart, L., Hillier, D. J., Audit, E., Livne, E., & Waldman, R. 2016, MNRAS, 458, 2094
Dessart, L., Hillier, D. J., Gezari, S., Basa, S., & Matheson, T. 2009, MNRAS, 394, 21
Dessart, L., Hillier, D. J., Sukhbold, T., Woosley, S., & Janka, H. T. 2021, arXiv e-prints, arXiv:2105.13029
Dessart, L., Hillier, D. J., Waldman, R., & Livne, E. 2013, MNRAS, 433, 1745
Dessart, L., & Jacobson-Galán, W. V. 2023, A&A, 677, A105
Dessart, L., John Hillier, D., & Audit, E. 2017, A&A, 605, A83
Dessart, L., Livne, E., & Waldman, R. 2010, MNRAS, 405, 2113
Dessart, L., Blondin, S., Brown, P. J., et al. 2008, ApJ, 675, 644
Di Stefano, R. 2010, ApJ, 712, 728
Dilday, B., Howell, D. A., Cenko, S. B., et al. 2012, Science, 337, 942
Dimitriadis, G., Siebert, M. R., Kilpatrick, C. D., et al. 2019, The Astronomer's Telegram, 12707, 1
Dimitriadis, G., Siebert, M. R., Taggart, K., Tinyanont, S., & Foley, R. J. 2020, Transient Name Server Classification Report, 2020-2840, 1
Dimitriadis, G., Sullivan, M., Kerzendorf, W., et al. 2017, MNRAS, 468, 3798
Doctor, Z., Kessler, R., Chen, H. Y., et al. 2017, ApJ, 837, 57
Dolphin, A. E. 2000, PASP, 112, 1383
Dong, Y., Valenti, S., Bostroem, K. A., et al. 2021, ApJ, 906, 56
Dong, Y., Milisavljevic, D., Leja, J., et al. 2022, ApJ, 927, 199
Dong, Y., Tsuna, D., Valenti, S., et al. 2024, arXiv e-prints, arXiv:2405.04583
Dopita, M. A., Kewley, L. J., Sutherland, R. S., & Nicholls, D. C. 2016, Ap&SS, 361, 61
Dressler, A., Bigelow, B., Hare, T., et al. 2011, PASP, 123, 288
Drory, N. 2003, A&A, 397, 371
Drout, M. R., Milisavljevic, D., Parrent, J., et al. 2016, ApJ, 821, 57
Duffell, P. C. 2016, RT1D: 1D code for Rayleigh-Taylor instability
Eldridge, J. J., Stanway, E. R., Xiao, L., et al. 2017, PASA, 34, e058
Fabricant, D., Fata, R., Epps, H., et al. 2019a, PASP, 131, 075004
—. 2019b, PASP, 131, 075004
Fan, Y.-F., Bai, J.-M., Zhang, J.-J., et al. 2015, Research in Astronomy and Astrophysics, 15, 918
Fassia, A., Meikle, W. P. S., Vacca, W. D., et al. 2000, MNRAS, 318, 1093
Fassia, A., Meikle, W. P. S., Chugai, N., et al. 2001, MNRAS, 325, 907
Fernández, R., Margalit, B., & Metzger, B. D. 2019, MNRAS, 488, 259
Ferrari, L., Folatelli, G., Kuncarayakti, H., et al. 2024, MNRAS, 529, L33
Filippenko, A. V. 1982, PASP, 94, 715
—. 1997, ARA&A, 35, 309
Filippenko, A. V., Chornock, R., Swift, B., et al. 2003, IAU Circ., 8159, 2

Fink, M., Röpke, F. K., Hillebrandt, W., et al. 2010, A&A, 514, A53
Fink, M., Kromer, M., Seitenzahl, I. R., et al. 2014, MNRAS, 438, 1762
Finkbeiner, D. P., Schlafly, E. F., Schlegel, D. J., et al. 2016, ApJ, 822, 66
Fitzpatrick, E. L. 1999, PASP, 111, 63
Flewelling, H. A., Magnier, E. A., Chambers, K. C., et al. 2016a, arXiv e-prints, arXiv:1612.05243 [astro-ph.IM]
—. 2016b, arXiv e-prints, arXiv:1612.05243
Folatelli, G., Phillips, M. M., Burns, C. R., et al. 2010, AJ, 139, 120
Foley, R. J. 2015, MNRAS, 452, 2463
Foley, R. J., Berger, E., Fox, O., et al. 2011, ApJ, 732, 32
Foley, R. J., Jha, S. W., Pan, Y.-C., et al. 2016, MNRAS, 461, 433
Foley, R. J., Smith, N., Ganeshalingam, M., et al. 2007, ApJ, 657, L105
Foley, R. J., Papenkova, M. S., Swift, B. J., et al. 2003, PASP, 115, 1220
Foley, R. J., Chornock, R., Filippenko, A. V., et al. 2009, AJ, 138, 376
Foley, R. J., Challis, P. J., Chornock, R., et al. 2013, ApJ, 767, 57
Foley, R. J., Scolnic, D., Rest, A., et al. 2018, MNRAS, 475, 193
Foreman-Mackey, D., Hogg, D. W., Lang, D., & Goodman, J. 2013, PASP, 125, 306
Fox, O. D., Chevalier, R. A., Dwek, E., et al. 2010, ApJ, 725, 1768
Fox, O. D., Chevalier, R. A., Skrutskie, M. F., et al. 2011, ApJ, 741, 7
Fox, O. D., Johansson, J., Kasliwal, M., et al. 2016, ApJ, 816, L13
Fransson, C., & Jerkstrand, A. 2015, ApJ, 814, L2
Fransson, C., & Kozma, C. 1993, ApJ, 408, L25
Fransson, C., Lundqvist, P., & Chevalier, R. A. 1996, ApJ, 461, 993
Fransson, C., Ergon, M., Challis, P. J., et al. 2014, ApJ, 797, 118
Fraser, M., Stritzinger, M. D., Brennan, S. J., et al. 2021, arXiv e-prints, arXiv:2108.07278
Freedman, W. L., Madore, B. F., Gibson, B. K., et al. 2001, ApJ, 553, 47
Fremling, C., Sollerman, J., Taddia, F., et al. 2016, A&A, 593, A68
Frohmaier, C., Sullivan, M., Maguire, K., & Nugent, P. 2018, ApJ, 858, 50
Fuller, J. 2017, MNRAS, 470, 1642
Fuller, J., & Tsuna, D. 2024, arXiv e-prints, arXiv:2405.21049
Gagliano, A., Izzo, L., Kilpatrick, C. D., et al. 2022, ApJ, 924, 55
Gaia Collaboration. 2022, VizieR Online Data Catalog, I/355
Gal-Yam, A., & Leonard, D. C. 2009, Nature, 458, 865
Gal-Yam, A., Leonard, D. C., Fox, D. B., et al. 2007, ApJ, 656, 372
Gal-Yam, A., Arcavi, I., Ofek, E. O., et al. 2014, Nature, 509, 471
Gal-Yam, A., Bruch, R., Schulze, S., et al. 2022, Nature, 601, 201
Galbany, L., Anderson, J. P., Rosales-Ortega, F. F., et al. 2016, MNRAS, 455, 4087
Galbany, L., Anderson, J. P., Sánchez, S. F., et al. 2018, ApJ, 855, 107
Galbany, L., Ashall, C., Hoeflich, P., et al. 2019, arXiv e-prints, arXiv:1904.10034
Gall, C., Hjorth, J., Watson, D., et al. 2014, Nature, 511, 326
Gayley, K. G. 1995, ApJ, 454, 410
Gehrels, N., Chincarini, G., Giommi, P., et al. 2004, ApJ, 611, 1005

Gehrz, R. D., & Woolf, N. J. 1971, ApJ, 165, 285
Gokhale, V., Peng, X. M., & Frank, J. 2007, ApJ, 655, 1010
Goldberg, J. A., Jiang, Y.-F., & Bildsten, L. 2022, ApJ, 933, 164
Gonzaga, S. 2012, The DrizzlePac Handbook
González, M., Audit, E., & Huynh, P. 2007, A&A, 464, 429
Graham, M. J., Kulkarni, S. R., Bellm, E. C., et al. 2019, PASP, 131, 078001
Granot, J., & Sari, R. 2002, ApJ, 568, 820
Graur, O., Zurek, D., Shara, M. M., et al. 2016, ApJ, 819, 31
Graur, O., Zurek, D. R., Rest, A., et al. 2017, ArXiv e-prints, arXiv:1711.01275 [astro-ph.HE]
Grefenstette, B. W., Brightman, M., Earnshaw, H. P., Harrison, F. A., & Margutti, R. 2023, ApJ, 952, L3
Groh, J. H. 2014, A&A, 572, L11
Grzegorzek, J. 2019, Transient Name Server Discovery Report, 2019-666, 1
Guevel, D., & Hosseinzadeh, G. 2017, dguevel/PyZOGY: Initial release
Guillochon, J., Nicholl, M., Villar, V. A., et al. 2018, ApJS, 236, 6
Hachinger, S., Mazzali, P. A., Taubenberger, S., et al. 2012, MNRAS, 422, 70
Hamuy, M., Phillips, M. M., Suntzeff, N. B., et al. 2003, Nature, 424, 651
Haynie, A., & Piro, A. L. 2021, ApJ, 910, 128
Hickish, J., Razavi-Ghods, N., Perrott, Y. C., et al. 2018, MNRAS, 475, 5677
Hillier, D. J., & Dessart, L. 2012, MNRAS, 424, 252
—. 2019, A&A, 631, A8
Hillier, D. J., & Miller, D. L. 1998, ApJ, 496, 407
Hiramatsu, D., Howell, D. A., Van Dyk, S. D., et al. 2021, Nature Astronomy, arXiv:2011.02176 [astro-ph.HE]
Hiramatsu, D., Tsuna, D., Berger, E., et al. 2023, ApJ, 955, L8
Ho, A. Y. Q., Goldstein, D. A., Schulze, S., et al. 2019, ApJ, 887, 169
Ho, A. Y. Q., Kulkarni, S. R., Perley, D. A., et al. 2020, ApJ, 902, 86
Holcomb, C., Guillochon, J., De Colle, F., & Ramirez-Ruiz, E. 2013, ApJ, 771, 14
Hoogendam, W., Auchettl, K., Tucker, M., et al. 2024, Transient Name Server AstroNote, 103, 1
Horne, K. 1986, PASP, 98, 609
Hosseinzadeh, G., Arcavi, I., Valenti, S., et al. 2017, ApJ, 836, 158
Hosseinzadeh, G., Valenti, S., McCully, C., et al. 2018, ApJ, 861, 63
Hosseinzadeh, G., Kilpatrick, C. D., Dong, Y., et al. 2022, ApJ, 935, 31
Hosseinzadeh, G., Farah, J., Shrestha, M., et al. 2023, ApJ, 953, L16
Huang, C., & Chevalier, R. A. 2018, MNRAS, 475, 1261
Huang, F., Wang, X. F., Hosseinzadeh, G., et al. 2018, MNRAS, 475, 3959
Hummer, D. G., & Storey, P. J. 1987, MNRAS, 224, 801
Hung, T., Tinyanont, S., Dimitriadis, G., & Foley, R. J. 2021, Transient Name Server Classification Report, 2021-884, 1
Irani, I., Morag, J., Gal-Yam, A., et al. 2023, arXiv e-prints, arXiv:2310.16885
Irani, I., Chen, P., Morag, J., et al. 2024, ApJ, 962, 109

Itagaki, K. 2023, Transient Name Server Discovery Report, 2023-1158, 1
Iwamoto, K., Brachwitz, F., Nomoto, K., et al. 1999, ApJS, 125, 439
Jacobson-Galán, W. V., Dimitriadis, G., Foley, R. J., & Kilpatrick, C. D. 2018, ApJ, 857, 88
Jacobson-Galán, W. V., Foley, R. J., Schwab, J., et al. 2019, MNRAS, 487, 2538
Jacobson-Galán, W. V., Polin, A., Foley, R. J., et al. 2020a, ApJ, 896, 165
Jacobson-Galán, W. V., Margutti, R., Kilpatrick, C. D., et al. 2020b, ApJ, 898, 166
—. 2021, ApJ, 908, L32
Jacobson-Galán, W. V., Dessart, L., Jones, D. O., et al. 2022a, ApJ, 924, 15
Jacobson-Galán, W. V., Venkatraman, P., Margutti, R., et al. 2022b, ApJ, 932, 58
Jacobson-Galán, W. V., Dessart, L., Margutti, R., et al. 2023, ApJ, 954, L42
Jacobson-Galán, W. V., Dessart, L., Davis, K. W., et al. 2024, ApJ, 970, 189
Jarrett, T. H., Chester, T., Cutri, R., et al. 2000, AJ, 119, 2498
Jencson, J. E., Kasliwal, M. M., Adams, S. M., et al. 2019, ApJ, 886, 40
Jencson, J. E., Pearson, J., Beasor, E. R., et al. 2023, ApJ, 952, L30
Jerkstrand, A., Smartt, S. J., Fraser, M., et al. 2014, MNRAS, 439, 3694
Johnson, S. A., Kochanek, C. S., & Adams, S. M. 2018, MNRAS, 480, 1696
Jones, D. O., Scolnic, D. M., Riess, A. G., et al. 2017, ApJ, 843, 6
Jones, D. O., Riess, A. G., Scolnic, D. M., et al. 2018, ApJ, 867, 108
Jones, D. O., Scolnic, D. M., Foley, R. J., et al. 2019, ApJ, 881, 19
Jones, D. O., Foley, R. J., Narayan, G., et al. 2021, ApJ, 908, 143
Jordan, George C., I., Perets, H. B., Fisher, R. T., & van Rossum, D. R. 2012, ApJ, 761, L23
Julienne, P. S., Davis, J., & Oran, E. 1974, J. Geophys. Res., 79, 2540
Jung, M.-K., Yoon, S.-C., & Kim, H.-J. 2021, arXiv e-prints, arXiv:2112.00272
Kaiser, N., Aussel, H., Burke, B. E., et al. 2002, in Society of Photo-Optical Instrumentation Engineers (SPIE) Conference Series, Vol. 4836, Survey and Other Telescope Technologies and Discoveries, ed. J. A. Tyson & S. Wolff, 154
Kalberla, P. M. W., Burton, W. B., Hartmann, D., et al. 2005, A&A, 440, 775
Kamble, A., Margutti, R., Soderberg, A. M., et al. 2016, ApJ, 818, 111
Karthik Yadavalli, S., Villar, V. A., Izzo, L., et al. 2023, arXiv e-prints, arXiv:2308.12991
Kasen, D., Thomas, R. C., & Nugent, P. 2006, ApJ, 651, 366
Kasliwal, M., Cao, Y., Surace, J., et al. 2013, SPIRITS: SPitzer InfraRed Intensive Transients Survey, Spitzer Proposal
Kasliwal, M., Cao, Y., Masci, F., et al. 2014, SPIRITS: SPitzer InfraRed Intensive Transients Survey, Spitzer Proposal
Kasliwal, M., Lau, R., Cao, Y., et al. 2016, SPIRITS: SPitzer InfraRed Intensive Transients Survey, Spitzer Proposal
Kasliwal, M., Jencson, J., Lau, R., et al. 2018, SPIRITS: SPitzer InfraRed Intensive Transients Survey, Spitzer Proposal
Kasliwal, M. M., Kulkarni, S. R., Gal-Yam, A., et al. 2010, ApJ, 723, L98
—. 2012, ApJ, 755, 161

Kawabata, M., Kawabata, K. S., Maeda, K., et al. 2018, PASJ, 70, 111
Kennicutt, Robert C., J. 1998, ARA&A, 36, 189
Kessler, R., Marriner, J., Childress, M., et al. 2015, AJ, 150, 172
Kewley, L. J., & Ellison, S. L. 2008, ApJ, 681, 1183
Khatami, D., & Kasen, D. 2023, arXiv e-prints, arXiv:2304.03360
Khazov, D., Yaron, O., Gal-Yam, A., et al. 2016, ApJ, 818, 3
Kilpatrick, C. D., & Foley, R. J. 2018, MNRAS, 481, 2536
Kilpatrick, C. D., Takaro, T., Foley, R. J., et al. 2018a, MNRAS, 480, 2072
Kilpatrick, C. D., Foley, R. J., Drout, M. R., et al. 2018b, MNRAS, 473, 4805
Kilpatrick, C. D., Foley, R. J., Jacobson-Galán, W. V., et al. 2023a, ApJ, 952, L23
Kilpatrick, C. D., Izzo, L., Bentley, R. O., et al. 2023b, MNRAS, 524, 2161
Kirkpatrick, J. D., Cushing, M. C., Gelino, C. R., et al. 2011, ApJS, 197, 19
Kochanek, C. S. 2019, MNRAS, 483, 3762
Kochanek, C. S., Adams, S. M., & Belczynski, K. 2014, MNRAS, 443, 1319
Kochanek, C. S., Fraser, M., Adams, S. M., et al. 2017, MNRAS, 467, 3347
Kolb, U., & Ritter, H. 1990, A&A, 236, 385
Kool, E. C., Johansson, J., Sollerman, J., et al. 2023, Nature, 617, 477
Kouveliotou, C., Woosley, S. E., Patel, S. K., et al. 2004, ApJ, 608, 872
Kriek, M., van Dokkum, P. G., Labbé, I., et al. 2009, ApJ, 700, 221
Kromer, M., Fink, M., Stanishev, V., et al. 2013a, MNRAS, 429, 2287
Kromer, M., Pakmor, R., Taubenberger, S., et al. 2013b, ApJ, 778, L18
Kromer, M., Fremling, C., Pakmor, R., et al. 2016, MNRAS, 459, 4428
Kuncarayakti, H., Anderson, J. P., Galbany, L., et al. 2018, A&A, 613, A35
Labrie, K., Simpson, C., Cardenes, R., et al. 2023, Research Notes of the American Astronomical Society, 7, 214
Lang, D., Hogg, D. W., Mierle, K., Blanton, M., & Roweis, S. 2010, AJ, 139, 1782
Langer, N. 2012, ARA&A, 50, 107
Lawlor, T. M., & MacDonald, J. 2006, MNRAS, 371, 263
Leonard, D. C., Filippenko, A. V., Barth, A. J., & Matheson, T. 2000, ApJ, 536, 239
Levanon, N., & Soker, N. 2017, MNRAS, 470, 2510
Li, G., Hu, M., Li, W., et al. 2024, Nature, 627, 754
Li, W., Bloom, J. S., Podsiadlowski, P., et al. 2011, Nature, 480, 348
Lin, H., Wang, X., Zhang, J., et al. 2021, MNRAS, 505, 4890
Liu, L.-D., Zhang, B., Wang, L.-J., & Dai, Z.-G. 2018, ApJ, 868, L24
Longair, M. S. 2011, High Energy Astrophysics
Lucy, L. B., & Solomon, P. M. 1970, ApJ, 159, 879
Lundqvist, P., & Fransson, C. 1996, ApJ, 464, 924
Lunnan, R., Kasliwal, M. M., Cao, Y., et al. 2017, ApJ, 836, 60
Lyman, J. D., James, P. A., Perets, H. B., et al. 2013a, MNRAS, 434, 527
—. 2013b, MNRAS, 434, 527
Lyman, J. D., Levan, A. J., Church, R. P., Davies, M. B., & Tanvir, N. R. 2014, MNRAS, 444, 2157

MacLeod, M., Goldstein, J., Ramirez-Ruiz, E., Guillochon, J., & Samsing, J. 2014, ApJ, 794, 9
Magnier, E. A., Schlafly, E., Finkbeiner, D., et al. 2013, ApJS, 205, 20
Magnier, E. A., Schlafly, E. F., Finkbeiner, D. P., et al. 2020, The Astrophysical Journal Supplement Series, 251, 6
Malesani, D., Fynbo, J. P. U., Hjorth, J., et al. 2009, ApJ, 692, L84
Mao, Y., Zhang, M., Cai, G., et al. 2023, Transient Name Server AstroNote, 130, 1
Margalit, B., & Metzger, B. D. 2016, MNRAS, 461, 1154
Margalit, B., Quataert, E., & Ho, A. Y. Q. 2022, ApJ, 928, 122
Margutti, R., & Grefenstette, B. 2024, The Astronomer's Telegram, 16587, 1
Margutti, R., Zaninoni, E., Bernardini, M. G., et al. 2013, MNRAS, 428, 729
Margutti, R., Milisavljevic, D., Soderberg, A. M., et al. 2014, ApJ, 780, 21
Margutti, R., Kamble, A., Milisavljevic, D., et al. 2017, ApJ, 835, 140
Marquardt, K. S., Sim, S. A., Ruiter, A. J., et al. 2015, A&A, 580, A118
Marsh, T. R., Nelemans, G., & Steeghs, D. 2004, MNRAS, 350, 113
Martini, P., Elias, J., Points, S., et al. 2014, in Society of Photo-Optical Instrumentation Engineers (SPIE) Conference Series, Vol. 9147, Ground-based and Airborne Instrumentation for Astronomy V, ed. S. K. Ramsay, I. S. McLean, & H. Takami, 91470Z
Masci, F. J., Laher, R. R., Rusholme, B., et al. 2019, PASP, 131, 018003
Massey, P., Neugent, K. F., & Morrell, N. 2015, ApJ, 807, 81
Matsuoka, T., & Maeda, K. 2020, ApJ, 898, 158
Matthews, D., Margutti, R., Alexander, K. D., et al. 2023, Transient Name Server AstroNote, 146, 1
Matzner, C. D., & McKee, C. F. 1999, ApJ, 510, 379
Mauerhan, J. C., Smith, N., Filippenko, A. V., et al. 2013, MNRAS, 430, 1801
Maund, J. R., Fraser, M., Ergon, M., et al. 2011, ApJ, 739, L37
McCully, C., Volgenau, N. H., Harbeck, D.-R., et al. 2018, in Society of Photo-Optical Instrumentation Engineers (SPIE) Conference Series, Vol. 10707, Software and Cyberinfrastructure for Astronomy V, ed. J. C. Guzman & J. Ibsen, 107070K
McCully, C., Jha, S. W., Foley, R. J., et al. 2014, Nature, 512, 54
McMullin, J. P., Waters, B., Schiebel, D., Young, W., & Golap, K. 2007, in Astronomical Society of the Pacific Conference Series, Vol. 376, Astronomical Data Analysis Software and Systems XVI, ed. R. A. Shaw, F. Hill, & D. J. Bell, 127
Meakin, C. A., & Arnett, D. 2007, ApJ, 667, 448
Metzger, B. D. 2012, MNRAS, 419, 827
Milisavljevic, D., Margutti, R., Kamble, A., et al. 2015, ApJ, 815, 120
Milisavljevic, D., Patnaude, D. J., Raymond, J. C., et al. 2017, ApJ, 846, 50
Miller, J. S., & Stone, R. P. S. 1993, LOTRM
Modjaz, M., Li, W., Butler, N., et al. 2009, ApJ, 702, 226
Moriya, T., Tominaga, N., Blinnikov, S. I., Baklanov, P. V., & Sorokina, E. I. 2011, MNRAS, 415, 199
Moriya, T. J., & Eldridge, J. J. 2016, MNRAS, 461, 2155

Moriya, T. J., Subrayan, B. M., Milisavljevic, D., & Blinnikov, S. I. 2023, PASJ, 75, 634
Moriya, T. J., Yoon, S.-C., Gräfener, G., & Blinnikov, S. I. 2017a, MNRAS, 469, L108
Moriya, T. J., Mazzali, P. A., Tominaga, N., et al. 2017b, MNRAS, 466, 2085
Morozova, V., Ott, C. D., & Piro, A. L. 2015, SNEC: SuperNova Explosion Code, Astrophysics Source Code Library, record ascl:1505.033
Morozova, V., Piro, A. L., & Valenti, S. 2017, ApJ, 838, 28
—. 2018, ApJ, 858, 15
Müller-Bravo, T. E., Gutiérrez, C. P., Sullivan, M., et al. 2020, MNRAS, 497, 361
Munoz-Arancibia, A., Forster, F., Bauer, F. E., et al. 2021, Transient Name Server Discovery Report, 2021-1092, 1
Murase, K., Thompson, T. A., Lacki, B. C., & Beacom, J. F. 2011, Phys. Rev. D, 84, 043003
Murase, K., Thompson, T. A., & Ofek, E. O. 2014, MNRAS, 440, 2528
Nakaoka, T., Kawabata, K. S., Maeda, K., et al. 2018, ApJ, 859, 78
Nakaoka, T., Maeda, K., Yamanaka, M., et al. 2020, arXiv e-prints, arXiv:2005.02992
Nakar, E., & Piro, A. L. 2014, ApJ, 788, 193
Nakar, E., & Sari, R. 2010, ApJ, 725, 904
Nasa High Energy Astrophysics Science Archive Research Center (Heasarc). 2014, HEAsoft: Unified Release of FTOOLS and XANADU, Astrophysics Source Code Library, record ascl:1408.004
Neugent, K. F., Massey, P., Skiff, B., & Meynet, G. 2012, ApJ, 749, 177
Nicholl, M., Short, P., Angus, C. R., et al. 2019, The Astronomer's Telegram, 12697, 1
Niemela, V. S., Ruiz, M. T., & Phillips, M. M. 1985, ApJ, 289, 52
Niu, Z., Sun, N.-C., Maund, J. R., et al. 2023, ApJ, 955, L15
Nomoto, K. 1982, ApJ, 257, 780
Nyholm, A., Sollerman, J., Taddia, F., et al. 2017, A&A, 605, A6
Nyholm, A., Sollerman, J., Tartaglia, L., et al. 2020, A&A, 637, A73
Ofek, E. O., Lin, L., Kouveliotou, C., et al. 2013a, ApJ, 768, 47
Ofek, E. O., Cameron, P. B., Kasliwal, M. M., et al. 2007, ApJ, 659, L13
Ofek, E. O., Sullivan, M., Cenko, S. B., et al. 2013b, Nature, 494, 65
Ofek, E. O., Sullivan, M., Shaviv, N. J., et al. 2014, ApJ, 789, 104
Ofek, E. O., Cenko, S. B., Shaviv, N. J., et al. 2016, ApJ, 824, 6
Oke, J. B., Cohen, J. G., Carr, M., et al. 1995, PASP, 107, 375
Onken, C. A., Wolf, C., Bessell, M. S., et al. 2024, arXiv e-prints, arXiv:2402.02015
Oosterloo, T., & Shostak, S. 1993, A&AS, 99, 379
Osterbrock, D. E., & Ferland, G. J. 2006, Astrophysics of gaseous nebulae and active galactic nuclei
Owocki, S. P., Gayley, K. G., & Shaviv, N. J. 2004, ApJ, 616, 525
Owocki, S. P., Townsend, R. H. D., & Quataert, E. 2017, MNRAS, 472, 3749
Pakmor, R., Kromer, M., Röpke, F. K., et al. 2010, Nature, 463, 61
Pakmor, R., Kromer, M., Taubenberger, S., et al. 2012, ApJ, 747, L10
Pan, Y. C., Foley, R. J., Jones, D. O., Filippenko, A. V., & Kuin, N. P. M. 2020, MNRAS, 491, 5897

Panjkov, S., Auchettl, K., Shappee, B. J., et al. 2023, arXiv e-prints, arXiv:2308.13101
Pastorello, A., Smartt, S. J., Mattila, S., et al. 2007, Nature, 447, 829
Pastorello, A., Cappellaro, E., Inserra, C., et al. 2013, ApJ, 767, 1
Pastorello, A., Benetti, S., Brown, P. J., et al. 2015, MNRAS, 449, 1921
Pastorello, A., Kochanek, C. S., Fraser, M., et al. 2018, MNRAS, 474, 197
Pastorello, A., Reguitti, A., Morales-Garoffolo, A., et al. 2019, A&A, 628, A93
Pearson, J., Hosseinzadeh, G., Sand, D. J., et al. 2023, ApJ, 945, 107
Pejcha, O., Metzger, B. D., Tyles, J. G., & Tomida, K. 2017, ApJ, 850, 59
Pellegrino, C., Howell, D. A., Terreran, G., et al. 2022, ApJ, 938, 73
Perets, H. B. 2014a, arXiv e-prints, arXiv:1407.2254
—. 2014b, arXiv e-prints, arXiv:1407.2254
Perets, H. B., Badenes, C., Arcavi, I., Simon, J. D., & Gal-yam, A. 2011, ApJ, 730, 89
Perets, H. B., & Beniamini, P. 2021, MNRAS, 503, 5997
Perets, H. B., Zenati, Y., Toonen, S., & Bobrick, A. 2019, arXiv e-prints, arXiv:1910.07532
Perets, H. B., Gal-Yam, A., Mazzali, P. A., et al. 2010a, Nature, 465, 322
—. 2010b, Nature, 465, 322
Perley, D. A., Gal-Yam, A., Irani, I., & Zimmerman, E. 2023, Transient Name Server AstroNote, 119, 1
Perley, D. A., Sollerman, J., Schulze, S., et al. 2022, ApJ, 927, 180
Perrott, Y. C., Scaife, A. M. M., Green, D. A., et al. 2013, MNRAS, 429, 3330
Pettini, M., & Pagel, B. E. J. 2004, MNRAS, 348, L59
Phillips, M. M. 1993, ApJ, 413, L105
Phillips, M. M., Simon, J. D., Morrell, N., et al. 2013, ApJ, 779, 38
Piro, A. L. 2015, ApJ, 808, L51
Piro, A. L., Haynie, A., & Yao, Y. 2021, ApJ, 909, 209
Piro, A. L., Muhleisen, M., Arcavi, I., et al. 2017, ApJ, 846, 94
Pohlen, M., Cortese, L., Smith, M. W. L., et al. 2010, A&A, 518, L72
Polin, A., Nugent, P., & Kasen, D. 2019a, arXiv e-prints, arXiv:1910.12434
—. 2019b, ApJ, 873, 84
Poznanski, D., Prochaska, J. X., & Bloom, J. S. 2012, MNRAS, 426, 1465
Prentice, S. J., Maguire, K., Flörs, A., et al. 2019, arXiv e-prints, arXiv:1909.05567
Puls, J., Vink, J. S., & Najarro, F. 2008, A&A Rev., 16, 209
Qin, Y.-J., Zhang, K., Bloom, J., et al. 2023, arXiv e-prints, arXiv:2309.10022
Quataert, E., Fernández, R., Kasen, D., Klion, H., & Paxton, B. 2016, MNRAS, 458, 1214
Quataert, E., & Shiode, J. 2012, MNRAS, 423, L92
Rabinak, I., & Waxman, E. 2011, ApJ, 728, 63
Ransome, C. L., Villar, V. A., Tartaglia, A., et al. 2024, ApJ, 965, 93
Raskin, C., & Kasen, D. 2013, ApJ, 772, 1
Rayner, J. T., Toomey, D. W., Onaka, P. M., et al. 2003, PASP, 115, 362
Rest, A., Stubbs, C., Becker, A. C., et al. 2005, ApJ, 634, 1103
Rest, A., Scolnic, D., Foley, R. J., et al. 2014, ApJ, 795, 44
Rest, A., Garnavich, P. M., Khatami, D., et al. 2018, Nature Astronomy, 2, 307

Rest, A., Dhawan, S., Mandel, K., et al. 2022, Transient Name Server AstroNote, 24, 1
Rho, J., Geballe, T. R., Banerjee, D. P. K., et al. 2018, ApJ, 864, L20
Ricker, G. R., Winn, J. N., Vanderspek, R., et al. 2015, Journal of Astronomical Telescopes, Instruments, and Systems, 1, 014003
Ridden-Harper, R., Rest, A., Hounsell, R., et al. 2021, arXiv e-prints, arXiv:2111.15006
Riess, A. G., Macri, L. M., Hoffmann, S. L., et al. 2016, ApJ, 826, 56
Riess, A. G., Yuan, W., Macri, L. M., et al. 2022, ApJ, 934, L7
Roming, P. W. A., Kennedy, T. E., Mason, K. O., et al. 2005, Space Sci. Rev., 120, 95
Rosswog, S., Ramirez-Ruiz, E., & Hix, W. R. 2008, ApJ, 679, 1385
Roth, N., & Kasen, D. 2015, ApJS, 217, 9
Rui, L., Wang, X., Mo, J., et al. 2019, MNRAS, 485, 1990
Saha, A., Thim, F., Tammann, G. A., Reindl, B., & Sandage, A. 2006, ApJS, 165, 108
Sahu, D. K., Tanaka, M., Anupama, G. C., et al. 2008, ApJ, 680, 580
Salpeter, E. E. 1955, ApJ, 121, 161
Sana, H., & Evans, C. J. 2011, in Active OB Stars: Structure, Evolution, Mass Loss, and Critical Limits, ed. C. Neiner, G. Wade, G. Meynet, & G. Peters, Vol. 272, 474
Sana, H., de Mink, S. E., de Koter, A., et al. 2012, Science, 337, 444
Sand, D. J. 2018, The Identification of Failed Supernovae, HST Proposal
Santos, A., Kilpatrick, C. D., Bom, C. R., et al. 2024, MNRAS, 529, 59
Sapir, N., & Waxman, E. 2017, ApJ, 838, 130
Sarin, N., Hübner, M., Omand, C. M. B., et al. 2023, arXiv e-prints, arXiv:2308.12806
Schechter, P. L., Mateo, M., & Saha, A. 1993, PASP, 105, 1342
Schlafly, E. F., & Finkbeiner, D. P. 2011, ApJ, 737, 103
Schlegel, D. J., Finkbeiner, D. P., & Davis, M. 1998, ApJ, 500, 525
Schwab, J., Quataert, E., & Kasen, D. 2016, MNRAS, 463, 3461
Scolnic, D., Casertano, S., Riess, A., et al. 2015, ApJ, 815, 117
Scolnic, D. M., Jones, D. O., Rest, A., et al. 2018, ApJ, 859, 101
Seibert, M., Wyder, T., Neill, J., et al. 2012, in American Astronomical Society Meeting Abstracts, Vol. 219, American Astronomical Society Meeting Abstracts #219, 340.01
Seitenzahl, I. R., Cescutti, G., Röpke, F. K., Ruiter, A. J., & Pakmor, R. 2013a, A&A, 559, L5
Seitenzahl, I. R., Taubenberger, S., & Sim, S. A. 2009, MNRAS, 400, 531
Seitenzahl, I. R., Timmes, F. X., & Magkotsios, G. 2014, ApJ, 792, 10
Seitenzahl, I. R., Ciaraldi-Schoolmann, F., Röpke, F. K., et al. 2013b, MNRAS, 429, 1156
Seitenzahl, I. R., Kromer, M., Ohlmann, S. T., et al. 2016, A&A, 592, A57
Sell, P. H., Arur, K., Maccarone, T. J., et al. 2018, MNRAS, 475, L111
Sell, P. H., Maccarone, T. J., Kotak, R., Knigge, C., & Sand, D. J. 2015, MNRAS, 450, 4198
Shahbandeh, M., Sarangi, A., Temim, T., et al. 2023, MNRAS, 523, 6048
Shappee, B. J., Stanek, K. Z., Kochanek, C. S., & Garnavich, P. M. 2017, ApJ, 841, 48
Shaviv, N. J. 2001a, ApJ, 549, 1093
—. 2001b, MNRAS, 326, 126
Shen, K. J., & Bildsten, L. 2007, ApJ, 660, 1444

—. 2009, ApJ, 692, 324
Shen, K. J., Bildsten, L., Kasen, D., & Quataert, E. 2012, ApJ, 748, 35
Shen, K. J., Quataert, E., & Pakmor, R. 2019, ApJ, 887, 180
Shen, K. J., & Schwab, J. 2017, ApJ, 834, 180
Shiode, J. H., & Quataert, E. 2014, ApJ, 780, 96
Shivvers, I., Groh, J. H., Mauerhan, J. C., et al. 2015, ApJ, 806, 213
Shrestha, M., Pearson, J., Wyatt, S., et al. 2024, ApJ, 961, 247
Silverman, J. M., Foley, R. J., Filippenko, A. V., et al. 2012, MNRAS, 425, 1789
Silverman, J. M., Nugent, P. E., Gal-Yam, A., et al. 2013, ApJS, 207, 3
Silverman, J. M., Pickett, S., Wheeler, J. C., et al. 2017, MNRAS, 467, 369
Sim, S. A., Fink, M., Kromer, M., et al. 2012, MNRAS, 420, 3003
Sim, S. A., Röpke, F. K., Hillebrandt, W., et al. 2010, ApJ, 714, L52
Smartt, S. J. 2009, ARA&A, 47, 63
Smartt, S. J., Valenti, S., Fraser, M., et al. 2015, A&A, 579, A40
Smith, K. W., Smartt, S. J., Young, D. R., et al. 2020, PASP, 132, 085002
Smith, M., Sullivan, M., D'Andrea, C. B., et al. 2016, ApJ, 818, L8
Smith, N. 2014, ARA&A, 52, 487
—. 2017, in Handbook of Supernovae, ed. A. W. Alsabti & P. Murdin, 403
Smith, N., & Arnett, W. D. 2014, ApJ, 785, 82
Smith, N., Chornock, R., Silverman, J. M., Filippenko, A. V., & Foley, R. J. 2010, ApJ, 709, 856
Smith, N., & Frew, D. J. 2011, MNRAS, 415, 2009
Smith, N., Hinkle, K. H., & Ryde, N. 2009, AJ, 137, 3558
Smith, N., Humphreys, R. M., Davidson, K., et al. 2001, AJ, 121, 1111
Smith, N., Li, W., Filippenko, A. V., & Chornock, R. 2011a, MNRAS, 412, 1522
Smith, N., & Owocki, S. P. 2006, ApJ, 645, L45
Smith, N., Pearson, J., Sand, D. J., et al. 2023, arXiv e-prints, arXiv:2306.07964
Smith, N., Li, W., Foley, R. J., et al. 2007, ApJ, 666, 1116
Smith, N., Li, W., Miller, A. A., et al. 2011b, ApJ, 732, 63
Smith, N., Mauerhan, J. C., Cenko, S. B., et al. 2015, MNRAS, 449, 1876
Soderberg, A. M., Chevalier, R. A., Kulkarni, S. R., & Frail, D. A. 2006, ApJ, 651, 1005
Soderberg, A. M., Berger, E., Page, K. L., et al. 2008, Nature, 453, 469
Soker, N. 2021, ApJ, 906, 1
Soraisam, M. D., Szalai, T., Van Dyk, S. D., et al. 2023, ApJ, 957, 64
Soumagnac, M. T., Ganot, N., Irani, I., et al. 2020, ApJ, 902, 6
Srivastav, S., Anupama, G. C., & Sahu, D. K. 2014, MNRAS, 445, 1932
Srivastav, S., Chen, T. W., Smartt, S. J., et al. 2024, Transient Name Server AstroNote, 100, 1
Stetson, P. B. 2000, PASP, 112, 925
Stritzinger, M., Valerin, G., Elias-Rosa, N., et al. 2023, Transient Name Server AstroNote, 145, 1
Stritzinger, M. D., Taddia, F., Burns, C. R., et al. 2018, A&A, 609, A135

Stroh, M. C., Terreran, G., Coppejans, D. L., et al. 2021, ApJ, 923, L24
Strotjohann, N. L., Ofek, E. O., Gal-Yam, A., et al. 2021, ApJ, 907, 99
Subrayan, B. M., Milisavljevic, D., Moriya, T. J., et al. 2023, ApJ, 945, 46
Sullivan, M., Kasliwal, M. M., Nugent, P. E., et al. 2011, ApJ, 732, 118
Sundqvist, J. O., & Owocki, S. P. 2013, MNRAS, 428, 1837
Sutherland, P. G., & Wheeler, J. C. 1984, ApJ, 280, 282
Svirski, G., Nakar, E., & Sari, R. 2012, ApJ, 759, 108
Szalai, T., Vinkó, J., Könyves-Tóth, R., et al. 2019, ApJ, 876, 19
Taddia, F., Stritzinger, M. D., Sollerman, J., et al. 2013, A&A, 555, A10
Taggart, K., Rojas-Bravo, C., Foley, R. J., & Angus, C. R. 2021, Transient Name Server Classification Report, 2021-1196, 1
Takei, Y., Tsuna, D., Kuriyama, N., Ko, T., & Shigeyama, T. 2022, ApJ, 929, 177
Tanikawa, A., Sato, Y., Nomoto, K., et al. 2017, ApJ, 839, 81
Tartaglia, L., Pastorello, A., Sullivan, M., et al. 2016, MNRAS, 459, 1039
Tartaglia, L., Sand, D. J., Groh, J. H., et al. 2021, ApJ, 907, 52
Taubenberger, S. 2017, The Extremes of Thermonuclear Supernovae, 317
Teja, R. S., Singh, A., Sahu, D. K., et al. 2022, ApJ, 930, 34
Teja, R. S., Singh, A., Basu, J., et al. 2023, ApJ, 954, L12
Terreran, G., Jerkstrand, A., Benetti, S., et al. 2016, MNRAS, 462, 137
Terreran, G., Jacobson-Galán, W. V., Groh, J. H., et al. 2022, ApJ, 926, 20
Theureau, G., Hanski, M. O., Coudreau, N., Hallet, N., & Martin, J. M. 2007, A&A, 465, 71
Thomas, R. C., Nugent, P. E., & Meza, J. C. 2011, PASP, 123, 237
Timmes, F. X., & Swesty, F. D. 2000, ApJS, 126, 501
Tinyanont, S., Kasliwal, M. M., Krafton, K., et al. 2019, ApJ, 873, 127
Tinyanont, S., Ridden-Harper, R., Foley, R. J., et al. 2022, MNRAS, 512, 2777
Tomita, H., Deng, J., Maeda, K., et al. 2006, ApJ, 644, 400
Tonry, J., Denneau, L., Heinze, A., et al. 2020, Transient Name Server Discovery Report, 2020-2815, 1
Tonry, J., Denneau, L., Weiland, H., et al. 2024, Transient Name Server Discovery Report, 2024-1020, 1
Tonry, J. L., Denneau, L., Heinze, A. N., et al. 2018a, Publications of the Astronomical Society of the Pacific, 130, 064505
—. 2018b, PASP, 130, 064505
Tonry, J. L., Denneau, L., Flewelling, H., et al. 2018c, ApJ, 867, 105
Toonen, S., Perets, H. B., Igoshev, A. P., Michaely, E., & Zenati, Y. 2018, A&A, 619, A53
Townsley, D. M., Miles, B. J., Shen, K. J., & Kasen, D. 2019, arXiv e-prints, arXiv:1903.10960
Tsang, B. T. H., Kasen, D., & Bildsten, L. 2022, ApJ, 936, 28
Tsuna, D., Murase, K., & Moriya, T. J. 2023, arXiv e-prints, arXiv:2301.10667
Uomoto, A. 1986, ApJ, 310, L35
Vacca, W. D., Cushing, M. C., & Rayner, J. T. 2003, PASP, 115, 389

Valenti, S., Benetti, S., Cappellaro, E., et al. 2008a, MNRAS, 383, 1485
Valenti, S., Elias-Rosa, N., Taubenberger, S., et al. 2008b, ApJ, 673, L155
Valenti, S., Yuan, F., Taubenberger, S., et al. 2014a, MNRAS, 437, 1519
Valenti, S., Sand, D., Pastorello, A., et al. 2014b, MNRAS, 438, L101
Van Dyk, S. D., Zheng, W., Maund, J. R., et al. 2019, ApJ, 875, 136
Van Dyk, S. D., Srinivasan, S., Andrews, J. E., et al. 2023, arXiv e-prints, arXiv:2308.14844
Vasylyev, S. S., Yang, Y., Filippenko, A. V., et al. 2023, ApJ, 955, L37
Vaytet, N. M. H., Audit, E., Dubroca, B., & Delahaye, F. 2011, J. Quant. Spec. Radiat. Transf., 112, 1323
Victor, G. A., Raymond, J. C., & Fox, J. L. 1994, ApJ, 435, 864
Villar, V. A., Berger, E., Metzger, B. D., & Guillochon, J. 2017, ApJ, 849, 70
Virtanen, P., Gommers, R., Oliphant, T. E., et al. 2020, Nature Methods, 17, 261
Wade, R. A., & Horne, K. 1988, ApJ, 324, 411
Waldman, R., Sauer, D., Livne, E., et al. 2011, ApJ, 738, 21
Wanajo, S., Müller, B., Janka, H.-T., & Heger, A. 2018, ApJ, 852, 40
Wang, Q., Goel, A., Dessart, L., et al. 2023, arXiv e-prints, arXiv:2305.05015
Waters, C. Z., Magnier, E. A., Price, P. A., et al. 2020, ApJS, 251, 4
Waxman, E., & Katz, B. 2017, in Handbook of Supernovae, ed. A. W. Alsabti & P. Murdin, 967
Weiler, K. W., Panagia, N., Montes, M. J., & Sramek, R. A. 2002, ARA&A, 40, 387
Wellons, S., Soderberg, A. M., & Chevalier, R. A. 2012, ApJ, 752, 17
Wheeler, J. C., Johnson, V., & Clocchiatti, A. 2015, MNRAS, 450, 1295
Wheeler, J. C., Barker, E., Benjamin, R., et al. 1993, ApJ, 417, L71
Wilson, C. D., Scoville, N., Madden, S. C., & Charmandaris, V. 2000, ApJ, 542, 120
Woosley, S. E., & Heger, A. 2015, ApJ, 810, 34
Woosley, S. E., & Kasen, D. 2011, ApJ, 734, 38
Woosley, S. E., Pinto, P. A., & Hartmann, D. 1989, ApJ, 346, 395
Woosley, S. E., Taam, R. E., & Weaver, T. A. 1986, ApJ, 301, 601
Woosley, S. E., Weaver, T. A., & Taam, R. E. 1980, in Texas Workshop on Type I Supernovae, ed. J. C. Wheeler, 96
Wu, S., & Fuller, J. 2021, ApJ, 906, 3
Yamanaka, M., Fujii, M., & Nagayama, T. 2023, arXiv e-prints, arXiv:2306.00263
Yao, Y., De, K., Kasliwal, M. M., et al. 2020, ApJ, 900, 46
Yaron, O., Perley, D. A., Gal-Yam, A., et al. 2017, Nature Physics, 13, 510
Yoon, S.-C., & Cantiello, M. 2010, ApJ, 717, L62
Yoon, S.-C., Dessart, L., & Clocchiatti, A. 2017, ApJ, 840, 10
Yoshida, T., Suwa, Y., Umeda, H., Shibata, M., & Takahashi, K. 2017, MNRAS, 471, 4275
Zackay, B., Ofek, E. O., & Gal-Yam, A. 2016, ApJ, 830, 27
Zenati, Y., Bobrick, A., & Perets, H. B. 2020, MNRAS, 493, 3956
Zenati, Y., Perets, H. B., Dessart, L., et al. 2023, ApJ, 944, 22
Zenati, Y., Perets, H. B., & Toonen, S. 2019a, MNRAS, 486, 1805
Zenati, Y., Toonen, S., & Perets, H. B. 2019b, MNRAS, 482, 1135

Zhai, Q., Li, L., Zhang, J., & Wang, X. 2024, Transient Name Server Classification Report, 2024-1031, 1
Zhang, J., Wang, X., Mazzali, P. A., et al. 2014, ApJ, 797, 5
Zhang, J., Wang, X., József, V., et al. 2020, MNRAS, 498, 84
Zhang, J., Li, C. K., Cheng, H. Q., et al. 2024, The Astronomer's Telegram, 16588, 1
Zhang, K., Wang, X., Zhang, J., et al. 2016, ApJ, 820, 67
Zhang, T., Wang, X., Zhou, X., et al. 2004, AJ, 128, 1857
Zimmerman, E. A., Irani, I., Chen, P., et al. 2024, Nature, 627, 759
Zwart, J. T. L., Barker, R. W., Biddulph, P., et al. 2008, MNRAS, 391, 1545